9-8-2015 12:00 AM

Behaviour of Helical Pile connectors for New Foundations

Muhammad Ahmad Muhammad Diab
The University of Western Ontario

Supervisor
Dr. M. Hesham El Naggar
The University of Western Ontario

BEHAVIOUR OF HELICAL PILE CONNECTORS FOR NEW FOUNDATIONS

(Thesis format: Integrated-Article)

by

Muhammad Ahmad Muhammad <u>Diab</u>

Graduate Program in Engineering Science
Department of Civil and Environmental Engineering

A thesis submitted in partial fulfillment
of the requirements for the degree of
Doctor of Philosophy

The School of Graduate and Postdoctoral Studies
The University of Western Ontario
London, Ontario, Canada

ABSTRACT

Despite the wide application of the connections between slender pile types, which end with a mono steel bar at the ground level (e.g. helical piles and micro piles), and new reinforced concrete foundations with limited width (e.g. RC grade beams) in the piling industry in North America, neither a clear understanding of the connections' behaviour nor a specific design criteria for their implementation is presented.

The main goal of this research was to clearly understand the behaviour of these connections and their failure mechanism under monotonic and cyclic loadings. The research methodology involved conducting experimental tests on 33 full-scale pile-foundation connections subjected to tension, compression, and shear loadings. The experimental results were used to calibrate a three-dimensional nonlinear finite element model that accurately simulated the structural behaviour and captured the possible failure modes of these connections. Based on the findings from the experimental and numerical investigations, analytical equations were developed to determine the connection capacity.

Both the experimental and the numerical investigations confirmed that it is unsafe to ignore the connection capacity in the foundation design considering only the grade beam capacity. It was shown that the connection behaviour under tension and compression loadings can be represented by the behaviour of the reinforced concrete beams subjected to indirect shear loading, while the connection behaviour under shear loading can be represented by the behaviour of cast-in-place headed anchors subjected to shear loading. The connection behaviour was mainly affected by the concrete compressive strength, the

ii

pile embedment depth, the beam's reinforcement, the pile cap configurations, and some other variables depending on the type of loading. Cyclic compression loading had a limited effect on the connection behaviour, while alternating cyclic shear loading had a major effect on the connection behaviour.

The developed connection design equations took into consideration the main factors affecting the connection behaviour under different cases of loading including cyclic loading and they were consistent with the recorded results from the experimental and numerical investigations.

Finally, the research objectives were achieved by providing a design aid and design precautions for helical pile-RC grade beam connections design.

Key words: Helical pile, Grade beam, New reinforced concrete foundations, pile cap, New construction bracket, pile connectors, pile-foundation connection, Tension, Compression, Shear, Monotonic and cyclic loading, Load transfer mechanism, breakout, embedment depth, Numerical modelling, indirect shear loading, Micropile, Design equations.

CO-AUTHORSHIP STATEMENT

All the experimental testing, numerical modeling, interpretation of results and writing the draft and the final thesis were carried out by the candidate himself, under the supervision of Dr. M. Hesham El Naggar. The supervisor's contribution consisted of providing advice throughout the research program and reviewing the draft, the final thesis, and the publications resulting from this research.

ACKNOWLEDGMENTS

TABLE OF CONTENTS

LIST OF TABLES

LIST OF FIGURES

xxiii

xxv

LIST OF APPENDICES

LIST OF ABBREVATIONS, SYMBOLS, NOMENCLATURE

a — Shear Span

a^* — The effective shear Span (the distance from the pile caps' plate end to the support in the studied case)

$\left(a/d\right)$ — Shear span to depth ratio

A_{anchor} — The anchor reinforcement contained in the pile cap's plate width

a_g — Specified nominal maximum size of coarse aggregate

A_s — The main longitudinal steel cross section area

A_{se} — Effective cross-sectional area of anchor; equal to the least cross-section area of the pile shaft

A_v — Area of shear reinforcement within a distance s

A_{vc} — Projected area of the failure surface as shown in Figure 10-3 for the different applicable cases

A_{vo} — Projected area for a single anchor in a deep member

b — Specimen width

BED — Distance from back row of studs to front edge

b_{plate} — Pile cap's plate width

b_{pile} — Pile shaft diameter or width

C_c — The cracked concrete contribution to the connection ultimate load under compression loading

C_{Cr} — The connection breakout cracking load under compression loading

C_s — The transverse reinforcement contribution to the connection ultimate load under compression loading

c' — Concrete cover

C_{ev3} Coefficient for eccentric shear force

C_{h3} Coefficient for member thickness

$C_{u\,Actual}$ The actual connection ultimate capacity under compression loading

$C_{u_{conc.}}$ The limit state of concrete ultimate capacity under compression loading

$C_{u\,Design}$ The recommended connection design load under compression loading

$Cu_{reinf.}$ The limit state of transverse reinforcement ultimate capacity under compression loading

$Cu_{support}$ The recommended crushing at supports limit state for (a/d)<1

C_{vcr} Coefficient for cracking in a member loaded in shear

C_{x3} Coefficient for overall X spacing of a connection with two or more rows

d   Specimen depth

da Anchor diameter

d_{bolt} The highest bolt depth

d_{emb} The pile embedment depth in the reinforced concrete beam

d_{rem} The remaining beam depth; $d_{rem} = h - d_{emb} - t_{plate}$

d_v The effective shear depth, taken as the greater of 0.9d or 0.72h

e Load eccentricity from the load location to the concrete surface

E_s Modulus of elasticity of non-prestressed reinforcement

fc' Specified compressive strength of concrete

f_{cc} Cubic compressive strength of concrete

f_u Transverse reinforcement ultimate stress

f_{ult} Specified tensile strength of anchor steel or pile shaft steel

f_v Transverse reinforcement stress accompanying with the cracked concrete contribution, C_c

f_{yp}	The pile shaft yield stress
h	Specimen height
L	Specimen Span
l	The load-bearing length of the anchor for shear
$M_{concrete}$	Moment sustained by the concrete due to the induced bearing stresses
M_f	Factored applied moment
M_{rsteel}	Anchor maximum moment capacity due to flexural at its weakest point
n	Number of anchors or pile shafts involved
P_f	The pile shaft friction capacity
R	resistance modification factor
r_p	Pile friction ratio
s	Maximum centre-to-centre spacing of transverse reinforcement
S_p	The pile shaft's section modulus at the critical section
s_z	The crack spacing parameter dependent on crack control characteristics of longitudinal Reinforcement
s_{ze}	The equivalent value of sz that allows for influence of aggregate size
T_c	The cracked concrete contribution to the connection ultimate load under tension loading
T_{Cr}	The connection breakout cracking load under tension loading
t_{plate}	Pile cap's plate thickness
T_s	The transverse reinforcement contribution to the connection ultimate load under tension loading
$T_{u\,Actual}$	The actual connection ultimate capacity under tension loading
$T_{u_{conc.}}$	The limit state of the concrete ultimate capacity under tension loading

$T_{u\,Design}$ The recommended connection design load under tension loading

$Tu_{reinf.}$ The limit state of the transverse reinforcement ultimate capacity under tension loading

$Tu_{support}$ The recommended crushing at supports limit state for (a/d)<1

v_c Factored shear stress resistance provided by the concrete

V_C Shear resistance attributed to the concrete

V_{Cr} The diagonal tension cracking shear strength

V_{br} Factored concrete breakout resistance in shear in cracked concrete

V_{cbr} Factored concrete breakout resistance in shear of a group of anchors or helical piles

$V_{crushing}$ The concrete crushing in front of the pile shaft limit state

V_{co3} Concrete breakout strength for a single stud or pile connection unaffected by connection or member geometry

V_f Factored applied shear load

V_r Factored shear resistance for a single or multiple stud or pile connections, accounting for member and connection geometry

V_s Shear resistance provided by shear reinforcement

V_{sr} Factored resistance in shear of a single anchor or a single pile shaft

$V_{sr,mu}$ The anchor/ pile maximum steel shear capacity due to induced flexural stresses

β Factor accounting for shear resistance of cracked concrete

θ Angle of inclination of diagonal compressive stresses to the longitudinal axis of the member

λ Modification factor reflecting the reduced mechanical properties of lightweight concrete

μ The average coefficient of friction between concrete and steel; approximately=0.47 as reported by Baltay et al., (1990)

ρ Ratio of non-prestressed tension reinforcement, equal to As/bd

$\emptyset_c$ Resistance factor for concrete

$\emptyset_s$ Resistance factor for non-prestressed reinforcing bars

ε_x Longitudinal strain at mid-depth of the member due to factored loads

ε_z Longitudinal strain at mid-depth of the breakout cone due to factored loads

$\psi_{c,v}$ The modification factor for cracked concrete

$\psi_{ed,v}$ The modification factor for edge

$\psi_{h,v}$ The modification factor for anchors/ piles located in a concrete member where the concrete element height (ha) < 1.5ca1

$\psi_{c,v}$ The modification factor for cracked concrete

INTRODUCTION

1.1 Helical Piles

Helical piles are a deep foundation system that can be used to support different light and moderately loaded structures such as low-rise buildings, medium-rise buildings, pipelines, and transmission towers. They can be used for both underpinning of deficient foundations of existing buildings and for supporting new foundations. This research is focussed on the connection of segmented helical (screw) pile (HSP) with a relatively small galvanized central square shaft (SS) of only 45 mm x 45 mm dimensions to concrete foundations. This type of helical piles is widely used in practice, and it enjoys growing popularity. In addition, the industry is continually pursuing further development to use it for supporting higher loads, to overcome its drawbacks, and to improve its installation techniques.

The load carrying capacity of slender shaft helical piles has been the focus of several studies including experimental testing and numerical modeling of the pile performance under monotonic and cyclic loading. These studies were as early as (Clemence & Smithling, 1983). Recently, Vickars & Clemence (2000), Abdelghany and El Naggar (2010) and El Sharnouby & El Naggar (2012) studied the performance of steel fibre-reinforced helical pulldown micropiles (RHPM), and fibre-reinforced polymer-steel fibre-reinforced pulldown micropiles (FRP-RHPM). In these innovative applications, the helical pile is installed with a special grout column surrounding the pile central shaft

along its extensions, which enhance its performance and increase its capacity under axial and lateral monotonic and cyclic loading conditions. These researchers concluded that the grout shaft significantly improves the helical pile axial performance under the monotonic and cyclic loading. To take advantage of this increase of the slender shaft helical pile capacity, it is important to properly design the pile-foundation connection in order to transfer the increased load.

1.2 New reinforced concrete foundations and the new construction bracket "pile cap"

"New foundations" refers to the installation of helical piles and tiebacks for new structures as shown in Figure 1-1. Helical piles have been used with different types of new reinforced concrete foundations such as grade beam foundations, column bases, or raft foundations.
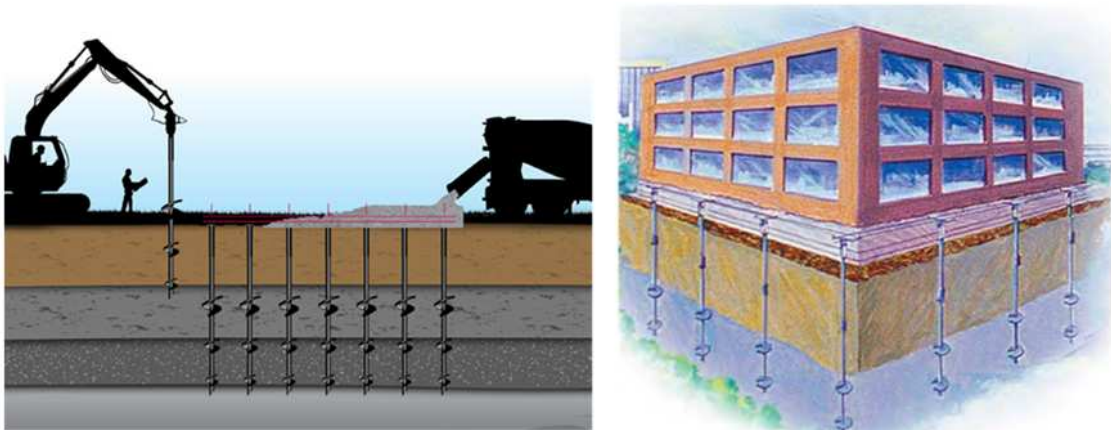
Figure 1- 1 Using helical pile in the new construction foundations (Perko, H. A. , 2009)

Typically, new construction steel brackets "pile caps" are used to transfer loads from the new reinforced concrete foundation to the helical piles in order to decrease the bearing stresses induced from the small pile shaft cross section under compression loading. This

bracket, shown in Figure 1-2, usually consists of a square plate with adequate thickness welded to a coupling tube (152 mm long) with adequate inner diameter to insert the pile in it, and sometimes the square plate is welded to the pile itself directly.

Figure 1- 2 The commonly used pile cap (i.e. New construction bracket) and its application in different types of the new reinforced concrete foundations (Perko, H. A. , 2009).

Pack (2009) reported experimental tests that were conducted to investigate the ultimate bearing capacity of the concrete in front of the pile cap's plate and it was found that it was compatible with the International Building Code (2003). Thus, the new foundations with the pile cap connection can be used and should be designed for shear and flexural as a regular reinforced concrete foundation. The only additional design step recommended is to account for the interaction between the new construction bracket and the reinforced concrete foundation by checking the bearing strength of the concrete in front of the new construction bracket. This can be true and accurate for helical piles supporting a column base. However, the failure mechanism for a helical pile connection attached to a grade

3

beam between two columns or carrying walls is different, and the proposed design method should be verified for these conditions. Furthermore, most of the new reinforced concrete foundations used with helical piles are grade beams with limited width, which may affect the connection capacity. Therefore, experimental evidence is necessary to confirm the connection capacity and its ability to transfer the applied loads successfully without cracking.

1.3 Research Objectives

The main objectives of this research are twofold: first, to fully understand the behaviour of the studied connection and its failure mechanisms under monotonic and cyclic loadings; second, to develop practical and reliable equations that can express the behaviour and state the capacity of the used connection between helical piles and new reinforced concrete grade beams foundation. In order to achieve these objectives, the following specific objectives are articulated:

1. Conduct an experimental parametric study in order to investigate the performance of connections between helical piles and grade beams loaded monotonically in compression, tension, and shear.

2. Conduct an experimental parametric study in order to investigate the performance of connections between helical piles and grade beams under compression and shear cyclic loadings.

3. Develop three dimensional non-linear finite element representative models that can be used to predict the overall behaviour of the connection between helical

piles and grade beams with the aid of LS-DYNA software and extend the studied variables in the experimental study.

4. Propose design equations that can reliably predict the studied connection capacity under tension, compression, and shear loading and/or indicate the required design precautions required to have the best connection performance.

1.4 Thesis Outline

This thesis has been produced in accordance with the guidelines of the School of Graduate and Postdoctoral Studies. The thesis is organized as follows.

Chapter 2 provides a brief review of the previous studies conducted on different types of helical piles and the new construction bracket used in practise. In addition, it reviews investigations on reinforced concrete elements that have similar failure mechanisms and similar load transfer mechanisms, which can be used to correlate the behaviour of the connection under investigation.

In Chapter 3, the behaviour of the helical pile connectors for new foundation is investigated experimentally under monotonic tension loading using full-scale testing.

Chapter 4 presents the development and verification of a nonlinear finite element model of the studied connection under monotonic tension loading. In addition, this model was used to conduct a comprehensive parametric study to investigate additional connection configurations that complement the results of cases covered in the experimental study.

Chapter 5 presents the development of the connection capacity equations and a design aid for the studied connections under monotonic tension loading using the results obtained from both the experimental and analytical studies.

Chapter 6 investigates the connection behaviour under monotonic and cyclic compression loading through experimental load testing of full-scale connection-foundation models.

Chapter 7 describes the development and verification of a nonlinear finite element model of the studied connection under monotonic compression loading. Moreover, a comprehensive parametric study was conducted using the verified finite element model to investigate additional connection configurations that complement the results of the experimentally studied variables.

In Chapter 8, equations were developed in order to calculate the connection capacity and a design aid was established based on the results obtained from both experimental and analytical studies for the studied connections when subjected to monotonic or cyclic compression loading.

In Chapter 9, the helical pile connectors for new foundation was investigated experimentally under monotonic and cyclic shear loading using full-scale testing. The connection behaviour along with its different failure mechanisms is indicated.

In Chapter 10, equations were developed in order to calculate the connection capacity and a design aid was established based on the results obtained from both experimental and

analytical studies for the studied connections when subjected to monotonic or cyclic shear loading.

Finally, Chapter 11 provides a summary of the research work, conclusions, and recommendations for future research.

1.5 References

Abdelghany, Y., and El Naggar, M.H., 2010. Full-scale experimental investigations and numerical analysis of different innovative instrumented helical screw piles under axial and lateral monotonic and cyclic loadings. *Environmental Engineering*, pp.319–329.

Clemence & Smithling, A.P., 1983. Dynamic uplift capacity of helical anchors in sand. *Civil Eng for Practicing and Design Engineers*, 2.

IBC, 2003. International building code. *International Code Council, Inc.*

Pack, J., 2009. *Design and Inspection Guide for Helical Piles and Helical Tension Anchors*, Denver, Colorado, U.S.A.

El Sharnouby, M.M. & El Naggar, M.H., 2012. Axial monotonic and cyclic performance of fibre-reinforced polymer (FRP) - steel fibre-reinforced helical pulldown micropiles (FRP-RHPM). *Canadian Geotechnical Journal*, 49(October), pp.1378–1392.

Perko, H. A. , 2009. Helical piles: a practical guide to design and installation. John Wiley & Sons.

Vickars, R.A. & Clemence, S.P., 2000. Performance of helical piles with grouted shafts. In *New Technological and Design Developments in Deep Foundations. Proceedings of Sessions of Geo-Denver 2000.*

LITERATURE REVIEW

2.1 Introduction

When helical piles are used with new reinforced concrete foundations, a new construction bracket (i.e. pile cap) is used to connect the steel pile to the reinforced concrete member. The main purpose of this pile cap is to transfer vertical tension or compression loads from the foundation to the piles through the bearing stresses induced between the pile cap's plate and the concrete beneath or above of it, while the horizontal shear forces are expected to transfer through the bearing in front of the embedded part of the pile shaft inside the reinforced concrete member.

Due to the lack of understanding of the behaviour of the connection between the pile and the reinforced concrete grade beam, designers design the grade beam for flexure and shear, and check the bearing capacity under the pile cap; however, this connection may be subjected to a breakout failure similar to the failure mechanism of the headed anchors in concrete subjected to tension or shear loading, or the failure mechanism of the reinforced concrete beams subjected to indirect shear loading when the connection is subjected to tension or compression loading. Also, the connection behaviour may be similar to the punching shear behaviour of the reinforced concrete foundations when wide grade beams or raft foundations are used.

Up to the author's knowledge, there is no previous research that investigated the connection between the helical piles and new foundation represented by the grade beams. The only directly related study was conducted by Pack (2009) to investigate the bearing capacity of the concrete in front of the new construction bracket (i.e. the pile cap) and it was conducted on concrete cylinders not on full scale specimens. Thus, the literature review covers different subjects that can be relevant to the studied connection behaviour in order to help understand the different expected failure and load transfer mechanisms that can occur for the connection when subjected to tension, compression, and shear loadings. The extensive review of the available literature related to the reinforced concrete behaviour revealed that the behaviour of the studied connection in the grade beam may be similar to the behaviour of the cast-in-place headed anchors under tension loading, the cast-in-place headed anchors under shear loading, the shear strength of the reinforced concrete beams, the shear strength of the reinforced concrete beams under indirect loading, and the punching shear strength of the reinforced concrete foundations.

A brief review of the different types of helical piles, their installation technique and load transfer mechanism will be presented, and the installation technique of the new foundation bracket used in practise will be demonstrated.

2.2 Helical piles

Helical piles are deep foundation systems used extensively in North America for light and medium weight structures. It is widely used because of its great advantages related to small equipment required to install the piles by mechanical equipment, which cause minimal noise and vibration. Also, this equipment can facilitate pile installation in limited

9

access areas. Furthermore, by monitoring the installation torque, onsite quality control of the helical pile and onsite prediction of the helical pile capacity can be achieved. As shown in Figure 2-1, the pile considered in this research is a segmented helical (screw) pile (HSP), which consists of relatively small galvanized central square shaft (SS). Its cross-sectional dimension is 45 mm x 45 mm and it can be fitted with one or more helices. The lead section contains the helices, which provide the bearing capacity of the helical pile, while the extensions are added and connected by bolts to install the helical pile to the required bearing layer. In this research, a segment of the extension pile shaft was used as part of the connection investigated.

In order to increase the helical pile capacity and enhance its performance, several helical pile modifications were introduced. Vickars & Clemence (2000) presented the Helical Pulldown® Micropile (HPM), shown in Figure 2-2, which has a grout column surrounding the pile shaft to increase the axial capacity of the helical pile. Also, the HPM was modified by adding steel fiber reinforcement to the grout mix to produce the steel fibre-reinforced helical pulldown micropile (RHPM) to enhance the helical pile ductility and ability to dissipate energy under cyclic loading conditions (Elsharnouby and El Naggar, 2012). Recently, to enhance the corrosion and the environmental resistance of piles, FRP tubes have been introduced (Sakr et al., 2004) as piling option. It employs an FRP tube surrounding self-consolidating concrete (SCC) as shown in Figure 2-2 (b). The FRP-SCC piles and steel piles were found to provide comparable performance for axial loads but the lateral capacity of the FRP-SCC piles was less than that of the steel piles.
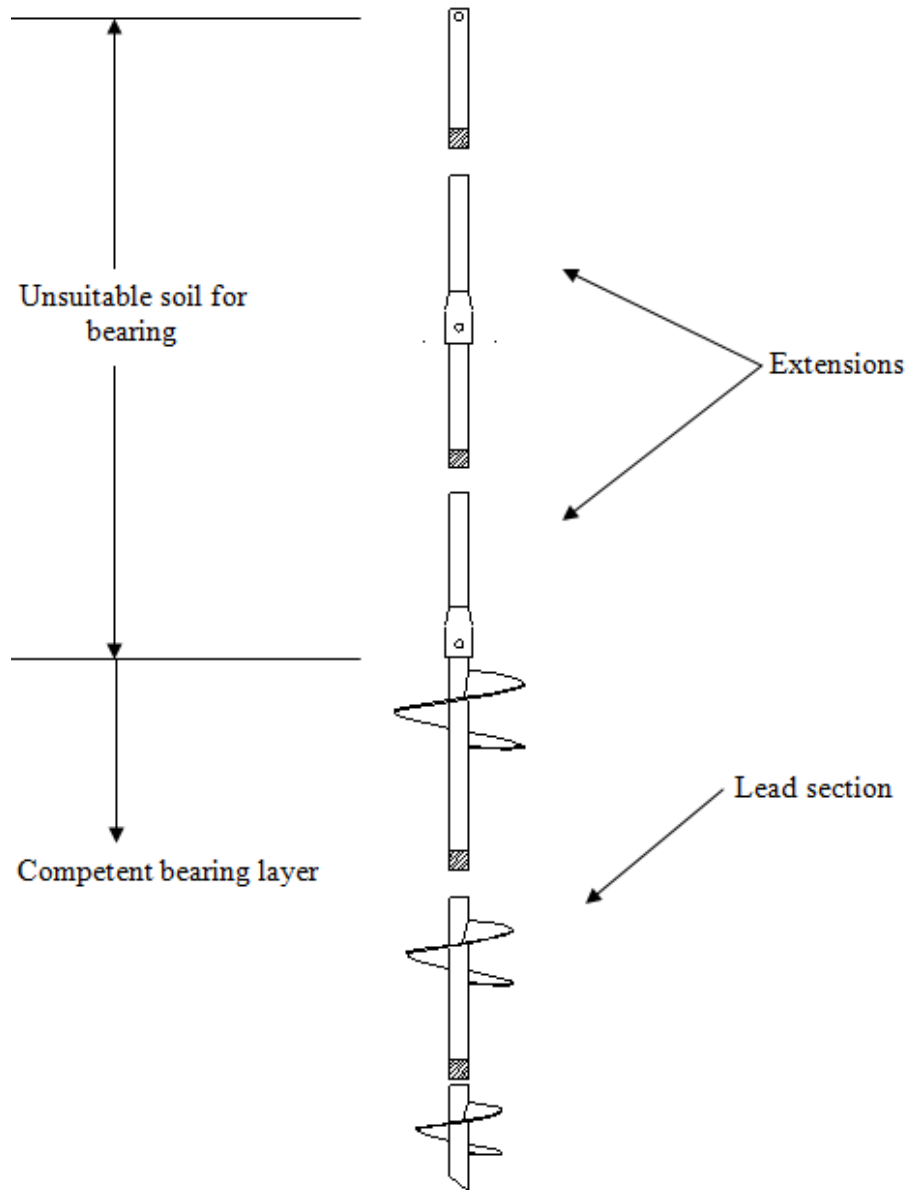
Figure 2- 1 Typical helical pile assembly; lead section and two extensions. Modifed from El Sharnouby, 2012
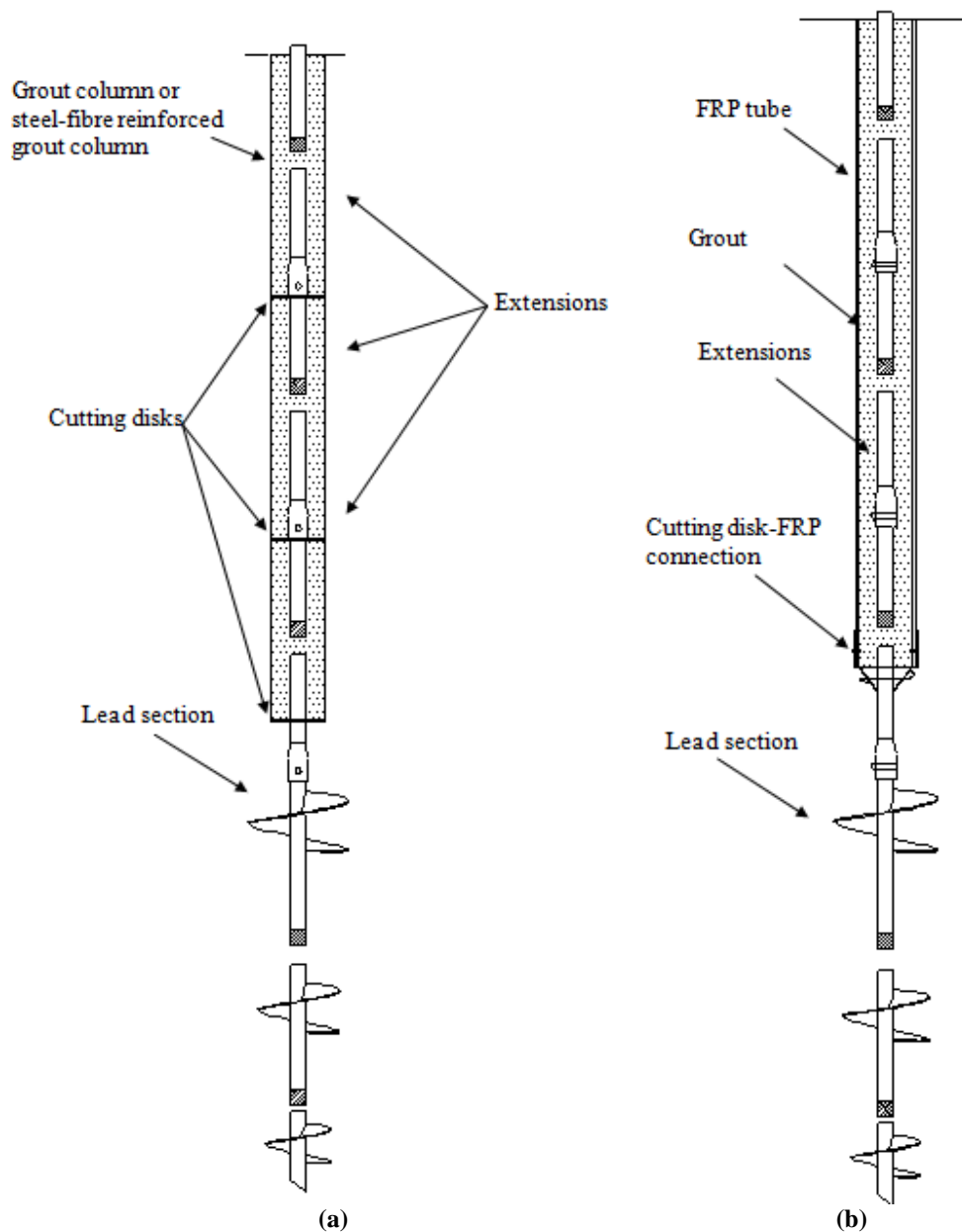
Figure 2- 2 Typical schematic of (a) HPM or RHPM, (b) FRP-SCC helical pile. Modifed from El Sharnouby and El Naggar (2012)

The load transfer mechanism between the different helical pile types and the soil can be demonstrated by one of two methods. The first method, denoted as individual helix

bearing method, assumes that the pile capacity is the summation of the bearing capacity of each helical plate. The second method, denoted as the cylinder shear method, calculates the friction capacity between a cylinder of soil mass enclosed by the highest and lowest helical piles and add it to the bearing capacity of the lowest helix under compression loading or the highest helix under tension loading.

2.3 New construction bracket (pile cap)

The new construction pile cap investigated herein is intended for use with the type Square Shaft (SS) helical piles in the connection to new reinforced concrete foundations with different configurations. The new construction bracket consists of one bearing plate welded to a steel tube sleeve to form the pile cap shown in Figure 2-3. For transfer of compression forces only, the pile cap shown in Figure 2-3 (a) is recommended and no bolted connection between the helical pile and the pile shaft is needed. If uplift is expected with the compression loading or if the pile shaft will be subjected to tension loading, holes in the steel tube should be provided to connect the pile cap to the pile shaft by one or two bolts as shown in Figures 2-3 (b) and (c). The pile cap in Figure 2-3 (d) is only used when equally high compression and uplift capacities are required from the helical pile. Moreover, if welding on site with appropriate quality is available, direct welding between the bearing plate and the pile shaft can be provided when the helical pile will be subjected to tension loading.
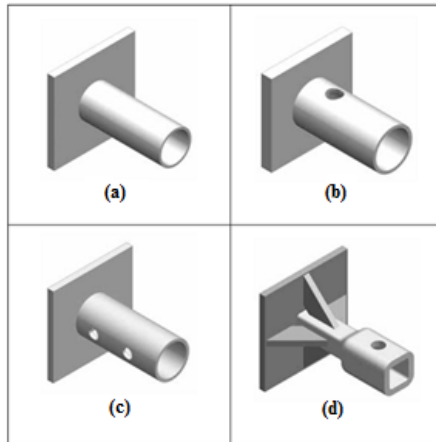
Figure 2- 3 Different commonly used new construction bracket in the new foundations construction (Hubbell Power Systems Inc., 2014)

The pile cap's plate size can change according to the application as this pile cap can be used in grade beams, spread footings, raft slabs, column bases, and different reinforced concrete pile caps.

The only experimental testing on these new construction brackets was indicated by Pack (2009). He reported on experimental tests to investigate the compressive strength of the connection between helical piles and plain concrete of fc'=21 MPa using a similar pile cap. These tests were conducted on the connection subjected to direct compression loading simulating the connection below a column base. The ultimate bearing stress was reported to be 9.3 MPa, and it was compatible with the International Building Code (2003). Also, a recent design manual (Hubbell Power Systems Inc., 2014) and report (Hubbell Power Systems Inc., 2016) provided tables of the proposed new construction pile caps under compression and tension loadings.

2.4 Shear behaviour of the reinforced concrete beams (one way shear)

Because of the limited width of the grade beam, a failure mechanism may occur due to shear failure at the connection position. Thus, it is important to understand the shear behaviour failure mechanism and its associated load transfer mechanism.

2.4.1   Importance of understanding shear behaviour

Mirza & MacGregor (1982) stated "No completely satisfactory mechanical model exists for predicting shear strength". Since then, significant research efforts have been dedicated to develop models and equations that can explain the shear behaviour in reinforced concrete (RC) beams. Different models currently exist, but they do not yield the same results for the same studied beams. Furthermore, because of the shear failure of RC beams is brittle, in contrast with their flexural failure if under reinforced section was used, most designers prefer to have a flexural failure mechanism before a shear failure mechanism can take place. Also, to avoid the brittle failure of the concrete beams, at least the minimum shear reinforcement should be provided to increase the shear strength of the concrete; however, shear reinforcement contributes to the shear capacity only if the diagonal shear cracks cross it.

2.4.2   Factors affecting the shear strength of the RC beam

MacGregor (1992) indicated that when no transverse reinforcement (i.e. shear reinforcement) is used, the ratio between the shear span to the effective depth (i.e. a/d ratio), the longitudinal reinforcement ratio, the presence of axial force, and the concrete tensile strength are the main factors that affect the concrete shear strength. Moreover, the size effect was found to affect the shear strength of the beams without stirrups as

15

indicated by Kani (1967), who concluded that the shear strength of the beam decreases with the beam depth increase. Moreover, Collins & Kuchma (1999) reported that increasing the course aggregate size increases the aggregate interlock contribution to the beam shear capacity. Joint ASCE-ACI Task Committee 426 (1973) indicated that the main advantage of providing shear reinforcement is to restrain the growth of inclined cracking and to increase ductility. Also, size effect of the beam with transverse reinforcement was found to be "small but nevertheless appreciable" (Bazant & Sun, 1987).

2.4.3 Classification of RC beams according to shear span/depth ratio (a/d)

The shear span is the distance from the applied load to the supports. The ratio between the shear span to the beam depth was found to have a remarkable effect on the beam behaviour, and a change in (a/d) may cause a total change in the beam failure mechanism (Kani, 1967). Thus, beams are classified as deep, short, and slender beams using (a/d) ratio and depending on the different observed behaviours. Kani (1967) identified "the valley of shear" shown in Figure 2-4. From Figure 2-4 and according to MacGregor (1992), the beam is considered as deep beam when (a/d)≤1.0, where cracking extends between the applied load and the supports, the shear is resisted by the arch action as shown in Figure 2-5. Also, when 1.0<(a/d)<2.5 the beam is considered as short beam and part of the loads are transferred by the arch action as a transition from the arch action failure to the beam-type failure. The failure mechanism of this type is either by shear-tension failure or shear compression failure after a diagonal crack formation as shown in Figure 2-6. When 2.5<(a/d)<6.0, the beam is considered slender beam and it fails just

after the diagonal cracks formation if no shear reinforcement was provided. Finally, if (a/d)>6.0, inclined cracks do not form and only flexural cracks develop causing flexural failure. Thus, both deep beams and short beams can sustain more shear loading than that of slender beams and beams failing in flexure.
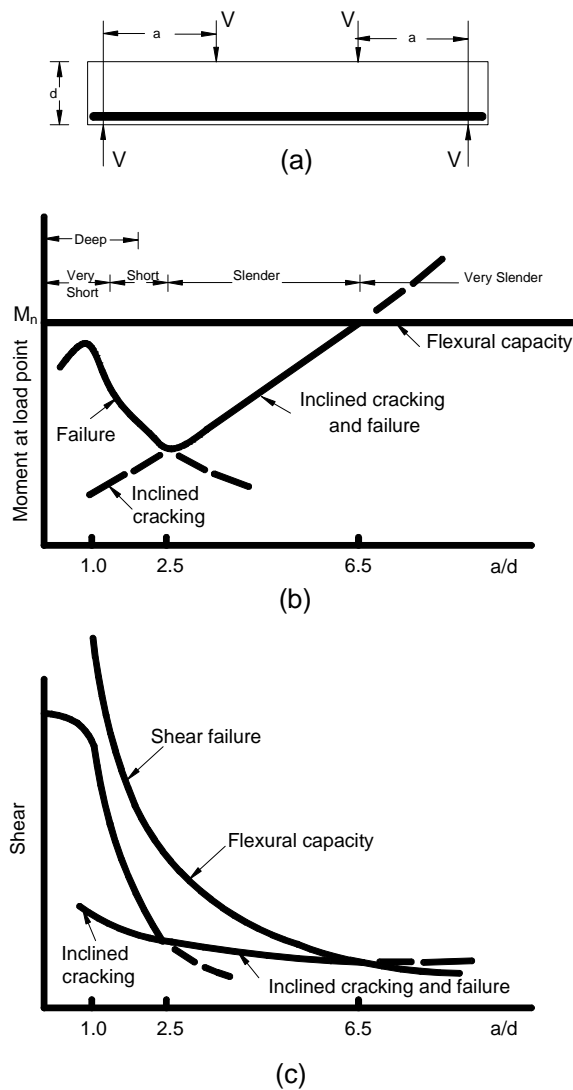
Figure 2- 4 The effect of a/d ratio on the shear strenth of beams without stirrups indicated by Kani (1967): (a) the loaded beam; (b) moments at cracking and failure and the valley of shear; and (c) shear at cracking and failure.
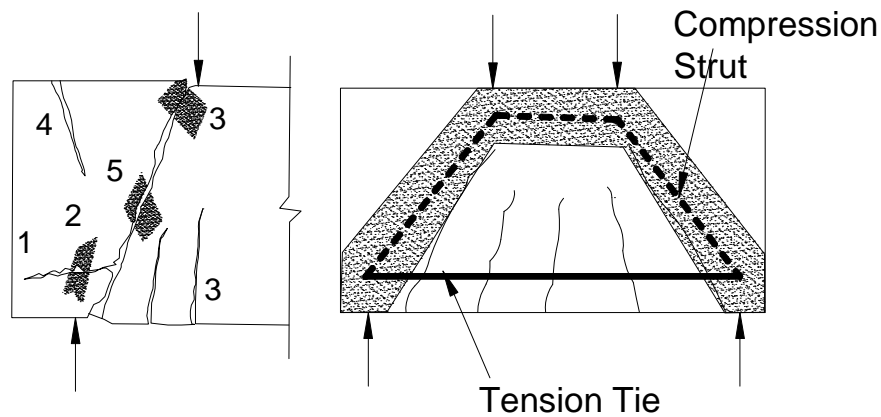
Figure 2- 5 The different modes of failures recorded for deep beams with (a/d) from 0.5 to 2. Modified from Joint ASCE-ACI Task Committee 426, 1973. The types of failure are: 1-Anchorage failure; 2- Bearing failure; 3- flexural failure; and 4,5-failure of compression strut.
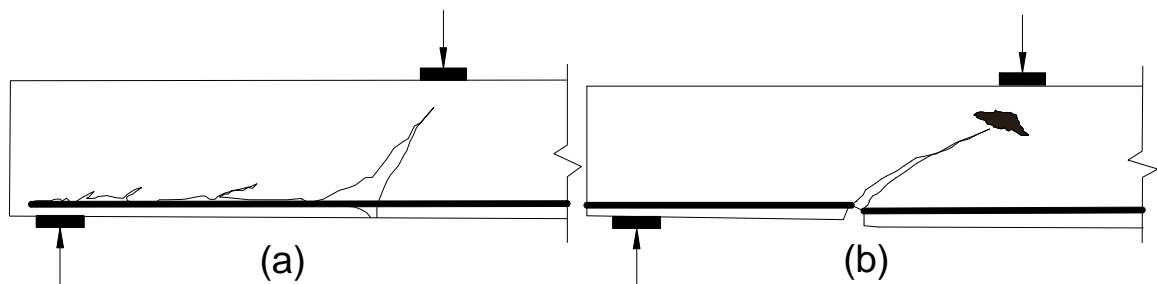
Figure 2- 6 The different modes of failures recorded for short beams with (a/d) from 1.5 to 2.5. Modified from Joint ASCE-ACI Task Committee 426, 1973. (a) shear-tension failure; and (b) shear compression failure.

2.4.4 Inclined shear cracking

Shear failure occurs only after the formation of inclined shear cracking. Two main types of cracking were observed in the RC beams failing in shear. The first type: the web shear cracks, which form when the principal tensile stress is equal to the concrete tensile strength as shown in Figure 2-7. These cracks are not regularly observed in the rectangular RC beams because the flexural cracks occur first, then they bend due to shear causing the second crack type named flexural shear crack shown in Figure 2-7.
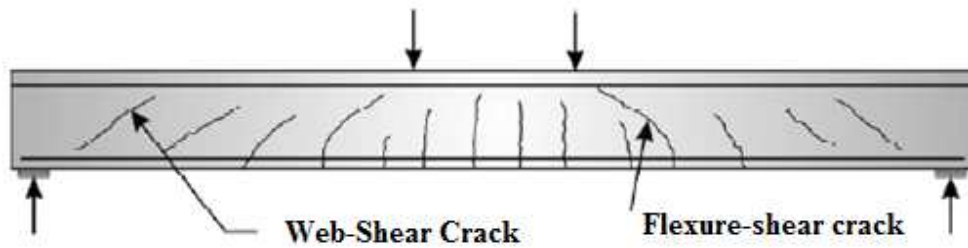
Figure 2- 7 The inclined shear cracking presenting the web shear crack and the Flexural shear crack

2.4.5 Shear transfer mechanism of RC beams after inclined crack formation

From previous studies, the inclined crack form and shear can transfer through some basic actions as shown in Figure 2-8. These basic actions are: (1) the shear stresses in the uncracked concrete (V_{cz}), (2) the interface shear transfer (V_{ca}) (i.e. aggregate interlock), (3) the residual tensile stresses in concrete (V_{rt}), (4) the arch action in deep and short beams, (5) the dowel action of the longitudinal reinforcement (V_d), (6) the vertical component of prestressing steel if existed (V_p), and (7) the shear reinforcement contribution if existed (V_s). These actions are discussed below from the literature for more understanding.
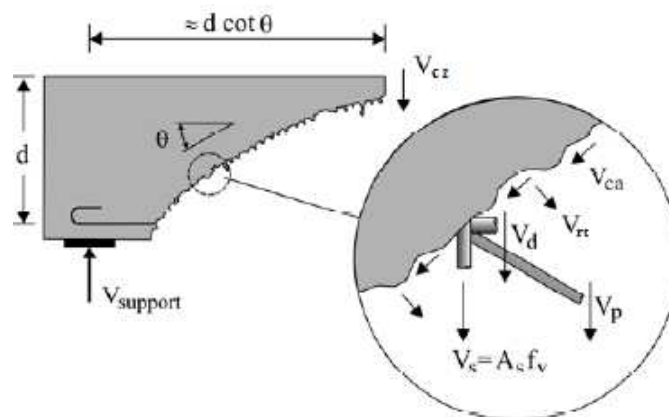
Figure 2- 8 Shear resistance Mechanism. Modified from NCHRP Report 549, 2005

2.4.5.1   The uncracked compression zone contribution to RC beam shear strength

Failure occurs when the inclined shear crack penetrates the compression zone or the compression zone crushes due to the high compressive shear stresses on it. It was found that the deeper the compression zone the higher the RC beam capacity. (Bresler and Pister (1958) and Zwoyer and Siess (1954) concluded that the compression zone carries all the RC beam shear load, while Reineck (1991) reported that the compression zone cannot contribute more than 30% of the RC beam shear strength. Recently, many researchers considered the failure mechanism of the compression zone to evaluate its shear strength from the interaction between the normal stresses induced by flexural and the shear stresses (e.g. Choi et al., 2007; and Zararis & Papadakis, 2001).

2.4.5.2   The interface shear transfer (i.e. aggregate interlock)

According to Reineck (1991), friction between the two cracked surfaces exists due to the roughness of the cracked surface and the existence of the aggregates that prevent the slippage. It was found that the beam shear strength increases with the maximum aggregate size increase and the crack width reduction. On the other hand, Zararis & Papadakis (2001) indicated that the existence of the compression zone is the main reason for slippage prevention and there is no contribution from either the aggregate interlock nor the longitudinal reinforcement dowel action.

2.4.5.3   The residual tensile stresses in concrete (i.e crack-bridging stresses in concrete)

Gopalaratnam & Shah (1985) conducted experimental testing to capture the post beak behaviour of the concrete after cracking. They concluded that cracked concrete can resist tension and the larger the crack width the less the tensile force it can sustain, which means that there is contribution from the tensile resistance of the cracked concrete. Bažant (1997) stated that even if the cracks are cohesive cracks capable of transmitting crack-bridging tensile stresses, the crack-bridging stresses are much less than the concrete tensile strength and its contribution to the RC beam shear capacity is negligible.

2.4.5.4   The arch action

Arch action is mainly effective when small (a/d) ratio exists. In order to consider the arch action contribution to the beam shear capacity, the strut and tie model which was first discussed by Mörsch (1908) and Drucker (1960) has been used by many researchers (e.g. Marti, 1985).

2.4.5.5   The longitudinal reinforcement dowel action

Watstein & Mathey (1958) conducted an experimental study on 9 RC beams with stirrups. They concluded that the shear carried by the longitudinal reinforcement by dowel action ranged from 38% to 75% when the load was from 42% to 46% of the maximum shear capacity. Then, the dowel action decreases as the shear crack width increases until it is equal to zero at failure. Acharya (1965) confirmed that it is of a great importance to consider the dowel action contribution to the shear strength as the longitudinal reinforcement can change the beam failure mechanism.

2.4.5.6   The vertical component of prestressing steel or the axial force in general

It is widely accepted that the axial compression force due to applied normal loads or prestressing increases the shear strength of concrete members. It was found that the axial compression force increases the height of concrete compression zone as well as narrows the crack width and so, it raises the shear resistance of the beam. Moreover, if the prestressing steel was inclined, the vertical component of the prestressing force should be considered as a contribution to the beam shear capacity.

2.4.5.7   The shear reinforcement (e.g. Stirrups)

Stirrups come into play only after the inclined cracks have formed and its contribution to the beam shear strength increases as the crack width increases up to its yielding strength. Generally, only the stirrups crossing the inclined shear cracks are assumed to carry a maximum tensile force equal to their cross-section area multiplied by their yielding stress. Also, many researchers reported that because the shear reinforcement controls the shear crack width, it contributes to the beam shear capacity by increasing contributions from the actions affected by the crack width like the dowel action, the aggregate interlock, and the arch action. Belarbi & Hsu (1994) experimentally found that the yield strength of the mild reinforced bars embedded in the concrete is less than that when same bars are in a bare condition and there is a linear relation between the actual yielding stress of the bars embedded in the concrete and the parameter equal to $\left(\frac{1}{\rho}\right) \left(f_{cr}/f_y\right)^{1.5}$ where f_{cr}

is the concrete cracking stress and ρ is the reinforcement percentage. They reported that this difference is mainly due to the strain localization at the crack location and tension

stiffening. Also, they reported that bars do not behave in elastic-perfectly plastic behaviour as their plastic modulus is 1.8 % to 2.35% less than its elastic modulus. Most of the shear models neglect these findings and still consider an elastic-perfectly plastic behaviour for the stirrups and the longitudinal reinforcement.

Figure 2-9 summarises the loading history and the shear transfer mechanism in a slender RC beam without prestressing force or axial forces reported by Joint ASCE-ACI Task Committee 426 (1973). In short, prior to the flexural cracks, all shear forces are resisted by the uncracked concrete. After the first flexural crack formation and before the inclined shear cracks formation, the external shear is resisted by the uncracked concrete, the dowel action, and the aggregate interlock. Just before the inclined cracking formation, the strain in the concrete is equal to the strain in the stirrups due to strain compatibility and since the concrete cracks at a very small strain, the stress in the stirrups will be so small (i.e. will not exceed 40 MPa). Thus, stirrups will not prevent cracking from forming and do not contribute to the beam shear capacity before cracking. Once the inclined crack forms, the load carried by the stirrups increases as the crack width increases up to its yielding capacity; however, the increase in the crack width decreases both the dowel action and the aggregate interlock shear loads till splitting failure occurs or cover spalling occurs and their values equal zero. At this stage, only RC beam shear capacity will be equal to the shear load carried by the compression zone and the stirrups yielding capacity up to the beam shear failure. Thus, most of the international codes and the shear equations consider only those two terms in the RC beam shear capacity.
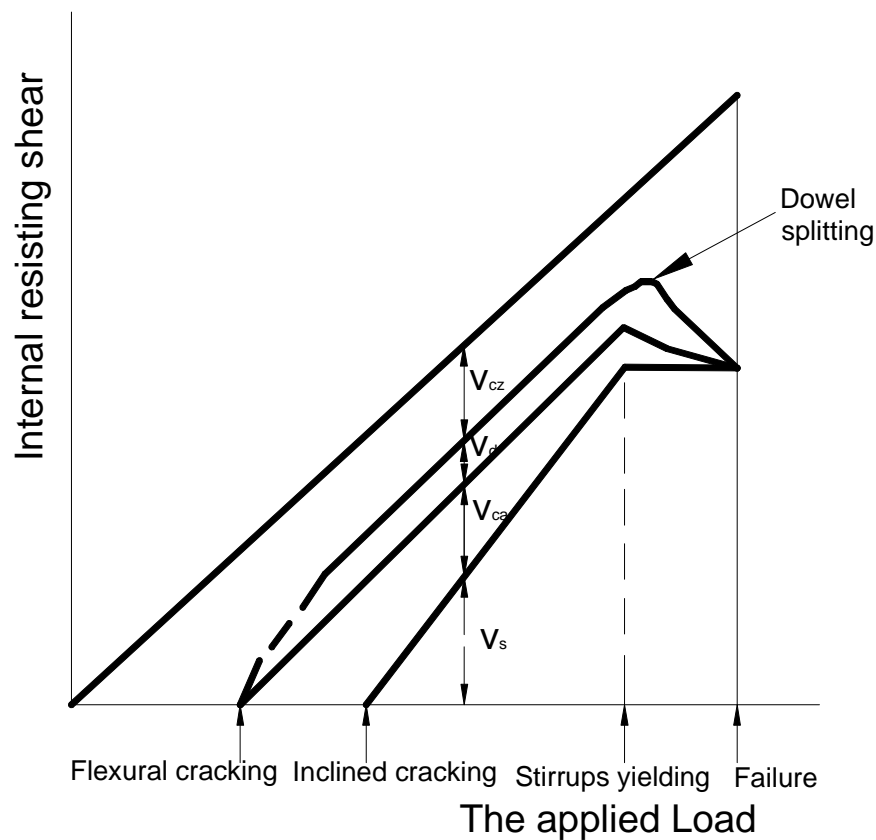
Figure 2- 9 The internal shear forces contributing to the RC beam shear strength in the different loading stages. Modified from Joint ASCE-ACI Task Committee 426, 1973.

2.5 Indirectly Loaded Reinforced Concrete Beams

The load applied on the grade beam may be transferred to the helical pile through the plate embedded in the concrete, i.e., the load is not directly applied on the extreme fibers of the beam as is the case in the typically loaded beams. Thus, the shear behaviour of the beam may differ and behaves similar to the beam loaded indirectly and failing in shear.

2.5.1 Importance of Indirect Shear behaviour

Ferguson (1956) drew attention to the possible effect of the manner of loading and supporting the beam on the RC beam shear capacity. He confirmed that there is a clear effect on the shear behaviour and crack pattern of the RC beams loaded indirectly. One of his tested RC beams without stirrups was loaded through transverse beams with height equal to half the height of the main beam. When the load was applied on these transverse beams entirely within the lower half depth of the beam, flat crack was developed between the two loaded beams and the failure was sudden. He reported that because of this type of loading, internal vertical tension loads induced over the loading zone. Also, Ferguson (1956) indicated that this beam capacity was smaller than other beams loaded directly. Smith & Fereig (1974) found that indirect loading affects the deflections, crack widths, steel strains, and the ultimate load. He also indicated that the arch action concept in indirectly loaded beam does not completely represent the behaviour after the inclined cracking initiation.

Taylor (1960) reported that "Beams loaded and supported through nibs can only sustain the diagonal cracking load. Beams loaded and supported directly on top and bottom surface can, under certain conditions, sustain loads beyond the diagonal cracking load". He also stated that the shear capacity of the beams loaded indirectly should not be calculated using the diagonal cracking load equations. On the other hand, Taub & Neville (1960) testing showed that there is a slight difference between the beams loaded directly and indirectly, however, it should be mentioned that all of the transverse beams used to indirectly load the main beams in their study had the same height of the main beam. Also,

25

he stated that the effects of vertical restraint at load points observed by Ferguson (1956) are believed to be limited to beams with a very low a/d ratio. He recommended using the diagonal tension cracking load, and not the collapse load, as the ultimate shear load on a beam without web reinforcement.

Taylor (1963) tested the manner of loading in RC beams with stirrups. He concluded that if the load indirectly applied near the bottom of the beam, a reduction in the beam capacity will be remarkable, and if the load is applied through the secondary beam with the same main beam height, a small reduction will occur as the loading will be approximate to a directly applied load.

2.5.2 Factors affecting the shear strength of the RC beam loaded indirectly and its shear transfer mechanism

Zuhua Wang (1987) compared the behaviour of beams loaded directly and indirectly by testing 41 specimens. He found that the reduction in the shear strength of the beam can go up to 63.4% of its shear capacity when directly loaded. He specified the factors that control how much reduction in the shear capacity of indirectly loaded beams. He implemented these factors as a reduction factor to the equation of Zsutty (1971). These factors are; (a/d) ratio, the position over the bottom surface of the beam, and the shear reinforcement ratio.

2.5.2.1 The (a/d) ratio effect

Zsutty (1971) investigated the test results provided by Ferguson (1956) and Leonhardt et al. (1968) and reported that his equation can predict the shear strength of the beam

accurately for indirect shear loading too if a reduction factor is considered depending on (a/d). Wang (1987) found that in case of a small shear span-depth ratio (a/d) was used, the decrease in the beam shear strength was great and conversely little variation was observed for large (a/d) ratios. Smith & Fereig (1974) found that for beam indirectly loaded without web reinforcement, the beam shear strength decreased to 1/2 to 2/3 of that in the directly loaded beam. The reduction in the shear-compression zone strength due to indirect loading is the main reason for the beam shear strength reduction (Smith & Fereig, 1974). Fereig & Smith (1977) investigated effect of (a/d) on the observed reduction due to indirect loading, and found that this effect decreases with increasing (a/d) and for (a/d)= 2.0 it was no longer significant.

2.5.2.2   The position over the bottom surface of the beam effect

Godycki-Cwirko (1973) conducted tests on a group of I beam specimens with varied secondary beam position. He indicated that there was 26% reduction in the beam shear capacity when the secondary beam was placed in the beam' tension zone and 16% reduction when the two beams had the same depth. Also, Taylor (1963) found that indirect loading at a closer point to the bottom surface of the beam had a major effect on the beam shear capacity. Smith & Fereig (1974) found that after the inclined cracking formation, higher beam deflection was recorded in the indirectly loaded beam on the lower portion of the beam sides than that in the beam directly loaded or indirectly loaded on the upper portion of the beam sides. CIRIA Guide 2 (1977) and Kong & Sharp (2006) provided design recommendations for deep beams bottom-loaded and for combined top- and -bottom case.

2.5.2.3   The shear reinforcement ratio effect

Wang (1987) stated that as the web reinforcement decreases the beam shear capacity decreases due to indirect shear loading especially if no web reinforcement was provided. Also, it was found that vertical shear reinforcement is more effective than the 45° shear reinforcement because the former can control the extension of the diagonal tension crack close to the applied load. Smith & Fereig (1974) found that shear reinforcement can reduce the indirectly loaded beam deflections, crack widths, and tensile steel strains. Paul (1978) recommended using hanger reinforcement anchored to the compression zone to transfer the applied load in case of indirect loading. Wang (1987) recommended using more vertical shear reinforcement for beams indirectly loaded to compensate for the reduction in the concrete shear capacity. Also, CSA A23.3 (2004) recommended using "hanger reinforcement" in the main beam indirectly loaded by a transverse beam.

2.5.3   Change in failure mechanism due to indirect shear loading,

Wang (1987) reported that loading the beam indirectly can change the mode of failure and he observed the following due to indirect loading of beams.

1- beams with large (a/d) ratio had same mode of failure as directly loaded beams.

2- beams with small (a/d) ratio loaded through secondary beams with the same depth of the main beams experience shear compression accompanied with flexural shear failure character.

3- beams with small (a/d) ratio loaded with secondary beams placed in the tension zone of the main beams experience diagonal tension failure.

4- Using additional vertical shear reinforcement can keep the mode of failure as that of the directly loaded beams.

2.6 Punching Shear (two-way shear)

A helical pile attached to raft slabs, wide pile caps, or wide beams employing the new construction bracket and subjected to compression loading may experience punching shear failure. Figure 2-10 reported by Ciria Report 89 (1981) shows that cases (e) and (f) represent loading conditions similar to the studied connection under tension and compression and may be considered failing due to punching shear.
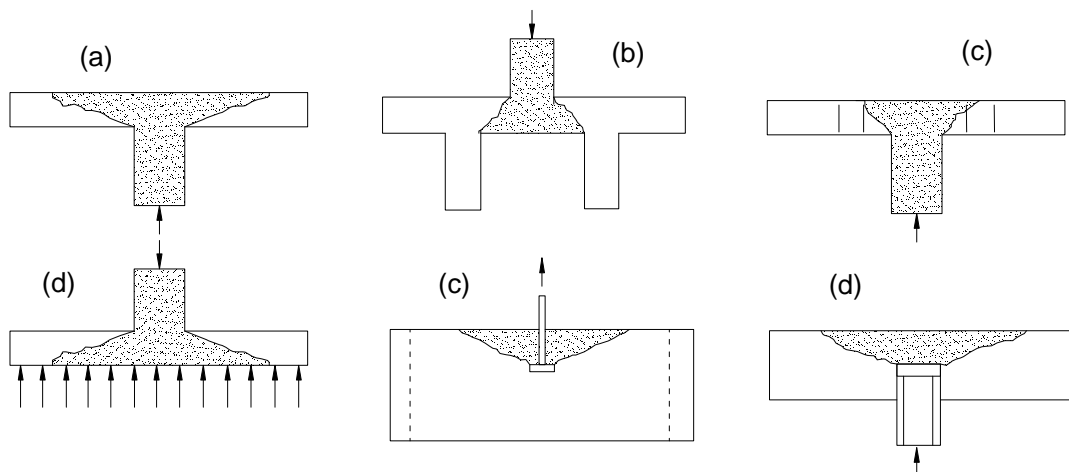
Figure 2- 10 Use of fracture surface approach to deal with various punching shear situations. Modified from Ciria Report 89, 1981

2.6.1   Punching Shear behaviour

Punching shear failure is a local phenomenon, which generally occurs in a brittle manner, at concentrated load regions (e.g. column support). This type of failure is catastrophic because no external, visible signs are displayed prior to the occurrence of the failure. It

occurs when the concentrated load punches through the RC element (mainly RC slabs), and is characterised by a pyramid failure surface formed at different inclinations of 30°, 45°, and 60°.

After diagonal tension cracking occurs, the slab carries the shear forces by shear across the compression zone, aggregate interlock, and dowel action. The ultimate shear strength developed in a slab in two-way shear was found to be much higher than that in a beam. This increase in punching shear strength of slabs is due to the three-dimensional nature of the slab shear-failure mechanism (Hassan, 2013). Ruiz & Muttoni (2010) summarized the different expected punching shear failure modes with shear reinforcement.

2.6.2   Factors affecting punching shear strength

Several variables affect the punching shear strength, including: the concrete strength, compression and tension longitudinal reinforcement ratio and their arrangement, concrete cover, shear reinforcement, loading type and area, column shape and size, size effect, span/depth ratio, slab thickness, In addition, the boundary restraint at supports, the location of the applied load in respect to the slab edge, as well as the presence of moment straining actions affect the punching shear strength.

2.7 Cast-in place headed anchors in concrete.

Anchors are used to transfer forces to concrete elements by tension, shear, and combination of both. The similarity between the studied connection between helical pile and new RC foundation using the new construction bracket (i.e. pile cap) and the cast-in-place headed anchors in concrete shown in Figure 2-11 is obvious. Therefore, these

anchors' behaviour and failure mechanisms under both tension and shear loading are briefly discussed herein, including evaluation of their capacities.
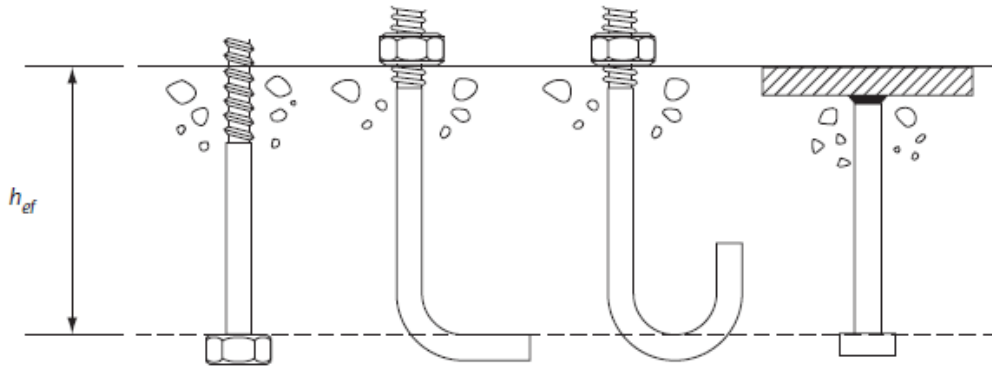
Figure 2- 11 Examples of cast-in-place anchors in concrete

2.7.1 Cast-in place headed anchors in concrete under tension loading

2.7.1.1 Anchor failure modes under tension loading

Under tension loading, anchors can fail in either ductile or brittle manner. The ductile failure mode refers to failure of the anchor shank, while the brittle failure mode refers to anchor pullout, concrete breakout, concrete splitting, and side face blowout. These failure modes are demonstrated in Figure 2-12 and they are briefly defined below.
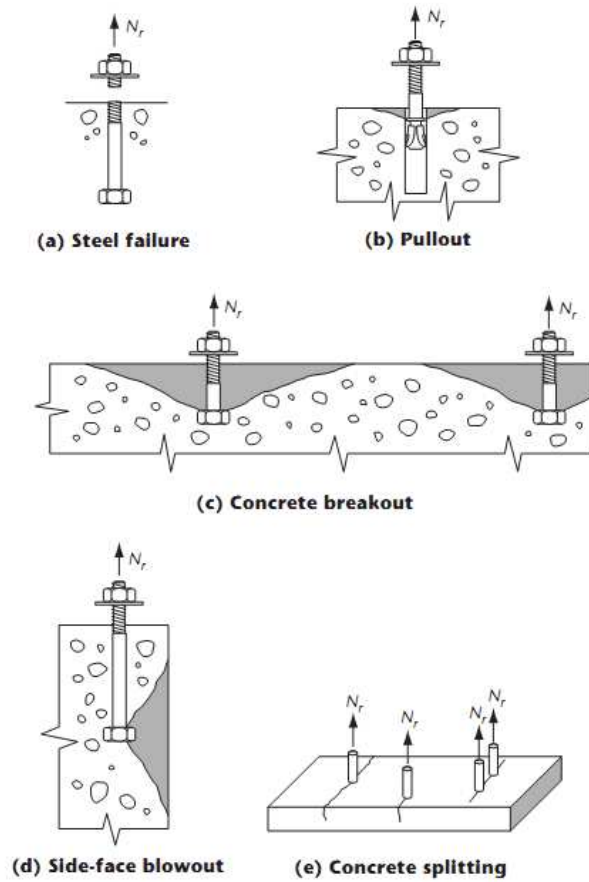
Figure 2- 12 Failure modes of anchors under tensile loading, after CSA A23.3, 2004.

2.7.1.1.1   Steel failure (The ductile failure)

This failure occurs when the anchor shank yields and fractures. It is classified as ductile if the anchor steel material is ductile. Collins et al. (1989) reported that it happens when the anchor embedment depth is sufficient to prevent the other types of failure modes.

2.7.1.1.2 Pullout failure

It takes place when the frictional resistance is less than the applied load. Eligehausen et al. (2013) reported that this failure mechanism may occur in headed anchors if the mechanical interlock at the bearing surface of the anchor head is inadequate.

2.7.1.1.3 Splitting failure

Splitting failure occurs due to the limited dimensions of the concrete component. It occurs when the anchor is installed close to the concrete edge or close to another anchor. Fuchs et al. (1995) indicated that it is not yet possible to determine theoretically the failure load to be expected in splitting failure. Therefore, most of the international codes determine edge distances (i.e. the distance between the anchor and the concrete edge), anchor spacing, and concrete member thickness to avoid it.

2.7.1.1.4 Concrete breakout failure

Concrete cone breakout failure mode is characterized by a conical crack that starts at the anchor tip and propagates towards the free edge of the concrete member. The angle between the failure surface and surface of the concrete member varies between 35° for shallow embedment to 45° for deep embedment, flattening out near the concrete surface (Hallowell, 1996). Eligehausen & Sawade (1985) tests headed studs and detected the crack pattern as follow. At approximately 40% of the breakout ultimate load, a short initial crack formed in the region of the stud head. This crack length increased slowly as the load rises. Then, the crack growth accelerated at approximately 90% to 95% of the

ultimate load. At the ultimate load, the crack had not reached the surface of the specimen yet. With displacement increase, the breakout cracks propagated to reach the concrete surface forming the breakout cone and brittle failure took place.

Eligehausen & Sawade (1985, 1989) measured the perpendicular strain to the diagonal fractural crack at two different locations and found that at concrete strain of 0.01%, micro cracks formed and extended with the load increase from the stud head location towards the concrete surface diagonally. They observed that at different stages of loading, the closer the strain gauge to the anchor, the higher the strain was recorded and the high strains' region moved with the load increase from the anchor location towards the concrete surface due to the micro cracks formation. Also, it was observed that just before reaching the concrete breakout load, the area of cracked concrete was only 25% to 30% of the whole surface of the fracture cone. Furthermore, Eligehausen et al. (1992) indicated that the breakout diagonal cracks' angle is approximately 35° and Eligehausen et al. (2013) stated that this angle depends on the stress condition in the concrete surrounding the anchor. Compression or tension stresses acting perpendicular to the direction of loading on the anchor caused the failure surface slope to be steeper or shallower, respectively. Furthermore, they stated that headed studs with an adequately large bearing surface will generate concrete breakout failure if the steel capacity is not exceeded and that the breakout failure is a brittle failure.

2.7.1.1.5 Side face blowout failure

This failure occurs when a headed anchor with deep embedment is close to an edge. It occurs due to the hydrostatic pressure at the stud head, which fails the concrete between the anchor head and the concrete edge, and the failure load is independent of the embedment depth. This failure may occur when the ratio of edge distance to anchor embedment depth is 0.3 to 0.5 (i.e. $\frac{c_1}{d_{emb}} = 0.3$ to 0.5), and the diameter of the side blowout cone was found to be approximately 6 c_1 (Senkiw & Lancelot, 1991).

2.7.1.2 Factors affecting cast-in-place anchor behaviour under tension loading

Many factors affect the cast-in-place anchor behaviour under tension loading, including: the anchor embedment depth, the size effect, the concrete mechanical properties, the maximum aggregate size, the used concrete mix, the anchor edge distance, the anchor spacing, the longitudinal reinforcement and its arrangement, the anchor reinforcement and its arrangement, the anchor head size, the concrete cracking condition before and during loading, the thickness of the concrete member, the stresses perpendicular to the anchor loading direction, the anchor capacity and material properties, the anchor type, the eccentricity in the applied load and presence of moments, loading type, span/depth ratio, the confinement effect, and the presence of shear loads with the applied tension loads. The factors which are most relevant to the studied connection are discussed below.

2.7.1.2.1 Anchor embedment depth and size effect

Eligehausen & Sawade (1989) concluded that anchors with small embedment depth should be described using non-linear fracture mechanics, whereas anchors with large embedment depth may be approximated using linear fracture mechanics. Eligehausen et al. (1992) indicated that concrete breakout load increases in proportion to the embedment depth, i.e. $d_{emb}^{1.5}$. The embedment depth influences the slope of the concrete failure cone, whereby the angle increases with increasing embedment depth (Eligehausen et al., 2013). Primavera et al. (1997) found that the embedment depth is the most important parameter for increasing the anchor tension capacity for anchors installed in high compressive strength concrete. Eligehausen et al. (1992) concluded that the concrete breakout load is affected by size as the linear fracture mechanics solution suggests, and recommended accounting for it in the design of fastenings.

2.7.1.2.2 Concrete mechanical properties, maximum aggregate size and concrete mix

Eligehausen et al. (2013) concluded that the tensile capacity of concrete can be used when designing anchors with an acceptable factor of safety. Eligehausen & Sawade (1985) demonstrated that the concrete breakout load depends on its fracture energy. Sawade (1994) conducted pull-out testing on a headed stud anchored in optical glass with tensile strength of approximately 25 times that of concrete while maintain $E_c . G_f$ (i.e. the modulus of elasticity multiplied by the fracture energy) approximately the same for both glass and concrete. He observed the same breakout cracking in glass and concrete. He demonstrated that the breakout load calculated using the glass tensile strength would be

36

770 kN, while its actual value was only 19 kN, which was close to that calculated by the equation based on the fracture energy. As the concrete modulus of elasticity and the fracture energy are related to the concrete compressive strength, it is assumed in some design equations that the concrete breakout load is proportional to $\sqrt{f_c'}$ (i.e. the square root of the concrete compressive strength), however, it should be mentioned that the concrete modulus of elasticity and the fracture energy are mainly affected by the maximum aggregate size and the concrete mix too and this explains why the anchors tested in concrete specimens having the same compressive strength but with varying mix designs exhibited varying concrete breakout loads.

Remmel (1994) evaluated the capacity of anchors embedded in concrete with compressive strength varying between 25 MPa and 125 MPa. He found that as the concrete compressive strength increased, the fracture process in tension became increasingly brittle.

2.7.1.2.3 Edge distance and anchor spacing

Eligehausen et al. (2013) showed that the tensile capacity decreases for closely spaced anchors or those installed close to an edge. Fuchs et al. (1995) recommended that minimum anchors spacing of 3 times the anchor embedment depth (i.e. 3 d_{emb}) to assure full anchor capacity, and the spacing should be even higher for shallow anchor bolts but may reduce to 2 for deeper anchor bolts. They concluded that increasing the anchor spacing up to spacing = 3 d_{emb}, increased the anchor breakout load capacity. They also

concluded that anchors should be placed at least 1.5 d_{emb} from the concrete edge to achieve the full concrete breakout capacity.

2.7.1.2.4 Longitudinal and anchor reinforcement

Eligehausen et al. (2013) reported that the longitudinal reinforcement perpendicular to the anchor orientation near the concrete surface does not typically increase the tension capacity of anchors. However, closely spaced longitudinal reinforcement can enhance the post cracking behaviour. They also demonstrated that hanger reinforcement similar to that shown in Figure 2-13 is only fully activated when the breakout cone forms. The anchor reinforcement located close to the anchor and adequately anchored inside and outside the breakout cone can increase the concrete breakout failure load and enhance the connection ductility.
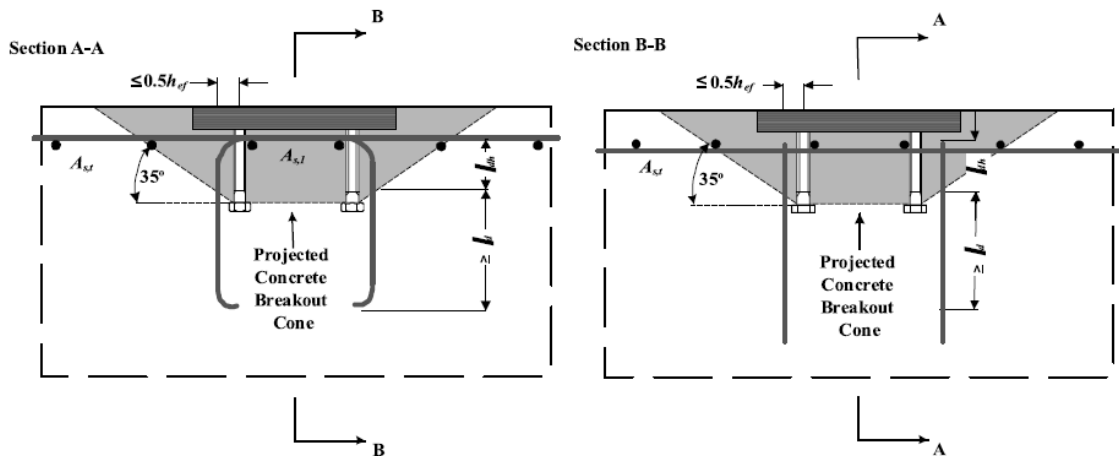
Figure 2- 13 Anchor reinforcement presented as hairpins. Modified from ACI 318 , 2014

2.7.1.2.5 Anchor head size

Eligehausen et al. (2013) indicated that the capacity of headed studs is approximately 15% higher than those of expansion anchors due to the favourable effect of the anchor head, which develops larger fracture surface and lower concrete stresses in the force transfer zone. Furche (1994) found that the critical maximum bearing pressure is approximately 10 to 14 times the cubic concrete compression strength (i.e. 10-14 $f_{cc,200}$). He observed that the concrete breakout load decreases as the anchor head size decreases due to local crushing in the concrete in front of the anchor head and the anchor displacement increases.

2.7.1.2.6 Cracking condition of concrete before and during loading

Ozbolt & Eligehausen (1992) observed that concrete breakout failure load decreases with increasing crack width up to a width of 0.15 mm to approximately 70 % of the failure load obtained for non-cracked concrete. Based on their results, they proposed simplified mechanism of the load transfer in uncracked and cracked concrete. Eligehausen & Balogh (1995) reported that anchors may attract cracks or induce cracking, thus they should be designed assuming cracked concrete. They observed that concrete breakout failure load of anchors located close to cracks with width 0.3 to 0.4 mm decrease by about 25% to 35% compared to uncracked concrete.

2.7.1.3   Capacity calculation of the concrete breakout under tension

Many empirical formulas have been proposed to calculate the breakout concrete capacity (e.g. CEB, 1993; Farrow & Klingner, 1995; Frigui, 1992; Fuchs et al., 1995; Klingner et al., 1982; and Walther et al., 1992).   The ACI 349 Appendix B (1990), ACI 349 Appendix B (1997), and PCI (1978) employed a 45-degree breakout cone model, considering a conical failure surface, in order to predict the concrete brittle failure. Recently, the Concrete Capacity Method (CCD), (Fuchs et al. 1995) has been proposed as a derivative of the so-called Kappa Method (CEB 1993).   The 45-degree cone method and the CCD Method have been compared against a large database of test results (Farrow & Klingner, 1995; Frigui, 1992; Fuchs et al., 1995). The CCD method was found to be accurate.   Thus, PCI (2004) and ACI 318-14 Appendix D adopted the CCD method to compute tension strength of anchors assuming uncracked concrete. Moreover, the CSA 23.3-04 Appendix D, and ACI 349 Appendix B (2001) used the same approach adopted in ACI 318-14 Appendix D. Furthermore, UBC-IBC (1997-2000), IBC (2003, 2006, and 2009) recommended design of anchors in concrete in accordance with Appendix D of ACI 318. The 45-Degree Cone Method and the CCD Method are discussed briefly below.

2.7.1.3.1   The 45-Degree Cone Method

The 45-Degree Cone Method assumes that a constant tensile stress of $0.96\sqrt{f_c'}$ (MPa) is applied on the projected area of the breakout cone, which has 45° cracking inclination propagating from the anchor end to the concrete surface as shown in Figure 2-14. Thus,

the anchor breakout cracking load for an anchor far from the concrete free edge will be

equal to $T_o = 0.96\sqrt{fc'}\pi d_{emb}^2(1 + d_b/d_{emb})$ (N)   **2.1**

If a short edge distance presented ($c_1 < d_{emb}$) or an adjacent concrete breakout cone (spacing< 2. d_{emb}) affected the behaviour, the breakout capacity will be equal to:

$$T_n = \frac{\text{Actual projected area of failure cone or cones}}{\text{Projected area of a single cone unaffected by edges}} * T_0 \qquad \textbf{2.2}$$
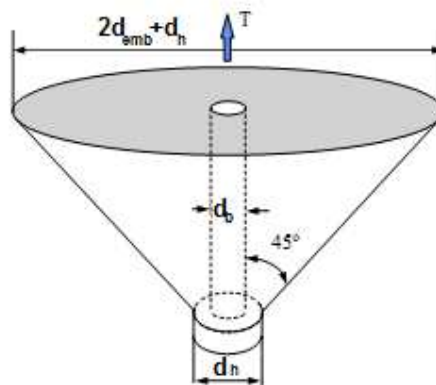
Figure 2- 14 Concrete Tensile Breakout cone regarding the 45° Cone Method

2.7.1.3.2   The Concrete Capacity Design Method (CCD Method)

The CCD Method is based on large amount of test results as well as extensive fracture mechanics studies to calculate the concrete breakout strength (Eligehausen & Sawade, 1989). The breakout tensile capacity for an anchor located far from the concrete free edge can be given by :

$$T_o = k\sqrt{fc'}.d_{emb}^{1.5} \qquad \text{;where k=17 for headed anchors} \qquad \textbf{2.3}$$

In the CCD Method, the breakout cone is presented as a pyramid with an inclination of 35° between the concrete surface and the failure surface as shown in Figure 2-15. The projected area of a single cone (i.e. the pyramid base) is $9.d_{emb}^{2}$. For small edge distance ($c_1 < 1.5.d_{emb}$) or short anchor spacing, the concrete breakout capacity is given by:

$$T_n = \frac{\text{Actual projected area of failure cone}}{\text{Projected area of a single cone unaffected by edges}} * \text{disturbance of symmetric stress factor} * T_0 \quad \textbf{2.4}$$
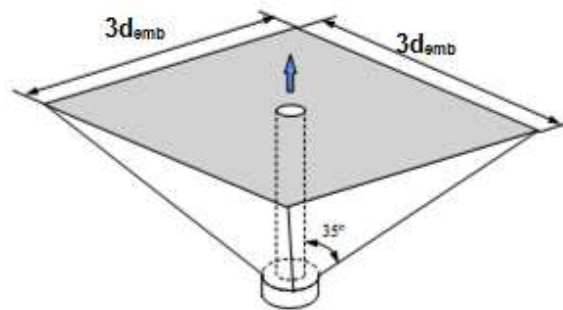
Figure 2- 15 Concrete Tensile Breakout cone regarding the CCD method

2.7.2 Cast-in place headed anchors in concrete under shear loading

2.7.2.1 Anchor failure modes under shear loading

Under shear loading, anchors can fail in a ductile or brittle manner. The ductile failure mode refers to failure of the anchor shank (i.e steel failure), while the brittle failure mode refers to concrete breakout (i.e. concrete edge failure) and concrete pryout failure. These failure modes are demonstrated in Figure 2-16. In some cases, these failure modes are preceded by crushing of the concrete close to the surface in front of the fastener. This is called concrete spalling (Figures 2-16a).
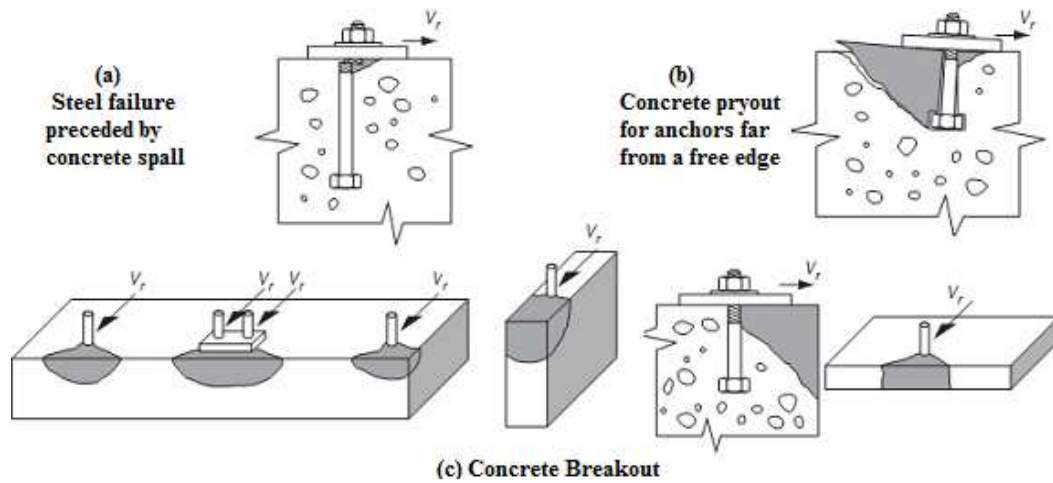
Figure 2- 16 Failure modes of anchors under shear loading, after CSA A23.3, 2004.

2.7.2.1.1 Steel failure

This failure is usually preceded by a concrete spall in front of the anchor and happens when the edge distance and the embedment depth are large enough to prevent the other failures modes from occurring. Anchors made of a ductile material can produce large deformation before failing. Fuchs (1992) observed that when the anchor bears on the concrete surface it produces high bearing stresses, which causes the concrete crushing (spall). The concrete crushing transfers the bearing point to a point farther from the concrete surface, causing an increase in the lever arm and associated flexural stresses in the anchor. Furthermore, Eligehausen et al. (2013) demonstrated that anchor bolts with variable cross-section may fail at the reduced cross-section due to the extra tension and flexural stresses in the shaft. Vintzeleou & Tassios (1987) and Fuchs (1992) proposed equations to calculate the concrete bearing strength in front of the anchor that causes the concrete crushing.

2.7.2.1.2   Concrete breakout failure (concrete edge failure)

Concrete breakout usually occurs when the anchor is located close to the free edge of a member and is loaded in shear towards the edge developing a semi-conical surface (Figure 2-16c). This semi-conical fracture surface originates from the bearing point in front of the anchor to the free edge of the concrete. Fuchs (1992) and Petersen & Zhao (2013) indicated that the fracture crack angle with the concrete edge is approximately 35° and develops to a depth of 1.3 to 1.5 times the edge distance. Thus, the breakout concrete cone is mainly affected by the edge distance. The breakout cracking load is based on brittle failure, which is not recommended for anchors design; however, designers used to consider it when limitation in the edge distance is presented.

2.7.2.1.3   Pryout failure

Anchors exhibit pry-out failure mode if they are located relatively far from the free edge and have a relatively small anchor embedment depth. Based on test results, Anderson (2005) described the pryout mechanism as follows: short and stiff anchors bend in a single curvature after the concrete spalling occurs in front of the anchor causing bearing at the anchor head "kicking back", which breaks out a crater of concrete behind the stud. The bearing pressure developed in front of the anchor cause the pryout rotational resistance. Eligehausen et al. (2013) indicated that the embedment depth required to ensure that pryout failure will not occur before the anchor steel failure depends on the steel strength, the anchor diameter, and the concrete strength. On the other hand, Hawkins (1987) indicated that for anchor embedment depth to the anchor diameter ratio,

$\left(d_{emb} / d_a \right) > 4$, pryout failure will not occur, while Anderson (2000) suggested

$\left(d_{emb} / d_a \right) > 4.5$.

2.7.2.2 Factors affecting cast-in-place anchor behaviour under shear loading

The variables that affect the cast-in-place anchor behaviour under shear loading include: anchor embedment depth, concrete mechanical properties, maximum aggregate size and concrete mix, anchor edge distance, size effect, longitudinal reinforcement and its arrangement, anchor reinforcement and its arrangement, anchor head size, concrete cracking condition, thickness of concrete member, concrete cover, stresses perpendicular to the anchor loading direction, anchor capacity and material properties, anchor type, lever arm of loading and presence of moments, loading type, span/depth ratio, confinement effect, and presence of tension loads with the applied shear loads. The factors which are most relevant to the studied connection are discussed below.

2.7.2.2.1 Anchor embedment depth and anchor diameter

Both anchor embedment depth and diameter affect the bearing stresses in front of the anchor shaft. Eligehausen et al. (2013) indicated that they have a small influence on the concrete breakout load for small edge distance, while it has negligible effect in case of large edge distances. Grosser (2012) found that no significant increase in the breakout failure load was observed for anchor diameter larger than 25 mm. Anderson (2005) concluded that increasing the embedment depth increases the pryout capacity remarkably.

Hawkins (1987) and Anderson (2000) indicated that $\left(d_{emb}/d_a\right)$ ratio is the main factor that indicates if pryout failure may occur or not.

2.7.2.2.2 Concrete mechanical properties, maximum aggregate size and concrete mix

The concrete bearing strength has a major effect on the anchor shear capacity. The concrete bearing capacity at the concrete surface increases linearly with the concrete compressive strength. Grosser (2012) reported that when expanded clay was used instead of round aggregate, the breakout failure load decreased significantly indicating the effect of the aggregate material on the concrete behaviour.

2.7.2.2.3 Edge distance, size effect and anchor spacing.

The edge distance affects the anchor shear behaviour and capacity. It governs if a steel failure, breakout failure, or pryout failure can take place. Klingner et al. (1982) and Ueda (1990) found that increasing the edge distance, increases the fracture surface area subjected to tension load and as a result it will increase the anchor breakout failure load. Also, Eligehausen et al. (2013) indicated that if the anchors are installed next to a corner or in a narrow member, the concrete resistance will decrease significantly due to the reduction in the area of the fracture surface.

ACI-349 (1990) proposed the critical spacing at which anchors will not affect each other breakout load as 2 times the edge distance (i.e. $2.c_1$), while Fuchs et al. (1995) concluded that the critical spacing should be approximately $3.c_1$.

2.7.2.2.4   Concrete member thickness

Fuchs et al. (1995) indicated that the effect of the concrete member thickness is negligible if it exceeded 1.5 c_1 from all anchor sides. If the concrete member thickness was less than 1.5.c_1, the breakout cone fracture surface will decrease and the resisting tension load of the concrete will decrease as a result. Also, size effect is more obvious for large concrete member thickness.

2.7.2.2.5   Anchor head size

The anchor head does not affect the breakout failure, however, it can add more fixation to the anchor (Eligehausen et al., 2013). Also, the larger the anchor head, the lower the bearing stresses in front of it, and pryout failure is less likely to occur.

2.7.2.2.6   Cracking condition of the concrete before and during loading

Concrete breakout failure loads decrease due to the presence of cracking compared to the non-cracked concrete as a function of the concrete crack width (Eligehausen et al., 2013). The shear breakout capacity of an anchor in cracked concrete decreases by approximately 18% under static loading compared to otherwise identical anchor in uncracked concrete (Hallowell, 1996), while Muratli et al. (2004) proposed a reduction factor of 0.714 to account for the effect of cracked concrete on the anchor capacity.

2.7.2.2.7 Longitudinal reinforcement

Petersen & Zhao (2013) indicated that the longitudinal reinforcement restrain splitting cracks and they should be fully developed at both sides of the anchor. Also, they recommended placing longitudinal bars directly in front of the anchor in direct contact with it to enhance the system behaviour by distributing the localized high compression stresses in front of the anchor especially if subjected to cyclic loading.

2.7.2.2.8 Anchor reinforcement (i.e. hanger reinforcement)

Eligehausen et al. (2013) stated that using hanger reinforcement can increase the shear capacity of anchors. He reported that using a single longitudinal bar restrained by ordinary stirrups had relatively small effect on the anchor failure capacity. On the other hand, adding hairpin reinforcement increased the anchor failure capacity remarkably, especially when the hairpin reinforcement was in direct contact to the anchor before loading. The initial stiffness of the system was not affected by the anchor reinforcement presence as the anchor reinforcement was only effective after the breakout cracking. Swirsky (1977) found that some minor improvement of the anchor shear capacity was recorded when using stirrups reinforcement.

2.7.2.3 Capacity calculation of the concrete breakout under shear loading

Several equations were generated to calculate the anchor breakout shear capacity (e.g. CEB, 1993; Fuchs et al., 1995; Klingner et al., 1982). Two methods are widely used in most codes: the 45-Degree Cone Method and the CCD Method.

2.7.2.3.1 The 45-Degree Cone Method

Assuming concrete tensile strength of $0.96\sqrt{f_c'}$ (MPa) as that used for anchors under tension loading applied on a 45° concrete half-cone as shown in Figure 2-17, The shear capacity may be given by:

$$V_{no} = 0.48\sqrt{fc'}.c_1^2 \text{ (N)}; \text{ where } c_1 = \text{edge distance in loading direction.} \qquad 2\text{-}5$$
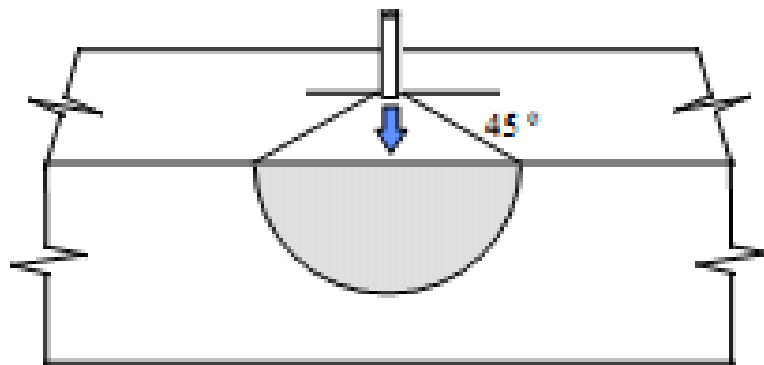
Figure 2- 17 Shear breakout cone of a single anchor regarding 45° cone method

2.7.2.3.2 The Concrete Capacity Design Method (CCD Method)

The CCD method presents the breakout cone as a half pyramid and its base is at the concrete member side face. The breakout angle is 35° from the concrete surface as shown in Figure 2-18. Using the CCD method, the anchor shear capacity can be given by:

$$V_{no} = (d_b fc')^{0.5}(l/d_b)^{0.2}c_1^{1.5} \text{ (N)} \qquad 2\text{-}6$$

where d_b=anchor outside diameter and l =d_{emb} for fasteners with constant stiffness.
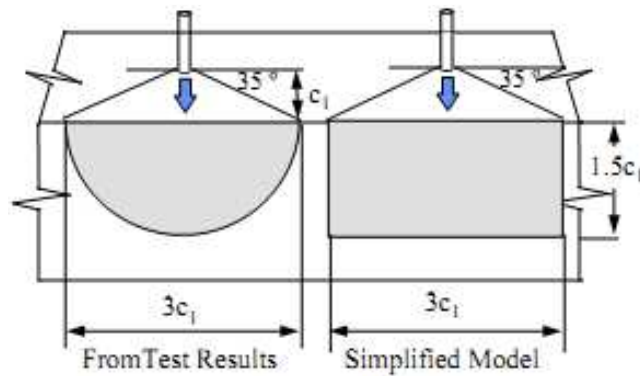
Figure 2- 18 The simplified model for a single anchor subjected to shear loading

2.8 Summary

Due to the shortage in understanding the behaviour of the studied connection, the different mechanisms related to the studied connection was described briefly including its load transfer mechanism, crack patterns, and the factors affecting each of them. These mechanisms include the behaviour of RC beams failing in shear, the behaviour of indirectly loaded RC beams failing in shear, punching shear behaviour, and cast-in-place headed anchors under tension and shear loadings. It was found that the most critical variables that should be studied in the pile-new foundation connection are: pile embedment depth in concrete, pile cap dimension, longitudinal reinforcement, and transverse reinforcement. It is expected that this brief literature review will provide good guidance to the analysis of the experimental and numerical investigations on the connection between the pile cap and the reinforced concrete grade beam under compression, tension, and shear loadings. Finally, the literature review revealed that there is no appropriate research was conducted on the connection which is already used on a wide range in North America. Therefore, it is of great importance to develop appropriate

50

design equations to predict the connection capacity considering different variables and under different loading cases.

2.9 References

Acharya, D.N., 1965. Significance of Dowel Forces on the Shear Failure of Rectangular Reinforced Concrete Beams Without Web Reinforcement. *Journal Of The American Concrete Institute*, 62(10), pp.1265–1279.

ACI 318, 2014. *Building code requirements for structural concrete (ACI 318-14) and commentary (ACI 318-14)*, Farmington Hills, MI: American Concrete Institute.

ACI-349, 1997. *Code Requirements for Nuclear Safety Related Concrete Structures*, Farmington Hills, MI.

ACI-349, 1990. *Code Requirements for Nuclear Safety Related Concrete Structures*, Farmington Hills, MI.

ACI 349, 2001. *ACI 349-01 Code Requirements for Nuclear Safety Related Concrete Structures*, Farmington Hills, MI: American Concrete Institute.

Anderson N. S., & M.D.F., 2000. Design criteria for headed stud groups in shear : Part 1 - Steel capacity and back edge effects. *PCI journal*, 45(5), pp.46–75.

Anderson N. S., & M.D.F., 2005. Pryout capacity of cast-in headed stud anchors. *PCI journal*, 50(2), pp.90–112.

Bažant, Z.P., 1997. Fracturing Truss Model: Size Effect in Shear Failure of Reinforced Concrete. *Journal of Engineering Mechanics*, 123(12), pp.1276–1288.

Bazant, Z.P. & Sun, H.-H., 1987. Size Effect in Diagonal Shear Failure: Influence of Aggregate Size and Stirrups. *Materials Journal*, 84(4), pp.259–272.

Belarbi, A., & Hsu, T.T., 1994. Constitutive Laws of Concrete in Tension and Reinforcing Bars Stiffened By Concrete. *ACI Structural Journal*, 91(4), pp.465–474.

Bresler, B. and Pister, K. S. 1958. Strength of concrete under combined stress. *ACI journal proceedings*, 55(9), pp.321–345.

CEB, 1993. *CEB-FIP model code 1993: design code*, Thomas Telford.

Choi, K.-K., Park, H.-G. & Wight, J.K., 2007. Unified Shear Strength Model for Reinforced Concrete Beams—Part I: Development. *ACI Structural Journal*, 104(2), pp.142–152.

CIRIA Guide 2, 1977. *Design of Deep Beams in Reinforced Concrete*, London: CIRIA.

Ciria Report 89, 1981. *Behaviour of Reinforced Concrete Flat Slabs*, London.

Collins, D., Klingner, R. & Polyzois, D., 1989. *Load-deflection behavior of cast-in-place and retrofit concrete anchors subjected to static, fatigue, and impact tensile loads*, Austin, Texas.

Collins, M.P. & Kuchma, D., 1999. How Safe Are Our Large, Lightly Reinforced Concrete Beams, Slabs, and Footings? *ACI Structural Journal*, 96(4), pp.482–490.

CSA A23.3, 2004. *A23. 3-04: design of concrete structures*,

Drucker, D., 1960. On structural concrete and the theorems of limit analysis. *IABSE Proceedings*, 21, pp.49–59.

Eligehausen, R. et al., 1992. Size effect of the concrete cone failure load of anchor bolts. In Z. P. Bazant, ed. *Fracture mechanics of concrete structures*. London: Elsevier Applied Science, pp. 517–525.

Eligehausen, R. & Balogh, T., 1995. Behavior of Fasteners Loaded in Tension in Cracked Reinforced Concrete. *Structural Journal*, 92(3), pp.365–379.

Eligehausen, R., Mallée, R. & Silva, J.F., 2013. *Anchorage in Concrete Construction*, John Wiley & Sons.

Eligehausen, R. & Sawade, G., 1989. A fracture mechanics based description of the pull-out behavior of headed studs embedded in concrete. In L. Elfgren, ed. *Fracture mechanics of concrete structures*. London: Chapman and Hall, pp. 281–299.

Eligehausen, R. & Sawade, G., 1985. Verhalten von Beton auf Zug. (Behaviour of concrete under Tension). *Betnwerk. Fertigteil-Technik*, 5, pp.315–322.

Farrow, C. Ben & Klingner, R.E., 1995. Tensile Capacity of Anchors with Partial or Overlapping Failure Surfaces: Evaluation of Existing Formulas on an LRFD Basis. *ACI Structural Journal*, 92(6), pp.698–710.

Fereig, S. M., & Smith, K.N., 1977. Indirect Loading on Beams with Short Shear Spans. *Magazine of Concrete Research*, 74(5), pp.220–222.

Ferguson, P., 1956. Some implications of recent diagonal tension tests. *ACI Journal Proceedings*, 53(8), pp.157–172.

Frigui, I., 1992. *Tensile Capacity of Single Anchors in Concrete: Evaluation of Existing Formulas on an LRFD Basis*. The University of Texas at Austin.

Fuchs, W., 1992. *Tragverhalten von Befestigungen unter Querlasten in ungerissenem Beton.(Load-bearing behaviour of fastenings under shear loading in non-cracked concrete)*. Universität Stuttgart. In German.

Fuchs, W., Eligehausen, R. & Breen, J.E., 1995. Concrete Capacity Design (CCD) Approach for Fastening to Concrete. *ACI Structural Journal*, 92(1), pp.73–94.

Furche, J., 1994. *Zum Trag-und Verschiebungsverhalten von Kopfbolzen bei zentrischem Zug (Load-Bearing and Displacement Behavior of Headed Bolts under Centric). In German.* Universität Stuttgart.

Godycki-Cwirko, T., 1973. *Schubrobleme im Stahlbetonbau. In German.* Duesseldorf.

Gopalaratnam, V.S. & Shah, S.P., 1985. Softening response of plain concrete in direct tension. *Journal Proceedings*, 82(3), pp.310–323.

Grosser, P.R., 2012. Load-bearing behavior and design of anchorages subjected to shear and torsion loading in uncracked concrete.

Hallowell, J.M., 1996. *Tensile and shear behavior of anchors in uncracked and cracked concrete under static and dynamic loading.* University of Texas at Austin.

Hassan, M.A.W., 2013. *Punching shear behaviour of concrete two-way slabs reinforced with glass fiber-reinforced polymer (GFRP) bars.* Université de Sherbrooke.

Hawkins, N.M., 1987. Strength in Shear and Tension of Cast-in-Place Anchor Bolts. *ACI Special Publication*, 103, pp.233–256.

Hubbell Power Systems Inc., 2016. *ICC-ES Report: Chance type ss6 and ss175 helical foundations systems*,

Hubbell Power Systems Inc., 2014. *Technical design manual* 3rd ed.,

IBC, 2003. International building code. *International Code Council, Inc.*

Joint ASCE-ACI Task Committee 426, 1973. The Shear Strength of Reinforced Concrete Members. *Journal of the Structural Division*, 99(6), pp.1091–1187.

Kani, G., 1967. How safe are our large reinforced concrete beams?. ACI journal proceedings, 64, pp.128–141.

Klingner, R.E., Mendonca, J. a. & Malik, J.B., 1982. Effect of Reinforcing Details on the Shear Resistance of Anchor Bolts Under Reversed Cyclic Loading. *ACI Journal*, 79(1), pp.3–12.

Kong, F. K., & Sharp, G.R., 2006. *Reinforced Concrete Deep Beams*, CRC Press.

Leonhardt, F., Walther, R. & Dilger, W., 1968. Schubversuche an indirekt gelagerten, einfeldrigen und durchlaufenden Stahlbetonbalken. In German. *Ernst*, pp.1–69.

Lim, F.K. & Rangan, B.V., 1995. Studies on Concrete Slabs with Stud Reinforcement in the Vicinity of Edge and Corner Columns. *ACI Structural Journal*, 92(5), pp.515–525.

Lovrovich, J. S., & McLean, D.I., 1990. Punching Shear Behavior of Slabs With Varying Span-Depth Ratios. *ACI Structural Journal*, 87(5), pp.507–512.

MacGregor, J.G., 1992. *Reinforced concrete : mechanics and design* 2nd Edition., Prentice-Hall, Incorporated.

Marti, P., 1985. Basic tools of reinforced concrete beam design. *ACI Journal Proceedings*, 82(1), pp.46–56.

Menétrey, P., 2002. Synthesis of punching failure in reinforced concrete. *Cement and Concrete Composites*, 24(6), pp.497–507.

Mirza, S.A. & MacGregor, J.G., 1982. Probabilistic study of strength of reinforced concrete members. *Canadian Journal of Civil Engineering*, 9(3), pp.431–448.

Mörsch, E., 1908. *Reinforced concrete construction, theory and application* Edition 5. K. Wittwer& Stuttgart, ed.,

Muratli, H., Klingner, R.E. & Herman L. Graves, 2004. Breakout Capacity of Anchors in Concrete—Part 2: Shear. *ACI Structural Journal*, 101(6), pp.821–829.

Muttoni, A., 2008. Punching shear strength of reinforced concrete slabs without transverse reinforcement. *ACI Structural Journal*, 105(4), pp.440–450.

NCHRP Report 549, 2005. *Simplified Shear Design of Structural Concrete Members*, Washington, D.C.

Ozbolt, J. & Eligehausen, R., 1992. Influence of crack width on the concrete cone failure load.

Pack, J., 2009. *Design and Inspection Guide for Helical Piles and Helical Tension Anchors*, Denver, Colorado, U.S.A.

Paul, I.S., 1978. *Behaviour of indirectly loaded reinforced concrete thin-wall ribbed panels*. Concordia University.

PCI, 2004. *PCI Design Handbook: Precast and Prestressed Concrete* 6th-Edition ed., Chicago, Ill.

PCI, 1978. *Precast and Prestressed Concrete (PCI Design Handbook)* 2nd-Edition ed., Chicago, , Ill.

Petersen, D. & Zhao, J., 2013. Design of Anchor Reinforcement for Seismic Shear Loads. *ACI Structural Journal*, 110(1), pp.53–62.

Primavera, E.J., Pinelli, J.-P. & Kalajian, E.H., 1997. Tensile Behavior of Cast-in-Place and Undercut Anchors in High-Strength Concrete. *ACI Structural Journal*, 94(5), pp.583–594.

Reineck, K.-H., 1991. Ultimate shear force of structural concrete members Without Transverse Reinforcement Derived From a Mechanical Model (SP-885). *ACI Structural Journal*, 88(5), pp.592–602.

Remmel, G., 1994. *Zum Zug- und Schubtragverhalten von Bauteilen aus hochfestem Beton (Tension and shear behaviour of building components made from high-strength concrete). In german* Deutscher Ausschuss für Stahlbeton, ed., Berlin: Beuth Verlag.

Ruiz, F. M. & Muttoni, A., 2010. Performance and Design of Punching-Shear Reinforcing Systems. *3rd fib International Congress*, 437, p.14.

Sakr, M., Naggar, M.H. El & Nehdi, M., 2004. Load transfer of fibre-reinforced polymer (FRP) composite tapered piles in dense sand. *Canadian Geotechnical Journal*, 41(1), pp.70–88.

Sawade, G., 1994. *Ein energetisches Materialmodell zur Berechnung des Tragverhaltens von zugbeanspruchtem Beton(Energetic material model to describe the load-bearing behaviour of concrete under tension). In German*. Universität Stuttgart.

Senkiw, G. & Lancelot, H., 1991. *Anchors in concrete--design and behavior* H. B. L. I. George A. Senkiw, ed., American Concrete Institute.

Smith, K.N. & Fereig, S.M., 1974. Effect of Loading and Supporting Conditions on the Shear Strength of Deep Beams. *ACI Special Publication*, 42, pp.441–460.

Swirsky, R., 1977. *Lateral resistance of anchor bolts installed in concrete*, California.

Taub, J., & Neville, A.M., 1960. Resistance to Shear of Reinforced Concrete Beams Port 1- Beams without Web Reinforcement. *Journal Of The American Concrete Institute*, 57(8), pp.193–220.

Taylor, R., 1963. Some aspects of the problem of shear in reinforced concrete beams*. *Civil engineering and Public works*, 17(1-2), pp.9–26.

Taylor, R., 1960. Some shear tests on reinforced concrete beams without shear reinforcement*. *Magazine of Concrete Research*, 12(36), pp.145–154.

UBC-IBC, 2000. *UBC-IBC Structural Comparison and Cross Reference (1997-2000)*, Whittier, CA.

Ueda, T., Kitipornchai, S. & Ling, K., 1990. Experimental Investigation of Anchor Bolts under Shear. *Journal of Structural Engineering*, 116(4), pp.910–921.

Vickars, R.A. & Clemence, S.P., 2000. Performance of helical piles with grouted shafts. In New Technological and Design Developments in Deep Foundations. Proceedings of Sessions of Geo-Denver 2000.

Vintzeleou, E.N. & Tassios, T.P., 1987. Behavior of Dowels Under Cyclic Deformations. *ACI Structural Journal*, 84(1), pp.18–30.

Walther, R., Sutton, C. & Meinheit, D., 1992. Evaluation of Expansion Anchor Ultimate Tensile Capacity Prediction Equations. *ACI Special Publication*, 130, pp.19–46.

Watstein, B.D. & Mathey, R.G., 1958. Beams Having Diagonal Cracks. *Journal Of The American Concrete Institute*, 58(55), pp.717–728.

Zararis, P.D. & Papadakis, G.C., 2001. Diagonal Shear Failure and Size Effect in RC Beams without Web Reinforcement. *Journal of Structural Engineering*, 127(7), pp.733–742.

Zsutty, T., 1971. Shear Strength Prediction for Separate Categories of Simple Beam Tests. *ACI Journal Proceedings*, 68(2), pp.138–143.

Zuhua Wang, 1987. shear strength of slender concrete beams loaded indirectly. *International journal of structures*, 7(1), pp.17–42.

Zwoyer, E. M. and Siess, C. P., 1954. Ultimate Strength in Shear of Simply-Supported Prestressed Concrete Beams Without Web Reinforcement. *ACI Journal Proceedings*, 51(10), pp.181–200.

BEHAVIOUR OF HELICAL PILE CONNECTORS FOR NEW FOUNDATIONS SUBJECTED TO TENSION LOADING: EXPERIMENTAL INVESTIGATION

3.1 Introduction

This research investigates the behaviour of the connection between slender solid shaft pile types, which end with a mono steel bar at the ground level (e.g. square shaft helical piles and micro piles) and a new reinforced concrete foundation (e.g. grade beams). Typically, steel brackets (plates) are used in order to transfer loads from the new reinforced concrete foundation to the steel pile. The bracket is a steel plate, which can be connected to the steel pile by welding or by bolts. Thus, the connection behaviour can be considered as a headed anchor. However, these types of anchors are not addressed by current design codes (e.g. A23.3-04 Appendix D, ACI 318-11 Appendix D, or ACI 349-01 Appendix B), because they are developed assuming linear fracture mechanics (Lee et al., 2007) based on tests on anchors with high bearing pressure (i.e. anchors with small heads). Furthermore, helical pile new construction may involve grade beams with limited width, which reduces the connection capacity.

In the research described herein, 9 full-scale pile-foundation connection models were experimentally tested under monotonic tension loading in order to clearly understand the behaviour of the connection and to indicate its failure mechanism.

Four groups of specimens were constructed and tested in this study. The main factors varied in these test specimens included: the embedment depth of the pile into the

foundation; the width of the pile cap's plate; the longitudinal reinforcement of the reinforced concrete grade beam; and the transverse reinforcement of the grade beam.

3.2 Research significance

The connection considered in this research is widely used in the construction of helical piles and micropiles in North America. Despite the wide application of these connections in the piling industry, there are no specific design criteria for their implementation in design. Given the growing popularity of these foundation options, especially in seismic active areas, there is a pressing need to understand their behaviour and develop a methodology for their design under different loading conditions. Thus, the main objective of this study is to examine the behaviour and capacity of the new construction brackets used to connect helical piles and micropiles to new reinforced concrete grade beam foundation subjected to monotonic tension loading. The experimental results obtained from full scale tests are used to describe the full behaviour of the connection and to help in assessing the applicability of existing design formulas for slender shaft anchors, indirect shear loading on beams, or other design formulas to this connection.

3.3 Experimental program

Nine simply supported reinforced concrete beams of dimensions 500 mm x 500 mm x 1600 mm, representing grade beams typically used in buildings foundations, were subjected to monotonic tension loading. The tested beams were categorized into four groups according to the parameters investigated. Each group has three beams, including the control beam T2. In each group only one variable was investigated, while other variables were kept constant. In the first group: various typical embedment depths, 254,

203 and 152 mm (10, 8, and 6 in) were investigated. In the second group, the width of the steel square plate (i.e. new construction bracket) was varied between 165 and 229 mm (6.5 and 9 in) to study the effect of the bracket size on the beam capacity. In the third group, the effect of the beam longitudinal reinforcement was investigated. Four longitudinal bars were used with different diameters (16mm (15M) , 19.5mm (20M) , 25.2mm (25M)) resulting in longitudinal reinforcement ratios of (0.31%, 0.56%, and 0.87%), respectively. In the forth group, the effect of the beam transverse reinforcement was examined considering stirrups spacing of 100 mm and 200mm, and the number of stirrup vertical branches of 2 branches and 4 branches. Table 3-1 and figure 3-1 summarize the dimensions and details of the nine tested specimens. Figure 3-2 shows the commonly used pile cap. Appendix B demonstrates the several steps conducted for the specimens preparation.
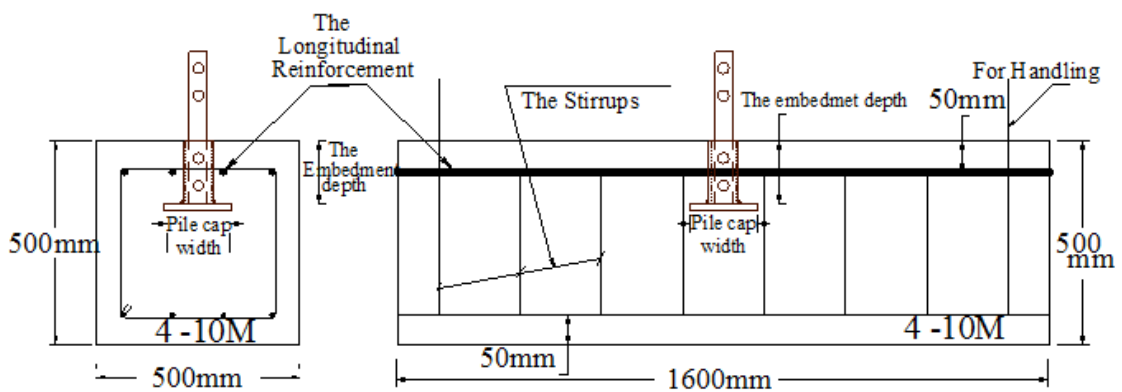
Figure 3- 1 Dimensions and full details for the tested specimens

Figure 3- 2 Commonly used pile cap (i.e. New construction bracket)

Table 3- 1 Details of studied Specimens

Beam Name	Beam Dimensions (mm)	Concrete Strength fc'(N/mm^2)	The embedment depth (mm)	Pile cap width (mm)	Longitudinal Reinforcement	Stirrups
T1	500x500x1600	30	152	165	4-15M	2 branches #2@200mm
T2	500x500x1600	30	203	165	4-15M	2 branches #2@200mm
T3	500x500x1600	30	254	165	4-15M	2 branches #2@200mm
T4	500x500x1600	40	203	190	4-15M	2 branches #2@200mm
T5	500x500x1600	40	203	229	4-15M	2 branches #2@200mm
T6	500x500x1600	40	203	165	4-20M	2 branches #2@200mm
T7	500x500x1600	40	203	165	4-25M	2 branches #2@200mm
T8	500x500x1600	40	203	165	4-15M	4 branches #2@200mm
T9	500x500x1600	40	203	165	4-15M	2 branches #2@100mm

3.4 Materials

It was planned to use only one concrete mix throughout the experimental work in two similar patches. In the first patch, beams T1, T2, and T3 were casted, and in the second patch beams T4, T5, T6, T7, T8 and T9 were casted. The concrete was delivered as a ready mix concrete with specific compressive strength. The concrete mix consisted of

ordinary Portland cement, sand, and gravel with 20 mm maximum nominal aggregate size. The concrete mix for one cubic meter consisted of 1100 kg of coarse aggregate, 780 kg of sand, 245 kg Type 10Gu cement, 145 litre of water, 250 millilitre of super-plasticizer, and 80 kg slag. All of the results from the concrete cylinder compression and splitting tests can be found in Appendix A. It was planned that the concrete mix will achieve 80 mm slump and characteristic cylinder compressive strength of 30 MPa; however, two different concrete strength values were recorded. Mostly, the provided concrete had higher cement content but the aggregate size was the same in the second patch. As a result, the concrete strength of the first 3 test specimens was 30 MPa while the strength of the remaining 6 test specimens was 40 MPa. Thus, modification to the control beam T2 to capture the behaviour of the same beam if the concrete strength was 40 MPa instead of 30 MPa was done as will be presented later.

The longitudinal reinforcing bars were 15M, 20M, and 25M high strength deformed steel conforms to CSA G30.18M-09 grade 400W. The compression longitudinal reinforcement comprised 10M high strength deformed steel conforms to CSA G30.18M-09 grade 400W. Plain bars of #2 (i.e. 6.35 mm or 1/4" diameter) cold formed steel, with grade 450/550, were used for stirrups. All of reinforcement bars direct tensile test result are presented in Appendix A. The steel pile model was a central steel shaft which is made of hot rolled round-cornered-square (RCS) solid steel bar (45 mmx45 mm) conforming to the dimensional and workmanship requirements of ASTM A29, with minimum yield and tensile strengths of 483 and 689 MPa.

The new construction bracket (i.e. the pile cap) is shown in Figure 3-2. It consists of a square steel plate with adequate thickness welded to 152 mm (6") long coupling tube with adequate inner diameter to insert the pile in it. The plate and tube conform to ASTM A36. The tube has one or two holes to connect the pile cap with the pile shaft using bolts. The used bolt was a 25 mm (1") diameter bolt complying with ASTM A 193 Grade B7 (minimum yield strength is 655 MPa, and minimum tensile strength is 793 MPa). The welding between the cylinder and the pile cap's plate was 10mm filet welding with E43XX metric electrode classification.

3.5 Instrumentation

Figure 3-3 shows the details of the test setup. The load was applied using a calibrated hydraulic jack of 1500 kN capacity with a maximum stoke of 500 mm. Two strong clamping beams, spaced at 1220 mm, attached with steel rods to the rigid floor of the laboratory were used to take the reaction of the tension loading. Two strong HEA 260 beams were used to raise the specimen elevation in order to detect the cracks and deformations expected to take place during loading.

As shown in Figure 3-3, at least seven linear displacement transducers (LDT) were used to monitor the displacements at the mid-span and quarter-span points of the beam, and the out of plane displacement as well as the displacement of the pile shaft. To accomplish these measurements, the LDTs were placed at the middle of upper and lower levels and the side of the beam. For each beam, five or more electrical strain gauges per beam were used to measure strain in different stirrups and different branches and in the outer and inner longitudinal steel (i.e. the longitudinal rebar close to the beams surface and the

64

longitudinal rebar close to the beam core, respectively). The strain readings were also used to evaluate magnitude and distribution of the plate deformation along its width. The strain gauges were 10 mm long and had 120±0.3% Ω resistance. The strain gauges, the loading cell, and the displacement transducers were connected to a data acquisition system to monitor and record the strains, the applied loads, and the displacements.

Figure 3- 3 Test rig and locations of displacement transducers

3.6 Test procedure

The load was applied monotonically at a loading rate of 7 kN/min, and cracks were marked. The deformations were recorded from the LDTs and the observed steel strains were recorded using the strain gages. The total duration of each test was about one hour. The test was stopped when breakout cone cracks opened excessively causing total separation of the breakout cone, accompanied by excessive strength reduction below 60% of the ultimate load. In most cases, the test was stopped when necking occurred in the stirrups causing failure (often after the strength dropped below 60% of the ultimate load).

3.7 Test results

3.7.1   General Crack patterns, failure modes and beam ductility

The crack patterns of the nine tested beams are shown in Figure 3-4. Most of the beams had approximately the same crack pattern. First, bond failure between the pile and the surrounding concrete was observed as shown in Figure 3-5 indicating that no load will be transferred through pile-concrete bond or pile-concrete friction as the crack will get wider due to the internal tension due to flexure. This bond crack was followed by the initiation of the first flexural crack as shown in Figure 3-6. As the load continued to increase, the flexural crack propagated towards the compression zone going beyond the pile cap level. At breakout cracking load, two inclined cracks initiated from pile cap's plate ends extending toward the tension load with approximately 35° reaching the level of the longitudinal reinforcement. These diagonal cracks extended horizontally in the width direction as shown in Figure 3-7 and Figure 3-8, which confirms that the cracking began from the plate ends. Also, cracks at 45° initiated from the pile corners; mostly from the

bolts, extending towards the beam borders as other cracking inside the breakout cone was observed as shown in Figure 3-9. After the breakout cracking load was reached, the breakout cracks opened wider causing dowel action in the longitudinal steel and yielding of stirrups took place (i.e. when steel strains are greater than 0.002 strain). At failure, the stirrups failed after necking as shown in Figure 3-10 causing the beam to disintegrate and the load transfer mechanism failed. As demonstrated in Figure 3-11, some splitting cracks appeared at the top of the beam after the breakout cracking and close to failure due to flexural stresses on the breakout cone because of the load transferred through the longitudinal reinforcement and stirrups.

It was clear that the crack extends approximately flat in the unsupported direction of the beam, which means a behaviour closer to single shear failure rather than anchors breakout failure, or punching failure. One may observe that the flexural cracks in all the specimens have minor effect on the breakout crack pattern and as a result on the breakout cracking load capacity.

Most specimens exhibited a vertical crack at the compression side of the beam as shown in Figure 3-12, just after the ultimate load was reached and close to failure (precisely after the stirrups yielding). This could be explained as follows. When the breakout cone began to move with the pile and the stirrups did not transfer the load vertically to the rest of the beam; this is associated with a sharp increase in the longitudinal reinforcement stress causing more tension load to the beam sides next to the breakout cone leading to inverted moment to the rest of the beam. Thus, tension occurred in the fibers that were

previously under compression. Also, this sharp increase in the steel stress caused bond and splitting cracks around the longitudinal reinforcement. Similar behaviour was observed by Watstein et al. (1958) and Smith and Fereig (1974).

The failure mechanism appears to be brittle at ultimate load; however, increasing the transverse reinforcement increased the ductility of the beam before failure. Also, as the breakout cracks initiated from the pile cap ends, the pile cap did not contribute to the ultimate load as the pile cap's plate strain was less than 66×10^{-6} (i.e. only 3% of its yielding strain) as will be discussed later.
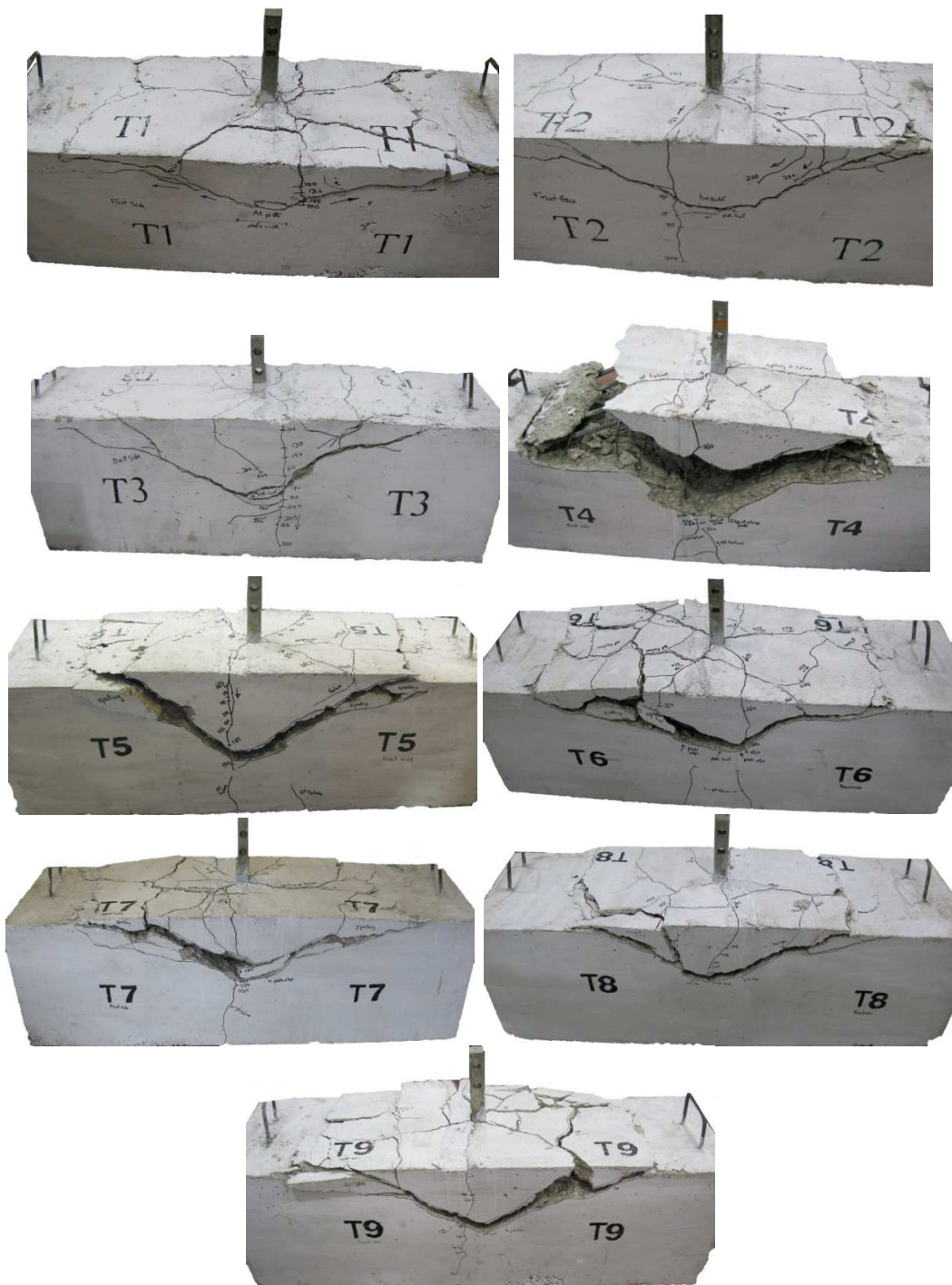
Figure 3- 4 Crack patterns of the tested beams

Figure 3- 5 Bond failure between the pile shaft and the surrounding concrete

Figure 3- 6 First flexural crack initiation and propagation
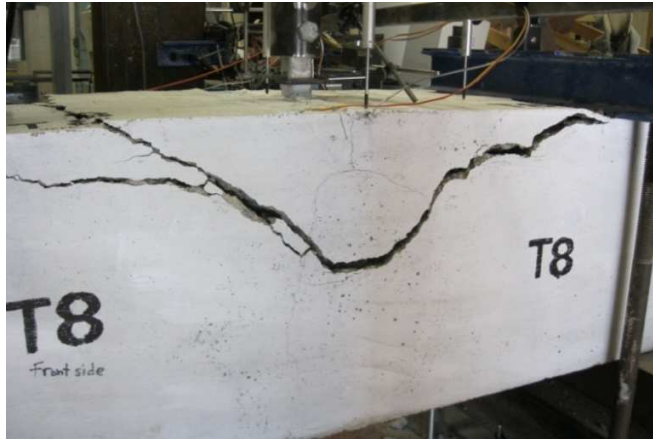
Figure 3- 7 Breakout cracking and the breakout cone

Figure 3- 8 Breakout cracking initiation from the plate ends
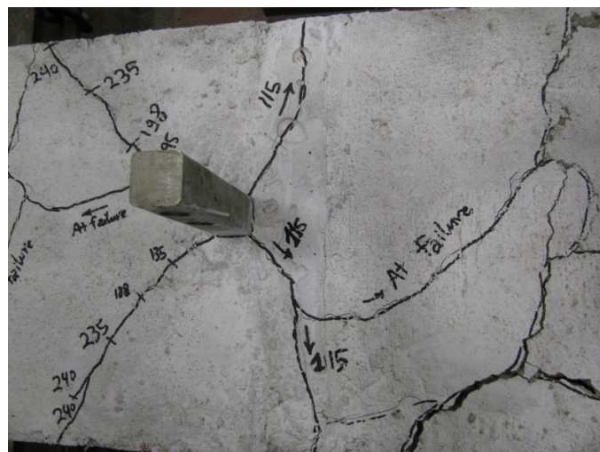
Figure 3-9 Observed surface cracking

Figure 3- 10 Stirrups failure by necking after the breakout cone formation
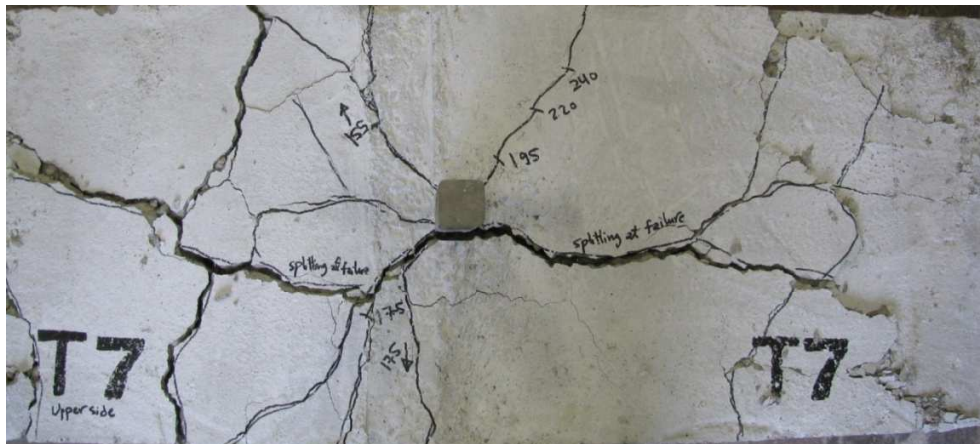
Figure 3- 11 Splitting cracks after reaching the connection ultimate load

Figure 3- 12 Vertical cracks initiation after the stirrups failure on the other side of the beam

3.7.2 General load transfer mechanism

The load transferred initially from the pile to concrete or vice versa through the bond between them up to a small load level depending on the embedment depth of the pile in the concrete. The load then transferred to the bolt, which caused cracks in front of the bolt, and then most of the load transferred to the pile cap's plate. The plate experienced concentration of stresses at its ends and cracking began gradually from the plate ends extending to the concrete surface producing tensile stresses on a diagonal plan inside the concrete. During the last three steps, the beam was still working with its full height. Afterwards, the tensile stresses acting on the remaining uncracked concrete next to the plate exceeded the concrete tensile strength and the breakout cracking extended to the beam edges. At this point, as shown in figures 3-13 and 3-14, the beam behaviour would fully depend on three resistance components: the longitudinal reinforcement, the transverse reinforcement, and the aggregate interlock. These three components provide breakout crack bridging to the forces. If those three components are enough to transfer the loads, the beam will continue to resist more loads. Also, the connection capacity may be higher than the beam flexural and shear capacities causing a beam failure before the connection failure or the beam capacity may be higher and the connection may fail first. Thus, it is really important to calculate the breakout cracking load, the ultimate load of the connection, and the beam ultimate capacity. Also, if the cracking width was too wide, two of the three connection capacity components, i.e. the concrete aggregate interlock and the dowel action of the longitudinal reinforcement, would have negligible values. In

this case, the connection ultimate capacity will be equal to the vertical tensile strength of the transverse reinforcement.

Comparing this load transfer mechanism with the load transfer mechanism for a beam failing in single shear indicates that the shear carried by the concrete in the compression zone is another component that can resist the beam shear failure which is missing in the current case as confirmed by Zuhua Wang (1987) when testing indirectly loaded beams. Also, Smith & Fereig (1974) recorded a sudden reduction in the compression zone compression strain and a sudden tensile strain increase in the longitudinal reinforcement after the diagonal cracking initiation for indirectly loaded beams as a confirmation that the compression zone is not that effective in the indirectly loaded beams. Thus, it is logic to use the embedment depth instead of the full beam depth in the breakout cracking load and the ultimate load calculation of the pile connection. Additionally, the stiffness of the beam just after the bond cracks around the pile will be less than the stiffness of the same beam loaded from the top in compression because of the cracking inside the beam at the bolts and the plate ends and because of the breakout cracks afterwards.
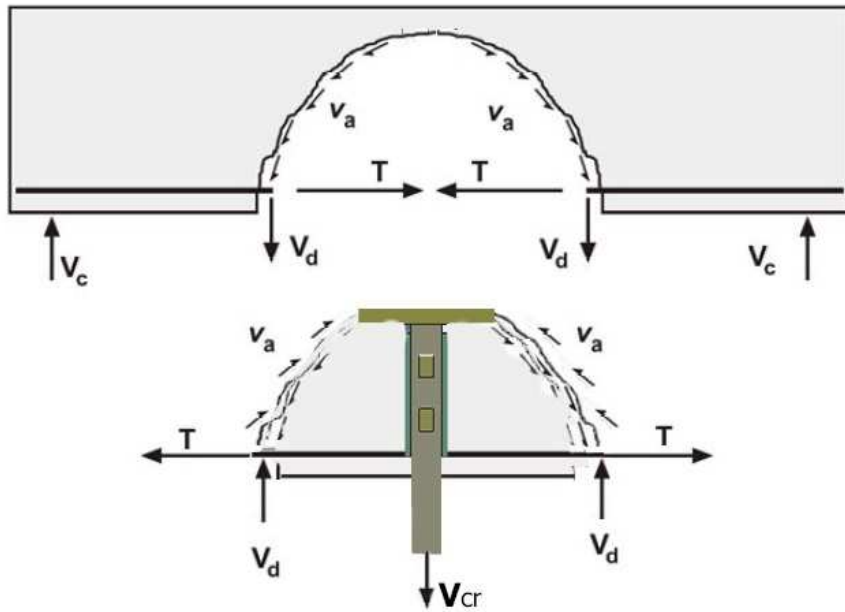
Figure 3-13 Load transfer mechanism for the connection without transverse reinforcement
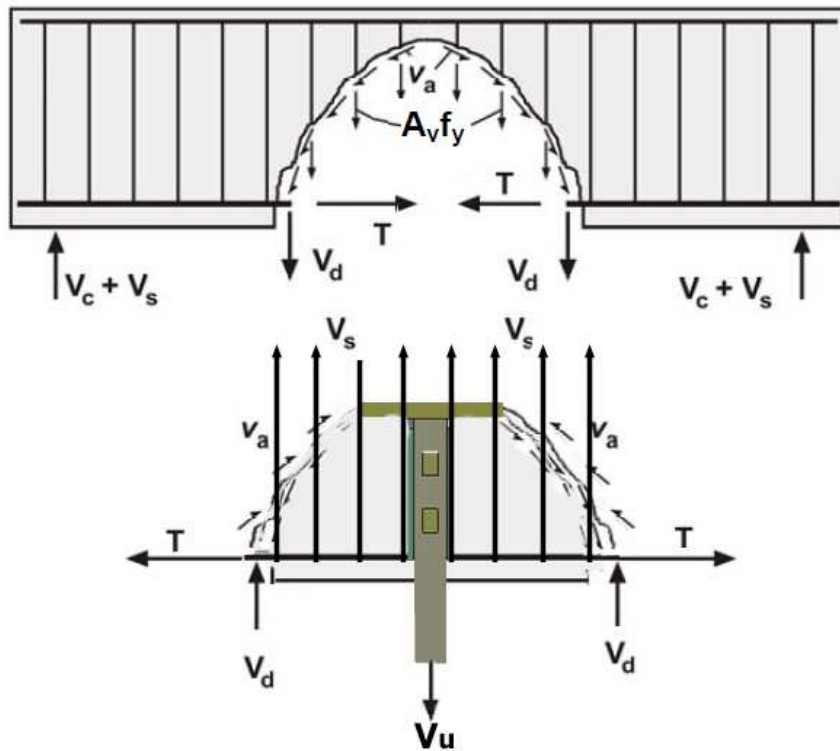
Figure 3-14 Load transfer mechanism for the connection with transverse reinforcement (Stirrups)

3.7.3   General Ultimate Load and Load Displacement Relationship

The observed breakout cracking behaviour was closer to the single shear cracking behaviour of a concrete beam because cracking propagated diagonally in one direction only. The capacity of the specimen upon reaching the breakout cracking load was primarily comprised of three components: dowel action of longitudinal reinforcement; stirrups resistance; and aggregate interlocking resistance. If the sum of the three components was less than the breakout cracking load, the ultimate load would be equal to the breakout cracking load; and if the sum is higher than the breakout cracking load, the ultimate load would be more than the breakout cracking load.

The load-deformation responses of specimens can be generally described as follows. The beam's mid-span vertical displacement increased linearly until the first flexural crack occurred. Then the displacement increased approximately linearly with higher rate up to the breakout cone formation when a small load increase caused excessive displacement. Depending on the beam variables, the beam either gained stiffness again after the breakout cracking load and the load increased as displacement increased causing higher ultimate load than the breakout cracking load, or the beam softened till failure took place.

The mid-span displacement at the lower level of the beam (i.e. the other side of the beam) was also recorded. It was observed that it was approximately the same as that at the upper level of the beam until breakout cracks were formed. After the breakout cracks formation, the displacement of the upper level of the beam increased excessively and the displacement of the lower level of the beam began to decrease gradually and the rest of the beam (i.e. the beam body excluding the breakout cone) began to bounce back with a

76

small rate. The difference between the two displacement values represented the breakout crack opening and the movement of the breakout cone. This confirms the reason for the cracks occurring at the unloaded side of the beam after reaching the ultimate load (which was subjected to internal compression not tension forces up to the breakout cracking load).

Moreover, it was observed that the vertical displacement in the pile shaft was slightly higher than that at the mid-span of the beam. This is due to number of displacements: displacement between the pile and the bolt due to the hole clearance, displacement between the bolt and the cylinder due to the hole clearance, displacement due to cracking in front of the bolt, and the deformation of the pile and pile cap components.

3.7.4   General Ductility:

Ductility is a desirable feature of any structural design as it safeguards a structure against unpredicted overloading. Generally, ductility factor is indicated as the ratio of displacement at failure to that at yielding. Most of the international codes prefer to use ductile design rather than a brittle one. They also indicate lower capacity reduction factors when using brittle beams design especially during an unexpected event requiring ductile behaviour as seismic events. Although, most of the tested beams had brittle failure, the presence of the reinforcement can enhance the ductility of the beams till it reaches an acceptable behaviour. Thus, the ductility of the tested beams will be compared to indicate the effects of different variables on the connection ductility.

Unfortunately, some of the specimens did not reach yielding till failure. Thus, the ductility factor cannot be calculated for all of the beams, however, we need a criteria to compare the tested specimens with each other regarding their ductility rather than to have a global criteria. Thus, the maximum mid-span deflection was used as a measure for ductility. Table 3-2 shows the measured mid-span displacement to indicate the beam ductility. It is clear that mid-span displacement can only be used as an indicator to the connection ductility if the compared specimens had approximately the same stiffness or they had similar ultimate loads at different displacements to achieve comparable patterns, which was not the case in some of the tested groups. Thus, the strain energy absorbed by the specimen up to failure was used as a comparison tool to indicate the ductility enhancement due to variables change in the specimens. Thus, the beam toughness/ strain energy, defined as the area under the load-mid-span displacement curve up to the 0.6 of the beam ultimate load after the beam softening, was calculated to measure the energy absorbed by the tested beams and the results are presented in table 3-2.

It should be mentioned that, in spite of the very small mid-span displacement that was recorded at the ultimate load for most of the beams, it is clear that the tested beams failed at a much higher mid-span displacement combined with lower connection capacity. This means the connection will have ductile behaviour before failure with adequate warning when it is subjected to displacement control loading (i.e. yielding of support, seismic event, etc.). However, if the connection is subjected to load control loading (i.e. gravity loads on the foundation) the connection will fail in a very brittle manner without warning.

Table 3- 2 Test results of the four tested groups

Group	Specimen	First cracking load(kN)	Breakout cracking load(kN)	Ultimate load (kN)	mid-span Displacement at breakout (mm)	mid-span Displacement at ultimate (mm)	Strain Energy at 0.6 of the Ultimate Load** (kN.mm)
First group	T1	100	154	154	2.55	2.55	1187***
	T2	100	200	201	1.64	3.6	2031***
	T3	100	232	232	2	2	2371***
Second group	T2	100	200	201	2.3	2.3	2031***
	T2-40*	115	211	211	1	1	4639
	T4	110	201.7	204	1.2	2.0	5641
	T5	115	239.5	239.5	1.6	1.6	5978
Third group	T2	100	200	201	2.3	2.3	2031***
	T2-40*	115	211	211	1	1	4639
	T6	150	222.5	222.5	1.3	1.3	7280
	T7	155	252.3	252.3	1	1	8340
Forth group	T2	100	200	201	2.3	2.3	2031***
	T2-40*	115	211	211	1	1	4639
	T8	105	208.5	256.3	1	6.4	8994
	T9	110	208.4	253.2	1.01	27.3	8170

* T2-40 is the modified beam of beam T2 to account for the concrete strength change from 30MPa to 40MPa.

** Strain energy is mainly measured at first load equal to 0.6 of the ultimate load to have the same criteria for each group, but the full strain energy up to failure can be much higher than the calculated values in this table.

*** This strain energy was not up to 0.6 of the ultimate load it was up to approximately 0.8 of it.

3.7.5 General Reinforcement Steel Strain, and Pile Cap's Plate Strain:

The longitudinal steel strain, transverse steel strain, and pile cap's plate strain were helpful to understand the actual internal behavior and cracking inside the tested specimens, especially if the strain gauges were located appropriately where cracking is expected to occur.

The main longitudinal reinforcement strain increased linearly as the applied load increased until the first flexural cracking load was reached; subsequently, the strain

increased excessively as the steel carried all the internal tension at the cracks. As load continued to increase up to the breakout cracking load, the steel strain increased at a much higher rate. At the breakout cracking load, it was obvious that the longitudinal steel strain increased suddenly without load increase due to the dowel action of the longitudinal reinforcement after the breakout cracking occurred and the extra normal force in the longitudinal steel induced from the horizontal pressure from the aggregates at the two sides of the breakout cracks. At this point, the behavior depended on whether the stirrups and the concrete cover could provide enough support to the longitudinal bars for its dowel action or not. When they provided enough support, the strain in the longitudinal steel continued to increase and the load continued to be transferred across the diagonal cracks to the rest of the beam. When the concrete cover failed, excessive vertical displacement took place at the breakout cone leading to large crack width which caused aggregate interlock loss and excessive longitudinal steel strains and stirrups strain began to increase excessively because most of the load was transferred to the stirrups. Consequently, the longitudinal steel strain reduced even if the breakout cone displacement was increasing.

It was observed in all of the tested beams that the interior longitudinal reinforcement recorded higher strains than that of the exterior longitudinal reinforcement. Also, the stirrups' strain was negligible before the breakout cracking initiation when a sudden increase in the stirrups strain occurred. It was clear that the stirrups closer to the pile shaft experienced higher strains than that of the stirrups farther from it. This behaviour was also recorded and indicated by Talbot, A. N. (1909) when they tested Reinforced concrete

beams failing in shear mechanism. The stirrups strain increased with the vertical displacement until the stirrups yielded and necking was observed just before stirrups failure.

Finally, the pile cap's plate strain indicated the amount of bending the plate experienced at the location of the strain gauge (i.e. approximately quarter the plate width). Thus, when the breakout cone initiated at the plate sides or farther, the plate experienced small strain compared to the case of the breakout crack crossing the plate. When the crack crossed the plate, it experienced excessive strain due to crack bridging, i.e., part of the load was transferred through the plate between the two sides of the crack. At the beginning of loading, the plate deformed slightly. After the crack reached the plate level, mostly due to crack initiation at the tip of the plate, the plate strain decreased slightly. As the breakout cone moved, the plate strain increased apparently due to the load transferred from the stirrups through the crack to the concrete at the edge of the plate. Compression strains were noted in the pile cap's plate while only tension strains were expected at the top of the plate. This may be due to the deformation associated with volume change causing small compression strains.

3.8 Derived Behaviour of Beam T2 with 40 MPa Compressive Strength (T2-40)

Due to the unintended variation of concrete compressive strength from 30 MPa in first batch to 40 MPa in second batch, it is necessary to adjust the results to the control beam T2 cast with 30MPa compressive strength to reflect the behaviour of the same beam if the concrete strength were 40 MPa (will be denoted herein as T2-40). The adjusted results

will be used as the control specimen for the 6 beams which had 40 MPa compressive strength.

Three different methods were used as representative of the T2-40 as shown in Figure 3-15. These methods include: the modified ACI code shear equation; the modified CSA code shear equation; and using a well calibrated finite element model to simulate the behaviour of beam T2-40. The two modified equations are used for calculating the connection capacity as will be discussed in chapter 5, while the finite element model calibration is reported in detail in Chapter 4.

3.8.1   The modified ACI equation (Equation 5.3 in chapter 5)

In this method, the load capacity of the beam is multiplied by the ratio of the calculated cracking load (using Equation 5.3 in chapter 5) to the breakout cracking load of beam T2. The ultimate load is then given by the sum of stirrups capacity and the breakout cracking load. This method gives a reasonable load-displacement curve for the beam, but may not correspond to the strain gauge data for longitudinal steel and stirrups because different beam behaviour may apply. Also, the breakout cracking load is expected to be higher and may be equal to the ultimate load.

3.8.2   The modified general CSA equation (Equation 5.21 in chapter 5)

The load capacity of the beam is multiplied by the ratio of the calculated ultimate load (using Equation 5.21 in chapter 5) to the ultimate load of beam T2. The breakout cracking load is considered as the ratio between the two ultimate loads multiplied by the measured breakout cracking load of beam T2. This method may be preferred over the

ACI modified equation method because it accounts for the change in the concrete strain due to the change in fc'. (i.e. as fc' increases, the beam capacity increases and the concrete strain increases accordingly). This increased concrete strain will decrease the tensile capacity of the concrete. At the same time, increasing fc' caused the concrete tensile capacity to increase. Thus, this equation account for the overall behaviour of the beam more than the ACI equation. However, the strain gauge data for longitudinal steel and stirrups is still not accounted for.

3.8.3   The results of well calibrated finite element model (discussed in Chapter 4)

As will be discussed in Chapter 4, a detailed finite element model was developed using LS-DYNA and was calibrated using the nine tested beams and three specimens of Angelakos, et al. (2001). The calibrated finite element model (FEM) using the material properties of beams T4, T5, T6, T7, T8, and T9 was used to build a new model for beam T2-40. This model gave approximately the same load-displacement behaviour established using Equations 5.3 and 5.21 until the breakout cracking load was reached as shown in figure 3-15. The behaviour changed afterwards. The main advantage of this method is that strain at any point of the beam can be checked and compared with data recorded from the physical beams tests.

Figure 3-15 demonstrates that the three methods yielded similar load-displacement curves. The beam behaviour before the breakout cracking was approximately the same; however, the finite element model predicted that the connection ultimate load is equal to its breakout cracking load. The two other methods could not expect this behaviour, however, the expected ultimate loads from the three methods were so close (215.55 kN,

83

217.88 kN and 211 kN). Thus, the predictions of the finite element model for beam T2-40 will be used as the FEM can predict the strain in the longitudinal reinforcement, stirrups, and pile cap's plate, which can be compared with the other tested six beams having 40 MPa concrete compressive strength.
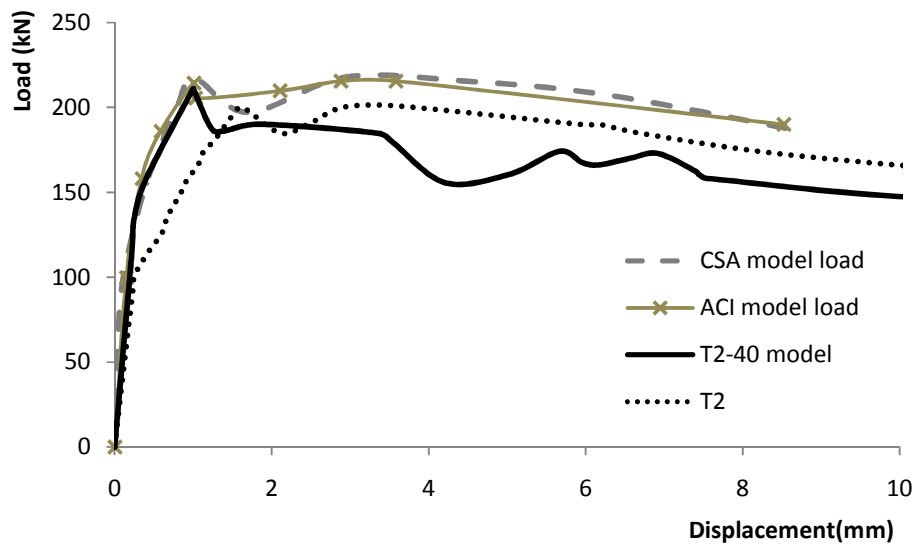
Figure 3- 15 Load displacement relationship for beam T2-40 using three methods

3.9 Discussion

3.9.1   First Group: Effect of pile embedment depth

Three specimens T1, T2, and T3 were tested in this group to investigate the effect of pile embedment depth in the grade beam. The tested embedment depths were: 152 mm (T1), 203 mm (T2), and 277 mm (T3). The concrete compressive strength, plate width and the longitudinal and transverse reinforcements were kept constant.

3.9.1.1 Crack pattern and mode of failure

T1, T2, and T3 had approximately the same crack pattern, but the size of the breakout cone increased as the embedment depth increased. Given that the angle of breakout crack was approximately the same in the three beams (i.e., $\theta = 35^o$), the size of the breakout cone at tension fibers can be given by:

$$\text{Breakout cone dimension} \cong \text{plate width} + 2\cot\Theta^o * \text{embedded depth} \qquad \textbf{3. 1}$$

Thus, the capacity of the connection increases approximately linearly with the embedment depth. Also, the failure mechanisms in T1, T2 and T3 were brittle at their ultimate load.

3.9.1.2 Cracking load, Breakout cracking load, and Ultimate load

As shown in table 3-2, the first cracking load was not affected at all by the variation in the embedment depth. However, the breakout cracking load and the ultimate load increased approximately linearly with the embedment depth. The breakout cracking loads for T1, T2, and T3 were 154, 200 and 232 kN, respectively, while the ultimate loads were 154, 201 and 232 kN, i.e. an increase of 30% and 51% as the embedment depth increased from 152mm to 203mm and to 254 mm, respectively. These ultimate load capacity values, however, are much less than the calculated ultimate load capacity of the beam in flexure or shear (650 kN, and 462 kN) using Response 2000. This indicates the importance of evaluating the connection capacity and not relying on the beam capacity.

The capacity of the specimen after reaching the breakout cracking load was primarily comprised of three components: the dowel action of longitudinal reinforcement; the stirrups resistance; and the aggregate interlock resistance. Both T2 and T3 gained more stiffness after the breakout cracking load, however, only T2 sustained more load beyond the breakout cracking load as the sum of the three components were more than that of the breakout cracking load. On the other hand, for T3, this sum was less than the breakout cracking load and as a result, the ultimate load was equal to the breakout cracking load. T1 (with the smallest embedment depth) failed directly after reaching the breakout cracking load mostly due to the small contribution of the aggregate interlock.

3.9.1.3 Stiffness and load displacement relationship

As shown in Figure 3-16, at the beginning of loading and before the initiation of cracks, the stiffness of the three beams was approximately the same and similar to the full beam stiffness when loaded by bearing on its extreme fibers. Then, the stiffness of the connection after the first flexural cracking increased as the pile embedment depth increased; however, the stiffness of the connection was much less than the full beam stiffness. As the load increased more than the breakout cracking load, stiffness of T1 decreased suddenly as the breakout cracking initiated. On the other hand, T2 and T3 exhibited increase in stiffness followed by softening behaviour as the displacement increased excessively with load reduction. Even though T1 had the same stirrups ratio and longitudinal reinforcement as T2 and T3, its stiffness did not increase again after the breakout cracking load, which indicated the importance of the aggregate interlock share to the ultimate load after the breakout cracking load. It was observed that the vertical

displacement at the unloaded side of the beam also increased with the load increase till the breakout crack initiation when it began to reduce and the rest of the beam began to bounce back with a small rate.
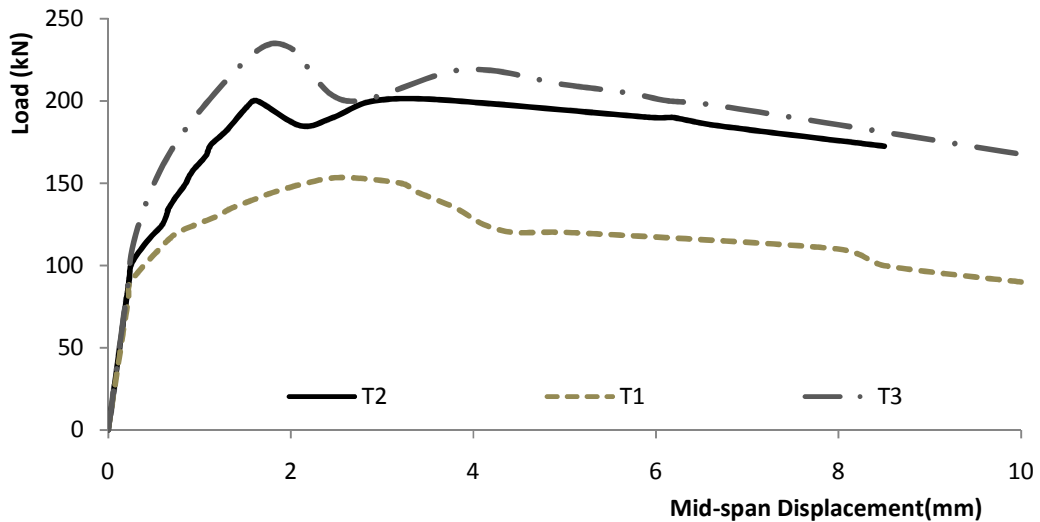
Figure 3- 16 Load mid-span displacement

3.9.1.4   Ductility and strain energy

Inspecting table 3- 2, it is clear that there is no specific pattern that can be concluded for the mid-span displacement, i.e., T1, T2, and T3 had displacements of 2.55, 3.6 and 2 mm at ultimate load. Even though T3 displayed the largest ultimate load, it gave the least mid-span displacement at that load. Also, T2 experienced higher mid-span displacement at ultimate load than T1 but its mid-span displacement at breakout cracking load was less than that of T1. Thus, it is more reliable to consider the strain energy as ductility indicator. From table 3- 2, the calculated strain energy was 1187, 2031 and 2371 kN.mm for T1, T2, and T3, respectively. As the embedment depth increased from 152 to 203 and

254mm the strain energy increased by 70%, and 100%, respectively indicating that the connection ability to absorb energy increases with the pile embedment depth increase.

3.9.1.5   Reinforcement Steel, and Pile Cap's Plate Strain

Figure 3-17 shows that the longitudinal steel strains in T1, T2 and T3 were the same till the first cracking load. The strain then suddenly increased for both the outer and inner longitudinal reinforcement. The more the embedment depth, the less the longitudinal reinforcement strain were observed. This indicates that the strain distribution in the beam depended mainly on the embedment depth. Thus, the connection capacity should be evaluated considering the embedment depth of the pile shaft. Also, beams with shallower embedment depths have higher tension strains indicating that its cracked concrete shear strength would decrease. After the breakout cracking load, the strain increased excessively till the stirrups yielded. At this point, the longitudinal reinforcement strain decreased due to concrete cover spalling and loss of bond occurred. The longitudinal steel did not reach yielding before ultimate load, which means less ductility and smaller displacements at the ultimate load, but its strain was so close to yielding at the connection ultimate load.
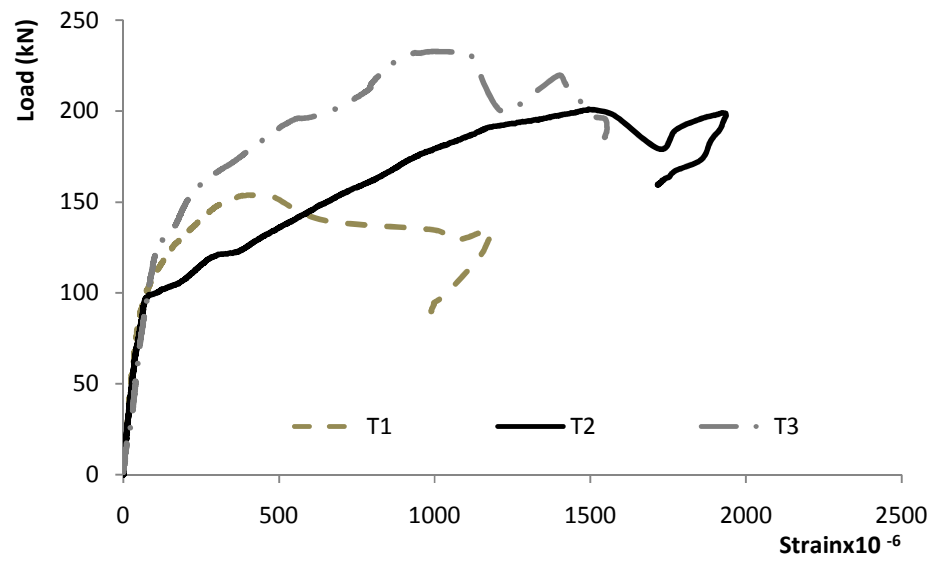
(a)
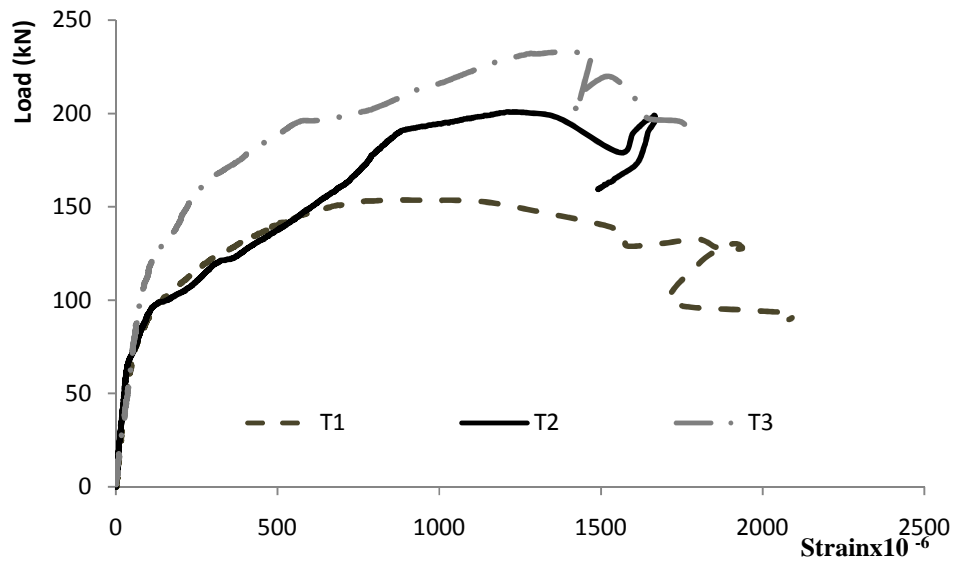
(b)

Figure 3- 17 Load-longitudinal steel strain: (a) outer bars; (b) inner bars

Figure 3-18 clearly shows that the stirrups contribution before the diagonal crack initiation was negligible. After the breakout cracking, the stirrups strain suddenly increased at constant rate until the beam and the stirrups failed (both outer and inner stirrups). Also, increasing the pile embedment, increased the breakout cracking load and

89

as a result delayed the strain increase in stirrups due to crack bridging and sustaining the beam integrity after the breakout cracking.

(a)
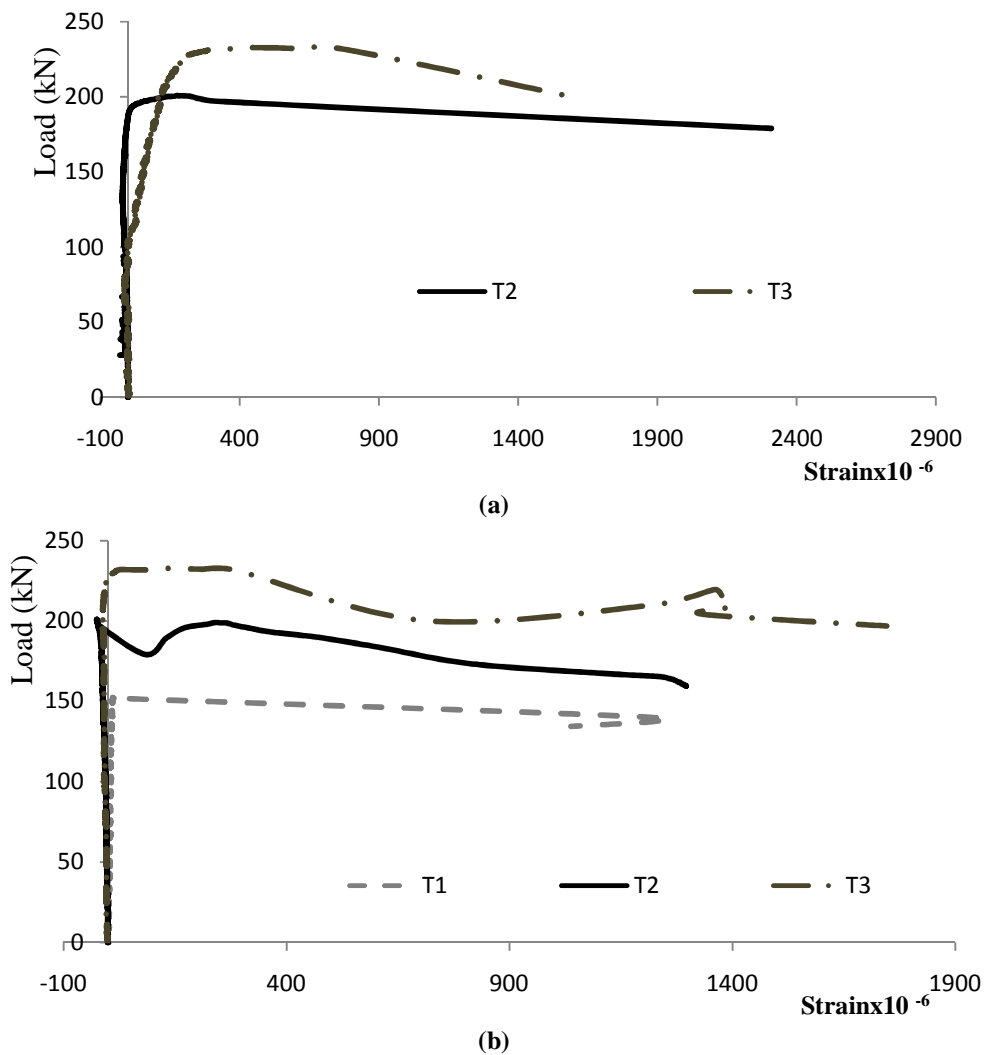
(b)
Figure 3-18 Load-stirrups strain: (a) outer stirrups; (b) inner stirrups

The strain of the pile cap's plate was approximately the same for T1, T2 and T3 till the first cracking occurred as shown in Figure 3-19. Afterwards, the strain was slightly less for beams with higher embedment depth owing to the lower beam deformation

accompanied with higher embedment depth. It is noted that the pile cap did not contribute to the breakout cracking load as its strain was less than 66×10^{-6} at the breakout cracking load.
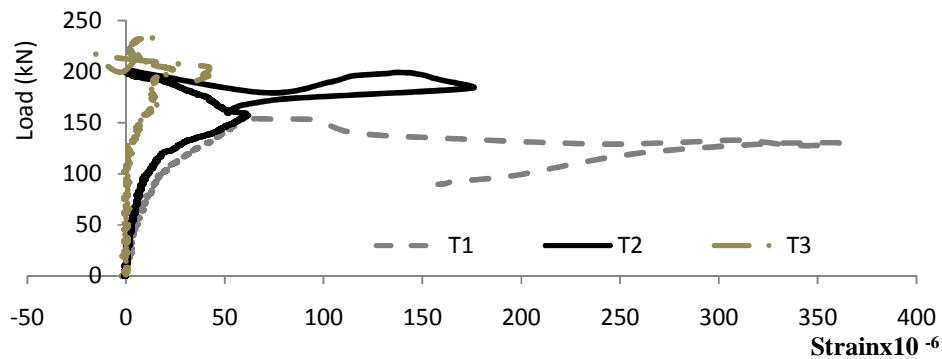
Figure 3-19 Load pile cap's plate strain relationship

3.9.2   Second Group: Effect of Pile Cap's Plate Width

Three different plate sizes, covering the range of pile cap configurations used in practice, were tested. They were as follows: 165 x165 x 19 mm (T2); 191 x191 x 19 mm (T4); and 229 x 229 x 25.4 mm (T5). The embedment depth, longitudinal reinforcement, and stirrups were kept constant as shown in table 3-1. The concrete compressive strength for T4 and T5 was 40 MPa, while it was only 30 MPa for T2. Thus, the modified response of T2-40 was established as discussed previously. However, the results will include both T2 (fc' = 30 MPa) and T2-40 (fc' = 40 MPa) for comparison purposes.

3.9.2.1   Crack pattern and mode of failure

T2, T4 and T5 had approximately the same crack pattern, but the size of the breakout cone differed; it increased as the plate width increased. Given that the angle of the breakout crack was approximately 35°, the size of the breakout cone at the tension fibers

91

was as indicated in equation 3.1 and can be approximated by using the lesser of (b_{plate}+2.5 d_{emb}) or (3 d_{emb}).. The breakout crack initiated at the plate edge (i.e. not at a distance equal to plate thickness as recommended in ACI 318 Appendix D) and the failure mechanism was brittle at ultimate load. Only 4 stirrups from the two sides were resisting the pile load and the stirrups component did not increase with the plate width increase. It is anticipated, though, that more stirrups would be involved for smaller stirrups spacing and larger plate sizes.

3.9.2.2   Cracking load, Breakout cracking load, and Ultimate load

As shown in table 3- 2, the first cracking loads were approximately the same for T2-40, T4, and T5, while the ultimate loads were equal to 211 kN, 204 kN, and 239.5 kN, respectively. The effect of the plate was complex: the capacity decreased slightly (4%) when the plate width increased from 165mm to 190mm, and increased by 13.5% when its width increased from 165 mm to 229mm. Several factors could interplay could cause this behavior including: increased breakout cone dimensions which increased the number of stirrups contributing to the connection ultimate capacity; a shift of the diagonal crack position to be farther from the load hence shortening the shear span and reduced flexural tension stresses; and decreased surface area of the concrete resisting cracking at the plate level. Thus, a finite element study was undertaken to better understand the effect of this variable on the connection behavior, which is reported in Chapter 4.

3.9.2.3 Stiffness and load displacement relationship

As shown in Figure 3-20, the connection stiffness was almost identical for all beams before the first cracking initiated. The beams had different breakout cracking load but their stiffness remained approximately the same. However, after the breakout cracking load (also ultimate load for T2-40 and T5), the connection stiffness decreased suddenly. Only T4 had slightly higher ultimate load than its breakout cracking load. The fact that T2-40, T4 and T5 had the same load capacity after the breakout cracking load suggests that the number of stirrups contributed to the resisting load was approximately the same. Thus, it is clear that the plate dimensions had minor effects on the beam stiffness up to the breakout cracking load.
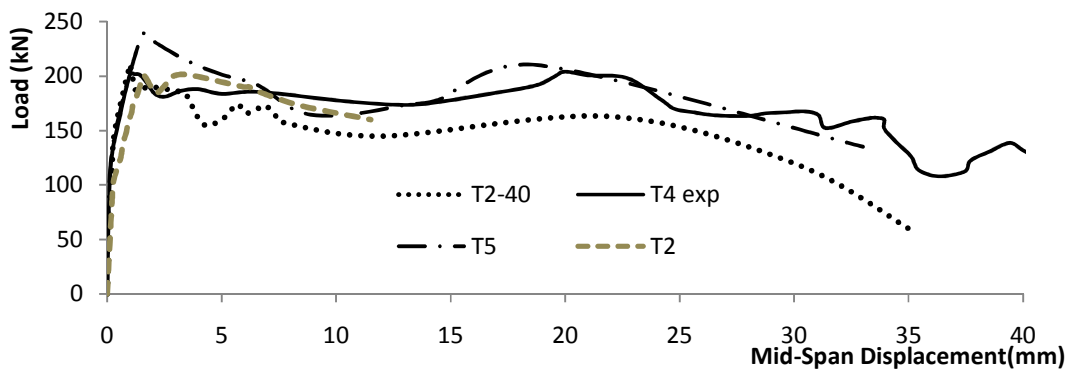
Figure 3-20 Load mid-span displacement

3.9.2.4 Ductility and strain energy

As shown in table 3-2, T2-40, T4, and T5 had strain energies equal to 4639, 5641, and 5978 kN.m, respectively. These results indicate that the strain energy, and hence the ductility slightly increased as the plate width increased.

3.9.2.5   Reinforcement Steel, and pile cap's plate Strain

Figure 3-21 shows that inner and outer longitudinal steel had approximately the same strain up to the breakout cracking load. Afterwards, the strain increased suddenly then loss of bond occurred.   In general, there was no observed clear trend for variation of strain in longitudinal reinforcement with plate width.
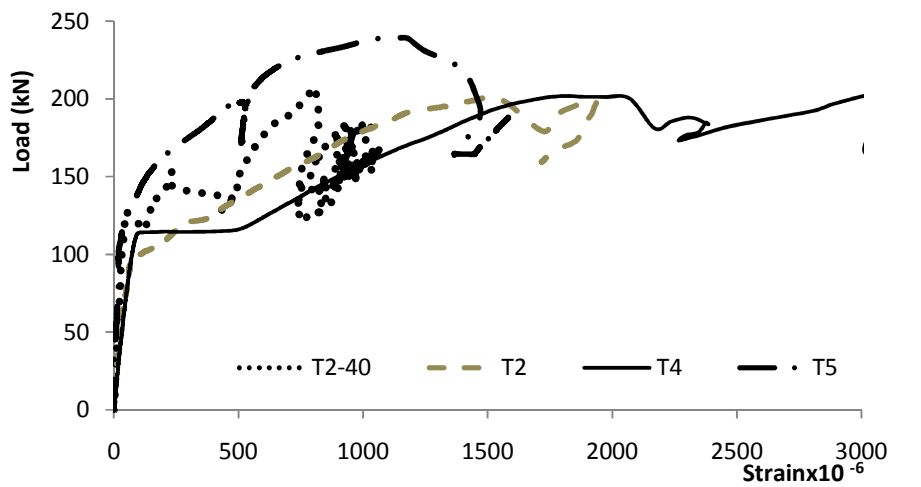
(a)
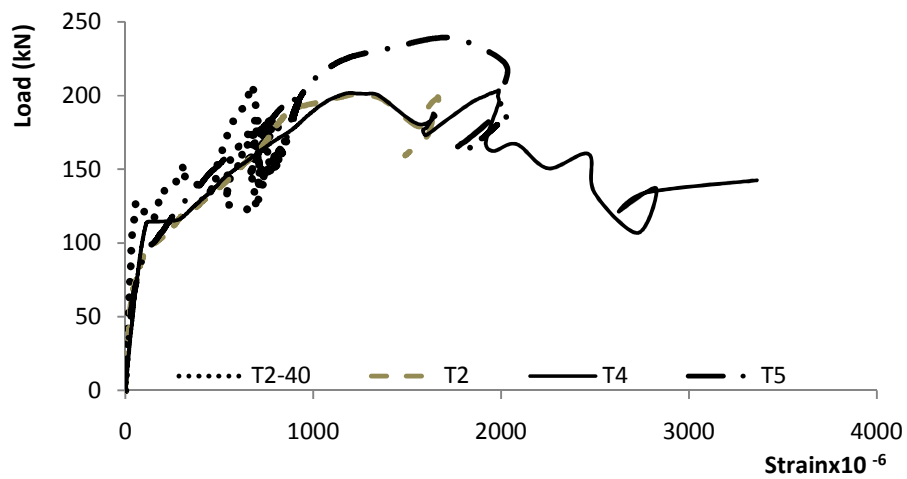
(b)

Figure 3- 21 load-longitudinal reinforcement strain: (a) outer bars; (b) inner bars

Figure 3-22 display the variation of stirrups strain with the applied load. It is noted that the strain was negligible before the diagonal crack initiated and a sudden increase in its strain was recorded just after the breakout crack initiated. An increase in the plate width increased the breakout cracking load in T5 and decreased it in T4. The stirrups in T4 contributed to higher ultimate load than the breakout cracking load. It is also noted that the strains in the inner stirrups were much higher than that of the outer stirrups as they were closer to the pile shaft.
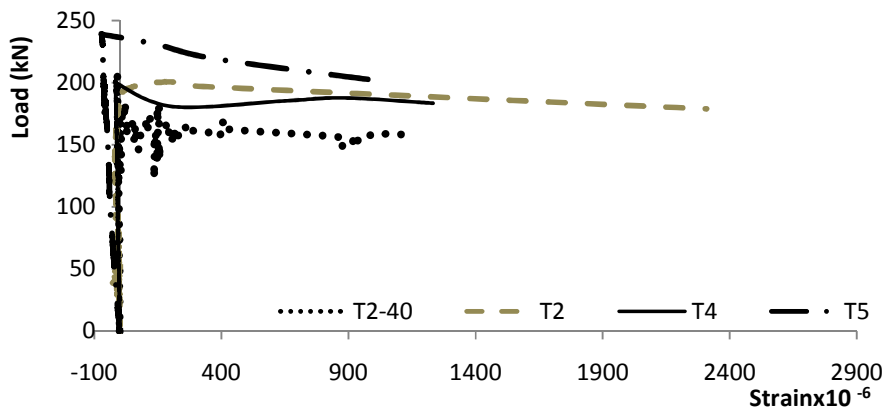
(a)
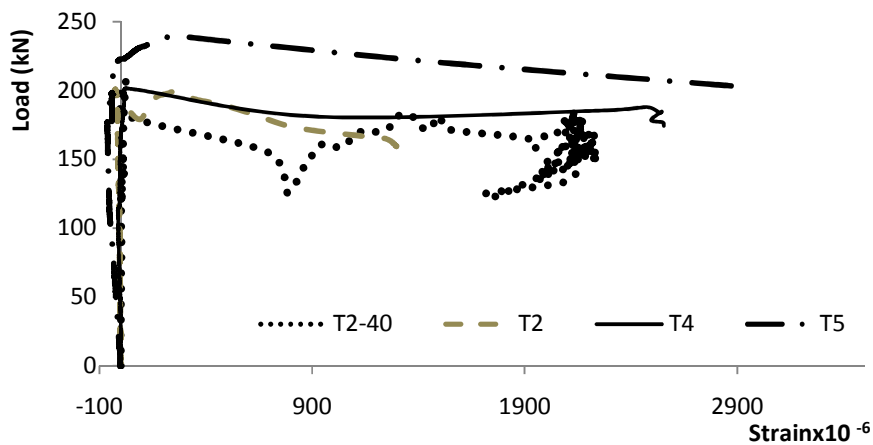
(b)

Figure 3-22 Load-stirrups strain: (a) outer stirrups; (b) inner stirrups

Figure 3-23 shows that the strain in the plate increased as the plate width increased, but it was so small (less than 110×10^{-6}), which indicates that the plate did not deflect much and that the breakout cracking began mainly from the tip of the plate.
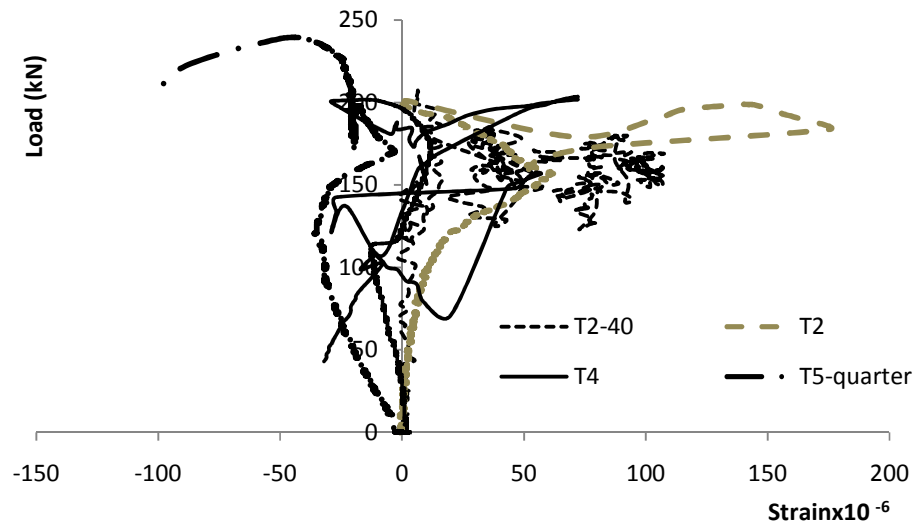
Figure 3-23 Load pile cap's plate strain relationship

3.9.3 Third Group: Effect of Longitudinal Reinforcement

In this group, three different longitudinal reinforcement ratios were tested, i.e. 0.35% (4-15M in T2-40), 0.53% (4-20M in T6), and 0.89% (4-25M in T7). The embedment depth, plate width and the stirrups configuration were kept constant.

3.9.3.1 Crack pattern and mode of failure

The tested beams had approximately the same crack pattern, but the crack widening occurred at higher load as the reinforcement ratio increased because of the dowel action effect. The angle of the breakout crack was approximately the same, 35°. The failure mechanism was brittle as the ultimate load was equal to the breakout cracking load.

96

However, the behaviour after reaching the ultimate load was enhanced by the increase in longitudinal reinforcement.

3.9.3.2 Cracking load, Breakout cracking load, and Ultimate load

As shown in table 3-2, the first cracking load increased as the longitudinal reinforcement ratio increased. The first cracking loads were 115, 150 and 155 kN for T2-40, T6, and T7, respectively, which are the same values as for three point direct loading without any reduction. This confirms that the connection did not affect the beam behaviour until the first cracking load was reached. The breakout cracking (and ultimate) loads of T2-40, T6, and T7 were 211, 222.5 and 252.3 kN, indicating an increase in the breakout cracking load as the longitudinal reinforcement ratio increased.

The sum of the contributions from concrete aggregate interlock, longitudinal reinforcement dowel action, and the stirrups was less than the breakout cracking load for the three beams. The beams failed after the failure of the stirrups by necking, indicating the importance of the transverse reinforcement. The longitudinal reinforcement and the stirrups formed a truss that transferred the load between the two beam segments separated by the breakout cracks. If the stirrups yielded, the longitudinal reinforcement lost its support and was only supported by the concrete cover causing its spalling.

3.9.3.3 Load-displacement relationship

Figure 3-24 shows that the stiffness of the specimens increased as the reinforcement ratio increased until first cracking occurred. This behavior was even more visible as the load increased till the breakout cracking initiated. Afterwards, the stiffness decreased suddenly

97

as the displacement increased excessively while the beam capacity decreased. It should be noted that after the first cracking load, the stiffness was much less than the directly loaded beam stiffness if subjected to three-point direct loading. In spite of the very small mid-span displacement that was recorded at the ultimate load, the three tested beams failed at a much higher mid-span displacement.
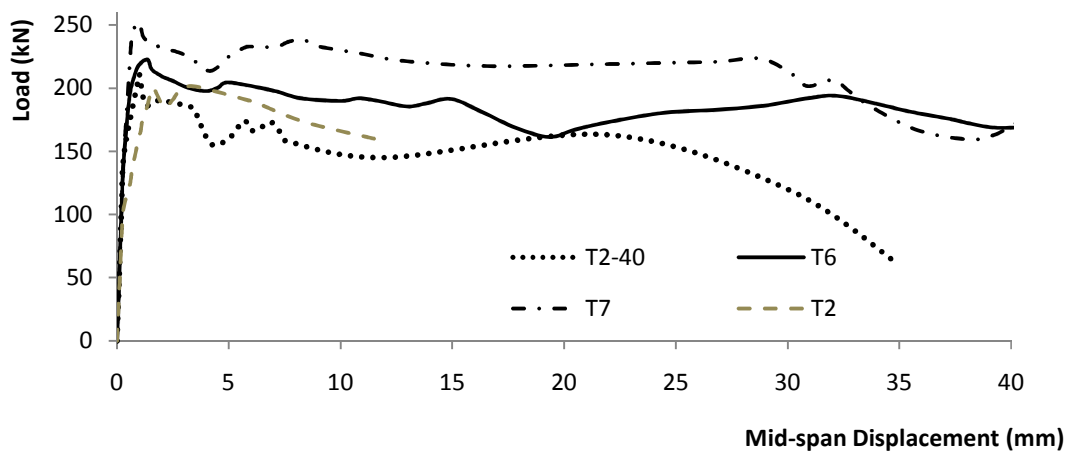
Figure 3-24 Load mid-span displacement

3.9.3.4 Ductility and strain energy

The strain energy for T2-40, T6, and T7 were calculated to be 4639, 7280 and 8340 kN.m, respectively, which indicates significant increase in the connections ductility as the longitudinal reinforcement ratio increased after their ultimate load. For example, as reinforcement ratio increased from 0.35% to 0.53% and 0.89%, the beam ability to absorb energy increased by 57%, and 80%.

3.9.3.5 Reinforcement Steel, and pile cap's plate Strain

Figure 3-25 shows that the longitudinal steel strain decreased as the longitudinal reinforcement ratio increased throughout the load test. It is also noted that the strain increased significantly after the first cracking load was achieved. However, beam T7 experienced small increase in strain as the forces transferred from the concrete to the steel were so small to cause large strain in the 4-25M steel bars. After the breakout cracking load was reached, the longitudinal steel strain increased excessively up to the concrete cover spalling or the stirrups necking. It is also observed that the longitudinal reinforcement did not yield before ultimate load; however, it yielded at the ultimate load and before failure occurred. This is consistent with the observed large difference between the beam deformation at ultimate load and its vertical displacement just before failure.

It is also observed from Figure 3-25 that the inner longitudinal reinforcement had higher strain than the outer longitudinal reinforcement, which indicates that the breakout cracking initiated at the plate edges and did not extend to the beam surface, hence initial load transfer mechanism failure only started when diagonal tension stress reached the concrete tensile strength, or the fracture energy at the cracking surface exceeded the fracture energy capacity of concrete. Thus, when higher reinforcement ratios are used in this connection, the inner reinforcement is more effective than the outer reinforcement and the longitudinal reinforcement is recommended to be distributed using a band width concept depending on the used longitudinal reinforcement ratio.
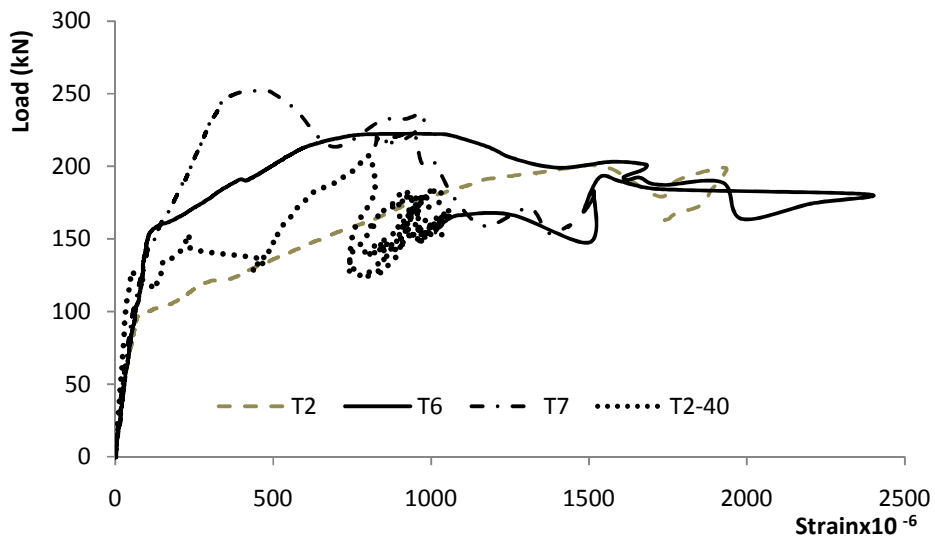
(a)
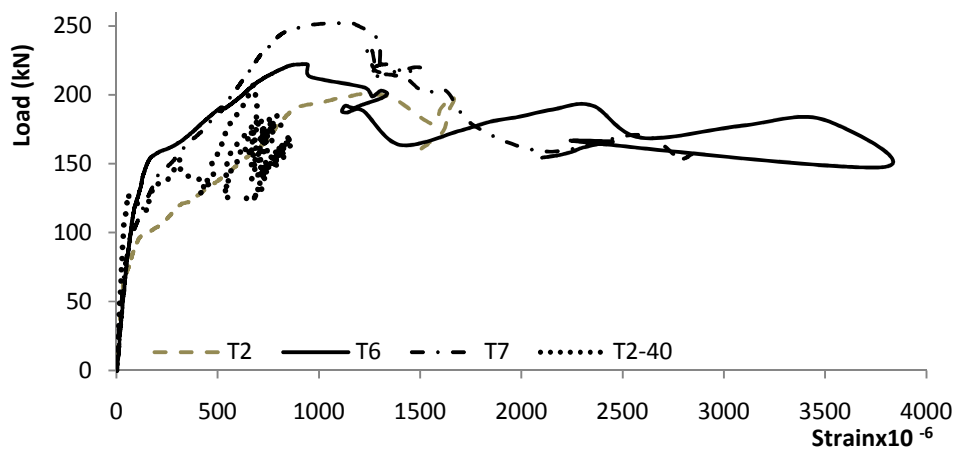
(b)

Figure 3-25 load-longitudinal reinforcement strain: (a) outer reinforcement; (b) inner reinforcement

Figure 3-26 shows that the stirrups contributed to the resistance only after the initiation of diagonal crack because the beams did not yield before ultimate load was reached. As a result, the deformation was small and failure was brittle. The breakout cracking load increased as the longitudinal reinforcement ratio increased. Consequently, high stirrups strains occurred at higher loads, reaching a peak that represented the stirrups ultimate

100

capacity. However, at this stage the crack width was too large to have adequate aggregate interlock, and consequently the breakout cracking load represented the ultimate load. Similar to second group, the inner stirrups contributed more to the beam capacity than the outer stirrups.

On the other hand, the stirrups can have significant effect on the beam behaviour especially with large longitudinal reinforcement ratios. This was inferred from the decrease of the longitudinal reinforcement strain due to concrete spalling only after the stirrups experienced large strains. Thus, higher percentage of transverse reinforcement can increase the connection capacity not only because of the stirrups contribution to the capacity but also because it enhances the contribution of the longitudinal reinforcement to the overall beam stiffness.

Finally, the maximum strain of the pile cap's plate up to the ultimate load was 183×10^{-6} which means the pile cap plate was not crossed with the breakout cracks and the crack initiated at the plate edges.
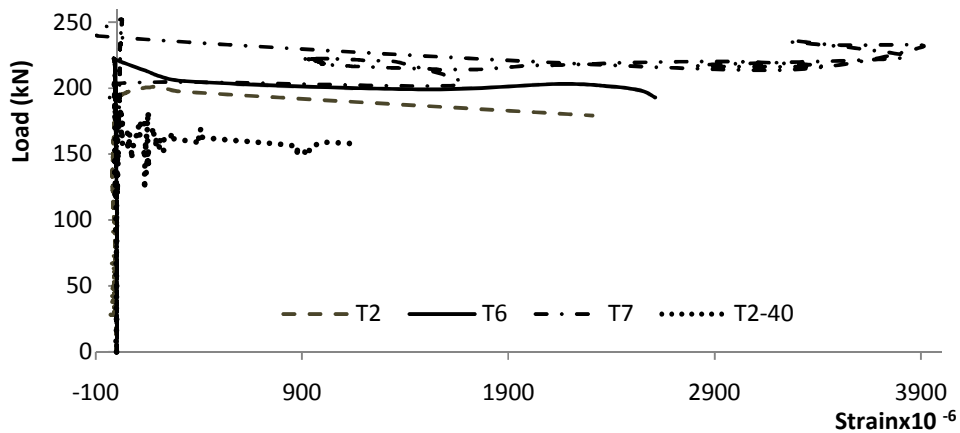
(a)
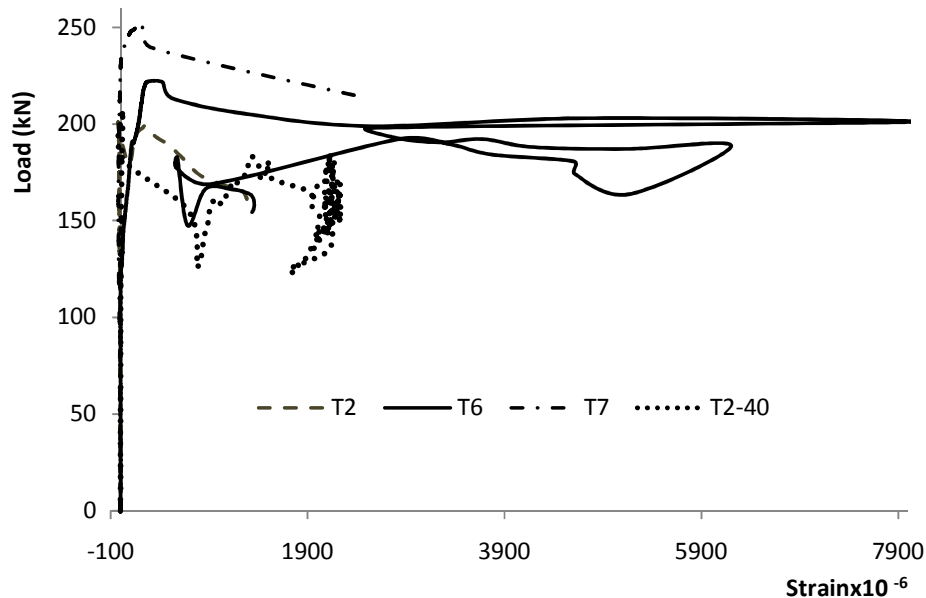
(b)
Figure 3-26 Load stirrups strain: (a) outer stirrups; (b) inner stirrups

3.9.4 Forth Group: Effect of transverse reinforcement

In this group, three beams with different transverse reinforcement (stirrups) were tested. All beams were reinforced with #2 rebar (6.35 mm diameter). T2 and T2-40 had two branches spaced at 200 mm (about 0.064% transverse reinforcement ratio). T8 had four branches spaced at 200 mm and T9 had two branches spaced at 100 mm (both about 0.127% transverse reinforcement ratio). The embedment depth, the width of pile cap's plate, and the longitudinal reinforcement were kept constant.

3.9.4.1 Crack pattern and mode of failure

The specimens had the same crack pattern but differed in the crack widening as the transverse reinforcement ratio increased especially in beam T8 because of the load transfer mechanism was successfully bridging the diagonal crack through the stirrups.

102

Moreover, the concrete cover spalling occurred at a higher load in T8 compared to that in T2 and T9. The angle of the breakout crack (35°) and the breakout cone dimension were approximately the same in T2-40, T8 and T9. The failure mechanism was brittle in T2 but ductile failure in T8 and T9. The ultimate loads of T8 and T9 were larger than the breakout cracking load and was reached after the inner stirrups yielded, confirming the influence of the transverse reinforcement on the mode of failure, the connection capacity, and the level of warning before failure.

3.9.4.2   Cracking load, Breakout cracking load, and Ultimate load

Table 3-2 provides the first cracking and breakout cracking loads as well as the ultimate loads for T2-40, T8 and T9. The results show that the variation in the transverse reinforcement ratio and configuration had negligible effect on the first cracking and the breakout cracking loads. However, the ultimate load increased as the transverse reinforcement ratio increased; the ultimate load for T2-40 was 211 kN, while ultimate load for T8, and T9 was 256.3 and 253.2 kN, respectively, i.e., an increase of approximately 20%.

Furthermore, in T9, the connection ultimate load was equal to the vertical tensile capacity of the stirrups contained within the breakout cone taking into consideration that the strain in different stirrups was not uniform and the inner stirrups resisted more load than the outer stirrups. The ultimate load of T9 was approximately equal to the full ultimate strength of 3 stirrups from each side, i.e., the number of stirrups contained in its breakout cone. On the other hand, T8 had one stirrup from each side with 4 branches contributed to

103

its yielding capacity and the outer stirrup contributed only a small part of its yielding capacity to the ultimate load and the balance is attributed to dowel action and aggregate interlock. Thus, it may be suggested that the connection capacity should be taken as the lesser of the ultimate capacity and the vertical tensile yielding capacity of the transverse reinforcement contained in the breakout cone (i.e. similar to equation suggested by ACI-Appendix D to determine anchor capacity considering anchor reinforcement). This behavior will be discussed further in terms of the variation of longitudinal and transverse reinforcement strain during loading.

3.9.4.3   Load displacement relationship

Figure 3-27 shows the variation of mid-span displacement with load for T2-40, T8 and T9. It is noted that the stiffness of the 3 beams were approximately the same until breakout cracking load was reached. Afterwards, they displayed different behavior. In T2-40 and T9, the stiffness decreased and concrete cover spalling occurred. However, T9 ultimate load was higher because of the stirrups' contribution increased as the crack width increased. On the other hand, T8 exhibited higher resistance and stiffness than T9 after the breakout cracking load up to the ultimate load but reached its ultimate capacity at a lower mid-span displacement. Nonetheless, it continued to sustain more displacement until the stirrups failed due to necking. It appears that for T8, the load resistance after the connection ultimate load was reached due to the vertical tensile resistance of the stirrups connecting the two separated parts of the beam.

It was observed that the unloaded side of the beam began to rebound only after the ultimate load in beam T8, while it began to rebound after the breakout cracking load in beams T2, and T9, confirming that the concrete aggregate interlock and longitudinal reinforcement dowel action was effective till the ultimate load in beam T8 where large ratio of transverse reinforcement was located just beside the pile shaft and plate end.

Thus, one can conclude that increasing the transverse reinforcement ratio enhances the connection stiffness remarkably after the breakout cracking load and enhance its overall behaviour. Also, using closer stirrups to the pile shaft and the pile ends can enhance the beam integrity remarkably by decreasing the breakout crack width at the location of its first initiation.
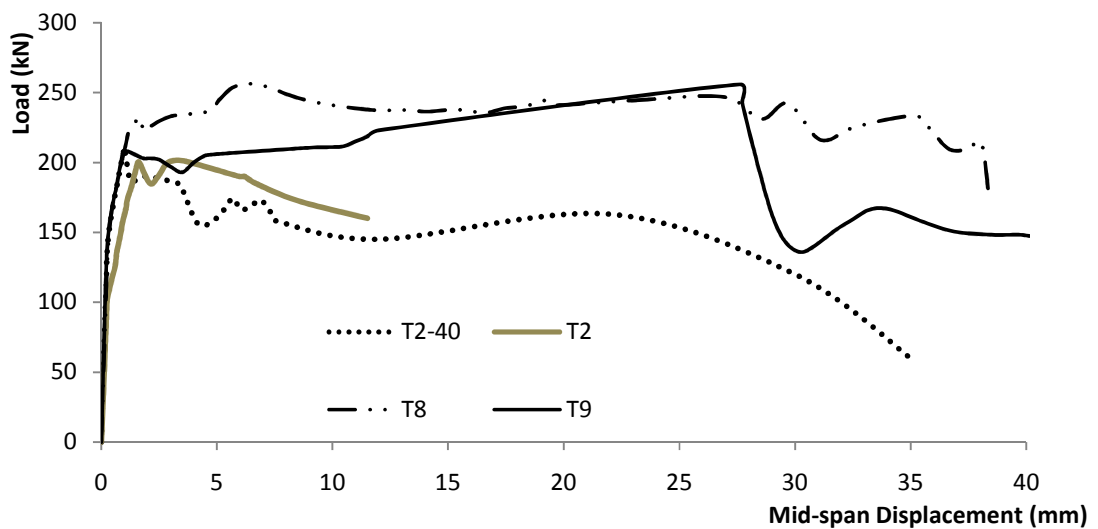
Figure 3-27 Load mid-span displacement

3.9.4.4 Ductility and strain energy

Table 3- 2 shows that the three tested beams had mid-span displacements of only 1 mm at the breakout cracking load. Meanwhile, at ultimate load the displacement was 1 mm, 6.4 mm, and 27.3 mm for T2-40, T8 and T9, respectively, which demonstrate the positive effect of the transverse reinforcement on the ductility. However, they failed at similar displacement levels due to stirrups failure.

Table 3-2 also shows that as the transverse reinforcement ratio increased from 0.064% to 0.127% the beam strain energy increased by about 94%, and 77% for T8 and T9 respectively. This underscores the importance of placing adequate stirrups at the position of the breakout cone. It should be noted that different transverse reinforcement configuration using the same transverse reinforcement ratio may affect the displacement at the ultimate load, but it would have a slight effect on the overall beam ductility.

3.9.4.5 Reinforcement Steel, and pile cap's plate Strain

Figure 3-28 presents the longitudinal steel strain for the three studied beams. It can be noted from Figure 3-28 that inner and outer bars had the same behaviour throughout loading and that all beams initially displayed the same behaviour. After the breakout cracking load was reached, the beams displayed different behaviour; the strain in T2-40 and T9 decreased due to concrete cover spalling and loss of bond, while no strain reduction was observed in T8. This confirms that both concrete aggregate interlock and dowel action of the longitudinal reinforcement contributed to the ultimate load T8 (and T2) but not in T2-40 and T9. It may be concluded that higher transverse reinforcement

106

ratio increased the connection load capacity, which allowed the longitudinal reinforcement to reach yielding prior to achieving the ultimate load, hence increasing the connection ductility.

(a)

(b)
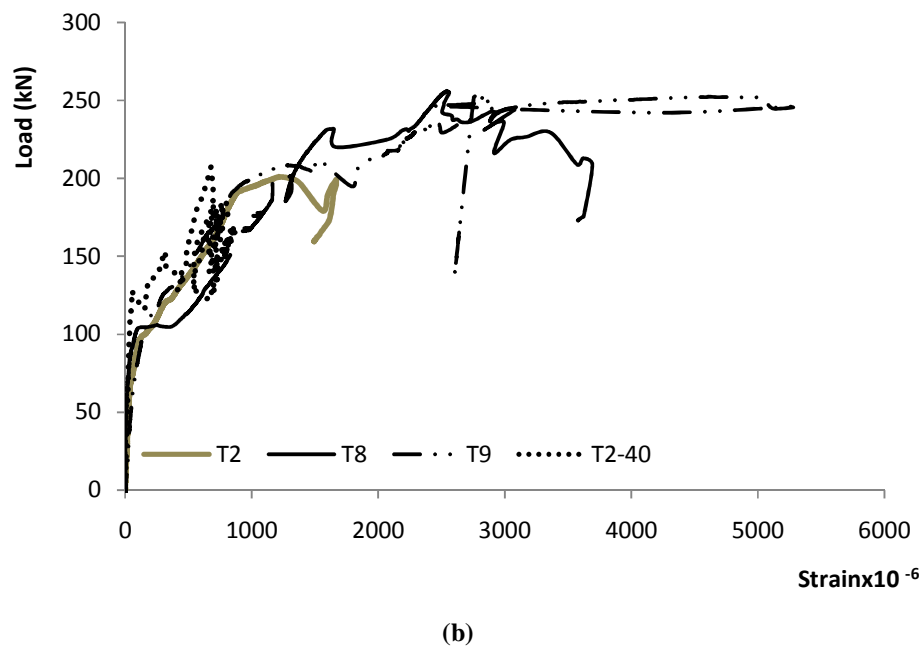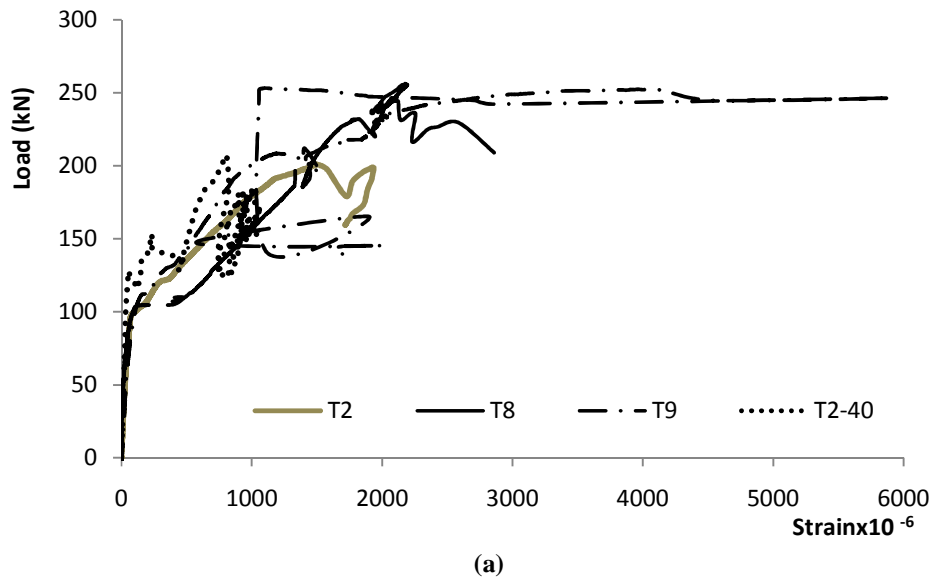
Figure 3-28 load-longitudinal reinforcement strain: (a) outer reinforcement; (b) inner reinforcement

Figure 3-29 shows the strain in transverse reinforcement. It is clear that the effect of the stirrups is negligible before the diagonal crack initiated. The location of the stirrups affected its strain remarkably; the closer the stirrups to the connection the higher the recorded strain and their contribution to the ultimate load.

In T8, the outer stirrups contributed to the connection capacity but their load was less than its yielding tensile capacity as it did not yield before the ultimate load and their strain at ultimate load was only about 400×10^{-6} which represents only 20% of the stirrups yield capacity. Similarly, the outer stirrups of T2-40 experienced small strains at ultimate load (less than 400×10^{-6}) and yielded after the ultimate load. On the other hand, in T9 the outer stirrups experienced strains higher than yielding at the ultimate load. This is mainly because of the wide crack opening at the ultimate load in T9 compared to that of T2-40 and T8. Finally, all inner stirrups' branches of T8 yielded before the ultimate load was reached and contributed to it. It seems that the longitudinal reinforcement did not distribute the load, rather the load transferred directly from the plate and the breakout cone to the inner stirrups.

In conclusion, using high transverse reinforcement ratio close to the pile shaft will increase the connection capacity remarkably after the breakout cracking load and can involve both aggregate interlock and longitudinal reinforcement dowel action similar to beam T8; however, distributing the stirrups along the breakout cone would increase the beam capacity but it would require larger displacement to transfer the load to several stirrups using the longitudinal reinforcement as a lower chord in a truss action with

vertical members presented by the stirrups as presented in figure 3-14. In addition, the contribution of vertical tensile capacity of stirrups within the breakout cone to the connection capacity should be based on their yield capacity. On the other hand, when considering the contribution of the aggregate interlock and the dowel action of the longitudinal reinforcement to the connection ultimate capacity, only the contribution of the transverse reinforcement close to the pile shaft (e.g. within the plate width) should be added to the connection capacity.

Finally, the maximum strain of the pile cap's plate for all beams was less than 183×10^{-6}, which means the pile cap had minimal effect on the connection capacity. This confirms that the plate was not crossed with the breakout cracks and the crack began from the plate sides.
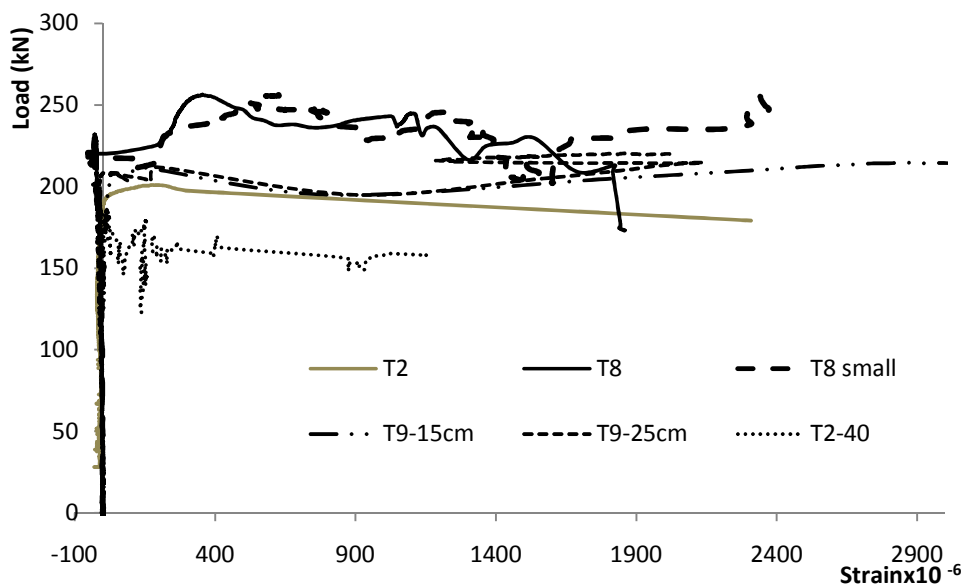
(a)
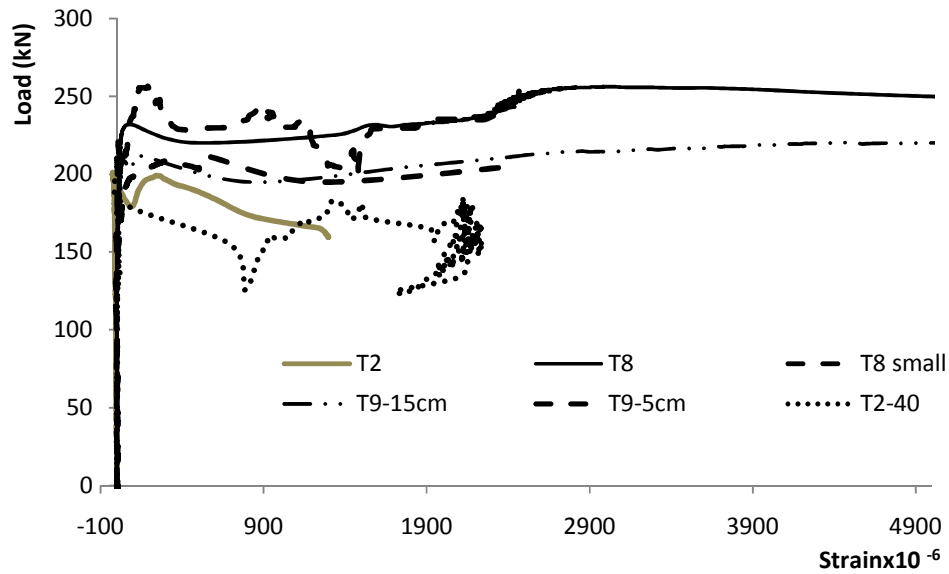
(b)
Figure 3-29 Load- stirrups strain: (a) outer stirrups; inner stirrups

3.10   Conclusions

The capacity of slender shaft piles- RC grade beam connection using steel brackets is investigated in a laboratory experimental program. Nine foundation models involving simply supported grade beams with new construction pile bracket were subjected to monotonic tension loading. The tested beams were categorized into four groups according to the parameters investigated. Each group has three beams. In each group only one variable was investigated, while the other variables were kept constant. The investigated variables are the: embedment depth of pile cap; the width of the steel plate; the beam longitudinal reinforcement; and the beam transverse reinforcement. The following conclusions may be drawn from the test results.

3.10.1 General

1) During loading, global beam behaviour was observed initially until first flexural cracking occurred. The response depended on the connection variables afterwards.

2) It is unsafe to only consider the grade beam capacity and ignore the connection capacity in foundation design and pile load transfer calculations.

3) The connection can be considered fixed (i.e. fixed pile head) up to the breakout cracking load. Afterwards, the connection becomes hinged and its stiffness and capacity depend on the longitudinal and transverse reinforcements.

4) Connection breakout cracking initiated from the pile cap's plate ends with a 35° angle, given that the distance to the support is more than three times the embedment depth, and no yielding of the pile cap's plate was observed.

5) Crack propagation in the longitudinal direction was similar to single shear cracking.

6) The dimension of the breakout cone can be approximated by the lesser of (b_{plate} +2.5 d_{emb}) or (3 d_{emb}) and can be accurately calculated using equation 3.1.

7) The pile shaft transfers the load to the concrete primarily through the pile cap's plate.

8) The breakout cracking load is mainly affected by the concrete strength and longitudinal reinforcement contributions and not by the transverse reinforcement.

9) The ultimate load of the connection is affected by the concrete strength, the longitudinal reinforcement, and the transverse reinforcement contributions.

10) The connection ductility depends mainly on the longitudinal and transverse reinforcements.

3.10.2 Effect of embedment depth

11) An increase in the pile cap embedment depth increases the breakout cracking and ultimate loads of the connection almost linearly and increases the size of the breakout cone. It also increases the connection stiffness after the first cracking load.

12) An increase in the pile embedment depth enhances the beam's ability to absorb energy before failure. However, it may decrease the load margin between breakout cracking and ultimate loads.

3.10.3 Effect of pile cap's plate width

13) The size of the breakout cone at the longitudinal reinforcement level increases with the increase of the plate width.

14) The plate dimensions have minor effects on the connection stiffness and their effect on the connection capacity was not clear.

15) The connection ductility and its ability to absorb energy enhances as the plate dimensions increase.

3.10.4 Effect of longitudinal reinforcement

16) The first flexural cracking load, the breakout cracking load, and the ultimate load of the connection increase by increasing the longitudinal reinforcement ratio. The breakout load increases because increased longitudinal reinforcement reduces the tensile strains in the surrounding concrete hence increasing the concrete diagonal tensile capacity. On the other hand, the ultimate load increases because of the enhanced dowel action.

17) Increasing the longitudinal reinforcement ratio increases the connection ability to absorb energy.

3.10.5 Effect of transverse reinforcement

18) The transverse reinforcement ratio has no effect on the first flexural cracking or breakout cracking loads, and had minor effect on the breakout cone dimensions.

19) Adequate transverse reinforcement can transfer the connection failure mechanism from brittle to ductile failure as it enhances the connection ability to absorb energy and the beam ductility. It also increases the connection capacity after the breakout cracking load.

20) The configuration of the transverse reinforcement can change the load transfer mechanism. Higher connection capacity can be achieved by placing higher percentage of transverse reinforcement closer to the pile shaft.

21) Placing transverse reinforcement closer to the pile shaft can reduce the breakout crack width, which maximizes the contributions of the concrete aggregate interlock and the longitudinal reinforcement dowel action.

22) The connection ultimate capacity is the larger of its capacity and the vertical tensile strength of the used transverse reinforcement within the breakout cone.

3.11 References

ACI 318, 2011. Building Code Requirements for Structural Concrete (ACI 318-11) and Commentary, Farmington Hills, MI: American Concrete Institute.

ACI 349, 2001. ACI 349-01 Code Requirements for Nuclear Safety Related Concrete Structures, Farmington Hills, MI: American Concrete Institute.

Angelakos, D., Bentz, E.C. & Collins, M.P., 2001. Effect of concrete strength and minimum stirrups on shear strength of large members. ACI Structural Journal, 98(3), pp.290–300.

CSA A23.3, 2004. A23. 3-04: design of concrete structures,

Lee, N.H. et al., 2007. Tensile-Headed Anchors with Large Diameter and Deep Embedment in Concrete. ACI Structural Journal, 104(4), pp.479–486.

Metwally, I.M., 2012. Evaluate the capability and accuracy of response-2000 program in prediction of the shear capacities of reinforced and prestressed concrete members. *HBRC Journal*, 8(2), pp.99–106.

Smith, K.N. & Fereig, S.M., 1974. Effect of Loading and Supporting Conditions on the Shear Strength of Deep Beams. ACI Special Publication, 42, pp.441–460.

Talbot, Arthur Newell, 1857-1942, 1909. Tests of reinforced concrete beams: : resistance to web stresses, University of Illinois at Urbana Champaign, College of Engineering. Engineering Experiment Station.

Watstein, B.D. & Mathey, R.G., 1958. Beams Having Diagonal Cracks. Journal Of The American Concrete Institute, 58(55), pp.717–728.

Zuhua Wang, 1987. shear strength of slender concrete beams loaded indirectly. International journal of structures, 7(1), pp.17–42.

BEHAVIOUR OF HELICAL PILE CONNECTORS FOR NEW FOUNDATIONS SUBJECTED TO TENSION LOADING: NONLINEAR FINITE ELEMENT ANALYSIS

4.1 Introduction

This research aims to develop nonlinear finite element models that can accurately mimic the structural behaviour and capture the possible failure modes of the connection between steel piles with slender shaft (i.e. helical piles and micropiles) and the reinforced concrete foundation (e.g. grade beams). The finite element model will be first calibrated and verified using the results from the accompanying experimental program and then will be used to conduct a comprehensive parametric study to investigate additional connection configurations that complement the results of cases covered in the experimental study. An overview of the literature relevant to nonlinear finite element modeling is presented first, followed by the details of the finite element model.

4.2 Numerical Model

The connection between the slender shaft pile and the reinforced concrete exhibits complex nonlinear structural behaviour as discussed in Chapter 3. The pile cap connection consists of a steel pile shaft, two high strength steel bolts, a steel cylinder, a steel plate, welding between the cylinder and the plate, and the concrete with longitudinal and transverse reinforcement. For proper modeling of nonlinear behaviour, the geometric and material properties should be simulated using proper meshing and material properties. In addition, specific interface conditions should be applied at the interface of

each two surfaces in order to simulate the nonlinear/discontinuity behaviour at the interfaces. All materials of the connection may exhibit nonlinear behaviour, especially near failure. Thus, the chosen numerical model must be able to handle the expected interactions between components such as gap opening/closing, nonlinear material behaviour, stress concentration, rate of loading, material deterioration with cyclic loading, and frictional and dowel forces. The general purpose implicit/explicit finite element program LS-DYNA (LSTC 1998 and LSTC 2009) was used in this study. It contains various material models capable of representing the complex behaviour recorded in the experimental work. In addition, the program offers different contact surface types with different advanced search algorithms that can facilitate modeling complex interface conditions.

4.3 Type of finite element analysis

The explicit analysis is used in the analysis to facilitate simulating nonlinearities and progressive damage/failure behaviour and to capture the accurate behaviour after cracking and softening behaviour. Furthermore, it is suitable for problems with large number of degrees of freedom and it is computationally more efficient as the solution can be achieved without forming a global stiffness matrix. Rather, the solution is obtained on an element-by element basis and as a result, it requires comparatively modest computer storage requirements. However, the explicit method is conditionally stable and therefore small time steps must be used. To ensure stable computations and convergence, quasi-static analysis was conducted using explicit FEM.

At each time step of the explicit analysis, the equilibrium equation is solved to calculate the displacement, i.e.

$$M\ddot{x}^{n+1} + D\dot{x}^{n+1} + k_t(x^n)\Delta x = P(x^n)^{n+1} - F(x^n) \qquad \textbf{4.1}$$

where $\ddot{x}^{n+1}$, $\dot{x}^{n+1}$, x^n, and Δx are the acceleration, the velocity, the coordination, and the displacement vectors. $P(x^n)^{n+1}$ is the external load vector and $F(x^n)$ is the stress divergence vector. M, D and K_t are the mass, damping and tangent stiffness matrices.

To ensure that the analysis can be static or quasi-static, the inertia and damping terms should be negligible. Pan (2006) suggested this can be achieved either through increased loading time (i.e. reduced rate of loading) or decreased system mass (i.e. reduced material density). Both approaches usually require numerous small time increments. For instance, decreasing the material density adds to the run time considerably as the appropriate time step is given by equation 4.2 (Ls-Dyna theory manual, 2006) .

$$\Delta t = \min\left(\frac{L_{min}}{S}\right), \qquad S = \sqrt{\frac{E}{\rho}} \qquad \textbf{4.2}$$

where L_{min} is the smallest dimension in an element; and S is the wave speed traveling through the element; E and ρ are the element Young's modulus and mass density.

In this study, both mass scaling and rate of loading reduction were used in order to achieve an appropriate running time with quasi-static behaviour. The material density was scaled to 1/1000 of the prototype density, and the rate of loading was optimized such that no effect of loading rate would be recorded. The best calibration was achieved, and the kinetic and inertial energies were minimized. These mass scaling ratio and loading

rate were kept constant for all investigated specimens. Moreover, the symmetry of the specimens about their main axes was exploited (i.e. only one quarter of the specimen was modeled) to further reduce the computational effort.

4.4 Element type

The plain concrete, steel pile shaft, steel bolts, steel cylinder, welding, and steel pile cap's plate were modeled using 8-node hexahedron solid constant-stress elements with three displacement degrees of freedom at each node with one integration point (element form 1 in LS-DYNA), which is shown in Figure 4-1. This element is preferred in analyses involving large nonlinear deformations because it is computationally efficient due to its one-integration point, yet it provides reasonably accurate results (Flanagan and Belytschko, 1981). However, it requires hourglass control.

Longitudinal and transverse reinforcement were modelled using two-node beam elements. Even though it has rotational degrees of freedom, it will behave as a truss element within the model as it was connected to solid element nodes that have no rotation.
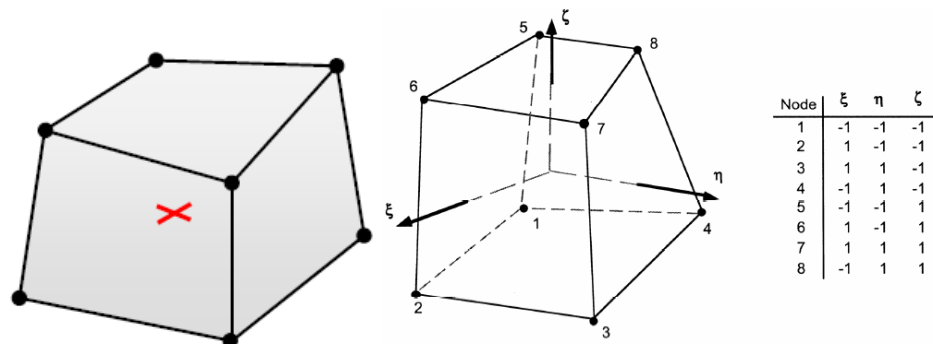
Figure 4-1 8-node solid hexahedron element with one integration point (LS-DYNA manual, 2006)

119

4.5 Material model

Proper definition of the mechanical properties of steel and concrete materials is necessary for modelling the realistic behaviour of the connection. Suitable material models for the plain concrete and steel were selected from LS-DYNA material library and their parameters were calibrated using the experimental results.

4.5.1 Concrete material model

Generally, modeling the behaviour of an element in a concrete continuum requires consideration of the triaxial stress-strain characteristics. As shown in Figure 4-2, the failure surface is a three-dimensional principle stress space as stated by Chen (2007). Also, for isotropic materials, the failure criterion based upon a state of stress must be an invariant function of the state of stresses and it does not depend on the chosen coordinates system.

In Figure 4-2, the elastic limit surface (yield surface) indicates the beginning of the material weakening. It has similar shape to the failure surface, but it is reduced in size. The failure surface is fixed in the principle stress space at a distance from the yield surface. The deviatoric stresses is considered in the elastic state till the stress reaches the yield surface, at which point the nonlinear behaviour takes place. The deviatoric stresses can then increase further until the failure surface is reached. Beyond this stage, the response can be perfectly plastic or softening behaviour can take place.
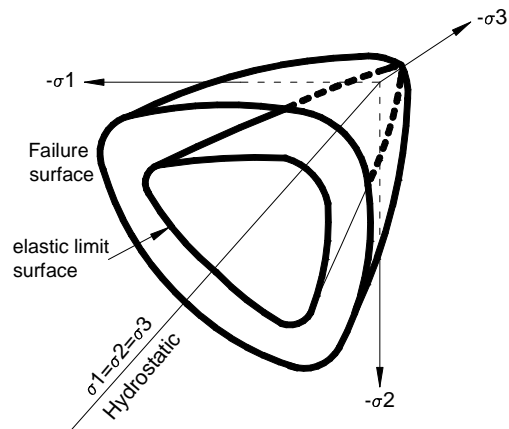
Figure 4-2 Schematic failure Surface of concrete in 3D stress space (Modifed from Chen, 2007)

4.5.1.1   Definition of concrete failure criterion

The failure surface in the 3-dimensional stress space can be demonstrated by the deviatoric plane (a cross-section shape perpendicular to the hydrostatic axis) with constant hydrostatic stress and its meridians (the intersection between a plane containing the hydrostatic axis and the failure surface) at a specific angle. For example, the cross-section in Figure 4-3 is approximately triangular and requires two points to be indicated. The first point is farthest from the hydrostatic axis with 60° angle, on the compressive meridian. The second point is nearest to the hydrostatic axis with 0° angle, on the tensile meridian. The path between the compressive and tensile meridians can be defined by an elliptical curve (Willam and Warnke, 1975) (distance *r* as a function of θ).

The failure curve can be considered triangular for tensile and small compression stresses and more circular for high compressive stresses. The ratio of tensile to compression deviatoric stress capacity at the same hydrostatic pressure is less than 1. This ratio

121

increases with the hydrostatic pressure increase, which means concrete can sustain higher tensile stresses when subjected to transverse compression stresses and pure hydrostatic loading cannot cause failure (Chin and zimmerman, 1965).

Figure 4-3 Deviatoric cross-section of the failure surface

4.5.1.2   Definition of fracture mechanics and failure criterion

When the tensile strength of a material is reached, cracking will take place. Fracture mechanics describe the condition around and in front of a crack tip (Elfgren, 1989). The behaviour of concrete subjected to tension or pure shear is best analyzed by combining fracture mechanics and finite element analysis, which allows modelling realistic crack initiation and propagation (Hillerborg, 1974).

It has been a common practise to ignore the tension strength of cracked concrete in design; however, Elighausen et al. (2013) confirmed its importance in finite element

analyses. Accounting for the cracked concrete tensile strength can accurately capture the failure mechanism of lightly reinforced concrete members and members failing in shear or tension, and allows better prediction of the member deformation. The crack is assumed to propagate when the stress at the crack tip reaches the tensile strength f_t. When the crack opens, the stress is not assumed to fall to zero at once, but to decrease with increasing the crack width, w (Hillerborg, 1976). Bazant and Oh (1983) demonstrated that stress-softening will occur at the crack location depending on the effective plastic strain at the crack. They defined the fracture energy, G_{Ft} as the consumed energy to form a unit area of crack surface. The 3-dimensional failure surface will indicate the initial yielding and the stress-strain relation for the material. Material damage will then occur after reaching the peak strength and the material continues to sustain loading till 99% damage value is reached depending on fracture mechanics (Chen 2007). The concrete tensile fracture energy G_{Ft} may be calculated by the (CEB-FIP model code ,1993), i.e.

$$G_{Ft} = \left(0.0469 \, d_a{}^2 - 0.5 d_a + 26\right)\left(\frac{f c'}{10}\right)^{0.7} \qquad\qquad \textbf{4.3}$$

where G_{Ft} is in N/m, $f c'$ is in MPa, d_a is the maximum aggregate size in mm.

Santiago and Hilsdorf (1973) observed concentrated deformation in certain zones after reaching the peak stress in their investigation of the behaviour of concrete loaded in compression. Nakamura and Hiagai (1999) indicated the importance of using compression fracture energy, especially when members are failing in compression under flexure or compression-shear. They proposed that concrete compressive fracture energy should be taken as 250 times concrete tensile fracture energy.

4.5.1.3 Concrete models in LS-DYNA

LS-DYNA has several comprehensive concrete models that can capture complex concrete behaviour including: biaxial and triaxial loading, biaxial stiffening, concrete-reinforcement interactions as well as nonlinear behaviour under tension, compression, and shear. table 4-1 lists the considered material models available in LS-DYNA. The important model features include: strain rate effects (SRATE); failure criteria (FAIL); equation of state for 3D solid and 2D continuum elements (EOS); damage effects (DAM); and different tension and compression behaviour (TENS). A material model possessing any of these attributes is marked with "Y" in the respective column. It should be noted, however, that concrete material models in LS-DYNA consider concrete as a homogenous continuum even though it is a heterogeneous material.

Table 4- 1 Attributes of concrete material models in LS-DYNA

Material No.	Name	SRATE	FAIL	EOS	DAM	TENS
84	Winfrith Concrete (with rate effect)	Y				Y
172	Concrete EC2		Y			Y
78	Soil Concrete		Y		Y	Y
26	Honeycomb	Y	Y			Y
126	Modified Hoenycomb	Y	Y		Y	Y
96	Brittle Damage	Y	Y		Y	Y
111	Johnson Holmquist Concrete	Y	Y		Y	Y
159	CSCM	Y	Y		Y	Y
72	Concrete Damage (K&C model)	Y	Y	Y	Y	Y

From table 4-1, it is obvious that Material 72 (denoted: K&C model, MAT_72, and MAT_72R3) offers comprehensive characterization of concrete. Initial analyses of the behavior of control specimen T2 during testing demonstrated that MAT_72R3 provided excellent match with observed behavior during loading tests. Moreover, numerous studies reported in the literature indicate the superiority of MAT_72R3 (e.g., John et al., 2012; Malvar et al., 1996, 1997 and 1999; Crawford et al, 1995, 1997, 2004, 2006, 2010, and 2012; Magallanes et al., 2007, 2008, 2011; Wesevich, 1997; Yonten et al., 2005; and Tu and Lu, 2009). Furthermore, MAT_72R3 has a default library for consistent different concrete strength, i.e., the model uses the concrete compression strength to generate the rest of the required variables. It also allows the user to set a particular material parameter that affects the damage evolution rate according to the mesh size to preserve energy to failure. The user can also implement available measured concrete characteristics (e.g. the concrete tensile strength), which can further improve the model predictions. Therefore, the constitutive model MAT_72R3 will be used herein. The model is discussed and the procedures done for evaluating its parameter affecting the damage evolution rate is discussed below.

4.5.1.4   MAT_CONCRETE_DAMAGE_REL3 (MAT_072R3)

The initial model was developed by Bažant and Cedolin (1979) and Bažant (1985). Malvar et al. (1997) incorporated automatic data generation feature in the model in order to calculate 72 input parameters given the unconfined uniaxial compressive strength of concrete. They also introduced a simple method to reduce mesh-dependencies due to strain softening. The model accounts for the effects of cracking by employing the

smeared crack band model. Crack initiation is based on strength criterion, i.e., when the maximum principal stress reaches the concrete tensile capacity, f_t. On the other hand, crack propagation is based on fracture mechanics criterion, i.e., considering fracture energy (Bažant and Cedolin, 1979). Smeared cracks are oriented perpendicular to the maximum principal stresses. The crack band model is defined by three material parameters: f_t, G_{ft}, and w (i.e. shear dialation factor). G_{Ft} is controlled by the input uniaxial tensile strain softening parameter, b2 and f_t. These two parameters should be modified to account for the effect of the used element size.

This model uses a limited shear dilation method to describe material deformation or flow, which accounts for confinement effect in reinforced concrete. For example, when steel stirrups are used, axial force in the stirrups will mobilize due to dilation and the concrete contained by the stirrups will be confined. The model specifies the concrete flow behaviour that is normal to surface (associative) and the flow at an angle Θ_n (non-associative). To capture the partial shear dilation of concrete caused by the aggregate interlock as shown in Figure 4-4, an associatively parameter, ranging from 0 to 1 is used. Noble el al. (2005) suggested a range to be used for w from 0.5 to 0.7. Also, maximum aggregate size is required to model the material flow.
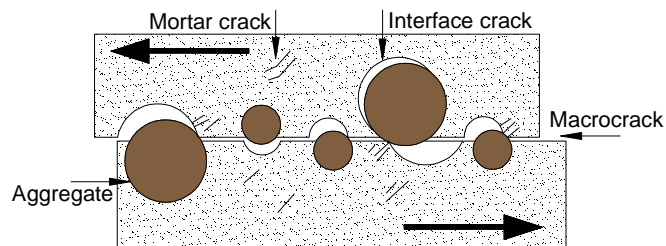
Figure 4-4 Influence of aggregate interlock on concrete fracturing process
(Modified from Noble el al., 2005)

4.5.1.4.1 Definition of failure surfaces for MAT_072R3

This model uses a plasticity based formulation with three independent dynamic failure surfaces: initial yielding, maximum, and residual failure surfaces (Crawford et al., 2012). The failure surface shape depends on the applied hydrostatic pressure and eight constants that can be calculated from the experimental data. This hydrostatic pressure invariant value is equal to P. The dynamic surfaces are given by:

The initial yielding surface: $\Delta\sigma_y = a_{oy} + \dfrac{P}{a_{1y} + a_{2y}p}$ **4.4**

The maximum failure surface: $\Delta\sigma_m = a_o + \dfrac{P}{a_1 + a_2 p}$ **4.5**

The residual failure surface: $\Delta\sigma_r = a_{of} + \dfrac{P}{a_{1f} + a_{2y}f}$ **4.6**

where $a_{oy}, a_o, a_{of}, a_{1y}, a_{2y}, a_1, a_2, a_{1f}, and\ a_{2f}$ are user-specified constants and can be estimated from laboratory triaxial tests in compression.

4.5.1.4.2 Softening parameters of MAT_72R3

The softening parameters $b1$, $b2$, and $b3$ establish the manner of softening exhibited by the model for different stress paths. Parameter $b1$ governs softening in compression, b_2 affects the uniaxial tensile strain softening, and $b3$ affects the triaxial tensile strain softening. In the current study, these values were determined by iterations until the values of fracture energies, Gft, Gfc,, and Gfs, converge with the calculated values using the (CEB-FIP Model code, 1993) as suggested by Magallanes (2010). Parameter b_2 governs

127

the tensile fracture energy G_{Ft} as it controls the softening branch of the stress-strain behaviour of concrete subjected to uniaxial tensile test. Malvar et al. (1997) indicated that the area under the stress-strain curve of one element should be adjusted to G_{Ft}/h_c, where h_c is the characteristic length of the element. To find the best representing parameter b_2, different finite element models were conducted using only one 3D solid element representing the concrete with a specific mesh size. This element is loaded perpendicular to one of its surfaces while the parallel surface was restrained from moving. The area under the stress-strain curve was then calculated and compared with the actual tensile fracture energy divided by the element length G_{Ft}/h_c. The parameter b_2 that gives the same tensile fracture energy G_{Ft} calculated with the (CEB-FIP Model code, 1993) is then used in the concrete material model.

These procedures were conducted for each studied mesh size. Table 4-2 presents the investigated b_2 parameters and resulting G_{ft} for fc' = 30 MPa (and f_t = 3.33 MPa) and fc' = 40 MPa (and f_t = 5.25 MPa) considering mesh size = 20mm and using one solid element. The calculated fracture energies from the (CEB-FIP Model code , 1993) were 80 N/mm and 96 N/mm for fc'=30 MPa and 40 MPa, respectively. Inspecting table 4-2, it is noted that Model E-3.1 with b2=3.1 best represented concrete with fc' =30 MPa, and model F-4.3 with b2=4.3 best represented concrete with fc' = 40 MPa.

Figure 4-5 presents the load displacement curves for different models with mesh size of 20 mm for fc'=30 and 40 MPa. Figure 4-5 demonstrates the effect of b_2 on the expected concrete behaviour and its ability to resist tension and displacement before cracking.

Table 4- 2 Calculated uniaxial tensile stran softening and corresponding tensile fracture energy

For compressive Strength, fc'=30 Mpa		For compressive Strength, fc'=40 Mpa	
b_2	G_{ft} (N/mm)	b_2	G_{ft} (N/mm)
1	140	1	221
2.3	99	3	132
3	82.405	4	102
3.1	**80.38**	**4.3**	**96.8**
4	63.65	4.4	95
5	52.27	4.5	92.5
6	42	5	82.85

(a)

(b)

Figure 4-5 Single element tensile load-displacement curve for different b_2 parameter for MAT_072R3: (a) with fc'=30 MPa; and (b) fc'=40 MPa

4.5.1.4.3 Elastic Parameters in MAT_72R3

The behaviour of concrete within the elastic range is described by two constants: the bulk modulus, K, and Poisson's ratio ν.

4.5.1.4.4 Damage function of MAT_72R3

Upon defining the three failure surfaces, the dynamic form of yield surface is obtained by interpolation between either the yield and max surfaces when hardening is occurring or the max and residual surfaces when softening is occurring. The interpolation is performed using a scalar quantity that is computed based on the extent of damage at the material point, which depends on the softening parameter (Crawford et al., 2012). The damage parameter is given by:

$$\lambda = \begin{cases} \int_0^{\overline{\varepsilon^p}} \dfrac{d\overline{\varepsilon^p}}{r_f\left(1+\frac{p}{r_f \cdot f_t}\right)^{b1}} & for \ p \geq 0 \\[4mm] \int_0^{\overline{\varepsilon^p}} \dfrac{d\overline{\varepsilon^p}}{r_f\left(1+\frac{p}{r_f \cdot f_t}\right)^{b2}} & for \ p < 0 \end{cases}$$

4. 7

where $d\overline{\varepsilon^p} = \sqrt{(\frac{2}{3})\varepsilon_{ij}^p \varepsilon_{ij}^p}$ is the effective plastic strain increment, r_f is a user-defined experimental rate enhancement factor from unconfined uniaxial compression tests.

This model implements shear damage accumulation and it treats the damage evolution differently in tension than in compression.

4.5.1.5   Concrete material input used in LS_DYNA

Two different concrete materials, fc' = 30MPa and 40 MPa, were used in the experimental program. Thus, two different concrete material inputs were generated automatically within the finite element program based on the average concrete compressive strength according to ASTM C39/ C39M and the average splitting tensile strength according to ASTM C496/ C496M-11 (see Appendix A). The generated keyword input data for the models used for the concrete material models are indicated in the Appendix C.

4.5.2   Steel Material Model

There are several material models to simulate steel in LS-DYNA. The model selected in this study was material MAT_024 (MAT_piecewise_linear _plasticity). It has piecewise linear plasticity curves that can capture effectively the strain localization behaviour of steel. It can capture steel rupture due to exceeding the maximum plastic strain and can mimic fractures at specific values of von Mises true strain. The element will be removed from the model if its maximum principle plastic strain exceeds the specified von Mises true strain, which depends on the steel grade. It can simulate isotropic and kinematic hardening plasticity materials such as steel. Both beam elements and solid elements can be simulated using this model. It was used to simulate 3 different rebar materials (upper and lower longitudinal reinforcement and stirrups), steel pile shaft, welding, steel cylinder, steel pile cap's plate, and high strength steel bolts. The predictions of this model matched well the observed behaviour of the tested specimens. An example for the generated input for the steel model is listed in the Appendix C.

131

4.6 Hourglass control

The 8-node hexahedral solid element used to simulate concrete has one integration point. It is necessary to control the zero energy modes, denoted as hourglassing modes, which arise when using this element (Flangan and Belytschko, 1981). They usually have much shorter periods than the structural response and hence cause oscillation of the response. Different hourglass control strategies are available in LS-DYNA. The viscous and stiffness hourglass controls are widely used. In general, viscous hourglass control is recommended for problems deformation with high velocities, while stiffness control is preferred for quasi-static analysis. Therefore, a stiffness form of hourglass control was used in the current analysis as suggested by LS-DYNA manual as shown in the keyword input data presented in Appendix C.

4.7 Rebar-concrete interface

The bond slip behavior of the rebar-concrete interface is complex. Its analysis requires incorporating the effects of actual size and shape of the bar and the explicit interference behaviour. Crawford et al. (1997) carried an extensive study to evaluate the importance of explicitly modeling the intricate details of this interface versus implicit modeling. They concluded that explicit modeling is problematic and the required effort is not worthwhile in light of the minimal difference in results compared with the implicitly modeled behaviour. Thus, the bond between the rebar and the concrete is generally analyzed implicitly by tying the rebars to the same nodes of the concrete elements. The bond-slip phenomena is thus captured by the behavior of the concrete strength attached to the rebars.

4.8 Welding at steel cylinder-pile cap plate interface

The welding was modeled as solid elements having the same multi-linear stress strain curve recorded for the welding connection. These elements were simulated using MAT_24 with a specific plastic stain and they shared the same nodes with the steel cylinder and the plate. Thus, loads were transferred through welding from the steel cylinder to the plate and any welding failure would be due to the welding material failure. This modeling strategy allowed monitoring different stresses acting on welding.

4.9 Steel elements interfaces

The interface conditions at steel pile shaft-bolts, steel pile-concrete, steel plate-concrete, bolt-steel cylinder, and bolt-concrete were modeled using a special arrangement. At each interface, two spring elements connected the adjacent nodes on the contacted surfaces. The springs are placed normal and parallel to the contact surface connecting a slave node on the slave surface and master node on the master surface. The contact algorithm within LS-DYNA applies the penalty method (Bala, 2001). It checks for slave points' penetration through the master surface at each time step. If penetration occurs, a restoring force (F_n) and a friction force (F_s) are applied to eliminate the penetration depending on the penetration depth, d, and the spring stiffness, k. The restoring force (F_n) is equal to the penetration depth multiplied by the spring stiffness while the friction force is computed based on the friction coefficient, μ, and the normal force F_n. When the acting force reaches the maximum friction force ($\mu.F_n$), the two surfaces begin to slide and the friction force (F_s) remain constant.

4.10 Boundary conditions

Due to symmetry in both the orthogonal directions, only one-quarter of the specimen is modeled to reduce the computational effort. All nodes across the axes of symmetry are restrained by roller support condition. Nodes corresponding to supports are restrained only in the vertical direction Y to accurately simulate the experimental setup, where only Y direction was restrained. Vertical loading was applied as an imposed upward constant velocity at the top surface of the pile shaft simulating tension loading. The small constant velocity loading resulted in small non oscillating kinetic energy compared to the internal energy of the system. The concrete overall dimensions, and support location are depicted in Figure 4-6a. The full model boundary conditions are shown in Figure 4-6b. To check the accuracy of the supporting system, the loads recorded from the system were compared with the model recorded reactions and they gave exactly the same values with inverted sign during the full loading and before total specimen failure.

a)
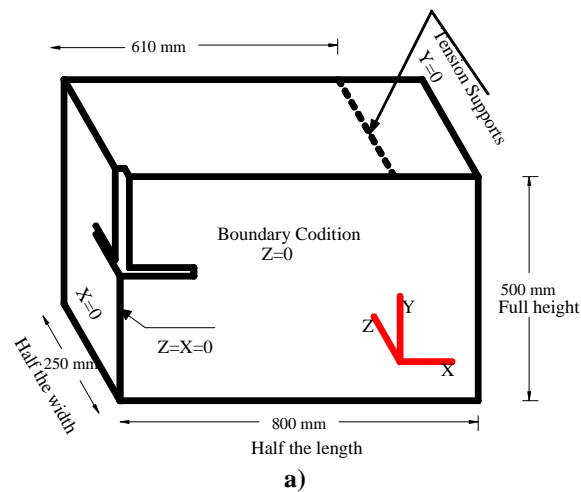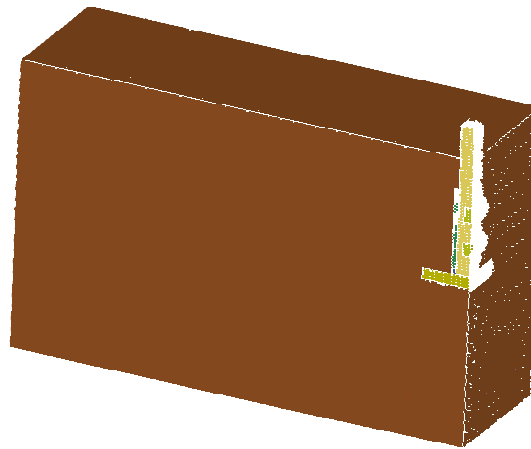
b)

Figure 4-6 Model boundary conditions: a) model dimensions; b) finite element mesh

4.11 Mesh size

Several element sizes were investigated, and for each model different value of b_2 was calculated to maintain the same fracture energy G_{ft}. The element size should be selected to correspond to the representative volume of the cracking and the fracture process zone, which is proportional to the maximum aggregate size (Bažant and Oh, 1983). On the other hand, small element sizes should be used with high strength concrete because its behaviour is more homogeneous. A sensitivity study was performed, which involved comparing the numerical predictions with the experimental observations. The model with concrete element size equal to the concrete maximum aggregate size of 20 mm and reber element length of 20 mm provided the best match with experimental results and hence was used for further analysis. Smaller element size was used for modeling the steel plate, bolts, welding, pile shaft and the steel cylinder due to their geometrical dimensions.

4.12 Verification of finite element model using the experimental results

Initially, to ensure proper modeling of quasi-static loading conditions, the total, internal, kinetic, and hourglass energies of the model were recorded as presented in Figure 4-7 for beam T2. It is clear that the kinetic energy is negligible compared to the internal energy, indicating the accuracy of modeling quasi-static loading conditions. The hourglass energy is also very small compared to the internal energy, which is acceptable in regards to the static equilibrium and energy aspects. The same energy behaviour was recorded in all investigated models.
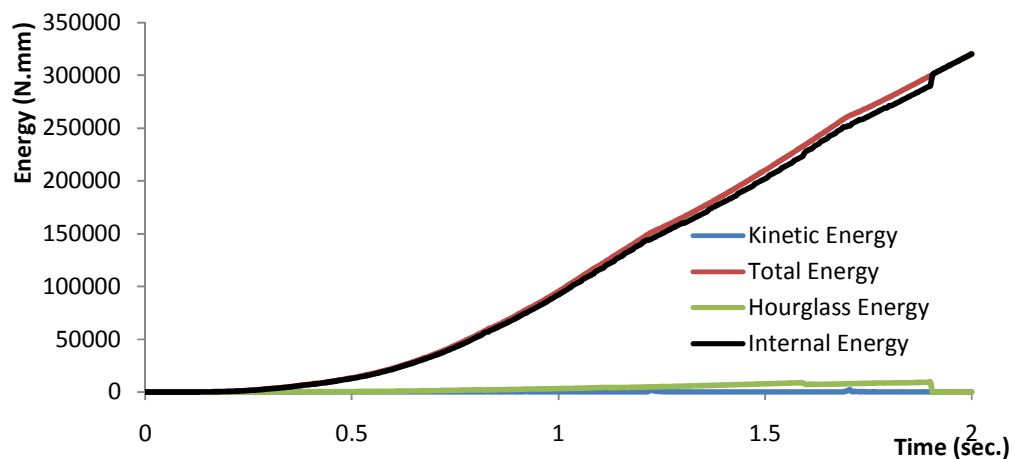
Figure 4-7 Total, internal, kinetic, and hourglass energies recorded in beam T2 Model

The finite element models were then verified through comparing their predictions with the experimental observations of the 9 specimens tested in this study. The comparison was conducted in terms of:

- Load-displacement behaviour including: breakout cracking and ultimate loads and corresponding displacements as well as connection stiffness.

136

- Longitudinal reinforcement strains for rebars next to the edge of the beam cross-section (denoted outer longitudinal reinforcement), and rebars inside the beam (denoted inner longitudinal reinforcement).

- Strain for stirrups next to the pile shaft (inner stirrups) and farther from the pile shaft (outer stirrups). For stirrups with 4 branches as in beam T8, strain in exterior and interior branches for outer and inner stirrups was monitored.

- The pile cap's plate strain.

- The failure mode and the crack pattern.

The results for beam T2 (control beam) are presented in Figures 4-8 to 4-12, which compare the recorded results for the experimental study (EXP.) and the finite element analysis (FEA). Figure 4-8 demonstrates that the numerical and experimental load displacement curves are in excellent agreement, except after the ultimate load was reached as the predicted softening curve was slightly different from the observed experimental results. Figure 4-8 also demonstrates the accuracy of the calculated first flexural cracking load, the breakout cracking load, and the ultimate load. Similarly, Figure 4-9 shows the accurate strain predictions in all longitudinal reinforcement bars. The numerical model also captured the release of strain in the longitudinal reinforcement after the stirrups yielded and concrete cover spalling occurred. In addition, Figure 4-10 demonstrates that there is a very good match between the calculated and measured stirrups strains; however, the finite element predicted slightly earlier initiation of strain in

the stirrups. This may be attributed to the difference in the location at which the strain was recorded on the stirrups between the model and the experimental setup. The strain of the pile cap's plate was also well predicted by the finite element model as shown in Figure 4-11. Finally, the crack patterns of half of beam T2 recorded experimentally is compared with the predicted crack pattern in Figure 4-12. It is clear from Figure 4-12 that the finite element model was able to correctly predict the crack patterns for flexural and breakout cracking even with approximately the same angles. It also predicted accurately the diagonal cracks at the top of the beam next to the pile shaft with the same angle during different stages of loading.

The same excellent agreement was observed through the comparison of the numerical predictions and the experimental results for the remaining 8 experimentally tested connections, including specimens with concrete compressive strength of fc' = 30 MPa and 40 MPa. These comparisons are included in Appendix D.
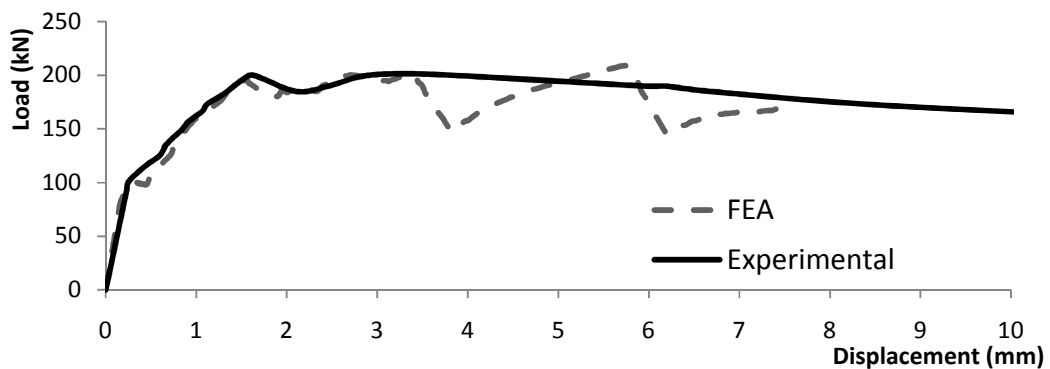
Figure 4-8 Load mid-span displacement from experimental test and finite element model for beam T2
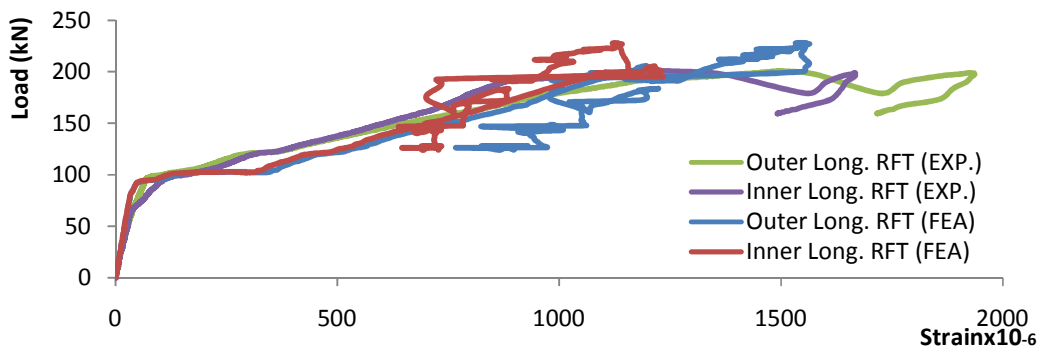
Figure 4-9 Load longitudinal reinforcement strain from experimental test and finite element model for beam T2
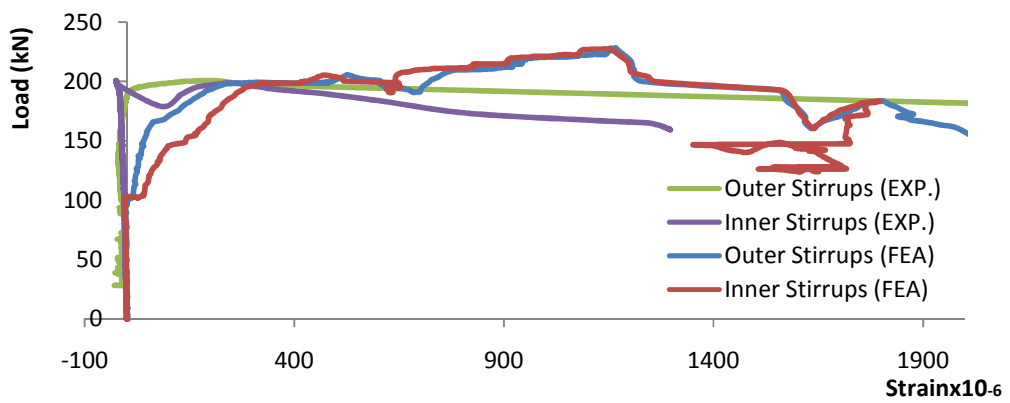
Figure 4-10 Load stirrups strain from experimental test and finite element model for beam T2
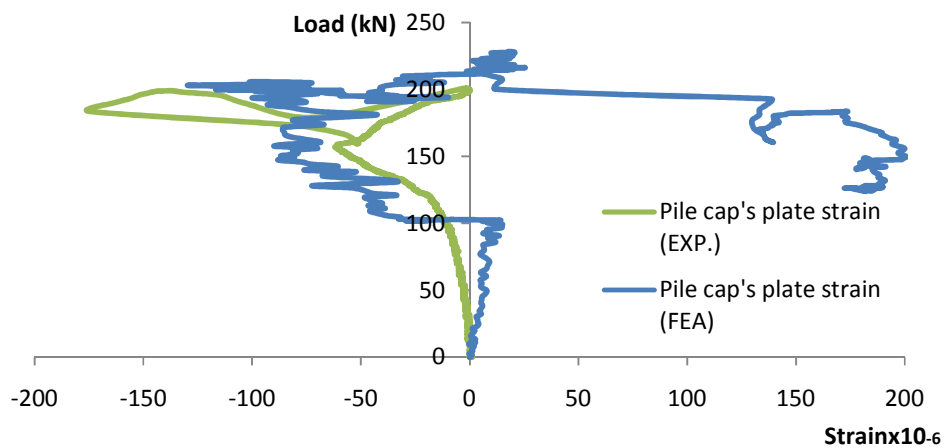
Figure 4-11 Load pile cap plate strain from experimental test and finite element model for beam T2

139
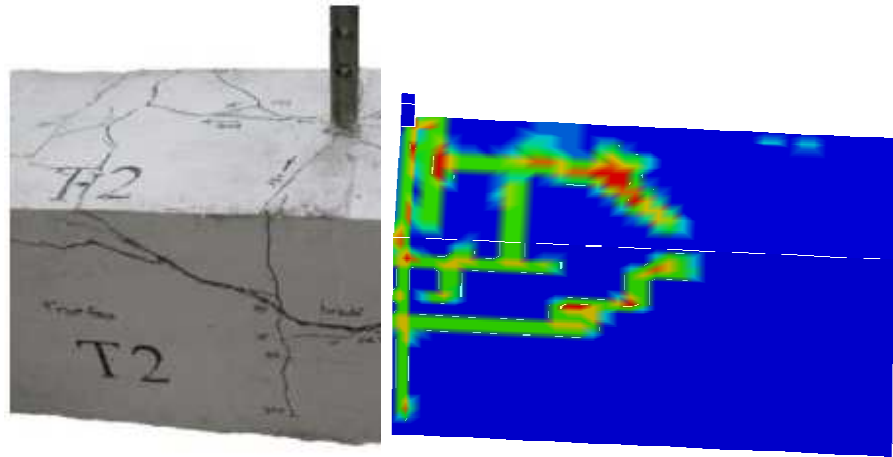
Figure 4-12 Crack patterns from experimental test and finite element model for beam T2

4.13 Verification of numerical model using published experimental results

In order to further verify the developed finite element model, it was used to analyze the experimental work reported by Angelakos et al. (2001). They investigated the influence of concrete compressive strength and minimum stirrups on the shear response of large lightly reinforced concrete members. The test beams DB120, DB130 and DB140 were analyzed using the finite element model described above. The full beams were modeled using 8-node hexahedron solid constant-stress elements with three displacement degrees of freedom at each node with one integration point and element size of 60 mm. Because the tensile capacity was not presented in the paper, the concrete material variables were calculated using the procedure of (Magallanes , 2010 ;and CEB-FIP model code , 1993). The same contact mechanism, loading, supporting system, and concrete and steel material models were employed. The calculated load-displacement curves for the three beams are compared with the measured responses from the experimental work of Angelakos et al. (2001) in figure 4-13. It is noted from figure 4-13 that the finite element model predicted

both the initial stiffness and the beam stiffness reduction due to flexural cracking accurately. It also captured the flexural shear cracking; however, it did not capture accurately the beam softening after the ultimate load. Figure 4-14 compares calculated and observed crack patterns of beams DB120, DB130, and DB140. Again, the finite element model predictions are in good agreement with the experimental observations.
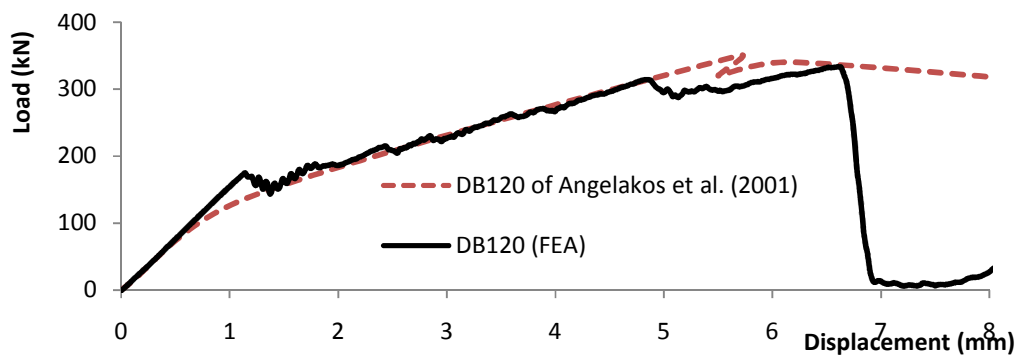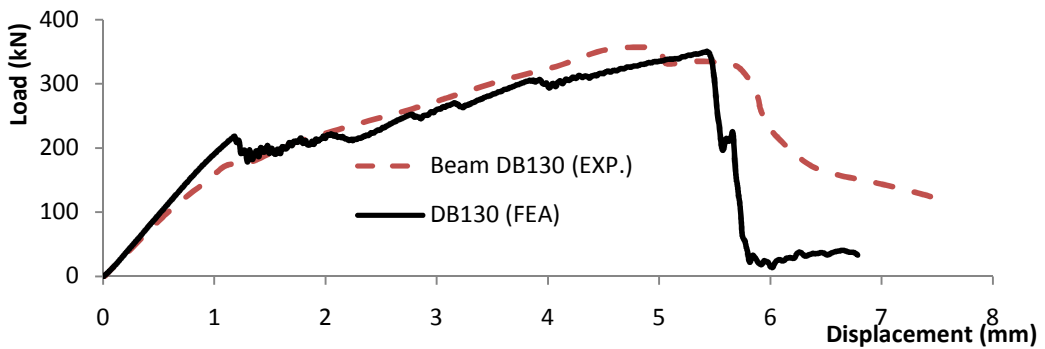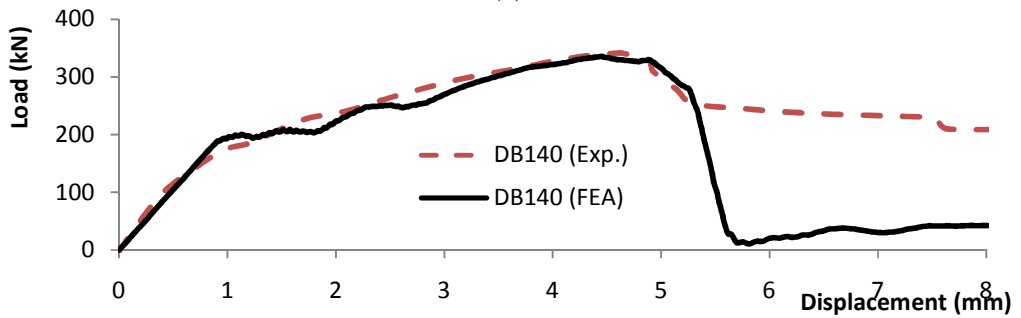
Figure 4-13 Load mid-span displacement curves for: (a) DB120; (b) DB130; and (c) DB140
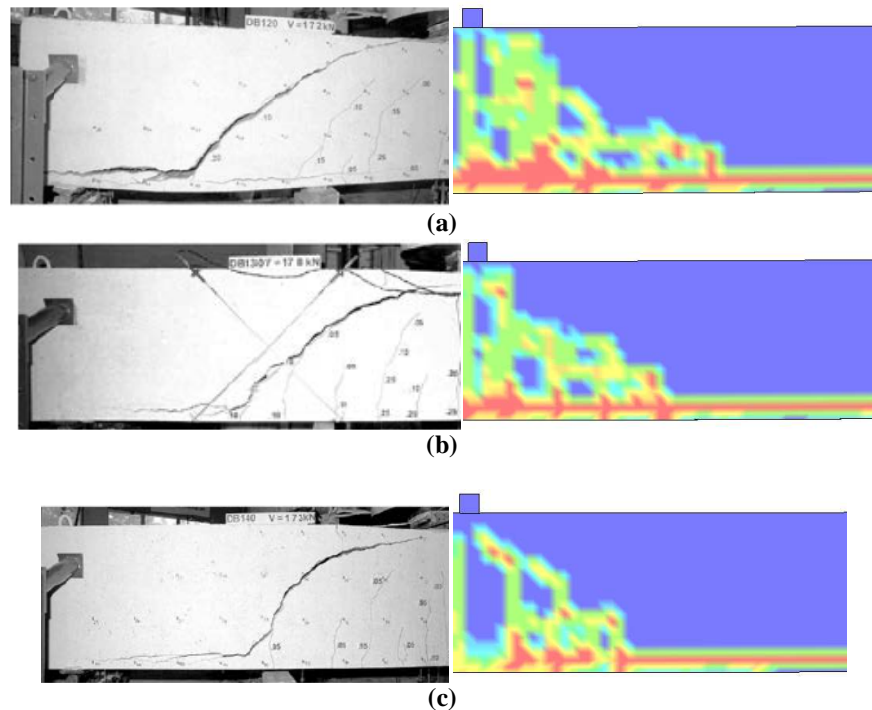
Figure 4-14 Crack patterns observed for: (a) DB120; (b) DB130; and (c) DB140

The excellent agreement between the finite element model predictions and the experimental results of the current study and those from Angelakos et al. (2001) confirms the ability of the numerical model to correctly simulate the behavior of reinforced concrete beams. Hence, it can be employed to examine the new construction bracket in an extensive parametric study to cover a range of parameters outside what was considered in the experimental study.

4.14 Numerical Parametric Study and Discussion of Results

The verified 3-dimensional finite element models are utilized to simulate the behaviour of the connection between the pile shaft and the grade beam using a pile cap detail or a welding detail. In order to cover the range of connection parameters used in practice, both

pile cap and concrete beam dimensions and strength properties were varied and their impact on the connection performance was evaluated.

4.14.1 Factors investigated in the parametric study

The parametric study investigated the influence of different factors on the connection response. These factors included: pile and pile cap parameters; concrete beam parameters and pile-beam connection parameters. The pile and pile cap parameters included: pile shaft embedment depth, pile cap plate size, and pile cap configuration (bolted or welded). The concrete beam parameters included: longitudinal reinforcement ratio, transverse reinforcement ratio and configuration, anchor reinforcement, concrete strength, shear span/depth ratio (i.e. a/d ratio) and beam height and width. The pile-beam connection parameters included: position of the pile shaft with respect to supports location, support detail (tensile anchor supports or bearing supports on the same side of the beam), corner effect and supports direction (one way or two way supports). All of the specimen data used in this parametric study are listed in Appendix E.

4.14.2 Discussion of results

For each factor of the studied factors several models were built to investigate its effect. The connection breakout cracking load, ultimate load capacity, the load-displacement relationship, the crack pattern, and the mode of failure are the main comparison criteria that will be used in their results discussion.

4.14.2.1 Specimens experimentally tested and used in the finite element investigation for

   comparison

To ensure that the finite element model is predicting realistic data, most of the test groups
of the factors that affect the pile connection had one or more of the beams experimentally
tested. The parameters of these experimentally tested beams are shown in Table 4- 3, and
Figure 4-15 summarizes their dimensions and details.

Table 4- 3 Details of studied experimentally tested Specimens

Beam Name	Beam Dimensions (mm)	Concrete Strength fc'(N/mm^2)	The embedment depth (mm)	Pile cap width (mm)	Longitudinal Reinforcement	Stirrups
T1	500x500x1600	30	152	165	4-15M	2 branches #2@200mm
T2	500x500x1600	30	203	165	4-15M	2 branches #2@200mm
T3	500x500x1600	30	254	165	4-15M	2 branches #2@200mm
T4	500x500x1600	40	203	190	4-15M	2 branches #2@200mm
T5	500x500x1600	40	203	229	4-15M	2 branches #2@200mm
T6	500x500x1600	40	203	165	4-20M	2 branches #2@200mm
T7	500x500x1600	40	203	165	4-25M	2 branches #2@200mm
T8	500x500x1600	40	203	165	4-15M	4 branches #2@200mm
T9	500x500x1600	40	203	165	4-15M	2 branches #2@100mm

Figure 4-15 Dimensions and full details for the tested specimens

4.14.2.2 Influence of the pile embedment depth

Three pile embedment depth, D, values were investigated considering beams that have the same variables of beam T2 (control beam). The investigated beams are denoted T-D-228 (D=228 mm), T-D-280 (D = 280 mm) and T-D-305 (D = 305 mm).

Figure 4-16 demonstrates the load-displacement curves for the investigated beams along with experimental results for the corresponding test beams. It can be noted from Figure 4-16 that the first flexural cracking load was approximately the same for all beams. Afterwards, the connection stiffness and ductility increased as the pile embedment depth increased. Figure 4-17 shows that the connection ultimate load increased as the embedment depth increased linearly until the embedment depth is equal to half the beam height. The connection capacity continues to increase as the embedment depth increases, but it is affected by the overall beam behavior, which will be discussed when considering the beam height on the connection behaviour. Finally, it was noted that cracks pattern was the same as that observed during the experiments.
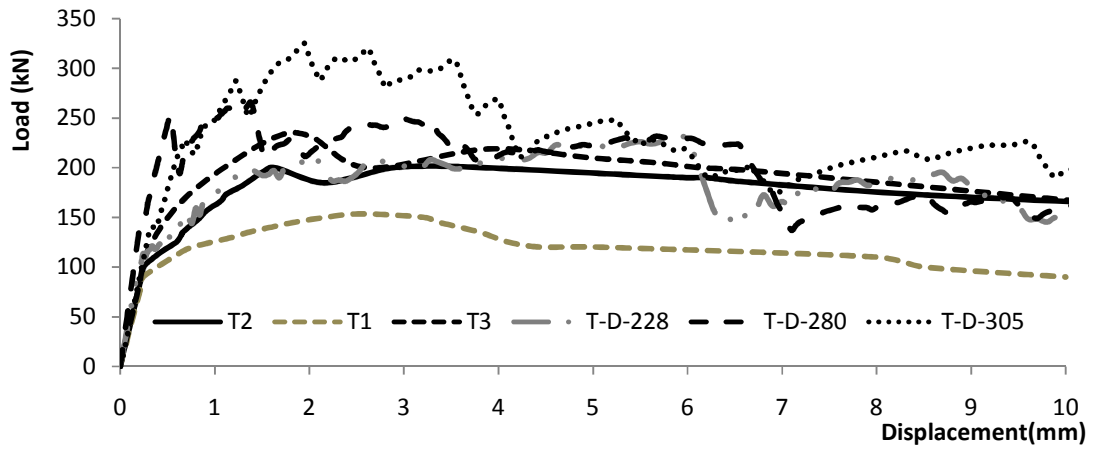
Figure 4-16 Effect of pile embedment depth on load mid-span displacement curve
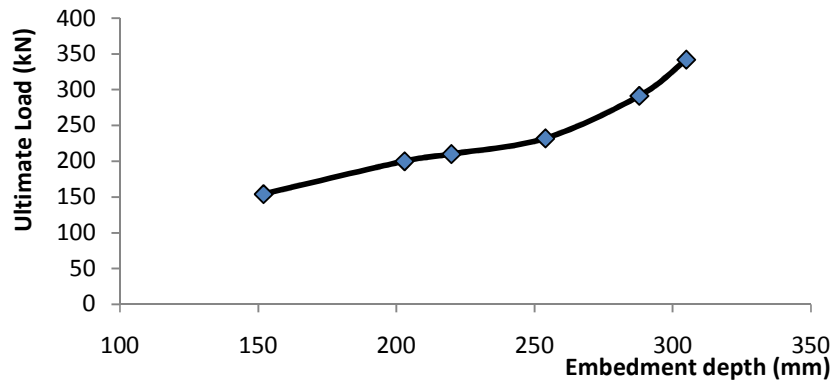
Figure 4-17 Effect of pile embedment depth on the connection load capacity

4.14.2.3 Influence of the size of pile cap plate

Three plate width, P, values were investigated considering beams that have the same variables of beam T2 (control beam). The investigated beams are denoted T-P-100 (P =100 mm), T-P-305 (P = 305 mm) and T-P-380 (P = 380 mm).

Figure 4-18 demonstrates the load-displacement curves for the investigated beams along with experimental results for the corresponding test beams. From figure 4-18, it is observed that the connection breakout load and the ultimate load increased as the plate

146

size increased. Only plate with P = 190 mm (investigated in the experimental program) exhibited some slight reduction in capacity compared to P = 165 mm. The numerical results also demonstrated that the size of the breakout cone increased as the plate width increased, which may explain the increase in the ultimate load. Figure 4-19 demonstrated that the connection capacity increases as the plate width increases; however, the increase in capacity was at a small rate as the plate width exceeded 250 mm. As the plate width increased beyond 300 x 300 x 20 mm, the plate yielded before the breakout cracking occurred. Thus, in order to increase the capacity of the connection, both the plate width and thickness have to be increased to ensure that the plate does not yield before the breakout cracking occurs (e.g. increase plate thickness to 25.4mm).
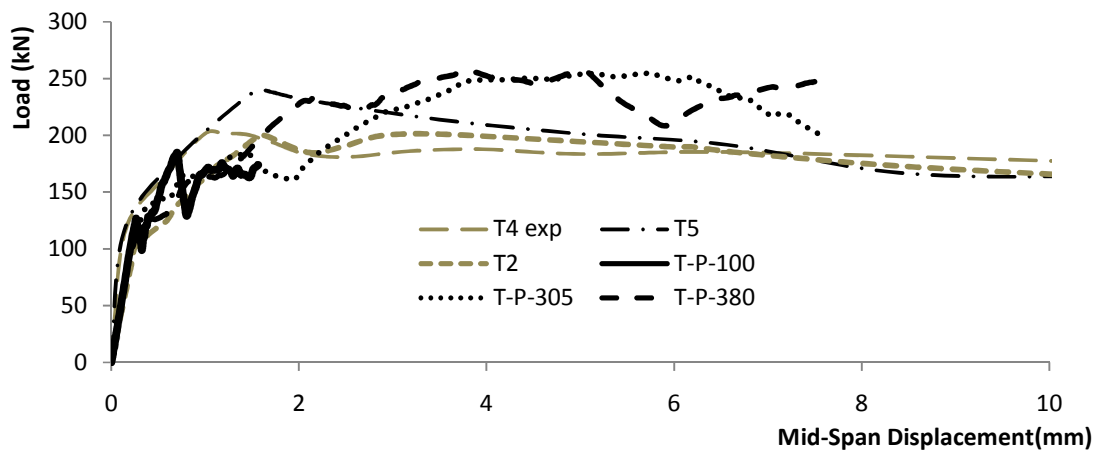
Figure 4-18 Effect of plate width on load mid-span displacement curve
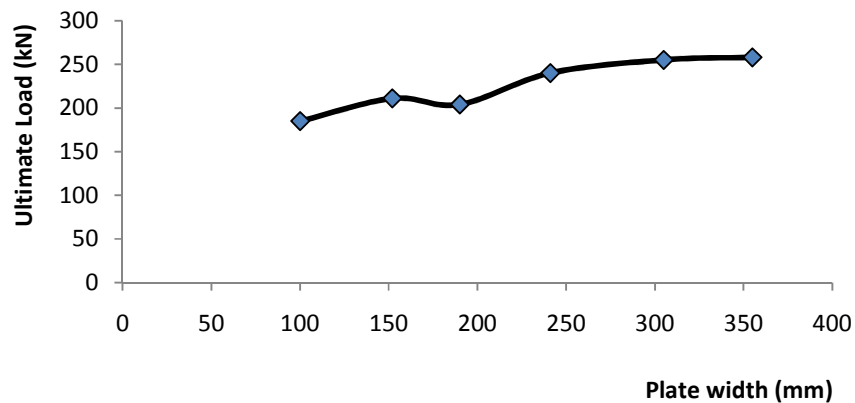
Figure 4-19 Effect of plate width on the connection ultimate load

4.14.2.4 Influence of the longitudinal reinforcement ratio

In this group, beams with two different values of concrete compressive strength (30 MPa and 40 MPa) and seven different values of steel reinforcement ratios were investigated. Four bars were used in all analyzed cases, but the bar designation changed in different beams, i.e. 10M, 15M, 20M, #7, 25M, 30M, and 35M were used in beams T-B-10, T-40, T6, T-B-7, T7, T-B-30, and T-B-35, respectively.

Figure 4-20 displays the load mid-span displacement curves for connections installed in beams with concrete compressive strength of 40 MPa. It is noted from Figure 4-20 that the stiffness of all connections was close to each other until first cracking occurred, and differed afterwards. It can also be noted that the breakout cracking load was almost equal to the ultimate load for all beams. Furthermore, it is clear that the connection stiffness and ductility increased as the longitudinal reinforcement ratio increased.

Figure 4-21 demonstrates the influence of longitudinal reinforcement ratio on connection breakout cracking load considering beams with fc' = 30 or 40 MPa. It is noted from the

148

figure that the connection ultimate load capacity increased as the longitudinal reinforcement ratio increased for both values of fc'. It is also noted that the connection ultimate load capacity increased slightly as fc' increased from 30 MPa to 40 MPa. Figure 4-22a shows that beam T-B-35 experienced failure mechanism similar to shear failure while T-B-25 (and the rest of beams) failed due to breakout cone formation from the plate ends as shown in Figure 4-22b.
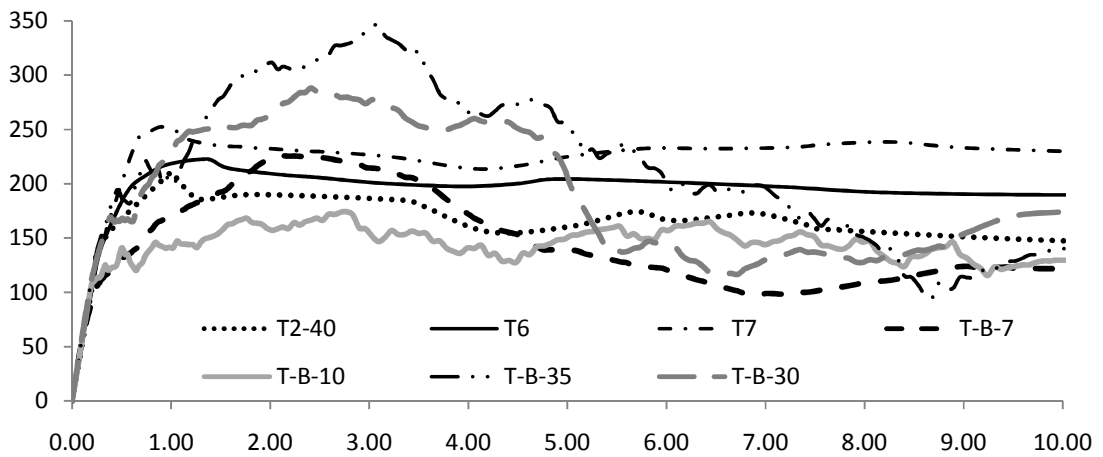
Figure 4-20 Load mid-span displacement curves for connections in beams with fc'=40 MPa
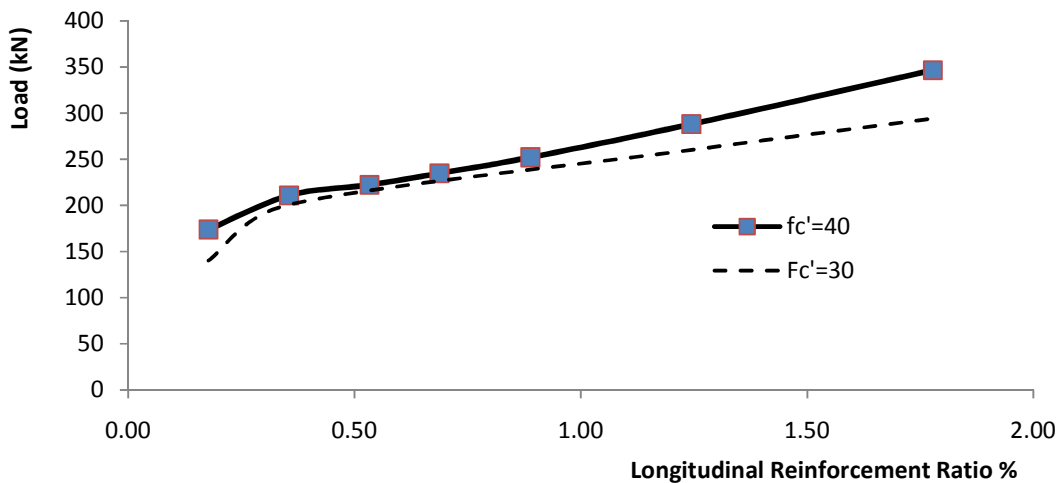
Figure 4-21 Influence of longitudinal reinforcement ratio on connection breakout cracking load

(a)

(b)
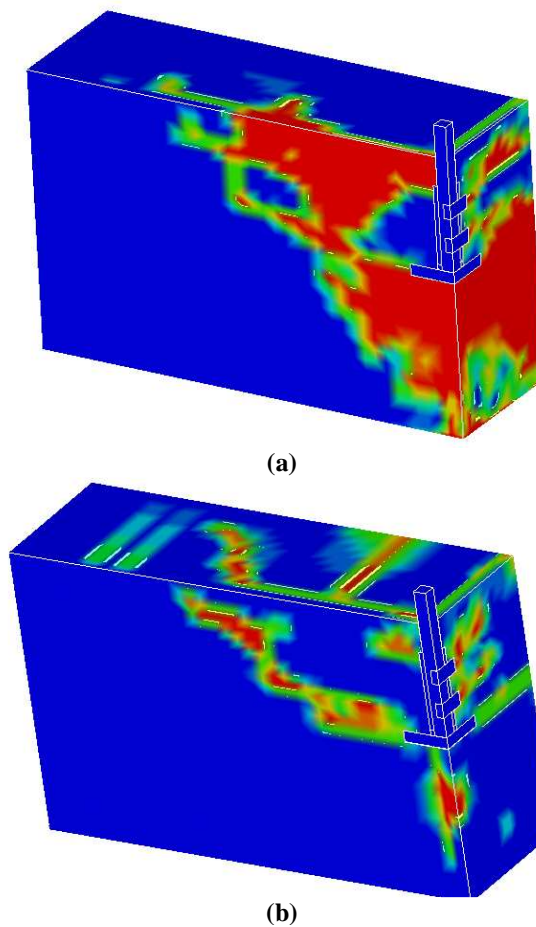
Figure 4-22 Crack pattern of the connection: (a) T-B-35 (fc'=40 MPa and 4-25M); (b) T-B-25 (fc'= 30 MPa and 4-25M)

4.14.2.5 Influence of the transverse reinforcement ratio and configuration

The effects of the transverse reinforcement on the connection performance were investigated considering closed stirrups with different bar designations, stirrups' spacing and number of branches in each stirrup. In addition, a beam without any stirrups, denoted T-S-0, was considered. The following stirrups arrangements were considered: 2br. #2@ 200 mm, 2br. 8mm@200 mm, 2br. #2@100 mm, 4br. #2 @200 mm, 2 br. 10M @200 mm, 2br. 8 mm @100 mm, 4br. 8 mm@200 mm, 2br. 15M @200 mm, 2br.

150

10M@100 mm, 4br. 10M @200mm, 2br. 15M @100mm, and 4br. 15M @200mm. All beams are considered to have concrete with fc'= 30 MPa and fs_y = 400 MPa.

The stirrups' effects on the connection performance were investigated in terms of the connection behavior versus that of a beam subjected to regular three-point direct loading. In addition, the effects of the stirrups configuration with varying reinforcing ratio and stirrups configuration with same reinforcing ratio on the connection performance were evaluated.

Figure 4-23 shows the load-displacement response for a beam subjected to three-point direct loading with and without stirrups compared to the same beam loaded using the pile connection with and without stirrups. The beam failed in flexure under three-point direct loading, however, the same beam without stirrups loaded through the pile connection experienced significant decrease (70%) of its capacity. It can be concluded from Figure 4-23 that a higher transverse reinforcement ratio may increase the connection ultimate load, however, it alters the failure mechanism to shear failure at a lower ultimate load compared to the beam capacity (obtained from 3-point direct loading) as shown for the beam with 2br.-15m@200 mm. In this case, the stirrups prevented a premature failure similar to that occurred in beam T-S-0, which occurred just after the flexural cracks reached the pile cap's plate level as shown in figure 4-24(a). In T-S-0, the failure initiated with a crack that extended from the plate ends to the support, and split the beam into two parts. The part that resists the loading will have a height equal to the embedment depth of the pile. In the finite element model, this small part of the beam failed in flexural at a low

load capacity because of the small resisting height. The presence of the stirrups with adequate percentage prevented cracks' initiation at the plate ends from widening and expanding horizontally. Thus, if there were no stirrups in the connection, a new limit state would be added equal to the capacity of a beam with a height equal to the embedment depth in shear or flexural wherever is less. In this case, the diagonal tension capacity of the separated part of the beam was lesser and the beam failed in shear. This ultimate load was close to the shear capacity calculated by Response 2000 using the embedment depth equal to the beam height. As shown in Figure 4-24, the finite element model predicted the behaviour of the beam loaded in a three point direct loading expected the occurrence of failure mechanism at a much higher load due to flexural failure and a shear failure was not expected to take place before the flexural failure, however, using the pile connection in the beam caused the beam to fail at a lower load and totally different failure mechanism.
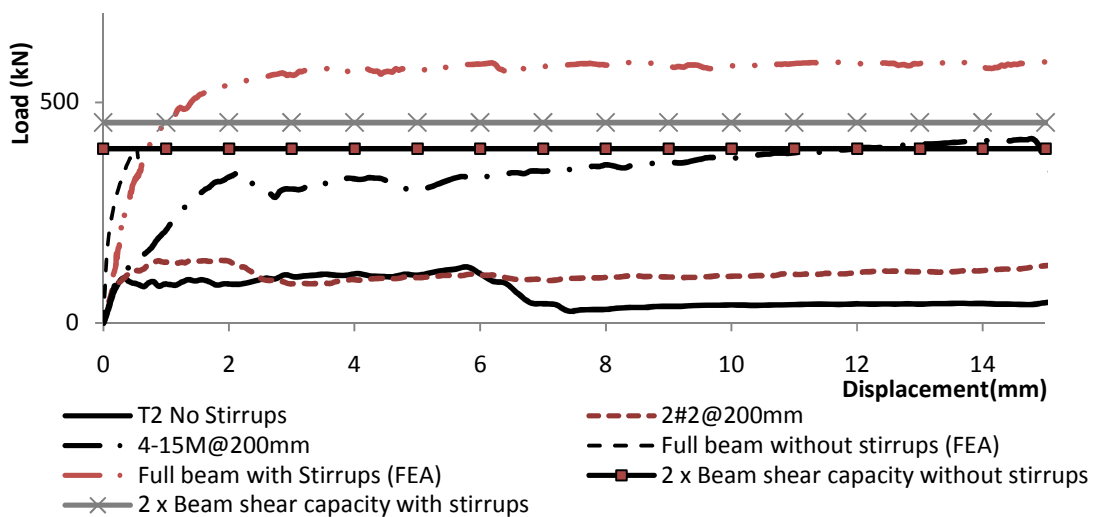
Figure 4-23 Load mid-span displacement response
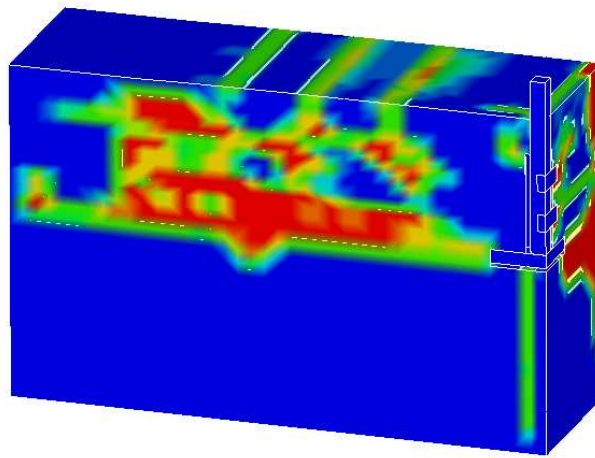
(a)
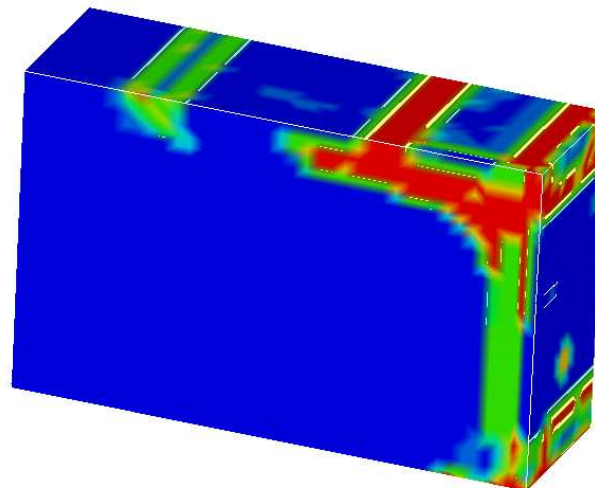
(b)

Figure 4-24 Crack pattern: (a) loaded through pile connection; (b) beam subjected to 3-point direct loading

Figure 4-25 presents the load-mid span displacement response for stirrups with different diameter but same spacing and number of branches. The figure shows that increasing the transverse reinforcement ratio increased the connection capacity but the maximum connection capacity was still much less than that of the beam subjected to 3-point direct loading.

153
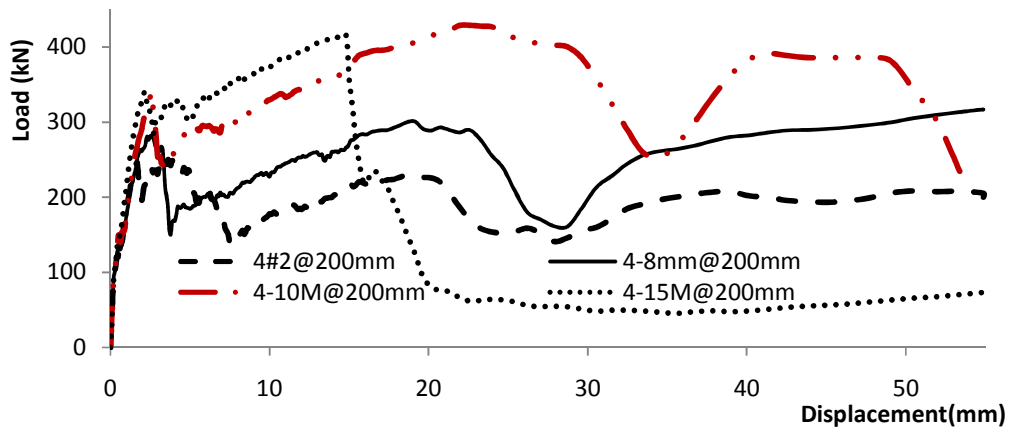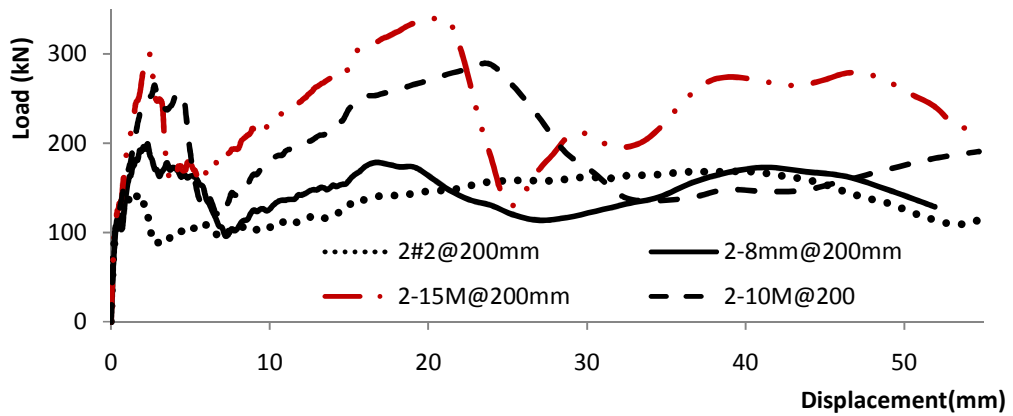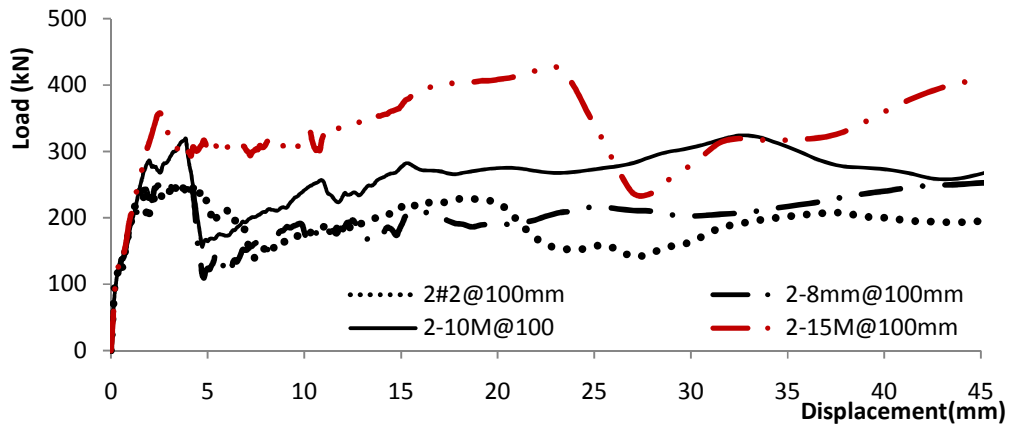
Figure 4-25 Load mid-span displacement response for stirrups (a) 2br@100 mm spacing; (b) 2br@200 mm spacing; (c) and 4br@200 mm

Figure 4-26 demonstrates the load-mid span displacement response for beams with same transverse reinforcement ratio but different stirrups configuration. It shows clearly that using more branches in each stirrup close to the pile shaft can achieve higher connection ultimate load at lower displacements. Using more branches near the plate ends enhances the beam integrity as it engages the dowel action of the longitudinal reinforcement and the concrete aggregate interlock. However, the connection ultimate load is approximately the same and equal to the tensile capacity of the stirrups contained in the breakout cone.
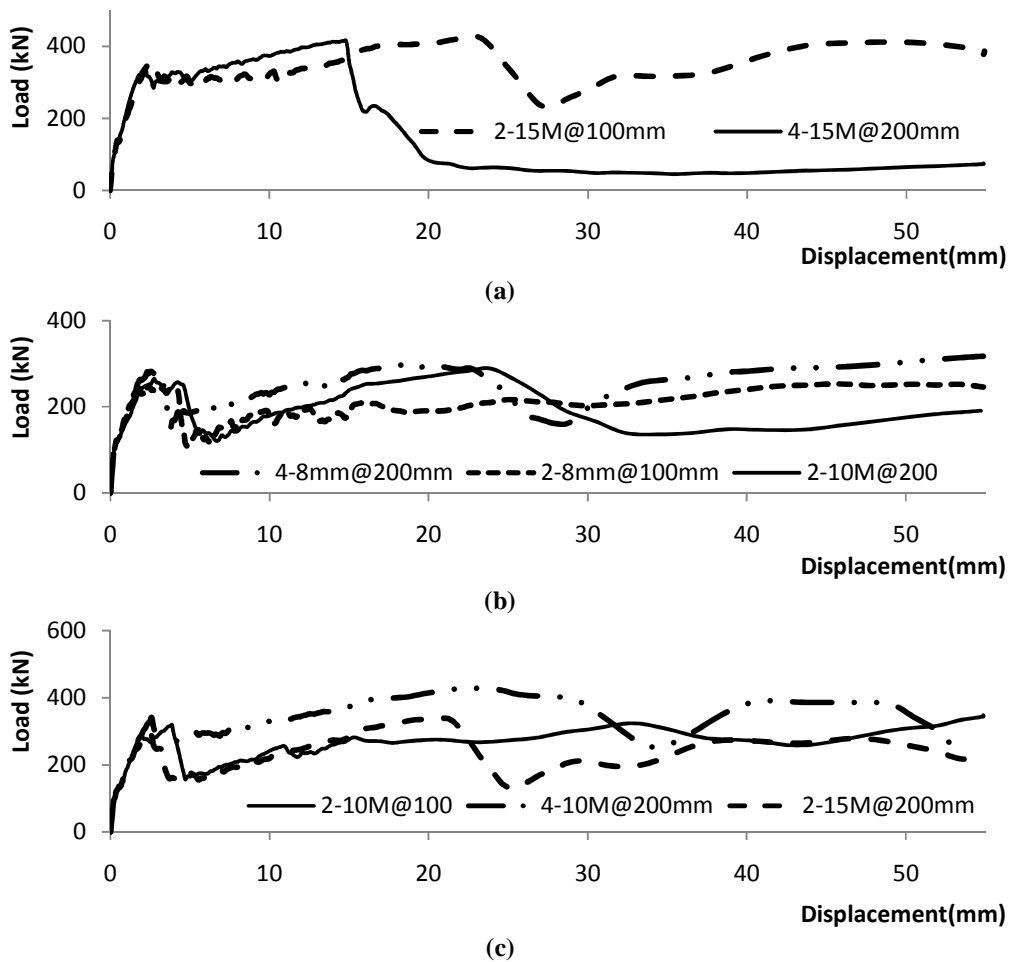
Figure 4-26 Load mid-span displacement response for the same transverse reinforcement ratios with different configurations : (a) 0.8%; (b)0.2%; (c)0.4%

Figure 4-27 indicates the effect of the transverse reinforcement ratio on the connection ultimate load. It is noted that for reinforcement ratio ≥ 0.4%, the connection capacity did not increase, probably because of beam shear failure due to the formation of a bigger breakout cone involving the full depth of the beam at the connection location as indication to the beam shear failure. The ultimate load was equal to twice the capacity of beam cross-section shear (454.2 kN as obtained from Response 2000). Thus, the connection capacity would be equal to the beam shear capacity if adequate transverse reinforcement was used.
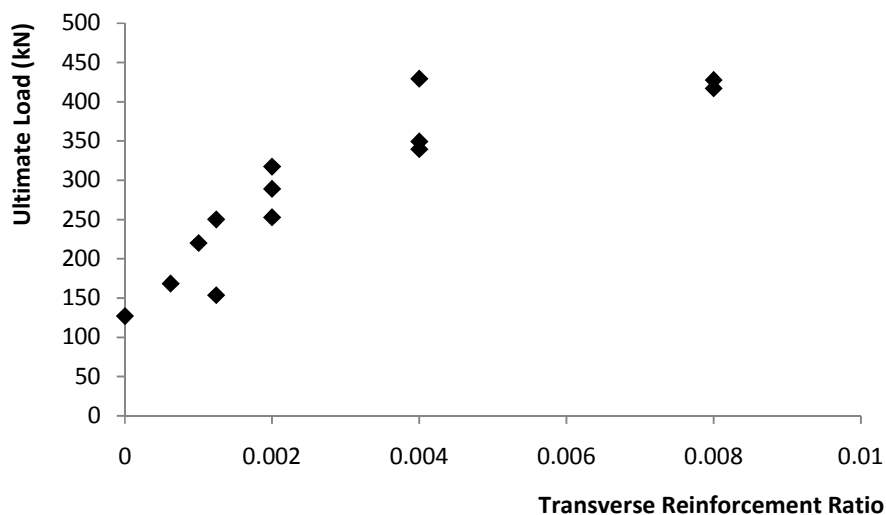
Figure 4-27 Relation between the connection ultimate load and the transverse reinforcement ratio

The crack patterns for beam T2 with low and high transverse reinforcement ratios are presented in Figure 4-28. It can be noted from Figure 4-28 that the breakout cone for the beam with high transverse reinforcement ratio extended to the full depth of the beam at the connection location. This was not the case for the beam with low reinforcement ratio.

156
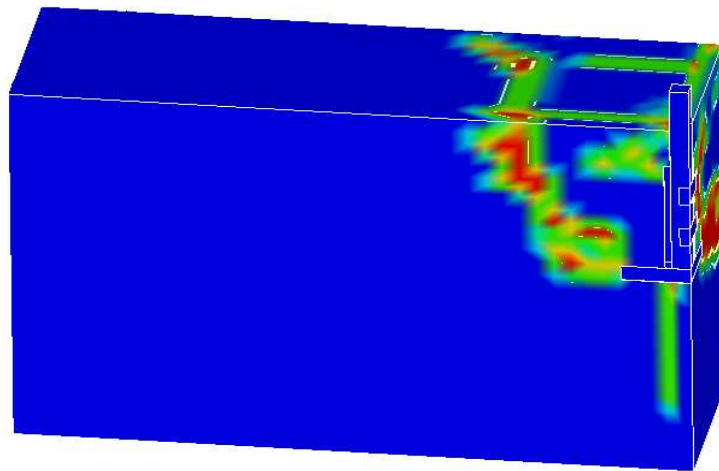
(a)
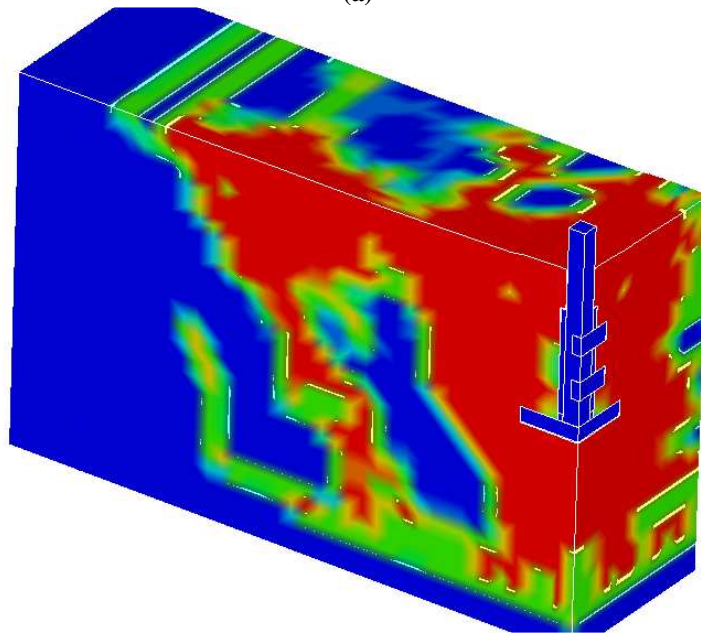
(b)

Figure 4-28 Crack pattern of connection in beam with: a) 2br.#2@200 mm; (b) 4br. 15M @200mm

4.14.2.6 Influence of anchor reinforcement

In this group, 6 beams were studied to capture the anchor reinforcement influence on the connection behaviour. All beams had only anchor reinforcement, i.e. 4 stirrups at the location of the pile shaft, two stirrups from each side, as shown in Figure 4-29. The

beams investigated are denoted T-A-6, T-A-8, T-A-10, T-A-15, T-A-20, and T-A-25 which had 4 bars of #2, 8mm, 10M, 15M, 20M, and 25M, respectively.
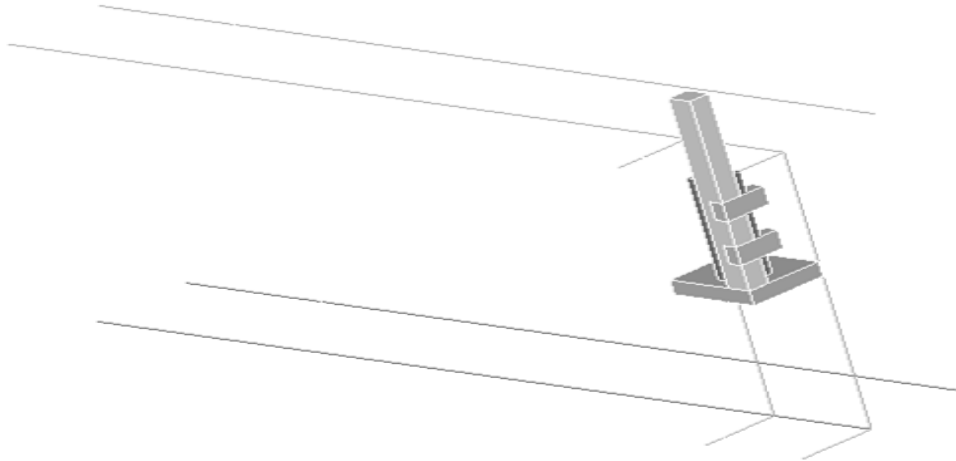
Figure 4-29 Anchor reinforcement configuration in one quarter of beam

Figure 4-30 shows the load displacement response of the investigated beams. It shows that as the anchor reinforcement strength increased the connection ultimate capacity, and will increase the breakout cracking load slightly. For beams T-A-6, T-A-8, and T-A-10, the connection ultimate load was equal to the ultimate tensile capacity of the anchor reinforcement. However, when the anchor reinforcement tensile strength exceeded twice the shear capacity of the beam (T-A-15, T-A-20, and T-A-25), the beam failed in shear before the anchor reinforcement failed. This is clearly presented in figure 4-31, as connection capacity did not increase for T-A-15 which had 4-15M anchor bars.
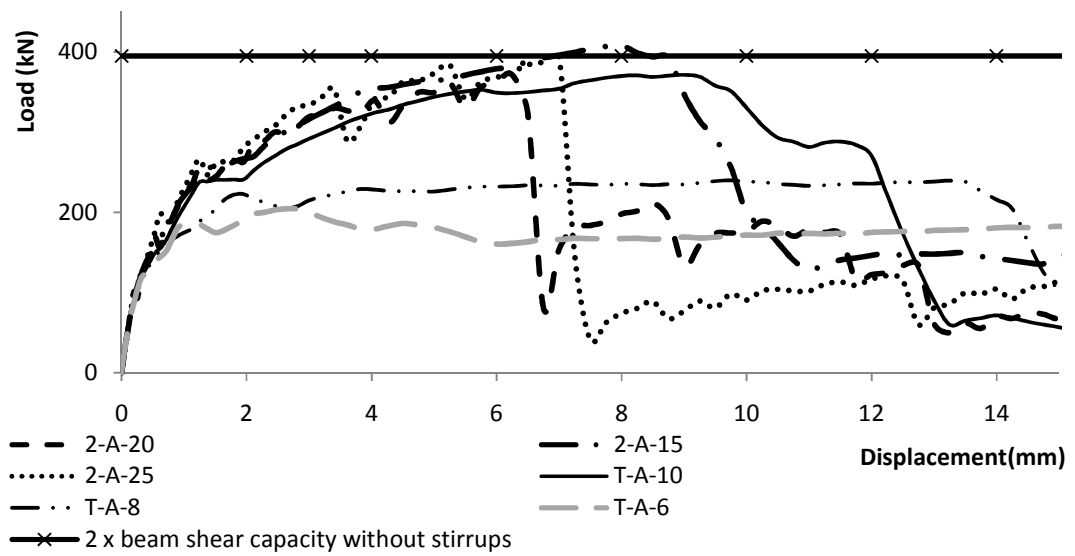
Figure 4-30 Load mid-span displacement relationship
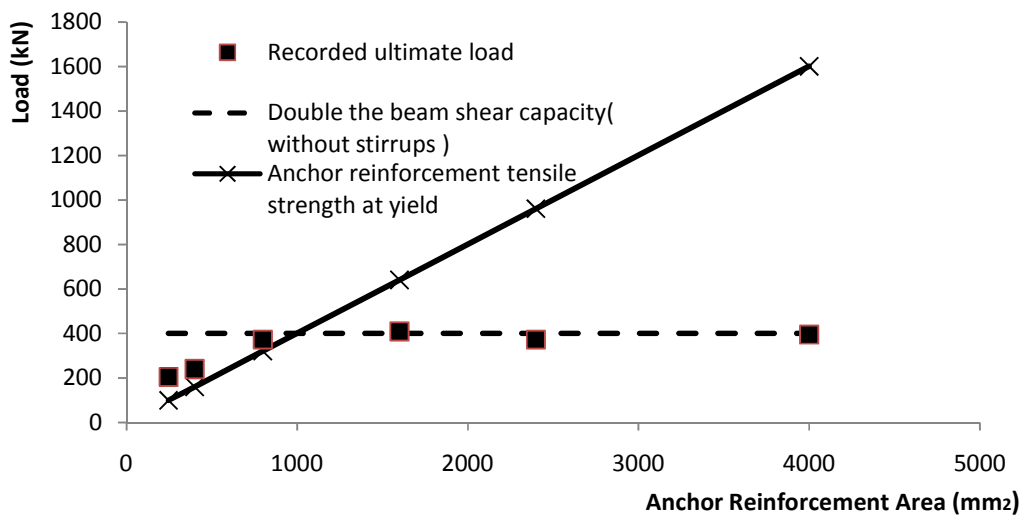
Figure 4-31 Effect of anchor reinforcement area on the connection load capacity

4.14.2.7 Influence of the concrete strength

The specimens tested in the experimental program were cast from two different concrete

batches with fc' = 30MPa and 40 MPa. In this numerical study, 3 beams with the

properties of beam T2 were examined considering concrete compressive strength, fc' = 20

159

MPa (T2-20), 30 MPa (T2) and 40 MPa (T2-40). All beams failed after the breakout cracking initiated and the breakout cone propagated vertically. Figure 4-32 presents the load-displacement response for the investigated beams, which shows that the breakout cracking load increased and the corresponding displacement decreased as the concrete strength increased.
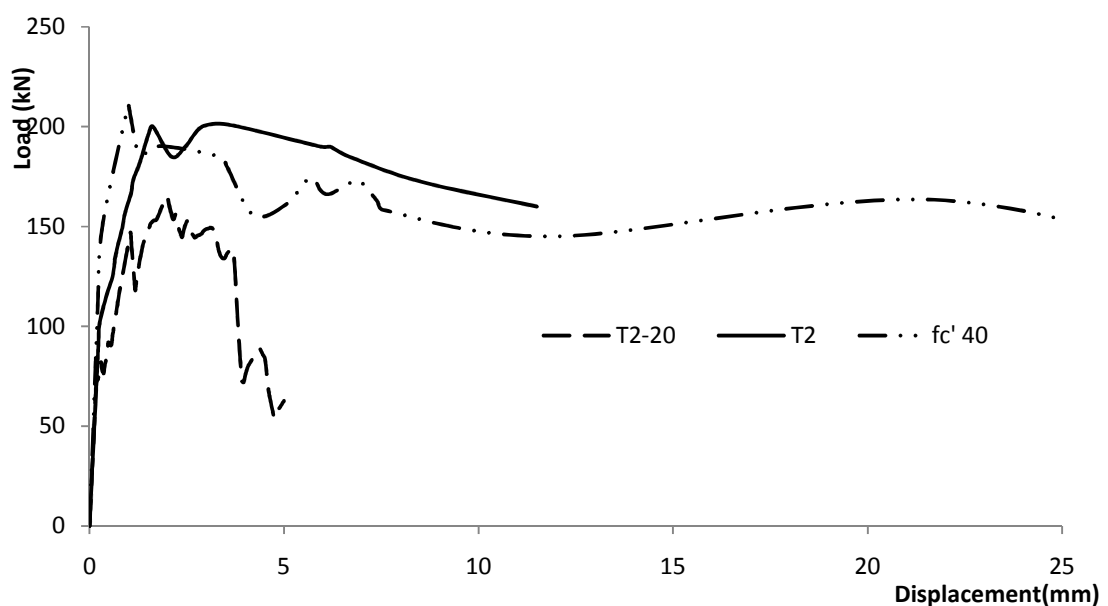
Figure 4-32 Load mid-span displacement response

4.14.2.8 Influence of beam shear span/depth ratio (a/d)

The beam shear span/ depth ratio has a significant influence on its behaviour and the expected failure mechanism. For beams with short span, i.e. 1.0 < a/d < 2.5, loads are transferred by arch action, and either shear compression failure or loss of bond failure is expected after cracking. For 2.5 < a/d < 5 to 6, diagonal tension failure is expected.

Finally, for (a/d) > 5 to 6, flexural failure is expected (MacGregor, 1988). In the current study, both beam depth and the pile embedment depth affect the beam behaviour.

To explore the effect of beam depth, 8 values of (a/d) were examined from: 0.25 to 2.75 for beams T-R-0.25 to T-R-2.75, respectively. The corresponding (a/d_{emb}) ratio varied between 0.55 and 6.1. It is clear that in the first two beams T-R-0.25, T-R-0.5 the connection behaviour will be close to the deep beam behaviour. All beams had the same variables of beam T2 including 4-15M longitudinal bars except for the location of the support, which depended on the beam span. The analyses were repeated for beams with longitudinal bars of 4-30M to prevent premature flexural in longer spans beams.

The load-displacement response curves for beams with 4-15M and 4-30M bars are presented in Figure 4-33. It is noted from Figure 4-33 that increasing (a/d) decreased the connection breakout cracking load and its ultimate load. A limit state (diagonal tension failure) was reached when a/d exceeded 2.25. Another limit state (compression strut failure) was reached when a/d < 0.5, which was discussed in ACI 318-99 and denoted as the sliding maximum shear strength and it was specified as $\sqrt{fc'}.b.d$. This limit state is affected by the longitudinal reinforcement ratio, i.e., failure occurred at 630 kN and 550 kN for longitudinal reinforcement of 4-30M and 4-15M, respectively. However, ACI 318 (2008) suggested neglecting the reinforcement' effect and specified that the shear capacity of deep beams shall not exceed 0.83 $\sqrt{fc'}.b.d$ (i.e. 550 kN for both reinforcement amounts).
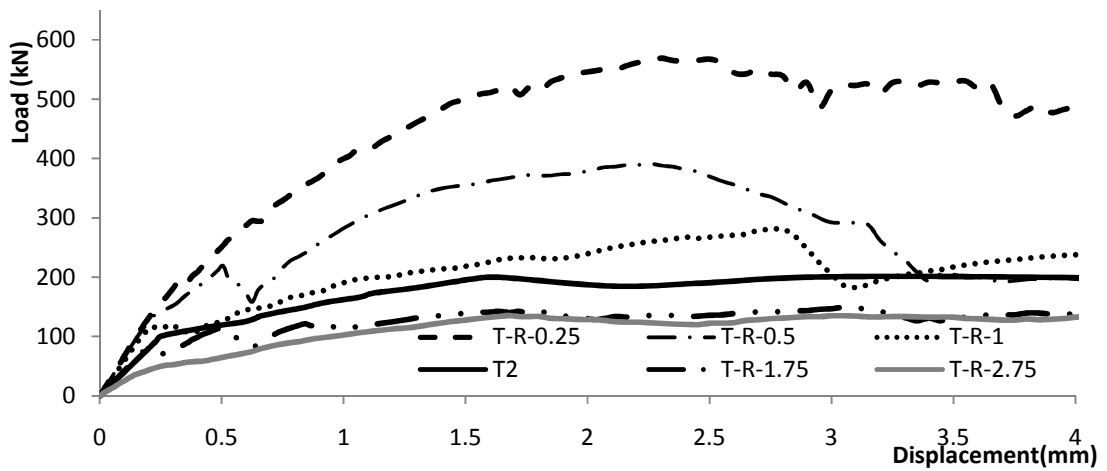
(a)
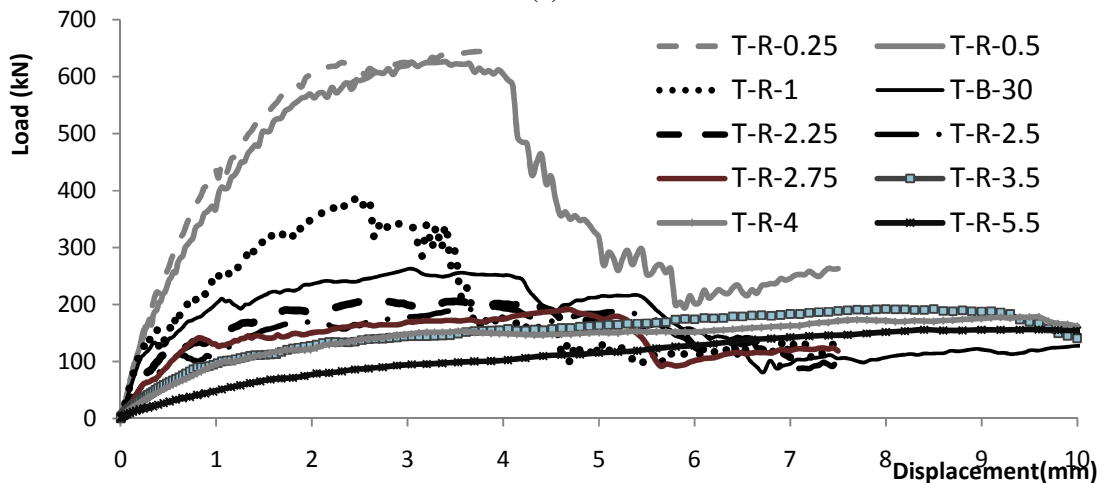
(b)

Figure 4-33 Load mid-span displacement response for different (a/d) ratios: (a) using 4-15M longitudinal bars, (b) using 4-30M longitudinal bars

4.14.2.9 Influence of beam height

In this group, four different beam heights were considered: 300, 500, 750 and 1500 mm, which results in (a/d) = 2.45, 1.35, 0.85, and 0.45 for beams T-H-300, T2, T-H-750, and T-H-1500, respectively. All beams had (a/d_{emb}) = 3 and same stirrups diameter and spacing of beam T2 (i.e. varying transverse reinforcement ratio).

162

Figure 4-34 shows the obtained load displacement response curves. It shows that even for constant d_{emb} and a/d_{emb} ratios, the connection load resistance and its breakout load increased as the beam height increased. This demonstrates the effect of the beam height, which is attributed to reduced strain in the concrete at the same load because of higher existing lever arm. In addition, beam T2-H-300 failed mainly due to shear failure and its ultimate load was higher than its breakout load. This was mainly because the pile embedment depth was greater than half of the beam depth.
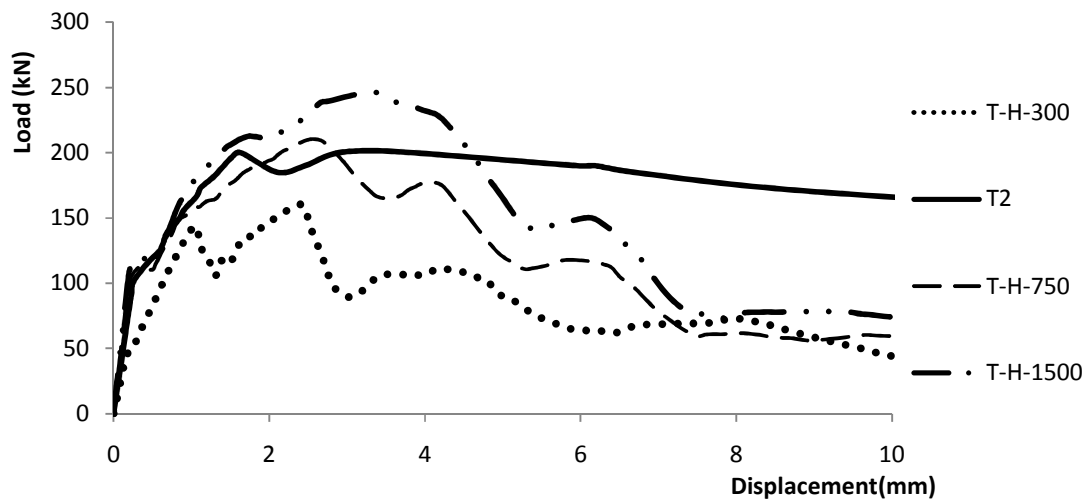
Figure 4-34 Load mid-span displacement relationship

4.14.2.10   Influence of beam width

To investigate the effect of the beam width on its breakout cracking load, four beams were investigated. Beams T2-S-0, T-W-800, T-W-1400, and T-W-1600 had a width of 500 mm, 800 mm, 1400 mm, and 1600 mm. They all had no stirrups to examine the effect of the concrete shear strength.

163

Figure 4-35 displays the crack pattern of T-W-1600. It is clear that the breakout cracks extended horizontally in the width direction and the failure was due to one way shear even though the beam width was equal to its depth. Similar observation was made in all experimental results. Figure 4-36a presents the load-displacement response of the examined beams. The results in Figure 4-36a show that the breakout cracking load increased as the beam width increased almost linearly when no stirrups were used as shown in Figure 4-36b.
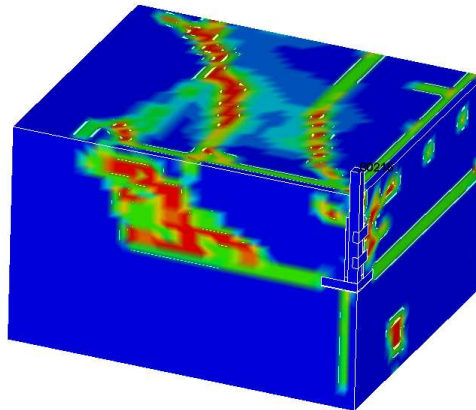
Figure 4-35 The crack pattern of the connection in T-W-1500 (beam width=1500mm)

(a)

164
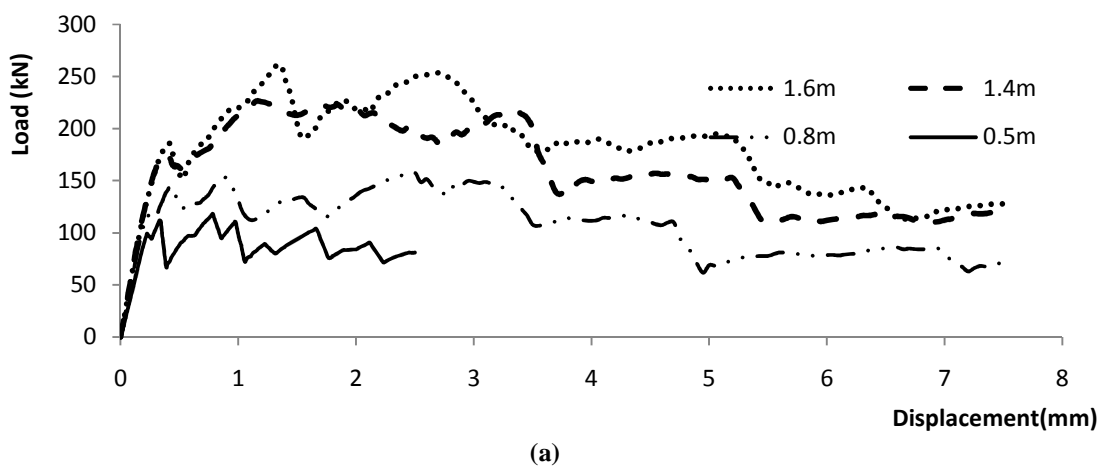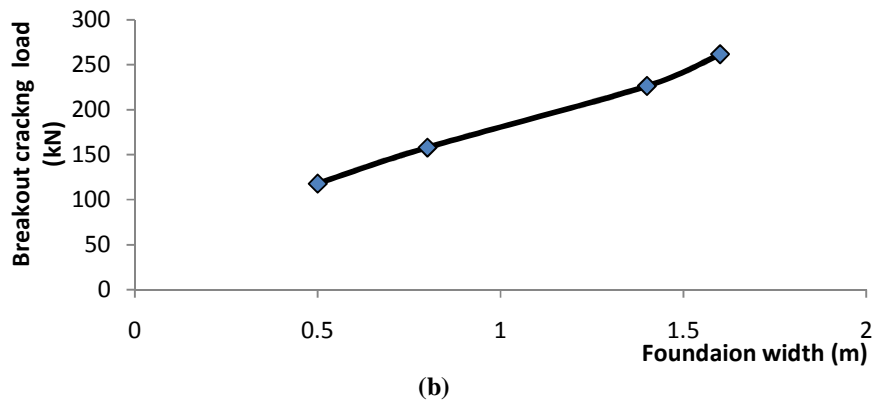
Figure 4-36 Effect of beam width on connection performance: (a) load-displacement curve; (b) breakout cracking load

4.14.2.11   Influence of position of pile shaft in respect to supports' location

The pile shaft could be connected to the grade beam at different locations relative to the supports. In order to examine the effect of distance of pile shaft to the support on the connection capacity, two beams with different (a/d) ratios from each side were studied and compared with the control beam. Beam T-L-0.75 had short spans as the pile shaft positioned such that (a/d) = 1.35 from one side and 0.75 from the other side. Beam T-L-3.8 had long span and the pile was positioned to achieve (a/d) = 1.35 from one side and 3.8 from the other side. The longitudinal reinforcement of T2-L-3.8 was increased to 4-30M to prevent beam flexural failure.

Figure 4-37 demonstrates the crack pattern of T2-L-3.8. It is clear that the angle of breakout cracking is not the same on both sides, and was different from the experimentally observed as 35° cracks in beam T2. As (a/d) increased, the angle with the horizontal axis decreased and the diagonal crack closer to the support initiated before the initiation of the cracks at the far side. Beam T-L-0.75 displayed the same behaviour.

165
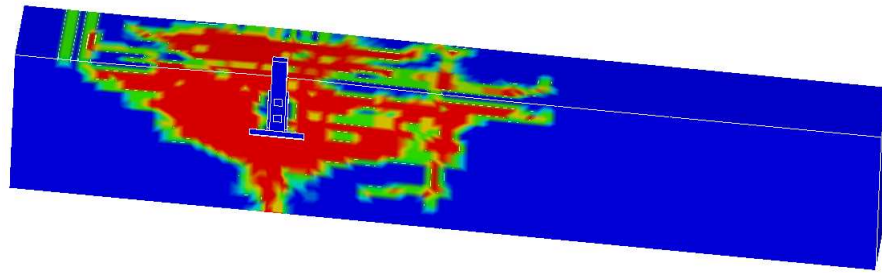
Figure 4-37 Crack pattern of connection in T2-L-3.8

Figure 4-38 presents the load-displacement response for T2-L-0.75 and T2-L-3.8 compared with the experimental results for T2. Beam T2-L-0.75 had higher breakout cracking load and higher ultimate load than that of beam T2 because it had lower (a/d) from one side. However, beam T2-L-3.8 had approximately the same breakout load as T2 because it had higher longitudinal reinforcement (4-30M compared to 4-15M in T2). Thus, the ratio (a/d) of both sides should be examined when calculating the connection capacity.
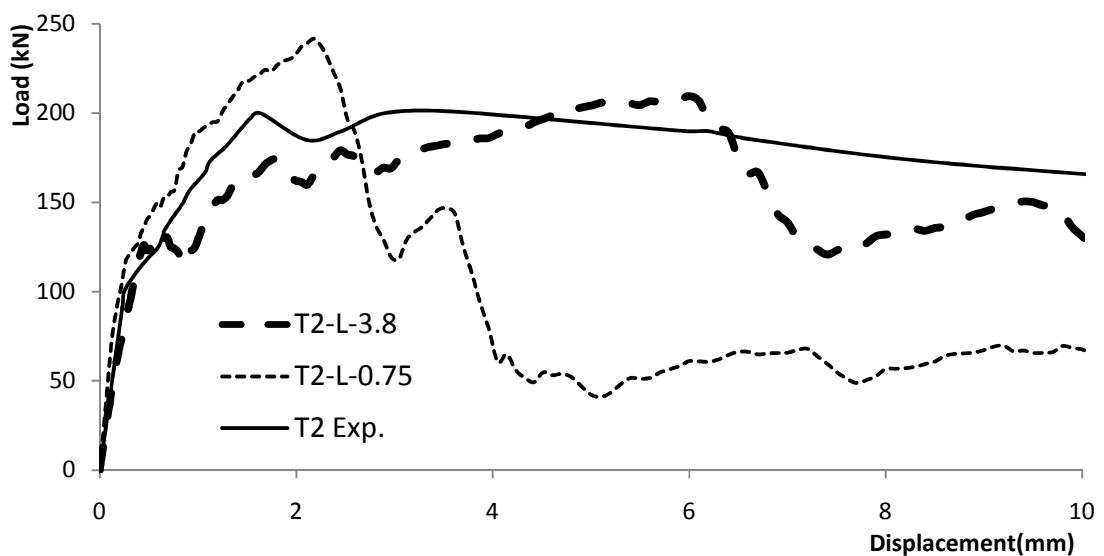
Figure 4-38 Load mid-span displacement relationship

4.14.2.12   Influence of pile cap configuration (Bolted and Welded details)

There are two methods implemented in practice to connect pile cap to helical piles or micropiles: bolted to pile shaft (same as that used in the experimental program) or welded to the pile shaft. In order to investigate the method used to connect the pile cap to the shaft on the connection performance, beam T2 was modeled considering a welded connection. This model is denoted T2W. All other variables of beam T2 were kept constant.

Figure 4-39 compares the calculated load-displacement responses of the bolted and welded connections as well as the measured response of the bolted connection. No obvious difference in behavior can be detected, suggesting that both methods of connectivity would have comparable performance in terms of stiffness, first cracking load, breakout cracking load, and ultimate load.
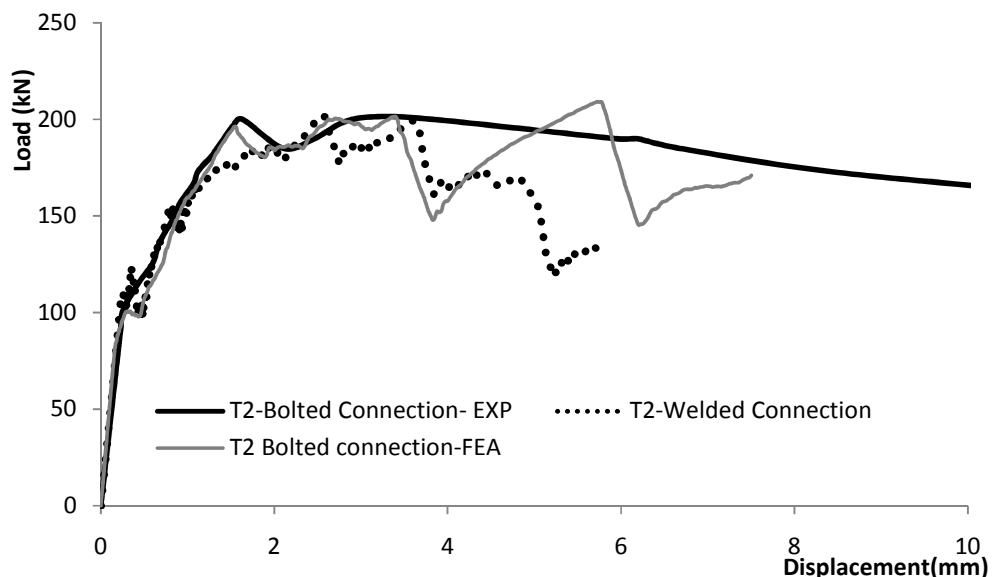
Figure 4-39 Load mid-span displacement relationship for different pile cap configurations

4.14.2.13   Influence of support detail (anchor support or bearing support)

In cases where columns or walls dowels are connected to the grade beam or anchors of steel towers (e.g. telecommunication towers) tied to the foundation, the anchor support may alter the connection behavior from the normal bearing support type. To explore this case, a finite element model is built to capture the effect of using an anchor as a support at the other side of the pile and the results were compared with the numerical and experimental results of beam T2. The model had the same variables of beam T2, but with anchors fully embedded in the concrete as shown in Figure 4-40.

Figure 4-41 compares the load-displacement response of this case with that obtained for beam T2. Both beams exhibited the same behaviour including connection stiffness as well as first flexural cracking, breakout cracking and ultimate loads, and both has approximately the same crack pattern. It should be noted that most codes locate the critical section for beam with tension supports at the support face, which increases the chance of beam shear failure in case of uniform loading for pile embedment depth greater than half of the beam depth.

The same analysis was repeated considering (a/d) = 1, 0.75, 0.5, and 0.25 while keeping other variables constant. For (a/d) < 1.0, the connection breakout load decreased and even the crack pattern changed. For example, for (a/d)<0.25, the breakout diagonal cracking did not extend to the loading points as happened in the ordinary loaded beams.
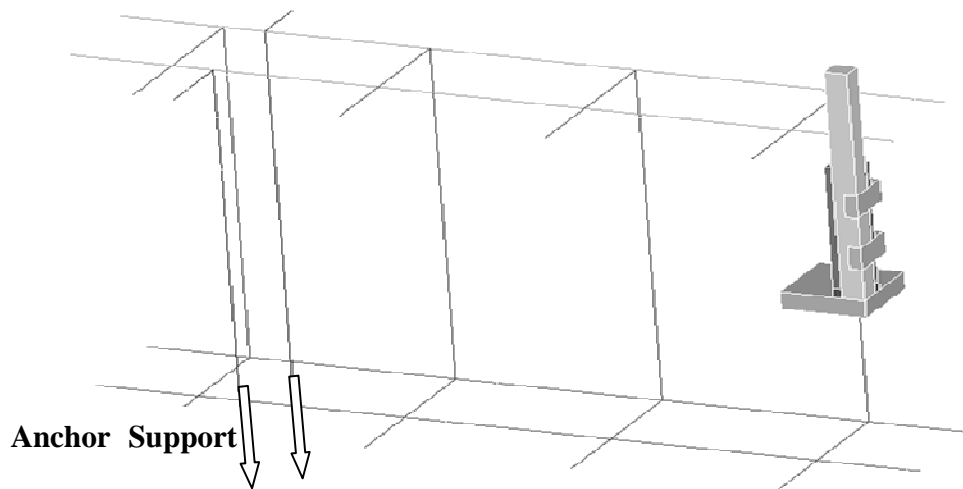
Anchor Support

Figure 4-40 Support configuration modeled as tension anchors fully embedded in the concrete
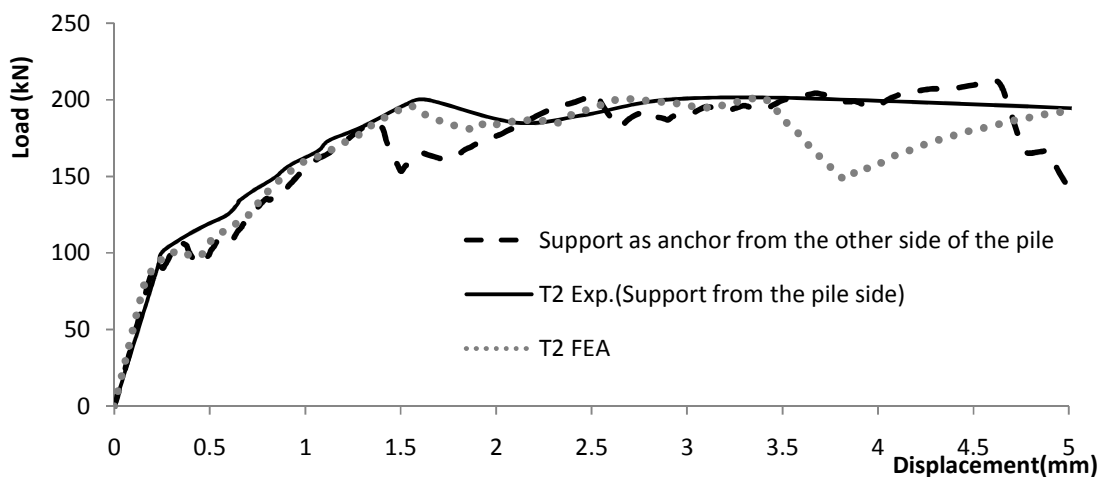
Figure 4-41 Load mid-span displacement response using anchor support for (a/d)=1.35

4.14.2.14   Influence of pile connection at corner of grade beam.

The pile connection was considered at the corner of the grade beam that had the same variables of beam T2. Figure 4-42 compares the load-displacement response of the corner connection with that obtained for T2. The results show that the corner connection

experienced higher displacement and exhibited lower stiffness compared to T2. This behavior is attributed to reduced constraint of the outside surface of the corner, which reduced the connection resistance. Also, the connection may experience torsion strains, which would also increase the applied shear stresses to the connection. As a result, the corner connection first cracking load, breakout cracking load, and ultimate load decreased as shown in Figure 4-42. Moreover, the stirrups contribution to the connection capacity decreased because they were farther from the pile shaft than that in an internal connection. Thus, it is recommended to add more anchor reinforcements at the corner locations.
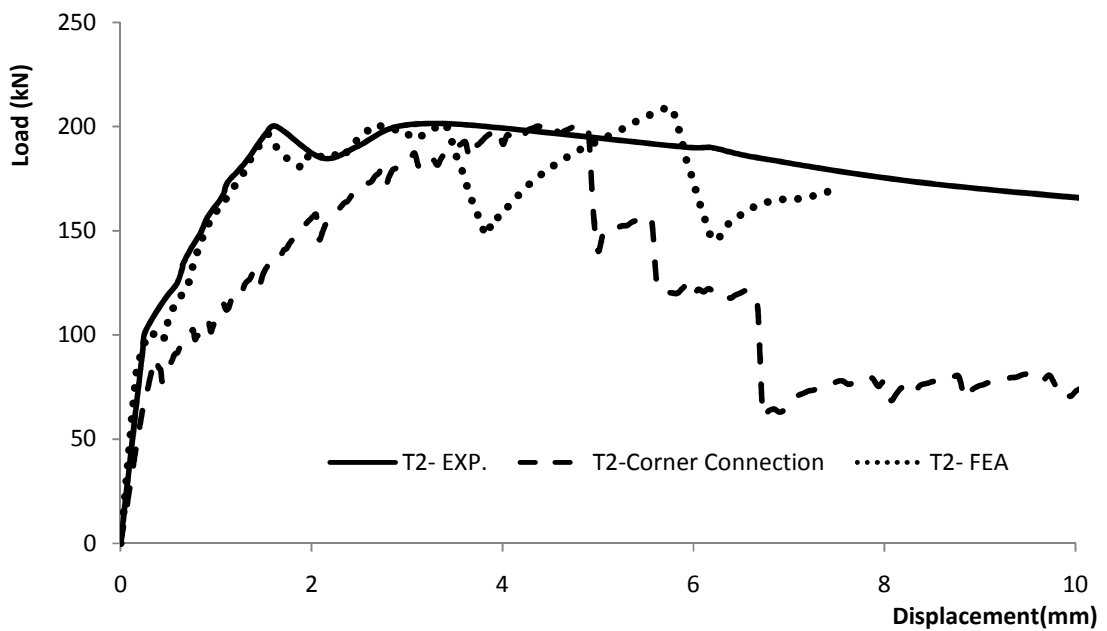
Figure 4-42 Load mid-span displacement reponse

4.14.2.15   Influence of supports direction (one way vs two way support)

Helical piles and micropiles may be used to support stiff pile caps or flexible rafts. In this case, the supports to the pile connection will be in two perpendicular directions. To explore the performance of the connection in this case, a two-way slab with same variables of beam T-W-1600 was analyzed considering the pile shaft at its centre with line supports from two directions.   The slab denoted T2-TWO had dimensions of 1600x500x1600 mm. The results from this analysis were compared with those obtained for beam T-W-1600.

The failure mechanism of T2-Two was due to breakout cracking similar to the crack pattern of anchors embedded in concrete with adequate edge distance and similar to the punching shear in slabs, but subjected to tension.

Figure 4-43 shows the load-displacement response for the investigated cases. It is noted from Figure 4-43 that T2-TWO and T-W-1600 had the same initial stiffness till cracking. Then, T2-two had higher load capacities, i.e., higher breakout cracking and ultimate loads. In conclusion, the connection behaviour in the two-way loading is better than that of the one-way loading and it is expected to resist more load and absorb more energy before its failure.
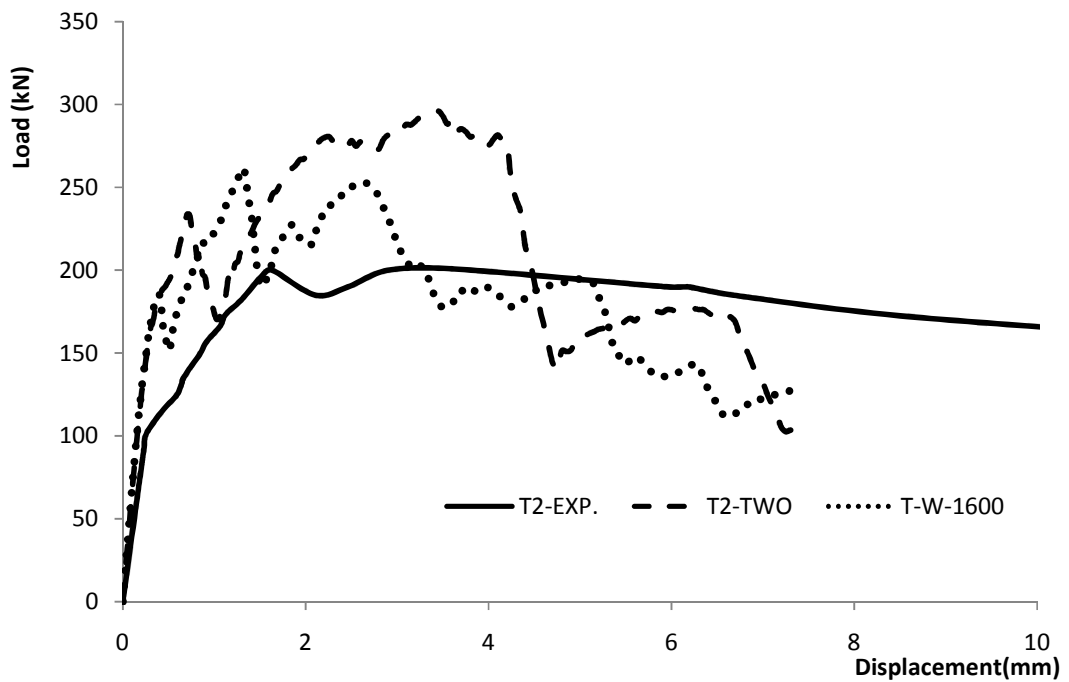
Figure 4-43 Load mid-span displacement relationship

4.15 Conclusions

1) The used finite element model is accurately predicting the behaviour of the helical pile-new reinforced concrete foundation connection, and it is recommended to be used for detailed design and analysis of the connection.

2) The connection capacity must be considered as part of the foundation design.

3) The connection can be considered fixed up to its breakout cracking load. The connection becomes hinged and its capacity would depend on its longitudinal and transverse reinforcements.

4) The breakout cracking initiates from the end of the pile cap's plate at 35° angle if the distance between the supports is $> 3 \, d_{emb}$ and the pile cap's plate will not yield during loading.

5) The observed crack propagation in the studied connection is similar to cracking under one ways shear.

6) The dimension of the breakout cone can be given by the lesser of ($b_{plate} +2.5 \, d_{emb}$) and ($3 \, d_{emb}$).

7) The pile shaft transfers the load to the beam primarily through the bolts and the pile cap's plate.

8) The breakout cracking load is affected by the concrete strength and longitudinal reinforcement contributions and is not affected by the transverse reinforcement.

9) The connection ultimate load is affected by the concrete strength, the longitudinal reinforcement, and the transverse reinforcement contributions.

10) For embedment depth less than one half of the beam height, the connection breakout cracking and ultimate loads increase almost linearly as the pile embedment depth increases.

11) An increase in the pile embedment depth enhances the beam ability to dissipate energy.

12) The plate width has minor effect on the connection stiffness, however, the larger the plate size, the higher the connection capacity and the larger the breakout cone dimensions was observed. This effect, however, is negligible if the plate yielded before the breakout cracking load.

13) The connection first flexural cracking, breakout cracking and ultimate loads increase as the longitudinal reinforcement ratio increases.

14) The transverse reinforcement ratio had no effect on the first flexural cracking and breakout cracking loads. However, using adequate transverse reinforcement ratio increases the connection capacity after the breakout cracking, and it can transfer the connection failure mechanism from brittle to ductile.

15) Using different transverse reinforcement configuration but same ratio can enhance the load transfer mechanism by placing higher percentage of transverse reinforcement close to the pile shaft. Only the transverse reinforcement contained in the breakout cone can add to the connection strength.

16) The connection ultimate capacity should be the lesser of the calculated capacity and the vertical tensile strength of the transverse reinforcement. The vertical tensile capacity should account for all stirrups within the breakout cone.

17) The capacity of a connection without transverse reinforcement is equal to the capacity of a beam with height equal to pile embedment depth if this beam is expected to fail in shear. Thus, minimum transverse reinforcement is

recommended at the connection location even if there is no transverse reinforcement in the beam.

18) The beam capacity in flexure and shear must be considered as limit states to the connection capacity.

19) The vertical tensile capacity of the anchor reinforcement within the plate width should be at least twice the required shear capacity of the beam at the pile location. As the anchor reinforcement tensile strength increases, the breakout cracking load will slightly increase and the ultimate loads will significantly increase.

20) As concrete strength increases the connection breakout capacity increases.

21) The ratio (a/d) affects the connection capacity. The breakout cracking load will increase for (a/d) < 2.5. For 2.5 <(a/d) < 6.0, the concrete shear strength and breakout cracking load will not change. However, for (a/d) < 1.0, the breakout cracking load increases remarkably higher than that for (a/d) > 2.5 because the load transfer mechanism changes to arch-type instead of beam-type, and the beam in this case is considered as a deep beam. Therefore, a strut and tie model is the best representative to the connection load transfer mechanism for a/d<1.

22) Increasing the beam height while maintaining the pile embedment depth and the shear span constant leads to increased connection capacity if stirrups are presented.

23) The connection breakout cracking load increases linearly with the beam width increase at the pile location when no stirrups are presented.

24) For connections shifted from the beam mid-span, its capacity should be the sum of shear strengths of the two sides using (a/d) representing each side; however, It is recommended to conservatively use twice the shear capacity of the side with higher (a/d) ratio as the connection shear capacity.

25) Welded and bolted pile cap connections have the same performance and capacity under tension loading.

26) The anchor support has negligible effect on the connection capacity for (a/d) >1, but the connection capacity decreases for a/d<1 than that of the beams loaded by bearing and the failure mechanism may change too.

27) The corner connection would have lower stiffness and slightly lower capacity than the internal connections. Anchor reinforcement may be recommended to be used in this case. In addition, shear stresses caused by torsion should be added to the shear stresses from vertical pile loading.

28) The pile connection can sustain higher breakout cracking load if the foundation was supported in two perpendicular directions.

4.16 References

ACI 318-99, 1999. Building Code Requirements for Structural Concrete (ACI 318-99) and Commentary (318R-99), Farmington Hills, MI: American Concrete Institute.

ACI 318-08, 2008. *Building Code Requirements for Structural Concrete (ACI 318-08) and Commentary*, Farmington Hills, MI: American Concrete Institute.

Angelakos, D., Bentz, E.C. & Collins, M.P., 2001. Effect of Concrete Strength and Minimum Stirrups on Shear Strength of Large Members. Structural Journal, 98(3), pp.291–300.

ASTM C39 / C39M-15a, 2015. *ASTM C39 / C39M-15a*, West Conshohocken, PA, USA: ASTM International.

ASTM C496 / C496M - 11, 2004. C496/C496M-11, Standard test method for splitting tensile strength of cylindrical concrete specimens, West Conshohocken, Pa, USA.

Bala, S., 2001. Contact Modeling in Ls-Dyna. Livermore Software Technology Corporation and FEA Information Inc, Livermore, CA.

Bažant, Z., 1985. Mechanics of fracture and progressive cracking in concrete structures. In A. M.-N. G. C. Sih, Di Tomasso, ed. *Fracture Mechanics of Concrete: Structural Application and Numerical Calculation*. Boston, pp. 1–91.

Bažant, Z. & Oh, B., 1983. Crack band theory for fracture of concrete. Material and Structures, 16(93), pp.155–177.

Bazant, Z.P. & Cedolin, L., 1979, Blunt Crack Band Propagation in Finite Element Analysis. Journal of the Engineering Mechanics Division, 105(2), pp.297–315.

CEB, 1993. CEB-FIP model code 1993: design code, Thomas Telford.

Chen, W., 2007. Plasticity in reinforced concrete, New York: McGraw-Hill Book Co.

Chinn, J. & Zimmerman, R., 1965. Behavior of plain concrete under various high triaxial compression loading conditions, CO, United States.

Crawford, J. & Malvar, L., 2006. *User's and theoretical manual for K&C concrete model*, Burbank, CA.

Crawford, J.E., Magallanes, J. & Zhang, Y., 2010. Determining the Effects of Cased Explosives on the Response of RC Columns. In *MABS21*. Jerusalem, Israel, pp. 3–8.

Crawford, J., 2012. Enhancing the Blast Resistance of RC Columns with FRP. In 6th International Conference on Advanced Composite Materials in Bridges and Structures. Kingston, Ontario, Canada, pp. 22–25.

Crawford, J. et al., 1995. Evaluation of jacketed columns as a means to improve the resistance of conventional structures to blast effects. In Proceedings, 66th Shock and Vibration Symposium. Biloxi, MS.

Crawford, J. et al., 2012a. Use and validation of the release II K&C concrete material model in LS-DYNA, Burbank, CA.

Crawford, J. et al., 2012b. Use and validation of the release II K&C concrete material model in LS-DYNA. Karagozian & Case, Glendale, July.

Crawford, J. & Wu, Y., 2012. Modeling of concrete materials under extreme loads. In I. H. H. & Z.-X. Li, ed. Advances in Protective Structures Research. London, UK: CRC Press/Balkema, pp. 1–32.

Eligehausen, R., Mallée, R. & Silva, J.F., 2013. Anchorage in Concrete Construction, John Wiley & Sons.

Flanagan, D.P. & Belytschko, T., 1981a. A uniform strain hexahedron and quadrilateral with orthogonal hourglass control. International Journal for Numerical Methods in Engineering, 17(5), pp.679–706.

Flanagan, D.P. & Belytschko, T., 1981b. A uniform strain hexahedron and quadrilateral with orthogonal hourglass control. International Journal for Numerical Methods in Engineering, 17(5), pp.679–706.

Hallquist, J., 2009. LS-DYNA keyword user's manual, Livermore, CA.

Hillerborg, A., Modéer, M. & Petersson, P.-E., 1976. Analysis of crack formation and crack growth in concrete by means of fracture mechanics and finite elements. Cement and Concrete Research, 6(6), pp.773–781.

Magallanes, J., Crawford, J. & Wu, Y., 2007. Evaluation of the K&C Concrete Model's Ability to Reproduce Standard Tests as Compared to Other LS-DYNA Material Models. In Workshop on Modeling Concrete Under High-Impulsive Loadings. Austin, TX.

Magallanes, J., Morrill, K. & Crawford, J., 2008. Finite element models for the analysis and design of CMU walls to blast loads. In Proceedings of the 80th DDESB Explosives Safety Seminar. Palm Springs, CA.

Magallanes, J. & Wu, Y., 2010. Recent improvements to release III of the K&C concrete model. 11th International LS-DYNA Users Conference, Dearborn, MI, pp.37–48.

Malvar, L. et al., 1996. A new concrete material model for DYNA3D-Release II: shear dilation and directional rate enhancements. A Report to Defense Nuclear ….

Malvar, L.J. et al., 1997. A plasticity concrete material model for DYNA3D. International Journal of Impact Engineering, 19(9-10), pp.847–873.

Malvar, L.J., Morrill, K.B. & Crawford, J.E., 2004. Numerical Modeling of Concrete Confined by Fiber-Reinforced Composites. Journal of Composites for Construction, 8(4), pp.315–322.

Metwally, I.M., 2012. Evaluate the capability and accuracy of response-2000 program in prediction of the shear capacities of reinforced and prestressed concrete members. *HBRC Journal*, 8(2), pp.99–106.

Nakamura, H. & Higai, T., 1999. Compressive fracture energy and fracture zone length of concrete. In JCI-C52E Seminar of post-peak behaviour of RC structures subjected to seismic loads. pp. 259–272.

Noble, C. et al., 2005. *Concrete Model Descriptions and Summary of Benchmark Studies for Blast Effects Simulations*, Livermore, CA.

Pan, F. & Zhu, J., 2006. Three point bending analysis of a mobile phone using LS-DYNA explicit integration method. 9th International LS-DYNA Users Conference, June, pp.4–6.

Reid, J.D., 1998. *LS-DYNA Examples Manual" LSTC 1998,"* Livermore, CA.

Santiago, S.D. & Hilsdorf, H.K., 1973. Fracture mechanisms of concrete under compressive loads. Cement and Concrete Research, 3(4), pp.363–388.

Tu, Z. & Lu, Y., 2009. Evaluation of typical concrete material models used in hydrocodes for high dynamic response simulations. International Journal of Impact Engineering, 36(1), pp.132–146.

Wesevich, J. W., L. J. Malvar, and J. E. Crawford, 1997, 1999. Comparison of Measured and Predicted Responses of Reinforced Concrete Walls Subjected to Close-in Blasts. In 9th International Symposium on Interaction of the Effects of Munitions with Structures. Berlin-Strausberg.

William, K. & Warnke, E., 1975. Constitutive model for the triaxial behavior of concrete. In *Seminar on Concrete Structures Subjected to Triaxial Stresses*. Bergamo, Italy, pp. 1–30.

Yonten, K. et al., 2005. An assessment of constitutive models of concrete in the crashworthiness simulation of roadside safety structures. International Journal of Crashworthiness, 10(1), pp.5–19.

BEHAVIOUR OF HELICAL PILE CONNECTORS FOR NEW FOUNDATIONS SUBJECTED TO TENSION LOADING: CONNECTION CAPACITY EQUATIONS AND DESIGN AID

5.1 Introduction

This chapter provides brief literature review and background information on breakout cracking of beams as well as discussions of the experimental and numerical studies on the behavior of helical piles and micropiles connectors for new foundations subjected to tension loading. Consequently, analytical equations will be developed to determine the connection capacity under tension loading. These equations are developed considering the findings of both the experimental and numerical investigations conducted in Chapter 3 and 4.

The experimental and numerical results demonstrated that the connection breakout cracking load and the connection ultimate load should be indicated as this connection involves the piles and pile caps, a limited crack width design may apply at the regions with high corrosion-conditions. Furthermore, it is usually assumed (and desirable) that the connection between the pile and the foundation is fixed for loads below the breakout load. However, the experimental and numerical results showed that the connection will become hinged if the breakout load is reached. Yahia and El Naggar (2015) demonstrated that the micropile capacity increases significantly for fixed connection over hinged connection between the micropile and the pile cap.

In order to develop an analytical solution that best describes both the connection breakout cracking and ultimate loads, the recorded behaviour of the tested connection was compared with different concrete failures reported by other researchers. This comparison should define the most representative concrete failure mechanism and identify the corresponding category of failure equations. The predictions of the identified equations are then compared with observed experimental and numerical results to verify the validity of the equations. In case the equations predictions are slightly different from observed results, the curve-fit constants of the equations are "fine tuned" to enhance the agreement of their predictions with observed behaviour. Finally, a statistical study is conducted to indicate the most suitable equation to be used for the evaluation of the connection capacity.

Following the development of a suitable equation to calculate the connection capacity and consideration of the different limit states that govern the connection failure mechanism, a design methodology is developed for the studied connection subjected to tension loading.

List of notations

a	Shear Span
a^*	The effective shear Span(the distance from the pile caps' plate end to the support in this case)
$\left(a/d\right)$	Shear span to depth ratio
A_{anchor}	The anchor reinforcement contained in the pile cap's plate width
a_g	Specified nominal maximum size of coarse aggregate
A_s	The longitudinal steel area
A_v	Area of shear reinforcement within a distance s
b	Specimen width
b_{plate}	Pile cap's plate width
T_c	The cracked concrete contribution to the connection ultimate load under tension loading
T_{Cr}	The connection breakout cracking load under tension loading
T_s	The transverse reinforcement contribution to the connection ultimate load under tension loading
c'	Concrete cover
$T_{u\,Actual}$	The actual connection ultimate capacity under tension loading
$T_{u_{conc.}}$	The limit state of the concrete ultimate capacity in the connection under tension loading
$T_{u\,Design}$	The recommended connection design load under tension loading
$Tu_{reinf.}$	The limit state of the transverse reinforcement ultimate capacity in the connection under tension loading
$Tu_{support}$	The recommended crushing limit state at supports for (a/d)<1
d	Specimen depth
d_{emb}	The pile embedment depth in the reinforced concrete beam
d_v	The effective shear depth, taken as the greater of 0.9d or 0.72h
E_s	Modulus of elasticity of non-prestressed reinforcement
fc'	Specified compressive strength of concrete
f_v	Transverse reinforcement stress accompanying with the cracked concrete contribution, C_c
f_u	Transverse reinforcement ultimate stress
h	Specimen height
M_f	Factored applied moment
L	Specimen Span
s	Maximum centre-to-centre spacing of transverse reinforcement
s_z	The crack spacing parameter dependent on crack control characteristics of longitudinal reinforcement
s_{ze}	The equivalent value of s_z that allows for influence of aggregate size

v_c	Factored shear stress resistance provided by the concrete
V_C	Shear resistance attributed to the concrete
V_{Cr}	The diagonal tension cracking shear strength
V_f	Factored applied shear load
V_s	Shear resistance provided by shear reinforcement
β	Factor accounting for shear resistance of cracked concrete
θ	Angle of inclination of diagonal compressive stresses to the longitudinal axis of the member
λ	Modification factor reflecting the reduced mechanical properties of lightweight concrete
μ	The average coefficient of friction between concrete and steel; approximately=0.47 as reported by Baltay et al. ,1990
ρ	Ratio of non-prestressed tension reinforcement, equal to A_s/bd
$\emptyset_c$	Resistance factor for concrete
$\emptyset_s$	Resistance factor for non-prestressed reinforcing bars
ε_x	Longitudinal strain at mid-depth of the member due to factored loads
ε_z	Longitudinal strain at mid-depth of the breakout cone due to factored loads

5.2 Main observed failure mechanism

The observations made from the experimental and numerical studies and the interpretation of their results demonstrated clearly that the breakout cracking resistance is closer to the single shear resistance of a concrete beam rather than the anchors nominal breakout resistance. This is because cracks propagated with inclination in one direction only (i.e. similar to single shear, especially when subjected to indirect loading) and not in two perpendicular directions (i.e. similar to breakout failure in anchors and punching shear). This behaviour is similar to that widely reported in the literature (e.g. Ferguson, 1956; Taylor, 1960; ACI-ASCE Committee 326, 1962; Zsutty, 1968 and 1971; Smith, 1974; Fereig, 1977; Cusens, 1985; Zuhua, 1987; Tan, 1997; and Lubell, 2009) for indirectly loaded beams failing under shear mechanism, not the behaviour reported for

the concrete breakout failure mechanism of anchors under shear loading (e.g. Carrato, 1996; Lee, 2007; and Yang, 2008). Therefore, it is appropriate to use the shear strength equations, with possible modifications to account for the embedment depth and pile cap width, for calculating the connection breakout capacity.

Furthermore, the single shear capacity should be doubled in case of pile shaft that is located at the grade beam mid-span in order to account for failure occurring along two sides at the same time as observed experimentally and analytically. In case of pile shaft that is not located at the mid-span between the considered supports, a superposition of the connection capacity contributions from the two sides should be accounted for, or else the capacity should be taken as twice the lower contribution as a conservative estimate.

5.3 Connection breakout cracking load calculation

There are several factors that affect the breakout cracking behavior and hence influence the connection breakout cracking load. These factors are listed herein.

5.3.1 Factors affecting connection breakout cracking load

1. The longitudinal reinforcement increases the breakout cracking load.

2. The plate width increases the breakout cracking load up to a specific width, after which the plate may yield before the breakout cracking occurs. This is because the crack initiates at the plate ends, which decreases the shear span. Thus, the shear span should be considered from the plate end to the support. However, if the plate yields before breakout cracking, the shear span extends to the pile shaft.

3. The embedment depth increases the breakout cracking linearly until it exceeds half the beam depth, at which it increases at a higher rate. Thus, conservatively, the breakout cracking load can be considered to increase linearly with embedment depth.

4. The anchor reinforcement can increase the connection capacity, but its contribution is mobilized mainly after the initiation of cracking. Thus, it can be neglected for the breakout cracking load calculations.

5. The shear span/ depth ratio (a/d) has an important effect on the connection capacity. For $2.5 < (a/d) < 6$ and $(a/d_{emb}) > 3$, the failure features diagonal tension cracking. For $(a/d) < 2.5$ and $(a/d_{emb}) < 3$, flexural shear cracks occurs, which mobilizes higher concrete shear resistance. Finally, for $(a/d) < 1$ or $(a/d_{emb}) < 1$, the failure features arching effect. Thus, the connection capacity may be evaluated considering diagonal tension cracking for $(a/d) > 2.5$, which will be conservative in case of $1 < (a/d) < 2.5$. For $(a/d) < 1$, the calculated capacity should be increased depending on (a/d) or (a/d_{emb}) or a strut and tie method may be used. Also, a limit state of $1.2\sqrt{fc'}.b.d_{emb}$ may be implemented as a maximum shear strength limit state.

6. The breakout cracking load increases linearly with the beam width increase.

7. For pile shafts connected to the beam off its mid-span, the connection capacity is given by the sum of resistance considering two diagonal tension failures. The connection capacity may be calculated conservatively using the larger (a/d) ratio.

8. Welded and bolted connections have almost the same capacity under tension loading.

9. For (a/d) > 1, the contribution of anchor support fully embedded in concrete subjected to tension is negligible, but bearing support can increase the connection capacity for $(a/d_{emb}) < 1$.

10. For connection attached at the corner of grade beams, additional shear stresses caused by torsion reduce the connection capacity.

11. Contribution of transverse reinforcement (i.e. stirrups) to the breakout load capacity is negligible.

12. The concrete above the plate level does not contribute to the connection capacity as that in the beams having compression shear failure mechanism.

5.3.2 Equation for the connection breakout cracking load

Table 5-1 lists different equations that are widely used for calculating the diagonal tension capacity of reinforced concrete beams without stirrups. These equations are employed herein to calculate the connection capacity, and their predictions are compared with the observed connection capacity (i.e. observed breakout cracking load from experimental and analytical results). The data of the specimens investigated experimentally and analytically that will be used in this study is presented in Appendix E.

It should be noted that the original expressions of the listed equations may not account properly for the pile embedment effect on the shear strength. Also, it is so important to

take the size effect into consideration especially if the beam height or the pile embedment depth are more than 1.0 m as reported by many researchers (e.g. Kani, 1966 and 1967; Collins and Kuchma, 1999; and Collins and Mitchell, 1996), especially for light weight longitudinal reinforcement. On the other hand, Qiang, et al. (2011) concluded that using stirrups decreases the size effect.

In order to examine the size effect and to explore whether full beam depth, d, or pile embedment depth, d_{emb}, should be utilized to determine the breakout cracking load, the equations listed in table 5-1 were modified to account for the size effect using either d or d_{emb}; and the concrete shear stress, v_c, obtained from the equations is multiplied by either b.d or b.d_{emb} (i.e. breakout cracking load = v_c.b.d or v_c.b.d_{emb}).

Finally, the shear strength predictions of these equations are multiplied by a factor of 2 to account for two equal contributions of the two sides of the connection because the pile shaft was located at the mid-span of the beam. Then, they will be compared with the experimentally recorded breakout cracking load of the control beam T2 (i.e. 200 kN). The calculated values of the connection capacity are presented in Table 5-2.

Table 5-1 Summary of shear strength equations for beams without stirrups loaded directly

Reference	Equations in MPa, and mm = [shear stress]
ACI 318-11 Code and KBCS Code	$v_c = \left[0.16\sqrt{fc'} + 17.\dfrac{\rho.V.d}{M} \right]$
CSA Code Simplified Method &Bentz (2005)	$v_c = \left[\left(\dfrac{230}{1000 + \dfrac{35.d}{15 + a_g}} \right) . \sqrt{fc'} \right]$
JSCE code (1997)	$v_c = \left[0.2(100.fc'.\rho)^{1/3}.(1000/d)^{1/4} \right]$
BS8110-1	$v_c = \left[0.79(100.\rho)^{1/3}.(400/d)^{1/4}.((fc^{'})/25)^{1/3} \right]$
CEB-FIP Model Code(1993)	$v_c = \left[0.15(3d/a)^{1/3}(100.\rho)^{1/3}.(1 + \sqrt{(200/d)}).(fc')^{1/3} \right]$
EC2 (2003)	$v_c = \left[0.18(1 + \sqrt{(200/d)})(95.\rho.fc')^{1/3} \right]$
DIN (2001)	$v_c = \left[0.15(1 + \sqrt{(200/d)})(95.\rho.fc')^{1/3} \right]$
AS 3600 Equation	$v_c = \left[1.1\,(1.6 - d/1000).(2d/a).(\rho.fc')^{1/3} \right]$
Zsutty (1968, 1971)	$v_c = \left[2.2(\rho.fc'.d/a)^{1/3} \right]$
Placas and regan (1971)	$v_c = \left[1.1956.(\rho.fc')^{1/3} \right]$
Al-zoubi (2014)	$v_c = \left[2.6\dfrac{1}{\sqrt{1 + d/(25.a_g)}}\left(\rho.fc'.\dfrac{d}{a} \right)^{1/3} \right]$
Bazant (1987)	$v_c = \left[0.54\sqrt[3]{\rho}\left(\dfrac{1 + \sqrt{5.08/a_g}}{\sqrt{1 + \dfrac{d}{25.a_g}}} \right)\left(\sqrt{fc'} + 249\sqrt{\dfrac{\rho}{(d/a)^5}} \right) \right]$
Bazant and YU (2005) & ACI Committee 446	$v_c = \left[1.1\rho^{3/8}\left(1 + \dfrac{d}{a} \right)\sqrt{\dfrac{fc'}{\left(1 + \dfrac{d}{687.5.fc'^{2/3}.\sqrt{a_g}} \right)}} \right]$
Ferguson (1968)	$v_c = \left[(0.066 + 8.3\rho)\sqrt{fc'} \right]$
Robert (1963)	$v_c = \left[0.2575\sqrt{fc'}(d/a) + 27.6\ \rho \right]$
Broujerdian (2004)	$v_c = \left[0.35\sqrt{fc'}\left(1 + \dfrac{75.a.\sqrt{fc'}}{\rho.Es.(a_g + 16)} \right)^{-1/2} \right]$
Jin-Keum (1996)	$v_c = \left[3.5(fc')^{1/3}.(\rho)^{3/8}.(0.4 + d/a)(\dfrac{1}{1 + 0.008d} + 0.18) \right]$

189

Table 5-2 Predicted breakout cracking load from different shear equation (using d or d_{emb})

Investigator	Using b.d (kN)	Using b.d_{emb} (kN)	($T_{theoretical}/T_{cr}$) % Using d	($T_{theoretical}/T_{cr}$) % Using d_{emb}
ACI 318-11 Code and KBCS Code	414	188	207	94
CSA Code Simplified Method &Bentz (2005)	394.4	213.8	197.2	106.9
JSCE code (1986)	242	133	121	66.5
BS8110-1	276	152	138	76
CEB-FIP Model Code(1993)	323	174	161.5	87
EC2 (2003)	292	158	146	79
DIN (2001)	243.4	132	121.7	66
AS 3600	274.3	150	137.15	75
Zsutty (1968, 1971)	424.2	191.4	212.1	95.7
Placas and regan (1971)	255	115	127.5	57.5
Al-zoubi (2014)	363.7	190.9	181.85	95.45
Bazant (1987)	502.5	263.7	251.25	131.85
Bazant &Yu (2004)&ACI 446	568.4	256.7	284.2	128.35
Ferguson (1968)	235.4	106.3	117.7	53.15
Robert (1963)	512.4	231.4	256.2	115.7
Broujerdian (2004)	263	119	131.5	59.5
Jin-Keum & Park (1996)	267	170.2	133.5	85.1

Comparing the predictions of the different equations presented in Table 5-2 with the observed breakout cracking load of beam T2 (200.0 kN), it is clear that using the beam full depth in these equations over estimate the breakout cracking load capacity of the connection. Thus, in order to predict the connection capacity, the pile embedment depth d_{emb} should be used. Also, it was found that d_{emb} should be used in the term representing the size effect instead of the beam depth, d. It is also noted that several equations

190

predicted the connection capacity reasonably close to the observed connection capacity, including: (ACI 318-11 Code, CSA simplified method, Zsutty (1971), and Al-zoubi (2014). The ACI 318-11 code and Zsutty (1971) equations were expected to give a reasonable expected values because they are mainly used to calculate the diagonal tension cracking load, which is similar to the observed failure mechanism. Based on these observations, the breakout cracking load may be given by:

$$T_{cr} = 2.v_c.b.d_{emb} \qquad\qquad \textbf{5. 1}$$

Both experimental and analytical investigations demonstrated clearly that the breakout cracking and diagonal tension cracking initiated at the plate ends. Therefore, the shear span (a) value should be reduced to (a^*), by subtracting one half of the plate width from (a), i.e.

$$a^* = a - \frac{b_{plate}}{2} \qquad\qquad \textbf{5. 2}$$

The connection capacity was calculated by applying this adjustment to the expressions listed in Table 5-1 and the results are presented in Table 5-3. It is clear that the predictions obtained from the revised Al-zoubi and Zsutty equations match the breakout cracking load for Beam T2, and the ACI 318-11 Code and CSA Code simplified method predictions are very close. It should be noted that the revised Al-zoubi equation accounts for both the (a*/d) ratio and the size effect, while the revised Zsutty and ACI318-11 Code equations account for (a*/d) only. On the other hand, CSA Code simplified method

accounts only for the size effect but does not account for the longitudinal reinforcement and the (a/d) effects.

Given the good performance of these revised equations utilizing d_{emb} and a^* (i.e. ACI318-11 Code, CSA Code simplified method, Zsutty , 1971, and Al-zoubi , 2014), they will be considered for further development of a suitable equation for the prediction of the connection capacity. The revised equations are:

ACI 318-11 Code: $T_{cr} = 2 . \left[0.16\sqrt{fc'} + 17.\frac{\rho.d}{a^*} \right].b.d_{emb}$ **5. 3**

CSA Simplified Method: $T_{cr} = 2 . \left[\left(\frac{230}{1000+\frac{35.d_{emb}}{15+a_g}} \right) . \sqrt{fc'} \right].b.d_{emb}$ **5. 4**

Zsutty (1971): $T_{cr} = 2 . \left[2.2 \left(\rho.fc'.\frac{d}{a^*} \right)^{1/3} \right].b.d_{emb}$ **5. 5**

Al-zoubi (2014): $T_{cr} = 2 . \left[2.6\frac{1}{\sqrt{1+d_{emb}/(25.a_g)}} \left(\rho.fc'.\frac{d}{a^*} \right)^{1/3} \right].b.d_{emb}$ **5. 6**

Table 5-3 Predicted breakout cracking load from different shear equations (for d and The d_{emb})

Equation Source	Using d_{emb} & a* (kN)	$(T_{theoretical}/T_{cr})\%$
ACI 318-11 Code and KBCS Code	189	95
CSA Code Simplified Method	213.8	107
JSCE code (1986)	133	66
BS8110-1	152	76
CEB-FIP Model Code(1993)	182.8	91
EC2 (2003)	158	79
DIN (2001)	132	66
AS 3600 Equation	150	75
Zsutty (1968, 1971)	201	100.5
Placas and regan (1971)	115	57.5
Al-zoubi (2014)	200	100
Bazant (1987)	328.3	164
Bazant&Yu(2004)& ACI 446	273.7	137
Ferguson (1968)	106.3	53
Robert G. Mathey (1963)	264.4	132
Broujerdian (2004)	118.6	60
Jin-Keum& yon park (1996)	187.4	93.7

Equations 5.3, 5.4, 5.5 and 5.6 are used to calculate the breakout cracking load for the beam connections tested in the experimental and numerical investigations considering: pile embedment depth; the pile cap plate width; and the beam longitudinal reinforcements. The calculated connection capacity from the four equations are compared with the recorded experimental and analytical results for a/d>1.0 in Table 5-4.

Table 5-4 Comparison of calculated and measured results for (a/d) > 1

Specimen	T_{cr} result (Breakout Cracking load) (kN)	$(T_{theoretical}/T_{cr})\%$ ACI Eq. 5.3	$(T_{theoretical}/T_{cr})\%$ CSA* Eq. 5.4	$(T_{theoretical}/T_{cr})\%$ Zsutty* Eq. 5.5	$(T_{theoretical}/T_{cr})\%$ Al-zoubi* Eq. 5.6
T1	154	91.6	107.9	97.7	101.1
T2	200	94.2	106.3	100.4	100.1
F-D-228	212.8	99.4	109.9	106.0	103.8
T3	232	101.6	110.0	108.3	104.3
F-D-280	290	89.6	95.0	95.5	90.4
F-D-305	324	87.4	90.9	93.2	86.8
T-P-100	184.5	116.7	133.0	117.5	117.1
T4	201.7	107.2	121.7	110.5	110.1
T5	239.5	90.4	102.5	94.3	93.9
T-P-305	255	85.3	96.3	90.9	90.6
T-P-380	258.6	84.5	94.9	92.2	91.9
T-B-10	174	121.1	141.1	100.9	100.5
T6	222.5	99.4	110.3	113.7	113.4
T7	252.3	91.8	97.3	118.9	118.5
T-B-30	288	84.0	85.2	116.6	116.2
T-B-35	345	74.7	71.1	109.6	109.2
T8	208.5	103.5	117.7	106.0	105.7
T9	208.4	103.6	117.8	106.1	105.7
Average%		95.9	106.1	104.4	103.3
Standard deviation%		11.8	16.9	9.1	9.8
Coefficient of variation%		12.3	15.9	8.7	9.5
Root mean squared error%		12.2	17.5	9.9	10.1

The results presented in Table 5-4 demonstrate that all four equations predicted the connection capacity reasonably well for the 18 investigated beams. Equation 5.4, however, provided non-conservative predictions of the breakout cracking load (up to 41% above observed cracking load) for beams with longitudinal reinforcement ratio less than 0.003 because this method does not account for the longitudinal reinforcement ratio

194

effect. Meanwhile, it underestimated the capacity (by up to 30%) for beams with high longitudinal reinforcement ratio. Thus, this equation is not suitable for the connection capacity prediction.

The modified ACI 318-11 Code equation (i.e. Equation 5.3) predicted the connection capacity for most of the investigated beams reasonably well. However, the predictions of the capacity for T-B-10 and T-B-35 were not as accurate because the ACI318-11 equation over predicts the concrete contribution and under estimate the longitudinal reinforcement contribution (Ozcebe, 1999 and Kani, 1966). Table 5-6 also shows that Equations 5.5 and 5.6 can accurately predict the capacity of beams with low and ordinary longitudinal reinforcement ratio. However, they may over predict the capacity of beams with high longitudinal reinforcement ratio. Both equations overestimate the effect of longitudinal reinforcement for beams with reinforcement ratio > 0.005. Thus, a limiting value of 0.005 will be used for longitudinal reinforcement ratio in both equations. On the other hand, Equations 5.5 and 5.6 predicted the breakout cracking loads very well with the lowest coefficient of variation (8.7% and 9.5%, respectively). However, the modified Al-zoubi's equation (Equation 5.6) is preferred as it accounts for size effect. It can be concluded from this discussion that Equation 5.5 and 5.6 are most appropriate for calculating the connection capacity, but should be modified to account for the longitudinal reinforcement ratio appropriately, i.e.

$$T_{cr} = 2 \cdot \left[2.2 \left(\rho . fc' . \frac{d}{a^*} \right)^{1/3} \right] . b . d_{emb} \, , where \; \rho \leq 0.5\% \qquad \textbf{5.7}$$

$$T_{cr} = 2 \cdot \left[2.6 \frac{1}{\sqrt{1 + d_{emb}/(25.a_g)}} \left(\rho . fc' . \frac{d}{a^*} \right)^{1/3} \right] . b . d_{emb} \text{ , where } \rho \leq 0.5\% \qquad \textbf{5.8}$$

5.3.3 Consideration of (a/d) effect

Most equations used to calculate the beam breakout capacity, listed in Table 5-1, were developed primarily for slender beams (a/d > 2.5) so they do not perform well for short beams (1 < a/d < 2.5) or deep beams (a/d < 1). Therefore, it is necessary to investigate the ability of the modified equations (i.e. Equations 5.7 and 5.8) to properly account for the effect of (a/d) or (a/d$_{emb}$) ratios on the connection capacity. Both equations were used to calculate connection capacity for beam configurations that were considered in the experimental and numerical investigations for evaluating effect of (a/d) and the results are presented in table 5-5. It is noted from Table 5-5 that Equations 5.7 and 5.8 provided conservative, but reasonable, predictions of the capacity of beams with (a/d) < 1. It is also noted that Equations 5.7 and 5.8 provided close predictions of the connection capacity for beams with low (a/d) ratios. Therefore, it is concluded that Equations 5.7 and 5.8 are generally suitable for calculating the connection breakout cracking load.

Table 5- 5 Calculated and recorded connection capacity for beams with varying (a/d) ratio

Specimen	T_{cr} (Breakout Cracking load) (kN)	$(T_{theoretical}/T_{cr})\%$ Modified Zsutty* Eq. 5.7	$(T_{theoretical}/T_{cr})\%$ Modified Al-zoubi* Eq. 5.8
T-R-2.75 (4-15M)	154	98	97
T-R-1.75 (4-15M)	216	82	82
T-R-1 (4-15M)	281	78	78
T-R-0.5 (4-15M)	392	77	77
T-R-0.25 (4-15M)	569	83	83
T-R-5.5 (4-30M)	175	80	80
T-R-4 (4-30M)	178	88	88
T-R-3.5 (4-30M)	192	85	85
T-R-2.75 (4-30M)	191	94	93
T-R-2.5(4-30M)	195	95	95
T-R-2.25 (4-30M)	210	91	91
T-R-1(4-30M)	386	68	68
T-R-0.5 4-30M)	626.4	55	55
T-R-0.25 (4-30M)	644	87	87
Average%		83.0	82.7
Standard deviation%		11.2	11.2
Coefficient of variation%		13.5	13.5
Root mean squared error%		31.7	33.2

Finally, several codes recommend using the strut and tie method for calculating the connection capacity for deep beams (e.g. CSA A23.3 code). In this case, compression struts will extend from the plate to the supports, i.e., not accounting for the full beam depth. In case of (a/d) < 1, the Strut and Tie model for the investigated connection is shown in Figure 5-1. It can be noted from Figure 5-1 that the effect of the beam depth is almost absent as the behaviour depends mainly on the embedment depth (d_{emb}). Only the effect of the beam flexural resistance contributes to the connection capacity, which should be accounted for by summing the tensile stresses from flexure and that of the

197

tension tie. However, the flexural tensile stress will be negligible compared to the tensile stress in the tension tie for beams when (a/d) < 1.
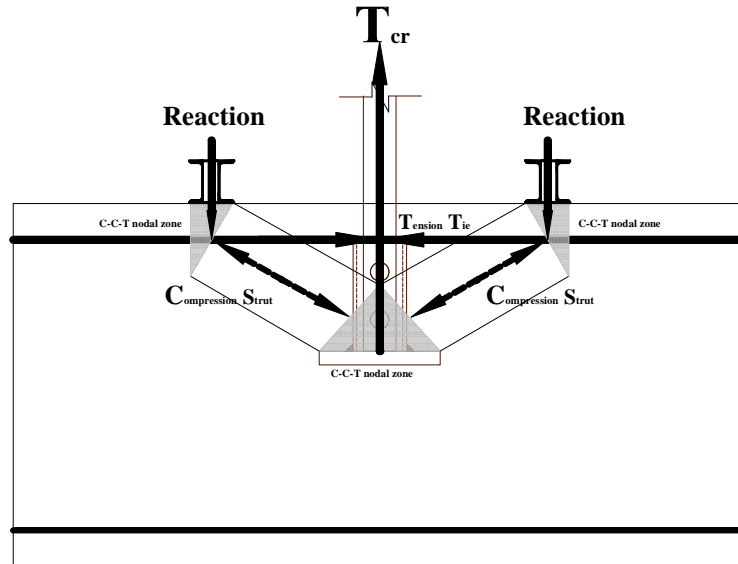
Figure 5- 1 Strut-and-tie model of a single span deep beam without stirrups with (a/d) < 1

5.3.4 Consideration of tension anchor support

The results of the numerical investigation demonstrated that the diagonal cracks pattern and the breakout cracking load were approximately the same for beams with either tension anchor supports or bearing supports for (a/d) > 1; however, for (a/d) < 1, the beams with tension anchors were governed by diagonal cracking while beams with bearing supports experienced deep beam compression strut failure. Table 5-6 compares the predicted breakout cracking loads using Equation 5.8 with the results obtained from the numerical study. The comparison shows that Equation 5.8 provided reasonable predictions of the connection capacity; the mean value of percentage of ($T_{theoretical}/T_{cr}$) is 87%, standard deviation is 12%, coefficient of variation is 13%, and root mean squared

error is only 7%. Thus, it is concluded that it is better to use the same equation used for

(a/d)>1 to expect the behaviour of a beam with tension anchor support.

Table 5- 6 Calculated and recorded connection capacity for beams with tension anchor support.

Specimen	Recorded T_{cr} (kN)	($T_{theoretical}$) (kN)	($T_{theoretical}/T_{cr}$)%
	(Breakout Cracking load) (kN)	Using Eq.5.8	Using Eq.5.8
Tension anchor (a/d=1.35)	200	200	100
Tension anchor (a/d=1)	242	226	93
Tension anchor (a/d=0.75)	330	254	77
Tension anchor (a/d=0.5)	424	310	73
Tension anchor (a/d=0.25)	516	484	94
Average%			87
Standard deviation%			12
Coefficient of variation%			13
Root mean squared error%			7

5.3.5 Consideration of position of pile shaft

Connecting the pile shaft to the beam off its mid-span leads to different (a/d) ratios on

either side of the pile connection. The numerical study showed that the connection

capacity may be given by either the sum of the contributions of both sides to the capacity

or twice the capacity of the longer side (i.e. side with higher (a/d)). Equation 5.8 can be

used to provide the capacity of the longer side (i.e. side with higher a/d) and the sum of

the contribution of both sides to the capacity can be given by Equation 5.9.

$$T_{cr} = \left[2.6 \frac{1}{\sqrt{1 + d_{emb}/(25.a_g)}} (\rho.fc'.d)^{1/3} . \left(\frac{\sqrt[3]{a^*_{right}} + \sqrt[3]{a^*_{left}}}{\sqrt[3]{a^*_{right}} \cdot \sqrt[3]{a^*_{left}}} \right) \right] . b. d_{emb} , where \ \rho \leq 0.5\% \qquad \textbf{5. 9}$$

Table 5-7 compares these two values with the breakout capacity obtained from the

numerical investigation. As can be noted from Table 5-7, Equation 5.9 provided capacity

prediction closer to that obtained from the numerical model than that obtained from

Equation 5.8 when using the higher (a/d) ratio. This finding suggests that Equation 5.8 can be used to calculate the connection capacity for piles connected to the beam at its mid-span, while Equation 5.9 is more appropriate for determining the capacity of the connection when the pile shaft is connected to the beam off its mid-span, however, using Equation 5.8 may lead to conservative results.

Table 5-7 Predicted connection capacity for pile shaft connected to beam off its mid-span

Specimen	T_{cr} (kN) (Breakout Cracking load) from FE modeling	$(T_{theoretical})$ (kN) Eq. 5.9	$(T_{theoretical})$ (kN) Eq.5.8	$(T_{theoretical}/T_{cr})\%$ Using Eq.9	$(T_{theoretical}/T_{cr})\%$ Using Eq.8
T2-L-0.75	241.64	227.1	200	94.0	82.8
T2-L-3.8	210	168.8	137.5	80.4	65.5
Average				87.2	74.1

5.4 Connection ultimate load calculation

5.4.1 Observations from experimental and analytical studies

1. The aggregate interlock, the dowel action of the longitudinal reinforcement, and the transverse reinforcement contribute to the connection ultimate load. However, the connection ultimate load should not be higher than the transverse reinforcement yielding tensile capacity.

2. The aggregate interlock is affected by the crack width in addition to all factors that influence breakout cracking load.

3. Only transverse reinforcement included in the breakout cone contributes to the connection ultimate capacity. The breakout cone size may be given by the lesser of b_{plate}+2.5 d_{emb} or 3 d_{emb}. Alternatively, it can be calculated by

Breakout cone dimension $=$ bplate $+ 2.\cot\theta°$x (demb)　　　　**5. 10**

4. The vertical reinforcement included in the width of the pile cap's plate contributes its full ultimate capacity to the connection ultimate capacity after propagating wide diagonal cracks. In this case, the longitudinal dowel action and the aggregate interlock should be neglected.

5. The following limit states should be considered for the connection ultimate load:

- Beam breakout cracking: especially for beams with low transverse reinforcement ratio.

- Crushing of support regions: this load may be given by $(2 . 0.6\sqrt{fc'}.b.d_{emb}) = 1.2\sqrt{fc'}.b.d_{emb}$ especially for (a/d) < 1.

- Bearing capacity of the concrete in front of the pile cap's plate: especially for loading applied directly to the pile connection (e.g. connection at column location) or small plate size.

- Beam shear failure: especially for beams with d < 2 d_{emb}, or high transverse reinforcement ratio was used.

- Beam flexural failure: especially for beams with a/d > 6 or low longitudinal reinforcement ratio was used.

- Pile shaft failure at the location of the bolts.

- Bolts double shear failure.

- Pile cap' cylinder failure at the bolt location or its bearing failure in front of bolts

- Welding failure at pile-plate or pile cap cylinder- plate interfaces

5.4.2 Development of ultimate load equation

After reviewing several concrete failure mechanisms discussed in the literature, it was concluded that the concrete ultimate load is best represented by the simplified modified compression field theory. However, it should be modified in order to differentiate between the failure of beams directly loaded failing in shear, and a pile-beam connection loaded in tension.

Vechio and Collins (1986) developed the Modified Compression Field Theory (MCFT) to evaluate the shear resistance of a reinforced concrete beam. Based on the MCFT, Collins and Mitchell (1991) developed the shear design method. The predictions of the shear design method were shown to agree well with the experimental observations, including excellent predictions of aggregate size effect. More recently, Bentz et al. (2006) developed the simplified Modified Compression Field Theory (SMCFT), which forms the basis for the CSA A23.3-04 general shear method. The SMCFT is modified slightly

in the current study to calculate the ultimate capacity of the connection. In the SMCFT, the shear resistance of a concrete section is given by:

$$V = V_c + V_s = \beta\sqrt{fc'}\text{b. d}_v + \frac{A_v.f_y}{s}.d_v.cot\theta \qquad\qquad \textbf{5. 11}$$

The shear factor, β, the concrete strain, ε_x (i.e.), and the crack angle, θ, are calculated using the following expressions:

$$\beta = \frac{0.40}{(1+1500.\varepsilon_x)} \cdot \frac{1300}{(1000+s_{ze})} \qquad\qquad \textbf{5. 12}$$

$$\varepsilon_x = \frac{M_f/d_v + V_f}{2.E_s.A_s} \qquad\qquad \textbf{5. 13}$$

$$d_v = \text{greater of} \begin{cases} 0.9d \\ 0.72h \end{cases} \qquad\qquad \textbf{5. 14}$$

$$s_{ze} = \frac{35\,s_x}{(15+a_g)} \geq 0.85\,s_z \qquad\qquad \textbf{5. 15}$$

$s_{ze} = 300mm$ *if the minimum transverse reinfrocement is used*   ,

s_z is the smaller of $\begin{cases} d_v \\ \textit{The maximum distance between longitudinal crack control steel} \end{cases}$,

$\theta = (29^o + 7000\varepsilon_x)(0.88 + s_{ze}/2500) \leq 75^o, and\ = (29^o + 7000\varepsilon_x)\ if\ s_{ze} = 300mm.$

As shown in Equation 5.11, to calculate β, ε_x, θ we use M_f and V_f which are known when it is a design process, however, in the analysis process their values are unknown. Also, it is clear that θ depends on ε_x which mainly depend on V_f which depend on ε_x again. The SMCFT was mainly developed to get rid of the iterations in the MCFT; however, the iteration problem is raised again when thinking of the accuracy of the used equations. If no stirrups were considered (i.e. $V_f = V_c$), when the factored shear force, V_f, increases the strain, ε_x, and the cracking angle, θ, will increase, but the shear factor, β , will decrease which decreases the concrete shear resistance V_c. Then, decreasing V_f

203

$(V_f = V_c)$ decreases the strain ε_x and the cracking angle, θ, but it increases β which increases the concrete shear resistance V_c. Thus, if we want to calculate the concrete shear capacity and the breakout cracking angle correctly it will be endless iterations of increasing and decreasing the values. One can conclude that only one equation should be used to calculate β, ε_x, and V_f because they are depending on each other. Thus, the author recommends employing a second order equation to calculate the concrete strain ε_x. Then, the other values can be calculated with the SMCFT but this time no iterations should be used to calculate V_c, and the first calculated concrete shear capacity V_c should be the accurate one without any iterations. The procedures to calculate this 2nd order equation are shown below.

1) Assume s_{xe}=300mm (considering minimum transverse reinforcement at the connection location).

2) Calculate $\beta = \dfrac{0.40}{(1+1500.\varepsilon_x)} \cdot \dfrac{1300}{(1000+s_{xe})} = \dfrac{0.40}{(1+1500.\varepsilon_x)}$

3) Calculate $V_c = \dfrac{0.40}{(1+1500.\varepsilon_x)} \sqrt{fc'} \text{b. d}_v$

4) $As\ \varepsilon_x = \dfrac{M_f/d_v+V_f}{2.E_s.A_s} \leq 3 * 10^{-3}$

5) $\varepsilon_x = \dfrac{(a/d_v+1)V_f}{2.E_s.A_s} = \dfrac{0.40}{(1+1500.\varepsilon_x)} \sqrt{fc'} \text{b. d}_v \dfrac{(\frac{a}{d_v}+1)}{2.E_s.A_s}$

By solving the 2nd degree equation, the new concrete strain will be denoted ε_z and may be given by:

$$\varepsilon_z = \frac{-1+\sqrt{1+6000z}}{3000} \qquad\qquad \textbf{5. 16}$$

Where:

$$z = \frac{0.4\sqrt{fc'}(1+\frac{a}{d_v})}{2E_s.\rho} \qquad\qquad \textbf{5. 17}$$

In the SMCFT, the term $2.E_s.A_s$ is used to account for the strain at the beam mid-height; however, for the connection under consideration the critical position is at the middle of the embedment depth. So, for the pile connection considered herein the average concrete strain should be calculated at this point, and Equation 5.17 should be replaced by:

$$z = \left(\frac{0.4\sqrt{fc'}b.d_{emb}\left(1+\frac{a}{d_v}\right)}{E_s.A_s}\right)\left(\frac{dv-d_{emb}/2+c'}{d_v}\right) \qquad\qquad \textbf{5. 18}$$

The concrete shear strength, V_c, and the diagonal cracking angle, θ, can then be calculated using the same equation of SMCFT. If the pile was in the mid-span, the concrete resistance (T_c) will be equal to double the concrete shear strength of one of the two failing sides. In addition, the embedment depth will be used instead of d_v as discussed before. Thus, the concrete resistance after cracking may be given by:

$$T_c = \frac{2*0.40}{(1+1500.\varepsilon_z)}\sqrt{fc'}b.d_{emb} \qquad\qquad \textbf{5. 19}$$

where,

$$\varepsilon_z = \frac{-1+\sqrt{1+6000z}}{3000} \qquad , \qquad z = \left(\frac{0.4\sqrt{fc'}b.d_{emb}\left(1+\frac{a}{d_v}\right)}{E_s.A_s}\right)\left(\frac{dv-d_{emb}/2+c'}{d_v}\right)$$

One of the major assumptions in the SMCFT is that aggregate interlock governs the shear failure of the beams without stirrups. Thus, SMCFT is developed for cracked sections, and the stirrups resistance should be included in the ultimate load calculations as T_s, which depends on the strain after the diagonal crack formed and the diagonal crack angle.

The experimental and numerical results demonstrated that only the stirrups within or close to the pile cap plate in the longitudinal direction contributed to the concrete ultimate load; however, all stirrups contained in the breakout cone should be accounted for in the connection ultimate load after the concrete fails experiencing wide cracks. The breakout cone size depends on the diagonal cracking angle, θ. So, the stirrups contribution to the concrete ultimate load may be given by:

$$T_s = A_v \cdot f_v \cdot \left(\frac{b_{plate}}{s} + 1 \right) \qquad \text{, where } f_v = \frac{f_y}{\varepsilon_y} \cdot \varepsilon_z \leq \varepsilon_y \qquad \textbf{5. 20}$$

For full bonding between the stirrups and the surrounding concrete, the strain in the stirrups and the concrete should be equal. Thus, the connection capacity can be given by the full cracked concrete capacity because the concrete strength can capture most factors that affect the concrete strength. Also, the concrete aggregate interlock and the longitudinal reinforcement dowel action were noted to be negligible at the stage of transverse reinforcement yielding in both the experimental and numerical investigations, which mean that the cracked concrete strength will be much smaller than Tc calculated using Equation 5.19 if the stirrups yielding strain was considered in calculating Ts in Equation 5.20.

Thus, when the pile is placed at the mid-span or the higher (a/d) ratio was conservatively used in the calculation, the concrete ultimate load may be given by:

$$T_{u_{conc.}} = T_c + T_s = \frac{2*0.40}{(1+1500.\varepsilon_z)}\sqrt{fc'}\text{b.d}_{emb} + A_v.f_v.\left(\frac{b_{plate}}{s} + 1\right) \qquad \textbf{5. 21}$$

Furthermore, the experimental and numerical results demonstrated that a limit state of the stirrups yielding strength should be compared with the concrete ultimate load and the lesser value should be considered for design purposes, but it should not be less than the concrete breakout cracking load. If anchor reinforcement is used, only the anchor reinforcement contained within the plate width contributes to the connection ultimate load, i.e.

$$Tu_{reinf.} = \frac{A_v.f_y}{s}.\left(2.\text{d}_{emb}.\cot\theta + b_{plate}\right) \text{ or } A_{anchor}.f_u \qquad \textbf{5. 22}$$

The ultimate strength of anchor reinforcement and stirrups considered in the design stage should not exceed $\emptyset_s.f_y$. Also, if the embedment depth is more than d/2 or large amount of transverse reinforcement was used at the connection, the full beam shear capacity should be considered as the upper limit of the connection ultimate capacity.

Finally, for (a/d) < 1, another limit state of $1.2\sqrt{fc'}.b.d_{emb}$ should be taken into consideration. This means the design ultimate load of the connection ($T_{u\ Design}$) should be the least of the four limit states in Equation 5.23, but not less than the concrete resistance, T_c .

$$T_{u\,Design} = the\;least\;of \begin{cases} Tu_{conc.} = \frac{2*0.40}{(1+1500.\varepsilon_z)}\sqrt{fc'}b.d_{emb} + A_v.f_v.\left(\frac{b_{plate}}{s}+1\right) \\ Tu_{support} = 1.2\sqrt{fc'}.b.d_{emb}\;\;if\;\left(\frac{a}{d}\right)<1 \\ Tu_{reinf.} = \frac{A_v.f_y}{s}.\left(2.d_{emb}.cot\theta + b_{plate}\right)\;or\;A_{anchor}.f_y \\ 2xBeam\;shear\;strength\;(using\;a_{max}) \end{cases} \geq T_c \quad \textbf{5.23}$$

On the other hand, for performance based design, the resistance of transverse reinforcement (stirrups or anchor reinforcement) should be accounted for ($Actual\;T_u$), i.e.

$$Actual\;T_u = Min.of \begin{cases} Max.of \begin{cases} Tu_{conc.} = \frac{2*0.40}{(1+1500.\varepsilon_z)}\sqrt{fc'}b.d_{emb} + A_v.f_v.\left(\frac{b_{plate}}{s}+1\right) \\ Tu_{reinf.} = \frac{A_v.f_y}{s}.\left(2.d_{emb}.cot\theta + b_{plate}\right)\;or\;A_{anchor}.f_u \end{cases} \\ Tu_{support} = 1.2\sqrt{fc'}.b.d_{emb}\;\;if\;\left(\frac{a}{d}\right)<1 \\ 2xBeam\;shear\;strength\;(using\;a_{max}) \end{cases} \geq T_c \quad \textbf{5.24}$$

This is particularly applicable when structures reach a state of near collapse (i.e. collapse prevention performance level). In this case, the concrete cracking width is not important, and the additional ductility provided by the transverse reinforcement is the main important factor. So, it is recommended to use transverse reinforcement with capacity equal to or more than the required beam ultimate load. To calculate the connection ultimate load and compare it with the results recorded from the experimental and analytical studies, it is clear that $Actual\;T_u$ should be used in this analysis stage.

Table 5-8 present the calculated concrete capacity (T_c), the steel capacity (T_s), and the reinforced concrete ultimate load ($Tu_{conc.}$) for different examined connections. These connections input data are presented in Appendix E. Also, in Table 5-9, the calculated concrete resistance (T_c) is compared with the recorded connection breakout cracking load (T_{cr}), the concrete ultimate strength ($Tu_{conc.}$) is compared with the recorded concrete

208

ultimate load, and the actual connection ultimate load ($Actual\ Tu$) is compared with the recorded connection ultimate load (T_u). For beams with high transverse reinforcement ratio close to the pile shaft, the ultimate concrete load and the breakout cracking load were almost the same, and hence the breakout cracking load was not indicated.

Tables 5-8 and 5-9 show that the concrete resistance (T_c) calculated by employing the modified SMCFT is close to the connection breakout cracking load. The mean value of the percentage T_c / T_{cr} is 89% and its standard deviation is 10%, with coefficient of variation of 12%. These values indicate the ability of the equation to predict the breakout cracking load well. In addition, Table 5-9 indicates the ability of Equation 5.21 to predict the concrete ultimate load with good accuracy for the beams that did not fail due to beam shear failure. Only the beams with high transverse reinforcement had a higher expected concrete ultimate load than the recorded ultimate load because the beam shear limit state was less than the connection capacity confirming the importance of comparing the connection capacity to the beam limit state designs.

Table 5-9 also confirmed that Equation 5.24 can accurately predict the actual behaviour of the pile connection, with mean percentage value of 104% and percentage standard deviation of 9%.

Table 5- 8 Calculated different components of connection capacity

Specimen	z	ε_z	Θ	Cone dim. (mm)	Cal. T_c (kN) Eq. 5.17	Cal. T_s (kN) Eq.5.18	Cal. $Tu_{conc.}$ (kN) Eq.5.19	Cal. $Tu_{reinf.}$ (kN) Eq.5.20	*2xBeam shear capacity (kN)	$T_{u\ Design}$ (kN) Eq. 5.23	$T_{u\ Actual}$ (kN) Eq. 5.24
T1	0.0021	0.0009	35.3	594	142	26	168	95	448	142	168
T2	0.0026	0.0010	36.2	719	174	30	204	129	448	174	204
F-D-228	0.0029	0.0011	36.6	779	190	32	222	140	448	190	222
T3	0.0031	0.0011	36.9	841	206	33	239	151	448	206	239
F-D-280	0.0032	0.0012	37.2	902	222	34	256	162	448	222	256
F-D-305	0.0034	0.0012	37.4	962	238	35	273	173	448	238	273
T-P-100	0.0031	0.0012	37.1	637	188	27	215	115	420	188	215
T4	0.0030	0.0011	36.8	732	192	35	227	132	457	192	227
T5	0.0029	0.0011	36.7	773	193	38	231	139	471	193	231
T-P-305	0.0028	0.0011	36.6	853	196	43	239	153	521	196	239
T-P-380	0.0027	0.0011	36.4	932	199	48	247	168	567	199	247
T-B-10	0.0061	0.0017	41.0	633	144	50	194	114	307	144	194
T6	0.0020	0.0009	35.1	742	222	25	247	134	632	222	247
T7	0.0012	0.0006	33.4	781	265	18	283	141	830.4	265	283
T-B-30	0.0009	0.0005	32.5	803	294	14	308	144	900	294	308
T-B-35	0.0006	0.0004	31.7	822	325	11	336	148	963	325	336
T8	0.0030	0.0011	36.9	706	191	66	257	254	527	254	257
T9	0.0030	0.0011	36.9	706	191	48	239	254	527	239	254
T-A-6	0.0026	0.0010	36.2	719	174	66	240	151	394	174	240
T-A-8	0.0026	0.0010	36.2	719	174	110	284	240	394	240	284
T-A-10	0.0026	0.0010	36.2	719	174	219	393	424	394	393	394
2-A-15	0.0026	0.0010	36.2	719	174	438	612	848	394	394	394
2-A-20	0.0026	0.0010	36.2	719	174	657	831	1272	394	394	394
2-A-25	0.0026	0.0010	36.2	719	174	1095	1269	2120	394	394	394
2br8@200	0.0026	0.0010	36.2	719	174	50	224	144	320	174	224
2 br 10@200	0.0026	0.0010	36.2	719	174	100	274	288	375	274	288
2 br 15@200	0.0026	0.0010	36.2	719	174	200	374	575	486	374	486
2 br 8@100	0.0026	0.0010	36.2	719	174	73	247	288	345	247	288
2 br 10@100	0.0026	0.0010	36.2	719	174	145	319	575	425	319	425
2 br 15@100	0.0026	0.0010	36.2	719	174	290	464	1150	494	464	494
4 br 8@200	0.0026	0.0010	36.2	719	174	100	274	288	494	274	288
4 br 10@200	0.0026	0.0010	36.2	719	174	200	374	575	494	374	494
4-15@200	0.0026	0.0010	36.2	719	174	400	574	1150	494	494	494

* *Using Response* 2000: This shear strength can be either due to reaching the shear or flexural capacity of the beam.

Table 5- 9 Comparison of capacity from recommended equations and recorded results

Specimen	Recorded T_{cr}	$\frac{Calculated\ T_c}{Recorded\ T_{cr}}$ %	Recorded $T_{uconc.}$	$\frac{calculated\ Tu_{conc.}}{Recorded\ Tu_{conc.}}$ %	Recorded T_u	$\frac{calculated\ Tu\ Actual}{Recorded\ T_u}$ %
T1	154	92	154	109	154	109
T2	200	87	201	101	201	101
F-D-228	212.8	83	229	97	229	97
T3	232	89	232	103	232	103
F-D-280	290	77	290	88	290	88
F-D-305	324	73	324	84	324	84
T-P-100	184.5	102	184.5	117	184.5	117
T4	201.7	95	201.7	112	201.7	112
T5	239.5	81	239.5	96	239.5	96
T-P-305	255	77	255	94	255	94
T-P-380	258.6	77	258.6	96	258.6	96
T-B-10	174	83	174	111	174	111
T6	222.5	100	222.5	111	222.5	111
T7	252.3	105	252.3	112	252.3	112
T-B-30	288	102	288	107	288	107
T-B-35	345	94	345	97	345	97
T8	208.5	91	231	111	256.3	100
T9	208.4	91	212	113	253.2	100
T-A-6	---	---	204	118	204	118
T-A-8	---	---	223	127	239.8	118
T-A-10	---	---	242	162	371.4	106
T-A-15	---	---	340	180	407.7	97
T-A-20	---	---	372	223	372	106
T-A-25	---	---	395	321	395	100
2br8@200	---	---	200	112	200	112
2 br 10@200	---	---	266	103	297	97
2 br 15@200	---	---	300	125	428	114
2 br 8@100	---	---	242	102	300	96
2 br 10@100	---	---	286	112	428	99
2 br 15@100	---	---	356	130	428	115
4 br 8@200	---	---	282	97	314	92
4 br 10@200	---	---	342	109	428	115
4-15@200	---	---	342	168	428	115
Average%		**89**				**104**
Standard deviation%		**10**				**9**
Coefficient of variation%		**11**				**9**
Root mean squared error%		**15**				**10**

5.4.3 Consideration of (a/d) ratio

To verify the ability of the developed equations to account for effect of (a/d) on the connection capacity, Equations 5.17, 5.18, 5.19, 5.20, and 5.24 were used to calculate the connection capacity of connections for beams with different (a/d) ratios and the results are presented in Tables 5-10 and 5-11. Table 5-10 presents the different components of the connection capacity and Table 5-11 compares the connection capacity values calculated from the proposed equations with those recorded from the experimental and numerical investigations. It is noted from Tables 5-10 and 5-11 that the recommended equations give good predictions for beams with (a/d) >1, while it gave conservative predictions for beams with (a/d) < 1.

It is suggested that a strut and tie model as shown in Figure 5-2 may be considered for calculating the connection capacity for beams with (a/d) < 1. However, the strut and tie model is not pursued in this research as deep beams with (a/d) < 1 is outside the scope of this research.

Table 5-10 Calculated different components of connection capacity for beams with different (a/d) ratios

Specimen	z	ε_z	Θ	Cone dim. (mm)	Cal. T_c (kN)	Cal. T_s (kN)	Cal. $Tu_{conc.}$ (kN)	Cal. Tu_{rein} (kN)	*2xBeam shear capacity (kN)	T_u Recorded (kN)	T_u Actual (kN)
T-R-2.75 (4-15M)	0.0041	0.00136	39	675	140	41	158	81	352	140	158
T-R-1.75 (4-15M)	0.0030	0.00112	37	707	159	33	174	85	387	159	174
T-R-1 (4-15M)	0.0021	0.00090	35	739	181	27	194	89	873	181	194
T-R-0.5 (4-15M)	0.0015	0.00073	34	764	203	22	213	92	1572	203	213
T-R-0.25 (4-15M)	0.0013	0.00064	33	779	217	19	226	93	1572	217	226
T-R-5.5 (4-30M)	0.0021	0.00089	35	739	182	27	194	89	390	182	194
T-R-4 (4-30M)	0.0016	0.00075	34	761	200	23	210	91	495	200	210
T-R-3.5 (4-30M)	0.0014	0.00070	34	769	208	21	217	92	521	208	217
T-R-2.75 (4-30M)	0.0012	0.00062	33	783	221	18	230	94	542	221	230
T-R-2.5 (4-30M)	0.0011	0.00058	33	788	227	18	235	95	480	227	235
T-R-2.25 (4-30M)	0.0010	0.00056	33	793	232	17	239	95	424	232	239
T-R-1 (4-30M)	0.0006	0.00038	32	823	270	11	276	99	1124	270	276
T-R-0.5 (4-30M)	0.0004	0.00031	31	837	292	9	296	100	2022	292	296
T-R-0.25 (4-30M)	0.0004	0.00026	31	846	307	8	310	101	2022	307	310

Table 5- 11 Calculated and measured capacity for beams with different (a/d) ratios

Specimen	Recorded T_{cr}	$\frac{Calculated\ T_c}{Recorded\ T_{cr}}$ %	Recorded $T_{uconc.}$	$\frac{calculated\ Tu_{conc.}}{Recorded\ T_{uconc.}}$ %	Recorded T_u	$\frac{calculated\ Tu\ Actual}{Recorded\ T_u}$ %
T-R-2.75 (4-15M)	154	91	154	103	154	103
T-R-1.75 (4-15M)	216	74	216	81	201	87
T-R-1 (4-15M)	281	65	281	69	229	85
T-R-0.5 (4-15M)	392	52	392	54	232	92
T-R-0.25 (4-15M)	569	38	569	40	290	78
T-R-5.5 (4-30M)	175	104	175	111	324	60
T-R-4 (4-30M)	178	112	178	118	184.5	114
T-R-3.5 (4-30M)	192	108	192	113	201.7	108
T-R-2.75 (4-30M)	191	116	191	120	239.5	96
T-R-2.5 (4-30M)	195	116	195	121	255	92
T-R-2.25 (4-30M)	210	110	210	114	258.6	92
T-R-1 (4-30M)	386	70	386	72	386	72
T-R-0.5 (4-30M)	626.4	47	626.4	47	626.4	47
T-R-0.25 (4-30M)	644	48	644	48	644	48
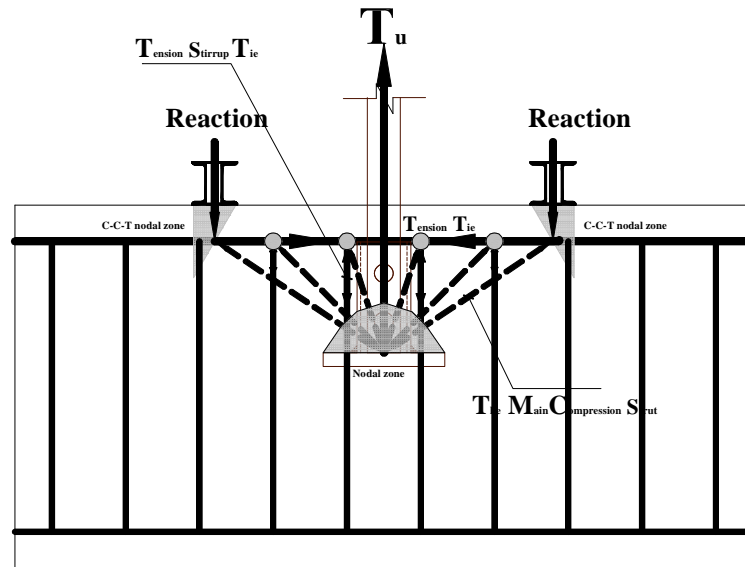
Figure 5- 2 Strut-and-tie model of single span deep beam with stirrups with (a/d)<1

5.4.4 Consideration of tension anchor supports

The connection capacity was calculated considering tension anchor supports instead of bearing supports and the results are presented in Tables 5-12 and 5-13. The results demonstrated that the proposed equations perform equally well for beams with anchor supports; however, the equation predictions is till applicable for (a/d) <1 because the concrete capacity with tension anchor supports is less than that of the bearing supports and diagonal tension cracking is still presented.

Table 5- 12 Calculated components of connection capacity for beams with different (a/d) ratios using tension anchor supports

Specimen	z	ε_z	Θ	Cone dim. (mm)	Cal. T_c (kN)	Cal. T_s (kN)	Cal. $Tu_{conc.}$ (kN)	Cal. Tu_{reinf} (kN)	*2xBeam shear capacity (kN)	T_u Recorded (kN)	T_u Actual (kN)
Tension anchor (a/d=1.35)	0.0026	0.001	36	719	174	45	188	86	450	174	188
Tension anchor (a/d=1)	0.00211	0.00090	35	739	181	34	194	89	873	181	194
Tension anchor (a/d=0.75)	0.00191	0.00084	35	747	196	27	319	90	1200	196	319
Tension anchor (a/d=0.5)	0.00153	0.00073	34	764	203	21	213	92	1572	203	213
Tension anchor (a/d=0.25)	0.00126	0.00064	33	779	217	15	226	93	1572	217	226

Table 5- 13 Calculated connection capacity compared with capacity recorded from experimental and numerical investigations for beams with different (a/d) ratios using tension anchor supports

Specimen	Recorded T_{cr}	$\frac{Calculated\ T_c}{Recorded\ T_{cr}}$ %	Recorded $T_{uconc.}$	$\frac{calculated\ Tu_{conc.}}{Recorded\ Tu_{conc.}}$ %	Recorded T_u	$\frac{calculated\ Tu\ Actual}{Recorded\ T_u}$ %
Tension anchor (a/d=1.35)	200	87	200	94	200	94
Tension anchor (a/d=1)	242	75	242	80	242	80
Tension anchor (a/d=0.75)	330	60	330	97	330	97
Tension anchor (a/d=0.5)	424	48	424	50	424	50
Tension anchor (a/d=0.25)	516	42	516	44	516	44

5.5 Recommended Equations for Connection Design

Considering the developed cracking load and ultimate load equations and the materials reduction factors, the design of the pile-grade beam connection may be accomplished according to the flow chart shown in Figure 5-6 taking into consideration the design conditions shown below:

1) For a fixed connection, it must be designed to prevent breakout cracking. Thus, the connection breakout cracking load T_{cr} must be equal to or more than the ultimate pile load. The connection breakout load will be given by Equation 5.25

$$T_{cr} = \left[2.6 \frac{1}{\sqrt{1+d_{emb}/(25.a_g)}} (\rho.\emptyset_c \lambda f c'.d)^{1/3}. \left(\frac{\sqrt[3]{a^*_{right}}+\sqrt[3]{a^*_{left}}}{\sqrt[3]{a^*_{right}}.\sqrt[3]{a^*_{left}}}\right)\right].b.d_{emb}, \rho \leq 0.5\% \quad \textbf{5. 25}$$

Figure 5-3 presents the ratio between the calculated values using equation 5.25 and the actual recorded values for 37 investigated connections using a unity concrete reduction factor and compared with the 1 and $\sqrt[3]{1/\emptyset_c}$ =1.154. Confirming that using Equation 5.25 is well expecting the connection breakout capacity and that using this equation will cause a conservative design.
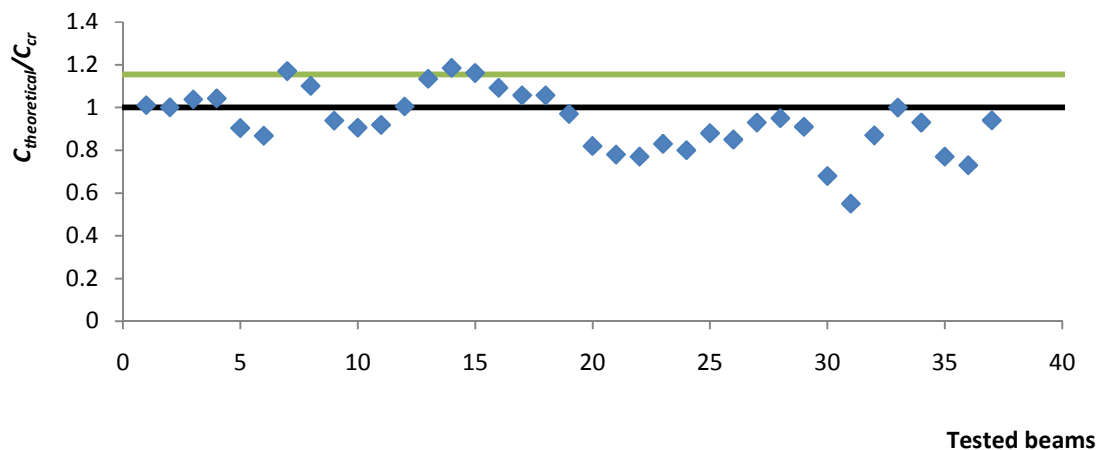
Figure 5- 3 The ratio between the calculated breakout cracking load using equation 5.25 and the recorded connection breakout cracking load

2) For a hinged connection in limit state design approach, the connection ultimate design load $T_{u\ Design}$ must be equal to or more than the ultimate pile load. The connection ultimate design load, $T_{u\ Design}$, is given by:

$$T_{u\,Design} = the\;least\;of \begin{cases} Tu_{conc.} = \dfrac{2*0.40}{(1+1500.\varepsilon_z)}\sqrt{\varnothing_c\lambda fc'}\text{b. d}_{emb} + A_v.\varnothing_s f_v.\left(\dfrac{b_{plate}}{s}+1\right) \\ Tu_{support} = 1.2\sqrt{\varnothing_c\lambda fc'}.\text{b. d}_{emb}\;\;if\;\left(\dfrac{a}{d}\right)<1 \\ Tu_{reinf.} = \dfrac{A_v.\varnothing_s f_y}{s}\left(2.\text{d}_{emb}.\cot\theta + \text{b}_{plate}\right)\;or\;A_{anchor}\varnothing_s f_y \\ 2xBeam\;shear\;strength\;(using\;a_{max}) \end{cases} \geq T_c \quad \textbf{5.26}$$

Figure 5-4 presents the ratio between the calculated values using Equation 5.26 and the actual recorded values for 52 investigated connections using a unity concrete and reinforcement reduction factors and compared with the 1 and $\sqrt{1/\varnothing_c}$=1.24. Confirming that equation 5.26 will cause a conservative design and it is recommended to be used in the connection design under tension loading. Figure 5-7 is a flow chart showing the design steps required when this design is required.
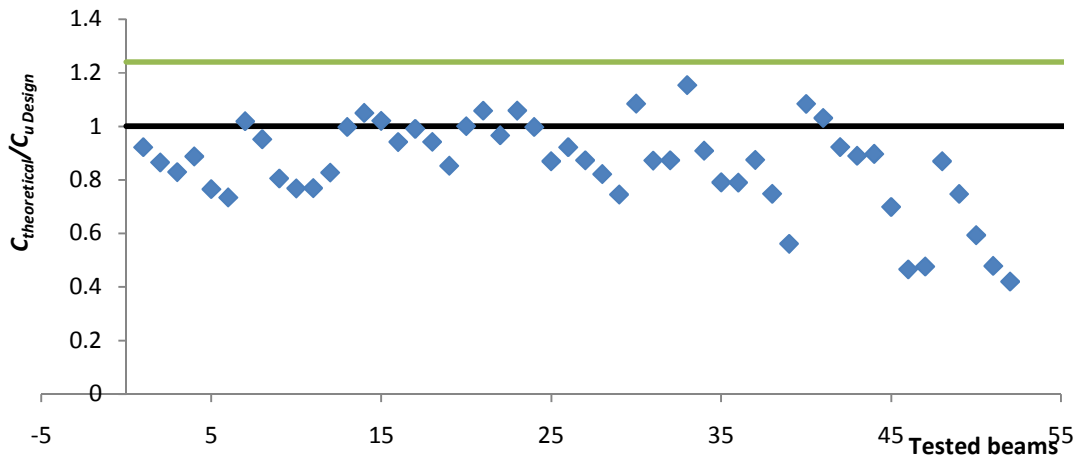
Figure 5-4 The ratio between the calculated connection design load using equation 5.26 and the recorded connection ultimate load

3) For collapse prevention level in performance based design, the connection can be designed for the actual ultimate load, $T_{u\,Actual}$. Thus, $T_{u\,Actual}$ must be equal to or more than the ultimate pile load. In this case, actual $T_{u\,Actual}$, is given by:

217

$$Actual\ T_u = Min.of \begin{cases} Max.of \begin{cases} Tu_{conc.} = \frac{2*0.40}{(1+1500.\varepsilon_z)}\sqrt{\emptyset_c \lambda f c'}b.d_{emb} + A_v.\emptyset_s f_v.\left(\frac{b_{plate}}{s}+1\right) \\ Tu_{reinf.} = \frac{A_v.\emptyset_s f_y}{s}\left(2.d_{emb}.\cot\theta + b_{plate}\right) or\ A_{anchor}.\emptyset_s f_y \\ Tu_{support} = 1.2\sqrt{f\emptyset_c \lambda c'}.b.d_{emb}\ \ if\ \left(\frac{a}{d}\right) < 1 \\ 2xBeam\ shear\ strength\ (using\ a_{max}) \end{cases} \end{cases} \geq T_c \quad \textbf{5.27}$$

Figure 5-5 presents the ratio between the calculated values using equation 5.27 and the actual recorded values for 52 investigated connections using a unity concrete and reinforcement reduction factors and compared with the 1 and $\sqrt{1/\emptyset_c}$ =1.24. Confirming that Equation 5.27 will cause a conservative design if the material reduction factors are used and it is recommended to be used in the connection design under tension loading when performance based design is used. Figure 5-8 is a flow chart showing the design steps required when this design is required.
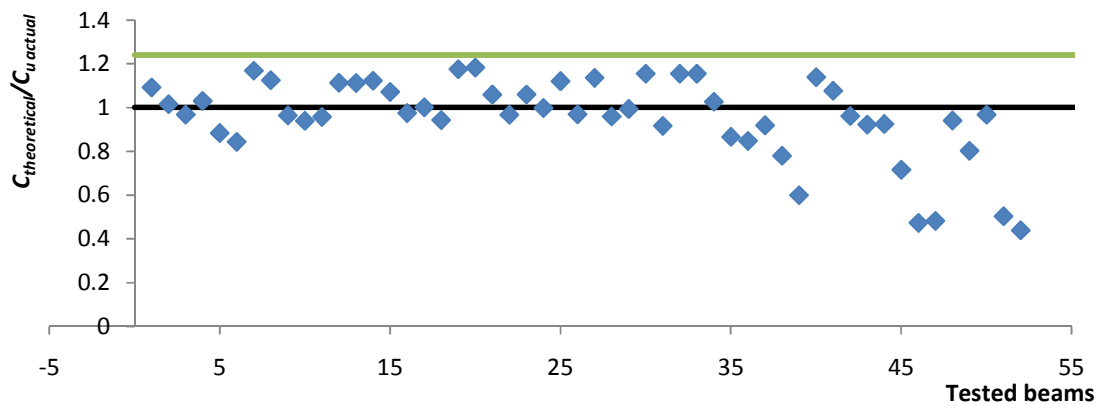
Figure 5-5 The ratio between the calculated connection actual load using equation 5.27 and the recorded connection ultimate load
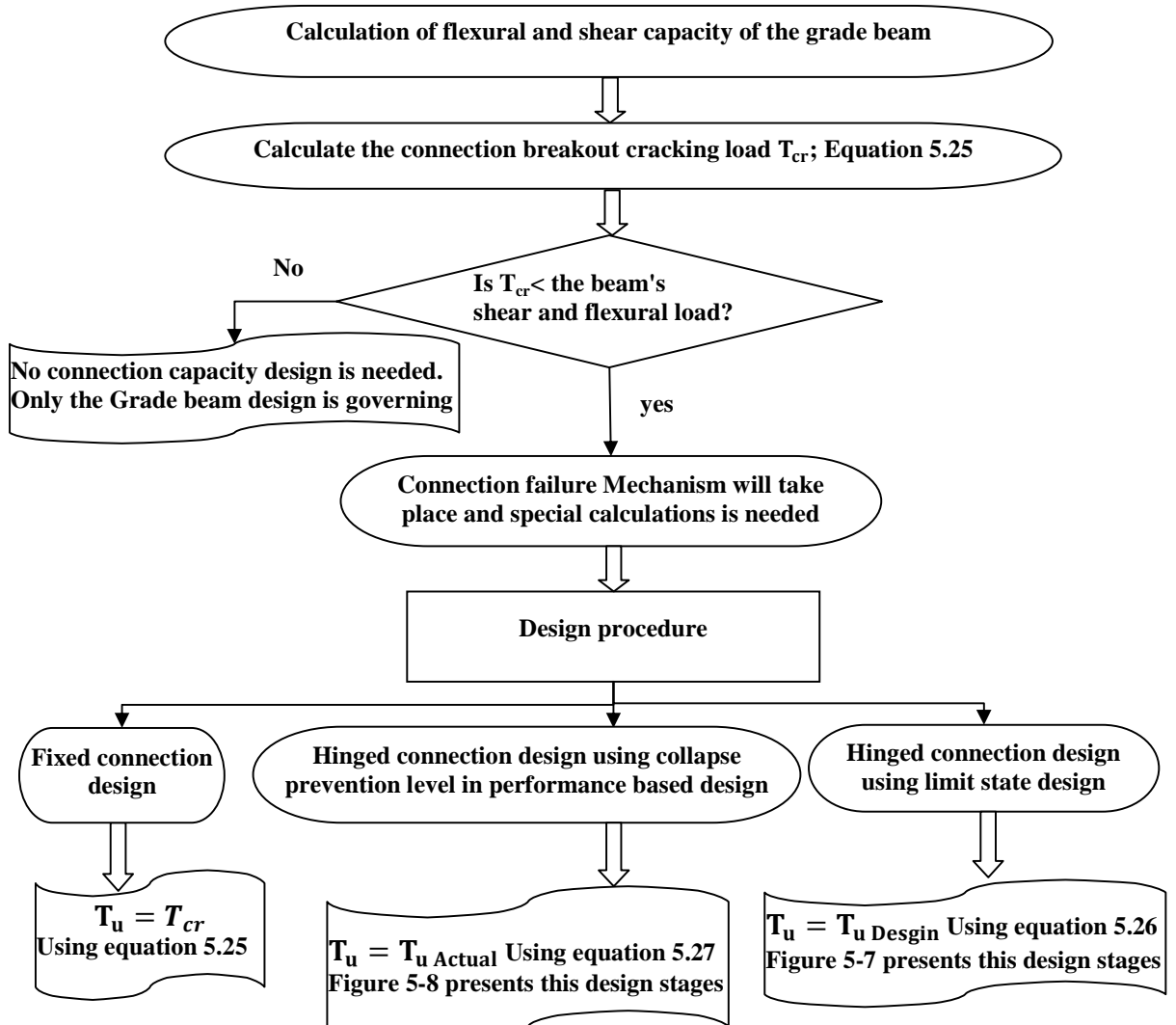
Figure 5- 6 The helical pile- RC grade beam connection's design stages

Calculate T_c, T_s, $Tu_{conc.}$ using equations 5.19, 5.20, and 5.21, respectively using concrete/steel reduction factors $\emptyset_c$=0.65, $\emptyset_s$=0.85

Calculate $T_{u\ reinf.}$ using equation 5.22 and steel reduction factor $\emptyset_s$=0.85

Calculate the sum of the shear capacities of the grade beam at the pile location from the two sides; $T_{u\ shear}$

Is $T_{u\ shear} < Tu_{conc.}$ & $T_{u\ reinf.}$?

yes

Single shear failure in the grade beam will take place and $T_u = T_{u\ shear}$

No

Is a/d<1?

yes

Calculate $Tu_{support} = 1.2\sqrt{\emptyset_c \lambda fc'}.b.d_{emh}$

No

Is $Tu_{support} < T_{u\ reinf.}$ & Tu_{conc}

No

yes

Crushing at the support region will occur & $T_u = T_{u\ support}$

Is $Tu_{conc.} > T_{u\ reinf.}$?

yes

$T_{udesign} = T_{u\ conc.}$ & non recommended brittle breakout failure will take place. Increase the transverse reinforcement till $Tu_{conc.} \leq T_{u\ reinf.}$.

No

$T_{udesign} = T_{u\ concrete}$ & recommended ductile failure after the concrete breakout cracking will occur

Figure 5- 7 The design steps required when a limit state design was used for hinged helical pile-RC grade beam connection.

Calculate T_c, T_s, $Tu_{conc.}$ using equations 5.19, 5.20, and 5.21, respectively using concrete/steel reduction factors $\emptyset_c$=0.65, $\emptyset_s$=0.85

Calculate $T_{u\ reinf.}$ using equation 5.22 and steel reduction factor $\emptyset_s$=0.85

Calculate the sum of the shear capacities of the grade beam at the pile location from the two sides; $T_{u\ shear}$

Is $T_{u\ shear} < Tu_{conc.}$ & $T_{u\ reinf.}$?

yes

Single shear failure in the grade beam will take place and $T_u = T_{u\ shear}$

No

Is a/d<1?

yes

Calculate $Tu_{support} = 1.2\sqrt{\emptyset_c \lambda fc'} . b. d_{emb}$

No

Is $Tu_{support} < T_{u\ reinf.}$ & $Tu_{conc.}$

No

yes

Crushing at the support region will occur & $T_u = T_{u\ support}$

Is $Tu_{conc.} > T_{u\ reinf.}$

No

yes

$T_u = T_{u\ conc.}$ & non recommended brittle breakout failure will take place. Increase the transverse reinforcement till $Tu_{conc.} \leq T_{u\ reinf.}$

$T_u = T_{u\ reinf.}$ & recommended ductile failure after the concrete breakout cracking will occur

Figure 5- 8 The design steps required when a collapse prevention level in performance based design was used for hinged helical pile-RC grade beam connection.

5.6 Conclusions

The breakout cracking behavior of helical piles and micropiles connections subjected to tension loads observed from experimental and numerical studies conducted as part of this research are discussed. In addition, methods available in the literature that are used to calculate beams capacity are reviewed with view of employing them to evaluate the connection capacity. Consequently, analytical equations are developed to determine the connection capacity under tension loading. These equations are developed considering the findings of both the experimental and numerical investigations conducted as well as relevant methods available in the literature. The following provides the main conclusions of this effort.

- Two equations are proposed to calculate the breakout cracking load of the helical pile connection. The first equation, Equation 5.25, is a modification of the equation proposed by Al-zoubi (2011). It predicted the breakout cracking load with almost 100% mean value and 9.5% COV. The second equation, Equation 5.19, is a modification of the SMCFT to calculate the concrete shear resistance accounting for difference in concrete strain due to pile connection. It allows calculating concrete capacity accurately without iterations.

- It is proposed to use the modified SMCFT, Equation 5.21, in order to calculate the contribution of concrete ultimate strength to the pile connection capacity. The modified SMCFT is accounting for the contribution of stirrups within the width of the pile cap plate considering the concrete strain.

- To calculate the pile-connection ultimate capacity, four different limit states were calculated and compared. These limit states are the concrete ultimate strength, the transverse reinforcement ultimate strength, double beam shear strength at the pile location, and the crushing of support region strength when (a/d) is less than 1. The value to be used in a limit state design is the least value of the four limit states, while the actual value that can be used in a serviceability performance level design is taking the bigger value of concrete ultimate load and the transverse reinforcement ultimate load and compare it with the other two values (Equations 5.26 and 5.27) to take the least value.

- It is recommended to use transverse reinforcement that has capacity $\geq$ $Tu_{conc.}$.

- For the connection design under Tension loading, three design equations were recommended taking into consideration the connection fixation condition and the design method as presented in Equations 5.25, 5.26, and 5.27 and the design procedures are demonstrated in Figures 5-6, 5-7, and 5-8.

5.7 References

Abd Elaziz, A.Y. & El Naggar, M.H., 2015. Performance of Hollow Bar Micropiles under Monotonic and Cyclic Lateral Loads. *Journal of Geotechnical and Geoenvironmental Engineering*, 141(5), pp.1–11.

ACI 318, 2011. *Building Code Requirements for Structural Concrete (ACI 318-11) and Commentary*, Farmington Hills, MI: American Concrete Institute.

ACI-ASCE Committee 326, 1962. Shear and Diagonal Tension. *ACI Journal Proceedings*, 59(1), pp.1–30.

AIK, K., 2009. *KBCS*,

Al-Zoubi, M., 2014. Diagonal Cracking Capacity and Ultimate Shear Strength of Slender RC Beams without Web Reinforcement. *Jordan Journal of Civil Engineering*, 8(1), pp.97–112.

AS 3600, 2001. *Australian Standard for Concrete Structures AS 3600-2001*, Australia, Sydney.

B8110-1, 1997. *Structural use of Concrete*, British Standard.

Baltay, P. & Gjelsvik, A., 1990. Coefficient of Friction for Steel on Concrete at High Normal Stress. *Journal of Materials in Civil Engineering*, 2(1), pp.46–49.

Bazant, Z.P. & Sun, H.-H., 1987. Size Effect in Diagonal Shear Failure: Influence of Aggregate Size and Stirrups. *ACI Materials Journal*, 84(4), pp.259–272.

Bazant, Z.P. & Yu, Q., 2007. Designing Against Size Effect on Shear Strength of Reinforced Concrete Beams Without Stirrups: I. Formulation. *Journal of Structural Engineering*, 131(12).

Bažant, Z.P. & Yu, Q., 2005. Designing Against Size Effect on Shear Strength of Reinforced Concrete Beams Without Stirrups: II. Verification and Calibration. *Journal of Structural Engineering*, 131(12), pp.1886–1897.

Bentz, E.C., 2005. Empirical Modeling of Reinforced Concrete Shear Strength Size Effect for Members without Stirrups. *ACI Structural Journal*, 102(2), pp.232–241.

Bentz, E.C. & Collins, M.P., 2006. Development of the 2004 Canadian Standards Association (CSA) A23.3 shear provisions for reinforced concrete. *Canadian Journal of Civil Engineering*, 33(5), pp.521–534.

Broujerdian, V., 2004. *Size effect on shear strength of reinforced concrete beams*. Sharif University of Technology.

Carrato, P.J., Krauss, K.W. & Kim, J.B., 1996. Tension Tests of Heavy-Duty Anchors with Embedments of 8 to 19 Inches. *ACI Structural Journal*, 93(3), pp.360–368.

CEB, 1993. *CEB-FIP model code 1993: design code*, Thomas Telford.

Collins, M.P. et al., 1996. A General Shear Design Method. *Structural Journal*, 93(1), pp.36–45.

Collins, M.P. & Kuchma, D., 1999. How Safe Are Our Large, Lightly Reinforced Concrete Beams, Slabs, and Footings? *ACI Structural Journal*, 96(4), pp.482–490.

Collins, M.P. & Mitchell, D., 1991. *Prestressed Concrete Structures*, Prentice Hall.

CSA A23.3, 2004. *A23. 3-04: design of concrete structures*,

Cusens, A. & Besser, I., 1985. Shear strength of reinforced concrete wall-beams under combined top and bottom loads. *Structural Engineer*, Part B,63(50), p.6.

Eurocode 2, 2003. *Commission of the European Communities, Eurocode No. 2: Design of Concrete Structures. Part 1: General Rules and Rules for Buildings.*, London: European Standards.

Fereig, S. M., & Smith, K.N., 1977. Indirect Loading on Beams with Short Shear Spans. *Magazine of Concrete Research*, 74(5), pp.220–222.

Ferguson, P., 1956. Some implications of recent diagonal tension tests. *ACI Journal Proceedings*, 53(8), pp.157–172.

JSCE, 1997. *Standard Specifications for Steel and Composite Structures* Japan Society of Civil Engineers, ed.,

Kani, G., 1966. Basic facts concerning shear failure. *ACI Journal Proceedings*, 63(6), pp.675–692.

Kani, G., 1967. How safe are our large reinforced concrete beams?. *ACI journal proceedings*, 64, pp.128–141.

Kim, J.-K. & Park, Y.-D., 1996. Prediction of Shear Strength of Reinforced Concrete Beams without Web Reinforcement. *ACI Materials Journal*, 93(3), pp.213–222.

Lee, N.H. et al., 2007. Tensile-Headed Anchors with Large Diameter and Deep Embedment in Concrete. *ACI Structural Journal*, 104(4), pp.479–486.

Lubell, A.S., Bentz, E.C. & Collins, M.P., 2009. Shear Reinforcement Spacing in Wide Members. *ACI Structural Journal*, 106(2), pp.205–214.

Mathey, R. & Watstein, D., 1963. Shear strength of beams without web reinforcement containing deformed bars of different yield strengths. *ACI journal proceedings*, 60(13), pp.183–207.

Metwally, I.M., 2012. Evaluate the capability and accuracy of response-2000 program in prediction of the shear capacities of reinforced and prestressed concrete members. *HBRC Journal*, 8(2), pp.99–106.

NCHRP Report 549, 2005. *Simplified Shear Design of Structural Concrete Members*, Washington, D.C.

Ozcebe, G., Ersoy, U. & Tankut, T., 1999. Evaluation of Minimum Shear Reinforcement Requirements for Higher Strength Concrete. *ACI Structural Journal*, 96(3), pp.361–368.

Paul, I.S., 1978. *Behaviour of indirectly loaded reinforced concrete thin-wall ribbed panels*. Concordia University.

Placas, A. & Regan, P., 1971. Shear failure of reinforced concrete beams. *ACI Journal Proceedings*.

Rajagopalan, K. & Ferguson, P., 1968. Exploratory shear tests emphasizing percentage of longitudinal steel. *ACI Journal Proceedings*, 65(46), pp.634–638.

Smith, K.N. & Fereig, S.M., 1974. Effect of Loading and Supporting Conditions on the Shear Strength of Deep Beams. *ACI Special Publication*, 42, pp.441–460.

Tan, K.H., KONG, F.K. & WENG, L.W., 1997. High strength concrete deep beams subjected to combined Top-and Bottom-Loading. *ACI Structural Engineer*, 75(11).

Taylor, R., 1960. Some shear tests on reinforced concrete beams without shear reinforcement*. *Magazine of Concrete Research*, 12(36), pp.145–154.

Vecchio, F. & Collins, M., 1986. The modified compression-field theory for reinforced concrete elements subjected to shear. *ACI Journal Proceedings*, 83(2), pp.219–231.

Yang, K.-H. & Ashour, A.F., 2008. Mechanism Analysis for Concrete Breakout Capacity of Single Anchors in Tension. *ACI Structural Journal*, 105(5), pp.609–616.

Yu, Q. & Bažant, Z.P., 2011. Can Stirrups Suppress Size Effect on Shear Strength of RC Beams? *Journal of Structural Engineering*, 137(5), pp.607–617.

Zsutty, B., 1968. Beam Shear Strength Prediction by. , 5(65), pp.943–951.

Zsutty, T., 1971. Shear Strength Prediction for Separate Categories of Simple Beam Tests. *ACI Journal Proceedings*, 68(2), pp.138–143.

Zuhua Wang, 1987. shear strength of slender concrete beams loaded indirectly. *International journal of structures*, 7(1), pp.17–42.

BEHAVIOUR OF HELICAL PILE CONNECTORS FOR NEW FOUNDATIONS SUBJECTED TO COMPRESSION LOADING: EXPERIMENTAL INVESTIGATION

6.1 Introduction

This research investigates the behaviour of the connection between slender solid shaft pile types, which end with a mono steel bar at the ground level (e.g. square shaft helical piles and micro piles) and a new reinforced concrete foundation (e.g. grade beams and footings). Typically, steel brackets (plates) are used in order to transfer loads from the new reinforced concrete foundation to the steel pile. The bracket is a steel plate, which can be connected to the steel pile by welding or by bolts. Thus, the connection behaviour can be considered as a headed anchor. However, these types of anchors are not addressed by current design codes (e.g. A23.3-04 Appendix D, ACI 318-11 Appendix D, or ACI 349-01 Appendix B), because they are developed assuming linear fracture mechanics (Lee et al., 2007) based on tests on anchors with high bearing pressure (i.e. anchors with small heads). Also, these codes are mainly concerned with the connections subjected to tension or shear not compression. Furthermore, helical pile new construction may involve grade beams with limited width, which reduces the connection capacity.

In the research described herein, full-scale pile-foundation connection models were tested experimentally under compression loading in order to clearly understand the behaviour of the connection and its failure mechanism under monotonic and cyclic loadings.

Four groups of specimens were constructed and tested under monotonic compression loading. The main factors varied in these test specimens included: the pile embedment depth into the foundation; the width of the pile cap's plate; and the longitudinal and transverse reinforcements of the grade beam. A fifth group, which include three specimens were subjected to cyclic compression loading and the results were compared with the same specimens tested in monotonic compression loading. Also, these three beams were compared with each other regarding the investigated variables.

6.2 Research significance

The connection considered in this research is widely used in the construction of helical piles and micropiles in North America. Figure 6-1 presents the configuration of the commonly used connector bracket (i.e. pile cap). Despite the wide application of these connections in the piling industry, there are no specific design criteria for their implementation in design. Given the growing popularity of these foundation options, especially in seismic active areas, there is a pressing need to understand their behaviour and develop a methodology for their design under different loading conditions. Thus, the main objective of this study is to examine the behaviour and capacity of the new construction brackets used to connect helical piles and micropiles to new reinforced concrete grade beam foundation subjected to monotonic and cyclic compression loading. The experimental results obtained from full scale tests are used to describe the full behaviour of the connection.

Figure 6- 1 Commonly used pile cap (i.e. New construction bracket)

6.3 Experimental program

Twelve specimens were experimentally tested under compression loading. The experimental program was divided into two phases. In the first phase, nine specimens were tested under monotonic compression loading. In the second phase, three other specimens were tested under cyclic compression loading. All tested specimens were simply supported reinforced concrete beams of dimensions 500 mm x 500 mm x 1600 mm, representing grade beams typically used in buildings foundations. In the first phase, the tested beams were categorized into four groups according to the parameters investigated. Each group has three beams, including the control beam C2. In each group only one variable was investigated, while the other variables were kept constant. In the first group: various typical pile embedment depths, 254 mm, 203 mm and 152 mm (10 in, 8 in, and 6 in) were investigated. The corresponding remaining depths (beam depth minus embedment depth and plate thickness) are 227 mm, 277 mm, and 330 mm. In the second group, the width of the steel square plate (i.e. new construction bracket) was varied between 165 and 229 mm (6.5 and 9 in) to study the effect of the bracket size on the beam capacity. In the third group, the effect of the beam's longitudinal reinforcement was

230

investigated. Four longitudinal bars were used with different diameters (16mm (15M), 19.5mm (20M), 25.2mm (25M)) resulting in longitudinal reinforcement ratios of 0.35%, 0.53%, and 0.89%, respectively. In the forth group, the effect of the beam's transverse reinforcement was examined considering stirrups spacing of 100 mm and 200mm, and the number of stirrup vertical branches of 2 and 4 branches. Table 6-1 and figure 6-2 summarize the dimensions and details of the nine specimens tested in the first phase. The second phase (i.e. fifth group) investigated the effect of cyclic loading on the connection behaviour concluded from the first phase. Three beams were tested under cyclic loading and the results are compared with those obtained from three similar beams tested under monotonic loading having the same variables. Also, this phase examined the effect of cyclic loading under different conditions including: different embedment depths (i.e.152 mm, and 203 mm); and different transverse reinforcement configurations (i.e. 2 branches of #2@ 200 mm, and 2 branches of #2 @ 100 mm). Table 6-2 summarizes the dimensions and details of the three specimens tested under cyclic loading in the second phase. Appendix B demonstrates the several steps conducted for the specimens preparation.
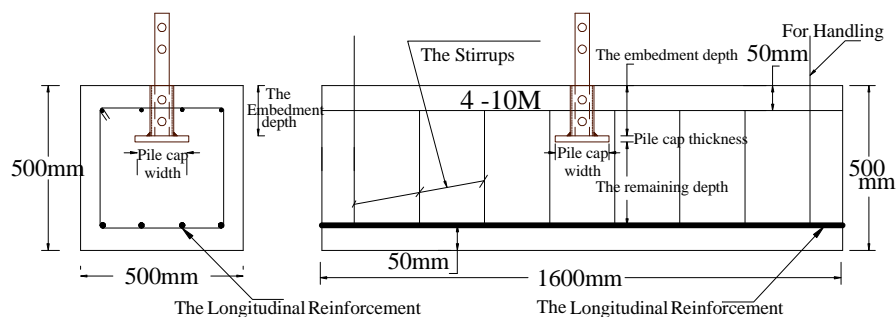
Figure 6- 2 Dimensions and full details for the tested specimens

Table 6- 1 Details of investigated specimens under monotonic compression loading

Beam Name	Beam Dimensions (mm)	Concrete Strength fc'(N/mm²)	The remaining depth (mm)	Pile cap width (mm)	Longitudinal Reinforcement	Stirrups
C1	500x500x1600	30	330	165	4-20M	2 branches #2@200mm
C2	500x500x1600	30	277	165	4-15M	2 branches #2@200mm
C3	500x500x1600	30	227	165	4-15M	2 branches #2@200mm
C4	500x500x1600	30	277	190	4-15M	2 branches #2@200mm
C5	500x500x1600	30	277	229	4-15M	2 branches #2@200mm
C6	500x500x1600	30	277	165	4-20M	2 branches #2@200mm
C7	500x500x1600	30	277	165	4-25M	2 branches #2@200mm
C8	500x500x1600	30	277	165	4-15M	4 branches #2@200mm
C9	500x500x1600	30	277	165	4-15M	2 branches #2@100mm

Table 6- 2 Details of studied Specimens in the second phase under cyclic compression loading

Beam Name	Beam Dimensions (mm)	Concrete Strength fc'(N/mm²)	The remaining depth (mm)	Pile cap width (mm)	Longitudinal Reinforcement	Used bolts	Stirrups
CC1	500x500x1600	30	330	165	4-20M	1-7/8"bolt &1-1" bolt	2 branches #2@200mm
CC2	500x500x1600	30	277	165	4-15M	2-1" bolts	2 branches #2@200mm
CC3	500x500x1600	30	277	165	4-15M	1-7/8"bolt &1-1" bolt	2 branches #2@100mm

6.4 Materials

The new construction bracket (shown in Figure 6-1) consists of a square steel plate with adequate thickness welded to 152 mm (6") long coupling tube with adequate inner diameter to insert the pile in it. The plate and tube conform to ASTM A36. The tube has one or two holes to connect the pile cap with the pile shaft using bolts. The used bolt was a 25 mm (1") diameter bolt complying with ASTM A 193 Grade B7 (minimum yield strength is 655 MPa, and minimum tensile strength is 793 MPa) with 152mm (6") length. Also, sometimes a 22 mm (7/8") diameter bolt with a length of 115mm (4 1/2") complying with ASTM A 193 Grade B7 was also used in case of tight space conditions (has been used in beams CC3 and CC1). The welding between the cylinder and the pile cap's plate was 10mm filet welding with E43XX metric electrode classification. The steel pile model was a central steel shaft which is made of hot rolled round-cornered-square (RCS) solid steel bar (45 mmx45 mm) conforming to the dimensional and workmanship requirements of ASTM A29, with minimum yield and tensile strengths of 483 and 689 MPa, respectively.

One concrete mix was used throughout the experimental work to cast the foundation models. Three concrete patches were used. Beams C1, C2, and C3 were casted in the first concrete patch. Beams C4, C5, C6, C7, C8, and C9 were casted in the second concrete patch. Beams CC1, CC2, and CC3 were casted in the third concrete patch. The three concrete patches had approximately the same concrete compressive strength of 30 MPa and their test data is presented in Appendix A. The concrete was delivered as a ready mix concrete. The concrete mix consisted of ordinary Portland cement, sand, and gravel with

20 mm maximum nominal aggregate size. The concrete mix for one cubic meter consisted of 1100 kg of coarse aggregate, 780 kg of sand, 245 kg Type 10Gu cement, 145 litre of water, 250 millilitre of super-plasticizer, and 80 kg slag. All of the results from the concrete cylinder compression and splitting tests can be found in Appendix A.

The longitudinal reinforcing bars were 15M, 20M, and 25M high strength deformed steel, which conforms to CSA G30.18M-09 grade 400W. The compression longitudinal reinforcement comprised 10M high strength deformed steel, which conforms to CSA G30.18M-09 grade 400W. Plain bars of #2 (i.e. 6.35 mm or 1/4" diameter) cold formed steel, with grade 450/550, were used for stirrups. All of reinforcement bars direct tensile test results are presented in Appendix A.

6.5 Instrumentation

Figure 6-3 shows the details of the test setup. The load was applied using a calibrated hydraulic jack of 1500 kN capacity with a maximum stoke of 500 mm. Two strong HEA 260 beams were used to support the specimens and to transfer the vertical load to the floor during loading. The two beams were spaced 1530 mm center-to-center and had a 1250 mm clear span resulting in beam span of 1440 mm center-to-center. The two strong HEA 260 beams allowed raising the specimen elevation in order to detect the cracks and deformations expected to take place during loading.

As shown in Figure 6-3, at least seven linear displacement transducers (LDT) were used to monitor the displacements at the mid-span and quarter-span points of the beam, and the out of plane displacement as well as the displacement of the pile shaft. To accomplish

these measurements, the LDTs were placed at the middle of upper and lower levels and the side of the beam. For each beam, five or more electrical strain gauges per beam were used to measure strain in different stirrups and different branches and in the outer and inner longitudinal steel (i.e. the longitudinal rebar close to the beams surface and the longitudinal rebar close to the beam core, respectively). The strain readings were also used to evaluate magnitude and distribution of the plate deformation along its width. The strain gauges were 10 mm long and had 120±0.3% Ω resistance. The strain gauges, the loading cell, and the displacement transducers were connected to a data acquisition system to monitor and record the strains, the applied loads, and the displacements.

Figure 6- 3 Test rig and locations of displacement transducers

6.6 Test procedure

In the first phase, monotonic loading was applied at a rate of 7 kN/min. In the second phase, cyclic loading was applied at frequency of 0.1 Hz. The load history of the cyclic compression loading applied in second phase was similar to that used by Esfahani (2008), and is shown in Figure 6-4. Initially, cyclic loading with amplitude 100 kN, which represented 30% of the expected ultimate load but less than the expected first cracking load, was applied to capture the effect of cyclic loading on the uncracked section. This was followed by cyclic loads, increasing in magnitude with 30 kN increments. Each increment was applied for 3 cycles before the next increment is applied, and the minimum load was maintained at 100 kN as seen in Figure 6-4. Observed cracks were marked, deformations were recorded from the LDTs, and the steel strains were recorded using the strain gauges. The total duration of each test was about one hour. The test was stopped when breakout cone cracks opened excessively causing total separation of the breakout cone, accompanied by excessive strength reduction below 60% of the ultimate load. In most cases, the test was stopped when necking occurred in the stirrups causing failure (often after the strength dropped below 60% of the ultimate load). To differentiate between the number of the cycle causing crack propagating while marking the crack pattern on the specimen, a dash (') was assigned to each loading cycle. Thus, 300' meant the first cycle of 300 kN, 300'' meant the second cycle of 300 kN, 300''' meant the third cycle of 300 kN.
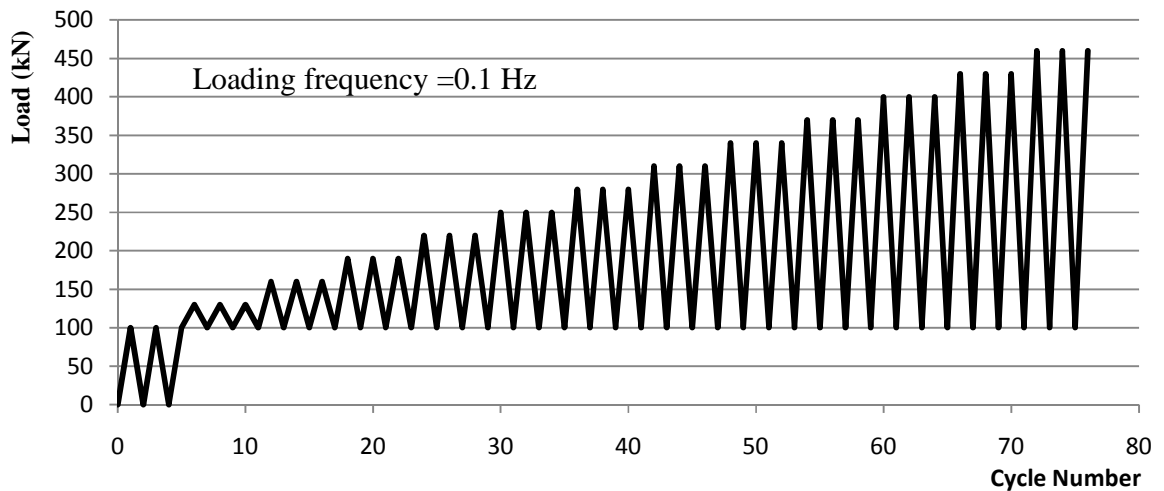
Figure 6- 4 The load history of the cyclic compression loading in phase two

6.7 Test results

The test result of the monotonic compression load tests will be discussed first. The results from the second phase (cyclic compression loading) will then be interpreted and compared with the results from the first phase.

6.8 General findings of first phase (Monotonic Compression Loading)

6.8.1   General Crack patterns, failure modes and beam ductility

The crack patterns of the nine tested beams are shown in Figure 6-5. Most of the beams had approximately the same crack pattern. The first flexural crack initiated as shown in Figure 6-6a, followed by bond failure between the pile and the surrounding concrete as shown in Figure 6-6b. As the load continued to increase, the flexural crack propagated towards the compression zone extending beyond the pile cap's plate and the bolt levels, and the cracks turned into flexural shear cracks after crossing the pile cap's plate and bolt levels. The cracks propagated towards each other and connected at the bolt level. The

237

formed cone was approximately rectangular. Probably due to shear friction at the crack location, this cone did not move vertically to separate from the specimen and the connection continued to resist more load till two inclined cracks were initiated forming another breakout cone. At this breakout cracking load, the inclined cracks began from the bolt level as shown in Figure 6-6c. Breakout cracks were formed by the flexural shear crack and the inclined cracks intersecting close to the longitudinal reinforcement level (mostly due to dowel action effect). In this case, the cracks angle changed from 60° at the flexural shear cracks to 35° close to the longitudinal reinforcement level as shown in Figure 6-6d. In beam C8, a new breakout cone formed by cracks inclined at 35° to 45° because only one flexural crack at the beam mid-span occurred when the breakout cracking load was reached.

Most specimens had the maximum load capacity (i.e. ultimate load) almost equal to the breakout cracking load because they did not have adequate transverse reinforcement to bridge the forces through the cracks. When adequate transverse reinforcement (e.g. stirrups) was used (e.g. C8 and C9), the ultimate load was higher than the concrete breakout cracking load. Dowel action in the longitudinal reinforcement, spalling of concrete and bond cracks were clear after the ultimate load was reached. At failure, the stirrups failed by necking as shown in Figure 6-6e causing the beam to disintegrate.

The crack extended approximately flat in the unsupported direction of the beam, which means the behaviour was closer to single shear failure rather than anchor breakout or punching failure. Furthermore, most specimens exhibited a vertical crack at the

compression side of the beam as shown in Figure 6-6f just after the ultimate load and close to failure (precisely after the stirrups yielding). This could be explained as follows. After the breakout cone moved with the loaded pile segment and the stirrups softened or failed, the longitudinal reinforcement stress increased sharply causing tensile stresses within concrete of the remaining part of the beam at the longitudinal steel level. This tension reversed the bending moment on the concrete above the bolt level and caused cracking releasing any pile-concrete friction. Similar behaviour was observed by Watstein et al. (1958) and Smith and Fereig (1974). Finally, the failure mechanism was brittle at ultimate load; however, the beam ductility increased as the transverse reinforcement increased.
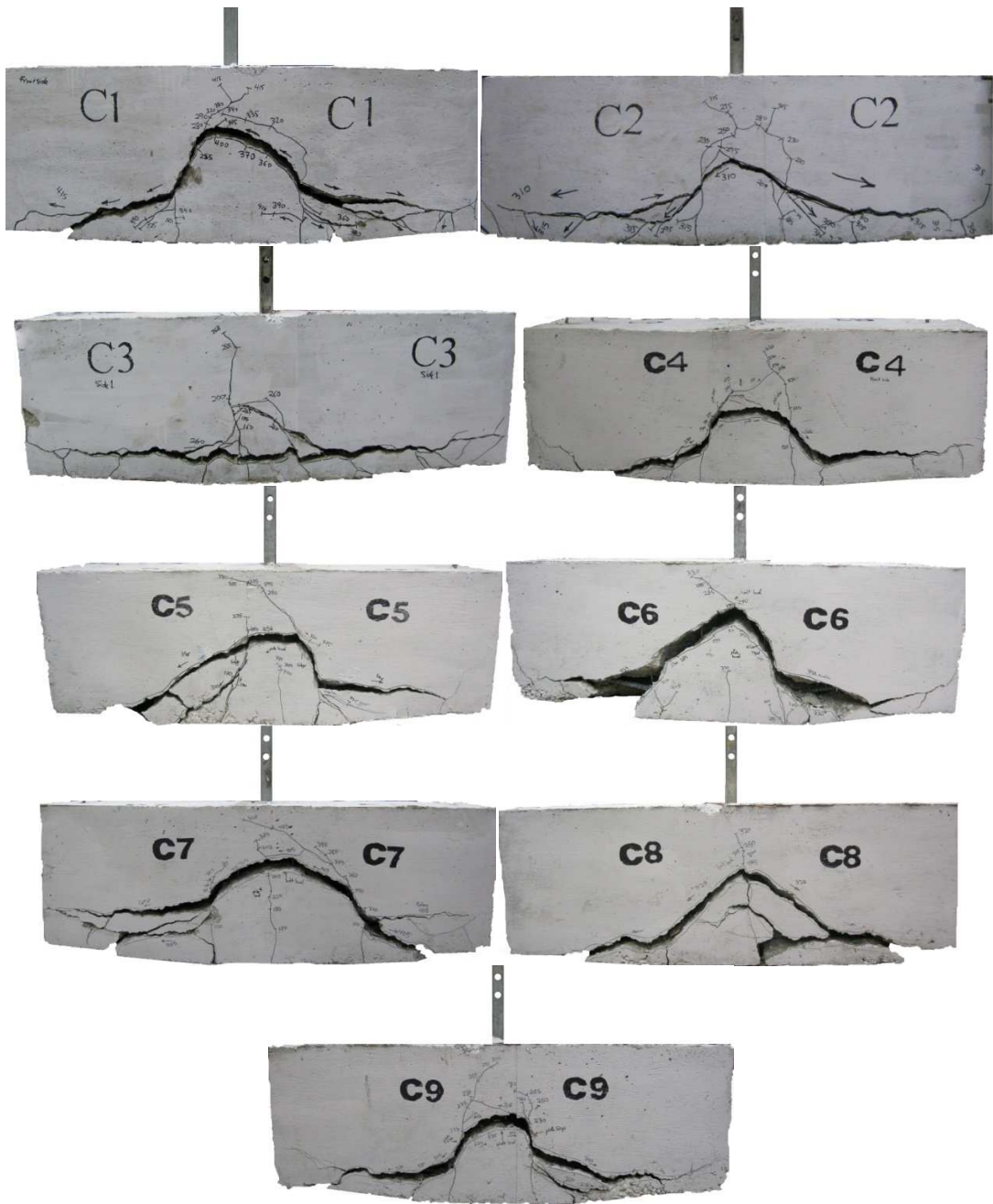
Figure 6- 5 Crack patterns of tested beams under monotonic compression loading
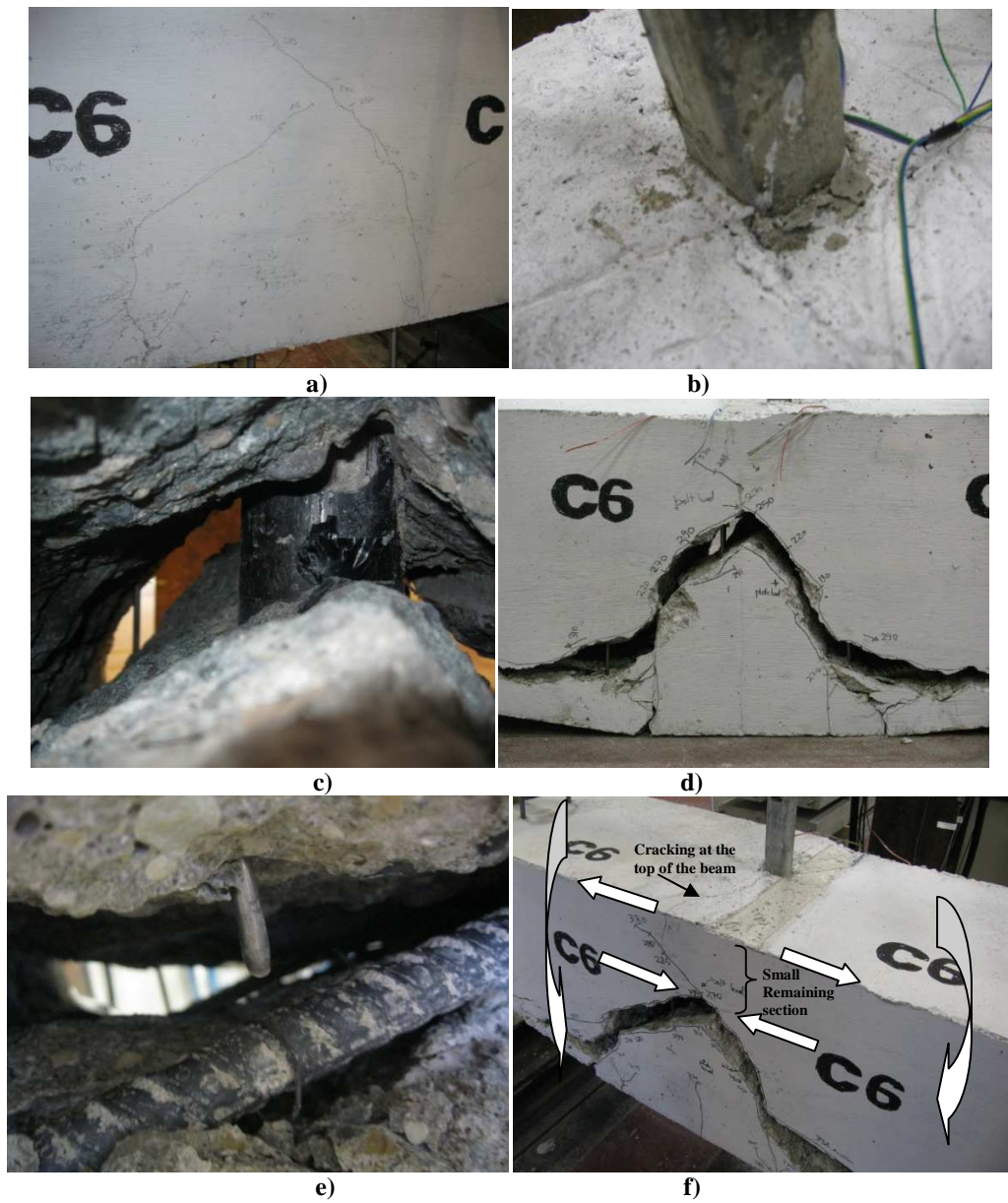
Figure 6- 6 a) flexural shear cracks initiation and propagation; b) Bond failure between the pile shaft and the surrounding concrete; c) Initiation of the breakout cracks under the bolt; d) Breakout cracking and the breakout cone formation; e) Stirrups failure by necking; f) Tension cracks initiation after the stirrups failure on the other side of the beam

6.8.2 General load transfer mechanism

The load transferred initially from the pile to concrete through their bond until slightly after the first flexural cracking, i.e., the beam still functioned as a full beam. The load then transferred by three different actions: the friction between the pile and the concrete; the bolt bearing on concrete; and pile cap's plate bearing on concrete. The friction between the pile and concrete was small due to the small pile width compared to the beam width. The load transferred through the bolt and the plate caused a breakout cone cracking from the bolt level. Cracks initiated mostly internally under the bolt then joined the flexural shear cracks to form the breakout cone. The aggregate interlock and the longitudinal reinforcement contributed the most to prevent the cone from moving, while the stirrups enclosed by the plate width contributed marginally at this stage.

When the load exceeded the capacity of aggregate interlock and longitudinal reinforcement dowel action, the cone moved slightly and the cracks widened causing the stirrups to transfer some load. The dowel action of the longitudinal reinforcement contribution dropped to approximately zero when the concrete cover spalled and longitudinal reinforcement bond failed at the cracks location, which consequently reduced aggregate interlock capacity. At this stage, the load mainly transferred through the vertical tensile capacity of the stirrups contained in the breakout cone. After the stirrups failure, the induced inverted moment in the rest of the beams causing internal tension on the pile-concrete interface eliminated the pile friction load and a total failure of the connection occurred.

The load transfer mechanism for a beam failing in single shear involves shear carried by the concrete in the compression zone, which was missing in the current case confirmed by Wang (1987) when testing indirectly loaded beams. Also, Smith & Fereig (1974) recorded a sudden reduction in the compression zone compression strain and a sudden tensile strain increase in the longitudinal reinforcement after the diagonal cracking initiation for indirectly loaded beams as a confirmation that the compression zone is not that effective in the indirectly loaded beams. Thus, the bolt depth, rather than the full beam depth, should be employed in calculating the connection breakout cracking and ultimate loads. Additionally, the stiffness of the beam just after bond cracks around the pile would be less than the stiffness of the same beam loaded from the top in compression because of the cracks inside the beam especially the breakout cracking from the bolt level. Thus, after breakout cracking, the connection compression capacity will be equal to the sum of aggregate interlock force (V_c), longitudinal reinforcement dowel action (V_d), and pile-concrete friction (V_f), as shown in Figure 6-7a, in addition to the stirrups contribution (V_s), as shown in Figure 6-7b, when stirrups are used. Furthermore, after the concrete cover spalling, the connection compression capacity is equal to stirrups tensile capacity (V_s) and pile friction (V_f).
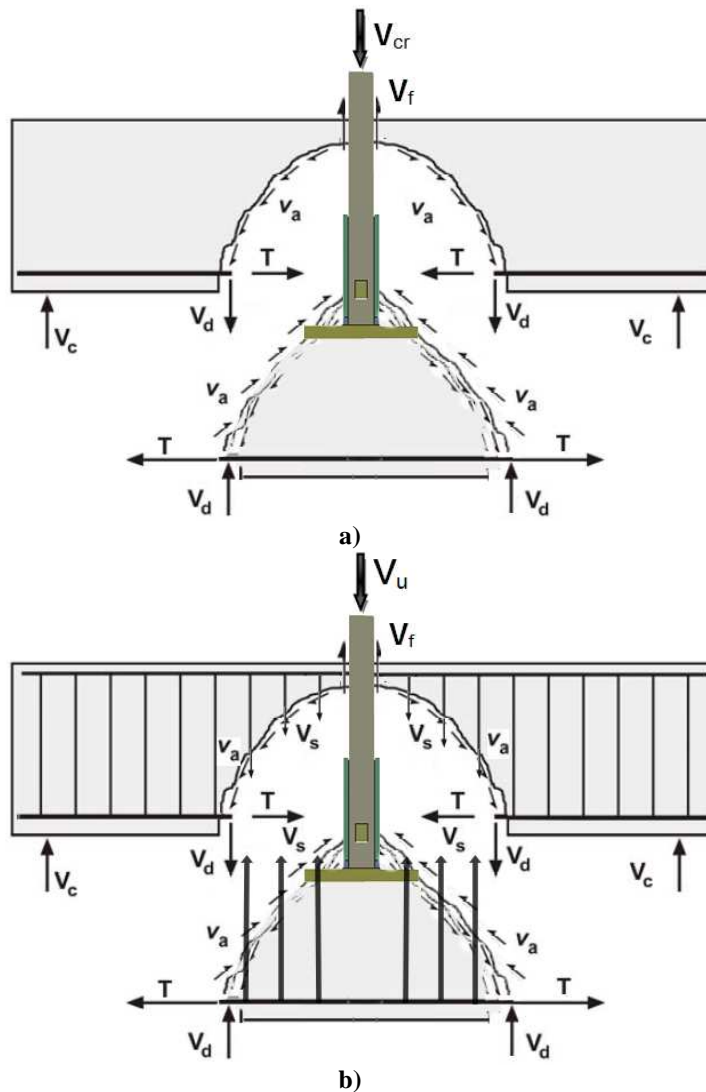
Figure 6- 7 Load transfer mechanism for the connection: a) without stirrups; and b) with stirrups)

6.8.3   General Ultimate Load and Load Displacement Relationship

The observed breakout cracking behaviour was similar to single shear cracking behaviour of a concrete beam because cracking propagated diagonally in one direction only. Most specimens experienced flexural shear cracking and, as a result, the breakout cracking load is expected to be slightly higher than the diagonal tension cracking capacity.

Upon reaching the breakout cracking load, the connection capacity comprised four components: pile-concrete friction; dowel action of longitudinal reinforcement; aggregate interlocking resistance; and stirrups resistance. The ultimate load would be greater than the breakout cracking load only when the sum of the four components is higher than the breakout cracking load.

The observed load-deformation responses of specimens can be generally described as follows. The beam's mid-span vertical displacement increased linearly with load until the first flexural crack occurred. The displacement then increased approximately linear with a higher rate up to the breakout cone formation. At this point, a small load increase caused excessive displacement. The connection stiffness decreased after the first flexural cracks, which extended to the bolt level and formed into flexural shear cracks from both sides. The stiffness decreased remarkably when the two flexural shear cracks joined together to form the breakout cone. At this stage, the displacement continued to increase at constant applied load. Some beams gained some stiffness again afterwards and higher ultimate load was achieved, while other beams softened and failure occurred.

The mid-span displacement at the other side of the beam was approximately the same as that at the lower level of the beam until breakout cracks formed. Afterwards, it decreased gradually and the beam (excluding the breakout cone) began to bounce back at a small rate. The difference between the displacements of both sides represented the breakout crack opening and the movement of the breakout cone. The vertical displacement of the pile shaft was slightly higher than that at the beam mid-span due to relative displacements

between the pile and bolt and between the bolt and the cylinder caused by the hole clearance, in addition to the deformation of the pile and the pile cap.

6.8.4   General Ductility:

Generally, ductility is indicated by the ductility factor indicated as the ratio of displacement at failure to that at yielding. As most codes recommend ductile, not brittle, design, the ductility of tested beams is compared to indicate the effects of different variables on the connection ductility. However, some specimens failed at the point of yielding (i.e. when steel strains are greater than 0.002 strain), and hence their ductility factor could not be calculated.   Therefore, there is a need to establish a criterion to compare the tested specimens regarding their ductility. One possibility is to use maximum mid-span deflection as a measure for ductility; however, it can only be used as an indicator of ductility if the compared specimens had approximately the same stiffness or they had similar ultimate loads at different displacements. Given that this was not the case for some specimens, it was decided to use the strain energy absorbed by the specimen up to failure for relative comparison of the ductility enhancement due to different specimen variables. Thus, the beam strain energy (toughness), defined as the area under the load-mid-span displacement curve up to 0.6 of the beam ultimate load after beam softening, was calculated to measure the beam absorbed energy and the results are presented in Table 6- 3.

In spite of the small mid-span displacement recorded at the ultimate load for most of the tested beams as shown in table 6-3, they failed at a higher mid-span displacement. This means the connection under displacement control loading (e.g. yielding of support,

seismic event, etc.) will exhibit more ductile response before failure with adequate warning. However, if the connection is subjected to load control loading (e.g. gravity loads on the foundation) the connection will fail in a brittle manner without warning. Although most tested beams had brittle failure, the presence of the reinforcement can enhance their ductility.

Table 6- 3 Test results of the four tested groups

Group	Specimen	First cracking load (kN)	Breakout cracking load(kN)	Ultimate load (kN)	mid-span Displacement at breakout (mm)	mid-span Displacement at ultimate (mm)	Strain Energy at 0.6 of Ultimate Load* (kN.mm)
First group	C1	165	400	415	2.6	3.4	11256
	C2	155	295	314	2.1	3.4	4952
	C3	150	250	268	2.9	3.8	2137
Second group	C2	155	295	314	2.1	3.4	4952
	C4	150	280	287	2.2	2.9	4836
	C5	140	289	348.5	1.9	3.5	6505
Third group	C2	155	295	314	2.1	3.4	4952
	C6	165	330	339	1.4	2.2	9144
	C7	170	400	409.3	1.2	1.3	11730
Forth group	C2	155	295	314	2.1	3.4	4952
	C8	156	320	340	1.4	2.2	8013
	C9	170	315	350.9	1.3	2.7	8282

* Strain energy measured at load equal to 0.6 of ultimate load, strain energy up to failure can be much higher.

6.8.5   General Reinforcement Steel Strain and Pile Cap's Plate Strain:

The longitudinal steel, transverse steel and pile cap's plate strains were recorded in order to aid in evaluating the internal behavior and cracking inside the specimens. The collected data indicated that the main longitudinal reinforcement strain increased linearly as the applied load increased until the first flexural cracking occurred. Subsequently, the

strain increased excessively as the steel carried all the internal tension at the cracks. As load increased until breakout cracking occurred, the steel strain increased at even higher rate. At breakout cracking, the strain increased suddenly without load increase. This is attributed to the dowel action of the longitudinal reinforcement and the additional normal force induced by the horizontal pressure from the aggregates at both sides of the breakout cracks due to aggregate interlock. At this point, the longitudinal steel strain continued to increase and the load continued to transfer across the shear cracks to the rest of the beam if the stirrups and the concrete cover provided enough support to the longitudinal bars for its dowel action. When the concrete cover failed, excessive vertical displacement took place at the breakout cone leading to large crack width, which caused aggregate interlock loss and excessive longitudinal steel strains and stirrups strain increased excessively because most of the load was transferred to the stirrups. Consequently, the longitudinal steel strain reduced even if the breakout cone displacement increased.

It was observed in all tested beams that the interior longitudinal reinforcing bars experienced higher strains than the exterior bars. Also, the stirrups' strain was negligible until breakout cracking initiated, then stirrups' strain increased suddenly and continued to increase up to stirrups yielding and necking was observed, just before their failure. Stirrups close to the pile shaft experienced higher strains than farther ones. The same behaviour of the stirrups was recorded by Talbot (1909) when they tested Reinforced concrete beams failing in shear.

Finally, the pile cap's plate strain indicated the amount of plate bending at the strain gauge location (i.e. approximately quarter the plate width). When the breakout cone initiated, the plate experienced small strain compared to the case of the breakout crack crossing the plate. On the other hand, when the crack crossed the plate, it experienced excessive strain due to crack bridging (i.e. part of the load was transferred through the plate). At initial loading, the plate deformed slightly. After the crack reached the bolt and plate levels, the plate strain decreased slightly. As the breakout cone moved, the plate strain increased apparently due to the load transferred from the stirrups through the crack to the concrete at the edge of the plate.

6.9 Discussion of the first phase groups (Monotonic Compression loading)

6.9.1   First Group: Effect of pile embedment depth

Three different embedment depths were examined: 152mm, 203mm and 254mm for beams C1, C2, and C3, respectively. The steel plate width was kept constant as 165 mm, and the stirrups diameter was 6.35 mm spaced at 200 mm. The longitudinal reinforcement was comprised of four bars of 15M high strength deformed steel for beams C2 and C3, while beam C1 had four bars of 20M to prevent the potential of flexural failure as this beam was expected to carry higher load.

6.9.1.1   Crack pattern and mode of failure

Beams C1, C2, and C3 had approximately the same crack pattern, but the size of the breakout cone increased as the embedment depth decreased. Beam C3 exhibited more bond cracks and splitting cracks (Figure 6- 8) than other beams because it had the highest embedment depth. The breakout cone size at longitudinal reinforcement level was

249

approximately 710mm, 625mm, and 420mm for beams C1, C2 and C3, respectively, i.e. it increased as the embedment depth decreased. The failure was brittle for all three beams and the embedment depth did not affect the failure mechanism.

Figure 6- 8 Observed splitting cracks in beam C3

6.9.1.2   Cracking load, Breakout cracking load, and Ultimate load

The results in table 6-3 show that the first cracking load was not affected by the variation in embedment depth but it was affected by amount of longitudinal reinforcement. The breakout cracking load and the ultimate load increased as the embedment depth decreased. The breakout cracking loads for beams C1, C2, and C3 were 400 kN, 295 kN, and 250 kN, respectively. The ultimate loads were 415 kN, 314 kN and 268 kN, respectively. An increase in the connection capacity of 17% and 55% was recorded when the remaining depth increased from 227mm to 277mm and to 330 mm, respectively. These ultimate load capacity values, however, are much less than the calculated ultimate load of the beam in flexure or shear (650 kN, and 448 kN). This indicates the importance of evaluating the connection capacity rather than the beam capacity. After the breakout

cracking, the three beams continued to resist load. This is attributed to dowel action and the longitudinal reinforcement normal force, which increased the aggregate interlock capacity, and the stirrups resistance. The pile friction existed before and after the breakout cracking load, but its value was small compared to the breakout cracking load or the connection ultimate load.

6.9.1.3 Stiffness and load displacement relationship

Figure 6-9 displays the load-mid span displacement curve for the three test beams. It shows that the stiffness of the three beams was approximately the same before cracks initiated. After the first flexural crack initiated and extended to the bolt level, the connection stiffness decreased because the flexural cracks formed flexural shear cracks from both sides. The stiffness decreased remarkably when the two flexural shear cracks joined together to form the breakout cone. At this stage, load displacement curve was approximately horizontal and the load increased slightly as the displacement increased until the connection ultimate load was reached. The connection stiffness was small after the breakout load was reached because of the light stirrups used. Also, Figure 6-9 demonstrates the effect of the embedment depth on the connection stiffness before the breakout cracking, which underscores the importance of the embedment depth on the connection behaviour. As the embedment depth decreased the connection stiffness after the first cracking load increased. After the ultimate load was reached, the connection capacity of beam C3 decreased suddenly due to longitudinal reinforcement bond failure and the load transferred to the stirrups with zero dowel action capacity and zero aggregate interlock capacity. On the other hand, Beams C1 and C2 experienced some contributions

251

from the longitudinal reinforcement and the aggregate interlock till the crack width increased and the connection capacity decreased.
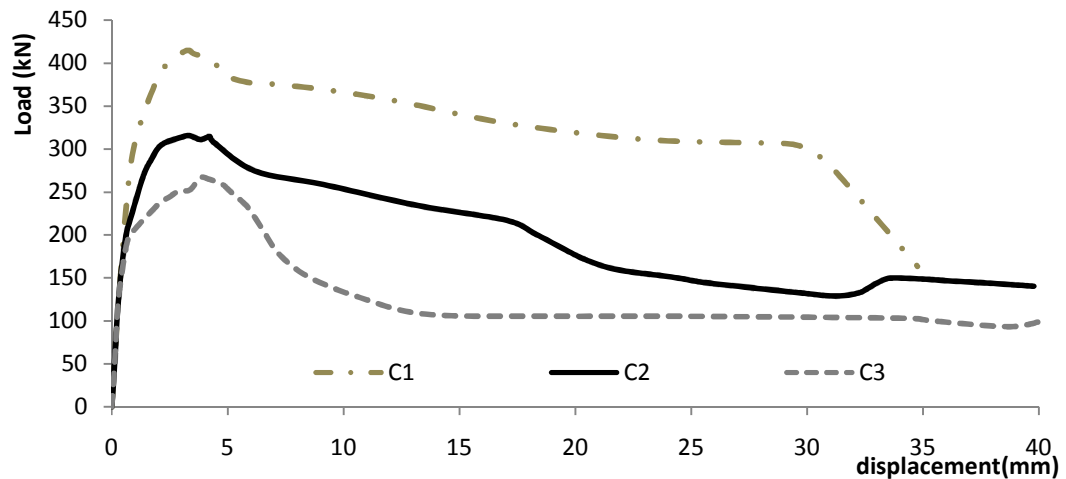
Figure 6- 9 Load mid-span displacement

6.9.1.4   Ductility and strain energy

Table 6- 3 shows that the ultimate load occurred at approximately the same mid-span displacement for all three beams (i.e. 3.4 mm, 3.4 mm and 3.8 mm for C1, C2 and C3). Also, most of the beams' longitudinal reinforcement did not yield before the ultimate load, suggesting that the three beams reached the ultimate load in a brittle manner. However, the embedment depth affected the connection ability to absorb energy before failure, i.e. the beam absorbed more energy as the embedment depth decreased. As shown in Table 6- 3, the strain energy were 2137, 4952 and 11256 kN.mm for C3, C2, and C1, respectively, which represented an increase of the strain energy by up to 427% as the embedment depth decreased (beam C1 compared to C3).

252

The ratio between the displacement at the ultimate load and the displacement at the breakout cracking load can be considered as an indication of warning before failure. This ratio was 1.307, 1.62, and 1.31 for beams C1, C2 and C3, which implies that even if the beams exhibited brittle behaviour at ultimate load, they gave warning signs.

6.9.1.5   Reinforcement Steel and Pile Cap's Plate Strain

Figure 6-10 shows that the longitudinal steel strains in C1, C2 and C3 were approximately the same until first cracking occurred. The strain increased sharply afterwards for both the outer and inner longitudinal reinforcement. The effect of embedment depth was to increase the longitudinal reinforcement strain, which is attributed to the reduction in the connection stiffness with the decrease in the remaining depth. The three beams reached ultimate capacity as the longitudinal reinforcement yielded due to the reduction in the shear friction capacity at the flexural shear cracks or the breakout cone. The same behaviour was observed by Collins and Mitchell (1996), Collins & Mitchell (1991),Vechio and Collins (1988), and Bentz et al. (2006).

a)

b)
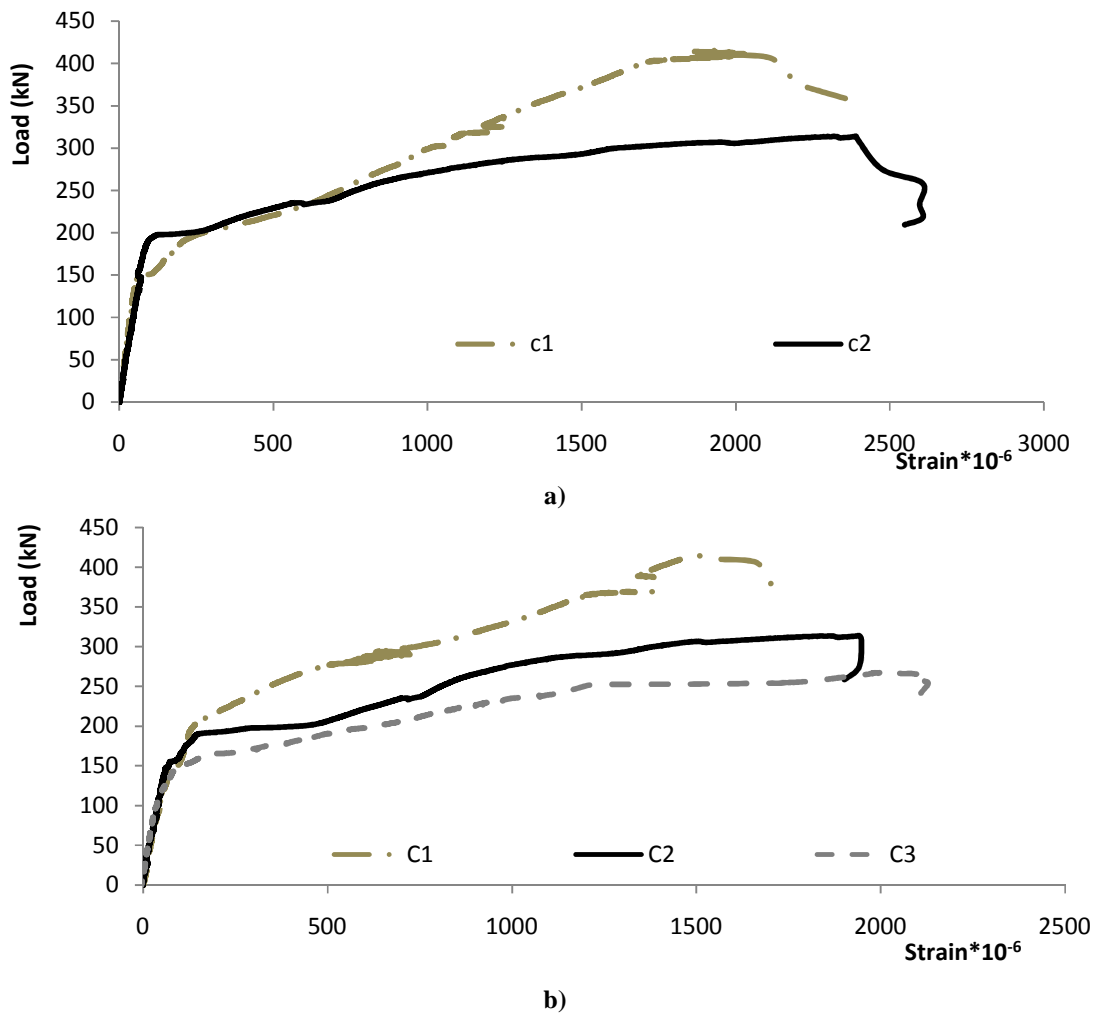
Figure 6- 10 Load-longitudinal steel strain: a) outer bars; and b) inner bars

Figure 6-11 displays the variation of stirrups strain with the applied loading. The figure shows that stirrups experienced a negligible strain before breakout cracking, and strain increased sharply afterwards indicating crack opening at stirrups locations and breakout cones movements. It is also noted that stirrups yielded only after ultimate load, which confirms that the connection ultimate load was resisted by the contributions of

254

longitudinal reinforcement dowel action, aggregate interlock and pile-concrete friction in addition to the stirrups vertical tensile strength.

The recorded pile cap's plate's strain was less than 100×10^{-6} mm/mm during the entire loading process, i.e., its flexural deformation was minimal. This observation is consistent with the observed crack pattern, as breakout cracking did not cross the pile cap's plate.
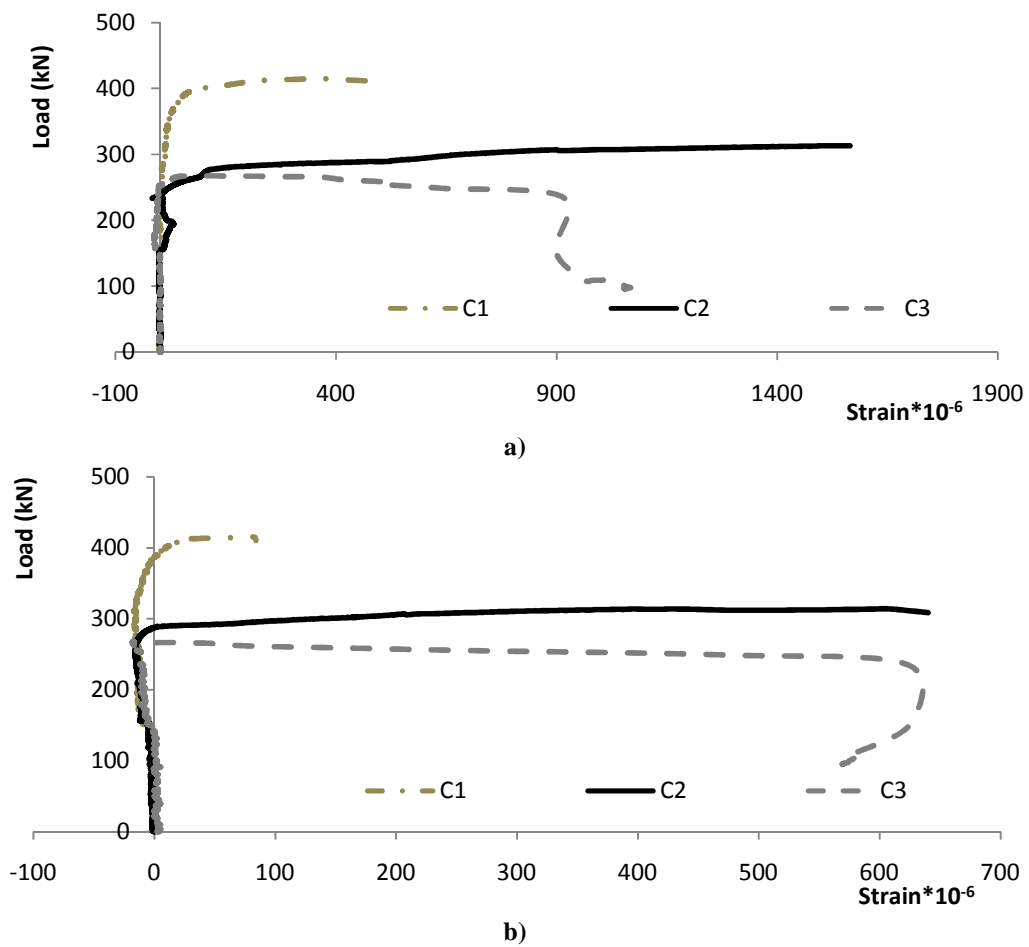
Figure 6- 11 Load-stirrups strain: a) outer stirrups; b) inner stirrups

6.9.2 Second Group: Effect of Pile Cap's Plate Width

Three different plate sizes, covering the range of pile cap configurations used in practice, were tested. They were as follows: 165 x165 x 19 mm (C2); 191 x191 x 19 mm (C4); and 229 x 229 x 25.4 mm (C5). The embedment depth, longitudinal reinforcement, concrete compressive strength, and stirrups were kept constant as shown in table 6-1.

6.9.2.1 Crack pattern and mode of failure

Both beams C2 and C4 experienced the general crack pattern described previously. Beam C5 experienced similar breakout cracking, but it was formed by the intersection between the wide pile cap's plate and the flexural shear cracks. This intersection had no affect on the breakout cracking load, but it contributed to the connection ultimate load as the plate bridged load across the crack. The ACI 318-11 Appendix D neglects the width of headed anchors if it is larger than the anchor head thickness. However, it was observed that the dimensions of the breakout cones at the longitudinal reinforcement level increased as the plat width increase, i.e., the plate width can add to the connection ultimate load. Finally, the three beams experienced brittle failure at the connection ultimate load, and the pile cap dimensions did not change the failure mechanism.

6.9.2.2 Cracking load, Breakout cracking load, and Ultimate load

The results presented in table 6-3 show that the three beams had approximately the same first cracking and breakout cracking loads. Furthermore, the ultimate loads were close to the breakout loads for beams C2 and C4 (106%, and 103% of their breakout loads). The ultimate load of C5, however, was 121% of its breakout load, which is attributed to the

crack bridging by the pile cap's plate. Beam C4 ultimate load was 92% of that of beam C2. This may be attributed to a variety of reasons including wider plate or yielding of plate at specific location. However, there is no clear evidence that the ultimate load increased as the plate width increased. Thus, the plate width should not be incorporated in the connection capacity equation, except it influences on decreasing the shear span distance.

6.9.2.3 Stiffness and load displacement relationship

Figure 6-12 displays the load-displacement behaviour of the test specimens. As noted from figure 6-12, the initial connection stiffness was almost identical for all beams until first cracking initiated. The stiffness decreased after cracking, but remained approximately the same for all three beams. After the ultimate load was reached, the three beams behaved similarly with approximately the same displacement for the same load capacity. This indicates that the same number of stirrups was involved in the three beams and the number of stirrups did not increase as the plate width increased.
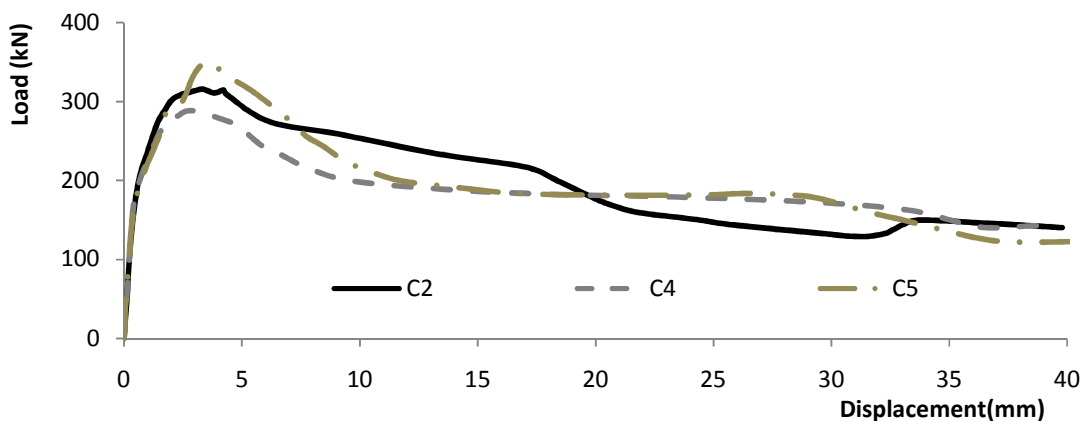
Figure 6- 12 Load mid-span displacement

6.9.2.4   Ductility and strain energy

The strain energies of beams C2, C4, and C5 were 4952, 4836, and 6505 kN.m, respectively, as shown in Table 6-3. These results indicate a slight increase in strain energy in beam C5, and hence the connection ductility, as the plate width increases to 192 mm. Furthermore, the ratio between the displacements at ultimate and breakout loads was equal to 1.62, 1.32, and 1.84 for beams C2, C4, and C5. This means the plate width had no direct effect on the warning margin before failure.

6.9.2.5   Reinforcement Steel, and pile cap's plate Strain

Figure 6-13 shows that the longitudinal steel strain for the test beams. Inner and outer longitudinal reinforcing bars had approximately the same strain up to breakout cracking, after which the strain increased suddenly and loss of bond occurred. In general, there was no observed connection between plate width and strain of longitudinal reinforcement. It is also noted from Figure 6-13 that reinforcing bars of C5 experienced higher strain than that of C2 and C4 because it experienced earlier flexural cracking, and reinforcing bars of C2 and C4 experienced approximately the same strain. Also, the outer steel bars reached yielding in beams C2 and C5 before ultimate load, and after ultimate load for beam C4. The inner longitudinal steel in C4, however, did not yield at all.
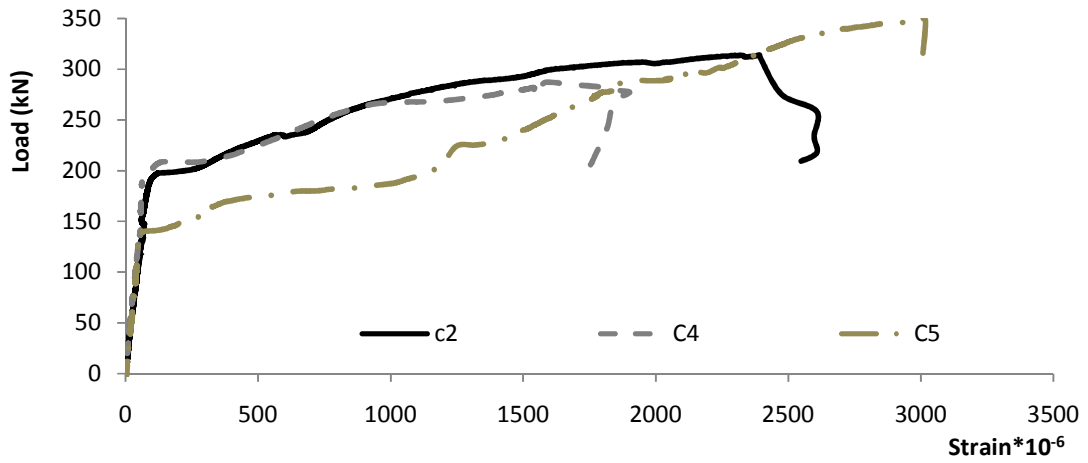
a)
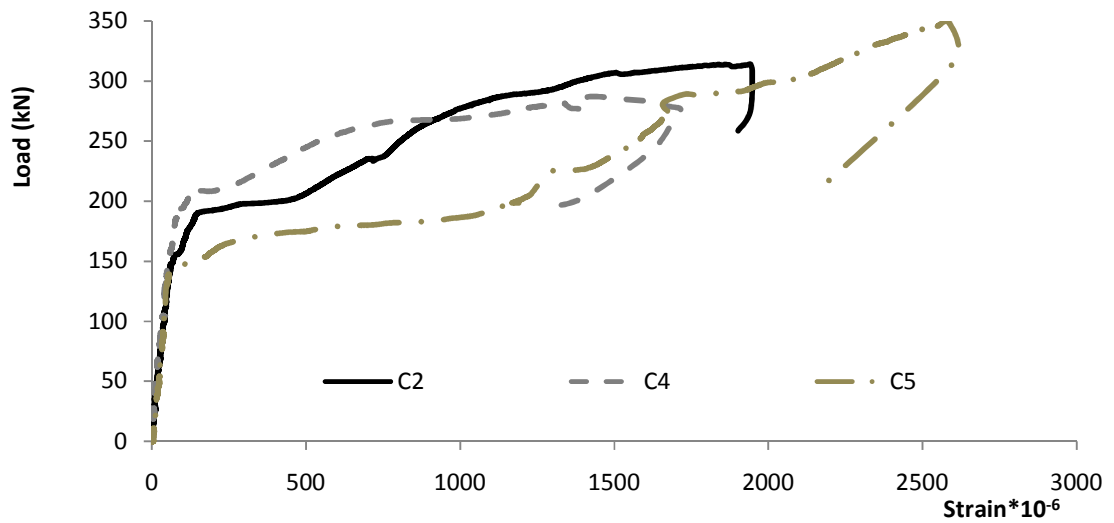
b)

Figure 6- 13 load-longitudinal reinforcement strain: a) outer bars; and b) inner bars

Figure 6-14 displays the variation of stirrups strain with the applied load. It shows that the strain was negligible before breakout cracking and increased sharply just after breakout crack initiated, especially in the inner stirrups. The contribution of the inner stirrups to the connection ultimate load was higher than that of the outer stirrups because they were closer to the pile shaft. However, none of the inner stirrups reached yielding

before ultimate load, and hence the yield strength of the stirrups should not be used to calculate their contribution to the connection ultimate load. Rather, the strain compatibility should be used to calculate both the concrete strength (i.e. the aggregate interlock) and the stirrups contributions. On the other hand, stirrups yielded after the ultimate load after excessive breakout cone movement and concrete cover spalling under the longitudinal reinforcement. For the stirrups spacing considered herein, the pile cap' plate width did not affect the stirrups contribution to the connection ultimate load; however, if smaller stirrups spacing is used, this may not be the case.
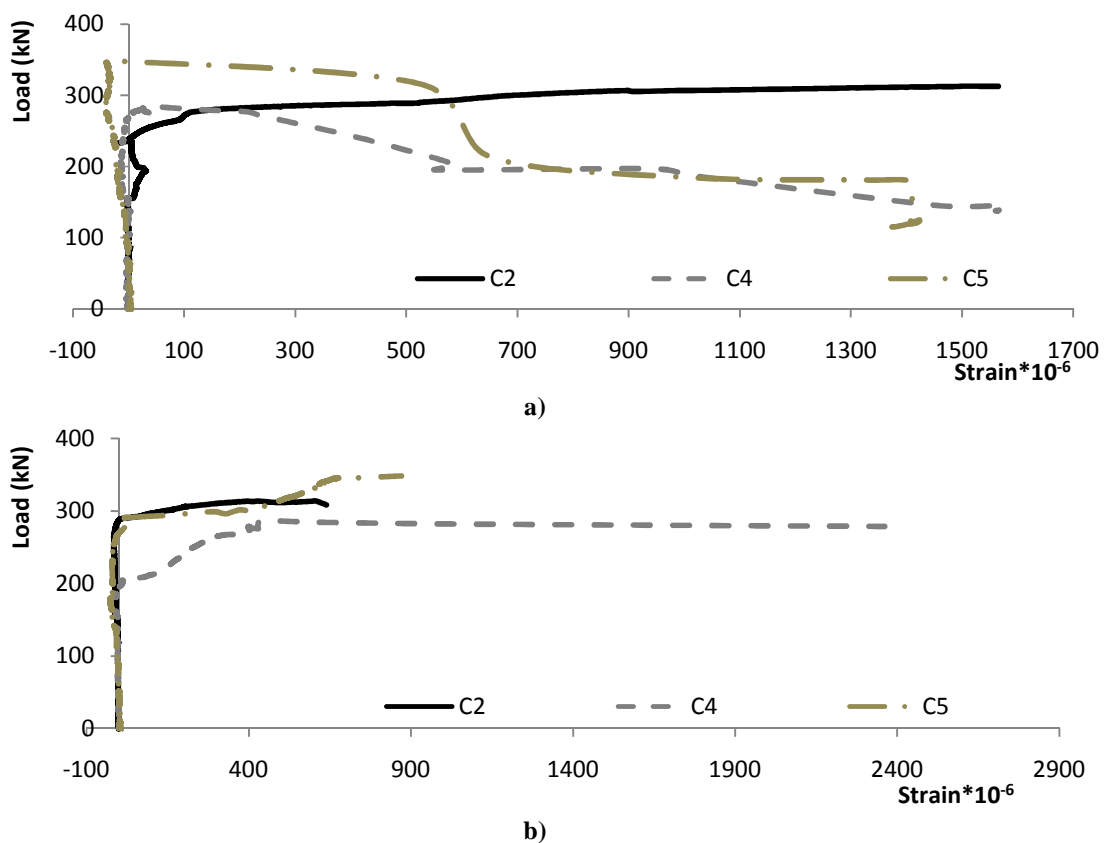
Figure 6- 14 Load-stirrups strain: a) outer stirrups; and b) inner stirrups

The strains in the pile cap's plate near the pile shaft in beams C2 and C4 were really small, indicating minimal flexure. On the other hand, for beam C5 the strain in the plate farther from the pile shaft was much higher than that next to the pile shaft (610×10^{-6} vs. 110×10^{-6}). Figure 6-15 presents the two locations of the strain gauges attached to the beam C5 pile cap's plate. This large difference in strain is attributed to the crack crossing the plate at this location. Finally, this large strain vanished at the ultimate load because the concrete under the tip of the plate failed.
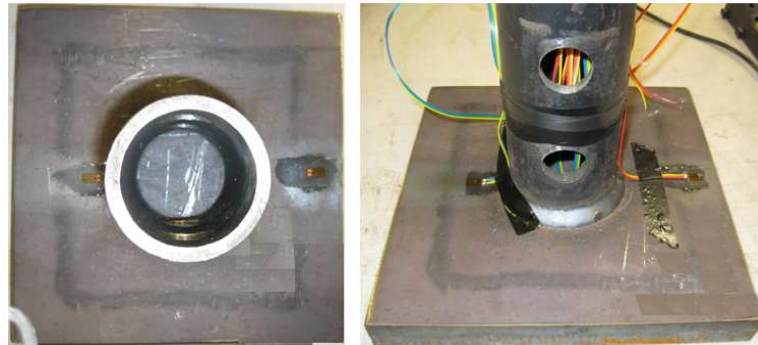
Figure 6- 15 Locations of the strain gages on the pile cap's plate of beam C5

6.9.3 Third Group: Effect of Longitudinal Reinforcement

In this group, three different longitudinal reinforcement ratios were tested, i.e. 0.35% (4-15M in C2), 0.53% (4-20M in C6), and 0.89% (4-25M in C7). The remaining depth, plate width, the concrete compressive strength, and the stirrups configuration were kept constant.

6.9.3.1 Crack pattern and mode of failure

The tested beams had approximately the same crack pattern; however the size of breakout cone increased as the longitudinal reinforcement ratio increased. The larger breakout cone moved the dowel action position closer to the beam supports, increasing the flexural and shear capacity of the rebars and hence contributed to the dowel action capacity. Bond failure occurred around the longitudinal reinforcement in beam C2 after the breakout cone formed because there was no sufficient support from the concrete cover. On the other hand, sufficient support existed for the dowel action in beams C6 and C7 because the larger breakout cone approached the dowel action position close to the supports. Also, after the connection ultimate load was reached the compression force transferred to the supports decreased causing sudden bond failure in beams C6 and C7.

6.9.3.2 Cracking load, Breakout cracking load, and Ultimate load

The results presented in table 6-3 demonstrate that the first cracking load increased as the longitudinal reinforcement ratio increased (i.e. 155, 165 and 170 kN for C2, C6, and C7, respectively). Almost the same values were calculated for a directly loaded beam supported on its extreme fiber, which implies the beams behaved as full beams until the first flexural cracking load. It should be mentioned that beams C1 and C6 had the same first flexural cracking load confirming that the embedment depth did not influence their first flexural cracking load. Table 6-3 also shows that the breakout load increased as reinforcement ratio increased. Also, the ultimate load increased as the longitudinal reinforcement ratio increased.

6.9.3.3 Stiffness and load displacement relationship

Figure 6-16 presents the load mid-span displacement curve for the test beams. The results show that the beams stiffness increased before first cracking as the longitudinal reinforcement ratio increased. It is clear that the connection stiffness increased with increasing the beam's longitudinal reinforcement ratio after the first flexural cracks initiation. After reaching ultimate load, similar softening behaviour was observed for the three beams. At this stage, differences in the resisted loads for same displacements are attributed to the dowel action capacity in longitudinal reinforcement.
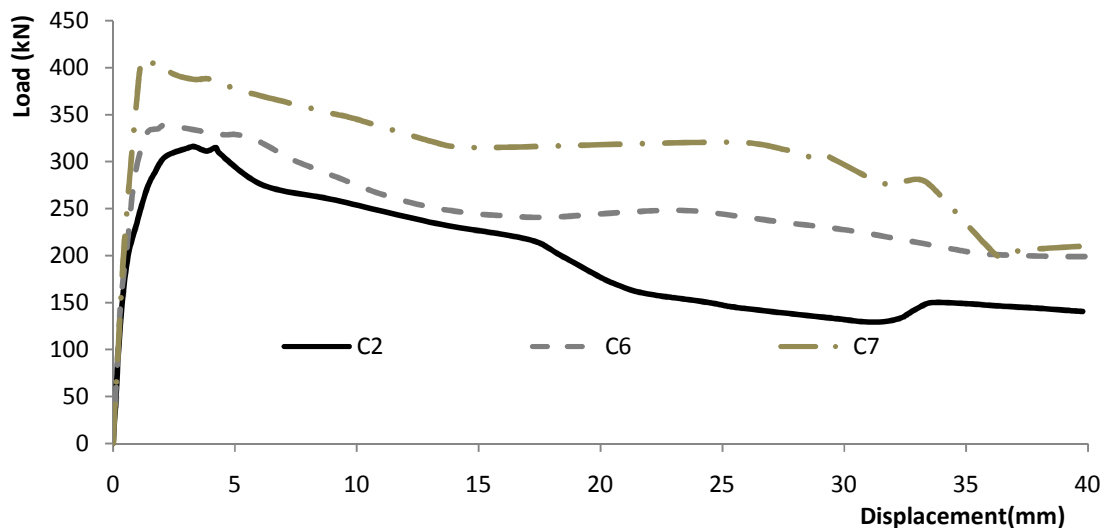
Figure 6- 16 Load mid-span displacement relationship

6.9.3.4 Ductility and strain energy

The mid-span displacement for beams C2, C6, and C7 were 2.1, 1.4 and 1.2 mm at the breakout cracking load and 3.4, 2.2 and 1.3 mm at ultimate load as shown in table 6-3. These results indicate that increasing the longitudinal reinforcement ratio reduced the

displacement corresponding to the breakout cracking and ultimate loads. On the other hand, the beams failed at such large mid-span displacement associated with substantial breakout cone movement.

The longitudinal reinforcement of beams C6 and C7 did not yield before reaching the connection ultimate load, i.e., the failure was brittle; however, the longitudinal reinforcement increased the connection ability to absorb energy before failing. The calculated strain energy for beams C2, C6, and C7 were 4952 kN.mm, 9144 kN.mm, and 11730 kN.mm, respectively, i.e., the absorbed energy increased by up to 137% as the reinforcement ratio increased.

6.9.3.5 Reinforcement Steel, and pile cap's plate Strain

Figure 6-17 shows the variation of longitudinal steel strain with the applied load. AS expected, beams with higher reinforcement ratio experienced smaller strain. It is also noted that the strain increased significantly after first cracking. After breakout cracking, the strain increased excessively accompanied by either concrete cover spalling and/or stirrups necking. The high strains are attributed to the dowel action contribution. At the ultimate load, outer longitudinal reinforcement reached yielding in beam C2 but not in beams C6 and C7. None of the inner longitudinal bars experienced yielding before ultimate load.
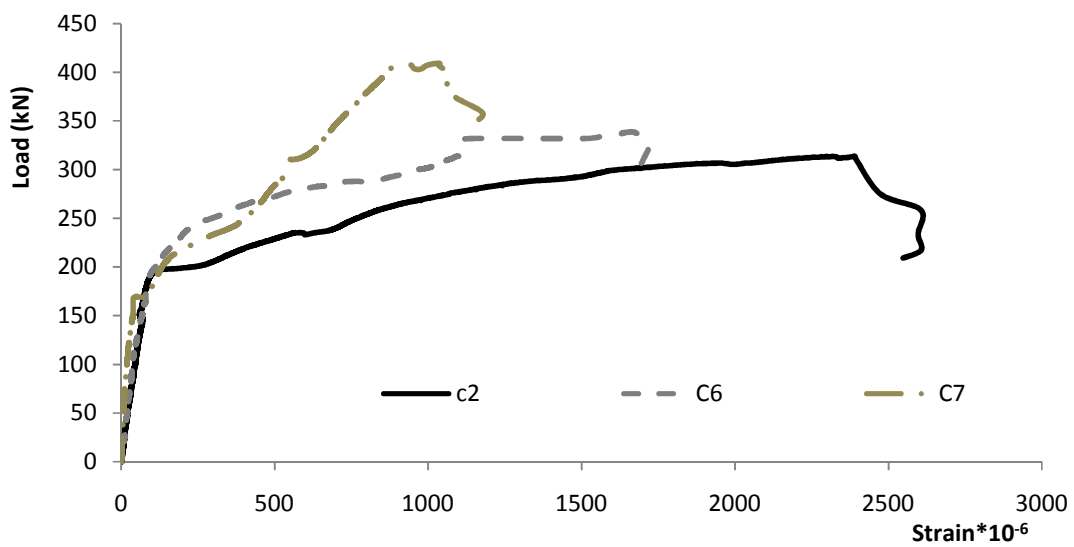
a)
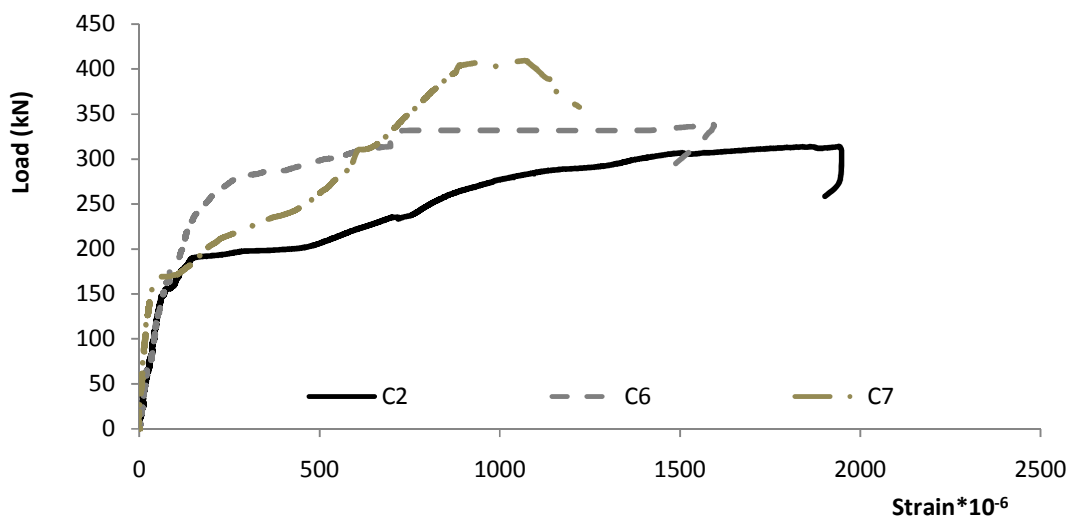
b)

Figure 6- 17 load-longitudinal reinforcement strain: a) outer reinforcement; b) inner reinforcement

Figure 6-18 shows the stirrups strains of the three test beams. The figure shows that the stirrups experienced large tensile strains only after breakout cracking occurred; however, they did not yield before ultimate loads. It should be mentioned that it is expected that increasing the transverse reinforcement ratio can increase the connection capacity not

265

only because of the stirrups contribution to the capacity but also because it enhances the

contribution of the longitudinal reinforcement to the overall beam stiffness.
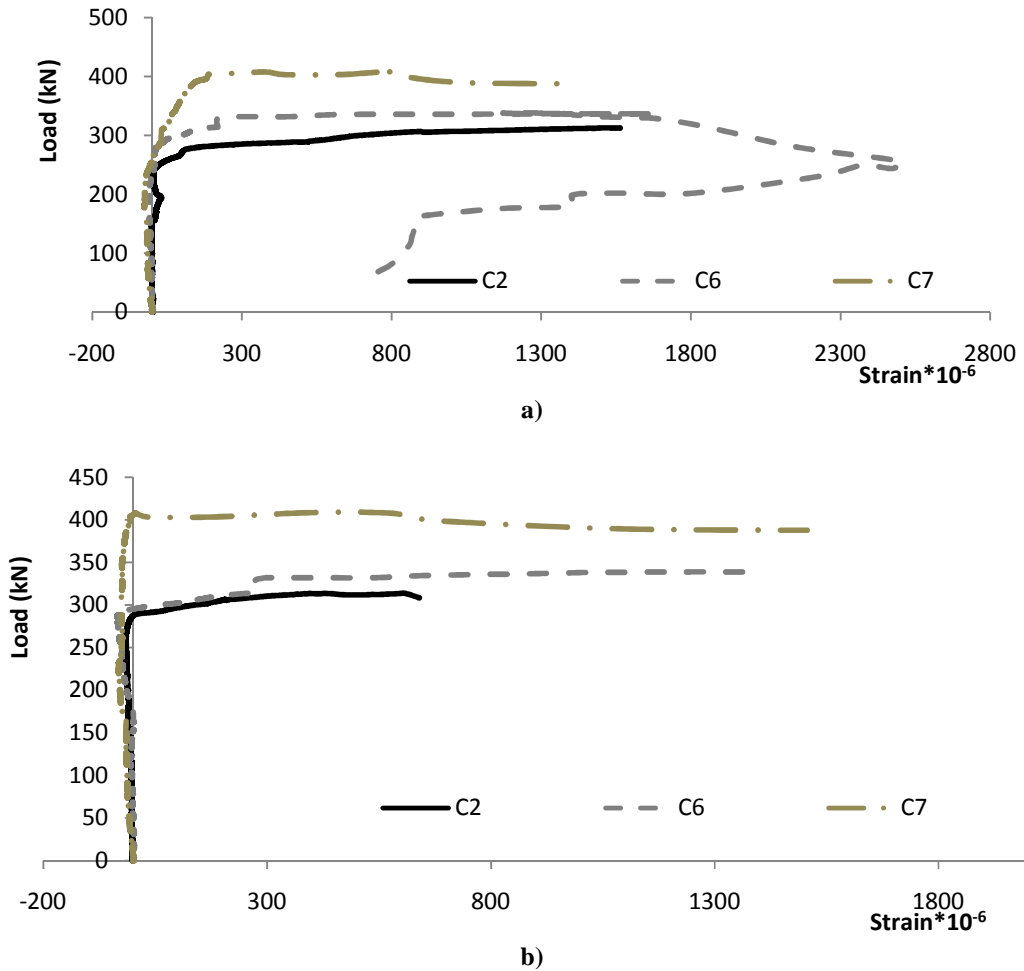
Figure 6- 18 Load stirrups strain: a) outer stirrups; b) inner stirrups

Figure 6-19 displays the variation of pile cap plate strain with load. It can be noted that

the plate experienced strain only after flexural cracks reached the plate level. Only beam

C6 experienced large strain (1800×10^{-6} mm/mm) at the breakout load, then decreased to

970×10^{-6} mm/mm at ultimate load. This increase in strain was because the crack intersected with the plate at one side near the strain gauge location.
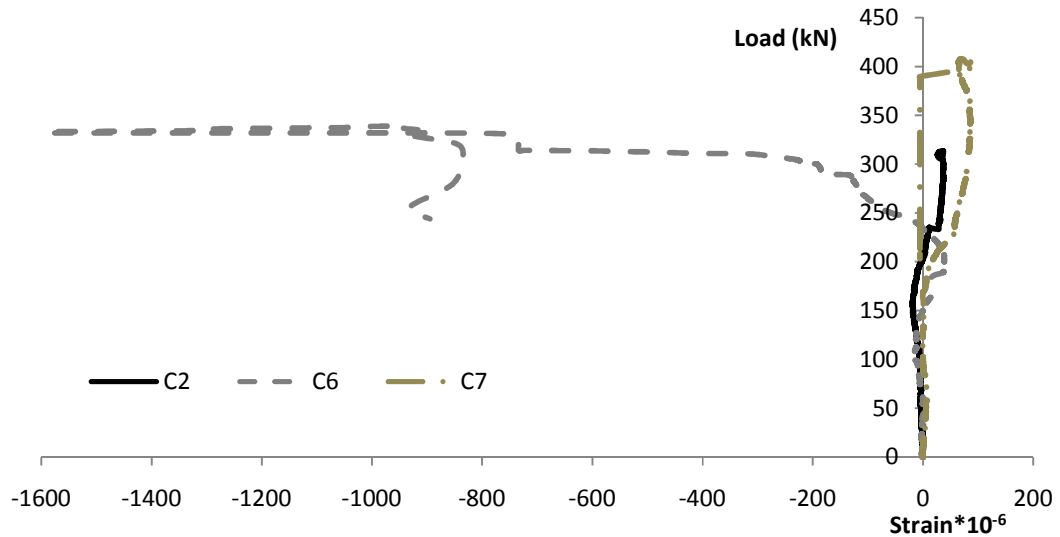
Figure 6- 19 Load pile cap's strain relationship

6.9.4 Forth Group: Effect of transverse reinforcement

Three beams with different stirrups configurations were tested. All beams were reinforced with #2 rebar (6.35 mm diameter) but different configurations. Beam C2 had two branches spaced at 200 mm (0.064% reinforcement ratio); Beam C8 had four branches spaced at 200 mm and Beam C9 had two branches spaced at 100 mm (i.e. 0.127% reinforcement ratio for both). The embedment depth, width of pile cap's plate, concrete compressive strength, and longitudinal reinforcement ratio were kept constant.

6.9.4.1 Crack pattern and mode of failure

The failure mechanism was brittle in beam C2 but ductile failures with large displacements before reaching failure were observed in beams C8 and C9. Wide cracks

267

and concrete cover spalling under the longitudinal reinforcement before ultimate load in beams C8 and C9 indicate that the concrete aggregate interlock and longitudinal reinforcement dowel action were negligible at their ultimate load. In beam C8, only one flexural crack extended vertically at the middle of the beam and no flexural shear cracks were observed. At breakout cracking, diagonal cracks formed at 40° angle at the bolt level. The concrete cover spalling indicated that longitudinal reinforcement dowel action took place. In beam C9, the crack pattern was similar but the breakout cracks initiated at the bolt level, which suggests taking the bolt depth into account when calculating the connection capacity. In addition, the breakout cracks crossed the pile cap's plate at some locations in beams C8 and C9. The size of the breakout cone was not affected by the transverse reinforcement ratio.

6.9.4.2   Cracking load, Breakout cracking load, and Ultimate load

The first cracking, breakout cracking and ultimate loads for beams C2, C8 and C9 are listed in table 6-3. These results demonstrate that stirrups did not affect the first cracking load but increased the breakout cracking and ultimate loads. Furthermore, after the concrete ultimate load was reached, ductile behaviour was observed as the stirrups sustained most of the applied load when the breakout crack width increased eliminating the aggregate interlock and dowel action contributions. In Beam C9, after the crack widened, the connection capacity was found to be equal to the vertical tensile capacity of the stirrups contained within the breakout cone, which was approximately equal to the full ultimate strength of 3 stirrups from each side (i.e. overall of 6 stirrups; 12 branches within the breakout cone). On the other hand, C8 had one stirrup from each side with 4

268

branches (i.e. overall of 2 stirrups; 8 branches within the breakout cone) contributed to connection capacity. It should be noted that the contribution of the outer stirrups to the connection capacity was small. Therefore, the connection design capacity should be taken as the lesser of the concrete ultimate capacity or the vertical tensile yielding capacity of the transverse reinforcement contained within the breakout cone (i.e. similar to equation suggested by ACI318-11 Appendix D to determine anchor capacity considering anchor reinforcement).

6.9.4.3 Load displacement relationship

Figure 6-20 shows the load-mid-span displacement curve for beams C2, C8, and C9. Beams C8 and C9 exhibited approximately the same response up to the breakout load and both had higher stiffness higher than that of beam C2. The breakout and ultimate mid-span deflections were 2.1, 1.4 and 1.3 mm, and 3.4, 2.2 and 2.7 mm for beams C2, C8, and C9, respectively. Comparing the behaviour of the beams past the ultimate load, it may be suggested that the stirrups contribution to the connection resistance after the ultimate load was higher for beam C9 than beams C2, and C8.
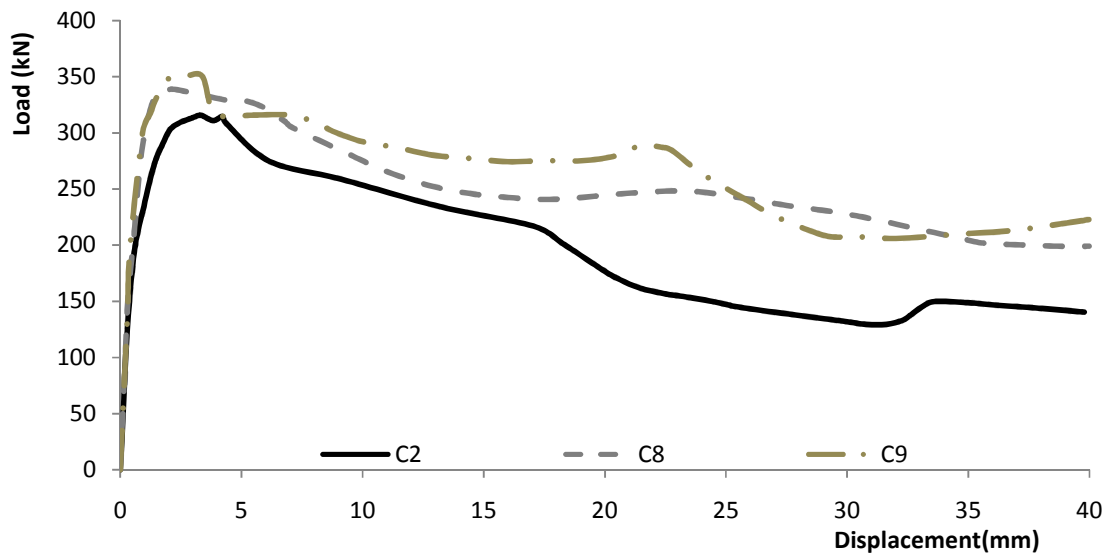
Figure 6- 20 Load mid-span displacement relationship

6.9.4.4 Ductility and strain energy

The small difference between the mid-span displacements at breakout and ultimate loads suggest that the effect of transverse reinforcement on the beam ductility was marginal; however, these results demonstrate that increasing the transverse reinforcement ratio increased the beam strain energy (i.e. the beam ability to absorb energy before failure). Also, all longitudinal reinforcement yielded before reaching the connection ultimate load in beams C8 and C9, which indicates enhanced beam ductility. This underscores the importance of placing adequate amount of stirrups at the position of the breakout cone.

6.9.4.5 Reinforcement Steel, and pile cap's plate Strain

Figure 6-21 presents the longitudinal steel strain for the three beams. The recorded strains indicate that all outer longitudinal reinforcement yielded (i.e. strains greater than 0.002 steel strain) and inner longitudinal reinforcement of beams C8, and C9.

270
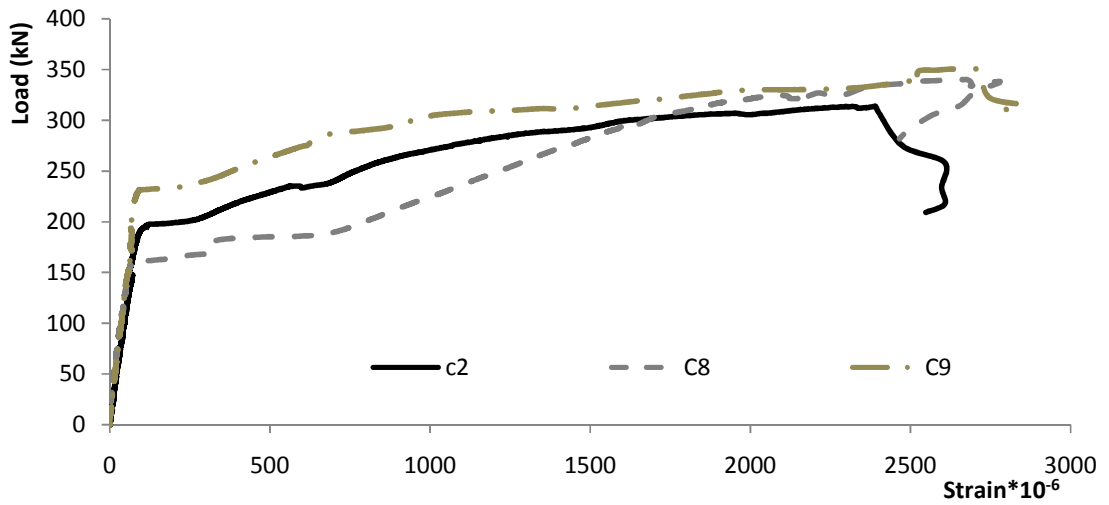
a)
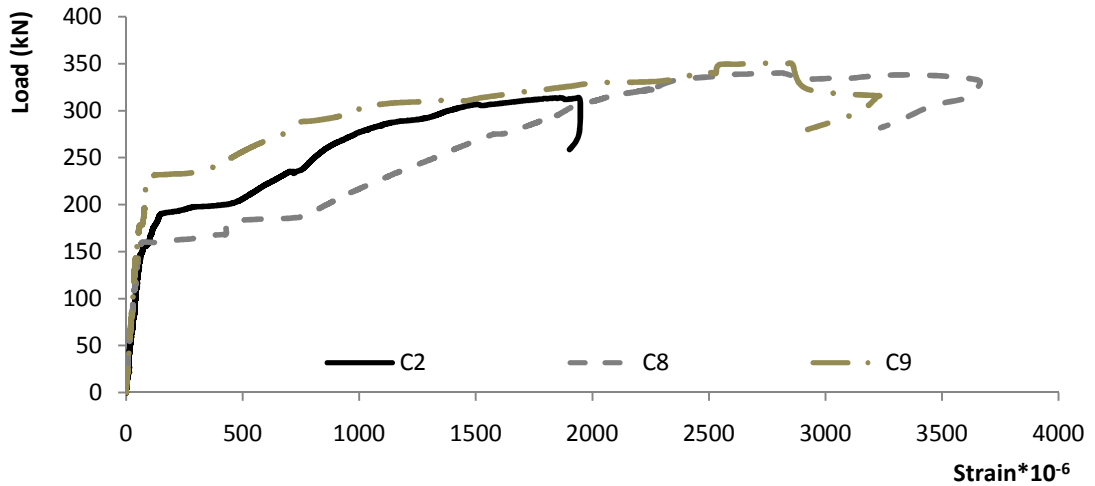
b)

Figure 6-21 load-longitudinal reinforcement strain: a) outer reinforcement; b) inner reinforcement

Figure 6-22 shows the strain in transverse reinforcement. Two strain gauges were attached to the inner and outer branches of the outer stirrups of beam C8. Both gauges recorded very small compression strain before breakout cracking. Afterwards, the compression strain decreased and even tensile strain was recorded. Two more strain gauges were attached to the inner stirrups of beam C8, which recorded strains of 460×10^{-6}

and 2150×10^{-6} mm/mm in the inner and outer branches at ultimate load. The inner stirrups experienced large tensile strains after the breakout cracking load, while the outer stirrups' contribution to the ultimate load was minimal. However, significant strain increase was observed after the ultimate load, which indicated enhanced beam ductility. In beam C9, there were three strain gauges attached to the stirrups located at 50mm, 150mm, and 250mm from the pile shaft. The strains recorded for these stirrups increased dramatically after flexural cracks propagated just before the breakout cracking load and continued to be large at the ultimate load, indicating the stirrups important contributions to both the breakout and ultimate loads.

It may be concluded that placing higher transverse reinforcement close to the pile shaft would increase the connection capacity substantially after breakout cracking, and can involve both aggregate interlock and longitudinal reinforcement dowel action when tight breakout cracks occur. In addition, the contribution of vertical tensile capacity of stirrups within the breakout cone to the connection capacity should be based on their yield capacity. Finally, only the contribution of aggregate interlock, dowel action, and stirrups close to the pile shaft (e.g. within the plate width) should be considered in calculating the connection capacity.

Both beams C8 and C9 exhibited large strains in the pile cap's plate, indicating its contribution to the connection capacity. The plate strain increased when flexural cracks reached the plate level, and it increased noticeably at the breakout load. Furthermore, the plate in beam C9 yielded before the ultimate load.
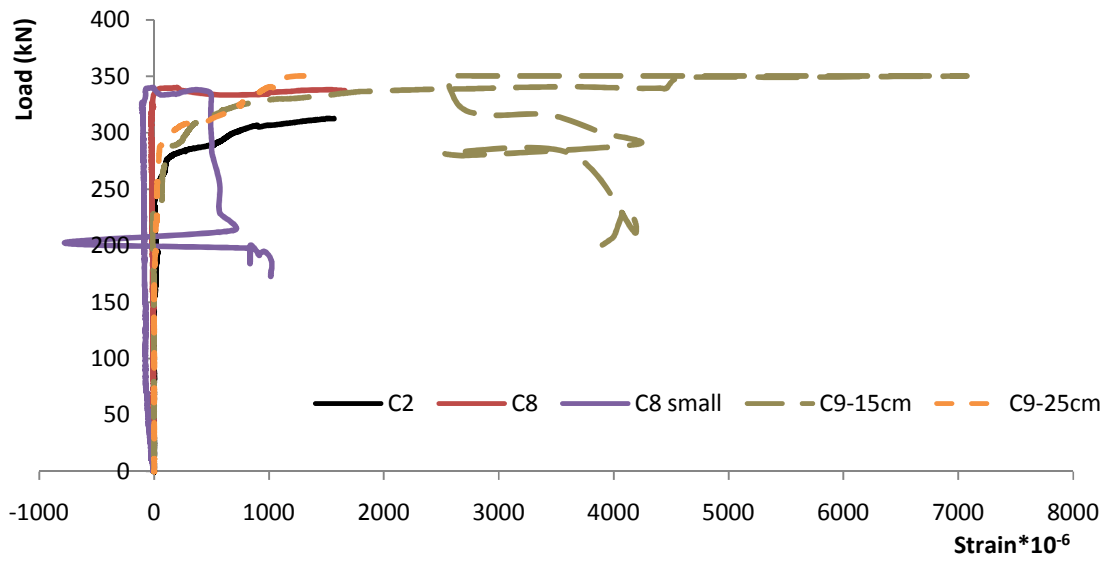
a)
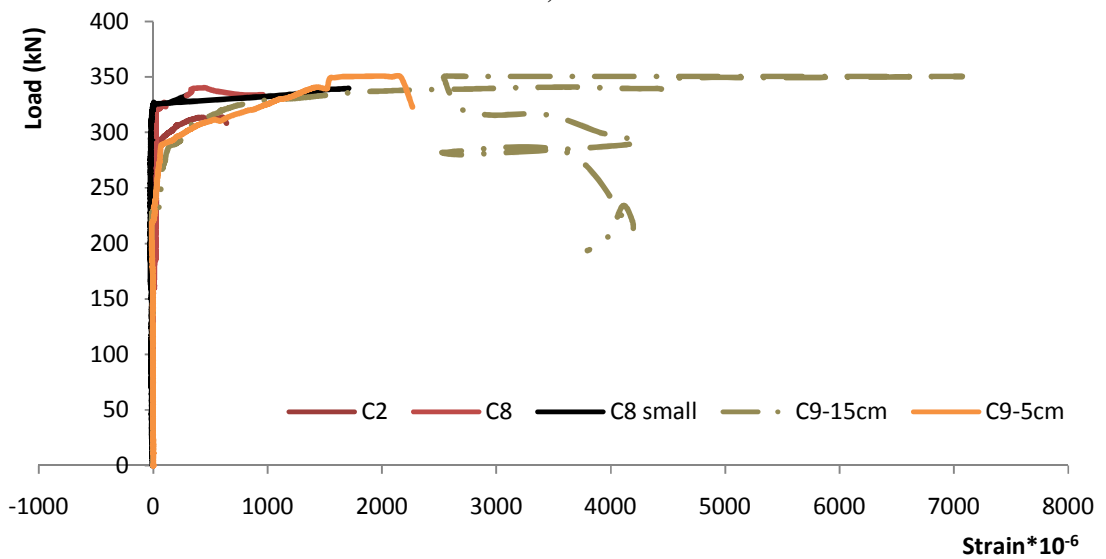
b)

Figure 6- 22 Load- stirrups strain: a) outer stirrups; b) inner stirrups

6.10 General findings of second phase: (Cyclic Compression Loading)

6.10.1 Derived Behaviour of Beams C1, C2, and C9 Considering 2-Bolts

The experimental observations demonstrated that the behaviour of 2-bolts connection is different than the one-bolt connection. Therefore, for the purpose of comparison between

273

the beams tested in monotonic loading (i.e. C1, C2, and C9) and having only one bolt with those tested in cyclic loading and having two bolts (i.e. CC1, CC2, and CC3), it was necessary to predict the performance of beams C1, C2, and C9 considering the effects of the second bolt.

As will be shown in Chapter 7, a detailed finite element model was built to simulate the behaviour of the connection under monotonic compression loading and was calibrated using the experimental results of the monotonic loading. The numerical model is shown to predict the connection behaviour accurately up to the connection ultimate load, and predicted the softening behaviour fairly reasonably. Figure 6-23 presents an example of the calculated load-displacement curve for beam C2 from the calibrated finite element analysis compared with the experimental results. This finite element model was then used to predict the performance of beams C1, C2, and C9 considering two-bolts connections. The derived load displacement relationship of these beams from the FEA along with that of the original beams and that of the corresponding beam subjected to cyclic loading are presented in Figure 6-25. The summary of the results is included in Table 6-4.
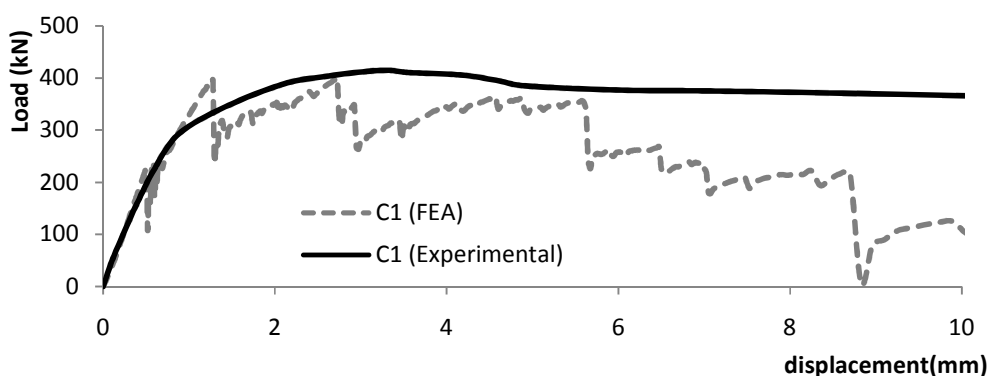
Figure 6- 23 Calculated and measured load-displacement curve for beam C1

6.10.2 General Crack Patterns, Failure Modes and General Load Transfer Mechanism

In the monotonic loading test specimens, one bolt was used to connect the pile cap to the pile shaft, while two bolts were used in the connection for specimens subjected to cyclic loading. This had some effects on the specimens' behaviour during the cyclic loading. In general, the crack pattern, shown in Figure 6-24, was similar to that observed for specimens subjected to monotonic loading, but the breakout cracking propagated below the top bolt. It was also observed that the crack initiated and propagated after a few cycles of the same load level, which clearly indicates that connection capacity degraded due to cyclic loading. It was also observed that the connection stiffness degraded as the number of load cycles increased, leading to stress concentrations at the cracks ends and causing extended crack propagation at the same load and as a result displacement increased at the same load level as the number of cycles increased.

The load transfer mechanism was similar to that observed during monotonic loading. However, the breakout cone was limited by the top bolt level and the aggregate interlock and shear friction behaviour extended up to this level. In addition, the pile shaft length subjected to friction decreased, but the additional resistance due to the second bolt was much higher than the reduction in the pile-concrete friction resistance resulting in net increase in the connection capacity.
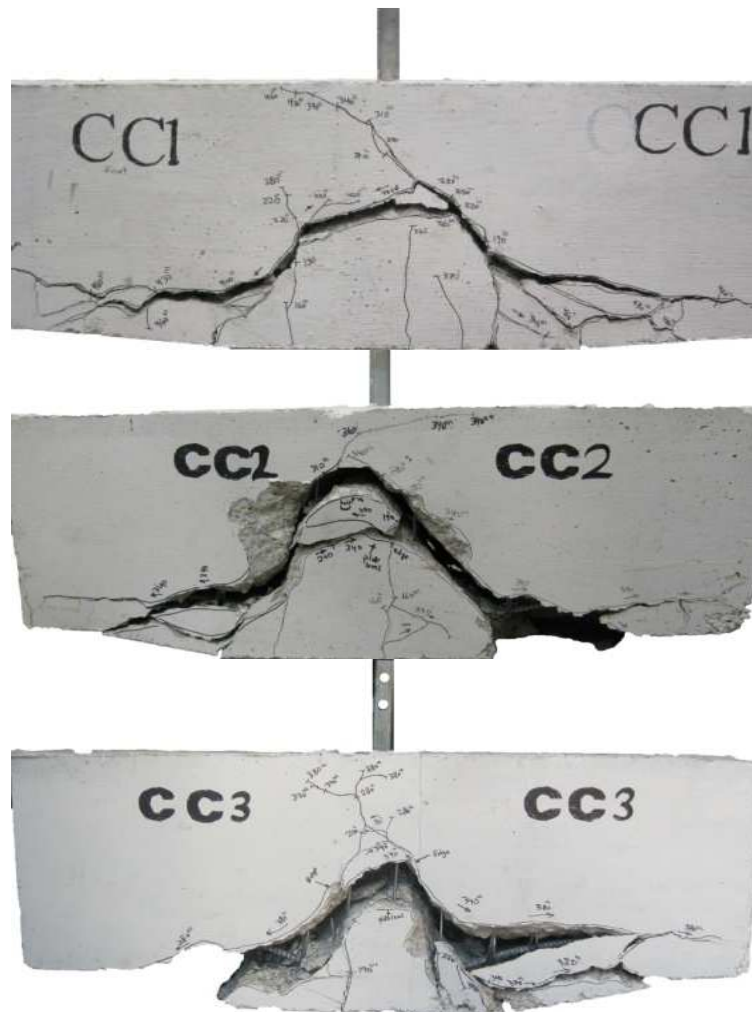
Figure 6- 24 Crack patterns of tested beams under cyclic compression loading

6.10.3 General Ultimate Load and Load Displacement Response

Figure 6-25 compares the load-displacement curves for the specimens subjected to monotonic and cyclic loading. The connection behaviour and its load-displacement responses were characterized by initiation of first cracking, breakout cracking and the connection failure. The cyclic loading affected the breakout cracking and ultimate loads, and hence affected the corresponding displacements due to deterioration in the concrete

mechanical properties under repeated cyclic loading within the inelastic range. The cyclic degradation of the concrete mechanical properties after cracking was reported by various researches (e.g. Erberik, 2010; and Shahnewaz, 2013).
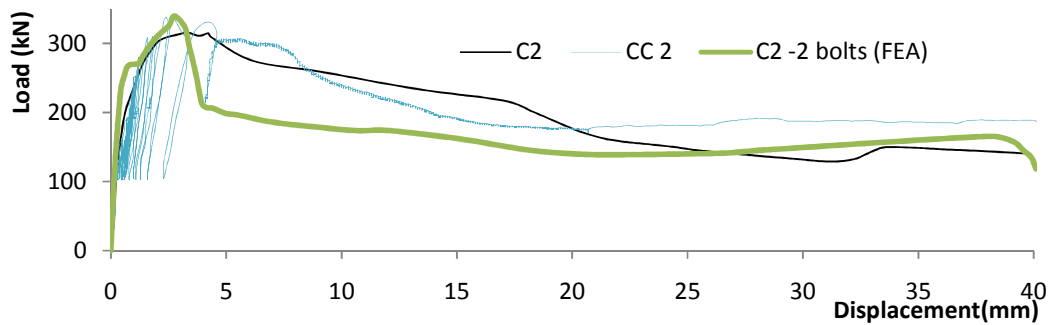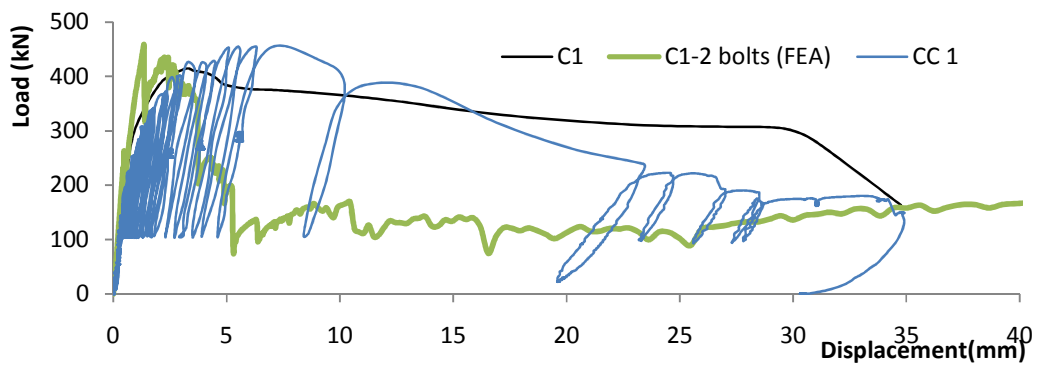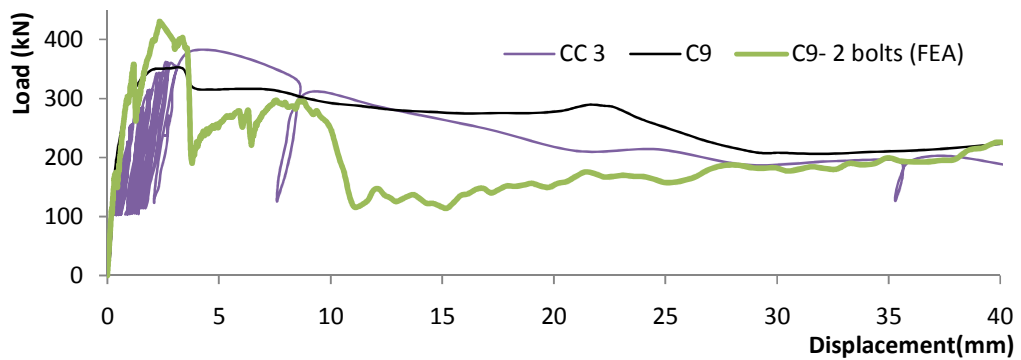
Figure 6- 25 Load mid-span displacement relationship: a) CC2; b) CC1; and c) CC3

Figure 6-25 shows that stiffness degradation occurred before reaching the ultimate connection capacity in all beams, especially CC1 because it had the largest breakout cone and the highest concrete resistance contribution. This affects both breakout cracking and ultimate loads of the connection because reduced stiffness leads to higher concrete tensile strains and lower shear capacity. Thus, load capacity reduction would be influenced by stiffness degradation and amplitude and number of load cycles. For example, before crack initiation the specimen exhibited linear elastic behaviour for both loading and unloading cycles, which means cyclic load has no effect on the beam behaviour at this loading level. On the other hand, after cracks initiated the connection behaviour was affected by cyclic loading and the effect was more pronounced as the load amplitude increased. As the applied load approached the connection ultimate capacity, all specimens experienced strength degradation and high residual deformations were recorded. This strength degradation is reflected in the fact that beams CC1 and CC2 failed after 4 cycles of loading and beam CC3 failed at the second cycle of loading.

6.10.4 Beam Ductility, Strain Energy and Energy Dissipation Capacity:

All specimens experienced brittle failure at their ultimate load, but they sustained increased displacement with decreasing load. The strain energy stored in the specimen is an indication of its ability to absorb energy before failure. Furthermore, the dissipated energy of a reinforced concrete member during cyclic loading is a favorable characteristic for structures subjected to earthquake, wind and impact loads. The energy dissipation capacity was calculated as the area of each hysteresis loop and the cumulative energy dissipated in each beam was calculated and used for evaluating the performance of

278

different beams. Calculated strain energy and cumulative energy dissipation for different

beams are presented in table 6-4.

Table 6- 4 Test results of the four tested groups

Group	Specimen	First cracking load(kN)	Breakout cracking load(kN)	Ultimate load (kN)	mid-span Displacement at breakout (mm)	mid-span Displacement at ultimate (mm)	Strain Energy at 0.6 of the Ultimate Load (kN.mm) *	Cumulative Dissipated Energy*** (kN.mm)
First comparison	C2 (one bolt)	155	295	314	2.1	3.4	4952	
	C2 FEA (two bolts)	160	325	339	2.5	2.71	**	
	CC2 (two bolts)	160	315	338	2.1	4.6	5000	127
Second comparison	C1 (one bolt)	165	400	415	2.6	3.4	11256	
	C1 FEA (two bolts)	165	458.8	458.8	1.3	1.3	**	
	CC1 (two bolts)	160	400	457	1.6	7.8	10516	240
Third comparison	C9 (one bolt)	170	315	350.9	1.3	2.7	8282	
	C9 FEA (two bolts)	174.4	353	430	1.16	2.35	**	
	CC3 (two bolts)	170	336.4	382.5	2.3	4.7	9512	364
Fourth comparison	CC2	160	315	338	2.1	4.6	5000	127
	CC1	160	430	457	3.3	7.8	10516	240
Fifth comparison	CC2	160	315	338	2.1	4.6	5000	127
	CC3	170	336.4	382.5	2.3	4.7	9512	364

* Strain energy at load equal to 0.6 of ultimate load, full strain energy up to failure can be much higher.

** Finite element analysis did not capture softening behaviour accurately. Thus, the calculated strain energy for
   FEA is not considered in the comparison.

***Cumulative dissipated energy is the sum of areas of hysteresis loops up to recorded ultimate load.

6.10.5 Reinforcement Steel Strain and Pile Cap's Plate Strain

Before first cracking initiated, the same strains were recorded during loading and unloading indicating linear elastic behaviour. After cracking initiated, the longitudinal reinforcement and pilecap's plate strains increased with the number of load cycles at the same applied load, and this was more pronounced as the amplitude of cyclic load increased. The stirrups did not experience residual strains due to cyclic loading up to the breakout cracking load. Afterwards, the strain increased with the number of load cycles and strains accumulation in each cycle increased as the load amplitude increased.

6.11 Discussion of the second phase groups (Cyclic Compression Loading)

6.11.1 Comparison of Connection Behaviour Under Monotonic and Cyclic Compression Loading

6.11.1.1 Beam C2 Vs beam CC2:

Beams CC2 was identical to C2, but had two bolts to connect the pile cap to the pile shaft. In order to facilitate proper comparison of response under monotonic and cyclic loading, the predicted response of beam C2-2bolts from FEA is used in the comparison.

From Table 6-4 and the load displacement curves shown in Figure 6-25a, it is noted that both C2-2bolts and CC2 had the same first cracking load, i.e., it was not affected by cyclic loading. The breakout cracking load decreased slightly (only 3%) and the ultimate load was almost the same (within 1%). Very small stiffness degradation was observed only after first cracking initiated and up to the connection ultimate capacity. Also, very small residual displacements existed due to load cycles at the same load level. It was also observed that the connection strength degraded due to load cycles when the load

approached the connection ultimate capacity. The connection reached its ultimate capacity in the 4th cycle at the same load level. Table 6-4 and Figure 6-25a show that for beam CC2 the mid-span displacement at ultimate load was much higher than that of beams C2 and C2-2bolts.

Figure 6-26 displays the variation of longitudinal and transverse reinforcement strains with the applied load for beam CC2. It can be noted from Figure 6-26a that CC2 experienced higher longitudinal reinforcement strains than C2. The concrete strength decreased slightly causing some strain increase of the longitudinal reinforcement in beam CC2. There were significant residual strains in the longitudinal steel for the load cycles just after flexural cracks initiated and at the ultimate load, but there was very small residual strain otherwise.

As shown in Figure 6-26b, the stirrups experienced very small strain initially, confirming that stirrups did not resist load before the breakout cracking in both monotonic and cyclic loading. After breakout cracking occurred, residual strains were recorded in the stirrups during cyclic loading indicating that stiffness of beam CC2 degraded due cyclic loading. The connection capacity, however, was not affected because the minimal reduction in concrete capacity due to cyclic loading was compensated by small increases in the longitudinal and stirrups strains as shown in Figure 6-26.

As shown in Table 6-4, both beams experienced brittle behaviour up to their ultimate loads. On the other hand, beam CC2 dissipated higher energy due to cyclic loading up to

its ultimate load that was 15% of the total energy absorbed by the specimen up to its

ultimate load.
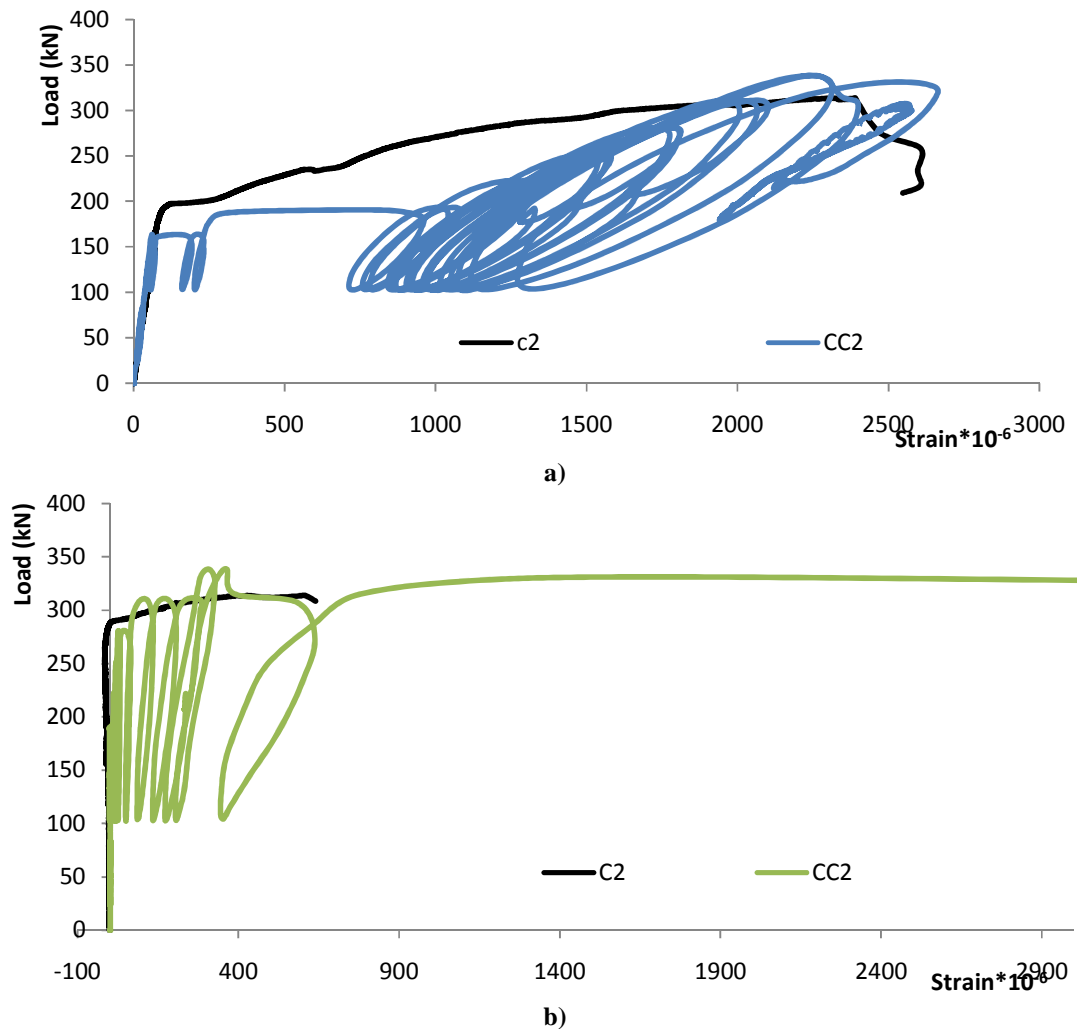
Figure 6-26 Load- reinforcement strains: a) longitudinal reinforcement; b) stirrups

6.11.1.2 Beam C1 Vs CC1

Both beams were identical, but beam CC1 had 2 bolts to connect the pile cap to its shaft. Thus, the calculated response of beam C1-2bolts obtained from FEA was used in the comparison.

Both beams had the same crack pattern, but the breakout cone in CC1and C1-2bolts initiated at the second bolt. The cracks propagated due to cyclic loading as shown in Figure 6-25b, and large flexural shear crack extended in one side of beam CC1 almost same as single shear failure. This may be attributed to the higher bolt position, which increased the overall governing depth close to the beam depth. This flexural shear crack rapidly propagated at each load cycle, even at the same load, due to the concrete deterioration.

Table 6-4 and Figure 6-25b demonstrate that both C1-2bolts and CC1 had approximately the same first cracking load, i.e., cyclic loading had no effect on connection performance up to the first cracking load because it behaved elastically. On the other hand, the breakout cracking load decreased by 13% and the ultimate load decreased by only 1%, which shows that stiffness degradation existed after first cracking and up to the connection breakout cracking. Also, residual displacements occurred due to cyclic loading as shown in Figure 6-25b. Finally, CC1 failed in the forth cycle at the ultimate load level and the corresponding mid-span displacement was much higher than that of C1 and C1-2 bolts.

Figure 6-27 presents the load-strain relationship for longitudinal and transverse reinforcements of beams C1 and CC1. Figure 6-27a shows that CC1 experienced lower longitudinal reinforcement strains than C1, which is attributed to the different number of connection bolts. It also shows that longitudinal steel accumulated significant residual strains in each load cycle after cracking initiated, which occurred in CC1 at a much lower load compared to C1.
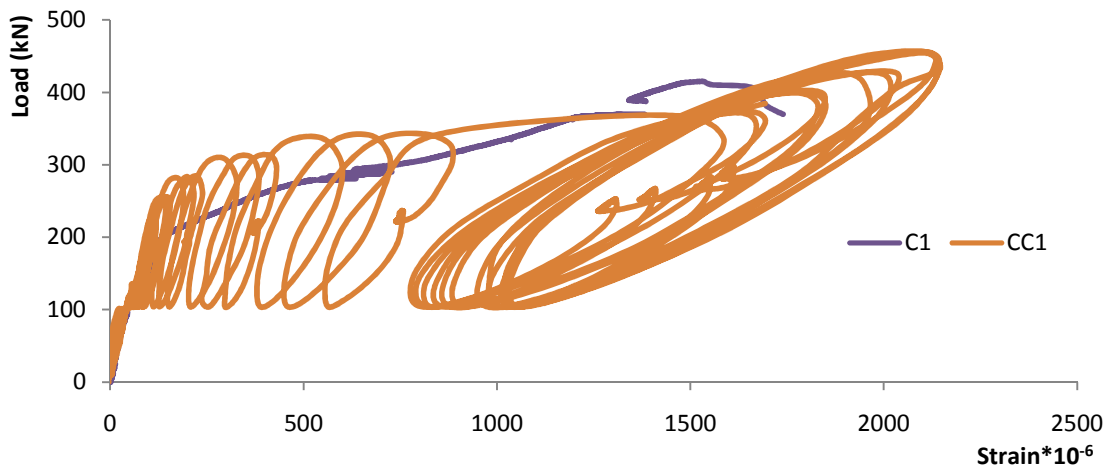
a)
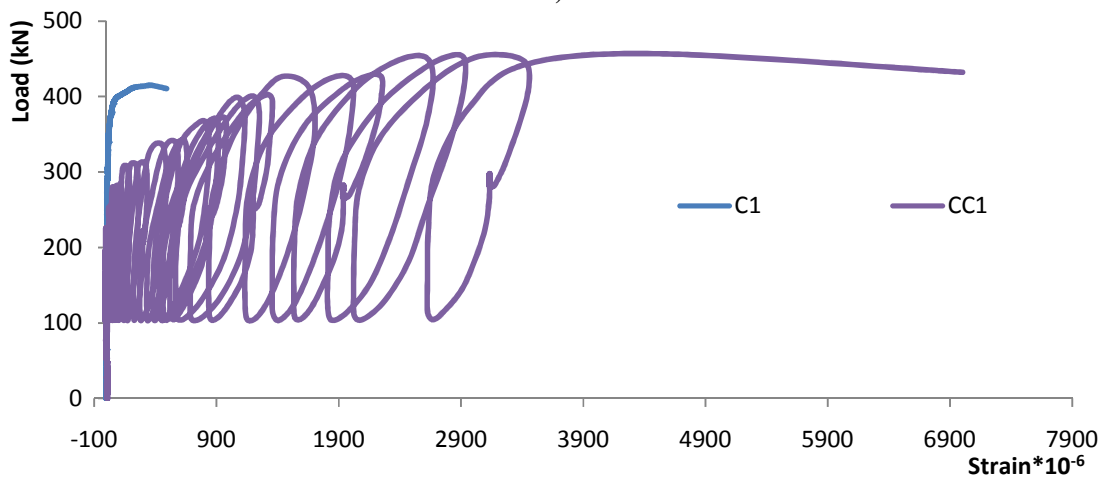
b)

Figure 6-27 load-strain relationship for: a) longitudinal reinforcement; b) stirrups

Figure 6-27b shows that the strain in stirrups of beam CC1 was much higher compared to beam C1 due to the early propagation of diagonal crack and associated deterioration of concrete strength. As a result, stirrups of CC1 yielded before the connection ultimate load was reached, i.e., the stirrups contributed to the connection capacity in beam CC1. Finally, both CC1 and C1 experienced relatively brittle failure, but longitudinal and transverse reinforcements of beam CC1 yielded before the connection ultimate load was reached, providing higher energy dissipation during cyclic loading.

6.11.1.3 Beam C9 Vs beam CC3

Both beams were identical, but Beam CC3 had 2 bolts connecting the pile cap to the pile shaft. Therefore, the response of beam C9-2bolts was calculated using the calibrated finite element model and was used in the comparison with beam CC3.

Beam CC3 had the same crack pattern (Figure 6-24), but the breakout cone initiated at the second bolt as that in beam C9-2bolts. Moreover, the cracks propagated further for each load cycle, even at the same load level.

Table 6-4 and Figure 6-25c show that CC3 and C9-2bolts had approximately the same first cracking load, i.e., the cyclic loading had no effect on it because the behaviour can be considered as elastic behaviour up to crack initiation. On the other hand, the breakout cracking load decreased by 5% and the ultimate load decreased by 11% due to degradation of concrete associated with cyclic loading. The connection stiffness degraded after first crack initiated and stiffness degradation increased up to the connection ultimate load. Additionally, cyclic loading caused accumulation of residual displacements. As

noted from Table 6-4 and Figure 6-25c, the mid-span displacements of CC3 at breakout cracking and ultimate loads were almost 75% higher than for C2 and C2-2 bolts due to stiffness degradation and residual displacement accumulation.

Figure 6-28 displays the load-strain curves for reinforcements in beams CC3 and C9. Figure 6-28a shows that longitudinal reinforcement of CC3 experienced strains higher than that in beam C9 for the same applied load. This is attributed to cyclic degradation of concrete strength; hence the load was transferred to the longitudinal reinforcement. The figure also shows accumulation of residual strains as the number of load cycles increased.

The cyclic loading resulted in rapid propagation of flexural shear cracks due to the concrete deterioration, which reduced the breakout crack load and some of the load was transferred to the stirrups, which is manifested in the recorded stirrups strain before breakout cone load as shown in Figure 6-28b. In addition, Figure 6-28b shows that the stirrups in beam C9 yielded before the ultimate was reached, and as would be expected, stirrups in beam CC3 also yielded and could not sustain more load after cyclic degradation of concrete strength. Thus, the ultimate capacity of beam CC3 was less than that of beam C9-2bolts.
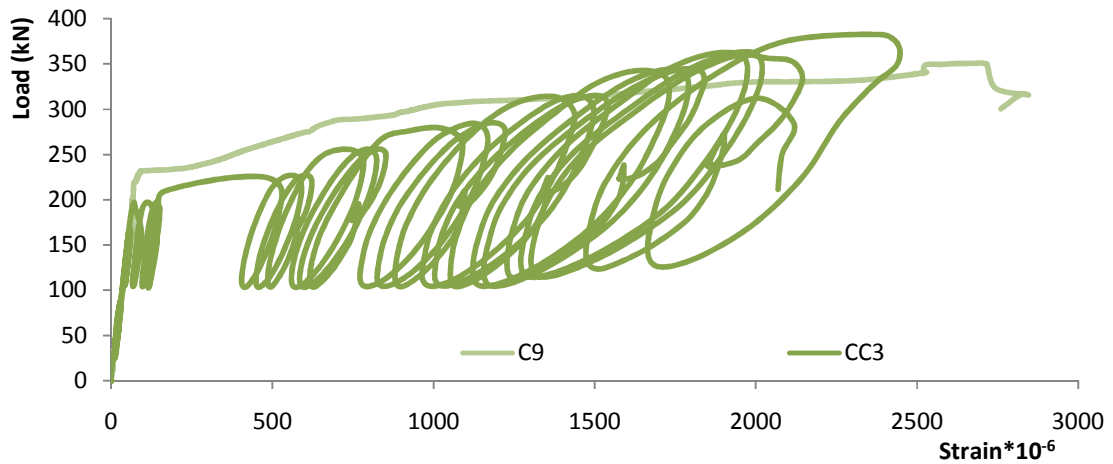
a)
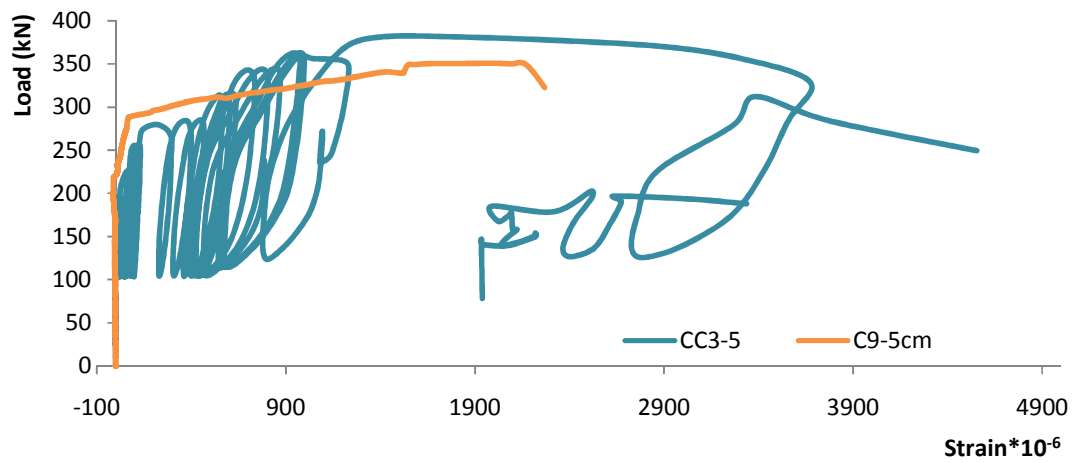
b)

Figure 6-28 load-strain in beams CC3 and C9 for: a) longitudinal reinforcement; b) stirrups

6.11.1.4 Beam CC2 and beam CC1

Both beams had the same variables, but beam CC1 had 152 mm pile embedment depth while beam CC2 had 203 mm pile embedment depth.

Both beams had the same crack pattern; however breakout cone dimension for CC1 was larger than that of beam CC2. Also, the cracking under the higher bolt in beam CC1 was initiated as an internal cone but beam CC2 had a horizontal crack at the level of the bolt.

287

Figure 6-29 shows the load displacement curves for both beams. It can be noted from Figure 6-29 and table 6-4 that the breakout cracking and ultimate loads increased as the remaining depth increased. In addition, the mid-span displacements at the breakout cracking and ultimate loads increased by more than 60% in beam CC1 compared to beam CC2, and the beam ability to absorb energy before failure increased by 110% as the remaining depth increased. On the other hand, Figure 6-29 shows that the residual displacement in beam CC1 was larger than that in beam CC2. This may be attributed higher contribution of concrete in the ultimate load for beam CC1 compared to CC2. Finally, Table 6-4 shows that the cumulative dissipated energy in beam CC1 was 89% higher than that in beam CC2 because of the increase in the connection remaining depth.
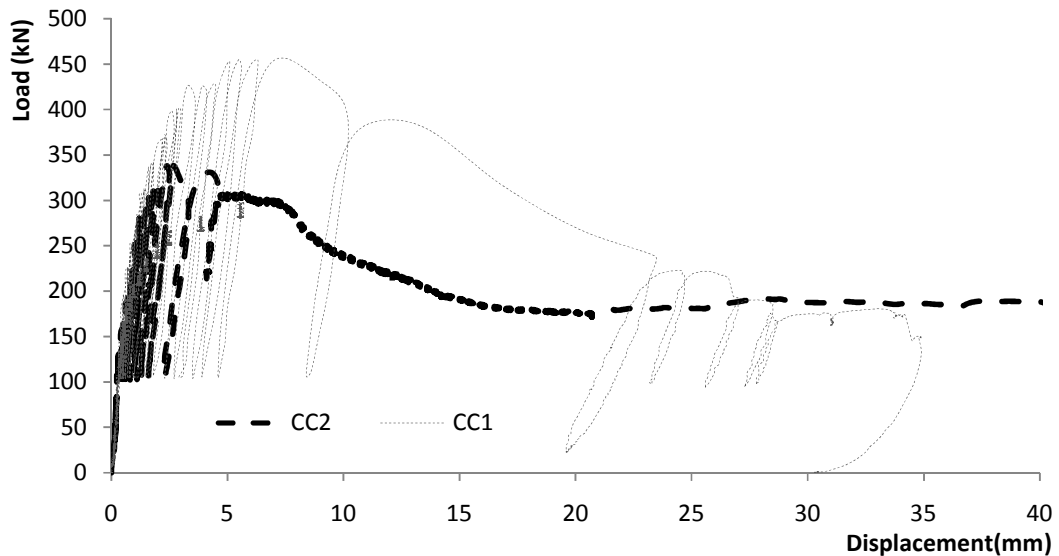
Figure 6- 29 Load mid-span displacement curve

6.11.1.5 Beam CC2 Vs beam CC3

Both beams had the same variables but beam CC2 had two branches of #2 rebar (6.35 mm diameter) spaced at 200 mm (about 0.064% transverse reinforcement ratio) while beam CC3 had two branches of #2 rebar (6.35 mm diameter) spaced at 100 mm (about 0.127% transverse reinforcement ratio). Both beams had the same crack patterns. However, cracking actions occurred at higher loads in beam CC3 compared to beam CC2.

Figure 6-30 compares the load displacement responses of beams CC2 and CC3. The results show that the breakout cracking and the ultimate loads increased by 6% and 13% as the transverse reinforcement ratio increased, but the mid-span displacements at the breakout cracking and ultimate loads, however, changed by only 2%. However, the absorbed energy before failure increased by 90% with the transverse reinforcement increase. Both beams had approximately the same loading and unloading stiffness during cyclic loading up to the breakout cracking load at which point the stiffness degraded, which demonstrates that the stirrups contribute to resisting the load only after breakout cracking occurred. Also, the cumulative dissipated energy of beam CC3 during loading up to its ultimate load increased by 187% over that of beam CC2 because of its higher transverse ratio. This confirms the important role of stirrups in enhancing the structural damping during cyclic loading events such as seismic and wind loading.
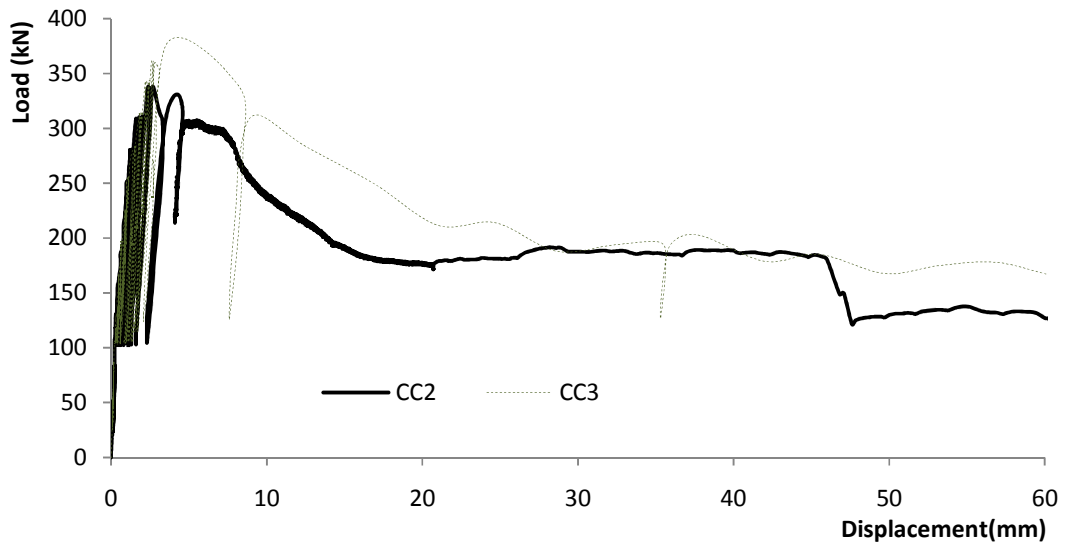
Figure 6- 30 Load mid-span displacement relationship

6.12 Conclusions

The capacity of new construction pile bracket used to connect slender shaft piles (e.g. helical piles and micropiles) to grade beams in new construction is investigated in a laboratory experimental program. In the first phase of the experimental program, nine foundation models involving simply supported grade beams with new construction pile brackets were subjected to monotonic compression loading. The test beams were categorized into four groups according to the parameters investigated. Each group had three beams and only one variable was investigated while the other variables were kept constant. The investigated variables are: embedment depth of pile cap; width of the steel plate; beam longitudinal reinforcement; and beam transverse reinforcement. In the second phase, three simply supported grade beams with new construction pile bracket were subjected to cyclic compression loading. The performance of these beams was compared with that of other similar beams tested under static compression loads. Because the beams

290

tested in phase one had only one bolt to connect the pile cap to the pile shaft, while two bolts were used in beams tested in second phase, finite element analyses were conducted to calculate the response of test beams accounting for the effect of the second bolt. The following conclusions may be drawn from the experimental and calculated results.

6.12.1 General

1) Global beam behaviour was observed initially until first flexural cracking occurred. The response depended on the connection variables afterwards.

2) The connection capacity may be less than the beam capacity, and must be considered in foundation design and pile load transfer calculations.

3) The connection can be considered fixed (i.e. fixed pile head) up to the breakout cracking load. Afterwards, the connection becomes hinged and its stiffness and capacity depend on the longitudinal and transverse reinforcements.

4) The breakout cracking initiated from the higher bolt level in the pile cap connection.

5) Crack propagation in the longitudinal direction was similar to single shear cracking.

6) The breakout cracking load is mainly affected by the concrete, pile-concrete friction, and longitudinal reinforcement contributions and not by the transverse reinforcement.

7) The connection ultimate load is affected by concrete, longitudinal reinforcement, pile-concrete friction, and transverse reinforcement contributions.

8) After the formation of wide breakout cracks, the load transfers by the stirrups and pile-concrete friction.

9) The connection ductility depends mainly on the longitudinal and transverse reinforcements.

6.12.2 Effect of embedment depth

10) An increase in the pile cap remaining depth increases the connection stiffness after first cracking, breakout cracking and ultimate loads, and size of breakout cone.

11) A decrease in pile cap remaining depth decreases the beam ability to absorb energy up to failure.

6.12.3 Effect of pile cap's plate width

12) The size of breakout cone at the longitudinal reinforcement level increases as the plate width increases.

13) The plate size has minor effect on the connection stiffness and its effect on the connection capacity was not clear; however, if breakout cracks cross the plate, it contributes substantially to the connection ultimate load.

14) The connection ductility and ability to absorb energy up to failure slightly improve for larger plates.

6.12.4 Effect of longitudinal reinforcement

15) The connection first flexural cracking, breakout cracking and ultimate loads increase with the longitudinal reinforcement ratio increase.

16) Increasing the longitudinal reinforcement ratio increases the connection ability to absorb energy till failure.

6.12.5 Effect of transverse reinforcement

17) The transverse reinforcement ratio has no effect on first flexural cracking or breakout cracking loads, and had minor effect on the breakout cone dimensions.

18) Adequate transverse reinforcement can transfer the connection failure mechanism from brittle to ductile and it enhances the connection ability to absorb energy.

19) The transverse reinforcement configuration can alter the load transfer mechanism. Higher connection capacity can be achieved by placing higher percentage of transverse reinforcement closer to the pile shaft and can reduce the breakout crack width, which maximizes the contributions of the concrete aggregate interlock and longitudinal reinforcement dowel action.

20) The connection ultimate capacity should be the larger of its ultimate concrete capacity or vertical tensile strength of transverse reinforcement within the breakout cone.

6.12.6 Effect of cyclic loading

21) Using more bolts to connect the pile shaft to the pile cap can increase the connection breakout cracking load and ultimate load.

22) During cyclic loading, the connection behaves in a linear elastic manner until its first flexural cracking load. After flexural cracking initiation, the connection behaviour becomes nonlinear inelastic characterized by concrete deterioration and residual deformations.

23) Longitudinal and transverse reinforcements can decrease the effect of concrete deterioration on the connection capacity, especially if they don't yield before the connection ultimate load is reached. If the reinforcement yields first, the connection ultimate load is expected to decrease due to cyclic loading.

24) The concrete deterioration is more pronounced for connections with larger remaining depth.

25) The dissipated energy during cyclic loading increases as the remaining depth increases.

26) The transverse reinforcement plays a very important role in enhancing the structure damping during cyclic loading by increasing the dissipated energy.

6.13 References

ACI 318, 2011. Building Code Requirements for Structural Concrete (ACI 318-11) and Commentary, Farmington Hills, MI: American Concrete Institute.

ACI 349, 2001. ACI 349-01 Code Requirements for Nuclear Safety Related Concrete Structures, Farmington Hills, MI: American Concrete Institute.

Bentz, E.C. & Collins, M.P., 2006. Development of the 2004 Canadian Standards Association (CSA) A23.3 shear provisions for reinforced concrete. Canadian Journal of Civil Engineering, 33(5), pp.521–534.

Collins, M.P. et al., 1996. A General Shear Design Method. Structural Journal, 93(1), pp.36–45.

Collins, M.P. & Mitchell, D., 1991. Prestressed Concrete Structures, Prentice Hall.

CSA A23.3, 2004. A23. 3-04: design of concrete structures,

Erberik, M.A. & Kurtman, B., 2010. a Detailed Evaluation on Degrading Behavior of Structural. In Proceedings of the 9th US National and 10 th Canadian Conference on Earthquake Engineering, (369), pp.1–10.

Esfahani, M.R., 2008. Effect of cyclic loading on punching shear strength of slabs strengthened with CFRP sheets. International Journal Of Civil Engineering, 6.

Lee, N.H. et al., 2007. Tensile-Headed Anchors with Large Diameter and Deep Embedment in Concrete. ACI Structural Journal, 104(4), pp.479–486.

Shahnewaz, M., 2013. Shear behavior of reinforced concrete deep beams under static and dynamic loads. University of British Columbia.

Smith, K.N. & Fereig, S.M., 1974. Effect of Loading and Supporting Conditions on the Shear Strength of Deep Beams. ACI Special Publication, 42, pp.441–460.

Talbot, Arthur Newell, 1857-1942, 1909. Tests of reinforced concrete beams: : resistance to web stresses, University of Illinois at Urbana Champaign, College of Engineering. Engineering Experiment Station.

Vecchio, F.J. & Collins, M.P., 1988. Predicting the Response of Reinforced Concrete Beams Subjected to Shear Using the Modified Compression Field Theory. Structural Journal, 85(3), pp.258–268.

Watstein, B.D. & Mathey, R.G., 1958. Beams Having Diagonal Cracks. Journal Of The American Concrete Institute, 58(55), pp.717–728.

Zuhua Wang, 1987. shear strength of slender concrete beams loaded indirectly. International journal of structures, 7(1), pp.17–42.

BEHAVIOUR OF HELICAL PILE CONNECTORS FOR NEW FOUNDATIONS SUBJECTED TO COMPRESSION LOADING:NONLINEAR FINITE ELEMENT ANALYSIS

7.1 Introduction

This research aims to develop nonlinear finite element models that can accurately mimic the structural behaviour and capture the possible failure modes of the connection between steel piles with slender shaft (i.e. helical piles and micropiles) and the reinforced concrete foundation (e.g. grade beams). The finite element model will be first calibrated and verified using the results from the accompanying experimental program and then will be used to conduct a comprehensive parametric study to investigate additional connection configurations that complement the results of cases covered in the experimental study. An overview of the literature relevant to nonlinear finite element modeling is presented first, followed by the details of the finite element model.

7.2 Numerical Model

The connection between the slender pile shaft and reinforced concrete foundation exhibits complex nonlinear structural behaviour as discussed in Chapter 6. The pile cap connection consists of a steel pile shaft, two high strength steel bolts, a steel cylinder, a steel plate, welding between the cylinder and the plate, and the concrete beam with its longitudinal and transverse reinforcement. For proper modeling of nonlinear behaviour, the geometric and material properties should be simulated using proper meshing and material properties. In addition, specific interface conditions should be applied at the

interface of each two surfaces in order to simulate the nonlinear/discontinuity behaviour at the interfaces. All materials of the connection may exhibit nonlinear behaviour, especially near failure. Thus, the chosen numerical model must be able to handle the expected interactions between components such as gap opening/closing, nonlinear material behaviour, stress concentration, rate of loading, material deterioration with cyclic loading, and frictional and dowel forces. The general purpose implicit/explicit finite element program LS-DYNA (LSTC 1998 and LSTC 2009) was used in this study. It contains various material models capable of representing the complex behaviour recorded in the experimental work. In addition, the program offers different contact surface types with different advanced search algorithms that can facilitate modeling complex interface conditions.

7.3 Type of finite element analysis

The explicit analysis is used in the calculations to facilitate simulating nonlinearities and progressive damage/failure behaviour and to calculate the response accurately including cracking and softening behaviour. Furthermore, it is suitable for problems with large number of degrees of freedom as it is computationally more efficient as the solution can be achieved without forming a global stiffness matrix. Rather, the solution is obtained on an element-by element basis and as a result, it requires comparatively modest computer storage requirements. However, the explicit method is conditionally stable and therefore small time steps must be used. To ensure stable computations and convergence, quasi-static analysis was conducted using explicit finite element modelling (FEM).

At each time step of the explicit analysis, the equilibrium equation is solved to calculate the displacement, i.e.

$$M\ddot{x}^{n+1} + D\dot{x}^{n+1} + k_t(x^n)\Delta x = P(x^n)^{n+1} - F(x^n) \qquad 7.1$$

where $\ddot{x}^{n+1}$, $\dot{x}^{n+1}$, x^n, and Δx are the acceleration, the velocity, the coordination, and the displacement vectors. $P(x^n)^{n+1}$ is the external load vector and $F(x^n)$ is the stress divergence vector. M, D and K_t are the mass, damping and tangent stiffness matrices.

To ensure that the analysis can be static or quasi-static, the inertia and damping terms should be negligible. Pan (2006) suggested this can be achieved either through increased loading time (i.e. reduced rate of loading) or decreased system mass (i.e. reduced material density). Both approaches usually require numerous small time increments. Decreasing the material density adds to the run time considerably as the appropriate time step is given by (Ls-Dyna theory manual, 2006):

$$\Delta t = \min\left(\frac{L_{min}}{S}\right), \qquad S = \sqrt{\frac{E}{\rho}} \qquad 7.2$$

where L_{min} is the smallest element dimension; S is wave speed traveling through the element; and E and ρ are the element Young's modulus and mass density.

In this study, both mass scaling and rate of loading reduction were used in order to achieve an appropriate running time with quasi-static behaviour. The material density was scaled to 1/1000 of the prototype density, and the rate of loading was optimized such that no effect of loading rate would be recorded and the best calibration was achieved.

Also, the kinetic and inertial energies were minimized. The mass scaling and the loading rate were kept constant for all investigated specimens. Moreover, the symmetry of the specimens about their main axes was exploited (i.e. only one quarter of the specimen was modeled) to further reduce the computational effort.

7.4 Element type

The plain concrete, steel pile shaft, steel bolts, steel cylinder, welding, and steel pile cap's plate were modeled using 8-node hexahedron solid constant-stress elements with three displacement degrees of freedom at each node with one integration point (element form 1 in LS-DYNA), which is shown in Figure 7-1. This element is preferred in analyses involving large nonlinear deformations because it is computationally efficient due to its one-integration point, yet it provides reasonably accurate results (Flanagan and Belytschko, 1981). However, it requires hourglass control.

Longitudinal and transverse reinforcement were modelled using two-node beam elements. Even though it has rotational degrees of freedom, it will behave as a truss element within the model as was connected to solid element nodes that have no rotation.
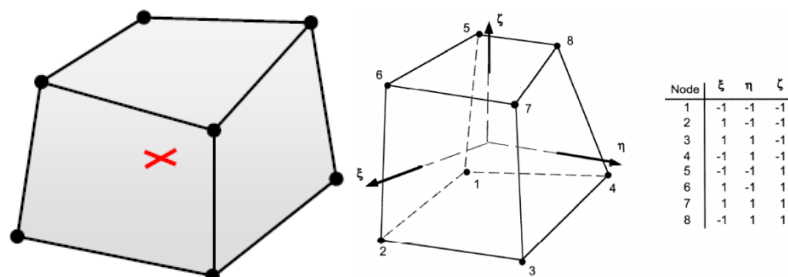
Figure 7- 1 8-node solid hexahedron element with one integration point (after LS-DYNA manual, 2006)

7.5 Material model

Proper definition of the mechanical properties of steel and concrete materials is necessary for modelling the realistic behaviour of the connection. Suitable material models for the plain concrete and steel were selected from LS-DYNA material library and their parameters were calibrated using the experimental results.

7.5.1 Concrete material model

Generally, modeling the behaviour of an element in a concrete continuum requires consideration of the triaxial stress-strain characteristics. As shown in Figure 7-2, the failure surface is a three-dimensional principle stress space (Chen, 2007). For isotropic materials, the failure criterion based upon a state of stress must be an invariant function of the state of stresses and it does not depend on the chosen coordinates system.

The elastic limit surface (yield surface) shown in Figure 7-2 indicates the beginning of the material weakening. It has similar shape to the failure surface, but it is reduced in size. The failure surface is fixed in the principle stress space at a distance from the yield surface. The deviatoric stresses are considered in the elastic state till the stress reaches the yield surface, at which point the nonlinear behaviour takes place. The deviatoric stresses can then increase further until the failure surface is reached. Beyond this stage, the response can be perfectly plastic or softening behaviour can take place.
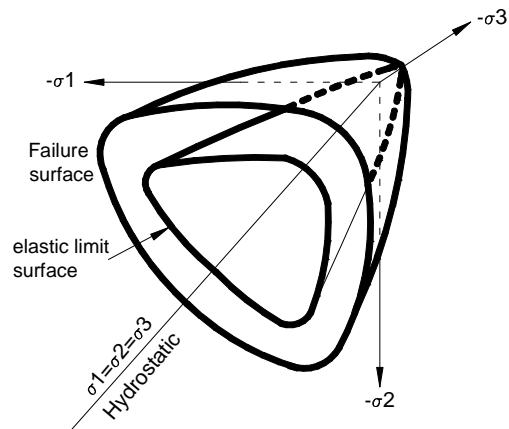
Figure 7- 2 Schematic failure Surface of concrete in 3D stress space (Modified from Chen, 2007)

7.5.1.1 Definition of concrete failure criterion

The failure surface in the 3-dimensional stress space can be demonstrated by the deviatoric plane (a cross-section shape perpendicular to the hydrostatic axis) with constant hydrostatic stress and its meridians (the intersection between a plane containing the hydrostatic axis and the failure surface) at a specific angle. For example, the cross-section in Figure 7-3 is approximately triangular and requires two points to be indicated. The first point is farthest from the hydrostatic axis with 60° angle, on the compressive meridian. The second point is nearest to the hydrostatic axis with 0° angle, on the tensile meridian. The path between the compressive and tensile meridians can be defined by an elliptical curve (Willam and Warnke, 1975) (distance r as a function of θ).
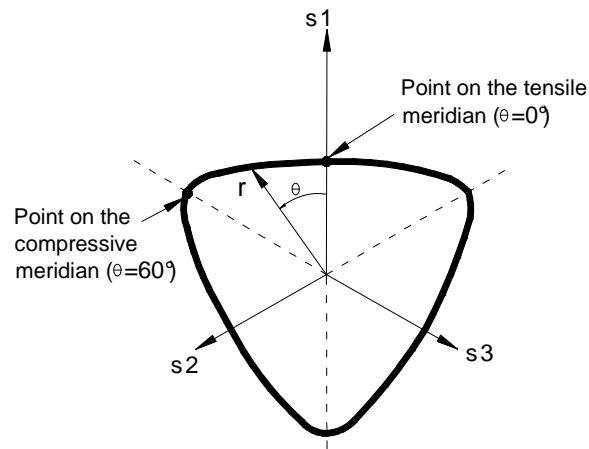
Figure 7- 3 Deviatoric cross-section of the failure surface

The failure curve can be considered triangular for tensile and small compression stresses and more circular for high compressive stresses. The ratio of tensile to compression deviatoric stress capacity at the same hydrostatic pressure is less than 1. This ratio increases with the hydrostatic pressure increase, which means concrete can sustain higher tensile stresses when subjected to transverse compression stresses and pure hydrostatic loading cannot cause failure (Chin and Zimmerman, 1965).

7.5.1.2   Definition of fracture mechanics and failure criterion

When the tensile strength of a material is reached, cracking will take place. Fracture mechanics describe the condition around and in front of a crack tip (Elfgren, 1989). The behaviour of concrete subjected to tension or pure shear is best analyzed by combining fracture mechanics and finite element analysis, which allows modelling realistic crack initiation and propagation (Hillerborg, 1976).

It has been a common practise to ignore the tension strength of cracked concrete in design; however, Elighausen et al. (2013) confirmed its importance in finite element analyses. Accounting for the cracked concrete tensile strength allows an accurate simulation of the failure mechanism for lightly reinforced concrete members and members failing in shear or tension. It also helps predicting the member deformation accurately. The crack is assumed to propagate when the stress at the crack tip reaches the tensile strength f$_t$. When the crack opens, the stress is not assumed to fall to zero at once, but to decrease with increasing the crack width (Hillerborg, 1976). Bazant and Oh (1983) demonstrated that stress-softening will occur at the crack location depending on the effective plastic strain at the crack. They defined the fracture energy, G_{ft} as the consumed energy to form a unit area of crack surface. The 3-dimensional failure surface will indicate the initial yielding and the stress-strain relation for the material. Material damage will then occur after reaching the peak strength and the material continues to sustain loading till 99% damage value is reached depending on fracture mechanics (Chen 2007). The concrete tensile fracture energy G_{ft} may be calculated by the CEB-FIP model code (1993), i.e.

$$G_{ft} = \left(0.0469\, d_a{}^2 - 0.5 d_a + 26\right)\left(\frac{fc'}{10}\right)^{0.7} \qquad\qquad \textbf{7.3}$$

where G_{ft} is in N/m, fc' is in MPa, d_a is the maximum aggregate size in mm.

Santiago and Hilsdorf (1973) observed concentrated deformation in certain zones after reaching the peak stress in their investigation of the behaviour of concrete loaded in

compression. Nakamura and Hiagai (1999) indicated the importance of compression fracture energy, especially when members are failing in compression under flexure or compression-shear. They proposed that the concrete compressive fracture energy should be taken as 250 times the concrete tensile fracture energy.

7.5.1.3 Concrete Constitutive Model

LS-DYNA has several comprehensive concrete models that can capture the complex concrete behaviour including: biaxial and triaxial loading, biaxial stiffening, concrete-reinforcement interactions as well as nonlinear behaviour under tension, compression, and shear.

The material model "Material 72", (denoted as K&C model, MAT_72, or MAT_72R3 in Ls-Dyna offers comprehensive characterization of concrete. MAT_72R3 provided excellent match with observed behavior during initial calibration tests. In addition, its superior performance is confirmed by many researchers (e.g., Malvar et al., 1997 and 1999; Crawford et al, 1995, 1997, 2004, 2006, 2010, and 2012; Magallanes et al., 2008, 2011; Wesevich, 1997; Yonten et al., 2005; and Tu and Lu 2009. Furthermore, has a default library for consistent different concrete strength, i.e., the model uses the concrete compression strength to generate the rest of the required variables. It also allows the user to set a particular material parameter that affects the damage evolution rate according to the mesh size to preserve energy to failure. The user can also implement available measured concrete characteristics (e.g. the concrete tensile strength), which can further improve the model predictions.

Finally, MAT_72R3 has important features including: strain rate effects; failure criteria; equation of state for 3D solid and 2D continuum elements; damage effects; and different tension and compression behaviour. Therefore, it will be used herein. The model and the procedure for evaluating its parameter affecting the damage evolution rate are discussed below. It should be noted, however, that concrete material models in LS-DYNA consider concrete as a homogenous continuum even though it is a heterogeneous material.

The model accounts for the effects of cracking by employing the smeared crack band model. Crack initiation is based on strength criterion, i.e., when the maximum principal stress reaches the concrete tensile capacity, f_t. On the other hand, crack propagation is based on fracture mechanics criterion, i.e., considering fracture energy (Bažant and Cedolin, 1979). Smeared cracks are oriented perpendicular to the maximum principal stresses. The crack band model is defined by three material parameters: f_t, G_{ft}, and w (i.e. shear dialation factor). G_{ft} is controlled by the input uniaxial tensile strain softening parameter, b2 and f_t. These two parameters should be modified to account for the effect of the used element size.

This model uses a limited shear dilation method to describe material deformation or flow, which accounts for confinement effect in reinforced concrete. For example, when steel stirrups are used, axial force in the stirrups will mobilize due to dilation and the concrete contained by the stirrups will be confined. The model can simulate both associative and non-associative flow behaviours. To capture the partial shear dilation of concrete caused by the aggregate interlock as shown in Figure 7-4, an associative parameter, ranging from

0 to 1 is used. Noble el al. (2005) suggested a range to be used for w from 0.5 to 0.7. Also, the maximum aggregate size is required to model the material flow.
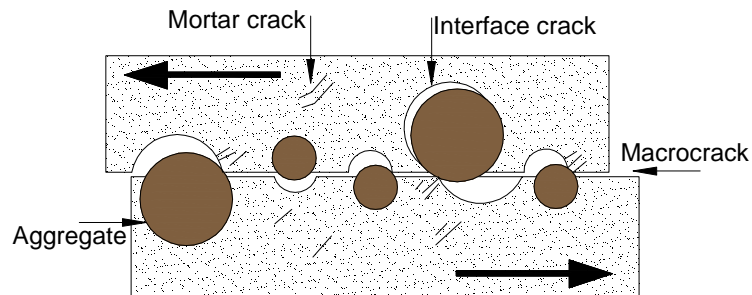
Figure 7- 4: Influence of aggregate interlock on concrete fracturing process
(Modifed from Noble el al., 2005)

7.5.1.4   Definition of failure surfaces for MAT_072R3

This model uses a plasticity based formulation with three independent dynamic failure surfaces: initial yielding, maximum, and residual failure surfaces (Crawford et al., 2012). The failure surface shape depends on the applied hydrostatic pressure and eight constants that can be calculated from the experimental data. This hydrostatic pressure invariant value is equal to P. The dynamic surfaces are given by:

The initial yielding surface: $\Delta\sigma_y = a_{oy} + \dfrac{P}{a_{1y}+a_{2y}p}$ **7.4**

The maximum failure surface: $\Delta\sigma_m = a_o + \dfrac{P}{a_1+a_2p}$ **7.5**

The residual failure surface: $\Delta\sigma_r = a_{of} + \dfrac{P}{a_{1f}+a_{2y}f}$ **7.6**

where $a_{oy}, a_o, a_{of}, a_{1y}, a_{2y}, a_1, a_2, a_{1f}, and\ a_{2f}$ are user-specified constants and can be estimated from laboratory triaxial tests in compression.

7.5.1.5 Softening parameters of MAT_72R3

The softening parameters $b1$, $b2$, and $b3$ establish the manner of softening exhibited by the model for different stress paths. Parameter $b1$ governs softening in compression, b_2 affects the uniaxial tensile strain softening, and $b3$ affects the triaxial tensile strain softening. In the current study, these values were determined by iterations until the values of fracture energies, G_{ft}, G_{fc}, and G_{fs}, converge with the calculated values using the CEB-FIP Model code (1993) as suggested by Magallanes (2010).

Parameter b_2 governs the tensile fracture energy G_{ft} as it controls the softening branch of the stress-strain behaviour of concrete subjected to uniaxial tensile test. Malvar et al. (1997) indicated that the area under the stress-strain curve of one element should be adjusted to G_{ft}/h_c, where h_c is the characteristic length of the element. To find the best representing parameter b_2, different finite element models were conducted using only one 3D solid element representing the concrete with a specific mesh size. This element is loaded perpendicular to one of its surfaces while the parallel surface was restrained from moving. The area under the stress-strain curve was then calculated and compared with the actual tensile fracture energy divided by the element length G_{ft}/h_c. The parameter b_2 that gives the same tensile fracture energy G_{ft} calculated with the (CEB-FIP Model code, 1993) is then used in the concrete material model.

These procedures were conducted for each studied mesh size. Table 7-1 presents the investigated b_2 parameters and resulting G_{ft} for fc' = 30 MPa (and f_t = 3.33 MPa) and fc' = 40 MPa (and f_t = 5.25 MPa) considering mesh size = 20mm and using one solid element. The calculated fracture energies from the CEB-FIP Model code (1993) were 80 N/mm and 96 N/mm for fc'=30 MPa and 40 MPa, respectively. Inspecting Table 7-1, it is noted that Model E-3.1 with b2=3.1 best represented concrete with fc' =30 MPa, and model F-4.3 with b2=4.3 best represented concrete with fc' = 40 MPa.

Figure 7-5 presents the load displacement curves for the different models of mesh size of 20 mm for fc'=30 and 40 MPa. Figure 7-5 demonstrates the effect of b_2 on the expected concrete behaviour and its ability to resist tension and displacement before cracking.

Table 7- 1 Calculated uniaxial tensile strain softening and corresponding tensile fracture energy

Compressive Strength, fc'=30 Mpa		Compressive Strength, fc'=30 Mpa	
b_2	G_{ft} (N/mm)	b_2	G_{ft} (N/mm)
1	140	1	221
2.3	99	3	132
3	82.405	4	102
3.1	**80.38**	**4.3**	**96.8**
4	63.65	4.4	95
5	52.27	4.5	92.5
6	42	5	82.85

Figure 7- 5 Single element tensile load-displacement curve for different b_2 parameter for MAT_072R3: a) with fc'=30 MPa; b) fc'=40 MPa

7.5.1.6 Elastic Parameters in MAT_72R3

The behaviour of concrete within the elastic range is described by two constants: the bulk modulus, K, and Poisson's ratio ν.

7.5.1.7 Damage function of MAT_72R3

Upon defining the three failure surfaces, the dynamic form of yield surface is obtained by interpolation between either the yield and max surfaces when hardening is occurring or the max and residual surfaces when softening is occurring. The interpolation is performed

using a scalar quantity that is computed based on the extent of damage at the material point, which depends on the softening parameter (Crawford et al., 2012). The damage parameter is given by:

$$\lambda = \begin{cases} \int_0^{\overline{\varepsilon^p}} \dfrac{d\overline{\varepsilon^p}}{r_f\left(1+\frac{p}{r_f \cdot f_t}\right)^{b1}} & for \; p \geq 0 \\[4mm] \int_0^{\overline{\varepsilon^p}} \dfrac{d\overline{\varepsilon^p}}{r_f\left(1+\frac{p}{r_f \cdot f_t}\right)^{b2}} & for \; p < 0 \end{cases} \qquad \textbf{7.7}$$

where $d\overline{\varepsilon^p} = \sqrt{(\frac{2}{3})\varepsilon_{ij}^p \varepsilon_{ij}^p}$ is the effective plastic strain increment, r_f is a user-defined experimental rate enhancement factor from unconfined uniaxial compression tests.

This model implements shear damage accumulation and it treats the damage evolution differently in tension than in compression.

7.5.1.8 Concrete material input used in LS_DYNA

The concrete material inputs were generated automatically within the finite element program based on the average concrete compressive strength according to ASTM C39/ C39M and the average splitting tensile strength according to ASTM C496/ C496M-11 (see Appendix A). The generated keyword input data for the models used for the concrete material models are indicated in the Appendix C.

7.5.2 Steel Material Model

There are several material models to simulate steel in LS-DYNA. The model selected in this study was material MAT_024 (MAT_piecewise_linear _plasticity). It has piecewise

linear plasticity curves that can capture effectively the strain localization behaviour of steel. It can capture steel rupture due to exceeding the maximum plastic strain and can mimic fractures at specific values of von Mises true strain. The element will be removed from the model if its maximum principle plastic strain exceeds the specified von Mises true strain, which depends on the steel grade. It can also simulate isotropic and kinematic hardening plasticity materials such as steel. Both beam elements and solid elements can be simulated using this model. It was used to simulate 3 different rebar materials (upper and lower longitudinal reinforcement and stirrups), steel pile shaft, welding, steel cylinder, steel pile cap's plate, and high strength steel bolts. The predictions of this model matched well the observed behaviour of the test specimens during the loading experiments. An example for the generated input for the steel model is listed in the Appendix C.

7.6 Hourglass control

The 8-node hexahedral solid element used to simulate the concrete has one integration point. It is necessary to control the zero energy modes, denoted as hourglassing modes, which arise when using this element (Flangan and Belytschko, 1981). They usually have much shorter periods than the structural response and hence cause oscillation of the response. Different hourglass control strategies are available in LS-DYNA. The viscous and stiffness hourglass controls are widely used. In general, viscous hourglass control is recommended for problems deformation with high velocities, while stiffness control is preferred for quasi-static analysis. Therefore, a stiffness form of hourglass control was used in the current analysis as suggested by LS-DYNA manual.

7.7 Rebar-concrete interface

The bond slip behavior of the rebar-concrete interface involves complex geometry and interference behaviour. Malvar et al. ,1997 investigated the importance of explicitly modeling the intricate details of this interface versus implicit modeling. They concluded that the bond between the rebar and the concrete is best simulated implicitly by tying the rebars to the same nodes of the concrete elements, which captures the bond-slip phenomena through the behavior of concrete attached to the rebars.

7.8 Welding at steel cylinder-pile cap's plate interface

The welding was modeled as elements having the same multi-linear stress strain curve recorded for the welding connection. These elements were simulated as solid elements using MAT_24 with specific plastic strain, while the steel cylinder and plate were connected to it using the common nodes. This allowed load transfer from the steel cylinder to the plate through welding. Hence, welding failure would be due to the failure of welding material.

7.9 Steel elements interfaces

The interface conditions at steel pile shaft-bolts, steel pile-concrete, steel plate-concrete, bolt-steel cylinder, and bolt-concrete were modeled using sets of two spring elements connecting the adjacent nodes on the contacted surfaces. The springs were placed normal and parallel to the contact surface connecting a slave node on the slave surface and master node on the master surface. It checks for slave points' penetration through the master surface at each time step. If penetration occurs, a restoring force (F_n) and a friction force (F_s) are applied to eliminate the penetration depending on the penetration depth, d,

313

and the spring stiffness, k (Bala, 2001). The restoring force (F_n) equals the penetration depth multiplied by the spring stiffness. The friction force is computed based on the friction coefficient, μ, and the normal force F_n. When the acting force reaches the maximum friction force ($\mu . F_n$), the two surfaces begin to slide and the friction force (F_s) remains constant.

7.10 Boundary conditions

Taking advantage of symmetry in both orthogonal directions, only one-quarter of the specimen was modeled. All nodes across the axes of symmetry were restrained by roller support condition. Nodes corresponding to supports were restrained only in the vertical direction Y to accurately simulate the experimental setup, where only Y direction was restrained. Vertical loading was applied as an imposed downward constant velocity at the top surface of the pile shaft simulating compression loading. The small constant velocity loading resulted in small non oscillating kinetic energy compared to the internal energy of the system. The concrete overall dimensions, and support location are depicted in Figure 7-6a. The full model boundary conditions are shown in Figure 7-6b. To check the accuracy of the supporting system, the loads recorded from the system was compared with the model recorded reactions and they gave exactly the same values with inverted sign during the full loading and before total specimen failure.

Half the length
800 mm

Half the width
250 mm

X=0

Boundary Codition
Z=0

500 mm

720 mm

Compression
Supports
Y=0
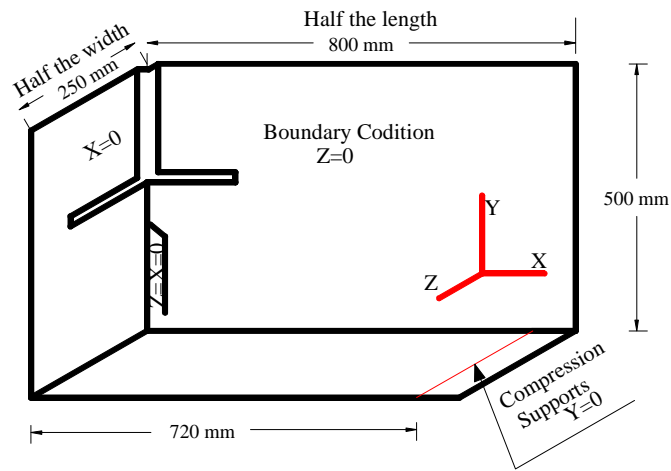
a)
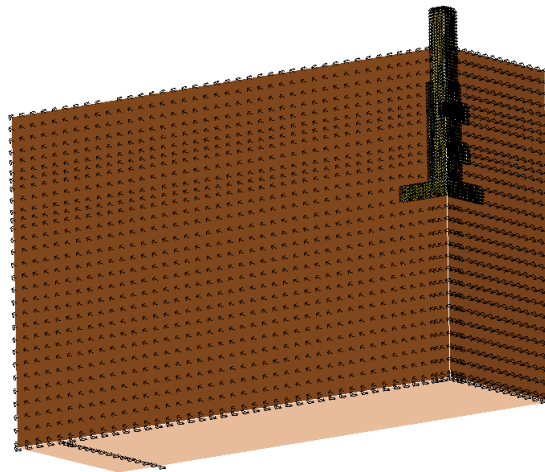
b)

Figure 7- 6 Model boundary conditions: a) with model dimensions; b) with model mesh

7.11 Mesh size

Several element sizes were investigated, and for each model different value of b_2 was calculated to maintain the same fracture energy G_{ft}. The element size was selected considering volume of cracking and fracture process zone, which is proportional to the maximum aggregate size (Bažant and Oh,1983), but maintaining small element sizes to ensure homogeneous behaviour. A sensitivity study was performed, which involved

315

comparing the numerical predictions with the experimental observations. The model with concrete element size equal to the concrete maximum aggregate size of 20 mm and reber element length of 20 mm provided best match with experimental results and hence was used for further analysis. Smaller element size was used for modeling the steel plate, bolts, welding, pile shaft and the steel cylinder due to their geometrical dimensions.

7.12 Verification of Finite Element Model

In order to ensure proper modeling of quasi-static loading conditions, the total, internal, kinetic, and hourglass energies of the model were initially recorded for beam C2 as presented in Figure 7-7. In all models, both kinetic energy and hourglass energy were negligible compared to the internal energy, which indicates the accuracy of modeling quasi-static loading conditions.
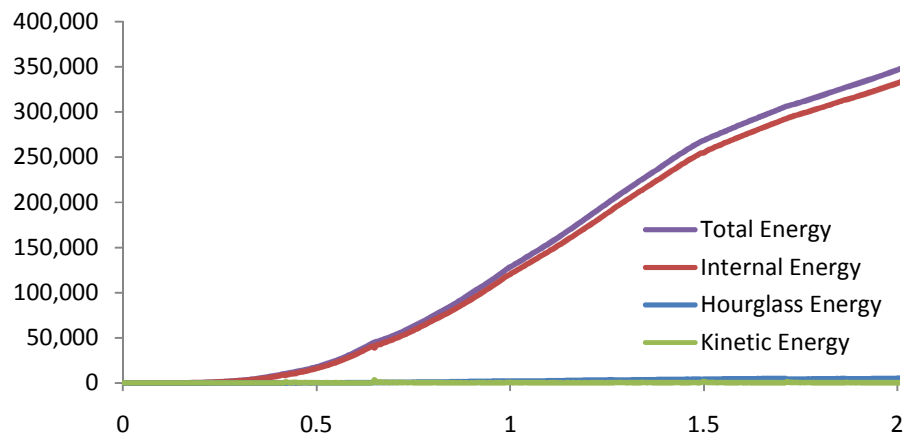
Figure 7- 7 Total, internal, kinetic, and hourglass energies recorded in beam C2 Model

The finite element models were then verified through comparing their predictions with the experimental observations of the 9 test specimens. The comparison focussed on:

- Load-displacement behaviour including: breakout cracking and ultimate loads and corresponding displacements as well as connection stiffness.

- Longitudinal reinforcement strains for rebars next to the edge of the beam cross-section (denoted outer longitudinal reinforcement), and rebars inside the beam (denoted inner longitudinal reinforcement).

- Strain for stirrups next to the pile shaft (inner stirrups) and farther from the pile shaft (outer stirrups). For 4 branches stirrups, strain in exterior and interior branches for outer and inner stirrups was also monitored.

- The pile cap's plate strain.

- The failure mode and the crack pattern.

The results for beam C1 are presented in figures 7-8 to 7-12, which compare the recorded results from the experimental study (EXP.) and the finite element analysis (FEA). Figure 7-8 demonstrates that the numerical and experimental load displacement curves are in excellent agreement, however, after the ultimate load, the predicted softening curve was slightly different from the observed experimental results. Figure 7-8 also demonstrates the accuracy of the calculated first cracking load, the breakout cracking load, and the ultimate load. Similarly, Figure 7-9 shows the accurate strain predictions in all longitudinal reinforcement bars. The numerical model also captured the release of strain in the longitudinal reinforcement after the stirrups yielded and concrete cover spalling occurrence. In addition, Figure 7-10 demonstrates the excellent match between the

317

calculated and measured stirrups strains. Also, the strain of the pile cap's plate was fairly predicted by the finite element model as shown in Figure 7-11. Finally, the crack patterns of beam C1 recorded experimentally is compared with the predicted crack pattern in Figure 7-12. It is clear from Figure 7-12 that the finite element model was able to correctly predict the crack patterns for flexural and breakout cracking even with approximately the same angles.

The same excellent agreement was observed through the comparison of the numerical predictions and experimental results for the remaining 8 samples. These results are included in Appendix D.
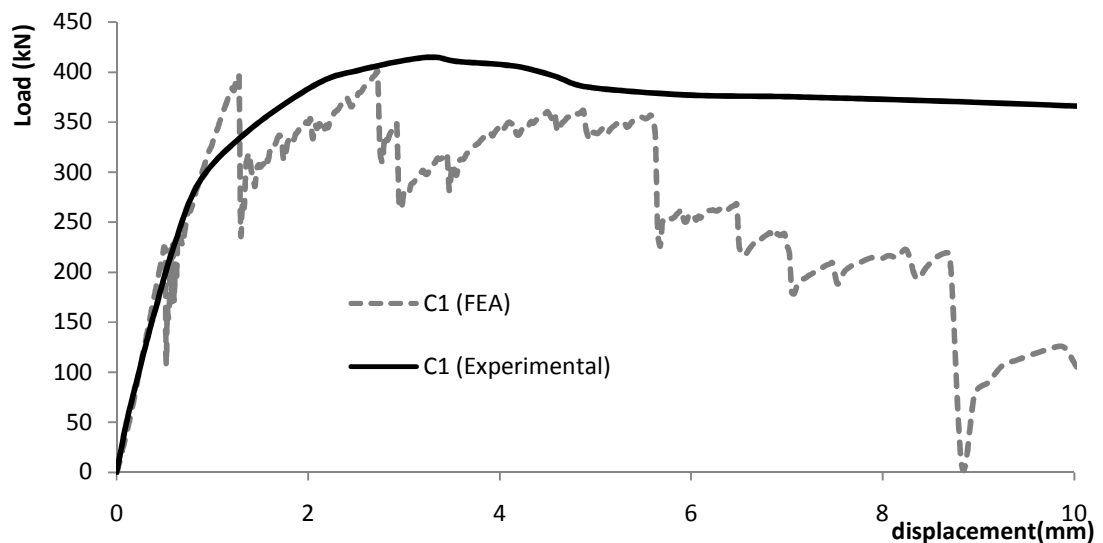
Figure 7- 8 Load mid-span displacement from experimental test and finite element model for beam C1

318
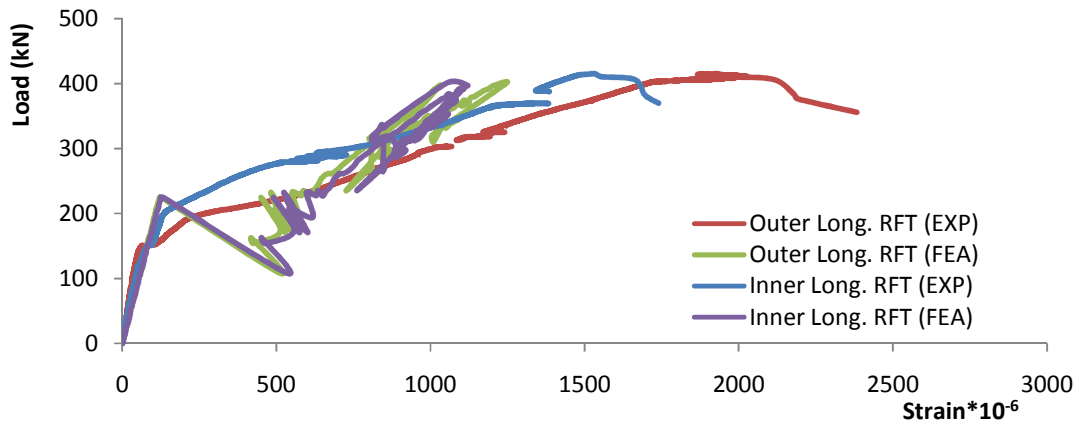
Figure 7- 9 Load longitudinal reinforcement strain from experimental test and finite element model for beam C1
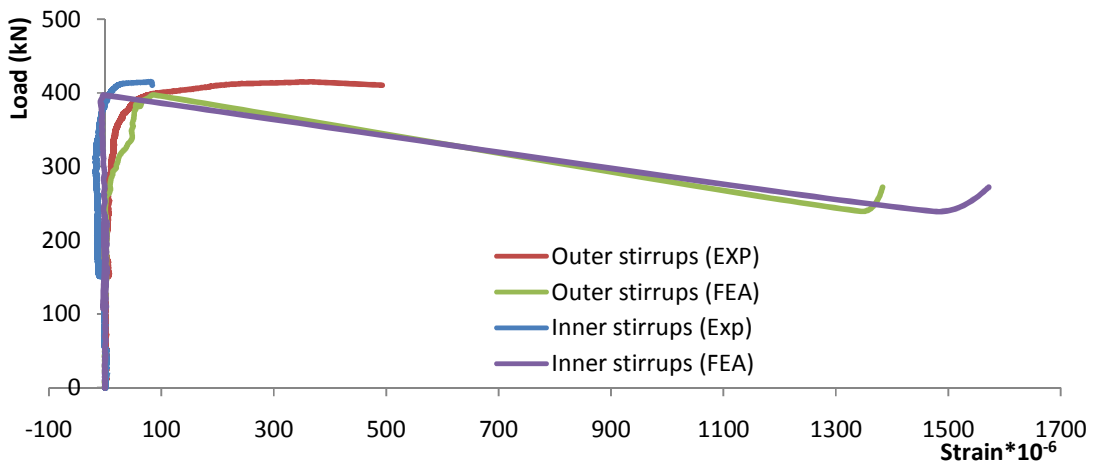
Figure 7- 10 Load stirrups strain from experimental test and finite element model for beam C1
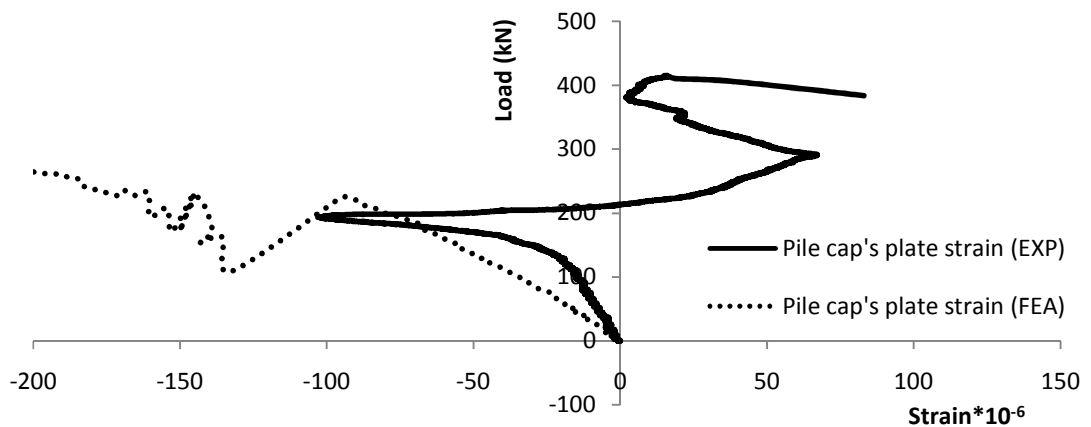
Figure 7- 11 Load pile cap plate strain from experimental test and finite element model for beam C1

319
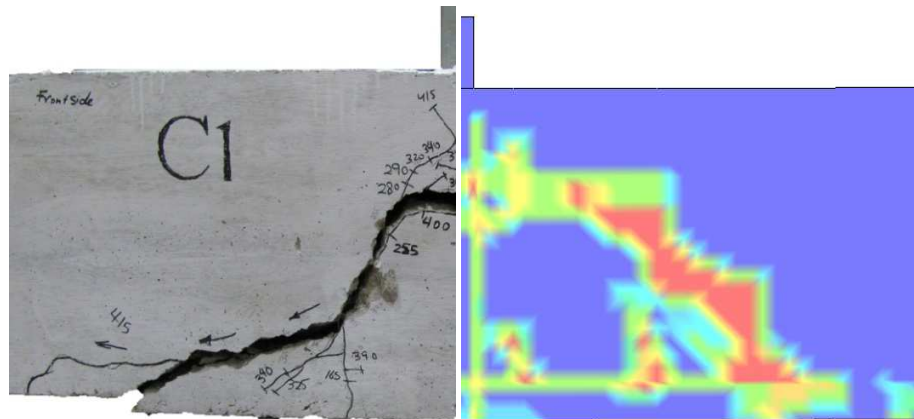
Figure 7- 12 Crack patterns from experimental test and finite element model for beam C1

7.13 Verification of numerical model using published experimental results

The same finite element variables were used to analyze the experimental work reported by Angelakos et al. (2001). They investigated the influence of concrete compressive strength and minimum stirrups on the shear response of large lightly reinforced concrete members. The test beams DB120, DB130 and DB140 were analyzed using the finite element model described above. The full beams were modeled using 8-node hexahedron solid constant-stress elements with three displacement degrees of freedom at each node with one integration-point and element side of 60 mm. The concrete material variables were calculated using the procedure of Magallanes (2010) and CEB-FIP model code (1990). The calculated load-displacement curves for the three beams are compared with the measured responses from the experimental work of Angelakos et al. (2001) in Figure 7-13. It is noted from Figure 7-13 that the initial stiffness and the beam stiffness reduction due to flexural cracking were predicted accurately; however, it did not capture

accurately the beam softening after the ultimate load. Finally, the finite element model predicted the crack patterns extremely well.

The excellent agreement between the finite element model predictions and the experimental results confirms the ability of the numerical model to correctly simulate the behavior of reinforced concrete beams. Hence, it can be employed to examine the new construction bracket in an extensive parametric study to cover a range of parameters outside what was considered in the experimental study.
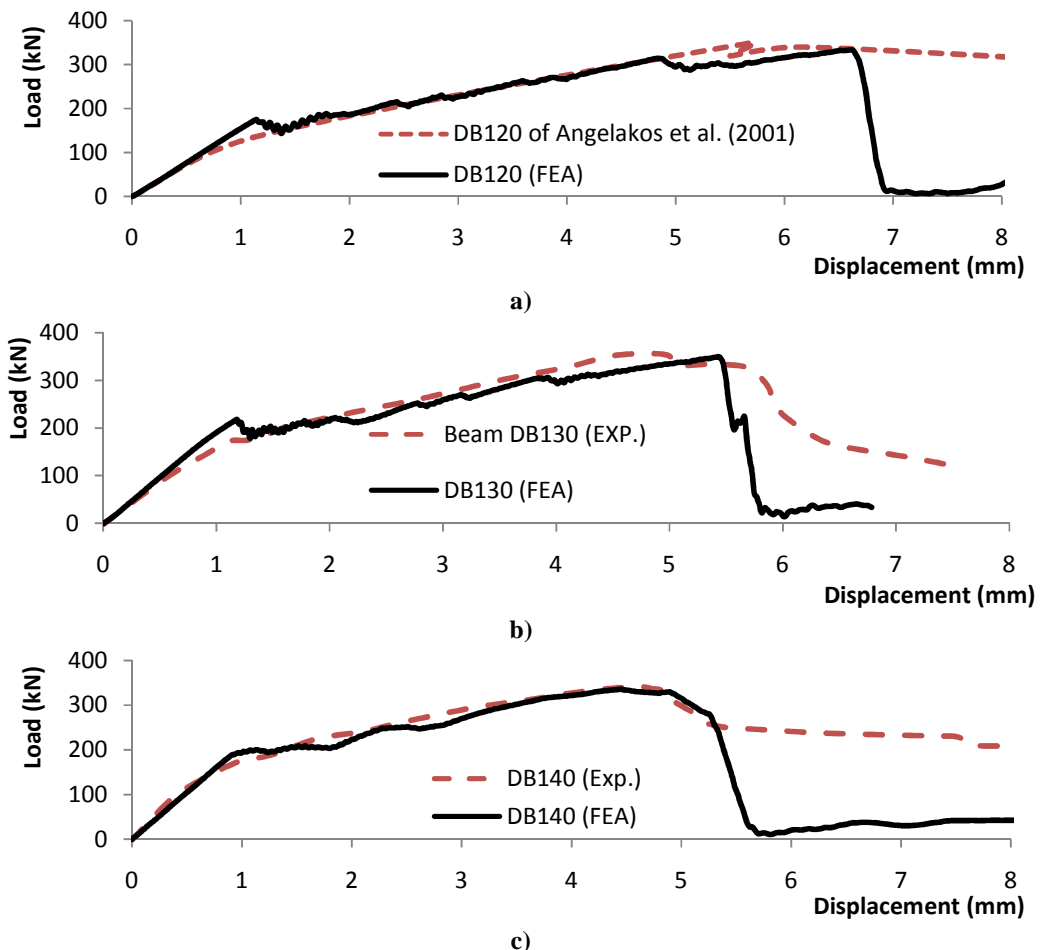
Figure 7- 13 Load mid-span displacement curves for: a) DB120; b) DB130; and c) DB140

7.14 Numerical Parametric Study

The verified 3-dimensional finite element models are utilized to simulate the behaviour of the connection between the pile shaft and the grade beam using a bolted pile cap detail or a welded pile cap detail. In order to cover the range of connection parameters used in practice, both pile cap and concrete beam dimensions and strength properties were varied and their impact on the connection performance was evaluated.

7.14.1 Factors investigated in parametric study

The parametric study investigated the connection performance considering the following factors: pile and pile cap parameters; concrete beam parameters and pile-beam connection parameters. The pile and pile cap parameters included: pile shaft embedment depth and pile cap configuration (bolted or welded). The concrete beam parameters included: longitudinal and transverse reinforcement, anchor reinforcement, concrete strength, shear span/depth ratio (i.e. a/d ratio) and beam width. The pile-beam connection parameters included: position of pile shaft in respect to supports location, corner effect and supports direction (one way or two way supports). All specimen data used in this parametric study are listed in Appendix E.

7.15 Discussion of results

For each investigated parameter, several models were analyzed. The connection breakout cracking and ultimate loads, load-displacement relationship, crack pattern, and mode of failure are the main comparison criteria that are used in the discussion of their results.

7.15.1 Specimens experimentally tested and used in the finite element investigation for comparison

To ensure that the finite element model is expecting a realistic data, most of the groups studying the factors affecting the pile connection will have one or more of the beams experimentally tested. The parameters of these experimentally tested beams are shown in table 7-2 and figure 7-14 summarize their dimensions and details.

Table 7- 2 Details of studied experimentally tested Specimens

Beam Name	Beam Dimensions (mm)	Concrete Strength fc'(MPa)	The remaining depth (mm)	Pile cap width (mm)	Longitudinal Reinforcement	Stirrups
C1	500x500x1600	30	330	165	4-20M	2 branches #2@200mm
C2	500x500x1600	30	277	165	4-15M	2 branches #2@200mm
C3	500x500x1600	30	289	165	4-15M	2 branches #2@200mm
C4	500x500x1600	30	277	190	4-15M	2 branches #2@200mm
C5	500x500x1600	30	277	229	4-15M	2 branches #2@200mm
C6	500x500x1600	30	277	165	4-20M	2 branches #2@200mm
C7	500x500x1600	30	277	165	4-25M	2 branches #2@200mm
C8	500x500x1600	30	277	165	4-15M	4 branches #2@200mm
C9	500x500x1600	30	277	165	4-15M	2 branches #2@100mm

Figure 7- 14 Dimensions and full details for the tested specimens

7.15.2 Influence of pile embedment depth

Two additional pile embedment depth values were investigated and the other variables of beam C2 (control beam) were kept constant. The remaining depth, d_{rem}, under the pile cap (i.e. beam height minus embedment depth and pile cap's plate thickness) was the main variable in this group. The investigated beams are denoted C-Dr-210 (d_{rem}=210 mm) and C-Dr-176 (d_{rem} = 176 mm). Figure 7-15 presents the calculated load-displacement curves along with the experimental results for the corresponding test beams. It can be noted from Figure 7-15 that first flexural cracking load was approximately the same for all beams. Afterwards, the connection stiffness and ductility increased as the remaining depth increased (i.e. the pile embedment depth decreased). Figure 7-16 demonstrates that the connection ultimate load increased as the embedment depth decreased.
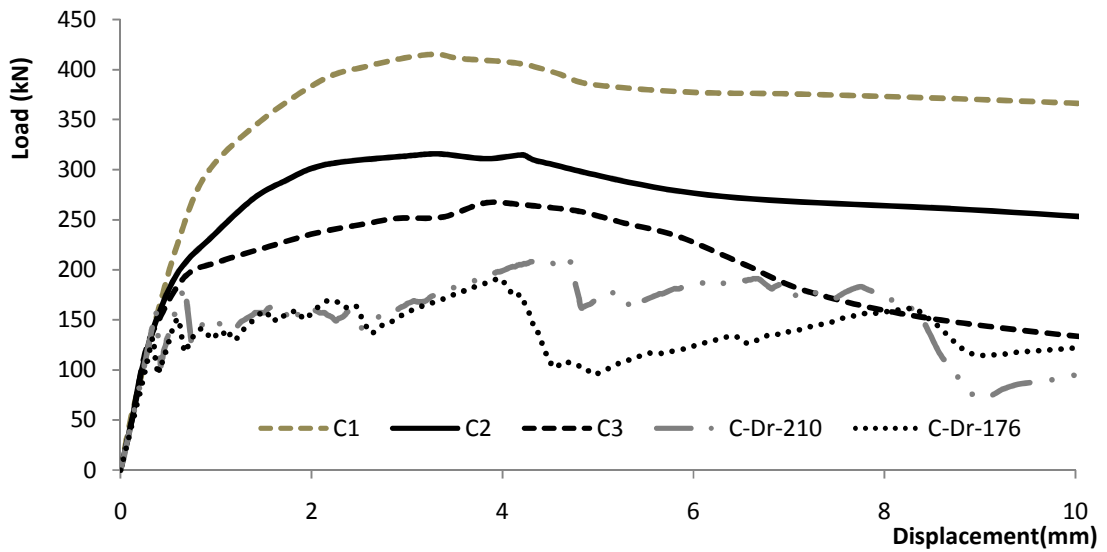
Figure 7- 15 Effect of pile embedment depth on load mid-span displacement curve for (a/d)=1.6
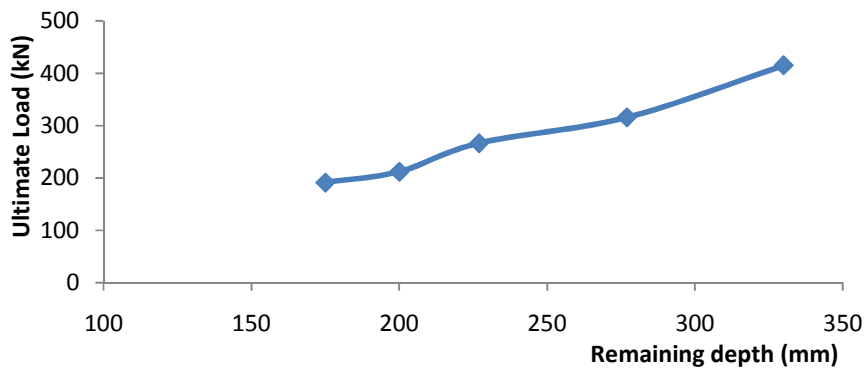
Figure 7- 16 Effect of pile embedment depth on connection load capacity for (a/d)=1.6

Three beams with different shear span to depth ratio (i.e. a/d =2.5) and different longitudinal reinforcement (4-25M) with the same other variables of beam C7 were investigated. The studied beams are denoted C-Dr-277 (d_{rem} =277 mm), C-Dr-227 (d_{rem} = 227 mm), and C-Dr-176R (d_{rem} =176 mm). Figure 7-17 shows the same behavior, i.e. first flexural cracking load was approximately the same for all beams. After cracking

325

occurred, the connection stiffness and ultimate load increased as the remaining depth increased.
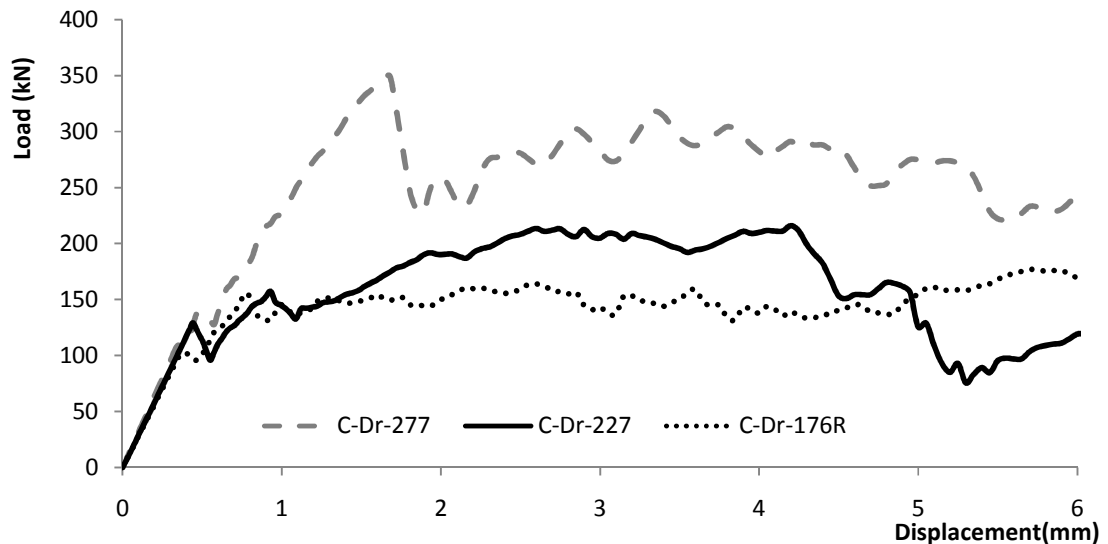
Figure 7- 17 Effect of pile embedment depth on load mid-span displacement curve for (a/d)=2.5

7.15.3 Influence of longitudinal reinforcement ratio

In this group, six beams with different values of steel reinforcement ratios were investigated for two different shear span to depth ratios (a/d). Four bars were used in all analyzed cases, but the bar designation were changed. 10M, 15M, 20M, #7, 25M, and 35M were used in beams C-B-10, C2, C6, C-B-7, C7, and C-B-35 , respectively for (a/d)=1.6 using the same variables of beam C2 except its longitudinal reinforcement. The longitudinal reinforcement was equivalent to the longitudinal reinforcement ratios of 0.18%, 0.36%, 0.53%, 0.69%, 0.89%, 1.78%, respectively.

Figure 7-18 displays the load mid-span displacement curves for these beams. It is noted from Figure 7-18 that the stiffness was almost the same for the investigated connections

326

until first cracking occurred. After cracking, the stiffness of the connection and its ability to absorb energy increased as the longitudinal reinforcement ratio increased.

The influence of longitudinal reinforcement ratio on the connection ultimate load using (a/d=1.6) is clear in Figure 7-18. It is noted from the figure that the connection ultimate load capacity increased as the longitudinal reinforcement ratio increased.
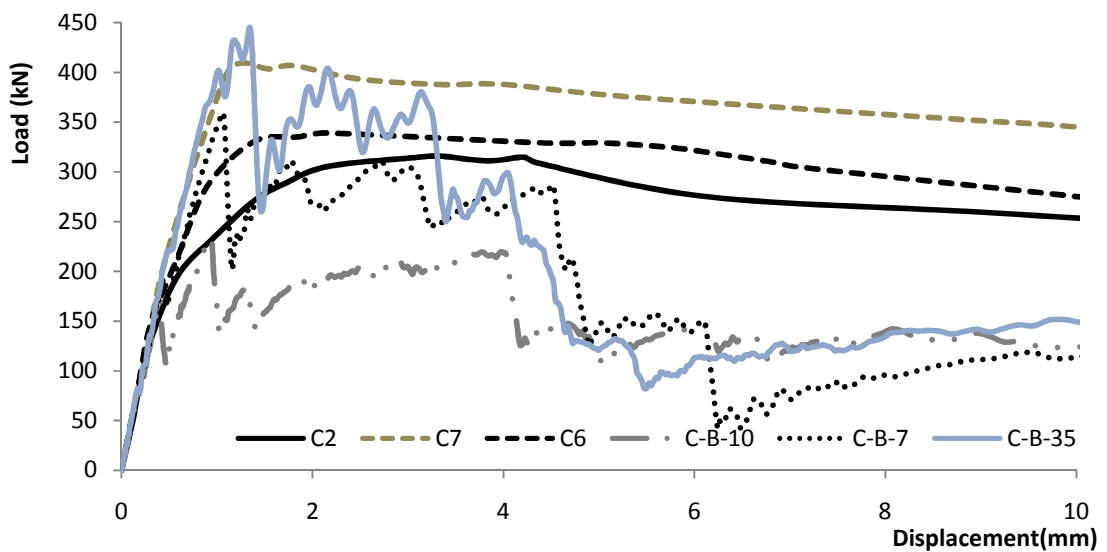
Figure 7- 18 Load mid-span displacement curves for (a/d=1.6)

To further investigate the longitudinal reinforcement effect, three beams with (a/d = 2.5) reinforced with 4-15M, 4-20M, and 4-25M (denoted C-B-15R, C-B-20R, and C-B-25R) were analyzed. Figures 7-19 and 7-20 indicate that with different (a/d) ratio the same finding was observed: the longitudinal reinforcement increased the connection stiffness after the first cracking load and increased the connection breakout and ultimate loads. Furthermore, Figure 7-20 shows that for the same beam and longitudinal reinforcement ratio, the connection ultimate load decreased as (a/d) increased.

327
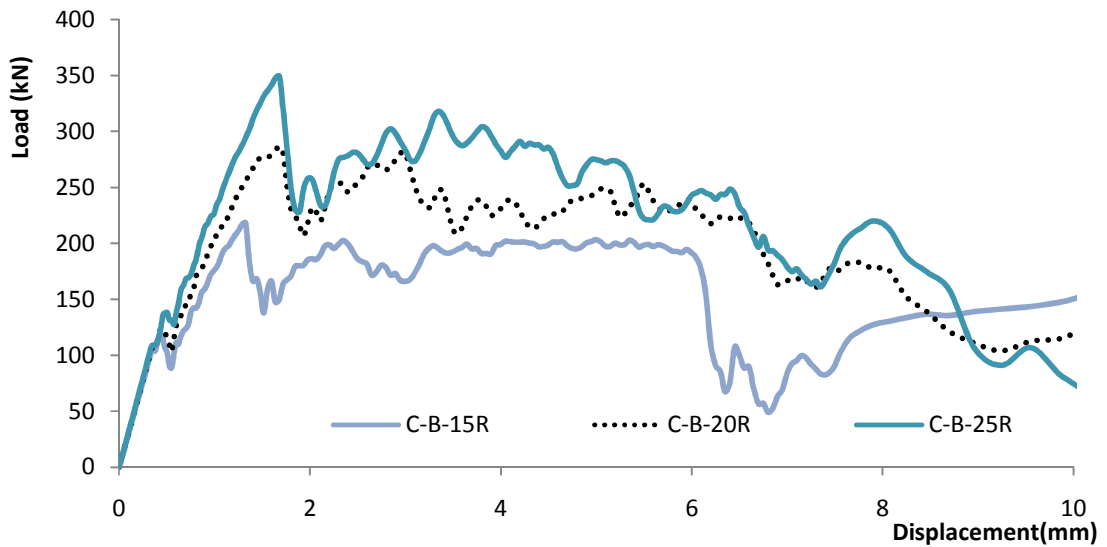
Figure 7- 19 Load mid-span displacement curves for (a/d=2.5)
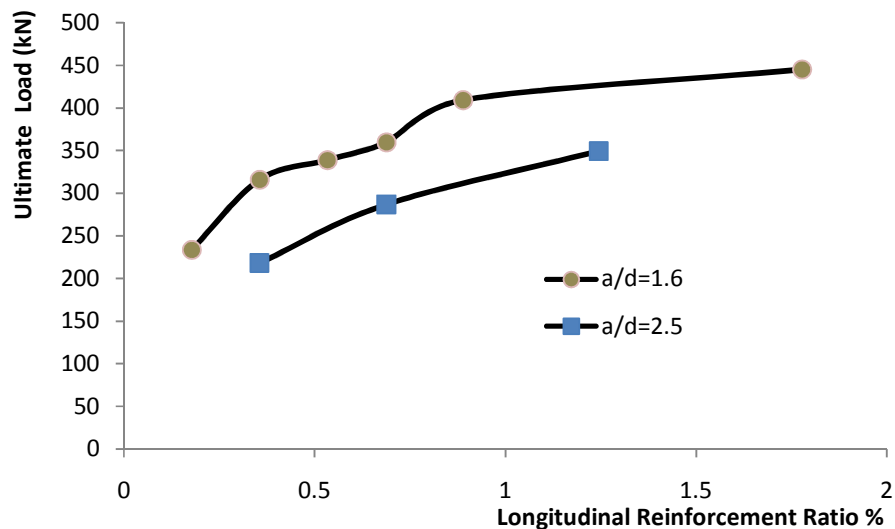
Figure 7- 20 Influence of longitudinal reinforcement ratio on the connection ultimate load for different (a/d) ratios

7.15.4 Influence of transverse reinforcement ratio and configuration

The effects of transverse reinforcement on the connection performance were investigated considering closed stirrups with different bar designations, stirrups' spacing and number

of branches in each stirrup. In addition, a beam without any stirrups, denoted C-S-0, was considered. The following stirrups arrangements were investigated: 2br. #2@ 200 mm, 2br. 8mm@200 mm, 2br. #2@100 mm, 4br. #2 @200 mm, 2 br. 10M @200 mm, 2br. 8 mm @100 mm, 4br. 8 mm@200 mm, 2br. 15M @200 mm, 2br. 10M@100 mm, 4br. 10M @200mm, 2br. 15M @100mm, and 4br. 15M @200mm. All beams were considered to have concrete with fc'= 30 MPa and fs_y = 430 MPa. The stirrups effects on the connection performance were investigated in terms of the connection behavior versus that of a beam subjected to regular three-point direct loading. In addition, the effects of the stirrups configuration with varying reinforcing ratio and stirrups configuration with same reinforcing ratio on the connection performance were evaluated.

Figure 7-21 shows the load-displacement response for a beam directly loaded on its extreme fibers and subjected to three-point direct loading with and without stirrups compared to the same beam loaded using the pile connection with and without stirrups. The used stirrups in the directly loaded beam was 2 br#2@200mm. The beam failed in flexure under three-point loading as shown in Figure 7-22 (b), however, the same beam without stirrups loaded through the pile connection and with the same variables experienced significant reduction in its load capacity of about 57% of the beam capacity without the pile connection. It can be concluded from Figure 7-21 that higher transverse reinforcement ratio (e.g. when using 4br.-10m@200 mm) increases the connection ultimate load, however, the connection capacity and beam stiffness will always be less than that obtained from 3-point loading for the same displacement. A premature failure was recorded in beam C-S-0 as shown in Figure 7-22 (a). This failure occurred just after

the formation of the breakout crack when the flexural cracks reached the bolt level. This crack extended at the longitudinal reinforcement level to the supports causing loss of bond in the longitudinal reinforcement. Thus, even if the expected failure of the beam under three point direct loading was due to flexural, loading through a pile connection changed both the failure mechanism and the beam behaviour. In brief, the higher the transverse reinforcement ratio, the closer the connection behaviour to the full beam (i.e. the beam directly loaded on top) without connection behaviour, and it is unsafe to not consider the connection capacity as a limit state when designing the foundation connected to the pile shaft.
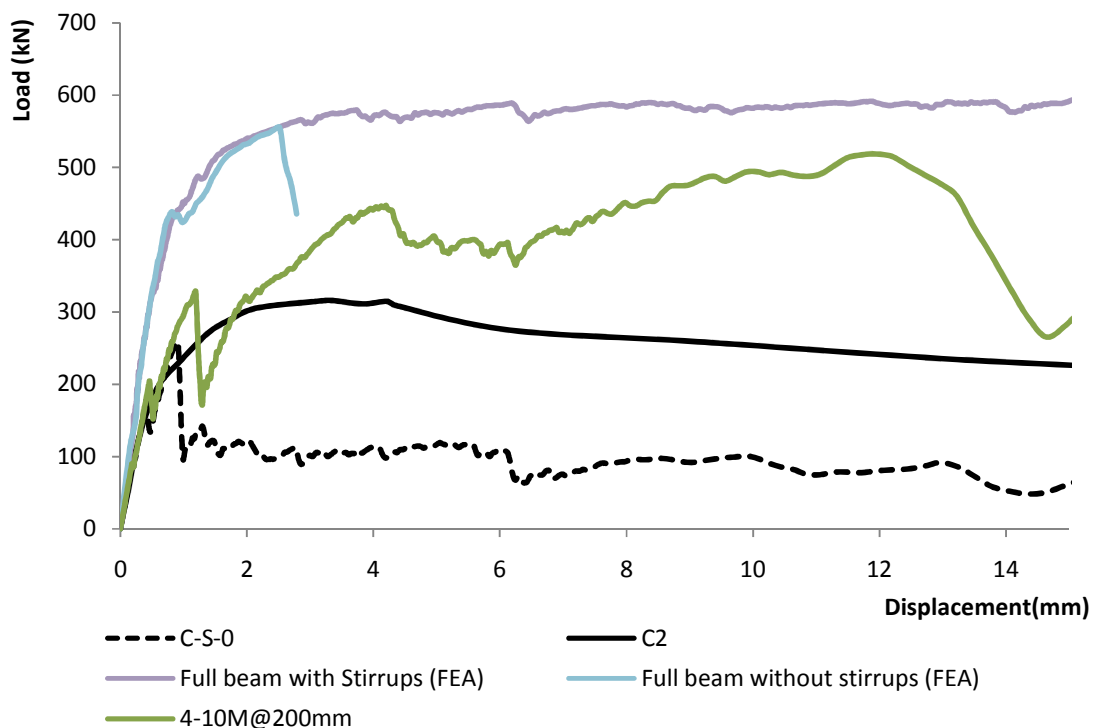
Figure 7- 21 Load mid-span displacement response

a)

b)
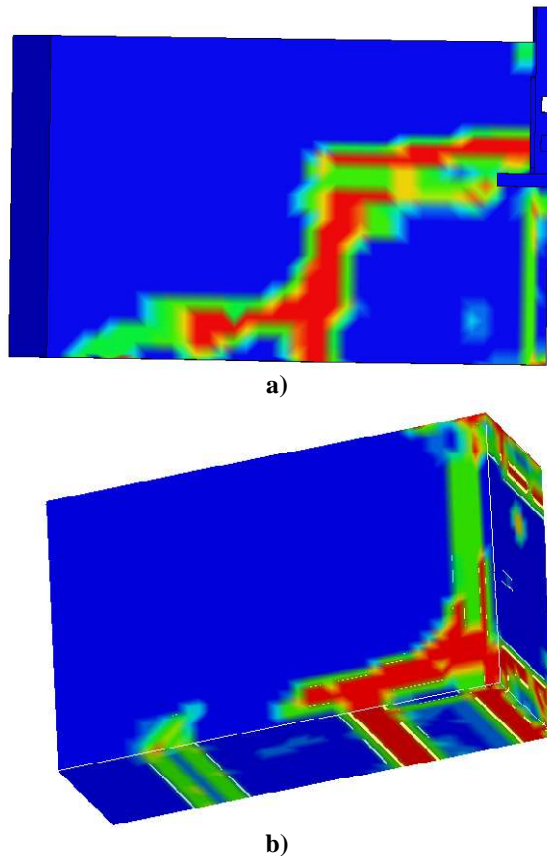
Figure 7- 22 Crack pattern: a) loaded through pile connection without stirrups; b) full beam directly loaded on its extreme fibers and subjected to 3-point loading

Figure 7-23 presents the load-mid span displacement response for stirrups with different diameter but same spacing and number of branches. This figure shows that the same initial stiffness was recorded from the four investigated beams and the difference in the behaviour began after the initiation of the breakout cracking load when the stiffness began to change according to the transverse reinforcement ratio. The higher the transverse reinforcement ratio the higher the beam stiffness would be, but still much less than the directly loaded beam. Also, increasing the transverse reinforcement ratio increased the connection capacity and the higher the transverse reinforcement ratio, the closer the connection behaviour to the directly loaded beam behaviour.

331
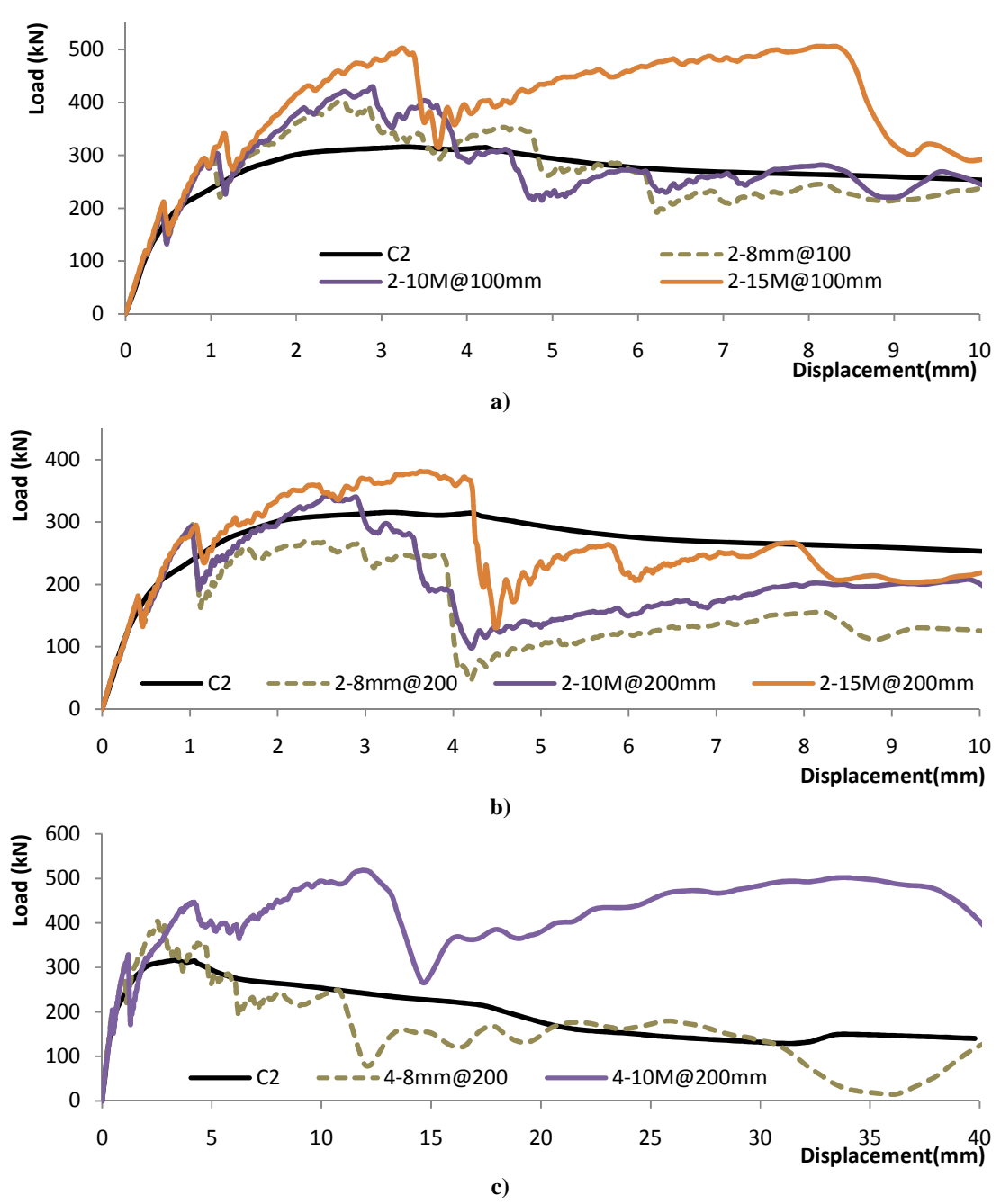
Figure 7- 23 Load mid-span displacement response for stirrups: a) 2br@100 mm spacing; b) 2br@200 mm spacing; and c) 4br@200 mm

Figure 7-24 demonstrates the load-mid span displacement response for beams with the same transverse reinforcement ratio but with different stirrups configuration. It shows clearly that using more branches in each stirrup close to the pile shaft can achieve higher connection ultimate load and higher connection stiffness after the breakout cracking load. It is clear that using more branches near the pile shaft enhances the beam integrity as it engages the stirrups contribution with the dowel action of the longitudinal reinforcement and the concrete aggregate interlock at the location of the highest strains and widest opening. It was observed that if the connection ultimate load was at a small mid-span displacement, this load value was produced from the four contributions of the concrete aggregate interlock, the dowel action of the longitudinal reinforcement, the stirrups, and the pile-concrete friction. On the other hand, if ultimate load occurred at large displacement at the ultimate load, it would be equal to the stirrups vertical tensile capacity plus the pile-concrete friction load. Also, it was observed that the pile-concrete friction load was around 10-20% of the connection capacity at its ultimate load. Thus, ignoring the pile-concrete friction contribution would underestimate the connection capacity by up to 20%.

Another investigation was conducted for the same beam but with (a/d) = 2.5 and longitudinal reinforcement of 4-25M. Three transverse reinforcement bar diameters with 2 branches spaced at 200 mm were considered: 2br. 8mm@200 mm, 2 br. 10M @200 mm, and 2br. 15M @200. Figure 7-25 shows the load mid-span displacement response recorded for those three beams. It confirms that the transverse reinforcement ratio can increase the connection ultimate capacity and enhance the connection behaviour greatly.
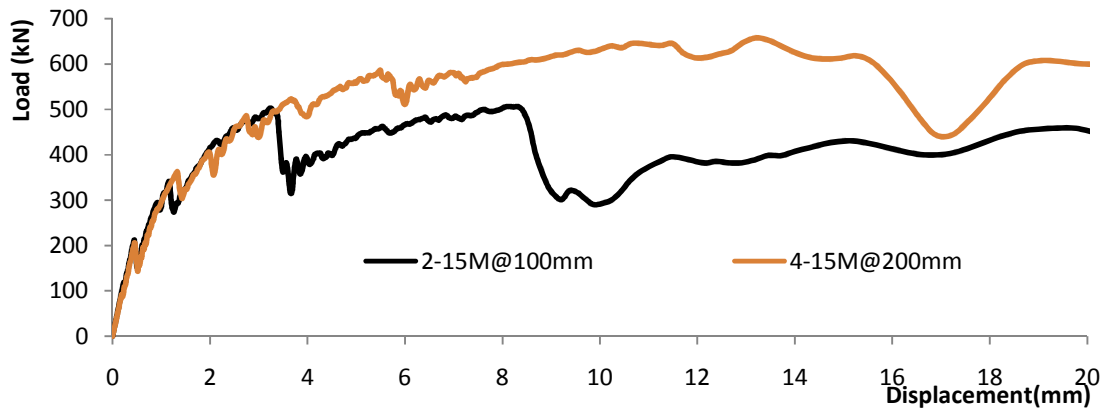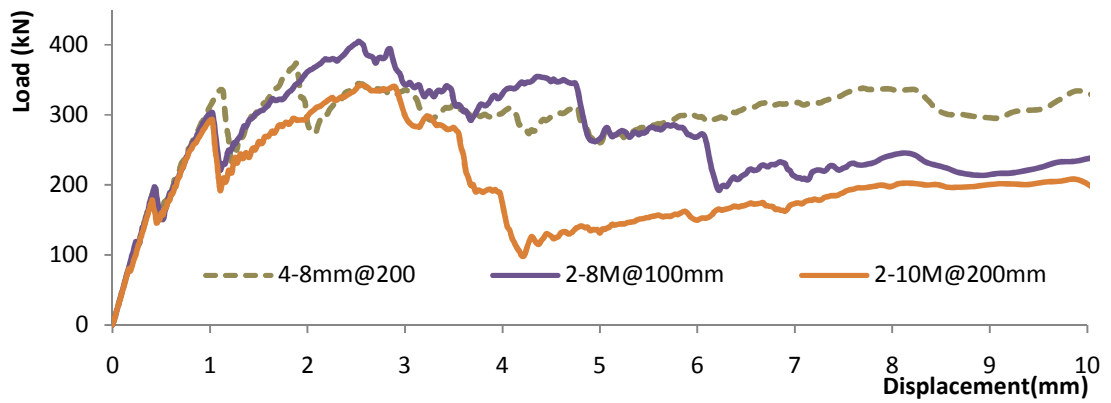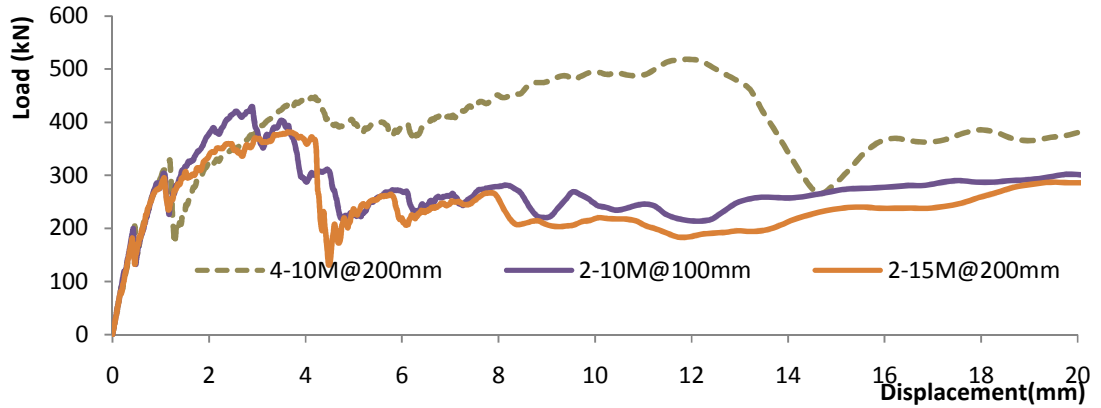
Figure 7- 24 Load mid-span displacement response for same transverse reinforcement ratios with different configurations: a) 0.8%; b) 0.2%; c) 0.4%
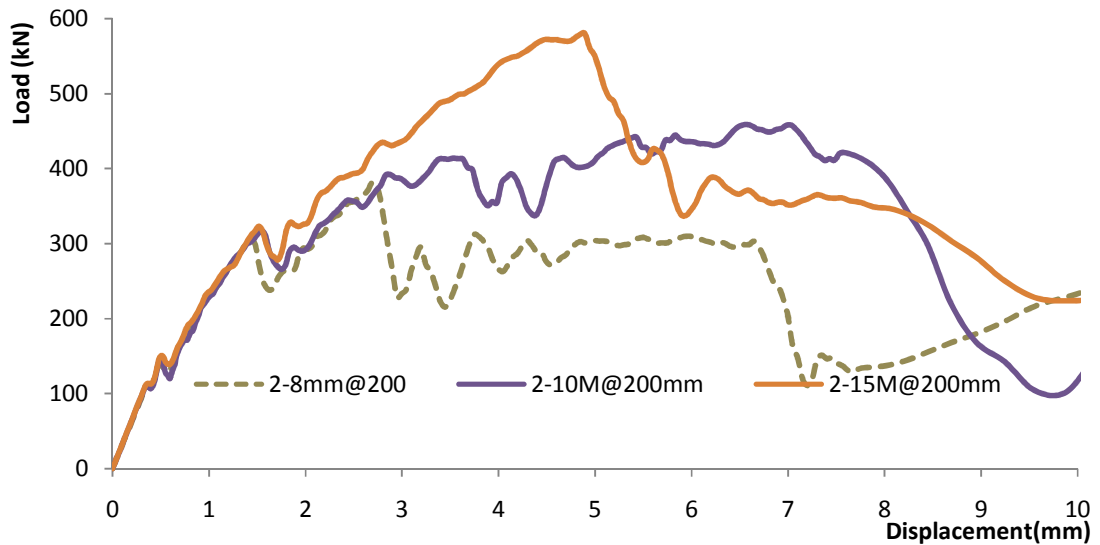
Figure 7- 25 Load mid-span displacement response (a/d=2.5) and 4-25M longitudinal reinforcement

Figure 7-26 shows the recorded ultimate loads for the investigated beams with different configurations and (a/d) ratios. It indicates that increasing the transverse reinforcement ratio for the same beam increases the connection ultimate load. Also, it indicates that the different configurations of the transverse reinforcement for the same transverse reinforcement ratio has a direct effect on the connection ultimate load as there are different ultimate loads for the same transverse reinforcement ratio and the more stirrups next to the pile shaft the more connection ultimate load was recorded. For connections with ultimate load equal to the directly loaded full beam ultimate capacity (i.e. the beam loaded by bearing on its top fibers as 3 point loading), increasing the transverse reinforcement will not increase the connection capacity. This is clear when the transverse reinforcement ratio $\geq 0.8\%$, the connection ultimate load was equal to the ultimate load of the full beam with the same variables. Because the full beam will fail in flexural, the limit

state of the beam ultimate flexural capacity was marked in Figure 7-26 as a limit state for the connection ultimate load.
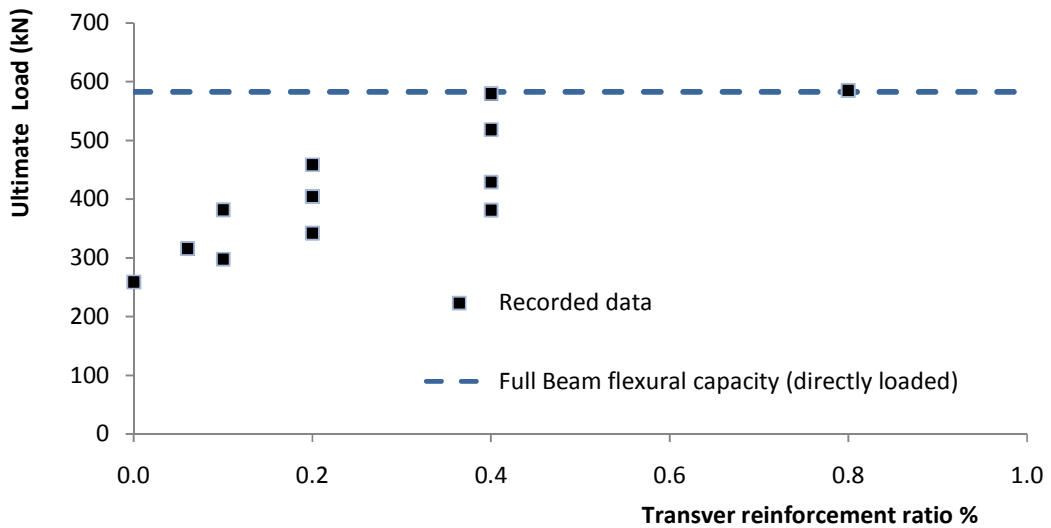
Figure 7- 26 Relation between the connection ultimate load and the transverse reinforcement ratio

7.15.5 Influence of anchor reinforcement

In this group, 6 beams were studied to evaluate the influence of anchor reinforcement on the connection behaviour. All beams had only anchor reinforcement without other transverse reinforcement, i.e. 4 stirrups at the location of the pile shaft, two stirrups from each side, as shown in Figure 7-27. The beams investigated are denoted C-A-6, C-A-8, C-A-10, C-A-15, C-A-20, and C-A-25. They had 4 anchor bars of #2, 8mm, 10M, 15M, 20M, and 25M, respectively. The anchor reinforcement had yield strength of 430 MPa.
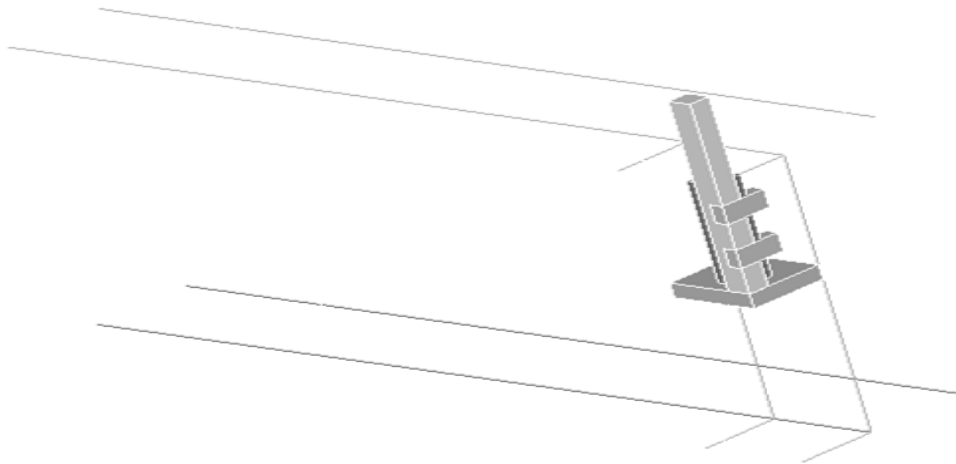
Figure 7- 27 Anchor reinforcement configuration in one quarter of the beam

Figure 7-28 shows the load displacement response of the investigated beams. It shows that as the anchor reinforcement strength increased the connection ultimate capacity increased, and it increased the breakout cracking load slightly. For beams C-A-6, C-A-8, and C-A-10, the connection ultimate load was close to the ultimate tensile capacity of the anchor reinforcement. However, when the anchor reinforcement tensile strength exceeded twice the beam shear capacity (e.g. C-A-15, C-A-20, and C-A-25), the beam failed in shear before the anchor reinforcement and the connection. Thus, increasing the anchor reinforcement more than a specific limit will not increase the connection capacity, as it would be constrained by the beam ultimate capacity. The connection capacity was compared with double the beam shear capacity calculated using Response 2000 as indicated in Figure 7-29.
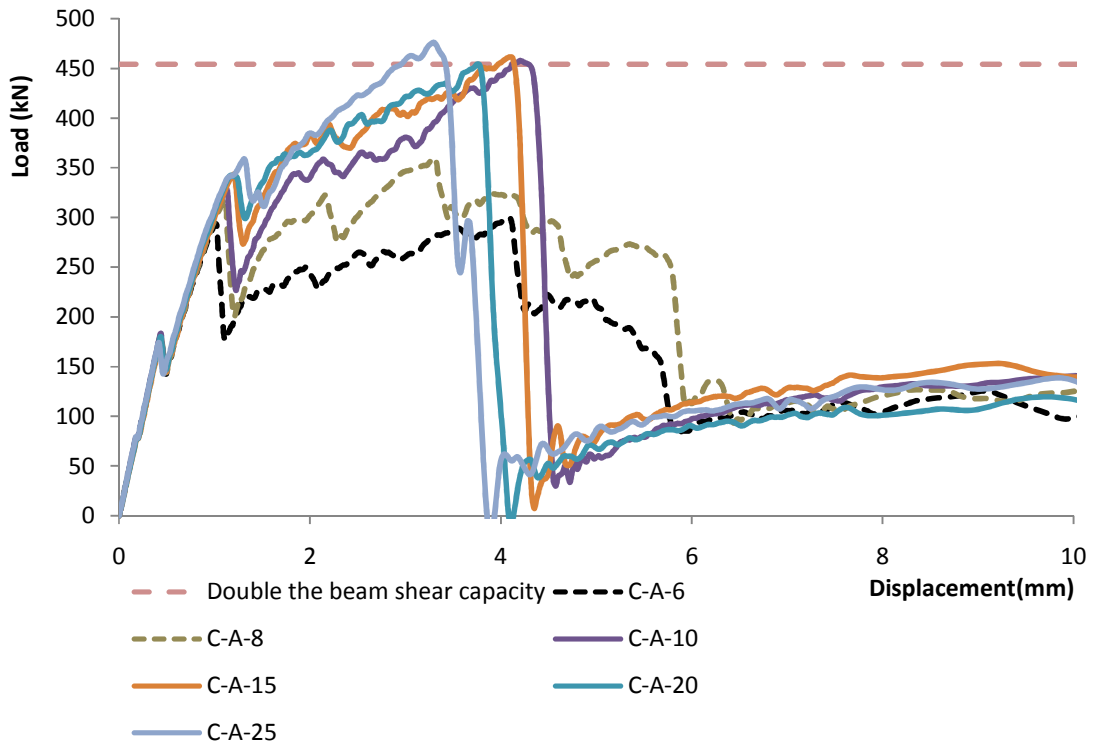
Figure 7- 28 Load mid-span displacement relationship
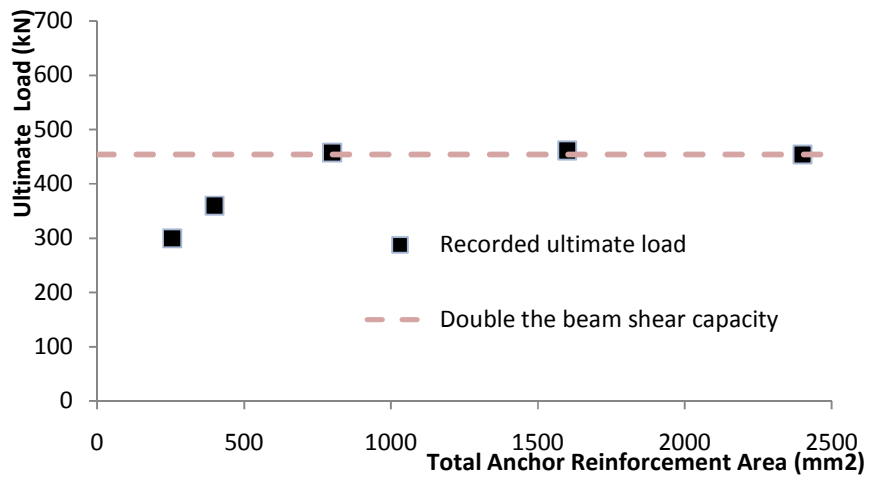
Figure 7-29 Effect of anchor reinforcement area on the connection load capacity

7.15.6 Influence of the concrete strength

Four beams similar to beam C2 were examined, but considering concrete compressive strength, fc' = 20 MPa (C2-20), 30 MPa (C2), 35 MPa (C2-35), and 40 MPa (C2-40). The concrete properties for C2 and C2-40 were the same as the experimental data presented in Appendix A. For beams C2-20 and C2-35, the concrete properties were calculated using the CEB-FIP Model Code-1993. Figure 7-30 presents the load-displacement response for the investigated beams. It shows that the initial stiffness, and first cracking, breakout cracking and ultimate loads increased, while the corresponding displacements decreased by increasing the concrete compressive strength.
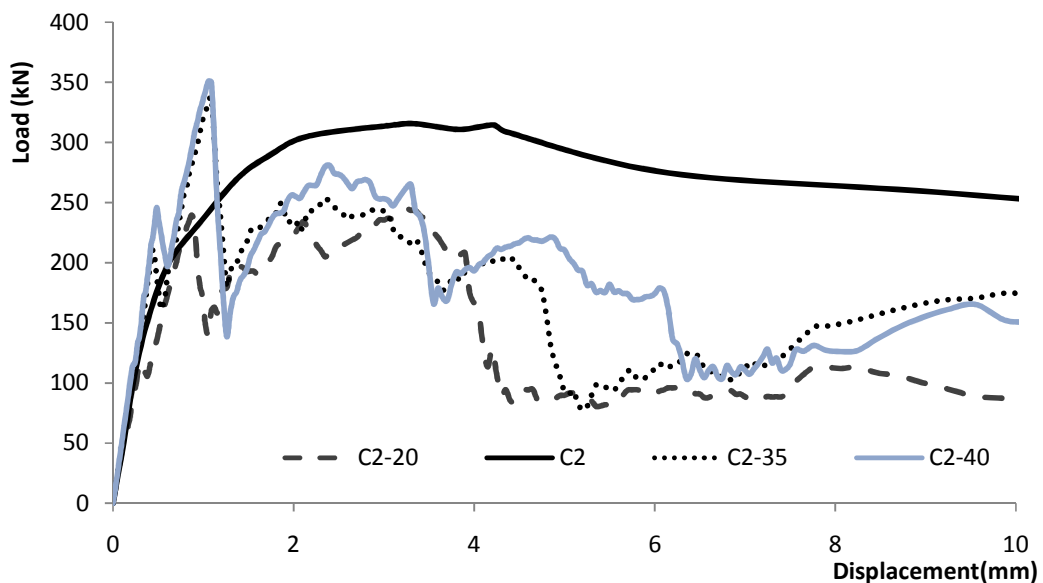
Figure 7- 30 Load mid-span displacement response

7.15.7 Influence of beam' shear span/depth ratio (a/d)

The beam shear span/ depth ratio has a significant influence on the connection behaviour and its expected failure mechanism. For beams with short span, i.e. 1.0 < a/d < 2.5, loads

339

are transferred by arch action, and either shear compression failure or loss of bond failure is expected after cracking. For $2.5 < a/d < 5$ to 6, diagonal tension or flexural shear failure is expected. Finally, for $(a/d) > 5$ to 6, flexural failure is expected (MacGregor, 1988).

Seven beams with (a/d) varying from 0.25 to 2.75 were examined for beams C-R-0.25 to C-R-2.75. The corresponding (a/d_{bolt}) ratio, defined as shear span to concrete depth under the high bolt level, varied between 0.33 and 3.7. The first two beams C-R-0.25, C-R-0.5 behaved like deep beams. All beams were similar to beam C7 (including its 4-25M longitudinal bars), but support location varied according to the used shear span. The analysis was repeated for longer beams considering 12 (a/d) ratios from 0.50 to 5.5 for beams C-R-0.5R to C-R-5.5R. The corresponding (a/d_{bolt}) for theses beams varied between 0.66 and 6. The beam longitudinal reinforcement included 4-30M bars to prevent premature flexural.

The load-displacement response curves for beams with 4-25M and 4-30M bars are presented in Figure 7-31. It is noted from Figure 7-31 that increasing (a/d) ratio decreased the connection breakout cracking load and its ultimate load. Also, the connection stiffness increased with the (a/d) ratio decrease. Figure 7-32 confirms the same finding and indicates that there is a limit state (diagonal tension failure) that was reached when (a/d) exceeded approximately 2.25 for the two different used longitudinal reinforcement ratios. It is also preferred to use another limit state (compression strut failure) when using small ratios of (a/d) as the cracking load did not increase much when the (a/d) ratio was closer

or less than 0.5. This limit state was discussed in ACI 318-99 and a sliding maximum shear strength was specified as $\sqrt{fc'}.\,b.\,d$. It is clear that this limit state should be affected by the longitudinal reinforcement ratio; however, ACI 318 (2008) suggested neglecting the reinforcement' effect and specified that the shear capacity of deep beams shall not exceed $0.83\sqrt{fc'}.\,b.\,d$. In our study, it is preferred to use the higher bolt depth (d_{bolt}) or the remaining depth (d_{rem}) instead of the full beam depth (d) because the compression strut most probably will began under the higher bolt or the pile cap's plate not at the top of the beam. Finally, Figure 7-32 confirms again the influence of the longitudinal reinforcement ratio on the connection behaviour for all (a/d) ratios.

a)
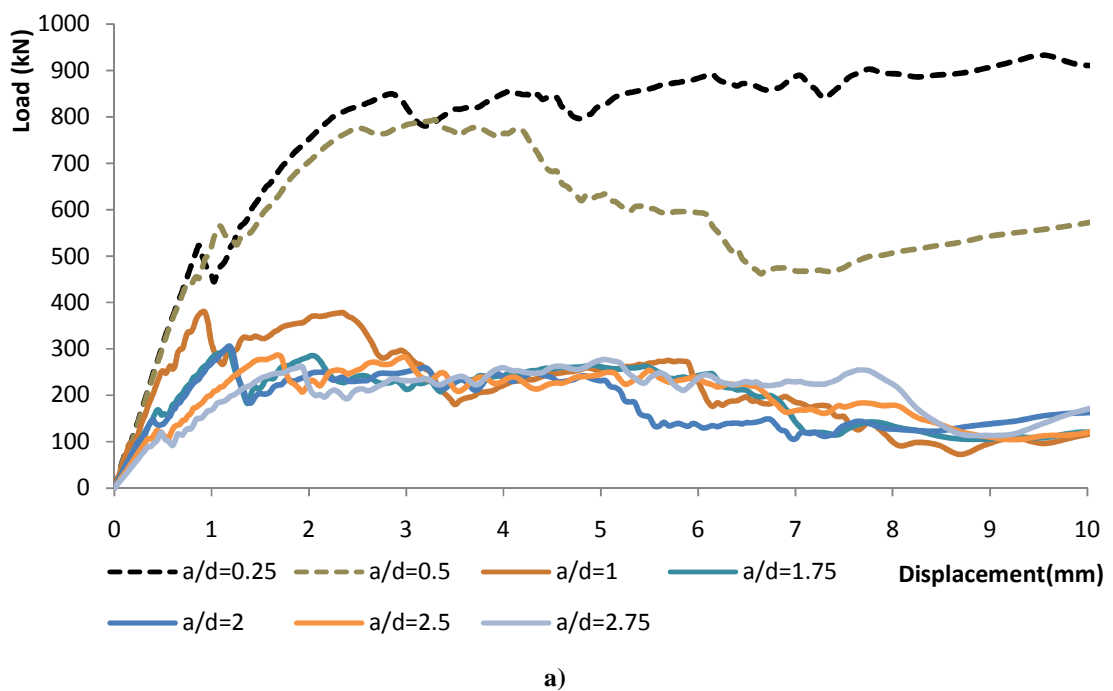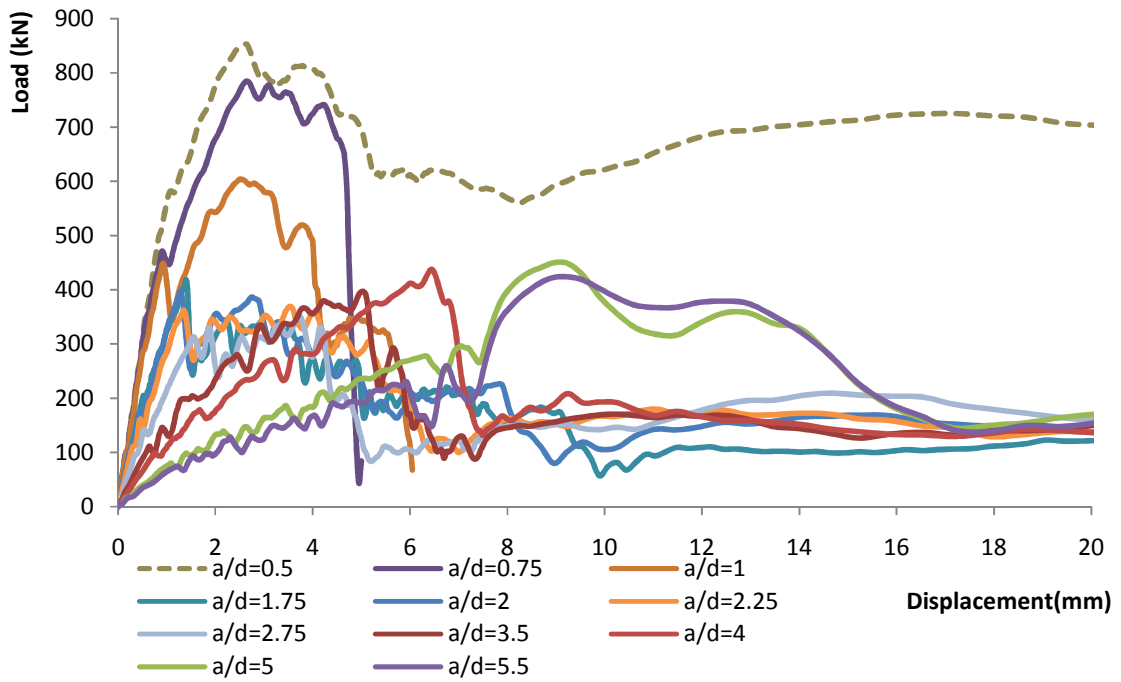
Figure 7- 31 Load mid-span displacement response for different (a/d) ratios: a) using 4-20M longitudinal bars, b) using 4-30M longitudinal bars
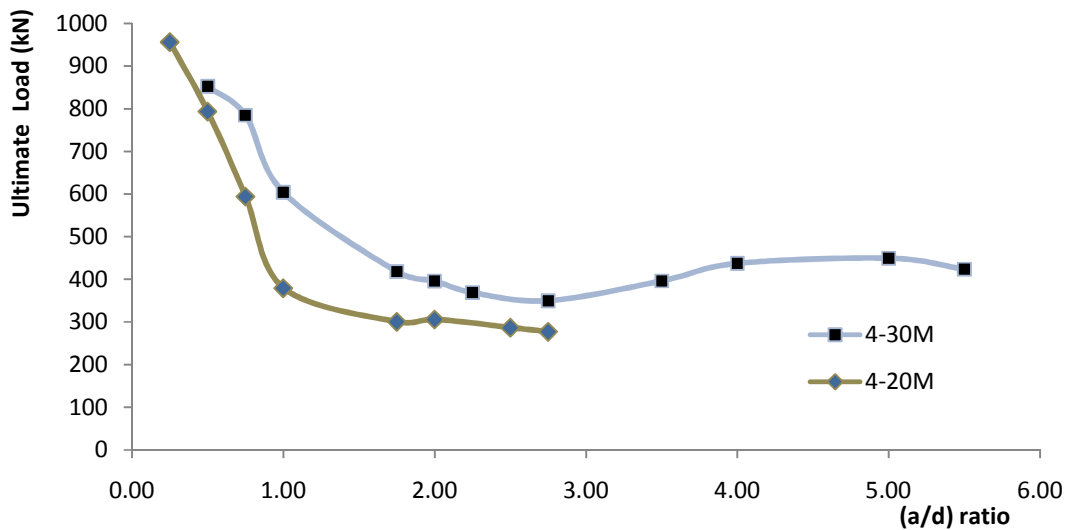
Figure 7- 32 Ultimate load for different (a/d) ratios for two different longitudinal reinforcement

7.15.8 Influence of beam width

To investigate the effect of the beam width on the connection behaviour, three beams were investigated. Beams C-W-800, C-W-1400, and C-W-1600 had widths of 800 mm, 1400 mm, and 1600 mm. Stirrups with f_{sy}=430 MPa were used and the same longitudinal reinforcement was provided in the width direction.

Figure 7-33 displays the crack patterns of investigated beams. In C-W-1400, and C-W-1600, horizontal crack was observed and a diagonal crack propagated in the longitudinal direction. Diagonal cracks then formed in the width direction closer to punching shear, rather than one way shear failure. On the other hand, C-W-800 had only horizontal cracks in the width direction causing one way shear failure as shown in Figure 7-33c.

It may be concluded that there is a width limit at which the limit state of punching shear will govern the behaviour if its capacity is less than the one ways shear strength. This width limit is proposed to be the lesser of $\left(2\sqrt{2}d_{bolt}\right)$ or $\left(2\sqrt{2}d_{rem} + b_{plate}\right)$ using a diagonal crack inclination of 45°. For larger beam width, the failure becomes similar to a punishing shear failure mechanism. This requires experimental verification to investigate the size effect, too.
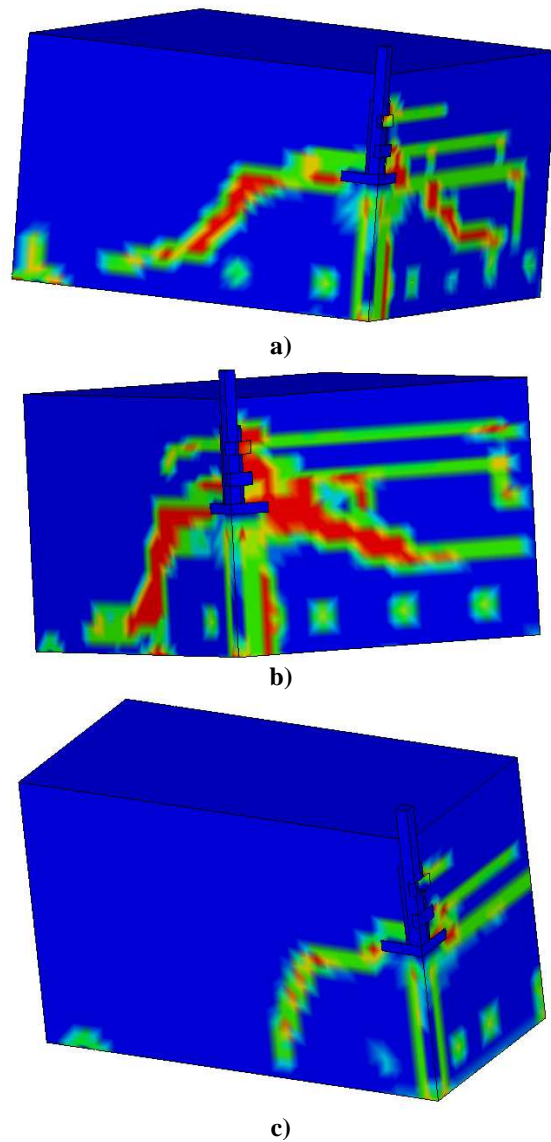
Figure 7- 33 Crack pattern of connections: a) C-W-1600; b) C-W-1400 and c) C-W-800

Figure 7-34 presents the load-displacement response of the examined beams, which shows that the breakout cracking load and the ultimate load increased as the beam width increased.
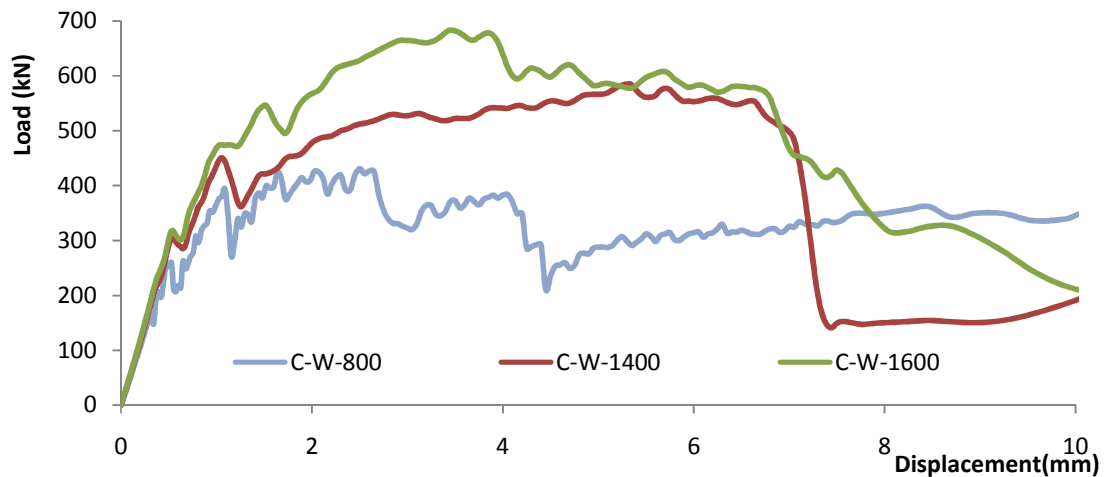
Figure 7-34 Effect of beam width on connection performance

7.15.9 Influence of position of pile shaft in respect to supports' location

The pile shaft may be connected to the grade beam at different locations relative to the supports. In order to examine the effect of pile shaft distance to the support on the connection capacity, two beams with properties similar to C6 but with different (a/d) ratio from each side were analyzed. Beam C-L-0.75 had a short span and the pile shaft positioned such that (a/d) = 1.6 from one side and (a/d) = 0.75 from the other side. Beam C-L-3.8 had a long span and the pile was positioned to achieve (a/d) = 1.6 from one side and (a/d) = 3.8 from the other side.

Figure 7-35 presents the crack pattern of C-L-3.8: (a) at initiation of breakout cracking and (b) at beam failure. Figure 7-35a shows that the angle of the breakout cracking was different on both sides. As (a/d) increased, the angle with the horizontal axis decreased and the diagonal crack closer to the support initiated before the far side. Beam T-L-0.75 displayed the same behaviour. Mostly, diagonal cracking was observed at the side with

345

the smaller (a/d) because it was stiffer and hence the other side yielded under loading.

Moreover, because the pile shaft was not at the mid-span, the shear force distribution in

the beam was not uniform and the side closer to the support carries higher shear force.

Because the bolt depth was higher than half the beam depth (d_{bolt}=352 mm; around 0.78

d) and the shear force was high in the support side, high probability of beam shear failure

occurrence was existed. Thus, the beam itself experienced shear failure when the load

increased as shown in Figure 7-35b.

(a)

(b)
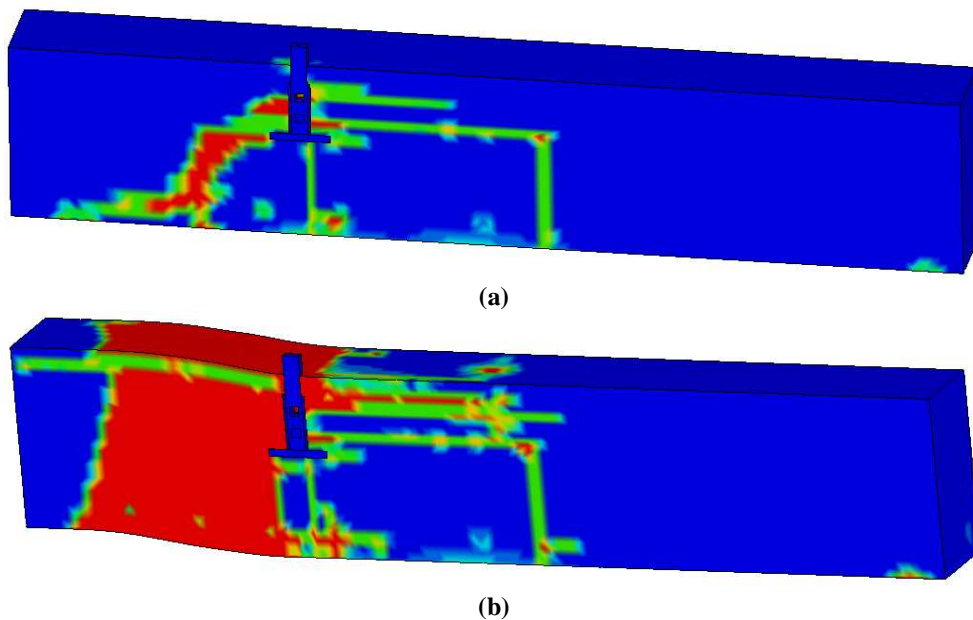
Figure 7-35 Crack pattern of connection in C-L-3.8;

a) Initiation of breakout cracks, b) the beam shear failure

Furthermore, the connection capacity would be compared with the shear capacity of the

beam at the side of the lesser (a/d) ratio multiplied by (L/(L-a)) (i.e. the beam span (L)

divided by the long distance from pile shaft to the support (L-a)). Thus, even if the

connection capacity limit state constitutes the superposition of the both sides' capacities, the beam's limit state design of single shear may govern the failure mechanism.

Figure 7-36 presents the load-displacement response C-L-0.75 and C-L-3.8 compared with the experimental results for C6. It was observed that the lower the (a/d) ratio the higher the ultimate load was observed even the pile shaft in beam C-L-0.75 was not in the mid-span and the failure was due to single shear. Thus, it is so important to have both the limit states of the beam shear failure and the connection capacity in the design procedure of the grade beams especially when the used resisting depth (i.e. resisting depth=d_{bolt} in this case) is more than half the beam depth.
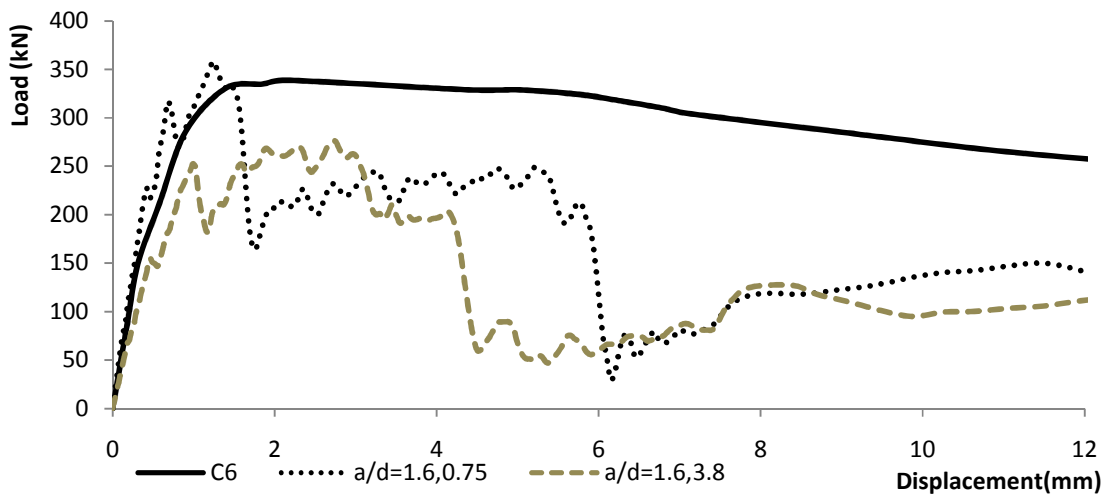
Figure 7- 36 Load mid-span displacement relationship

7.15.10 Influence of pile cap configuration (bolted and welded details)

There are two methods implemented in practice to connect pile cap to helical piles and micropiles: bolted to pile shaft (same as used in the experimental program) with one or two bolts, welded to the pile shaft or pile cap without bolts. In order to investigate the

effect of method used to connect the pile cap to the shaft on the connection performance, beam C2 was modeled twice: once considering a welded connection; and another considering bolted connection using 2-bolts. These models are denoted C2-W and C2-two bolt, respectively. All other variables of beam C2 were kept constant.

Figure 7-37 compares the calculated load-displacement responses of the bolted and welded connections as well as the experimentally measured response of beam C2 (using one bolt). Remarkable change in the behaviour was recorded. The results show that connection breakout cracking and ultimate loads were affected by the change in the connection configuration.
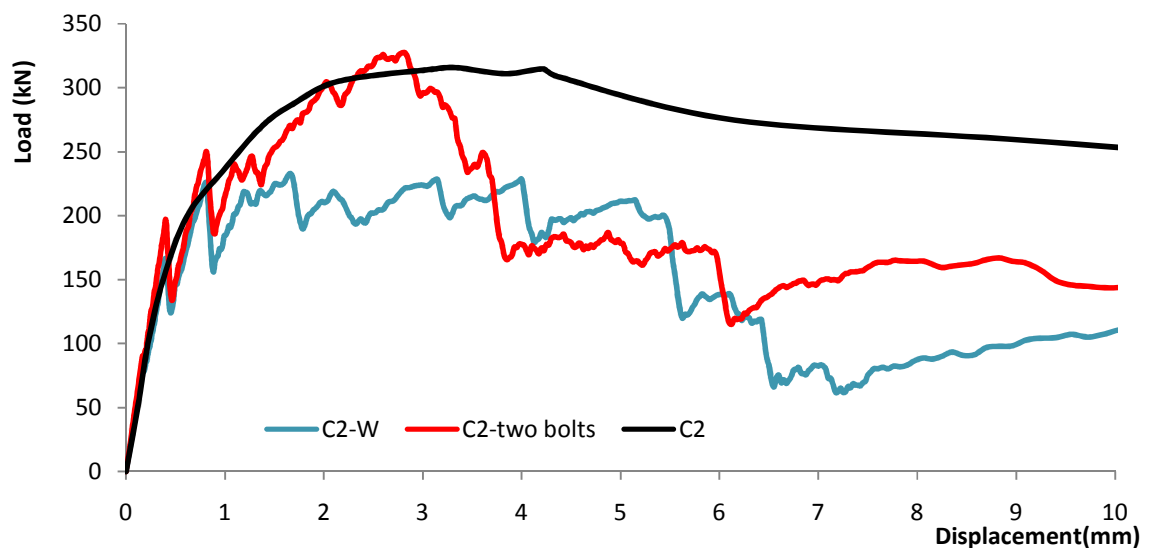
Figure 7- 37 Load mid-span displacement curves for different pile cap configurations for beam C2

As shown in Figure 7-38a, the breakout cone in a welded connection initiated at the tip of pile cap' plate. On the other hand, Figure 7-38b shows that for bolted connection the breakout cone initiated at the top bolt level. As the breakout cone initiated at higher level, the concrete contribution to the connection capacity increased. Similarly, the connection

348

stiffness after the breakout cracks initiation increased for the bolted connection than that of the welded connection.

dr (remaining depth) is governing

a)

d_{bolt} (top bolt depth) is governing

b)
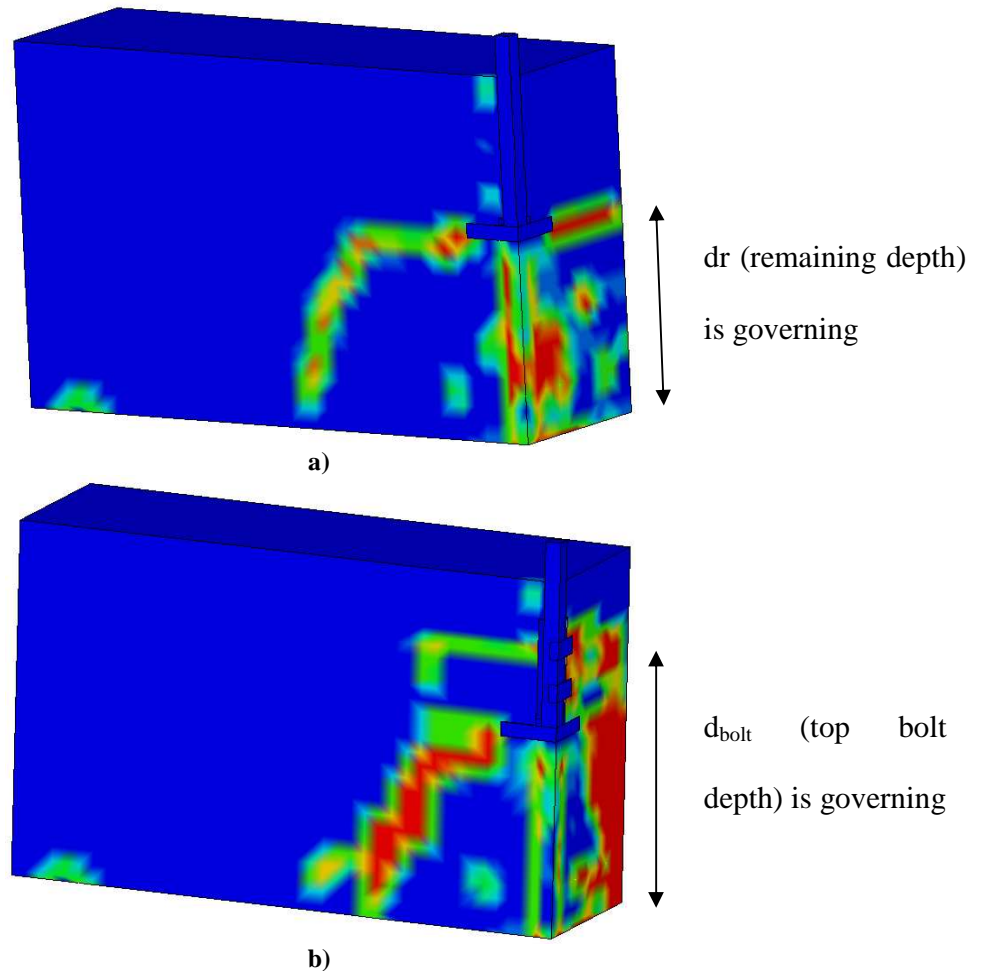
Figure 7- 38 Crack pattern of connection in: a) beam C2-W; b) beam C2-two

To investigate the effect of using 2 bolts instead of one bolt on the connection capacity, two other beam models with the same variables of two experimentally tested beams with one bolt were analyzed. The obtained load mid-span displacement curves of beams C1-two bolts and C9-two bolts are compared with those for beams C1 and C9 in Figure 7-39.

349

The results confirm that using a second bolt increases the connection breakout cracking and ultimate loads. It may be concluded that the welded connection capacity should be calculated based on the remaining depth, while the capacity of bolted connection should be calculated using the highest bolt depth. Furthermore, it was noted that the welding stresses were negligible, which suggests that pile cap connection without bolts is expected to have the same behaviour of the welded connection under compression loading.

a)

b)
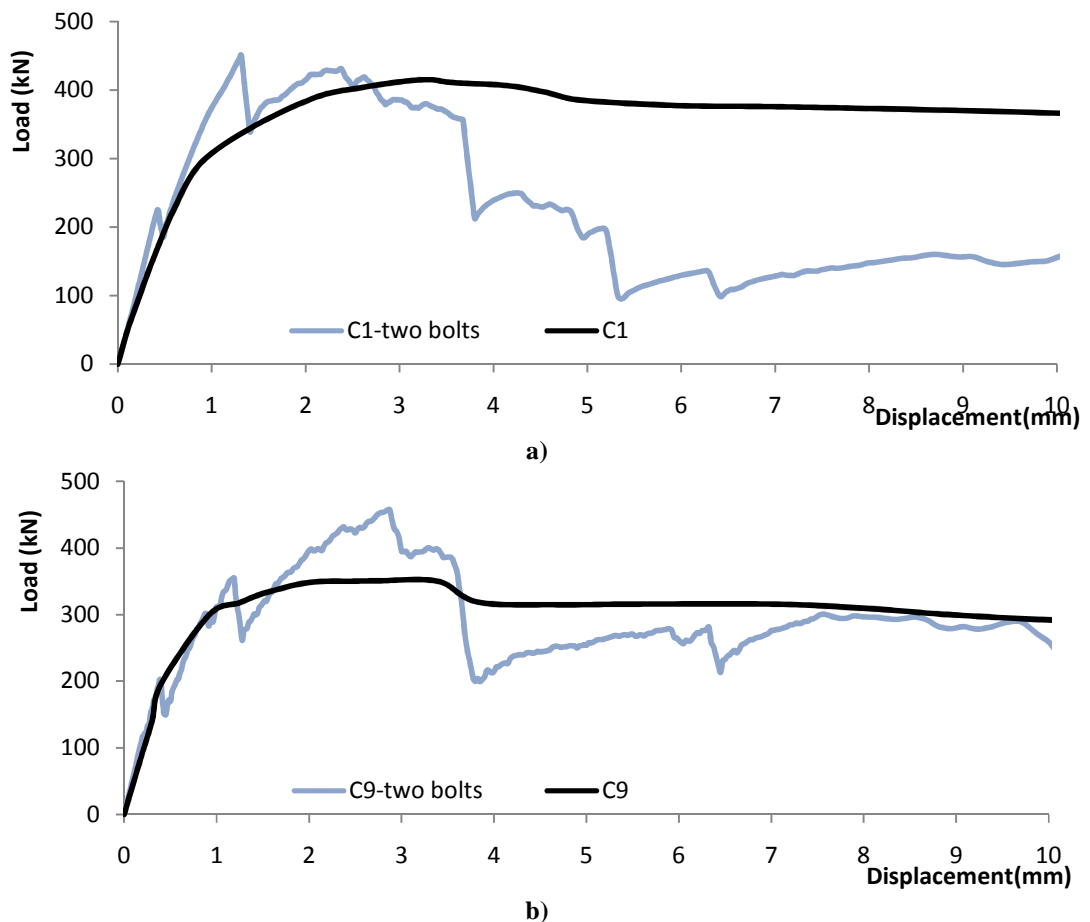
Figure 7- 39 Effect of pile cap configuration on connection performance for beam: a) C1; b) C9

7.15.11 Influence of pile connection at corner of grade beam.

The pile connection was considered at the corner of a grade beam that have the same variables of beam C2. Figure 7-40 compares the load-displacement response of the corner connection with that obtained for C2. The results show that the corner connection experienced higher displacement and exhibited lower stiffness compared to C2. This behavior is attributed to reduced constraint of the outside surface of the corner, which reduced the connection resistance. Also, the connection may experience torsion strains, which would also increase the applied shear stresses to the connection. As a result, the corner connection first cracking load, breakout cracking load and ultimate load decreased as shown in Figure 7-40. Moreover, the stirrups contribution to the connection capacity decreased because they were farther from the pile shaft. Thus, it is recommended to add anchor reinforcement at the corner locations.
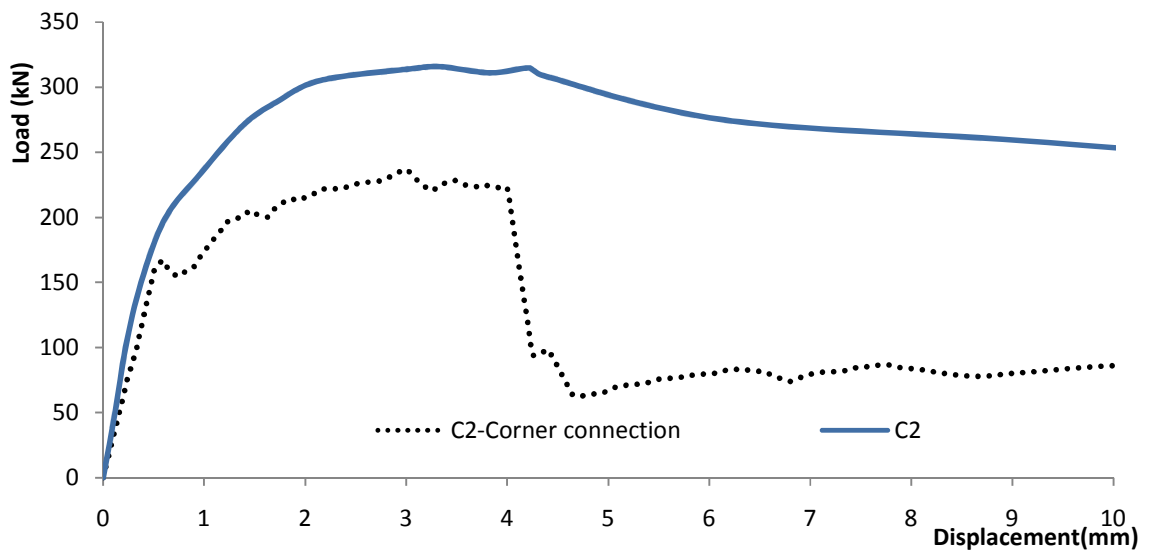
Figure 7- 40 Load mid-span displacement response

7.15.12 Influence of supports direction (one way vs two way support)

Helical piles and micropiles may be used to support stiff pile caps or flexible rafts. In this case, the supports to the pile connection will be in two perpendicular directions. To evaluate the connection performance in this case, a two-way slab denoted C2-TWO with same variables of beam C2 (but different width and longitudinal reinforcement in two directions) was analyzed. The slab had dimensions of 1600x500x1600 mm and the pile shaft was considered to be at its centre with line supports from two directions. The results from this analysis were compared with those obtained for beam C-W-1600 with the same dimensions of 1600x500x1600 mm but supported from only one direction.

As shown in Figure 7-41, the failure mechanism of C2-Two involved breakout cracking similar to the punching shear in slabs. On the other hand beam C-W-1600 experienced horizontal crack in the width direction then a diagonal crack initiated forming into punching shear behaviour as shown in Figure 7-33a.
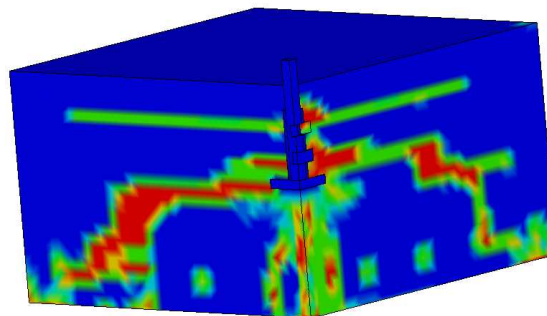
Figure 7- 41 Crack pattern of beam for C2-Two

Figure 7-42 shows that the first flexural cracking load of beam C2-TWO was higher than that of beam C2-W-1600 because the load was transferred in two directions, which

352

reduced the applied load and moment in each direction. After first cracking, stiffness of C-TWO was higher than that of C2- W-1600. Also, the connection breakout cracking and ultimate loads for beam C2-Two were higher than that of C-W-1600.
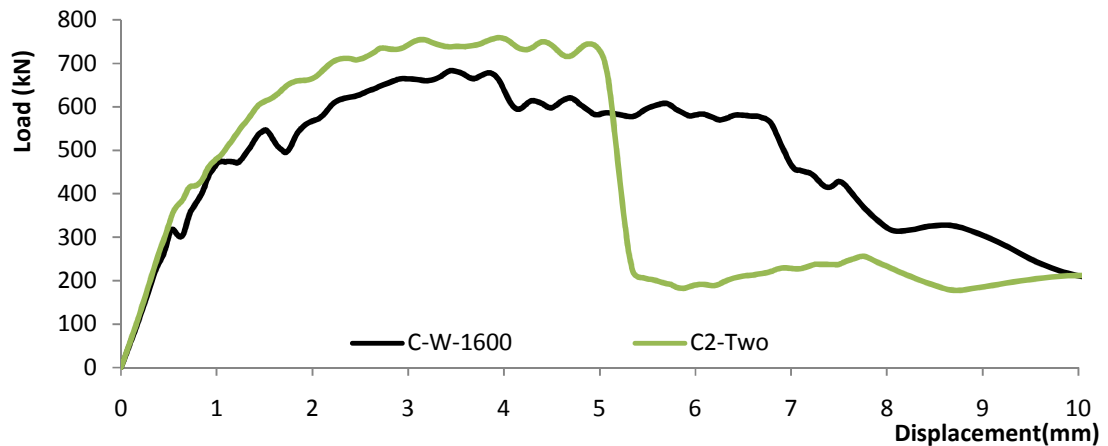
Figure 7- 42 Load mid-span displacement relationship

7.16 Conclusions

1) The finite element model accurately predicted the behaviour of pile-new reinforced concrete foundation connection.

2) Both grade beam capacity and connection capacity must be considered in the foundation design and pile load transfer calculations.

3) The connection can be considered fixed (i.e. fixed pile head) up to its breakout cracking load. Afterwards, the connection becomes hinged and its stiffness and capacity depend on the longitudinal and transverse reinforcements.

4) Up to breakout cracking, the connection load transfer is through bolt bearing on concrete, pile cap's plate bearing on concrete and pile-concrete friction. Thus, breakout cracking load is mainly affected by the concrete and longitudinal reinforcement contributions and not by the transverse reinforcement. After the breakout cracking, the load transfers by the stirrups, the pile-concrete friction, the dowel action of the longitudinal reinforcement, and the concrete aggregate interlock.

5) An increase in the pile cap remaining depth increases the connection breakout cracking and ultimate loads as well as its stiffness after first flexural cracking.

6) The connection first flexural cracking, breakout cracking and ultimate loads increase by increasing the concrete compressive strength and the longitudinal reinforcement ratio.

7) The transverse reinforcement ratio has no effect on the first flexural cracking or breakout cracking loads. The connection ultimate capacity, however, can be increased by placing higher percentage of transverse reinforcement closer to the pile shaft.

8) The connection ultimate capacity is the larger of its ultimate concrete capacity and the vertical tensile strength of transverse reinforcement within the breakout cone.

9) Adequate anchor reinforcement within the plate width should have vertical tensile capacity ≥ double the required shear capacity of the grade beam at the pile location.

10) The breakout cracking and ultimate loads increase as anchor reinforcement tensile strength increases, but the connection capacity will not exceed the beam capacity.

11) The shear span to beam depth ratio (a/d) affects the connection capacity significantly: for (a/d) < 2.25, the concrete shear strength, and consequently the breakout cracking, increases; for 2.5 < (a/d) < 6, the concrete shear strength and breakout cracking load will not change; for (a/d) < 1, the breakout cracking load is much higher than (a/d) = 2.5 because the beam would behave as deep beam and the load transfer mechanism switches to Arch-Type instead of Beam-Type.

12) Crack propagation was similar to single shear cracking for concrete member width $b < \left(2\sqrt{2}d_{rem} + b_{plate}\right) and 2\sqrt{2}d_{bolt}$. For larger b, cracks become similar to punching shear cracks. The connection breakout cracking load increases as the beam width increases up to this specific width if supports are provided in one direction only.

13) For connections off beam mid-span, the diagonal cracks do not initiate simultaneously from both sides. The side with the lower (a/d) ratio will initiate first. The connection capacity should be the sum of shear strengths of both sides using corresponding (a/d) ratio for each side. Conservatively, the connection shear

355

capacity may be given by double the shear capacity of the side with higher (a/d) ratio. Additionally, the connection capacity should be compared with the beam shear capacity considering the lower (a/d) ratio multiplied by $\left(\frac{Span}{long\ shear\ span}\right)$.

14) Connection breakout cracking initiated from the top bolt level in case of bolted connection and from the plate level in case of welded connection or pile cap without bolts. Therefore, the connection capacity should be calculated considering the high bolt depth for bolted connection and the remaining depth for welded connection.

15) The connection stiffness and capacity decreases if placed at the corner intersection of grade beams. Anchor reinforcement, rather than stirrups, is recommended in this case. Also, the shear stresses caused by the torsion should be considered along with shear stresses from vertical pile loading.

16) The connection breakout cracking load is higher for slabs and grade beams supported in two perpendicular directions because punching shear, not single shear, will govern the connection behaviour.

7.17 References

ACI 318-99, 1999. Building Code Requirements for Structural Concrete (ACI 318-99) and Commentary (318R-99), Farmington Hills, MI: American Concrete Institute.

ACI 318-08, 2008. *Building Code Requirements for Structural Concrete (ACI 318-08) and Commentary*, Farmington Hills, MI: American Concrete Institute.

Angelakos, D., Bentz, E.C. & Collins, M.P., 2001. Effect of Concrete Strength and Minimum Stirrups on Shear Strength of Large Members. Structural Journal, 98(3), pp.291–300.

ASTM C39 / C39M-15a, 2015. *ASTM C39 / C39M-15a*, West Conshohocken, PA, USA: ASTM International.

ASTM C496 / C496M - 11, 2004. C496/C496M-11, Standard test method for splitting tensile strength of cylindrical concrete specimens, West Conshohocken, Pa, USA.

Bala, S., 2001. Contact Modeling in Ls-Dyna. Livermore Software Technology Corporation and FEA Information Inc, Livermore, CA.

Bažant, Z., 1985. Mechanics of fracture and progressive cracking in concrete structures. In A. M.-N. G. C. Sih, Di Tomasso, ed. Fracture Mechanics of Concrete: Structural Application and Numerical Calculation. Boston, pp. 1–91.

Bažant, Z. & Oh, B., 1983. Crack band theory for fracture of concrete. Material and Structures, 16(93), pp.155–177.

Bazant, Z.P. & Cedolin, L., 1979, Blunt Crack Band Propagation in Finite Element Analysis. Journal of the Engineering Mechanics Division, 105(2), pp.297–315.

CEB, 1993. CEB-FIP model code 1993: design code, Thomas Telford.

Chen, W., 2007. Plasticity in reinforced concrete, New York: McGraw-Hill Book Co.

Chinn, J. & Zimmerman, R., 1965. Behavior of plain concrete under various high triaxial compression loading conditions, CO, United States.

Crawford, J. & Malvar, L., 2006. *User's and theoretical manual for K&C concrete model*, Burbank, CA.

Crawford, J.E., Magallanes, J. & Zhang, Y., 2010. Determining the Effects of Cased Explosives on the Response of RC Columns. In *MABS21*. Jerusalem, Israel, pp. 3–8.

Crawford, J., 2012. Enhancing the Blast Resistance of RC Columns with FRP. In 6th International Conference on Advanced Composite Materials in Bridges and Structures. Kingston, Ontario, Canada, pp. 22–25.

Crawford, J. et al., 1995. Evaluation of jacketed columns as a means to improve the resistance of conventional structures to blast effects. In Proceedings, 66th Shock and Vibration Symposium. Biloxi, MS.

Crawford, J. et al., 2012. Use and validation of the release II K&C concrete material model in LS-DYNA, Burbank, CA.

Crawford, J. & Wu, Y., 2012. Modeling of concrete materials under extreme loads. In I. H. H. & Z.-X. Li, ed. Advances in Protective Structures Research. London, UK: CRC Press/Balkema, pp. 1–32.

Crawford, J.E., Magallanes, J. & Zhang, Y., 2010. Determining the Effects of Cased Explosives on the Response of RC Columns. In MABS21. Jerusalem, Israel, pp. 3–8.

Elfgren, L., 1989. Fracture mechanics of concrete structures From theory to applications: Report of the Technical Committee 90-FMA Fracture Mechanics to Concrete/Applications, London, UK: Taylor and Francis Group.

Eligehausen, R., Mallée, R. & Silva, J.F., 2013. Anchorage in Concrete Construction, John Wiley & Sons.

Flanagan, D.P. & Belytschko, T., 1981. A uniform strain hexahedron and quadrilateral with orthogonal hourglass control. International Journal for Numerical Methods in Engineering, 17(5), pp.679–706.

Hallquist, J., 2009. LS-DYNA keyword user's manual, Livermore, CA.

Hillerborg, A., Modéer, M. & Petersson, P.-E., 1976. Analysis of crack formation and crack growth in concrete by means of fracture mechanics and finite elements. Cement and Concrete Research, 6(6), pp.773–781.

Jaime, M.C., 2012. Numerical Modeling Of Rock Cutting And Its Associated Fragmentation Process Using The Finite Element Method. , p.260.

Kupfer, H., Hilsdorf, H. & Rusch, H., 1969. Behavior of concrete under biaxial stresses. ACI Journal proceedings, 66(8), pp.656–666.

Launay, P. & Gachon, H., 1972. Strain and Ultimate Strength of Concrete Under Triaxial Stress. ACI Special Publication, 34, pp.269–282.

Magallanes, J., Crawford, J. & Wu, Y., 2007. Evaluation of the K&C Concrete Model's Ability to Reproduce Standard Tests as Compared to Other LS-DYNA Material Models. In Workshop on Modeling Concrete Under High-Impulsive Loadings. Austin, TX.

Magallanes, J., Morrill, K. & Crawford, J., 2008. Finite element models for the analysis and design of CMU walls to blast loads. In Proceedings of the 80th DDESB Explosives Safety Seminar. Palm Springs, CA.

Magallanes, J. & Wu, Y., 2010. Recent improvements to release III of the K&C concrete model. 11th International LS-DYNA Users Conference, Dearborn, MI, pp.37–48.

Malvar, L. et al., 1996. A new concrete material model for DYNA3D-Release II: shear dilation and directional rate enhancements. A Report to Defense Nuclear ….

Malvar, L.J. et al., 1997. A plasticity concrete material model for DYNA3D. International Journal of Impact Engineering, 19(9-10), pp.847–873.

Malvar, L.J., Morrill, K.B. & Crawford, J.E., 2004. Numerical Modeling of Concrete Confined by Fiber-Reinforced Composites. Journal of Composites for Construction, 8(4), pp.315–322.

Metwally, I.M., 2012. Evaluate the capability and accuracy of response-2000 program in prediction of the shear capacities of reinforced and prestressed concrete members. *HBRC Journal*, 8(2), pp.99–106.

Nakamura, H. & Higai, T., 1999. Compressive fracture energy and fracture zone length of concrete. In JCI-C52E Seminar of post-peak behaviour of RC structures subjected to seismic loads. pp. 259–272.

Noble, C. et al., 2005. Concrete Model Descriptions and Summary of Benchmark Studies for Blast Effects Simulations, Livermore, CA.

Pan, F. & Zhu, J., 2006. Three point bending analysis of a mobile phone using LS-DYNA explicit integration method. 9th International LS-DYNA Users Conference, June, pp.4–6.

Reid, J.D., 1998. *LS-DYNA Examples Manual" LSTC 1998,"* Livermore, CA.

Santiago, S.D. & Hilsdorf, H.K., 1973. Fracture mechanisms of concrete under compressive loads. Cement and Concrete Research, 3(4), pp.363–388.

Tu, Z. & Lu, Y., 2009. Evaluation of typical concrete material models used in hydrocodes for high dynamic response simulations. International Journal of Impact Engineering, 36(1), pp.132–146.

Wesevich, J. W., L. J. Malvar, and J. E. Crawford, 1997, 1999. Comparison of Measured and Predicted Responses of Reinforced Concrete Walls Subjected to Close-in Blasts. In

9th International Symposium on Interaction of the Effects of Munitions with Structures. Berlin-Strausberg.

William, K. & Warnke, E., 1975. Constitutive model for the triaxial behavior of concrete. In Seminar on Concrete Structures Subjected to Triaxial Stresses. Bergamo, Italy, pp. 1–30.

Yonten, K. et al., 2005. An assessment of constitutive models of concrete in the crashworthiness simulation of roadside safety structures. International Journal of Crashworthiness, 10(1), pp.5–19.

BEHAVIOUR OF HELICAL PILE CONNECTORS FOR NEW FOUNDATIONS SUBJECTED TO COMPRESSION LOADING: CONNECTION CAPACITY EQUATIUONS AND DESIGN AID

8.1 Introduction

The experimental and numerical results demonstrated that the breakout cracking and ultimate loads are different because the connection behaviour under compression loading may be governed by two different failure mechanisms. In addition, as this connection involves the pile and pile cap with its bolts, a limited crack width design may also apply at the regions with high corrosion-conditions. Furthermore, it is usually assumed (and desirable) that the connection between the pile and foundation is fixed for loads lower than the breakout load. However, the experimental and numerical results showed that the connection will become hinged if the breakout load is reached. Yahia and El Naggar (2015) demonstrated that the capacity of micropiles increases significantly for fixed connection between the micropile and the pile cap compared to a hinged connection.

In order to develop an analytical solution that best describes both the breakout cracking and ultimate loads, the recorded behaviour of the tested connection was compared with different concrete failure mechanisms reported by other researchers. This comparison should define the most representative concrete failure mechanism and identify the corresponding category of failure equations. The predictions of the identified equations are then compared with observed experimental and numerical results to verify the validity of the equations. In case the equations predictions are slightly different from observed

results, the curve-fit constants of the equations are "fine tuned" to enhance the agreement of their predictions with observed behaviour. Finally, a statistical study is conducted to indicate the most suitable equation to be used for evaluating the connection capacity. Following the development of a suitable equation to calculate the connection capacity and consideration of the different limit states that govern the connection failure mechanism, a design methodology is developed for the studied connection subjected to compression loading.

List of notations

a	Shear Span
a^*	The effective shear Span (the distance from the pile caps' plate end to the support in this case)
$\left(a/d\right)$	Shear span to depth ratio
A_{anchor}	The anchor reinforcement contained in the pile cap's plate width
a_g	Specified nominal maximum size of coarse aggregate
A_s	The longitudinal steel area
A_v	Area of shear reinforcement within a distance s
b	Specimen width
b_{plate}	pile cap's plate width
b_{pile}	pile shaft diameter or width; 44.45 mm (1.75") in our case
C_c	The cracked concrete contribution to the connection ultimate load under compression loading
C_{Cr}	The connection breakout cracking load under compression loading
C_s	The transverse reinforcement contribution to the connection ultimate load under compression loading
c'	Concrete cover
$C_{u\,Actual}$	The actual connection ultimate capacity under compression loading
$C_{u_{conc.}}$	The limit state of the concrete ultimate capacity in the connection under compression loading
$C_{u\,Design}$	The recommended connection design load under compression loading
$Cu_{reinf.}$	The limit state of the transverse reinforcement ultimate capacity in the connection under compression loading
$Cu_{support}$	The recommended crushing limit state at supports for (a/d)<1
d	Specimen depth
d_{bolt}	The highest bolt depth
d_{emb}	The pile embedment depth in the reinforced concrete beam

d_{rem}	The remaining beam depth; $d_{rem} = h_a - d_{emb} - pile\ cap's plate\ thickness$
d_v	The effective shear depth, taken as the greater of 0.9d or 0.72h
E_s	Modulus of elasticity of non-prestressed reinforcement
fc'	Specified compressive strength of concrete
f_v	Transverse reinforcement stress accompanying with the cracked concrete contribution, C_c
f_u	Transverse reinforcement ultimate stress
h	Specimen height
M_f	Factored applied moment
L	Specimen Span
P_f	The pile shaft friction capacity
r_p	Pile friction ratio
s	Maximum centre-to-centre spacing of transverse reinforcement
s_z	The crack spacing parameter dependent on crack control characteristics of longitudinal Reinforcement
s_{ze}	The equivalent value of s_z that allows for influence of aggregate size
t_{plate}	Pile cap's plate thickness
v_c	Factored shear stress resistance provided by the concrete
V_C	Shear resistance attributed to the concrete
V_{Cr}	The diagonal tension cracking shear strength
V_f	Factored applied shear load
V_s	Shear resistance provided by shear reinforcement
β	Factor accounting for shear resistance of cracked concrete
θ	Angle of inclination of diagonal compressive stresses to the longitudinal axis of the member
λ	Modification factor reflecting the reduced mechanical properties of lightweight concrete
μ	The average coefficient of friction between concrete and steel; approximately=0.47 as reported by Baltay et al. ,1990.
ρ	Ratio of non-prestressed tension reinforcement, equal to A_s/bd
$\emptyset_c$	Resistance factor for concrete
$\emptyset_s$	Resistance factor for non-prestressed reinforcing bars
ε_x	Longitudinal strain at mid-depth of the member due to factored loads
ε_z	Longitudinal strain at mid-depth of the breakout cone due to factored loads

8.2 Main Failure Mechanism

The observations made from the experimental and numerical studies and the interpretation of their results demonstrated clearly that the breakout cracking resistance is closer to the single shear resistance of a concrete beam rather than the anchors nominal breakout resistance. This is because cracking propagated with inclination in one direction only (i.e. similar to single shear, especially when subjected to indirect loading) and not in two perpendicular directions (i.e. similar to breakout failure in anchors and punching shear). This behaviour is similar to the behaviour widely reported in the literature (e.g. Ferguson, 1956; Taylor, 1960; ACI-ASCE Committee 326, 1962; Zsutty, 1968 and 1971; Smith, 1974; Fereig, 1977; Cusens, 1985; Zuhua, 1987; Tan, 1997; and Lubell, 2009) for indirectly loaded beams failing under shear mechanism, not the behaviour reported for the concrete breakout failure mechanism of anchors under shear loading (e.g. Carrato, 1996; Lee, 2007; and Yang, 2008).. On the other hand, for beams with width less than $\left(2\sqrt{2}d_{rem} + b_{plate}\right)$ and $\left(2\sqrt{2}d_{bolt}\right)$, diagonal cracks were observed in the width direction, i.e., similar to the punching shear cracks as indicated in Chapter 7.

Therefore, it is proposed to use the shear strength equations for calculating the connection capacity after modifying them to account for the pile embedment depth and pile cap plate width. Also, the connection capacity is twice the single shear capacity in case of the pile shaft located at the beam mid-span due to the contribution of both sides of the beam. In case of the pile shaft is connected to the beam off its mid span, the connection capacity should be obtained as the sum of the capacity of each side, or conservatively, twice the lesser capacity of either side.

Finally, the connection capacity represents a limit state that should be compared with the beam limit states and the system failure will be due to the lowest capacity of all limit states, which will govern the failure mechanism.

8.3 Connection Breakout Cracking Load Calculation

Based on the observations of the experimental and numerical studies, there are several factors that affect the connection breakout cracking behavior and hence influence the breakout cracking load. These factors are listed herein.

8.3.1   Factors affecting the breakout cracking load

1. The concrete above the plate level contributes to the shear resistance due to the bolt bearing on the concrete and the pile-concrete friction. Thus, the connection capacity should be calculated considering the depth of the higher bolt and the pile friction to the connection capacity.

2. The remaining depth should be used in calculating the connection capacity for welded connections and bolted connections with short bolts.

3. Increasing the longitudinal reinforcement increases the breakout cracking load.

4. Decreasing the pile embedment depth, increases the breakout cracking load.

5. The shear span/depth ratio (a/d) has an important effect on the connection capacity. For $2.5 < (a/d) < 6$, the failure depends on the diagonal tension cracking or the flexural shear cracking. For $(a/d) < 2.25$, the failure is similar to shear compressive failure, which involves higher concrete shear resistance. Finally, for (a/d) or $(a/d_{bolt}) < 1$, the failure mechanism depends on the arch effect. Thus, the diagonal tension cracking can be considered conservatively for $1 < (a/d) < 2.5$ too. while for $(a/d) < 1$ the connection capacity should be increased by a factor that

depends on (a/d) or (a/d_{bolt}), or strut and tie method may be used. Also, the connection capacity should be limited to $1.2\sqrt{fc'}.b.d_{rem}$.

6. The beam width used to calculate the single shear strength should be limited to the lesser of $\left(2\sqrt{2}d_{rem} + b_{plate}\right) or \left(2\sqrt{2}d_{bolt}\right)$, or a punching shear limit state should be considered.

7. For pile shaft connected at the beam mid-span, the connection capacity is given by the contributions of the two diagonal tension failure surfaces on the two sides. The connection capacity must be compared with the shear capacity of the beam at the side with lower (a/d) multiplied by $\left(\frac{Span}{long\ shear\ span}\right)$. Alternatively, the larger (a/d) ratio can be used to provide a conservative estimate of the connection capacity.

8. In case of the connection is at the corner of grade beam, the shear stresses caused by the torsion should be added to the shear stresses from vertical pile loading. Thus, the connection capacity would be reduced due to these torsional stresses.

9. Stirrups or transverse reinforcement contribution to the breakout cracking load capacity can be considered negligible. Thus, transverse reinforcement will not be considered in the breakout cracking load equation.

10. Using anchor reinforcement can increase the breakout cracking load but its effect will be neglected because its effect is mainly after the initiation of the cracking.

8.3.2 Equation for the connection breakout cracking load

To evaluate the diagonal tension or flexural shear capacity at the breakout cracking, different equations used for calculating the capacity of reinforced concrete beams without stirrups will be compared with the observed experimental and numerical results. These equations are reported by ACI 318-11, CEB-FIP Model (1993); Zsutty (1968); Zsutty

(1971); Al-zoubi (2014); Robert (1963); CSA Simplified Method, Bazant and Yu (2005) & ACI Committee 446. These equations are presented in Table 8-1. The data of the specimens investigated experimentally and analytically and will be used in this study is presented in Appendix E.

Table 8- 1 Summary of shear equations for beams without stirrups directly loaded

Investigator	Equations in Mpa, and mm = [shear strength]
ACI 318-11 Code and KBCS Code	$v_c = \left[0.16\sqrt{fc'} + 17.\dfrac{\rho.V.d}{M} \right]$
CSA Code Simplified Method &Bentz (2005)	$v_c = \left[\left(\dfrac{230}{1000 + \dfrac{35.d}{15 + a_g}} \right). \sqrt{fc'} \right]$
CEB-FIP Model Code(1993)	$v_c = \left[0.15(3d/a)^{1/3}(100.\rho)^{1/3}.(1 + \sqrt{(200/d)}).(fc')^{1/3} \right]$
Zsutty (1968, 1971)	$v_c = \left[2.2(\rho.fc'.d/a)^{1/3} \right].b.d$
Al-zoubi (2014)	$v_c = \left[2.6\dfrac{1}{\sqrt{1 + d/(25.a_g)}} \left(\rho.fc'.\dfrac{d}{a} \right)^{1/3} \right]$
Bazant (1987)	$v_c = \left[0.54\sqrt[3]{\rho} \left(\dfrac{1 + \sqrt{5.08/a_g}}{\sqrt{1 + \dfrac{d}{25.a_g}}} \right) \left(\sqrt{fc'} + 249\sqrt{\dfrac{\rho}{(d/a)^5}} \right) \right]$
Bazant and YU (2005) & ACI Committee 446	$v_c = \left[1.1\rho^{3/8} \left(1 + \dfrac{d}{a} \right) \sqrt{\dfrac{fc'}{\left(1 + \dfrac{d}{687.5.fc'^{2/3}.\sqrt{a_g}} \right)}} \right]$
Robert (1963)	$v_c = \left[0.2575\sqrt{fc'}(d/a) + 27.6\ \rho \right]$

As mentioned previously, the pile-concrete friction contributes to the breakout cracking load. This contribution depends on the internal compression force in the concrete induced

368

by the moment on the beam. The friction resistance is equal to the friction factor multiplied by the internal compression force. This internal force is considered equal to twice the full beam internal force multiplied by pile shaft width/beam width. Moreover, the numerical results demonstrated that this friction force represented 10-20% of the total connection breakout cracking capacity. Thus, it is recommended to consider an upper limit on the pile-concrete friction equal to 20% of the breakout cracking load. Therefore, the pile friction capacity, P_f, may be given by Equation 8.2. The following steps are the steps used to derive the pile-concrete friction equation.

$$P_f = \mu. \text{ beam internal compression load} . \frac{2\, b_{pile}}{b} \leq 0.2 C_{cr} \qquad \textbf{8. 1}$$

Where $\mu = 0.47$ is average coefficient of friction between concrete and steel (Baltay et al., 1990)

The beam internal compression load is approximately $\approx \frac{M_f}{0.9d} \approx \frac{C_{cr}/2 .a}{0.9\,d}$. Thus,

$$P_f \approx \left(\frac{a}{d}\right)\left(\frac{b_{pile}}{b}\right).\frac{C_{cr}}{2} = r_p. C_{cr} \leq 0.2 C_{cr} \qquad \textbf{8. 2}$$

Equation 8.2 represents the pile friction as a ratio (r_p) between the pile-concrete friction load and the applied compression load. This ratio as shown in Equation 8.3 can be considered as a geometry property of the connection and it cannot be more than 0.2, i.e.

$$r_p = \frac{1}{2}\left(\frac{a}{d}\right)\left(\frac{b_{pile}}{b}\right) \leq 0.2 \qquad \textbf{8.3}$$

Table 8-2 compares the experimentally recorded breakout cracking load of beam C2 (i.e. 295 kN) with the shear loads calculated by the different shear stress equations presented in Table 8-1 after multiplying them by 2.0 considering two symmetric diagonal cracks on both sides of the pile shaft (in case of the connection is located at the mid-span), adding the pile-concrete friction load to it, and multiplying it by the width and the effective depth. The pile-concrete friction at the breakout cracking load was calculated from its finite element model as 23 kN, which represented only 7.8% of the breakout cracking load. Thus, the expected breakout crack should be equal to $Ccr = (2V_{cr} + pile\ friction) = 2V_{cr} + 23kN$ for beam C2. Furthermore, to investigate whether the full beam depth, d, or higher bolt depth, d_{bolt}, should be used in calculating the connection capacity as the effective depth, the connection breakout load was calculated twice for each equation using both of the two depths (i,e d, and d_{bolt}) as shown in Table 8-2.

Table 8- 2 Predicted breakout cracking load using different shear equation (Using d and d_{bolt})

Investigator	Using d (kN)	Using d_{bolt} (kN)	$(T_{theoretical}/T_{cr})$ % Using d	$(T_{theoretical}/T_{cr})$ % Using d_{emb}
ACI 318-11 Code and KBCS Code	434	333	147.1	112.9
CSA Code Simplified Method &Bentz (2005)	414	318	140.3	107.8
CEB-FIP Model Code(1993)	329	253	111.5	85.8
Zsutty (1968, 1971)	424.4	325	143.9	110.2
Al-zoubi (2014)	367	282	124.4	95.6
Bazant (1987)	430	423	145.8	143.4
Bazant&Yu(2004)&ACI 446	555	423	188.1	143.4
Robert G. Mathey (1963)	464	355	157.3	120.3

The comparison presented in Table 8-2 demonstrate that using the beam full depth in calculating the breakout cracking load overestimates the connection capacity and show that it is more appropriate to use d_{bolt} instead. Also, the equations can be ranked in terms of the closeness of their predictions to the observed connection capacity in the following order:

1) Al-zoubi's equation, 2014; 2) CSA Code Simplified Method &Bentz, 2005; 3) Zsutty's equation, 1971; 4) ACI 318-11 code equation; 5) CEB-FIP Model Code, 1993; 6); Mathey, 1963.

The equations proposed by Al-zoubi (2014), CSA Simplified method, Zsutty (1971) and ACI 318-11 yielded the closest results because they evaluate the diagonal tension cracking resistance accurately. However, the ACI 318-11 and Zsutty equations do not account for effect of beam size on its shear strength. This can affect the calculated capacity of connections for beams with heights or embedment depths greater than 1m. Unfortunately, the CSA Code Simplified Method &Bentz (2005) does not account for the effect of the longitudinal reinforcement or the (a/d) ratio. On the other hand, Al-zoubi's equation accounts for the effects of both beam size, the longitudinal reinforcement, and the (a/d) ratio on the connection capacity. These 4 equations are further considered in calculating the connection capacity for all tested beams.

Several researchers indicated the size effect on beams without transverse reinforcement on their shear resistance (e.g. Collins and Kuchma, 1999; Collins and Mitchell, 1996; Bazant and Kazemi, 1991 and Kim and Park, 1997). On the other hand, Qiang, et al.

371

(2011) concluded that using stirrups decreases the size effect. Because the connection capacity was found to be affected by the bolt depth (d_{bolt}), it should be used in the size effect term too in the CSA code Simplified Method & Bentz, 2005 and Al-zoubi's equations. Furthermore, to account for the plate width effect, the shear span (a) is replaced with (a*), which is equal to the shear span (a) minus half the plate width (b_{plate}/2), i.e.

$$a^* = a - \frac{b_{plate}}{2}$$ **8. 4**

Accordingly, the four equations are modified to calculate the connection capacity accounting for the bolt depth, the beam size, as well as the pile friction contribution as a ratio from the applied load and are given by:

ACI 318-11 Code equation:
$$C_{cr} = 2(1 + r_p)\left[0.16\sqrt{fc'} + 17.\frac{\rho.d}{a^*}\right].b.d_{bolt}$$ **8. 5**

CSA Code Simplified Method and Bentz (2005) equation:
$$C_{cr} = 2(1 + r_p)\left[\left(\frac{230}{1000 + \frac{35.d_{bolt}}{15 + a_g}}\right).\sqrt{fc'}\right].b.d_{bolt}$$ **8. 6**

Zsutty's (1971) equation:
$$C_{cr} = 2(1 + r_p)\left[2.2\left(\rho.fc'.\frac{d}{a^*}\right)^{1/3}\right].b.d_{bolt}$$ **8. 7**

Al-zoubi's (2014) equation:
$$C_{cr} = 2(1 + r_p)\left[2.6\frac{1}{\sqrt{1 + d_{bolt}/(25.a_g)}}\left(\rho.fc'.\frac{d}{a^*}\right)^{1/3}\right].b.d_{bolt}$$ **8. 8**

The breakout cracking loads for test beams were calculated using the four modified equations and the results are compared in table 8-3 with the experimental results (from

Chapter 6). Table 8-3 shows that the modified equations predicted the breakout cracking load of the 9 tested beams reasonably well. It is also shown that Equation 8.8 provided excellent predictions of the beams breakout cracking load with a percentage mean value of 101%, 5% standard deviation and 5% root mean squared error. These results indicate suitability of Equation 8.8 for calculating the connection breakout cracking load.

Table 8-3 Comparison between calculated and measured connection breakout loads

Specimen	C_{cr} (Breakout Cracking load) (kN)	$(C_{theoretical}/C_{cr})\%$ Eq. 8.5	$(C_{theoretical}/C_{cr})\%$ Eq. 8.6	$(C_{theoretical}/C_{cr})\%$ Eq. 8.7	$(C_{theoretical}/C_{cr})\%$ Eq. 8.8
C1	400	98	84	105	96
C2	295	113	102	108	101
C3	250	113	107	109	105
C4	280	118	107	114	107
C5	289	115	104	112	105
C6	330	103	91	110	104
C7	400	88	75	108	101
C8	320	104	94	99	93
C9	315	105	96	101	95
Average%		106	96	107	101
Standard deviation%		9	11	5	5
Coefficient of variation%		9	11	4	5
Root mean squared error%		11	11	9	5

The modified equations were also used to calculate the breakout cracking load of the numerically investigated connections in beams with a/d > 1. The calculated values are compared in table 8-4 with those obtained from the numerical analysis (Chapter 7). All the used beams data in this table is presented in Appendix E.

Table 8- 4 Comparison of breakout cracking loads from modified equations and FEA for (a/d)>1

Specimen	C_{cr}(Breakout Cracking load) (kN)	$(C_{theoretical}/C_{cr})$% Eq. 8.5	$(C_{theoretical}/C_{cr})$% Eq. 8.6	$(C_{theoretical}/C_{cr})$% Eq. 8.7	$(C_{theoretical}/C_{cr})$% Eq. 8.8
C-B-10	234	138.3	145.0	113.6	103.7
C-B-7	360	96.1	94.2	116.0	105.8
C-B-35	445	88.3	76.2	128.7	117.4
C-B-15	219	154.3	160.8	134.8	123.0
C-B-20R	287	119.4	122.7	117.7	107.4
C-B-25R	349	101.0	100.9	114.8	104.7
C2-20	240	113.9	115.4	122.0	111.3
C2-35	338	105.5	108.4	104.4	95.2
C2-40	351	94.4	96.6	95.5	87.1
C2-W	226	119.8	128.6	121.1	114.8
C2-TWO BOLTS	305	129.8	126.7	131.2	115.3
C1-TWO BOLTS	451	99.3	93.3	100.4	85.7
C9-2 BOLTS	353	112.2	109.4	113.4	99.6
C-R-2.75 (4-20M)	260	118.9	122.7	113.8	103.8
C-R-2.50 (4-20M)	287	108.1	111.1	106.6	97.3
C-R-2.00 (4-20M)	305	103.0	104.6	108.8	99.3
C-R-1.75 (4-20M)	301	105.2	106.0	115.8	105.7
C-R-5.5 (4-30M)	231	134.4	138.1	104.4	95.3
C-R-5 (4-30M)	277	112.6	115.1	90.0	82.1
C-R-4 (4-30M)	269	117.4	118.6	100.2	91.4
C-R-3.5 (4-30M)	280	113.8	113.9	100.7	91.9
C-R-2.75 (4-30M)	313	103.8	101.9	98.2	89.6
C-R-2.25 (4-30M)	362	91.6	88.1	91.1	83.1
C-R-2.0 (4-30M)	396	84.9	80.5	87.1	79.5
C-R-1.75(4-30M)	418	81.9	76.2	86.6	79.0
Average%		109.9	110.2	108.7	98.8
Standard deviation%		17.2	20.6	13.5	12.4
Coefficient of variation%		15.7	18.7	12.4	12.5
Root mean squared error %		19.6	22.6	15.8	12.2

Table 8-4 shows that Equation 8.6 overestimated the breakout cracking load for the beams with light longitudinal reinforcement ratios because it does not account for the effect of the longitudinal reinforcement on the connection behavior.

Equation 8.6 overestimated the breakout cracking load of C-B-10 by 45%, while for beams with high longitudinal reinforcement ratio (e.g. C-B-35) it underestimated the

breakout cracking load by 24%. Moreover, for all the beams with different (a/d) ratios and different longitudinal reinforcement Equation 8.6 expected the same breakout load for all the beams in table 8-4, which is totally unrealistic. Similarly, Equation 8.5 overestimated the breakout cracking loads of beams C-B-10 and underestimated that of C-B-35 because it overestimated the contribution of the concrete resistance, and underestimates the longitudinal reinforcement contribution (Ozcebe, 1999; Kani, 1966).

On the other hand, Equations 8.7 and 8.8 predicted the breakout cracking loads of most beams reasonably well with percentage averages of 108.7% and 98.8% with standard deviation of 13.5% and 12.4%, respectively, however, Equation 8.8 involves the size effect in calculating the breakout cracking load and provides more conservative values and accurate predictions than that when using Equation 8.7. Therefore, it is recommended to use Equation 8.8 for calculating the connection capacity.

8.3.3 Consideration of (a/d) effect for deep beams

Most of the equations used to calculate the capacity of beams were derived primarily for cylinder beams (a/d > 2.5) not for short beams (1 < a/d < 2.5) or deep beams (a/d < 1). Thus, their accuracy in predicting the load resistance of deep beams is limited. To examine the applicability of the modified equations for calculating the capacity of connection in deep beams, the cracking load of the deep beams that were analyzed in the numerical study is calculated using the modified equations and the results are compared in Table 8-5. This comparison demonstrates that the breakout cracking loads for beams with low (a/d) calculated using Equations 8.7 and 8.8 were in agreement with those obtained from the numerical analyses. On the other hand, Equation 8.6 gave the same

375

calculated breakout loads for all beams in Table 8-5 as it does not account for (a/d) or longitudinal reinforcement, resulting in gross under estimation of connection capacity as can be noted from Table 8-5. Therefore, Equation 8.8 appears to be the most appropriate for calculating the connection breakout cracking load. Furthermore, the numerical results showed that the ultimate capacity of connections in beams with (a/d) < 1 should be limited to $1.2\sqrt{fc'}.\,b.\,d_{bolt}$, which should be respected when using Equation 8.8.

Finally, several codes recommend the strut and tie method for calculating the capacity of deep beams (e.g. CSA A23.3 code). Using this method for the pile connection considered, the compression struts will extend from the plate to the supports, without any consideration of the full beam depth or bolt level in evaluating the pile friction as the load will transfer primarily through the plate bearing. Thus, for beams with (a/d) < 1, the proposed model should be as shown in Figure 8-1. In this case, the effect of beam depth is negligible as the behaviour depends mainly on the remaining depth (d_{rem}). Only the effect of beam flexure should be taken into account by adding the tensile flexural stresses to the tensile stress from the tension tie. This tensile stress will be negligible in case of (a/d) <1 if compared to that calculated from the strut and tie model.

Table 8- 5 The comparison between the calculated results and the recorded results for (a/d)≤1

Specimen	C_{cr} result (Breakout Cracking load) (kN)	$(C_{theoretical}/C_{cr})\%$ ACI* Eq. 8.5	$(C_{theoretical}/C_{cr})\%$ CSA* Eq. 8.6	$(C_{theoretical}/C_{cr})\%$ Zsutty* Eq. 8.7	$(C_{theoretical}/C_{cr})\%$ Al-zoubi* Eq. 8.8
C-R-1 (4-20M)	380	88.3	84.2	114.3	104.3
C-R-0.5 (4-20M)	775	50.9	41.2	76.6	69.9
C-R-0.25 (4-20M)	850	89.2	37.5	117.5	107.2
C-R-1(4-30M)	443	86.9	72.0	101.7	92.8
C-R-0.75 (4-30M)	471	54.0	40.6	64.8	59.1
C-R-0.5 (4-30M)	580	58.9	37.4	70.1	63.9
Average%		71.3	52.1	90.8	82.9
Standard deviation%		18.6	20.5	23.2	21.2
Coefficient of variation%		26.0	39.3	25.5	25.5
Root mean squared error %		33.3	51.4	23.1	25.8
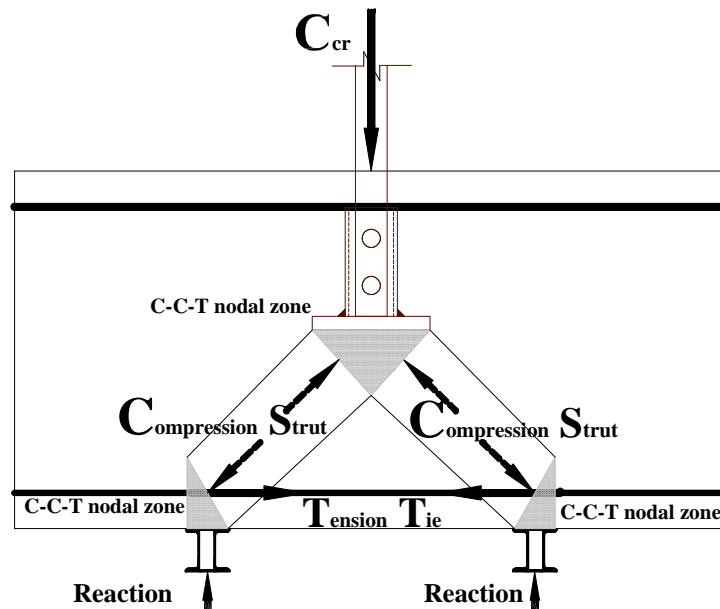
Figure 8- 1 Strut-and-tie model of a single span deep beam without stirrups with (a/d)<1

Based on the above discussion, it may be concluded that Equation 8.8 can be used to calculate the connection breakout cracking load. However, the following adjustments should be taken into consideration:

1- the used beam width in the calculation has a maximum that equals to the lesser of $\left(2\sqrt{2}d_{rem} + b_{plate}\right)$ or $\left(2\sqrt{2}d_{bolt}\right)$.

2- the longitudinal reinforcement ratio considered in the equation should be limited to 0.5%.

3- for piles connected to the beam off mid-span, the connection capacity is given by the resistance contribution of both sides. Thus, the connection breakout load can be given by:

$$C_{cr} = (1 + r_p)\left[2.6\frac{1}{\sqrt{1+d_{emb}/(25.a_g)}}(\rho.fc'.d)^{1/3}.\left(\frac{\sqrt[3]{a^*_{right}}+\sqrt[3]{a^*_{left}}}{\sqrt[3]{a^*_{right}}.\sqrt[3]{a^*_{left}}}\right)\right].b.d_{bolt} \quad \textbf{8.9}$$

or

$$C_{cr} = 2(1 + r_p)\left[2.6\frac{1}{\sqrt{1+d_{bolt}/(25.a_g)}}\left(\rho.fc'.\frac{d}{a^*_{max.}}\right)^{1/3}\right].b.d_{bolt} \quad \textbf{8.10}$$

where $\rho \le 0.5\%$, and $b \le \left(2\sqrt{2}d_{rem} + b_{plate}\right)$ & $\left(2\sqrt{2}d_{bolt}\right)$

4- for bolts shorter than half the width of the pile cap's plate, the remaining depth (drem) should be used instead of the top bolt depth (dbolt) because the contribution of the bolt bearing on the concrete may be negligible.

8.4 Connection Ultimate Load calculation

8.4.1 Observations from experimental and analytical studies

1. The connection ultimate load includes resistance contributions of the aggregate interlock, dowel action of the longitudinal reinforcement, pile-concrete friction,

378

and transverse reinforcement; however, the ultimate load should not exceed the stirrups yielding tensile capacity or the anchor reinforcement ultimate tensile strength. Also, the compression zone above the highest bolt does not contribute any shear resistance.

2. The vertical reinforcement within the width of the pile cap's plate contributes its ultimate capacity to the connection ultimate capacity after propagation of wide diagonal cracks, and the longitudinal dowel action and aggregate interlock become negligible.

3. The following limit states should be taken into consideration when calculating the connection ultimate load:

- The higher of beam breakout cracking load and concrete ultimate load.

- The crushing of support regions equal to $(2x \ 0.6\sqrt{fc'}.b.d_{emb})$ = $1.2\sqrt{fc'}.b.d_{emb}$, especially for (a/d) < 1.

- The bearing capacity of concrete under the plate for direct loading above the pile connection or small plate width.

- The beam shear failure for d < 2 d_{emb} or transverse reinforcement ratio > 0.8%.

- The beam flexural failure, especially for (a/d) > 6 or very low longitudinal reinforcement ratio.

- The pile shaft failure due to buckling at the bolts locations.

- The bolts double shear failure.

8.4.2 Development of the connection ultimate load equation

The simplified modified compression field theory was found to represent the concrete ultimate load well; however, some modifications are proposed to account for the difference in behavior between a beam directly loaded and failing in shear, and a pile-beam connection loaded in compression. The shear design methods based on the Modified Compression Filed Theory (MCFT) showed excellent agreement with the experimental results and predicted the size effects in shear and aggregate size. To reduce the excessive computational effort and excessive required design iterations involved in the general method of the MCFT, Bentz et al. (2006) introduced the Simplified Modified Compression field (SMCFT), which was adopted in the 2004 CSA A23.3 general shear method. The SMCFT will be used in this study to calculate the connection ultimate capacity with some modifications. In the SMCFT, the shear resistance of a reinforced concrete section comprises the shear resistance of the concrete and reinforcing steel, i.e.

$$V = V_c + V_s = \beta\sqrt{fc'}\mathrm{b}.\,\mathrm{d_v} + \frac{\mathrm{A_v.f_y}}{\mathrm{s}}.\,\mathrm{d_v}.\cot\theta \qquad \textbf{8. 11}$$

Where shear factor, β, concrete strain, ε_x and crack angle, θ are given by:

$$\beta = \frac{0.40}{(1+1500.\varepsilon_x)} \cdot \frac{1300}{(1000+s_{ze})} \qquad \textbf{8-12a}$$

$$\varepsilon_x = \frac{M_f/d_v + V_f}{2.E_s.A_s} \qquad \textbf{8-12b}$$

380

$$\theta = (29^o + 7000\varepsilon_x)\left(0.88 + \frac{s_{ze}}{2500}\right) \leq 75^o$$

$$\theta = (29^o + 7000\varepsilon_x) \; if \; s_{ze} = 300mm \qquad\qquad \textbf{8-12c}$$

and $\;$ dv is the greater of $\begin{cases} 0.9d \\ 0.72h \end{cases}$

$$s_{ze} = \frac{35 \; s_x}{(15 + a_g)} \geq 0.85 \; s_z$$

$s_{ze} = 300mm \; for \; minimum \; transverse \; reinfrocement$,

s_z is smaller of $\begin{cases} d_v \\ The \; max. distance \; between \; the \; crack \; control \; longitudinal \; steel \end{cases}$

In order to calculate β, ε_x, θ, factored moment and shear, M_f and V_f, are required. These values would be specified during the design process, but would not be available in the analysis process. Also, θ depends on ε_x, which depends on V_f, which in turn depends on ε_x. Specifically, in absence of stirrups $(i.e.\,V_f = V_c)$, an increase in V_f increases ε_x and θ but reduces β, which reduces the concrete shear resistance, V_c. Thus, an iterative procedure would be required. To eliminate this time consuming iterative procedure, only one equation should be used to calculate β, ε_x, and V_f. Therefore, it is proposed to use a second order equation to calculate the concrete strain ε_z, and consequently, the other values can be calculated using the SMCFT to calculate V_c without the iterative procedure. The 2nd order equation is developed as follow:

Assuming s_{xe}=300mm (considering the minimum transverse reinforcement at the connection location), and substituting in Equation 8.12a yields:

$$\beta = \frac{0.40}{(1+1500.\varepsilon_x)} \cdot \frac{1300}{(1000+s_{xe})} = \frac{0.40}{(1+1500.\varepsilon_x)}$$

Considering Equation 8.11, the concrete shear resistance can then be given by:

$$V_c = \frac{0.40}{(1+1500.\varepsilon_x)} \sqrt{fc'} \text{b. } d_v \qquad\qquad \textbf{8.13}$$

Finally, considering Equation 8.12b (i.e. $\varepsilon_x = \frac{M_f/d_v+V_f}{2.E_s.A_s} \leq 3 * 10^{-3}$), a 2nd degree equation for ε_x can be obtained, i.e.

$$\varepsilon_x = \frac{(a/d_v+1)V_f}{2.E_s.A_s} = \frac{0.40}{(1+1500.\varepsilon_x)} \sqrt{fc'} \text{b. } d_v \frac{(\frac{a}{d_v}+1)}{2.E_s.A_s} \qquad\qquad \textbf{8.14}$$

By solving the 2nd degree equation, the calculated concrete strain (denoted ε_z) is then given by:

$$\varepsilon_z = \frac{-1+\sqrt{1+6000z}}{3000} \qquad\qquad \textbf{8.15}$$

Where, for directly loaded beams:

$$z = \frac{0.4\sqrt{fc'}(1+\frac{a}{d_v})}{2E_s.\rho} \qquad\qquad \textbf{8.16}$$

In the SMCFT, the term $2.E_s.A_s$ is used to account for the strain at the beam mid-height; however, the critical position for the connection under consideration is at the middle of the highest bolt depth (d_{bolt}) or the remaining depth (d_{rem}). Therefore, Equation 8.16 should be adjusted for indirectly loaded pile connections using the ratio $\left(\frac{d_v-\frac{d_{bolt}}{2}+c'}{d_v}\right)$ instead of ½, i.e.

$$z = \left(\frac{0.4\sqrt{fc'}\text{b.d}_{\text{bolt}}\left(1+\frac{a}{d_v}\right)}{E_s.A_s}\right)\left(\frac{dv-d_{\text{bolt}}/2+c'}{d_v}\right)$$ **8.17**

The concrete shear strength, V_c, and diagonal cracking angle, θ, may then be calculated using the SMCFT equation. To account for two sides' contribution, concrete resistance (C_c) is equal to twice the concrete shear strength for piles connected at the beam mid-span. In addition, bolt depth (d_{bolt}) or remaining depth (d_{rem}) should be used instead of d_v as discussed previously. Thus, the concrete resistance after cracking is given by:

$$C_c = \frac{2*0.40}{(1+1500.\varepsilon_z)}\sqrt{fc'}\text{b.d}_{\text{bolt}}$$ **8.18**

Where ε_z and z are given by Equations. 8.15 and 8.17.

The SMCFT, developed mainly for cracked sections, assumes that the aggregate interlock governs the shear failure of members without stirrups. Thus, the stirrups resistance, C_s, should be incorporated into the ultimate load calculation as it depends on both strain after diagonal crack formation and diagonal crack angle.

The experimental and numerical results demonstrated that only stirrups included within the plate width in the longitudinal direction contributed to the concrete ultimate load. Therefore, the stirrups contribution to the concrete ultimate load is given by:

$$C_s = A_v.f_v.\left(\frac{b_{\text{plate}}}{s}+1\right)$$ **8.19**

Where $f_v = \frac{f_y}{\varepsilon_y} . \varepsilon_z \le \varepsilon_y$

Equation 8.19 assumes full bonding between the stirrups and concrete, and hence strain compatibility (stirrups and concrete strains are equal). Therefore, the steel resistance may be calculated using the concrete strain, ε_z, and the concrete ultimate load for connection of pile attached to the beam mid-span is given by:

$$C_{u_{conc.}} = C_c + C_s = \frac{2*0.40}{(1+1500.\varepsilon_z)} \sqrt{fc'} b. \, d_{bolt} + A_v. f_v. \left(\frac{b_{plate}}{s} + 1\right) \qquad \textbf{8.20}$$

Also, the pile-friction contribution may be evaluated using the pile friction ratio (r_p), i.e.

$$C_{u_{conc.}} = (1 + r_p) \left[\frac{2*0.40}{(1+1500.\varepsilon_z)} \sqrt{fc'} b. \, d_{bolt} + A_v. f_v. \left(\frac{b_{plate}}{s} + 1\right)\right] \qquad \textbf{8.21}$$

Furthermore, the resistance of stirrups contained within the breakout cone should be considered in calculating the connection ultimate load after concrete failure. The breakout cone size depends on the diagonal cracking angle, θ. For design purposes, knowing that the connection ultimate load should be the lesser of capacity of stirrups within the breakout cone (denoted the reinforcement ultimate load) and the concrete ultimate load, but it should not be less than the concrete breakout cracking load. Also, if anchor reinforcement is used, the reinforcement ultimate load calculation should consider only the anchor reinforcement within the plate width. Based on this discussion, it is proposed to calculate the reinforcement ultimate load as:

$$Cu_{reinf.} = \left(1 + r_p\right) \left[\frac{A_v.f_y}{s} . (2. \, d_{bolt}. \cot\theta)\right] \text{ or } (1 + r_p) [A_{anchor}. f_u] \qquad \textbf{8.22}$$

Also, for (a/d) < 1, the connection capacity is limited to $1.2\sqrt{fc'}.b.d_{emb}$. Therefore, the connection ultimate load capacity ($C_{u\,Actual}$) should be given as:

$$C_{u\,Actual} = Min.\,of \begin{cases} Max.\,of \begin{cases} Cu_{conc.} = (1 + r_p)\left[\frac{2*0.40}{(1+1500.\varepsilon_z)}\sqrt{fc'}b.d_{bolt} + A_v.f_v.\left(\frac{b_{plate}}{s} + 1\right)\right] \\ Cu_{reinf.} = (1 + r_p)\left[\frac{A_v.f_y}{s}.(2.d_{bolt}.\cot\theta)\ or\ A_{anchor}.f_u\right] \\ Cu_{support} = 1.2\sqrt{fc'}.b.d_{bolt}\ \ if\ \left(\frac{a}{d}\right) < 1 \\ 2xBeam\ shear\ strength(\ using\ a_{max}) \end{cases} \end{cases} \geq C_c\ \ \textbf{8.23}$$

The components of connection capacity (concrete capacity, C_c, steel capacity, C_s, concrete ultimate load, $Cu_{conc.}$, transverse reinforcement ultimate capacity, Cu_{reinf}, twice beams shear capacity, and actual connection ultimate load, $Actual\ C_u$) are used in table 8-6 for experimentally tested connections capacity calculation and Tables 8-7 and 8-8 for numerically investigated connections. The used specimens input data are indicated in Appendix E. It is clear in these tables that because most of the studied connections had a small transverse reinforcement ratio and the beam capacity was more than the connection capacity, the concrete ultimate strength ($Cu_{conc.}$) was equal to the actual connection ultimate load (Actual C_u) for most of them. Only when large transverse reinforcement ratio or heavy anchor reinforcement were used, the actual connection ultimate load (Actual C_u) was more than the concrete ultimate strength ($Cu_{conc.}$) because the transverse/ anchor reinforcement increased the reinforcement ultimate load to be more than the concrete ultimate load after wide concrete cracks formation.

Table 8- 6 Components of connection capacity for experimentally tested beams

Specimen	z	ε_z	Θ	Cone dim. (mm)	C_c (kN) Eq. 8.18	C_s (kN) Eq. 8.19	$Cu_{conc.}$ (kN) Eq. 8.21	$Cu_{reinf.}$ (kN) Eq. 8.22	*2xBeam shear capacity (kN)	$C_{u\ Actual}$ (kN) Eq. 8.23
C1	0.0028	0.0011	36	1061	331	32	386	185	632	386
C2	0.0040	0.0013	38	859	249	40	307	150	448	307
C3	0.0037	0.0013	38	744	219	38	273	130	448	273
C4	0.0039	0.0013	38	861	250	42	310	150	457	310
C5	0.0038	0.0013	38	865	252	46	316	151	471	316
C6	0.0026	0.0010	36	925	291	31	343	162	632	343
C7	0.0016	0.0007	34	997	350	22	397	174	830.4	397
C8	0.0040	0.0013	38	859	249	79	349	300	527	349
C9	0.0040	0.0013	38	859	249	58	326	300	527	326

* *Using Response* 2000 using a* and f_t from the material tests

Table 8-7 Components of connection capacity for numerically investigated beams with (a/d)>1

Specimen	z	ε_z	Θ	Cone dim. (mm)	C_c (kN) Eq. 8.18	C_s (kN) Eq. 8.19	$Cu_{conc.}$ (kN) Eq. 8.21	$Cu_{reinf.}$ (kN) Eq. 8.22	*2xBeam shear capacity (kN)	$C_{u\ Actual}$ (kN) Eq. 8.23
C-B-10	0.0079	0.0020	43	729	187	48	250	103	307	250
C-B-7	0.0020	0.0009	35	962	320	21	363	136	721	363
C-B-35	0.0008	0.0005	32	1074	437	11	477	152	963	477
C-B-15	0.0054	0.0016	40	803	219	39	284	118	282	282
C-B-20R	0.0036	0.0013	38	875	258	31	318	129	402	318
C-B-25R	0.0022	0.0009	35	954	313	22	370	140	556	370
C2-20	0.0032	0.0012	37	893	220	29	264	127	466	264
C2-35	0.0043	0.0014	39	846	261	34	313	120	521	313
C2-40	0.0039	0.0013	38	860	249	32	299	122	535	299
C2-W	0.0036	0.0012	38	716	211	30	257	102	448	257
C2-TWO BOLTS	0.0042	0.0014	39	1015	291	33	345	144	448	345
C1-TWO BOLTS	0.0042	0.0014	39	1145	327	34	384	162	632	384
C9-2 BOLTS	0.0042	0.0014	39	1015	291	48	361	288	527	361
C-A-6	0.0040	0.0013	38	859	249	73	342	158	454	342
C-A-8	0.0040	0.0013	38	859	249	114	386	247	454	386
C-A-10	0.0040	0.0013	38	859	249	228	507	494	454	454
C-A-20	0.0040	0.0013	38	859	249	683	991	1481	454	454
C-A-25	0.0040	0.0013	38	859	249	1139	1476	2468	454	454
2-8-200	0.0040	0.0013	38	859	249	52	320	197	410	320
2-10-200	0.0040	0.0013	38	859	249	104	375	393	450	393

Specimen										
2-15-200	0.0040	0.0013	38	859	249	208	486	786	450	450
2-8-100	0.0040	0.0013	38	859	249	75	345	393	450	393
2-10-100	0.0040	0.0013	38	859	249	151	425	786	450	450
2-15-100	0.0040	0.0013	38	859	249	302	586	1573	464	464
4-8-200	0.0040	0.0013	38	859	249	104	375	393	525	393
4-10-200	0.0040	0.0013	38	859	249	208	486	786	525	525
4-15-200	0.0040	0.0013	38	859	249	416	707	1573	525	525
2-8-200 (4-25M)	0.0217	0.0035	53	504	313	36	385	226	516	385
2-10-200 (4-25M)	0.0022	0.0009	35	954	313	72	425	453	525	453
2-15-200 (4-25M)	0.0022	0.0009	35	954	313	144	504	906	588	588
C-R-2.75 (4-20M)	0.0037	0.0013	38	1035	244	40	316	214	352	316
C-R-2.50 (4-20M)	0.0035	0.0012	38	1047	251	38	319	215	387	319
C-R-2.00 (4-20M)	0.0029	0.0011	37	1073	267	34	326	215	481	326
C-R-1.75 (4-20M)	0.0027	0.0010	36	1088	277	32	331	216	557	331
C-R-5.5 (4-30M)	0.0028	0.0011	37	1079	271	33	366	240	389	366
C-R-5 (4-30M)	0.0026	0.0010	36	1092	280	32	374	243	420	374
C-R-4 (4-30M)	0.0022	0.0009	35	1120	300	28	385	244	495	385
C-R-3.5 (4-30M)	0.0019	0.0009	35	1135	312	26	389	242	521	389
C-R-2.75 (4-30M)	0.0016	0.0008	34	1160	334	23	399	240	542	399
C-R-2.25 (4-30M)	0.0014	0.0007	34	1179	351	21	408	239	577	408
C-R-2.0 (4-30M)	0.0013	0.0006	33	1190	362	20	413	239	619	413
C-R-1.75(4-30M)	0.0011	0.0006	33	1200	373	19	420	238	717	420

* *Using Response* 2000 using a* and f_t from the material tests

Table 8- 8 Components of connection capacity for investigated beams with (a/d)$\leq$ 1

Specimen	z	ε_z	Θ	Cone dim. (mm)	C_c (kN) Eq. 8.18	C_s (kN) Eq. 8.19	$Cu_{conc.}$ (kN) Eq. 8.21	$Cu_{reinf.}$ (kN) Eq. 8.22	*2xBeam shear capacity (kN)	$C_{u\ Actual}$ (kN) Eq. 8.23
C-R-1 (4-20M)	0.0019	0.0008	35	1138	315	26	353	219	873	353
C-R-0.5 (4-20M)	0.0014	0.0007	34	1179	352	21	378	222	1572	378
C-R-0.25 (4-20M)	0.0011	0.0006	33	1204	377	18	397	224	1572	397
C-R-1(4-30M)	0.0008	0.0005	32	1236	415	15	446	238	1124	446
C-R-0.75(4-30M)	0.0007	0.0004	32	1250	433	13	458	238	1498	458
C-R-0.5 (4-30M)	0.0006	0.0004	32	1263	451	12	471	238	2022	471

* *Using Response* 2000 using a* and f_t from the material tests

Tables 8-9, 8-10, and 8-11 compare the calculated concrete resistance (C_c) to the recorded connection breakout cracking load (C_{cr}) after taking the effect of the pile friction into account, and the calculated actual connection ultimate strength ($Actual\ C_u$) to the recorded connection ultimate load.

Table 8-9 demonstrates that the concrete resistance (C_c) calculated by the modified SMCFT (Equation 8.18), taking into account the pile-concrete friction action, can predict the breakout cracking load reasonably well. The mean percentage ratio of the calculated concrete resistance $(1 + r_p)C_c$ and the recorded breakout cracking load C_{cr} is 90.2% and its standard deviation is only 4.4%, while the coefficient of variation is 4.9%.

These results indicate the ability of the proposed equations to predict the breakout cracking load reasonably. Also, table 8-9 confirms the accuracy of Equation 8.23 in predicting the connection ultimate load. The mean percentage ratio of the calculated connection ultimate load ($C_{u_{actual}}$) and the recorded connection ultimate load (C_u) is 98.3% and its standard deviation is only 5.7%, while the coefficient of variation is 5.8% and the root mean squared error is 5.6%. These values indicate that Equations 8.23 could capture the connection ultimate load accurately and may be used in the analysis/design of helical piles/micropiles connections to new foundations.

Table 8- 9 Comparison of calculated and experimentally recorded connection capacity

Specimen	Recorded C_{cr} (kN)	$\frac{Calculated\ C_c}{Recorded\ C_{cr}}(1+r_p)$ %	Recorded C_u (kN)	$\frac{calculated\ Cu_{actual.}}{Recorded\ C_{u.}}$ %
C1	400	88	415	93.3
C2	295	90	314	98.1
C3	250	93	268	102.2
C4	280	95	287	108.7
C5	289	92	348.5	91.0
C6	330	94	339	101.5
C7	400	93	409.3	97.0
C8	320	83	340	103.5
C9	315	84	350.9	93.5
Average%		90.2		98.3
Standard deviation%		4.4		5.7
Coefficient of variation%		4.9		5.8
Root mean squared error %		10.6		5.6

Table 8-7 shows that for beams with high transverse reinforcement ratios or heavy anchor reinforcement (e.g. beams C-A-25, C-A-20, 4-10-200, and 4-8-200), the pile connection failed either due to the failure of the transverse reinforcement or the shear failure in the beam at the connection. This confirms that the two limit states of the transverse reinforcement ultimate strength and the beam shear capacity must be considered in the calculation of the pile connection.

Table 8-10 compares the ratio of calculated and recorded connection ultimate load for analytically tested connections with (a/d)>1. The presented results confirm the ability of Equation 8.23 to accurately predict the actual behaviour of the pile connection, which is manifested by the calculated mean percentage value of 103.8%, percentage standard deviation of 14.8% and percentage coefficient of variation of 14.3%. Moreover, it is

clear that the concrete resistance (C_c) multiplied by $(1 + r_p)$ gives appropriate evaluation of the breakout cracking load. The mean value of the percentage ratio between the calculated concrete resistance $(1 + r_p)C_c$ and the recorded breakout cracking load C_{cr} is 96.1% and the standard deviation for this ratio is 15.9% and coefficient of variation is 16.2%.

It should be noted that the original SMCFT was developed for slender beams with (a/d) > 2.5. Also, CSA A23.3 Code recommends that for (a/d) < 1, the concrete strain should be calculated considering (a/d) = 1. Table 8-10 confirms the applicability of the proposed equation for different (a/d) ratios that are more than 1.

Table 8- 10 Comparison of calculated capacity using recommended equations with FE results for beams with (a/d)>1

Specimen	Recorded C_{cr} (kN)	$\frac{Calculated\ C_c}{Recorded\ C_{cr}}(1 + r_p)$ %	Recorded C_u (kN)	$\frac{calculated\ Cu_{actual}}{Recorded\ C_u}$ %
C-B-10	234	85	234	107
C-B-7	360	95	360	101
C-B-35	445	105	445	107
C-B-15	237	102	264	107
C-B-20R	287	99	287	111
C-B-25R	349	99	349	106
C2-20	240	98	245	108
C2-35	338	82	338	93
C2-40	351	75	351	85
C2-W	226	99	233	110
C2-TWO BOLTS	305	101	327	105
C1-TWO BOLTS	451	77	451	85
C9-2 BOLTS	353	88	455	79
C-A-6	294	90	300	114
C-A-8	319	83	360	107
C-A-10	330	80	458	99

C-A-20	341	78	454	100
C-A-25	357	74	476	95
2-8-200	295	90	298	107
2-10-200	295	90	342	115
2-15-200	295	90	382	118
2-8-100	303	87	405	97
2-10-100	304	87	429	105
2-15-100	341	78	586	79
4-8-200	303	87	405	97
4-10-200	328	81	518	101
4-15-200	362	73	694	76
2-8-200 (4-25M)	303	114	298	129
2-10-200 (4-25M)	317	109	342	132
2-15-200 (4-25M)	323	107	382	154
C-R-2.75 (4-20M)	260	105	277	114
C-R-2.50 (4-20M)	287	97	287	111
C-R-2.00 (4-20M)	305	95	305	107
C-R-1.75 (4-20M)	301	99	301	110
C-R-5.5 (4-30M)	231	141	424	86
C-R-5 (4-30M)	277	121	450	83
C-R-4 (4-30M)	269	131	438	88
C-R-3.5 (4-30M)	280	128	396	98
C-R-2.75 (4-30M)	313	119	350	114
C-R-2.25 (4-30M)	362	106	369	110
C-R-2.0 (4-30M)	396	99	396	104
C-R-1.75(4-30M)	418	96	418	100
Average%		96.1		103.8
Standard deviation%		15.9		14.8
Coefficient of variation%		16.5		14.3
Root mean squared error %		16.2		15.2

Table 8-11 indicates that the proposed equation will accurately predict the connection ultimate capacity for $(a/d) \geq 1$, but provides very conservative values for $(a/d) < 1$. Thus, for the connection with (a/d) ratio < 1, it is recommended to use a strut and tie model as

shown in Figures 8-1 and 8-2 to calculate the connection ultimate capacity. However, the strut and tie model is not investigated in the current research as deep beams with (a/d) < 1 is outside the scope of this research.

Table 8-11Comparison of calculated connection capacity using the recommended equations with FE results for beam with (a/d) ≤ 1

Specimen	Recorded C_{cr} (kN)	$\frac{Calculated\ C_c}{Recorded\ C_{cr}}(1 + r_p)$ %	Recorded C_u (kN)	$\frac{calculated\ Cu_{actual.}}{Recorded\ C_{u.}}$ %
C-R-1 (4-20M)	379	86	379.0	93
C-R-0.5 (4-20M)	775	46	793.0	48
C-R-0.25 (4-20M)	850	44	956.0	41
C-R-1(4-30M)	443	97	604.2	74
C-R-0.75(4-30M)	785	57	785.0	58
C-R-0.5 (4-30M)	853	54	852.7	55
Average%		64.0		61.6
Standard deviation%		22.1		19.0
Coefficient of variation%		34.6		30.8
Root mean squared error %		41.3		42.1
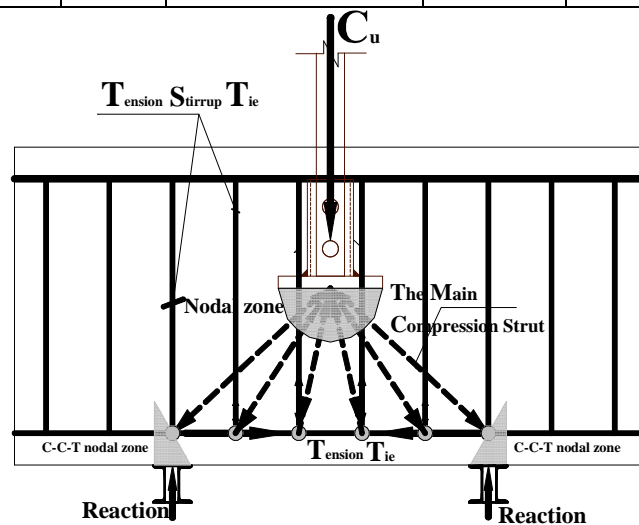
Figure 8- 2 Strut-and-tie model of a single span deep beam with stirrups with (a/d)<1

For transverse reinforcement, stirrups or anchor reinforcement, that can resist loading up to its ultimate capacity, the governing equation should be Equation 8.23 (*Actual C_u*):

however, the concrete crack width will be so wide to the extent the beam will no longer maintain its integrity. Alternatively, the connection design capacity ($C_{u\,Design}$) should be evaluated considering the lesser of four limit states, but will not be less than the concrete resistance C_c for limit state design analysis. Furthermore, the limit state of the transverse reinforcement ultimate capacity is equal to its yield strength instead of its ultimate tensile capacity. Therefore, the connection design capacity ($C_{u\,Design}$) may be given by:

$$C_{u\,Design} = \text{the least of} \begin{cases} Cu_{conc.} = \left(1 + r_p\right)\left[\frac{2*0.40}{(1+1500.\varepsilon_z)}\sqrt{fc'}\text{b}.\text{d}_{\text{bolt}} + \text{A}_\text{v}.\text{f}_\text{v}.\left(\frac{\text{b}_{\text{plate}}}{\text{s}} + 1\right)\right] \\ Cu_{support} = 1.2\sqrt{fc'}.b.\text{d}_{\text{bolt}}\;\;if\;\left(\frac{a}{d}\right) < 1 \\ Cu_{reinf.} = \left(1 + r_p\right)\left[\frac{\text{A}_\text{v}.\text{f}_\text{y}}{\text{s}}.(2.\,\text{d}_{\text{bolt}}.\cot\theta)\; or\; \text{A}_{\text{anchor}}.\text{f}_\text{y}\right] \\ 2xBeam\;shear\;strength(\;using\;a_{max}) \end{cases} \geq C_c \;\; \textbf{8.24}$$

Based on this discussion, it may be concluded that Equation 8.23 ($Actual\;C_u$) can be used in performance based design. For example, when designing for a maximum credible earthquake with very low probability of occurrence, structures may reach a state of near collapse and the structure may not be used after the earthquake (i.e. collapse prevention performance level). In this case, the concrete cracking width is not important, and the ductile failure provided by the transverse reinforcement is the important factor. A specific stirrups strain level can be specified as the governing design criterion. Therefore, it is recommended to use transverse reinforcement that has an ultimate capacity at least equal to $C_{u_{conc}}$.

8.5 Cyclic loading consideration

From the three specimens tested under cyclic compression loading in Chapter 6, it was found that cyclic loading can deteriorate the concrete mechanical properties causing a reduction in the connection capacity and a clear change in its stiffness specially after the breakout cracking load. The maximum recorded reduction in the connections ultimate capacity from the three tested specimens was only 11% of the same specimens' capacity if loaded under monotonic loading. For sure, more testing is required to exactly indicate the effect of cyclic loading on the connection capacity, however, it is recommended to use a reduction factor of at least 0.85 in case of cyclic compression load is expected as a case of loading on the helical pile- RC grade beam connection.

8.6 Recommended Equations for Connection Design

Employing the developed cracking load and ultimate load equations and considering the materials reduction factors, the pile-grade beam connection design may be accomplished according to the flow chart shown in Figure 8-6 and taking into consideration the following design conditions:

1) The effective shear span, a*, should be used instead of the shear span, a, if the plate is not allowed to yield. To achieve this, the plate thickness should be given by:

$$t_{plate} = \sqrt{\left(\frac{3}{8}\right).\left(\frac{C_{u\,actual}}{f_y}\right).\frac{(b_{plate}-50)^2}{b_{plate}^{\,2}}} \qquad \textbf{8.25}$$

394

2) The beam width used to calculate the single shear strength should be limited to the lesser of $\left(2\sqrt{2}d_{rem} + b_{plate}\right)\ or\ \left(2\sqrt{2}d_{bolt}\right)$.

3) For connections with bolts shorter than half the pile cap's plate width, the remaining depth (d_{rem}) should be used instead of the top bolt depth (d_{bolt}) because the contribution of the bolt bearing on the concrete may be negligible.

4) To ensure connection fixity, it must be designed to prevent breakout cracking. Thus, the breakout cracking load C_{cr} must be equal to or greater than the ultimate pile load. The breakout load is given by:

$$C_{cr} = \left[2.6\frac{1}{\sqrt{1+d_{rem}/(25.a_g)}}(\rho.\emptyset_c.\lambda.fc'.d)^{1/3}.\left(\frac{\sqrt[3]{a^*_{right}}+\sqrt[3]{a^*_{left}}}{\sqrt[3]{a^*_{right}}.\sqrt[3]{a^*_{left}}}\right)\right].b.d_{rem} \qquad \textbf{8.26}$$

Figure 8-3 presents the ratio between the calculated values using equation 8.26 and the actual recorded values for 40 investigated connections using a unity concrete reduction factor. Confirming that using the remaining depth instead of the bolt depth and neglecting the pile friction will cause a more conservative equation that will have all of its results less than the actual recorded values.
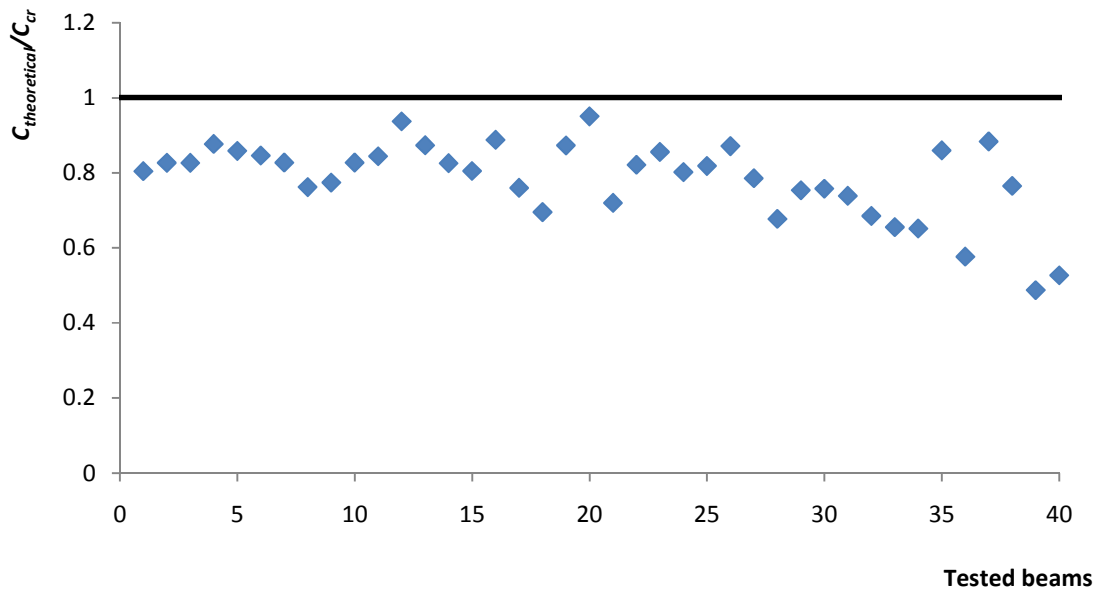
Figure 8- 3 The ratio between the calculated breakout cracking load using Equation 8.26 and the recorded values

5) For a hinged connection design using the limit state design approach, the ultimate design load $C_{u\ Design}$ must be equal to or greater than the ultimate pile load. The ultimate design load, $C_{u\ Design}$, should be calculated using equation 8.27.

$$C_{u\ Design} = the\ least\ of \begin{cases} Cu_{conc.} = \frac{2*0.40}{(1+1500.\varepsilon_z)}\sqrt{\emptyset_c\lambda fc'}\text{b}.\,\text{d}_{rem} + \emptyset_s\text{A}_v.\,\text{f}_v.\left(\frac{\text{b}_{plate}}{\text{s}} + 1\right) \\ Cu_{support} = 1.2\sqrt{\emptyset_c\lambda fc'}.b.d_{rem}\quad if\ \left(\frac{a}{d}\right) < 1 \\ Cu_{reinf.} = \frac{\text{A}_v.\emptyset_s\text{f}_y}{\text{s}}(2.\,\text{d}_{rem}.\cot\theta)\ or\ \text{A}_{anchor}.\emptyset_s\text{f}_y \\ 2xBeam\ shear\ strength(\ using\ a_{max}) \end{cases} \geq C_c \quad \textbf{8.27}$$

Figure 8-4 presents the ratio between the calculated values using Equation 8.27 and the actual recorded values for 57 investigated connections using a unity concrete and reinforcement reduction factor. Confirming that using the remaining depth instead of the

396

bolt depth and neglecting the pile friction will cause a more conservative equation that will have all of its results less than the actual recorded values. Figure 8-7 presents a flow chart showing the design steps required when this design is used.
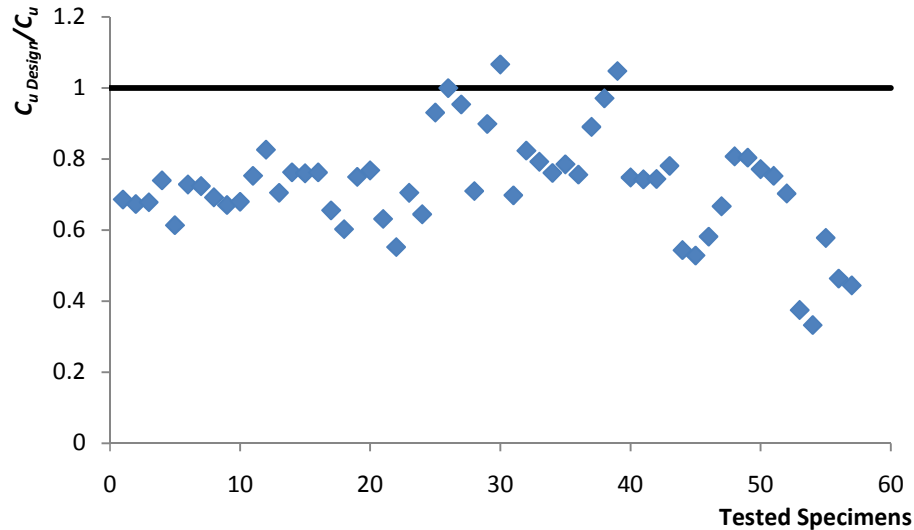
Figure 8-4 The ratio between the calculated connection design load using equation 8.27 and the recorded values

6) For a hinged connection design using the collapse prevention level in a performance based design approach, the connection can be designed for the actual ultimate load, $C_{u\,Actual}$. Thus, $C_{u\,Actual}$ must be equal to or more than the ultimate pile load. In this case, $C_{u\,Actual}$, should be calculated using equation 8.28.

$$C_{u\,Actual} = Min.of \begin{cases} Max.of \begin{cases} Cu_{conc.} = \left[\frac{2*0.40}{(1+1500.\varepsilon_z)}\sqrt{\emptyset_c\lambda fc'}\text{b.}\text{d}_{rem} + \emptyset_s A_v.f_v.\left(\frac{b_{plate}}{s}+1\right)\right] \\ Cu_{reinf.} = \left[\frac{A_v.\emptyset_s f_y}{s}.(2.\text{d}_{rem}.\cot\theta) \text{ or } A_{anchor}.\emptyset_s f_u\right] \end{cases} \\ Cu_{support} = 1.2\sqrt{\emptyset_c\lambda fc'}.\text{b.}\text{d}_{rem} \quad if \;\left(\frac{a}{d}\right) < 1 \\ 2xBeam\;shear\;strength(\,using\;a_{max}) \end{cases} \qquad \textbf{8.28}$$

Figure 8-5 presents the ratio between the calculated values using equation 8.28 and the actual recorded values for 57 investigated connections using a unity concrete and reinforcement reduction factor. It confirms that using the remaining depth instead of the bolt depth and neglecting the pile friction will cause a more conservative equation that will have most of its results less than the actual recorded values but so close to it. Also, it is clear that using the concrete and reinforcement reduction factors will confirm that all the calculated results will be conservative. Figure 8-8 presents a flow chart indicating the design steps required when this design is used.
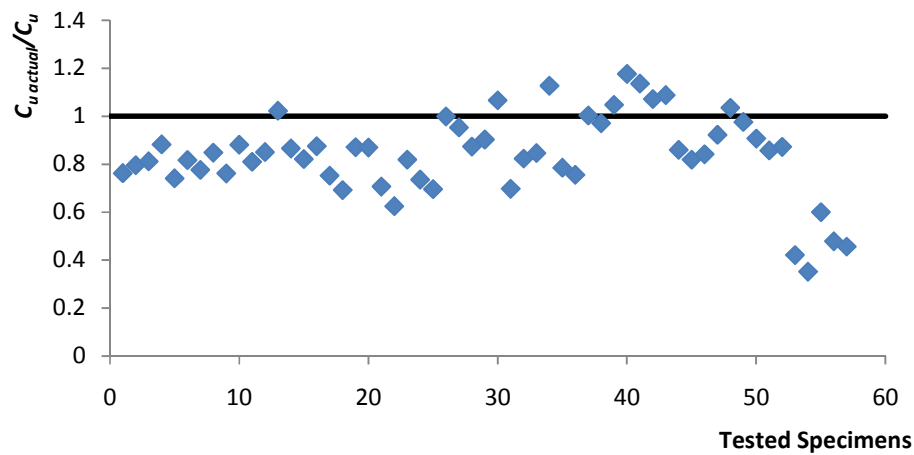
Figure 8- 5 The ratio between the calculated actual connection design load using equation 8.28 and the recorded values
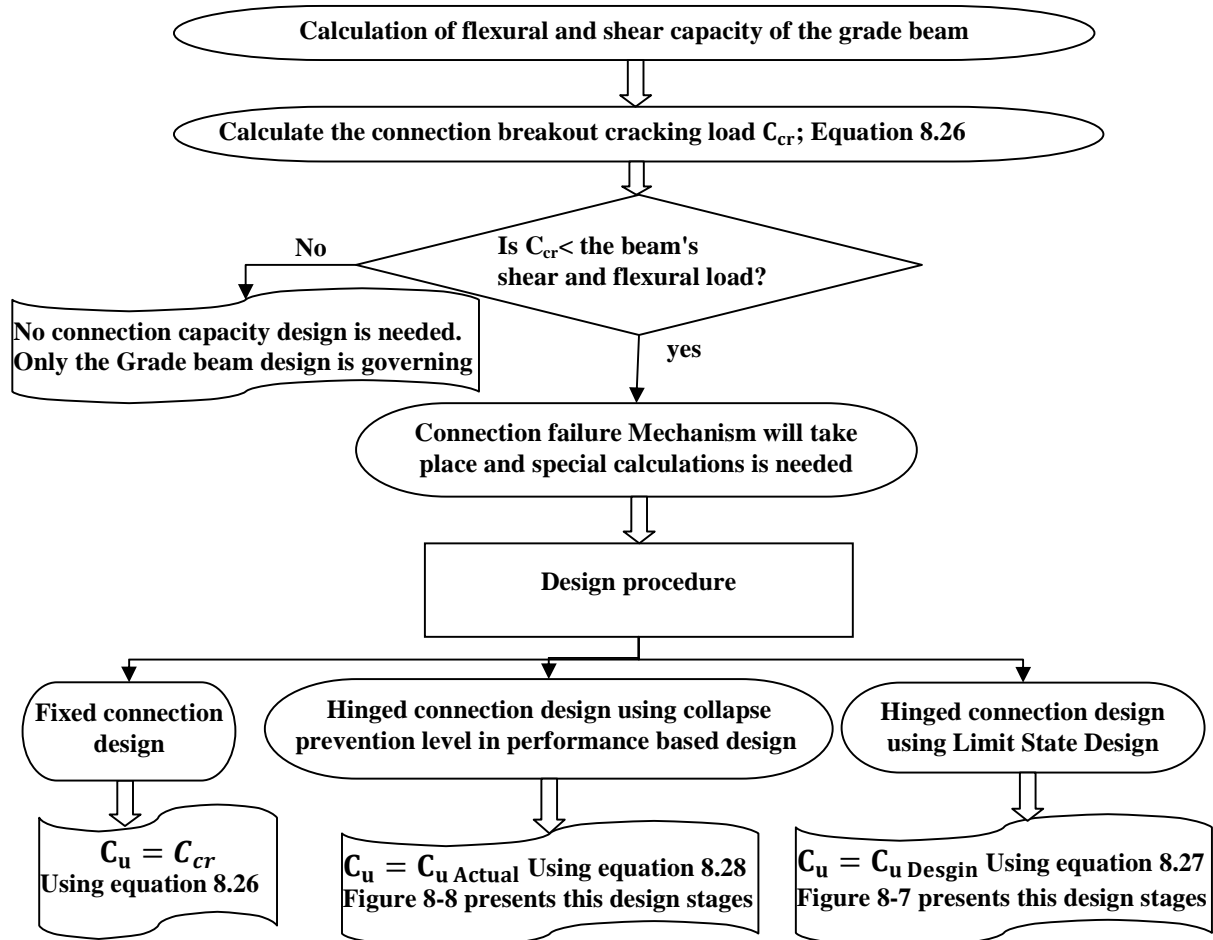
Figure 8- 6 The helical pile- RC grade beam connection's design stages

Calculate C_c, C_s, $Cu_{conc.}$ using equations 8.13, 8.14, and 8.15, respectively, using rp=1, d_{rem} instead of d_{bolt}, and using concrete/steel reduction factors $\emptyset_c$=0.65, $\emptyset_s$=0.85

Calculate $C_{u\,reinf.}$ using equation 8.17, using rp=1, d_{rem} instead of d_{bolt}, and using steel reduction factor $\emptyset_s$=0.85

Calculate the sum of the shear capacities of the grade beam at the pile location from the two sides; $C_{u\,shear}$

yes

Is $C_{u\,shear} <$ $Cu_{conc.}$&$C_{u\,reinf.}$?

Single shear failure in the grade beam will take place and $C_u = C_{u\,shear}$

No

Is a/d<1?

Calculate $Cu_{support} = 1.2\sqrt{\emptyset_c \lambda fc'}.b.d_{rem}$

yes

No

Is $Cu_{support} <$ $C_{u\,reinf.}$&$Cu_{conc.}$?

No

yes

Crushing at the support region will occur & $C_u = C_{u\,support}$

Is $Cu_{conc.} >$ $C_{u\,reinf.}$?

No

yes

$C_{udesign} = C_{u\,conc.}$ & non recommended brittle breakout failure will take place. Increase the transverse reinforcement till

$C_{udesign} = C_{u\,conc.}$ & recommended ductile failure after the concrete breakout cracking will occur

Figure 8- 7 The design steps required when a limit state design was used for hinged helical pile-RC grade beam connection.
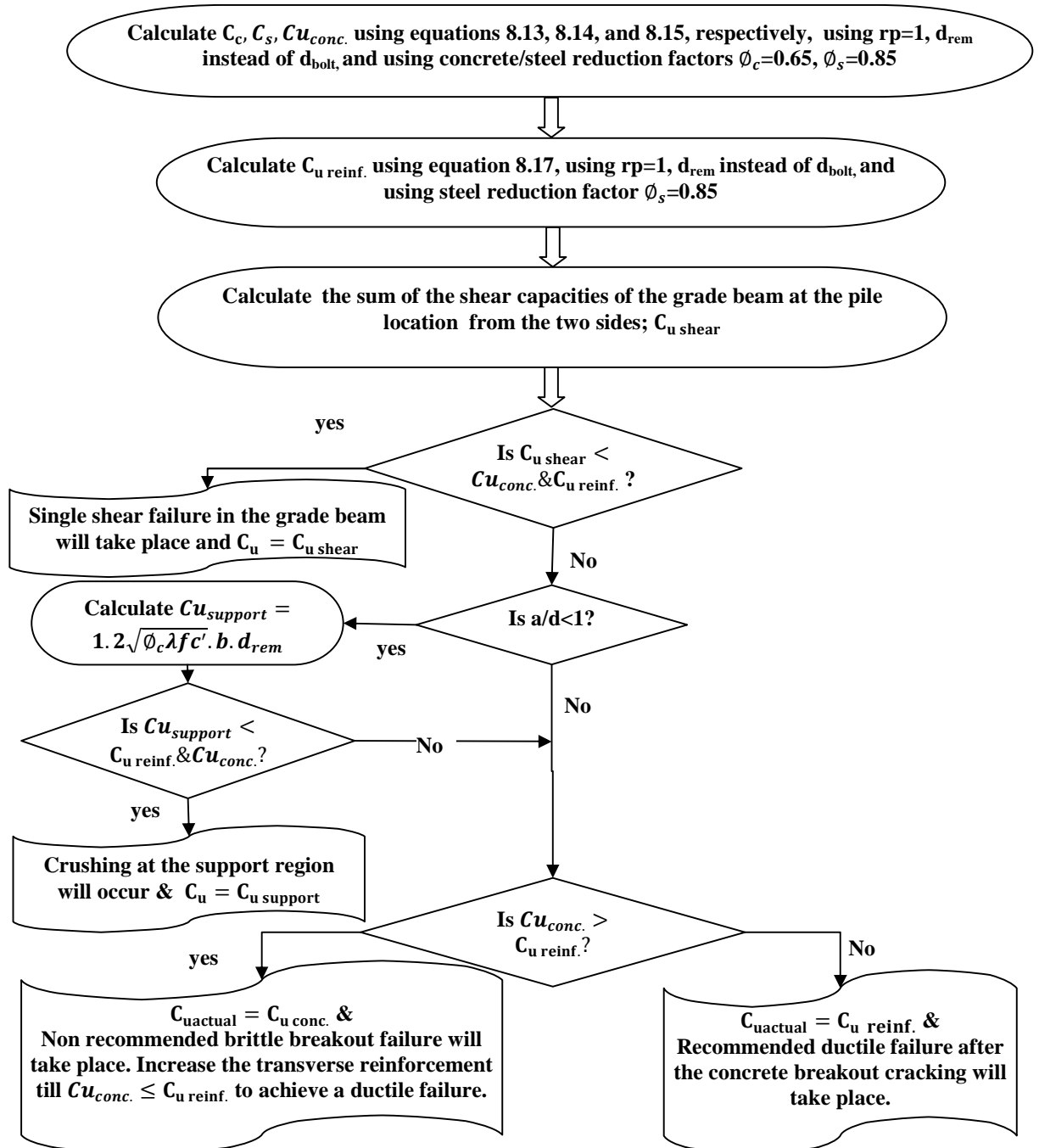
Figure 8- 8 The design steps required when a collapse prevention level in performance based design was used for hinged helical pile-RC grade beam connection.

8.7 Conclusions

Analytical equations were developed to determine the connection capacity under compression loading. These equations are developed considering the findings of both the experimental and numerical investigations conducted in this research in Chapters 6 and 7 as well as relevant methods available in the literature. The following provides the main conclusions of this effort.

- Two equations are proposed to calculate the breakout cracking load of the pile connection. The first equation (i.e. Equation 8.8) is a modification to Al-zoubi's equation (2011) and it predicted the breakout cracking load with almost 101% mean value with 5% COV. The second equation (i.e. Equation 8.9) is a modification of the cracked concrete shear resistance equation of the SMCFT. It accounts for the difference in the concrete strain due to pile condition and calculates the accurate concrete strength at once, i.e., eliminating the need for iterative procedure.

- The modified SMCFT (Equation 8.21) is recommended for calculating the concrete ultimate strength contribution to the pile connection capacity. The proposed modification accounts for the transverse reinforcement contribution considering the same concrete strain used for concrete resistance.

- To calculate the pile-connection ultimate capacity, four different limit states were calculated and compared. These limit states are the concrete ultimate strength, the transverse reinforcement ultimate strength, the beam shear strength at the pile

402

location, and the crushing of support region strength when (a/d) is less than 1. The value to be used in a limit state design is the least value of the four limit states, while the actual value that can be used in a serviceability performance level design is taking the bigger value of the concrete ultimate load and the transverse reinforcement ultimate load and compare it with the other two values to take the least value. These two equations are 8.23 and 8.24.

- It is recommended to use transverse reinforcement that has capacity $\geq$ $Cu_{conc.}$.

- For the connection design under compression loading, three design equations were recommended taking into consideration the materials reduction factors, the site conditions, the used connection details, and the connection fixation condition. These design equations are presented in Equations 8.26, 8.27, and 8.28 and the design procedures are demonstrated in Figures 8-6, 8-7, and 8-8.

- It is recommended to use a reduction factor of at least 0.85 in case of cyclic compression load is expected as a case of loading on the helical pile- RC grade beam connection.

8.8 References

Abd Elaziz, A.Y. & El Naggar, M.H., 2015. Performance of Hollow Bar Micropiles under Monotonic and Cyclic Lateral Loads. *Journal of Geotechnical and Geoenvironmental Engineering*, 141(5), pp.1–11.

ACI 318, 2011. *Building Code Requirements for Structural Concrete (ACI 318-11) and Commentary*, Farmington Hills, MI: American Concrete Institute.

ACI-ASCE Committee 326, 1962. Shear and Diagonal Tension. *ACI Journal Proceedings*, 59(1), pp.1–30.

Al-Zoubi, M., 2014. Diagonal Cracking Capacity and Ultimate Shear Strength of Slender RC Beams without Web Reinforcement. *Jordan Journal of Civil Engineering*, 8(1), pp.97–112.

Baltay, P. & Gjelsvik, A., 1990. Coefficient of Friction for Steel on Concrete at High Normal Stress. *Journal of Materials in Civil Engineering*, 2(1), pp.46–49.

Bažant, Z.P. et al., 2007. Justification of ACI 446 Proposal for Updating ACI Code Provisions for Shear Design of Reinforced Concrete Beams. *ACI Structural Journal*, 104(5), pp.601–610.

Bazant, Z.P. & Kazemi, M.T., 1991. Size Effect on Diagonal Shear Failure of Beams Without Stirrups. *Structural Journal*, 88(3), pp.268–276.

Bažant, Z.P. & Yu, Q., 2005. Designing Against Size Effect on Shear Strength of Reinforced Concrete Beams Without Stirrups: II. Verification and Calibration. *Journal of Structural Engineering*, 131(12), pp.1886–1897.

Bentz, E.C. & Collins, M.P., 2006. Development of the 2004 Canadian Standards Association (CSA) A23.3 shear provisions for reinforced concrete. *Canadian Journal of Civil Engineering*, 33(5), pp.521–534.

Carrato, P.J., Krauss, K.W. & Kim, J.B., 1996. Tension Tests of Heavy-Duty Anchors with Embedments of 8 to 19 Inches. *ACI Structural Journal*, 93(3), pp.360–368.

CEB, 1993. *CEB-FIP model code 1993: design code*, Thomas Telford.

Collins, M.P. et al., 1996. A General Shear Design Method. *Structural Journal*, 93(1), pp.36–45.

Collins, M.P. & Kuchma, D., 1999. How Safe Are Our Large, Lightly Reinforced Concrete Beams, Slabs, and Footings? *Structural Journal*, 96(4), pp.482–490.

Collins, M.P. & Mitchell, D., 1991. *Prestressed Concrete Structures*, Prentice Hall.

CSA A23.3, 2004. *A23. 3-04: design of concrete structures*,

Fereig, S. M., & Smith, K.N., 1977. Indirect Loading on Beams with Short Shear Spans. *Magazine of Concrete Research*, 74(5), pp.220–222.

Ferguson, P., 1956. Some implications of recent diagonal tension tests. *ACI Journal Proceedings*, 53(8), pp.157–172.

Kani, G., 1966. Basic facts concerning shear failure. *ACI Journal Proceedings*, 63(June), pp.675–692.

Kim, J. & Park, Y., 1997. Prediction of Shear Strength of Reinforced Concrete Beams without Web Reinforcement. *ACI Materials Journal*, 93(3), pp.213–222.

Lee, N.H. et al., 2007. Tensile-Headed Anchors with Large Diameter and Deep Embedment in Concrete. *ACI Structural Journal*, 104(4), pp.479–486.

Lubell, A.S., Bentz, E.C. & Collins, M.P., 2009. Shear Reinforcement Spacing in Wide Members. *ACI Structural Journal*, 106(2), pp.205–214.

Mathey, R. & Watstein, D., 1963. Shear strength of beams without web reinforcement containing deformed bars of different yield strengths. *ACI journal proceedings*, 60(13), pp.183–207.

Metwally, I.M., 2012. Evaluate the capability and accuracy of response-2000 program in prediction of the shear capacities of reinforced and prestressed concrete members. *HBRC Journal*, 8(2), pp.99–106.

Ozcebe, G., Ersoy, U. & Tankut, T., 1999. Evaluation of Minimum Shear Reinforcement Requirements for Higher Strength Concrete. *ACI Structural Journal*, 96(3), pp.361–368.

Smith, K.N. & Fereig, S.M., 1974. Effect of Loading and Supporting Conditions on the Shear Strength of Deep Beams. *ACI Special Publication*, 42, pp.441–460.

Tan, K.H., KONG, F.K. & WENG, L.W., 1997. High strength concrete deep beams subjected to combined Top-and Bottom-Loading. *ACI Structural Engineer*, 75(11).

Taylor, R., 1960. Some shear tests on reinforced concrete beams without shear reinforcement*. *Magazine of Concrete Research*, 12(36), pp.145–154.

Yang, K.-H. & Ashour, A.F., 2008. Mechanism Analysis for Concrete Breakout Capacity of Single Anchors in Tension. *ACI Structural Journal*, 105(5), pp.609–616.

Qiang, Yu, Q. & Bažant, Z.P., 2011. Can Stirrups Suppress Size Effect on Shear Strength of RC Beams? *Journal of Structural Engineering*, 137(5), pp.607–617.

Zsutty, B., 1968. Beam Shear Strength Prediction by. , 5(65), pp.943–951.

Zsutty, T., 1971. Shear Strength Prediction for Separate Categories of Simple Beam Tests. *ACI Journal Proceedings*, 68(2), pp.138–143.

Zuhua Wang, 1987. shear strength of slender concrete beams loaded indirectly. *International journal of structures*, 7(1), pp.17–42.

BEHAVIOUR OF HELICAL PILE CONNECTORS FOR NEW FOUNDATIONS SUBJECTED TO SHEAR LOADING: EXPERIMENTAL INVESTIGATION

9.1 Introduction

This research investigates the behaviour of the connection between slender solid shaft pile types (e.g. square shaft helical piles and micropiles) and a new reinforced concrete foundation (e.g. grade beams and footings). Typically, steel brackets (plates) are used in order to transfer loads from the new reinforced concrete foundation to the steel pile. The bracket can be connected to the pile by welding or by bolts, and the connection behaviour can be considered as a headed anchor. However, these types of anchors are not addressed by current design codes (e.g. A23.3-04 Appendix D, ACI 318-11 Appendix D, or ACI 349-01 Appendix B) because these codes are developed assuming linear fracture mechanics (Lee et al., 2007) based on test results of anchors with high bearing pressure. Furthermore, the piles may be connected to grade beams with limited width, which may reduce the connection capacity.

In the research described herein, full-scale pile-foundation connection models were tested experimentally under shear loading in order to evaluate the performance of the connection and its failure mechanism under monotonic and cyclic loadings. Four groups of specimens were tested under monotonic shear loading to evaluate the effects of: the pile embedment depth into the foundation; the width of the pile cap's plate; and the

longitudinal and transverse reinforcements of the grade beam. A fifth group, involving three more specimens, was tested under cyclic shear loading.

The connection behaviour was explicitly described and design recommendations were presented for the connection design under monotonic and cyclic shear loading.

9.2 Research significance

The connection considered in this research is widely used in the construction of square shaft helical piles and micropiles in North America. It comprises a steel bracket (plate) as shown in figure 9-1. Despite the wide application of this connection in the piling industry, there are no specific design criteria for its implementation in design. Given the growing popularity of helical piles and micropiles, especially in seismic active areas, there is a pressing need to understand the connection behaviour and develop a methodology for its design under different loading conditions. Accordingly, the main objective of this study is to examine the connection behaviour and capacity subjected to monotonic and cyclic shear loading, and to recommend suitable equations that can be used for the connection design under shear loading.

9.3 Experimental program

Twelve specimens were constructed and tested under shear loading in two phases: nine specimens were tested under monotonic shear loading in the first phase; and three specimens were tested under cyclic shear loading in the second phase. All the tested specimens were simply supported reinforced concrete beams of dimensions 500 mm x 450 mm x 1000 mm, representing grade beams typically used in building foundations. In

the first phase, the tested beams were categorized into four groups according to the parameters investigated. Each group has three beams, including the control beam S2. In each group it was planned that only one parameter was varied to investigate its effect, and the other variables were kept constant. In the first group: three typical pile embedment depths, 254 mm, 203 mm, and 152 mm were investigated. In the second group, three values of the steel bracket (square plate) width were considered (165mm, 190 mm, and 229 mm) to study its effect on the connection capacity. In the third group, the effect of the beam's longitudinal reinforcement was investigated. Four longitudinal bars were used with different diameters (16mm (15M), 19.5mm (20M) , 25.2mm (25M)) resulting in longitudinal reinforcement ratios of 0.4%, 0.6%, and 1.11%, respectively. In the forth group, the effect of the beam's transverse reinforcement was examined considering stirrups spacing of 100 mm and 200mm, and the stirrups bar diameter and type (#2, and 10M). Table 9-1 and figure 9-2 summarize the dimensions and details of the nine specimens tested in the first phase. The second phase involved testing three beams under cyclic loading. In this phase, the effects of cyclic loading were examined considering different embedment depths (i.e.152 mm, and 203 mm) and transverse reinforcement configurations (i.e. 2 branches of #2@ 200 mm, and 2 branches of #2 @ 100 mm). Table 9-2 summarizes the dimensions and details of the three specimens tested under cyclic loading in the second phase. Finally, Appendix B demonstrates the several steps conducted for the specimens preparation.

Figure 9- 1 Commonly used pile cap (i.e. New construction bracket)
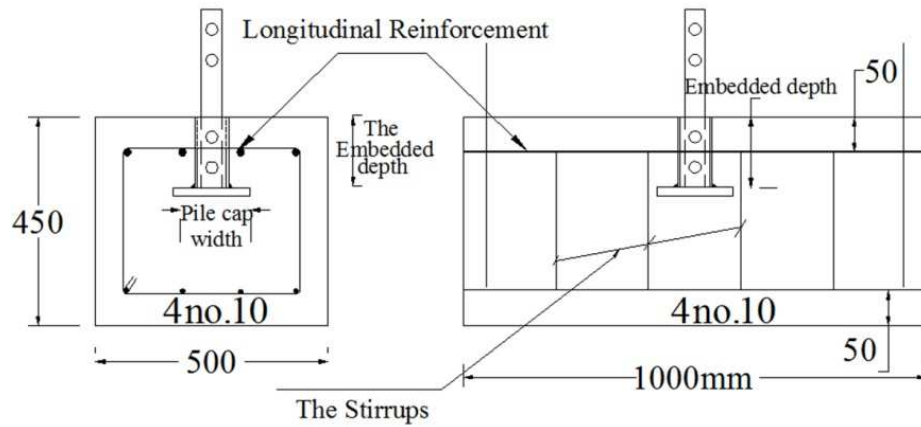
Figure 9-2 Dimensions and full details for the tested specimens

Table 9- 1 Details of specimens subjected to monotonic shear loading

Beam Name	Beam Dimensions (mm)	Concrete Strength fc'(N/mm2)	Pile embedment depth (mm)	Pile cap width (mm)	Longitudinal Reinforcement	Closed Stirrups	Notes
S1	500x450x1000	30	152	165	4-15M	2 branches #2@200mm	2 holes and 1 bolts to connect pile cap
S2	500x450x1000	30	203	165	4-15M	2 branches #2@200mm	2 holes and 1 bolts to connect pile cap
S3	500x450x1000	30	254	165	4-15M	2 branches #2@200mm	Hole next to the loaded beam surface existed
S4	500x450x1000	30	152	190	4-15M	2 branches #2@200mm	Only one hole/bolt to connect the pile cap
S5	500x450x1000	30	152	229	4-15M	2 branches #2@200mm	Only one hole/bolt to connect the pile cap
S6	500x450x1000	30	152	165	4-20M	2 branches #2@200mm	Only one hole/bolt to connect the pile cap
S7	500x450x1000	40	152	165	4-25M	2 branches #2@200mm	2 holes and 2 bolts to connect pile cap
S8	500x450x1000	40	152	165	4-15M	2 branches 10M @200mm	2 holes and 2 bolts to connect pile cap
S9	500x450x1000	40	152	165	4-15M	2 branches #2@100mm	2 holes and 2 bolts to connect pile cap

Table 9- 2 Details of specimens subjected to cyclic shear loading

Beam Name	Beam Dimensions (mm)	Concrete Strength fc'(N/mm2)	Pile embedment depth (mm)	Pile cap width (mm)	Longitudinal Reinforcement	Closed Stirrups	Notes
CS1	500x450x1000	30	152	165	4-15M	2 branches #2@200mm	Only one hole/bolt to connect the pile cap
CS2	500x450x1000	30	203	165	4-15M	2 branches #2@200mm	Only one hole/bolt to connect the pile cap
CS3	500x450x1000	30	203	165	4-15M	2 branches #2@100mm	Only one hole/bolt to connect the pile cap

9.4 Materials

The concrete was delivered as ready mix, which consisted of ordinary Portland cement, sand, and gravel with 20 mm maximum nominal aggregate size. The concrete mix for one cubic meter consisted of 1100 kg of coarse aggregate, 780 kg of sand, 245 kg Type 10Gu cement, 145 litre of water, 250 millilitre of super-plasticizer, and 80 kg slag. All of the

results from the concrete cylinder compression and splitting tests can be found in Appendix A.

Three concrete patches were used in casting the foundation models. Beams S1, S2, and S3 were casted using the first concrete patch. Beams S7, S8, and S9 were casted using the second concrete patch. Beams S4, S5, S6, CS1, CS2, and CS3 were casted using the third concrete patch. The first and third concrete patches had approximately the same concrete compressive strength of 30 MPa using the same concrete mix design while the second patch accidently had higher concrete compressive strength of 40 MPa.

The longitudinal reinforcing bars were 15M, 20M, and 25M high strength deformed steel conforming to CSA G30.18M-09 grade 400W. The compression longitudinal reinforcement comprised 10M high strength deformed steel conforming to CSA G30.18M-09 grade 400W. Plain bars of #2 (i.e. 6.35 mm diameter) cold formed steel, with grade 450/550, were used for stirrups. All reinforcement bars direct tensile test results are presented in Appendix A. The steel pile model was a central steel shaft made of hot rolled round-cornered-square (RCS) solid steel bar (45 mm x 45 mm) conforming to the dimensional and workmanship requirements of ASTM A29, with minimum yield and tensile strengths of 483 and 689 MPa.

The new construction bracket (also denoted as pile cap) consists of a square steel plate with adequate thickness welded to 152 mm long coupling tube with adequate inner diameter to insert the pile in it. The plate and tube conform to ASTM A36. The tube has one or two holes to connect the pile cap with the pile shaft using bolts. The used bolt was

412

25 mm in diameter and 152mm long, complying with ASTM A 193 Grade B7 (minimum yield strength of 655 MPa, and minimum tensile strength of 793 MPa). The welding between the cylinder and the plate was 10mm filet weld with E43XX metric electrode classification.

9.5 Instrumentation

Figure 9-3 shows the details of the test setup. The load was applied using a calibrated hydraulic jack of 1500 kN capacity and 500 mm maximum stroke. Two strong HEA 260 beams were used as supports for shear loading and to transfer the vertical load to the floor during loading. The two beams were spaced 925 mm center-to-center. Thus, the test beam center to center span was 835 mm. Also, Two strong clamping beams, spaced at 610 mm, attached with steel rods to the rigid floor of the laboratory were used were used to prevent the rotation of the specimen during shear loading.

As shown in Figure 9-3, at least seven linear displacement transducers (LDT) were used to monitor the displacements at the mid-span and quarter-span points of the beam, and the out of plane displacement as well as the displacement of the pile shaft. To accomplish these measurements, the LDTs were placed at the middle of upper and lower levels and the side of the beam. For each beam, five or more electrical strain gauges were used to measure strain in different stirrups and different branches and in the outer and inner longitudinal steel (i.e. the longitudinal rebar close to the beams surface and the longitudinal rebar close to the beam core, respectively). The strain readings were also used to evaluate magnitude and distribution of the plate deformation along its width. The strain gauges were 10 mm long and had 120±0.3% Ω resistance. The strain gauges, the

loading cell, and the displacement transducers were connected to a data acquisition system to monitor and record the strains, the applied loads, and the displacements.

a)

b)
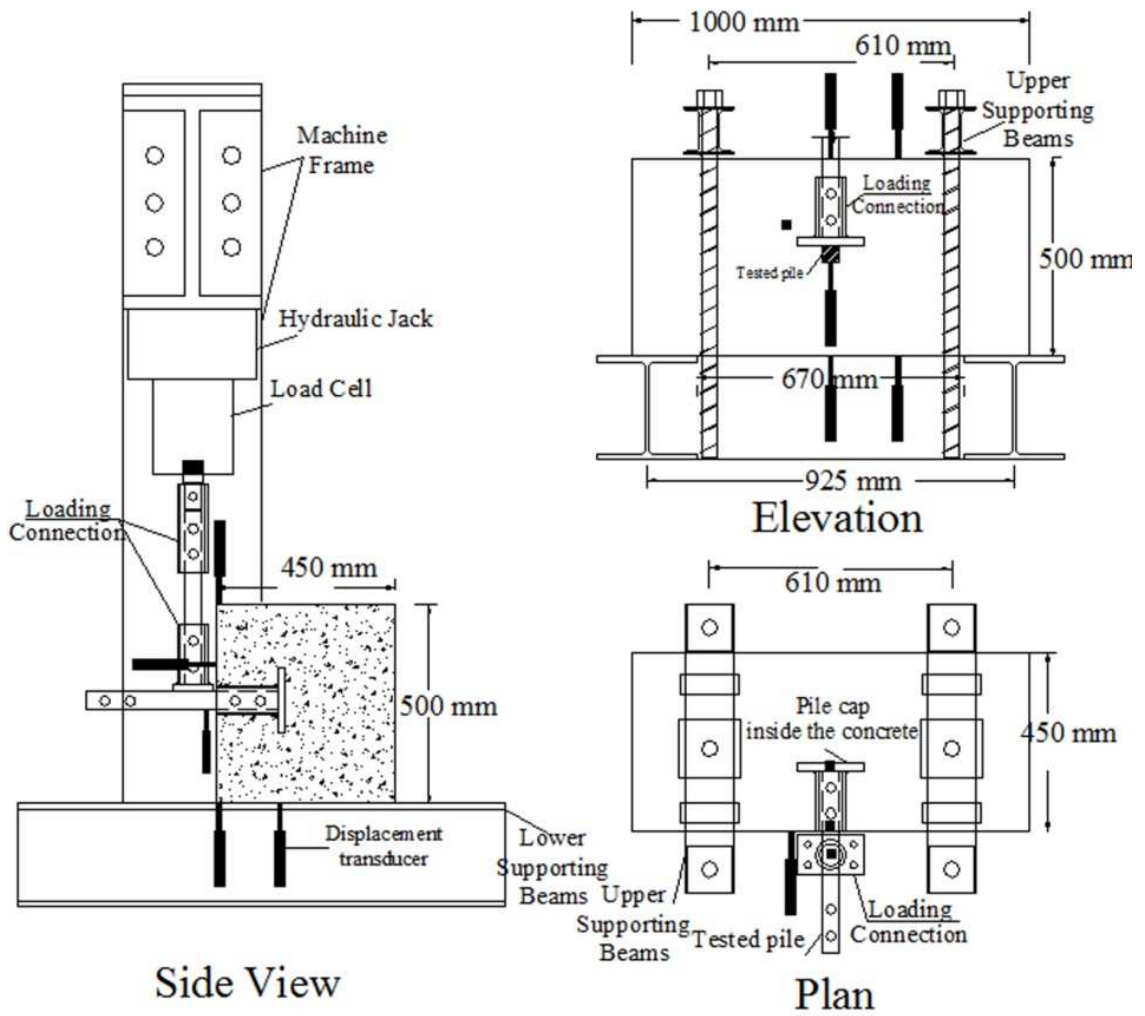
Figure 9-3 Test rig and locations of displacement transducers: a) schematic; b) actual setup

9.6 Test procedure

In the first phase, the load was applied monotonically at a loading rate of 5 kN/min, and cracks were marked. In the second phase, the load was applied as an alternating cyclic load at a cyclic rate of approximately 0.01 Hz, as shown in Figure 9-4. This loading scheme is similar to that specified by ASTM E2126 - 11 Test Method B (ISO 16670 Protocol) but using loading control instead of displacement control (also same as type I loading conducted by Klingner (1982). The loading scheme consisted of two load patterns. The first pattern consisted of five single fully reversed cycles at loads of approximately 1.25, 2.5, 5, 7.5 and 10 % of the expected connection ultimate load. The second pattern consisted of phases, each containing three fully reversed cycles of equal

415

amplitude, at load of approximately 20, 40, 60, 80, and 100 % of the expected connection ultimate load. To produce fully reversed cycles of equal amplitude, a clip (i.e. a loading connection) was used in the test rig, as shown in figure 9-5, to hold the pile during loading.

The cracks were marked, deformations were measured using the LDTs, and the observed steel strains were recorded using the strain gauges. The total duration of each test was about one hour. The test was stopped when breakout cone cracks opened excessively causing total separation of the breakout cone accompanied by excessive strength reduction below 60% of the ultimate load. In some cases, the test was stopped when necking occurred in the stirrups causing failure, when pile shaft failed, or when pile cap's welding failed (after the strength dropped below 60% of the ultimate load).
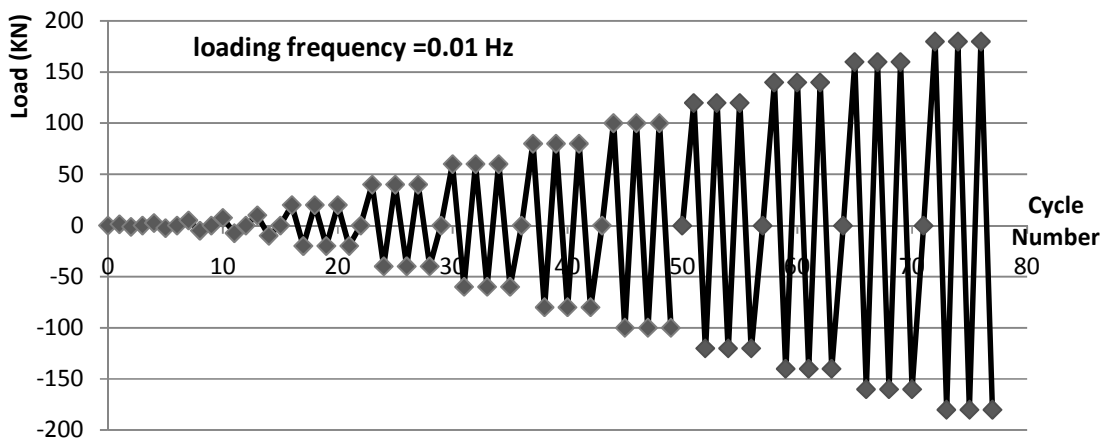
Figure 9- 4 Load history of cyclic shear loading in phase two
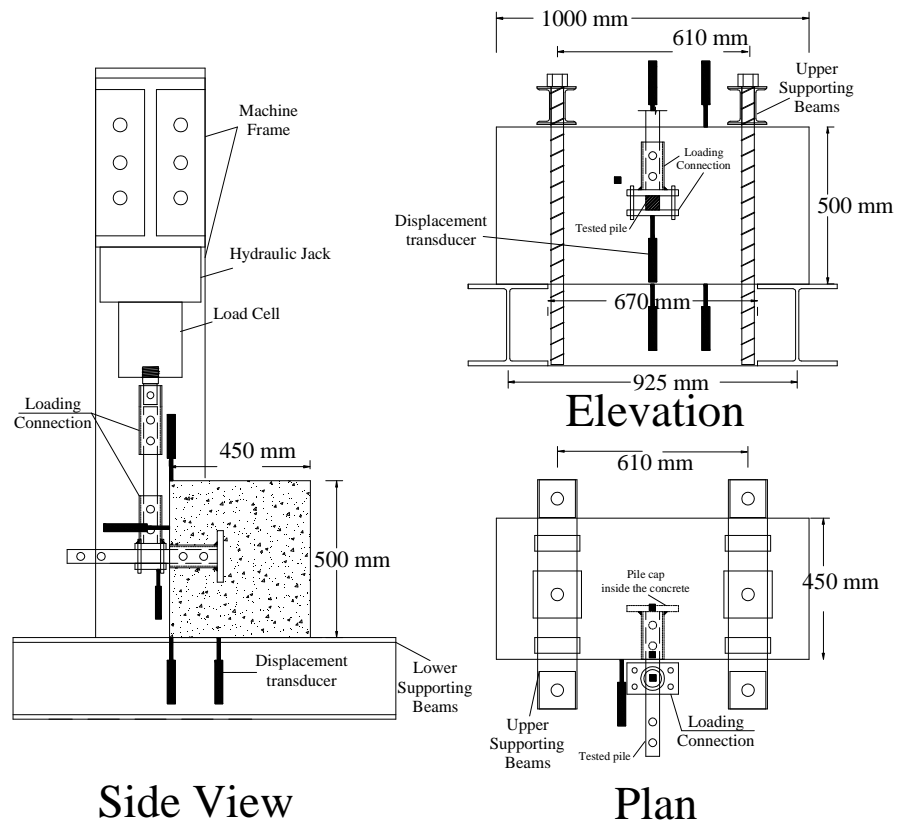
Figure 9- 5 Test rig and location of displacement transducers for cyclic shear loading: a) schematic; b) actual setup

417

9.7 Test results

The results of the monotonic shear load test are discussed first, followed by discussion of the cyclic shear load test results. In addition, the results from both sets of tests are compared.

9.8 General findings of monotonic shear loading

9.8.1   General crack pattern, failure mode, and beam ductility

The crack patterns of the tested beams are shown in figure 9-6. Most beams had approximately the same crack pattern until breakout cracking formation. However, the final failure mechanism varied due to different studied factors.

Initially, a very thin crack appeared next to the unloaded side of the pile due to bond failure. The cracks then initiated in the beam and extended gradually with a 20° angle longitudinally from the pile shaft towards the supports as the load increased. This was followed by a flexural crack at the mid-span of the beam, which occurred at a load approximately one quarter of the expected first flexural cracking load. The early flexural crack indicated that the concrete resistance in flexure mobilized over only one half of the flexural resisting depth. As load continued to increase, the 20° cracks reached the supports causing thin breakout cracks and eventually forming the first (large) breakout cone. As the load increased further, concrete crushing and spalling occurred in front of the pile shaft when concrete reached its bearing strength (Figure 9-7), and smaller breakout cone formed at approximately 35° extending from the pile shaft towards the beam side (Figure 9-8a). It was not possible to accurately record the concrete crushing load because it was progressive crushing. The breakout cracks (Figure 9-8a) occurred at

418

loads close to the values calculated by using equations reported by ACI 318-11 Appendix D and A23.3-04 CSA code Appendix D as will be discussed later in chapter 10. These equations were developed assuming half pyramid breakout cone with side length of (3 c_{a1}) and depth of (1.5 c_{a1}) with 35° crack angles (where ca_1 is the distance from the edge to the pile shaft axis as shown in Figure 9-8 (b). The test beams exhibited approximately the same breakout crack side length and angle (35°), but the pyramid height varied depending on the longitudinal reinforcement and the concrete cover dimension (Figure 9-8).

As the load continued to increase, the 35° cracks widened further and both longitudinal and transverse reinforcements carried more load (indicated by strain gauge readings). In some of the tested beams, the concrete cover separated suddenly from the rest of the 35° breakout cone (Figure 9-9c). At this stage, the failure mechanism formed. Similar cover failure was reported by Randl et al. (2001) in their study of the structural behaviour of fasteners at component edge subjected to lateral loads.

The connection failure mechanism depended on several factors: concrete compressive strength, beam's longitudinal and transverse reinforcement ratios, pile embedded depth, pile cap's plate width, position of connecting bolts/holes in the pile shaft, pile shaft material capacity, welding thickness and quality, clear cover dimension, etc. Four failure mechanisms were observed in the tested beams: Breakout failure, Breakout failure with pryout failure cracking, breakout failure with welding failure, and pile shaft failure before or after the breakout failure capacity.

Due to concrete spalling in front of the pile shaft and/or due to breakout cone movement, the bearing position of the pile shaft on the concrete shifted to a deeper location in the concrete member causing tension and flexure stresses on the pile shaft. This behaviour was also indicated by Zhao (1995) and Eligehausen (2013). When the stresses at the new position reached the pile shaft capacity, it failed even before the second breakout cone formation (i.e. beam S3 as shown in Figure 9-9a), or after the connection breakout load (i.e. beams S7, S8, and S9 as shown in Figures 9-9b and 9-9c). If the pile shaft capacity was not reached, the load was transferred to the pile cap welding as tension and flexural stresses, which failed when it reached its capacity (i.e. beams S4, S5, and S6 as shown in Figure 9-9e). If welding could resist these stresses, it would transfer the load to the pile cap's plate, causing compression on the adjacent concrete resulting in pryout cracks (i.e. beams S1). This pryout failure was not expected in the anchors near the beam edges because breakout failure would occur in earlier stages as indicated by Anderson et al. (2005). Additionally, in beams S4, and S5, the larger pile cap's plate size caused larger pryout capacity and welding failed before reaching the pryout capacity. Moreover, it appears that both the longitudinal reinforcement and stirrups maintained the specimen integrity and enhanced its ability to resist load after the breakout capacity until pry-out cracking occurred in some specimens. Some of the tested beams' stirrups failed due to stirrups necking and the longitudinal reinforcement had a clear bent due to their dowel action effect as shown in figure 9-9 (e) and presented in figure 9-11.

Figure 9- 6 Crack patterns of the tested beams under monotonic shear loading

Figure 9- 7 Concrete crushing under the pile shaft in two different specimens

(a)

(b)

Figure 9- 8 Connection breakout cracking: a) observed breakout cone failure (b) Breakout cone dimensions noted by the ACI 318-11 and A23.3-04 CSA code

a)

(b)

(c)

d)

e)

Figure 9- 9 Observed failure mechanisms: a) pile shaft failure after concrete crushing in front of the pile; b) pile shaft failure after the breakout failure of the concrete cover; (c) pile shaft failure with the concrete cover failure; d) Concrete pryout cracking at the unloaded side of the specimen; and e) breakout failure combined with the pile cap's welding failure

9.8.2 General Load Transfer Mechanism

Based on the experimental observations and measurements, the specimen structural behaviour and load transfer mechanisms during shear loading can be presented as shown in Figure 9-10. The specimen can be presented as a cantilevered beam. The cantilever is loaded with the shear load at its free end. The first support (vertical spring) represents the

424

breakout resistance of the reinforced concrete beam. This support deforms vertically with the breakout cone movement, and its location moves horizontally towards the second support. The second support has vertical and rotational springs, whose constants are derived from the pile cap and pryout resistance of the adjacent concrete.

At the start of loading, the vertical reaction at the first support is approximately equal to the shear load. As the applied load increases, the support moves inward due to concrete crushing under the pile and the reaction at the first support increases excessively. The second support (pile cap) experiences higher vertical reaction and small positive moment (i.e. causing compression at the top fibres and tension at the bottom fibres). With more breakout cone movement, the first spring deforms more and the pile cap experiences negative moment (causing tension at the top fibres and compression at the bottom fibres) due to pile shaft inclination. As concrete failure initiates (breakout cracking), the first support reaction decreases substantially and the beam turned into a cantilever. At this point, the pile shaft and the pile cap's welding are subjected to large stresses and may fail. The pile shaft experiences shear force and negative moment. If the induced stress exceeds the capacity of the pile shaft, a plastic hinge forms and failure ensues. If the induced stress exceeds the plate welding capacity, the welding fails causing separation between the pile cap and the pile shaft and consequently failure of the connection.

Finally, if the pryout capacity of the concrete in front of the pile cap's plate is exceeded, pryout cracks will occur and the pile shaft will rotate due to the loss of fixation in the second support (Figure 9-9d). This concluded failure mechanism is supported by the recorded strains of the pile cap's plate above and below the pile shaft, which initially

indicated compression strain in the plate above the pile and tension strain below the pile, and excessive tensile strains above the pile after the connection breakout load.
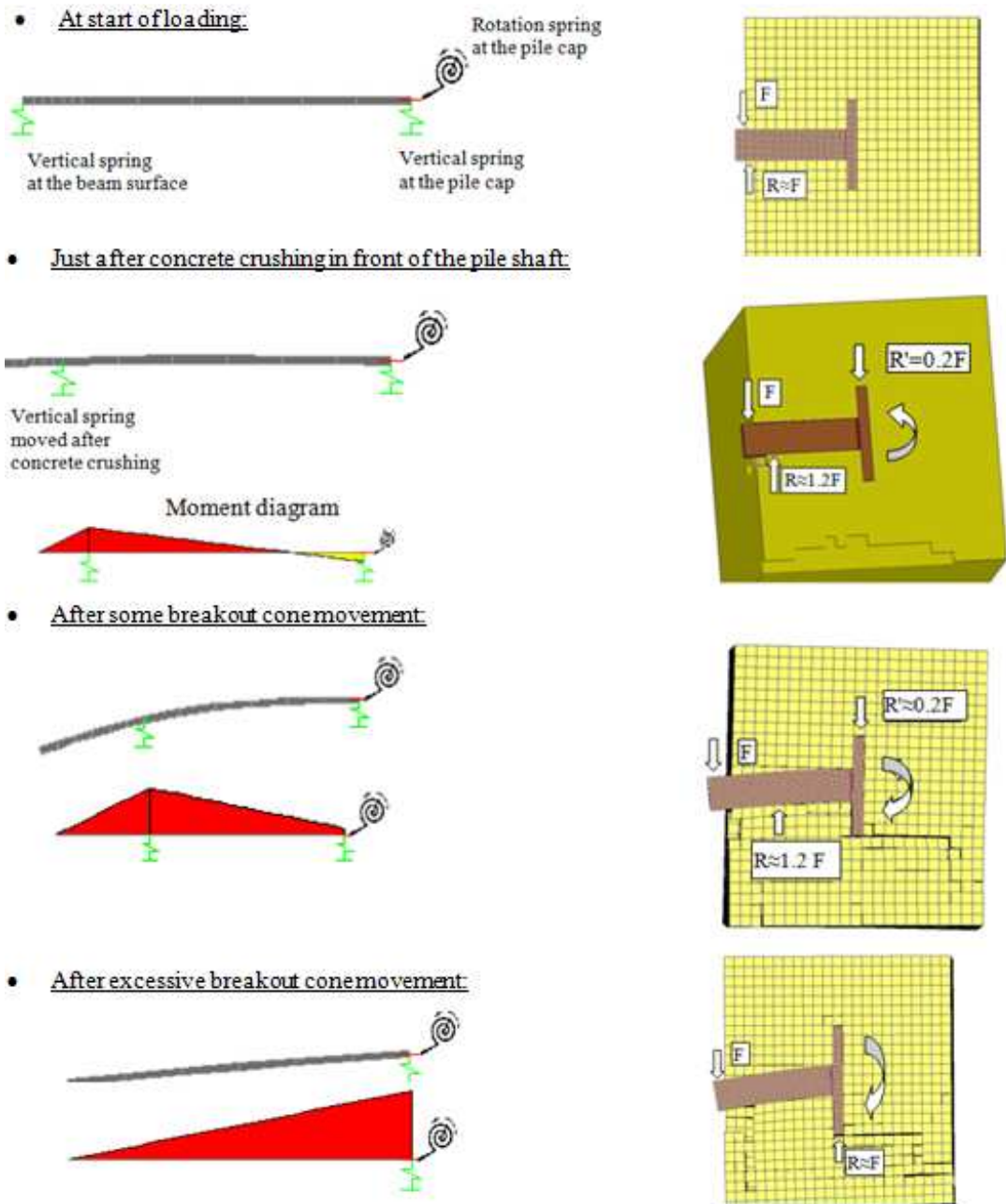
Figure 9- 10 Structural behaviour and load transfer mechanisms of the specimen subjected to shear loading

9.8.3 General Ultimate Load and Load Displacement Relationship

The first flexural cracking load, the connection breakout load, and the ultimate load for the tested beams are presented in table 9-3. The first cracking load was recorded when first flexural crack was observed at the beam side, which was associated with remarkable increase in the longitudinal steel strain. The connection breakout load occurred when the 35° breakout cone (i.e. the second cone) formed fully and moved causing substantial increase in the strains of longitudinal steel, stirrups, and pile cap. Also, at the connection breakout load, excessive displacement occurred at the loaded side of the beam and a small displacement at the unloaded side of the beam, which mean wide cracks formation was presented.

Thus, before the breakout cracking load, the connection can be considered as fixed connection, while the connection should be considered as hinged connection after the connection breakout cracking load and up to its failure. Abd Elaziz & El Naggar (2015) reported that helical piles and micropiles could resist much higher lateral load when their heads are fixed, rather than semi fixed or hinged, into the foundation. Therefore, the connection breakout load has a significant impact on the geotechnical lateral capacity of the pile because it approximately represents the load at which the connection condition changes from totally fixed to semi-fixed or hinged.

The ultimate load is defined as the maximum load that the specimen could resist, before its stiffness decreased substantially. The total specimen resistance at the ultimate load is comprised of four contributions: the dowel action of longitudinal reinforcement; the stirrups resistance; the pile cap contribution to the connection; and the aggregate interlock

resistance as shown in Figure 9-11. The pile cap contribution is caused by the transfered shear, tension, and flexure stresses from the pile shaft to the pile cap, then transfer of these stresses from the pile cap to the adjacent concrete as compression stresses. Thus, either the pile shaft , the welding of the pile cap, or the concrete in front of the pile cap's plate would fail after the connection breakout load is exceeded. Therefore, the location of the connecting bolts (and their holes) is important because the embedment depth of these holes affects the flexural capacity of the pile cap cylinder. For example, beam S3 had an ultimate load less than its connection breakout load because the connecting hole was close to the beam surface, which resulted in stress concentration at the hole. Thus, the pile shaft failed as soon as the concrete in front of the pile crushed, even before the 35° breakout cone fully formed.
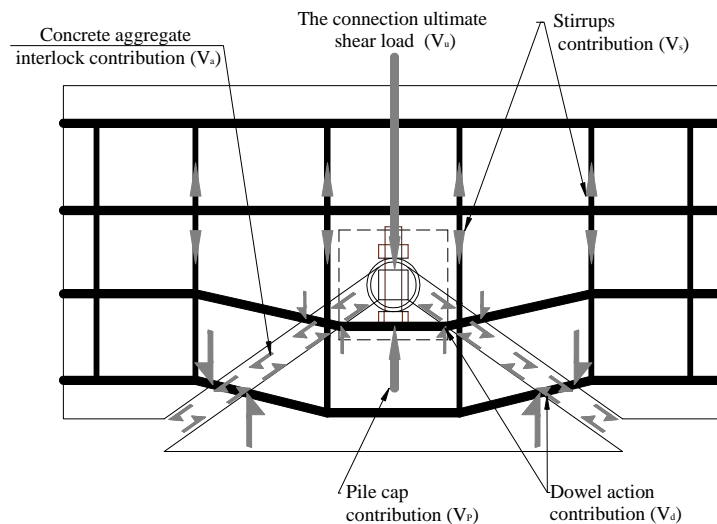
Figure 9- 11 Load transfer mechanism at the connection ultimate load for a beam with longitudinal and transverse reinforcements

The mid-span deformation in the concrete at the loaded beam side was recorded at each load increment. The observed load-deformation response can be generally subdivided into five stages as follows. Stage 1: the deformation increased linearly with the load until first flexural cracking occurred. Stage 2: the deformation increased with the load at an almost constant rate, but higher than the rate observed in stage 1, until the 20° cracks formed a large cone. Stage 3: the beam stiffness decreased and progressive deformation occurred until the 35° breakout cone formed (i.e. breakout load). Stage 4: the specimen stiffness decreased markedly as manifested by significant increase in deflection with negligible load increase and the ultimate load was reached. Stage 5: deformation increased while the load decreased until failure took place. The breakout and ultimate loads of the test beams as well as their mid-span deformations at these loads are presented in Table 9-3.

The results showed that all specimens with the same concrete strength exhibited almost the same stiffness until their breakout load was reached. Afterwards, the specimens' stiffness varied depending on their reinforcement and pile cap configurations.

Furthermore, the mid-span deformation at the unloaded beam side was recorded and was found to be approximately equal to that of the loaded side up to the connection breakout load. At this point, the deformation at the unloaded side decreased gradually. The difference between the two deformations represented the breakout crack opening and the movement of the breakout cone.

Table 9- 3 Test results of the beams under monotonic shear loading

Group	Specimen	First flexural cracking load(kN)	Connection breakout load(kN)	Connection ultimate load (kN)	Mid-span displacement at breakout load (mm)	Mid-span displacement at ultimate load (mm)	Strain energy at 0.6 of ultimate load (kN.mm) *	Strain energy of the connection (kN.mm) **	Failure mechanism
First group	S1	78.2	137.48	162.39	1.4	4.7	2556	4445	Breakout Failure then pryout cracking
	S2	50	145.03	151.4	3	5	4591	6851	Breakout Failure with wide pryout cracks
	S3	75	>136.86	136.83	------	3.2	318	2716	Pile shaft failure
Second group	S2	50	145.03	151.4	3	5	4591	6851	Breakout Failure then pryout cracking
	S4	38.4	148.4	176	4.5	8.6	3594	8019	Breakout failure then welding failure
	S5	45.4	145.4	160.1	3.7	8.5	2713	6555	Breakout failure then welding failure with pryout cracks
Third group	S2	50	145.03	151.4	3	5	4591	6851	Breakout Failure then pryout cracking
	S6	39.1	157.8	164.2	4.6	6.5	4527	6687	Breakout failure then welding failure with pryout cracks
	S7	87.7	183.5	183.5	4.2	4.2	903	7071	Breakout failure then pile failure
Forth group	S2	50	145.03	151.4	3	5	4591	6851	Breakout Failure then pryout cracking
	S8	77.1	185.2	185.2	2.9	2.9	1891	5520	Breakout failure then pile failure
	S9	83.5	190.6	190.6	5.5	5.5	2413	4642	Breakout failure then pile failure

(*)Strain Energy of Concrete is calculated using the mid-span deformation at the loaded beam side up to 0.6 of its ultimate load after reaching its ultimate load.

(**)Strain Energy of Connection is calculated using the loading jack displacement to take the pile deformation into account up to 0.6 of its ultimate load after reaching its ultimate load.

9.8.4 General Ductility

The connection ductility depends on the overall displacement of the connection, including that of the pile shaft. The connection ductility increases as the displacement before connection failure increases. It is recommended to design anchors and connections to have ductile failure (i.e. failure in the steel members rather than in the concrete). Ductile steel failure results in larger displacements and allows some warning before reaching the connection ultimate load.

Thus, specimens' ductility in the current study is evaluated using the ductility ratio $\left(\frac{\Delta u}{\Delta y}\right)$, defined as the ratio between the mid-span displacement at the ultimate load and the mid-span displacement recorded when the longitudinal or the transverse reinforcements began to yield (i.e at a steel strain approximately equal to 0.002). In addition, the strain energy was calculated to evaluate the beams ability to absorb energy before failure. Two strain energies are presented in table 9-3: the strain energy absorbed by the concrete using the recorded beam mid-span deflection; and the strain energy absorbed by the overall connection including the pile shaft using the loading jack displacement.

Most of the tested specimens reached their ultimate load before experiencing large deformations in the concrete as the maximum deflection in the beams at ultimate load was less than 10mm. However, deformations increased excessively after the breakout cracks formation and widening. In most of the tested specimens, the stirrups and longitudinal reinforcement reached yielding close to the ultimate load, which enhanced the specimens' ductility before and after the ultimate load. On the other hand, the failure

431

of beams S3, S7, S8, S9 occurred in the pile shaft at a relatively low load but they exhibited an overall ductile failure mechanism, which is favourable for elements subjected to earthquake loading because of the plastic hinge presented in the pile shaft before its failure .

9.8.5 General Reinforcement Steel and Pile Cap's Plate Strains:

The longitudinal steel strain, transverse steel strain, and pile cap's plate strain were recorded during loading to help understand the internal behavior and cracking inside the tested specimens.

The longitudinal reinforcement strain increased linearly with the applied load until the first flexural cracking occurred. With further increase in the load up to the connection breakout load, the strain increased at a higher rate as the steel carried the internal tension at the cracks. At the connection breakout load, the longitudinal steel strain spiked without load increase due to the dowel action of the longitudinal reinforcement after the connection breakout occurrence. This is attributed to the additional normal force in the longitudinal steel induced by the horizontal pressure from the aggregates at the two sides of the breakout cracks due to the aggregate interlock.

The inner longitudinal reinforcement strain was much less than that of the outer longitudinal reinforcement strain up to the connection breakout load. However, after the connection breakout occurance, the inner longitudinal reinforcement strain increased substantially compared to that in the outer longitudinal reinforcement due to the high dowel action contribution from the inner longitudinal reinforcement. The outer

432

longitudinal reinforcement experienced stresses from both flexural and breakout cracking, while the inner longitudinal reinforcement experienced stresses from breakout cracking only. Thus, the inner longitudinal bars were more affected by the breakout cracking because they were closer to pile shaft. Additionally, most of the longitudinal reinforcement in the specimens reached yielding before failure indicating to the connection ductility before failure.

The stirrups' strain was negligible before the 20° first breakout cone formed. After the formation of the 35^0 breakout cone, stirrups strain increased significantly. The inner stirrups experienced higher strain compared to the outer stirrups because they were closer to the pile shaft. Finally, necking was observed in stirrups of some beams indicating their important contribution to the connection ultimate shear load.

The maximum recorded strain in the pile cap's plates was far from yielding, which confirmed that no plastic hinges were developed and that the used plate sizes were enough to ensure fixation of the pile shaft. After the connection breakout, the transferred moments from the pile shaft to the pile cap caused compression strains at the loaded side of the plate and tensile strains in the unloaded side of the plate.

9.9 Discussion of results for monotonic shear loading

9.9.1   First Group: effect of pile embedment depth

Three different embedment depths were investigated: 152, 203 and 254 mm (beams S1, S2 and S3, respectively). The beams had concrete compression strength of 30 MPa, four bars of 15M high strength deformed steel longitudinal reinforcement, and stirrups with

diameter 6.35 mm spaced at 200 mm. The steel plate width was kept constant as 165 mm and the pile shaft dimensions, position of connecting holes, and welding thickness were all the same for the tested beams.

9.9.1.1   Crack pattern and mode of failure

Beams S1 and S2 had similar crack pattern. Anderson et al. ,2005 indicated that for anchors with embedment depth to diameter ratio (d_{emb}/b_{pile}) < 4.5, pryout failure can govern the anchor failure mechanism. Both S1 and S2 had pryout cracks because they had d_{emb}/b_{pile} < 4.5. In beam S3, the same crack pattern was observed till the concrete crushing under the pile shaft occurred (at a load of 136kN). The reduced pile cross-section at the hole next to the concrete surface caused the pile failure before the full formation of the 35° breakout crack. Vintzelou et al. (1992) and fuchs (1992) reported that high bearing stresses occur in the concrete in front of the loaded anchor, which causes concrete crushing and shear/bending failure of the anchor shank near the concrete surface.

9.9.1.2   first flexural cracking, Breakout and Ultimate Loads

Table 9-3 shows that increasing the plate embedment depth from 152mm to 203mm increased the connection breakout load by 5.5%, but it decreased the connection ultimate load by 6.7%. This may be explained as follows; After the connection breakout load was reached, larger breakout cone movement would be required to transfer the total load to the pile cap as the embedded depth of the pile shaft increased. In beam S1, the rotation of the pile shaft with small breakout cone movement due to the shallow pile embedment

434

depth, caused increase in the pryout contribution to the connection capacity. This increased the ultimate load remarkably before pryout cracks formation and breakout cone movement increased while the resisting load decreased. On the other hand, beam S2 had larger embedded depth, which necessitated larger breakout cone movement for transfer of forces to the pile cap and consequently larger resistance contributions from the longitudinal steel and stirrups to the connection ultimate load. When the crack width widened, the aggregate interlock contribution and the resisting load decreased gradually. In this process, the pryout resistance contributed to the resistance only when the resisting load decreased. This explanation is supported by the following: the load-displacement curves presented in Figure 9-12 demonstrate that the stiffness of beam S2 was much higher than that of beam S1 after the ultimate loads; and the strain at the top of the pile cap in beam S2 was less than that of beam S1 up to the ultimate load. Also, in spite of increasing the embedded depth in beam S3, the beam failed in the pile shaft before forming the 35° breakout cone after concrete crushing in front of the pile.

The lower ultimate load of beam S3 is attributed to the presence of the bolt hole close to the beam surface, which caused premature failure of the connection after concrete crushing in front of the pile shaft. Subsequently, the shear and flexural stresses transferred to the weakest point of the pile causing failure. Fuchs ,1992 and Randl et al. (2001) made similar conclusions for anchors embedded in uncracked unreinforced and reinforced concrete members, respectively.

9.9.1.3 Stiffness and load-concrete displacement relationship

As shown in Figure 9-12, the response of the three beams was essentially the same from start of loading until the 35° breakout cone formed. Subsequently, the stiffness decreased slightly for larger pile embedment depth. After the connection breakout occurred, the beam stiffness decreased substantially as the load increased until the ultimate load was reached, and the breakout cone moved. After reaching the ultimate load, the stiffness of beam S2 decreased gradually. It could resist 132 kN (87% of its ultimate load) at 28.4mm and 50% of its ultimate load at 50mm (10 times displacement at ultimate load), which presents high ductility after reaching the ultimate load. This resistance came mostly from the pile cap contribution to the connection capacity. On the other hand, the resistance and stiffness of beam S1 decreased rapidly as the pile cap already failed when wide pryout cracks occurred at the connection ultimate load. The connection of beam S3 failed due to failure of the pile shaft before reaching the connection breakout load, and the concrete beam specimen unloaded rapidly.

The recorded displacements at the other six locations, for the three beams, confirmed the same behaviour. Also, it was noted that the displacements at the loaded and unloaded sides at the same longitudinal locations started to deviate only after the connection breakout cracks opened. Furthermore, the out of plan displacement in beams S1 and S2 indicated that the bolts and the pile cap pushed the concrete in front of it causing pryout cracking and there was rotation in the connection inside the beam after the breakout crack widening.
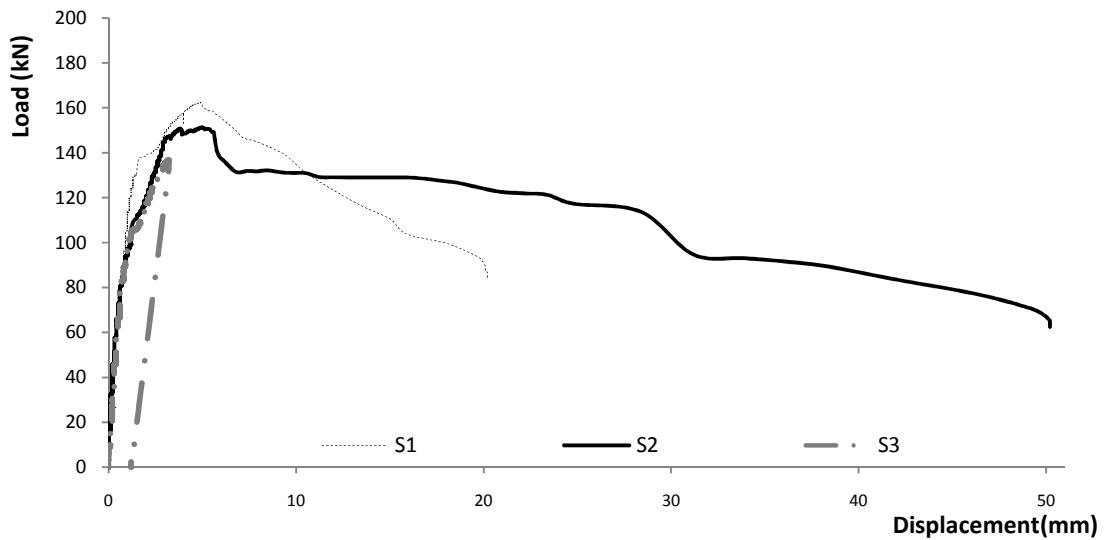
Figure 9- 12 Load mid-span concrete displacement response

9.9.1.4 Ductility and strain energy

The calculated $\left(\frac{\Delta u}{\Delta y}\right)$ values for beams S1 and S2 were 2.33 and 2.38, respectively, which represents a slight increase in ductility. On the other hand, the strain energy stored in beams S1 and S2 were 4445 kN.mm and 6851 kN.mm, demonstrating significant increase in the ability of the specimen to absorb more energy as the embedment depth increased from 203 mm to 254 mm. However, the strain energy stored in beam S3 was only 2716 kN.mm due to the premature failure in the pile shaft. Similar observation can be made by inspecting the strain energies of the tested specimens calculated using the mid-span displacement of the specimens (i.e. 2556 kN.mm, 4591 kN.mm, and 318 kN.mm for beams S1, S2 and S3).

9.9.1.5 Reinforcement Steel, and Pile Cap's Plate Strain

Figure 9-13 presents the measured strains in the longitudinal reinforcement. It shows that the strains in the reinforcement of all three beams were essentially the same until the first flexural cracking load was reached. Beam S2 had a lower first flexural cracking load, thus it displayed the highest longitudinal steel strain after that point. It is also noted from Figure 9-13 that the inner longitudinal bars were affected more by the breakout cracking because they were closer to pile shaft. They sustained extra shear and tension stresses when concrete crushing occurred in front of the pile shaft.

Figure 9-13 also demonstrates that the longitudinal steel sustained more load just after the connection breakout load; and they reached yield in beams S1, and S2, and were close to yield in beam S3. This observation confirms the ductility of the connections. Finally, the recorded plastic strain after the pile shaft failure of beam S3 (740×10^{-6}) indicated that the specimen would not return to its original condition after the initiation of the diagonal cracks.
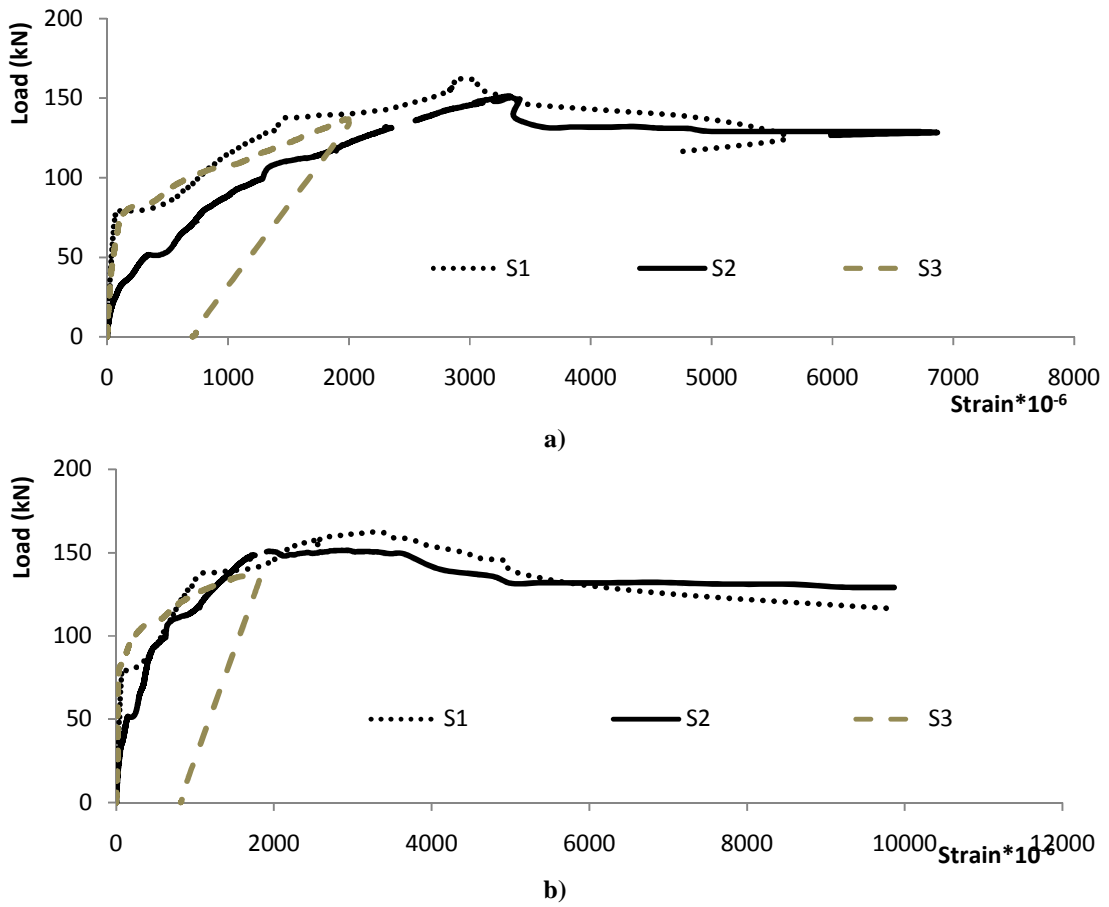
Figure 9- 13 Load-longitudinal steel strain: a) outer bars; b) inner bars

Figure 9-14 displays the stirrups strains. The results indicate that the stirrups contributed to the connection resistance only after the formation of the 20° diagonal cracks and sustained significant loads after the formation of the 35^0 breakout cone. All stirrups in beam S1 reached yielding before its ultimate load was reached, while stirrups in beam S2 yielded just after reaching its ultimate load. Figure 9-14 also shows that the inner stirrups sustained higher load than the outer stirrups after the breakout cone formed. Finally, the inner stirrups of the beam with larger pile embedment depth experienced higher strains.

439
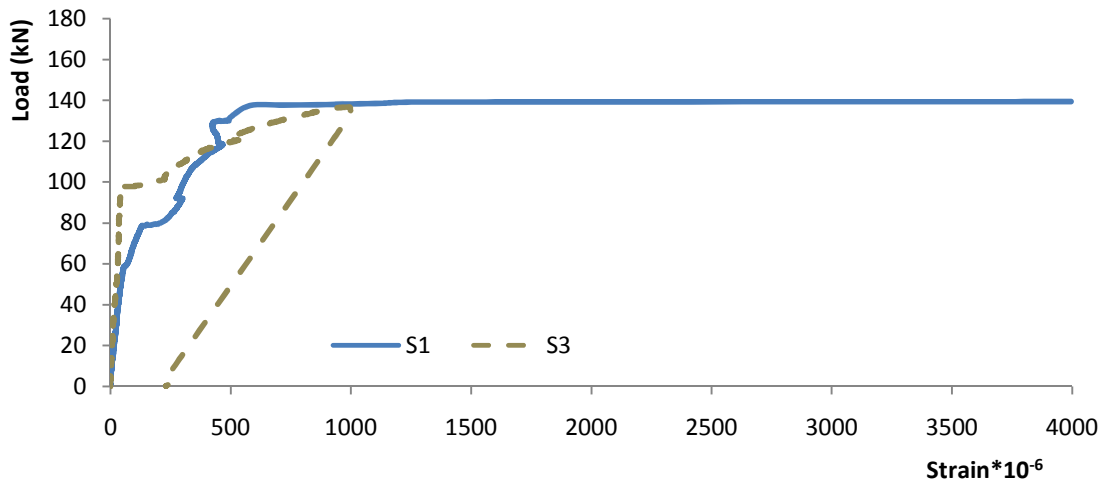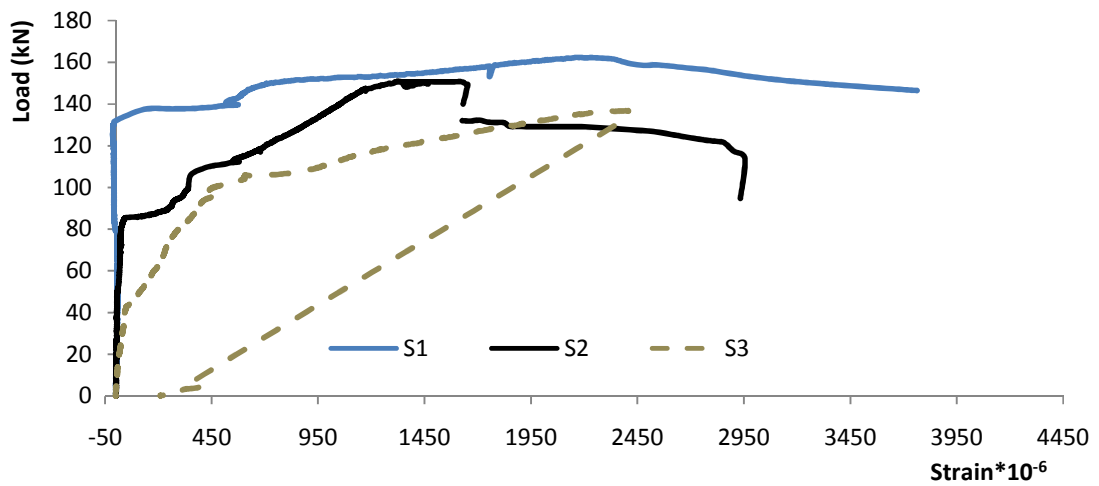
Figure 9- 14 Load-stirrups strain: a) outer stirrups; b) inner stirrups

The pile cap strain was less than 375×10^{-6} mm/mm during the entire loading process for all beams, which means it was far from yielding. Also, the pile cap strain did not decrease before reaching the ultimate load, which confirmed that the pile cap welding did not fail.

In addition, large strains were recorded in the pile cap only after the breakout crack opened. The strain of pile cap in beam S1 was highest followed by that of beam S2 and

beam S3. Thus, it may be concluded that increasing the pile embedment depth decreased the effect of the pile cap. This is because the specimen capacity would be derived mainly from the breakout capacity not the pryout capacity and the pile would act as a longer cantilever with larger displacement.

9.9.2   Second Group: Effect of Pile Cap's Plate Width

Three different plate sizes, covering the range of pile cap configurations used in practice, were tested. They were as follows: 165 x165 x 19 mm (S2); 191 x191 x 19 mm (S4); and 229 x 229 x 25.4 mm (S5). The embedment depth, longitudinal reinforcement, concrete compressive strength, and stirrups were kept constant as shown in Table 9-1.

9.9.2.1   Crack pattern and mode of failure

There are three main differences in behaviour related to the crack pattern of beams S4 and S5 compared to that of beam S2 due to change in pile cap's plate size: 1) the full breakout cone moved with the pile shaft movement and no pryout failure occurred in beams S4 and S5, while pryout cracks opened in beam S2 because the pile cap's contribution diminished the pile shaft rotated and the pile cap could not push the large pryout cone; and 2) the pile cap's welding in beams S4, and S5 failed, indicating large straining actions that were transferred to it; and 3) the stirrups failed by necking because of the large movement of the full breakout cone after the pile cap's welding yielding. These differences demonstrate that increasing the pile cap's plate size had a great effect on the connection behaviour only after reaching the connection breakout load because the

pile cap resistance prevented the connection rotation and altered the failure mechanism after the breakout cracking.

9.9.2.2 First flexural cracking, breakout and ultimate loads

The test results presented in table 9-3 show that the three beams had approximately the same first flexural cracking and breakout loads. The pile cap's plate size only affected the connection ultimate load; the connection ultimate load increased by 16% as the pile cap's width increased from 165 mm (beam S2) to 190 mm (beam S4), while it increased by only 6% for beam S5 which had pile cap width = 229 mm. This is because the stirrups failed in both S4 and S5, contributing their full tensile capacity to the connection ultimate load. However, it was observed that the pile cap contribution to the connection resistance was higher in beam S4 than in beam S5.

9.9.2.3 Stiffness and load displacement relationship

Figure 9-15 shows the load-mid span displacement response of the tested beams within this group. It can be noted from Figure 9-15 that the connection response was essentially the same for all beams until the first flexural cracking initiation and the breakout cone movement. After the connection breakout occurrence, beam S2 experienced large displacement with a small increase in load, while beams S4 and S5 continued to resist more load, but with reduced stiffness until the ultimate load was reached. The three beams exhibited softening behaviour afterwards until failure occurred: beam S2 failed with pryout cracking, while both beams S4 and S5 failed due to failure of pile cap's welding and stirrups necking.

442
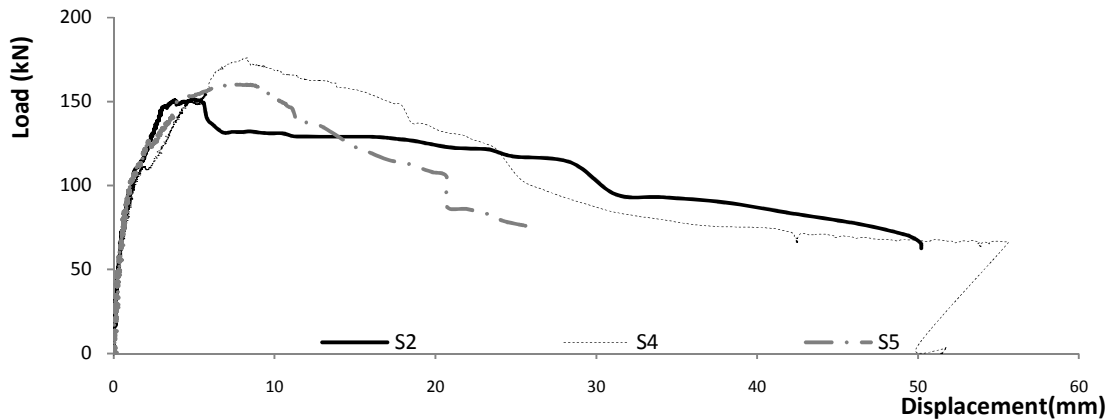
Figure 9- 15 Load mid-span displacement

9.9.2.4 Ductility and strain energy

As reported in Table 9-3, beams with wider pile cap's plate had larger mid-span displacement at ultimate load. Also, the ductility ratio, $\left(\frac{\Delta u}{\Delta y}\right)$ = 1.15, 1.596, and 2.237 for beams S2, S4, and S5, respectively, indicated increased ductility as the pile cap size increased. The strain energies calculated using the loading jack displacement were 6851, 8019, and 6555 kN.mm for beams S2, S4, and S5, demonstrating an increase in ability of connection to absorb energy as the pile cap plate size increased more than 165mm.

9.9.2.5 Reinforcement Steel, and pile cap's plate Strain

Figure 9-16 demonstrates the variation of longitudinal reinforcement strain of the tested beams with the applied load. The general trends of strain behaviour were similar until breakout load was reached for the 3 beams. Also, all longitudinal reinforcement bars reached yielding before the connection ultimate load and the inner longitudinal

reinforcement exhibited significant increase in strain after reaching the connection ultimate load.
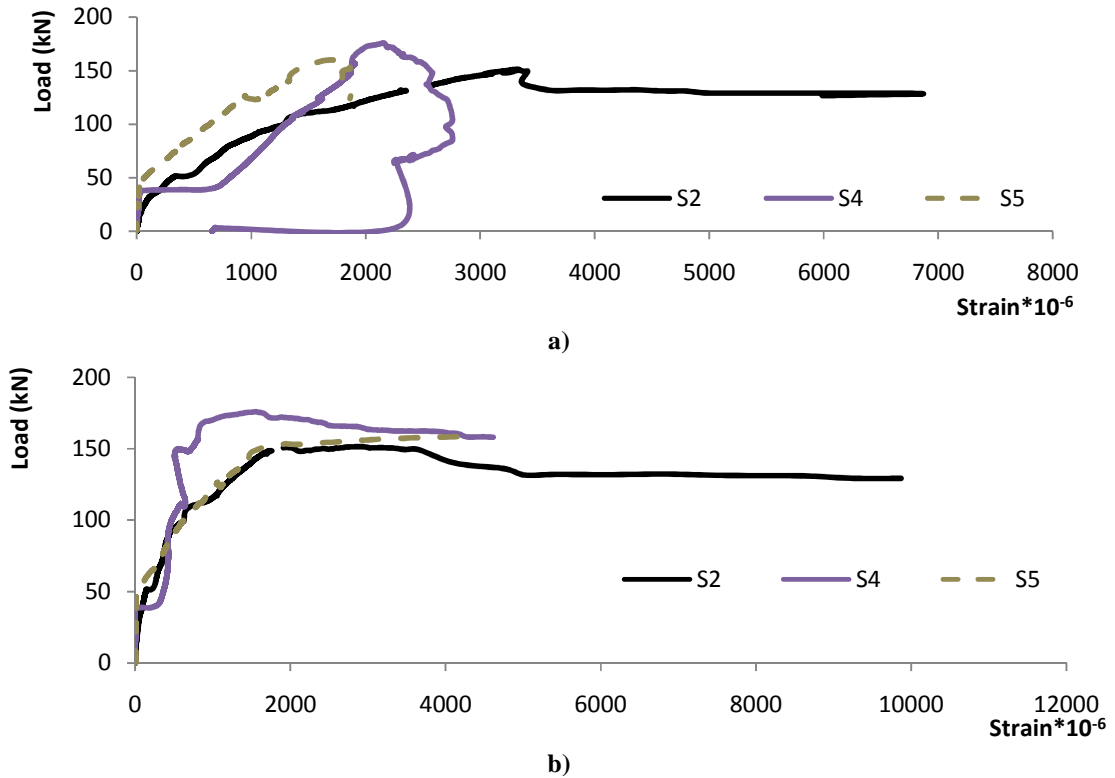
Figure 9- 16 load-longitudinal reinforcement strain: a) outer bars; b) inner bars

Figures 9-17 displays the variation of stirrups strain with the applied load. The three beams exhibited approximately the same behaviour up to their connection breakout load, at which point the inner stirrups in beams S4 and S5 experienced large increase in stirrups strains, reaching their tensile capacity at the connection ultimate load. The outer stirrups, however, were outside the 35° breakout cone and thus did not experience similar strain increase. It can be concluded that using wider pile cap's plate can increase the inner

444

stirrups contribution to the connection capacity by decreasing the chance of pryout failure after the breakout cone movement.
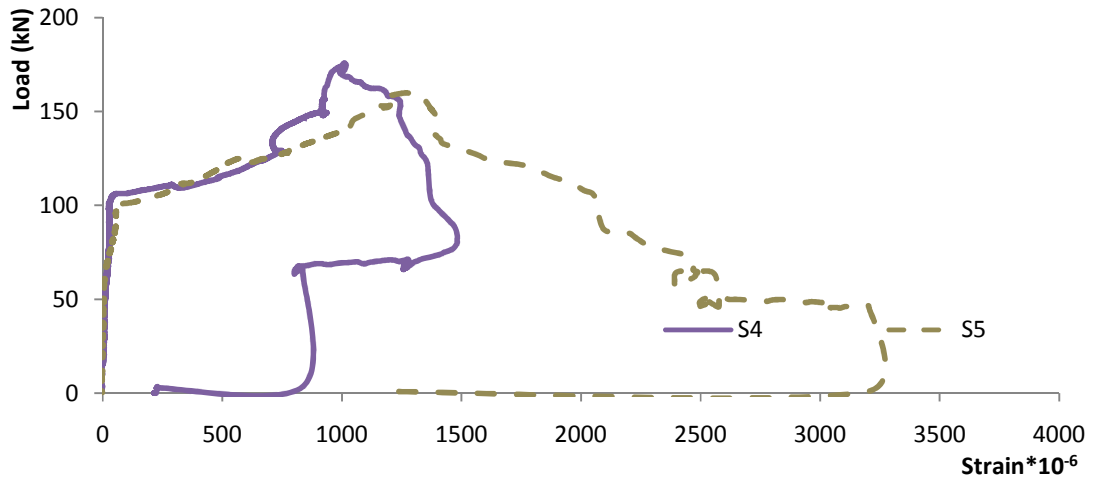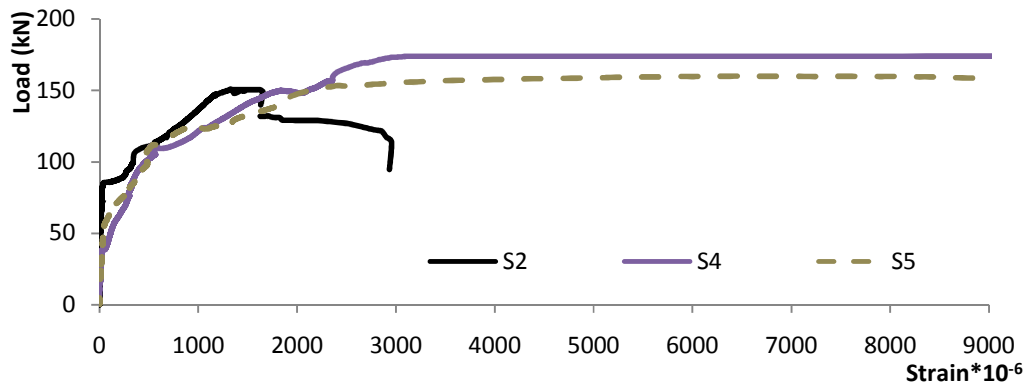
Figure 9- 17 Load-stirrups strain: a) outer stirrups; b) inner stirrups

The pile cap's plates of beams S4 and S5 experienced high levels of strain, and the plates yielded after the connection breakout load was reached. Initially, the strains on the upper and lower sides of the pile cap plate were tensile indicating that tensile forces, not moments, transferred through the pile cap. On the other hand, after the connection breakout in beams S4 and S5, the tensile strain in the lower side of the pile cap decreased

then increased again due to moment transfer from the pile shaft to the pile cap. Because the pile cap could transfer these forces and moments to the surrounding concrete without pryout failure, the connection capacities of beams S4 and S5 were higher than that of beam S2. Some cracking and large out of plane displacement were recorded for beam S5, and which explains the smaller ultimate load for S5 compared to S4. Finally, the pile cap's plate strains in beams S4 and S5 decreased at the failure stage when the pile cap's welding failed.

9.9.3 Third Group: Effect of Longitudinal Reinforcement

In this group, three different longitudinal reinforcement ratios were tested, i.e., 0.4% (4-15M in S2), 0.6% (4-20M in S6), and 1.11% (4-25M in S7). The pile embedment depth, plate width and stirrups configuration were kept constant. Accidently, beam S7 had compressive strength of 40 MPa while beams S2 and S6 had compressive strength of 30 MPa. Also, two bolts were used in beam S7 to connect the pile cap to the pile shaft instead of one bolt in beams S2 and S6.

9.9.3.1   Crack pattern and mode of failure

Beams S6 and S7 had different mechanism than that of beam S2 due to their higher longitudinal reinforcement ratio. Beam S2 experienced breakout failure manifested in concrete cover spalling in front of the pile. Similarly, beam S6 experienced breakout failure and thin pryout cracks; however, its pile cap's welding failed before pryout failure took place. On the other hand, beam S7 failed because the pile shaft failed after the formation of the breakout cone.

446

The higher longitudinal reinforcement ratio in beam S6 reduced the crack width of the first breakout cone and delayed the full formation of the breakout cone. After the connection breakout occurred and the breakout cone moved, the longitudinal reinforcement provided higher contribution to the connection resistance and the pile cap contributed to the connection capacity. Moreover, the stirrups of beam S6 failed by necking; however, its welding capacity was less than the connection pryout capacity and thus the welding failed causing a sudden loss of the pryout resistance and reduction in the connection capacity.

The behaviour of beam S7 was influenced by the high concrete strength (40 MPa) and the two-bolts pile shaft connection in addition to its high longitudinal reinforcement. All cracks formed at higher loads compared to S2 and S6, and the breakout crack width was so small until the connection failed. Also, the concrete crushing in front of the pile shaft occurred at a higher load due to the high concrete compressive strength.

After concrete crushing, the point of pile bearing on the concrete shifted deeper, large flexural stresses, in addition to shear stresses, transferred to the pile shaft causing it to yield at the fixation point (first bolt hole). Fuchs (1992) observed the same shell-shaped concrete spalling for a headed stud when subjected to shear loading far from the concrete edge due to the high local bearing stresses. Subsequently, the pile rotated causing more concrete crushing and the pile shaft failed due to a combination of shear and flexural stresses at the first bolt hole. Finally, it is clear that using 2 bolts did not enhance the shear behaviour of the connection. Eligehausen, Mallée, & Silva (2013) observed the

same behaviour when they studied anchors in concrete and stated that anchor bolts with variable cross-sectional area may fracture at the reduced cross-section due to the tensile forces induced in the anchor. Furthermore, Fuchs (1992) confirmed that it is not only the tension capacity of the concrete which affect the anchors behaviour in shear, but also the concrete bearing capacity in front of the anchor and its distribution.

9.9.3.2 First flexural cracking, breakout and ultimate loads

As expected, beam S7 had the highest first flexural cracking load as it had both the highest longitudinal reinforcement and the highest concrete strength. However, the first flexural cracking load for beam S6 was surprisingly less than that of beam S2, but its breakout and ultimate loads were higher than those of S2. Thus, it may be concluded that increasing the longitudinal reinforcement increases the connection breakout and ultimate loads.

In beam S7, the pile shaft failed at 75% of its minimum yielding capacity. Thus, in order to design the connection with capacity higher than the connection breakout or concrete crushing loads, high flexural stresses should be considered in the pile shaft design or a reduction factor should be used when calculating the shear capacity of the pile shaft.

9.9.3.3 Stiffness and load-displacement relationship

Figure 9-18 displays the load-mid span displacement during loading for the test specimens. It can be noted from Figure 9-18 that the initial response of the three beams was essentially identical despite the difference in their reinforcement ratio. This is because only one longitudinal bar was close to the extreme tension fibers in the shear

448

loading mode, in addition to one bar of the beam's secondary longitudinal reinforcement.

Beam S7, with 1.11% main longitudinal reinforcement ratio, had higher stiffness than that of beams S2 and S6 only after the formation of the first breakout cone, which is attributed to its higher concrete compressive strength. Figure 9-18 shows that beam S7 failed suddenly with very small beam displacement. However, the pile shaft sustained large displacement because it developed a plastic hinge before failing.
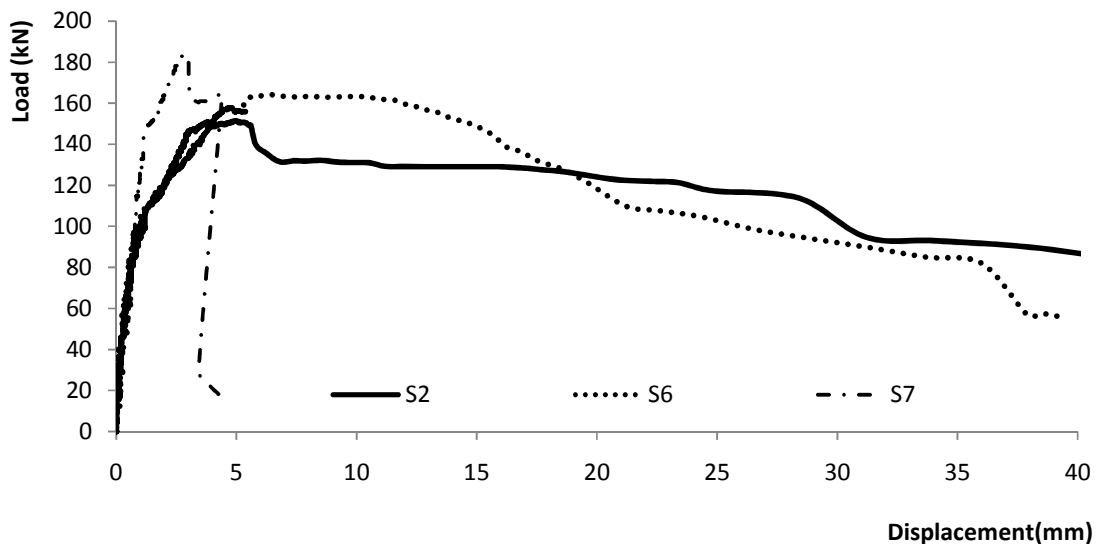
Figure 9- 18 Load mid-span concrete displacement relationship

9.9.3.4   Ductility and strain energy

Table 9-3 shows that the mid-span displacement of beam S6 was higher than that of beam S2 because it had higher connection breakout and ultimate loads. The ratio $\left(\frac{\Delta u}{\Delta y}\right) = 2.38$ and 2.1 for beams S2 and S6, respectively, which indicated that increasing the longitudinal reinforcement ratio did not apparently enhance the beam ductility because both the connection displacement and the displacement at which the reinforcement

449

yielded increased and hence the ratio $\left(\frac{\Delta u}{\Delta y}\right)$ decreased slightly. Similarly, the strain energy

for both beams was approximately equal. On the other hand, beam S7 had $\left(\frac{\Delta u}{\Delta y}\right) = 1.14$,

and absorbed much less strain energy than beams S2 and S6. On the other hand, the strain

energy stored in the beam calculated using the pile displacement was higher than that of

beams S2 and S6 and the overall failure of beam S7 could be considered ductile because

it was due to the failure of the pile shaft, which experienced remarkable deformation

before failure.

9.9.3.5 Reinforcement steel and pile cap's plate strain

Figure 9-19 presents the longitudinal steel strain for the test specimens. It shows that the

strain decreased as the longitudinal reinforcement ratio increased because it decreased the

concrete tensile strain and delayed its failure in addition to the higher required load to

strain larger bars. This explains the corresponding increase in the connection breakout

load. At the ultimate load, the outer longitudinal reinforcement of beam S2 reached

yielding strain (3332×10^{-6} mm/mm), but not in beam S6 (1299×10^{-6} mm/mm) and beam

S7 (931×10^{-6} mm/mm). The same behaviour was observed for the inner longitudinal

reinforcement. Figure 9-19 also shows that the outer longitudinal reinforcement

experienced higher strain than the inner longitudinal reinforcement due to the flexural

stresses; however, after the connection breakout occurrence, the inner bars' strain

increased because they carried more load by dowel action.

a)

b)
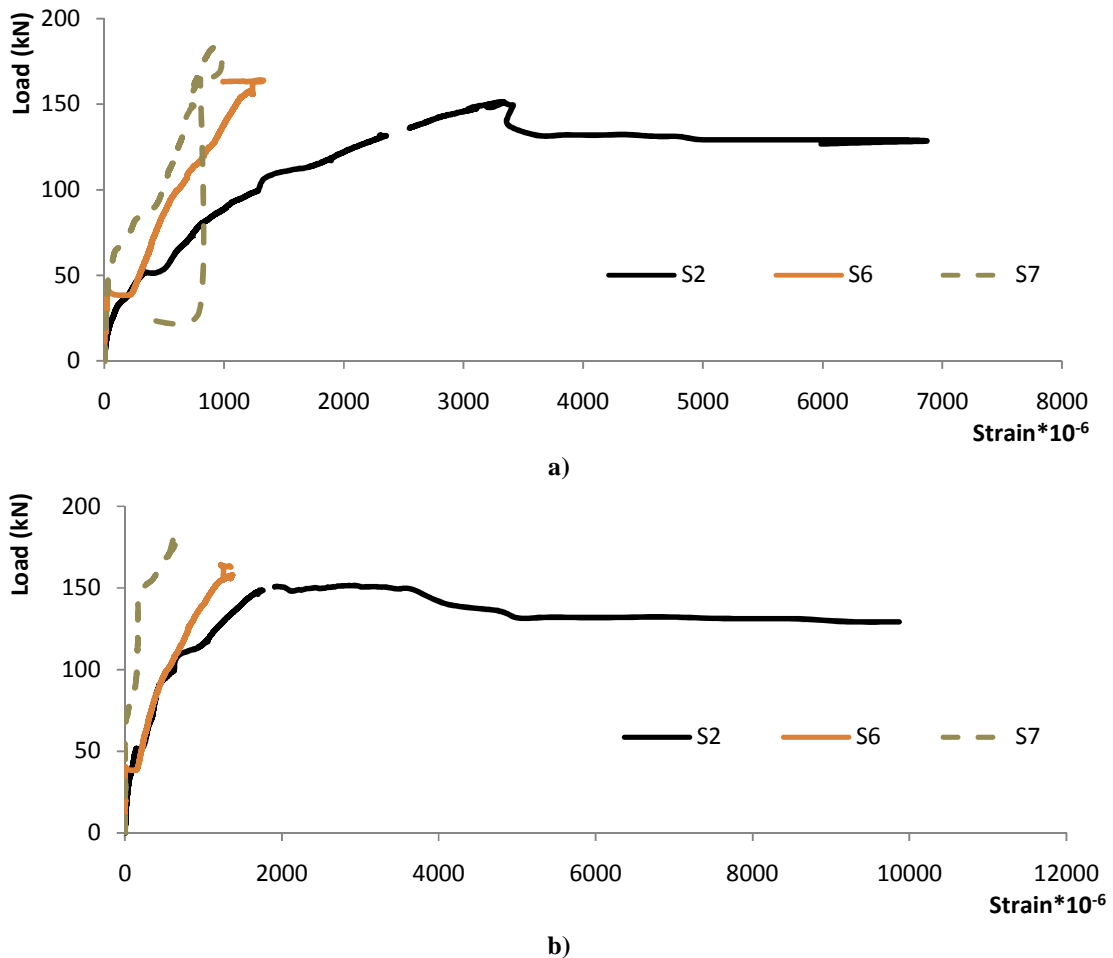
Figure 9- 19 load-longitudinal reinforcement strain: a) outer reinforcement; b) inner reinforcement

Figure 9-20 displays the stirrups strain for the test specimens. It indicates that stirrups contributed to resisting load only after the formation of 20° diagonal cracks (at an applied load of around 100 kN), and that the inner stirrups experienced higher strains than the outer ones. The stirrups of beams S6 and S2 experienced roughly the same strain levels until the breakout cone formed fully, at which point the strain increased rapidly and the inner stirrups exceeded its yield strain and failed by necking. Beam S7 exhibited lower stirrups strains because of its higher concrete compressive strength and longitudinal

451

reinforcement ratio, and breakout cone fully formed at a higher load compared to beams

S2 and S6. However, beam S7 had higher breakout and ultimate loads than beams S2 and

S6 and its inner stirrups also yielded (2417×10^{-6} mm/mm) before the pile failure.

a)

b)
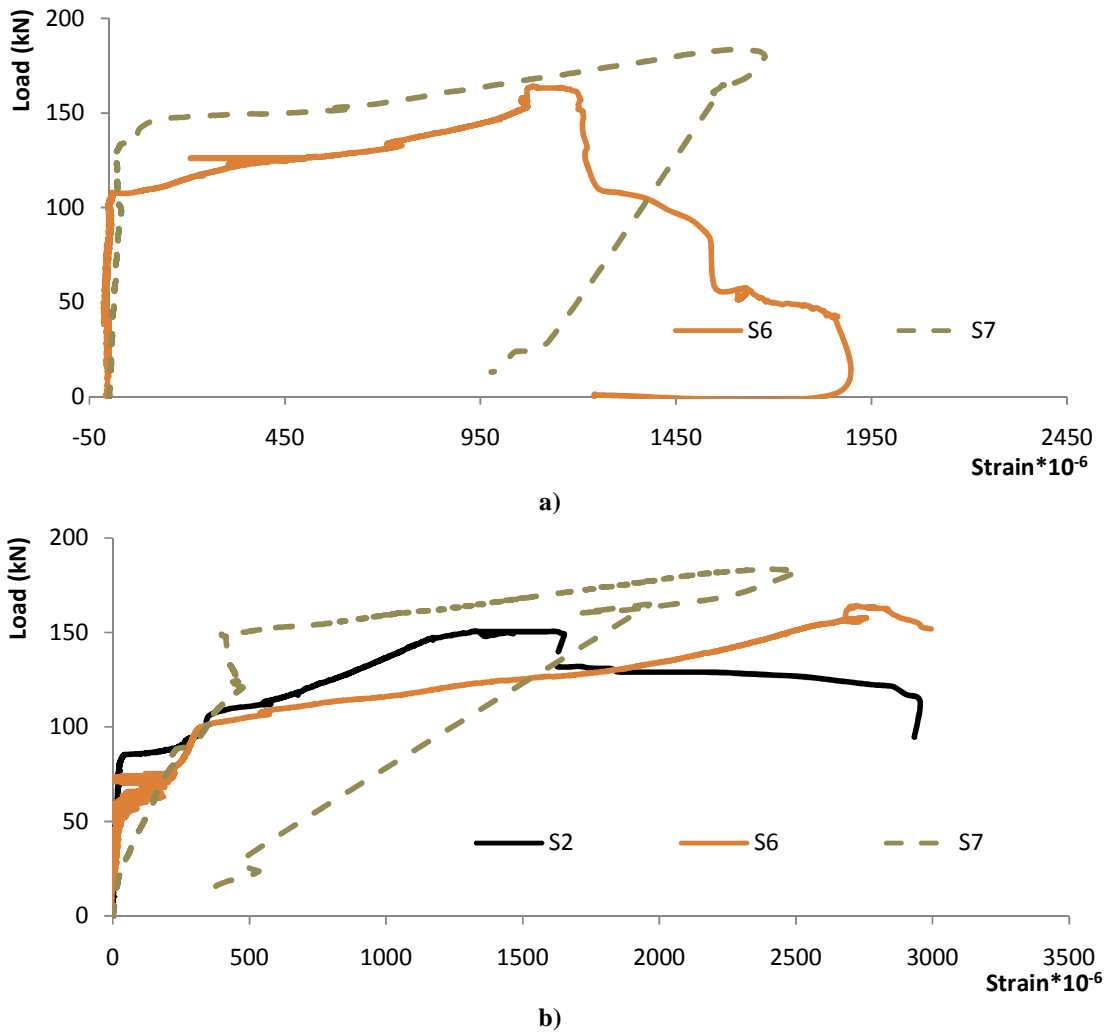
Figure 9- 20 Load stirrups strain: a) outer stirrups; b) inner stirrups

All three beams experienced small strains in the pile cap plate (less than 375×10^{-6}

mm/mm) before their ultimate loads were reached, i.e., the pile cap's plate did not yield

and the pryout contribution to the connection capacity was minimal. After the ultimate

load was reached, beams S2 and S6 experienced large pile cap's strains due to the large rotation of the pile shaft and pile cap mobilizing the pryout resistance. Beam S6 exhibited reduction in the pile cap strains after the ultimate load was exceeded, which is attributed to the failure of the plate's welding (at an applied load of 128 kN). In beam S7, the pile shaft developed a plastic hinge at its first bolt hole and the pile cap did rotate, which resulted in small pile cap strain at its ultimate load ($< 160 \times 10^{-6}$ mm/mm).

9.9.4 Forth Group: Effect of transverse reinforcement

In this group, three beams with different transverse reinforcement (stirrups) were tested. Beam S2 had two branches of #2 (6.35 mm diameter) spaced at 200 mm (about 0.07% transverse reinforcement ratio). Beam S8 had two branches of 10M spaced at 200 mm (about 0.22% transverse reinforcement ratio). Beam S9 had two branches of #2 spaced at 100 mm (about 0.14% transverse reinforcement ratio). The pile cap width, the embedment depth, and the longitudinal reinforcement were kept constant. The concrete compressive strength was 40 MPa for beams S8 and S9 and 30 MPa for beam S2. Finally, beams S8 and S9 had two-bolt pile cap connection and beam S2 had one-bolt connection.

9.9.4.1 Crack pattern and mode of failure

Beams S8 and S9 had different crack patterns than beam S2 due to higher transverse reinforcement and concrete compressive strength, and the number of connection bolts. The failure mechanism in beams S8 and S9 involved pile shaft failure after the breakout cracks formation, while beam S2's connection failed due to breakout cracking failure combined with pryout cracks. Thus, the pryout contribution to the connection capacity

was negligible for beams S8 and S9, but the bearing capacity of the concrete (i.e. concrete crushing load) in front of the pile shaft in beams S8 and S9 were more than that of beam S2. In addition, the high transverse reinforcement ratio of beams S8 and S9 decreased the breakout crack width, which increased the concrete aggregate interlock contribution. Furthermore, beams S8 and S9 developed plastic hinges in the pile shaft, which caused high stress concentration in the concrete in front of the pile shaft leading to concrete crushing and eventually the pile shaft failed. Also, using two-bolt connection may have contributed to the pile shaft failure. Finally, the higher concrete compressive strength in beams S8 and S9 caused cracking to occur at higher loads than that of beam S2, and the concrete in front of the pile could sustain more bearing stresses before the concrete crushing occurred. Finally, second breakout cone was observed in beams S8 and S9, which formed in the concrete cover bounded by the longitudinal reinforcement, the transverse reinforcement, the first breakout cone cracks and the flexural cracks. Rndla and Kunz (2014) reported similar breakout cone.

9.9.4.2   First flexural cracking, breakout and ultimate loads

The first flexural cracking load of beams S8 and S9 was not affected by the increase in the transverse reinforcement. On the other hand, beams S8 and S9 had higher flexural cracking load than beam S2, possibly due to their high concrete compressive strength. As shown in table 9-3, the higher transverse reinforcement ratio and concrete compressive strength of beams S8 and S9 increased the connection capacity by at least 23% compared to beam S2. At the same time, beams S8 and S9 had approximately the same ultimate load, which suggests that the reason for the increase in the connection breakout and

454

ultimate loads was the higher concrete compressive strength not the higher transverse reinforcement ratio. On the other hand, beam S9 ultimate load was slightly higher than that of S8, possibly due to its higher stirrups contribution.

9.9.4.3 Stiffness and load-displacement relationship

Because of the different concrete compressive strength of the beams in this group, the load mid-span displacement response curves shown in figure 9-21 also include beam S7 as a reference beam to help delineate the effects of concrete compressive strength from those due to the transverse reinforcement ratio. Beams S7, S8 and S9 had essentially the same stiffness and response until the first breakout cone initiated, which means the transverse reinforcement had no effect. As the breakout load was exceeded, the beam stiffness increased slightly as the transverse reinforcement ratio increased.
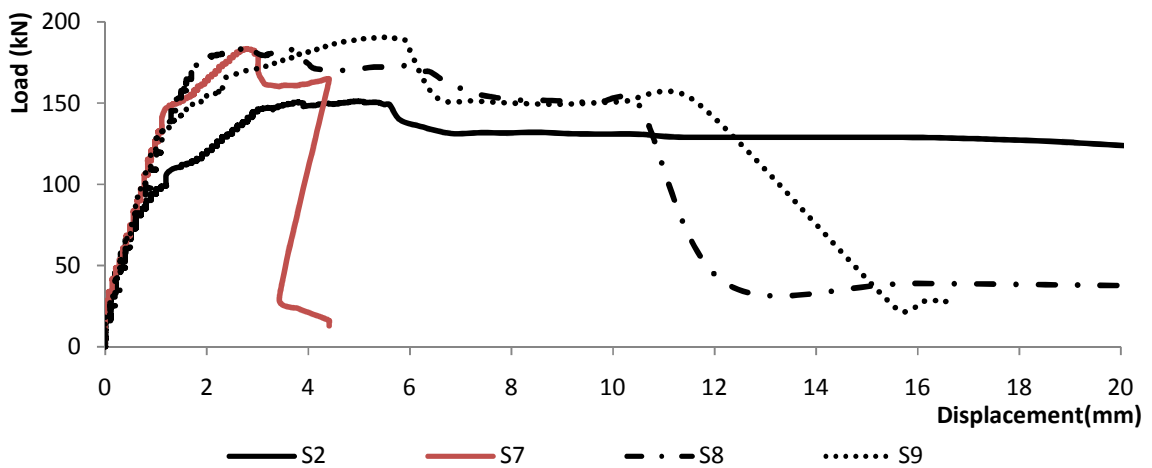
Figure 9- 21 Load mid-span displacement relationship

9.9.4.4   Ductility and strain energy

The calculated ductility, $\left(\frac{\Delta u}{\Delta y}\right)$, for beams S2, S8 and S9 was 2.38, 1.53 and 1.42, respectively. These values were influenced by the pile shaft failure, which negated the expected effect of higher transverse reinforcement ratio on enhancing ductility. Also, table 9-3 shows that the absorbed energies calculated using both the beam mid-span displacement and the pile displacements were less for beams S8 and S9 than that calculated for beam S2. On the other hand, beams S8 and S9 absorbed more energies compared to beam S7. Thus, the pile shaft failure overshadowed the effect of the transverse reinforcement on the connection ductility.

9.9.4.5   Reinforcement steel and pile cap strains

Figure 9-22 displays the strains in the longitudinal reinforcement bars. At the ultimate load, the outer longitudinal reinforcement exceeded yielding strain in beams S2 (3332×10^{-6} mm/mm) and S8 (2189×10^{-6} mm/mm), while it did not reach yielding in beam S9 (1586×10^{-6} mm/mm). The inner longitudinal reinforcement strains at the ultimate load were 2936×10^{-6} mm/mm, 852×10^{-6} mm/mm, and 1469×10^{-6} mm/mm for S2, S8 and S9, respectively. These results demonstrate that the outer longitudinal reinforcement in beams S8 and S9 experienced higher strain compared to the inner longitudinal reinforcement because they failed at the connection breakout load.
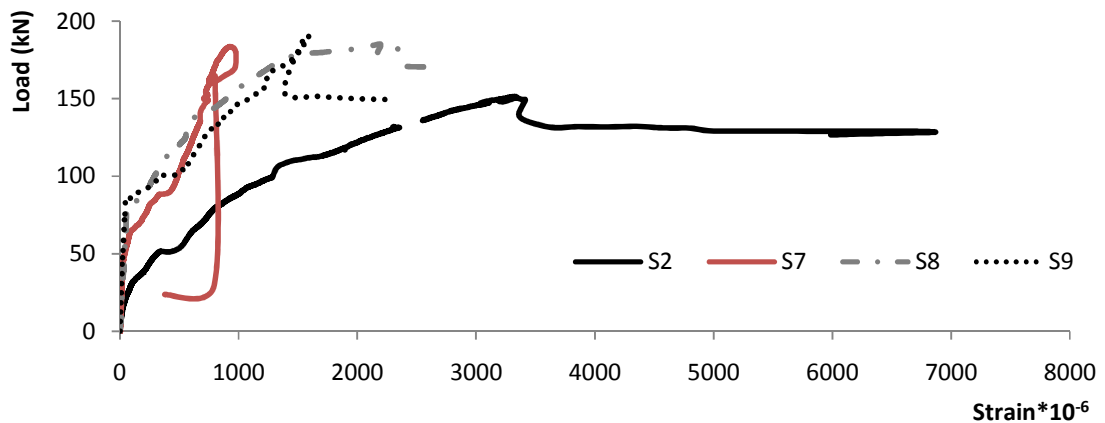
a)
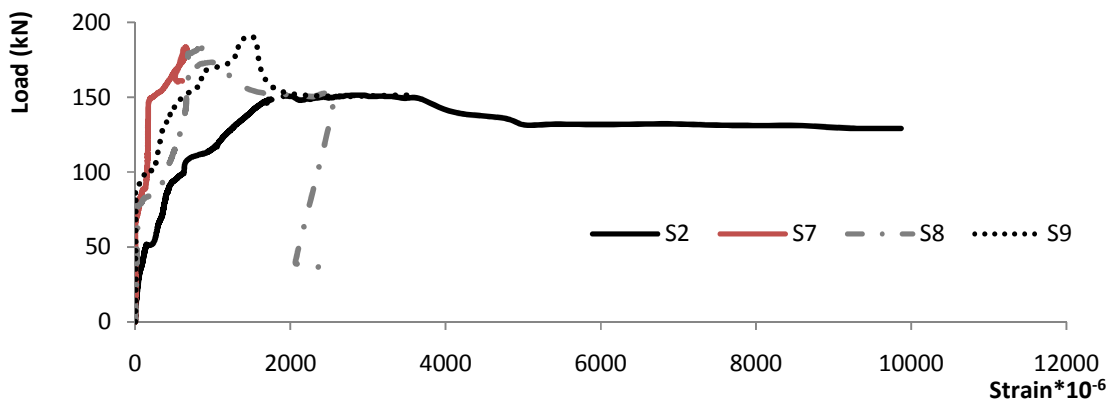
b)

Figure 9- 22 load-longitudinal reinforcement strain: a) outer reinforcement; b) inner reinforcement

Figure 9-23 presents the strains of the test beams' stirrups. It can be noted from the figure that stirrups contributed to the connection capacity only after the formation of the 20° diagonal cracks. Also, the stirrups close to the pile shaft experienced higher strains than that in the outer stirrups. In beam S8, the breakout cracks did not intersect with the outer stirrups at one side of the beam. Thus, its strain was negligible and the inner stirrups at the same beam side experienced large strains after the formation of the breakout cracks. However beams S7, S8, and S9 failed in the pile shaft, their inner stirrups reached yielding before the ultimate load.

457

The pile cap strain was less than 300×10^{-6} mm/mm in the four beams until the ultimate load was reached. In beams S7, S8, and S9, the pile shaft had a plastic hinge at its first bolt hole, the pile cap did not rotate and its strain was $< 150 \times 10^{-6}$ mm/mm. After the pile shaft failure, the strain reduced much further
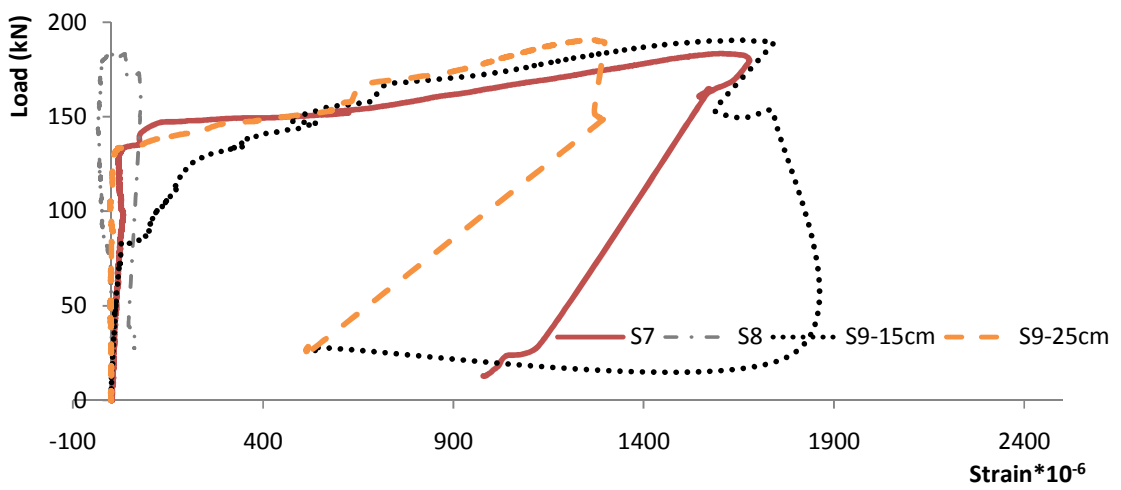
a)
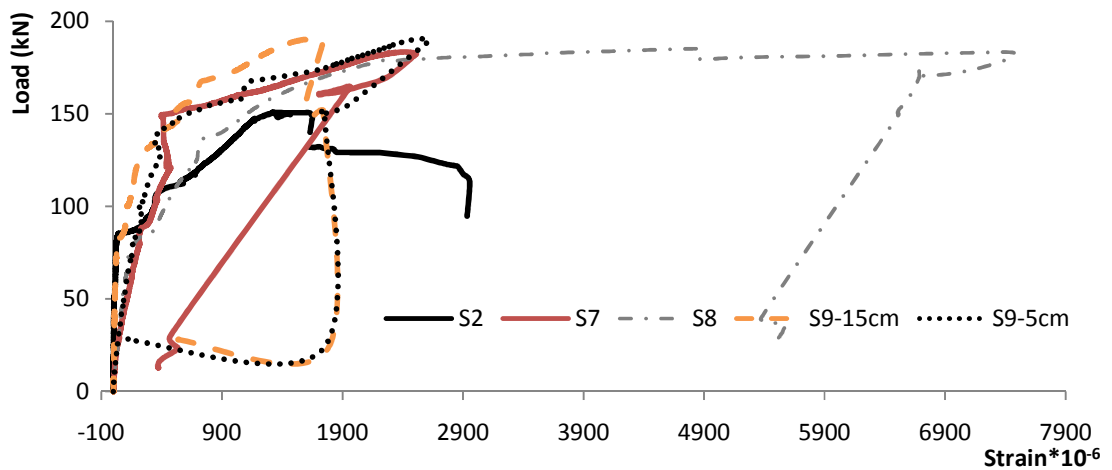
b)

Figure 9- 23 Load- stirrups strain: a) outer stirrups; b) inner stirrups

9.10 General findings of cyclic shear loading tests

9.10.1 General crack patterns, failure modes and general load transfer mechanism

Figure 9-24 presents the crack patterns of the tested specimens. As can be noted from figure 9-24, cyclic loading caused concrete cracking at both sides of the beam, but the cracking pattern was slightly different. The cracks initiated at the lower side of the test rig (which had a clear span of 670 mm), followed by cracks at the upper side (which had a span of 610 mm).

Thin cracks appeared first at the unloaded side of the pile, followed by cracks in the beam that extended gradually with a 20° angle longitudinally from the pile shaft towards the supports as the load increased. Flexural cracks then initiated at the mid-span of the beam, followed by breakout cracks, which extended from the pile shaft with approximately the same angle in the two loaded sides of the beam. Plastic deformations were observed due to concrete crushing and cracks opening even at earlier stages of loading as shown in Figure 9-24. For each cycle of the same load levels, cracks extended further due to degradation of concrete strength. Thus, concrete stiffness degradation was presented while cyclic loads were applied as that recorded by (Rieder & Strauss, 2009, Vintzelou & Eligehausen., 1992, Vintzeleou & Tassios, 1987, and Swirsky, 1977). The concrete crushing and plastic displacements caused large gap around the pile shaft, which reduced the concrete support to the pile shaft and the connection capacity. Finally, the pile cap welding failed and concrete cover spalling was observed after the connection breakout occurance. All three tested beams experienced the same failure mechanism, i.e., breakout failure followed by failure of the pile cap's welding.

459
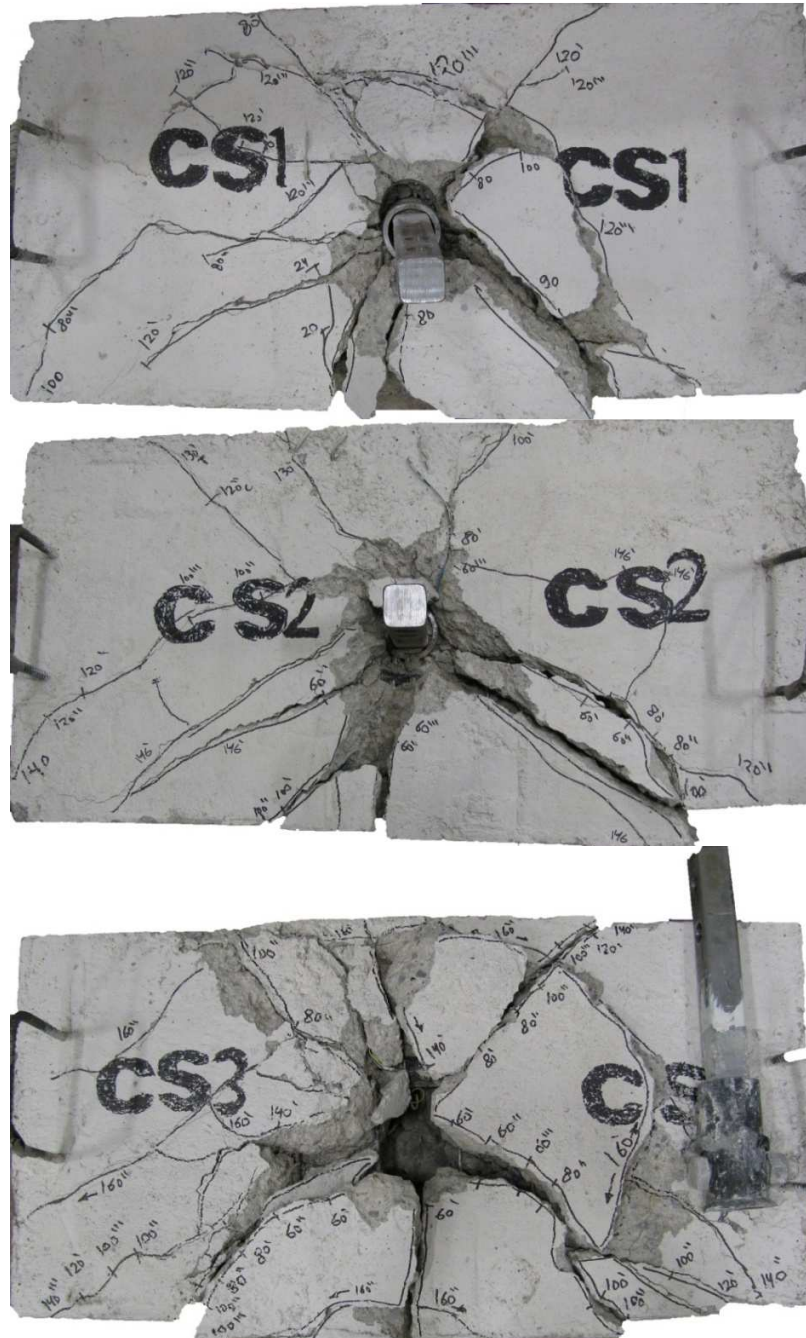
Figure 9- 24 Crack patterns of beams subjected to cyclic shear loading

The load transfer mechanism was similar to that observed during monotonic loading. The crushing of concrete at the surface around the pile shaft increased the pile shaft bending,

and possibly resulted in low cycle fatigue failure of the pile cap's welding due to the repeated yielding cycles (Eligehausen, Mallée, & Silva, 2013; Klingner, Mendonca, & Malik, 1982). The premature failure in the pile cap's welding due to the cyclic loading did not allow pryout cracking to occur, which eliminated its contribution to the connection ultimate capacity. Usami et al. (1980) reported similar results, which showed that low-cycle fatigue strength of an anchor could be less than 40% of its monotonic shear strength. Therefore, a strength reduction factor must be considered when designing the steel components that transfer the cyclic shear load to the foundation. Also, in order to prevent welding failure, stiffeners should be provided between the pile cap's plate and the pile cap's cylinder to increase its flexural capacity in case of large cyclic shear loading is expected.

9.10.2 General Ultimate Load and Load-Displacement Response

Figures 9-25 and 9-26 compare the load-displacement curves for the three specimens subjected to cyclic loading (i.e. CS1, CS2 and CS3) with the response of identical specimens subjected to monotonic loading (i.e. S1, S2 and S9). Figure 9-25 presents the beam mid-span displacements at one of the loaded sides, while Figure 9-26 presents the recorded displacements from the loading jack to account for the pile deformation.

Figures 9-25 and 9-26 show that the displacement increased as the number of load cycles increased due to the degradation of the concrete strength and stiffness. This resulted in reduced connection breakout and ultimate loads of the beams subjected to cyclic loading compared to those subjected to monotonic loading.

The connection load-displacement responses characterized by the initiation of the first flexural cracking, breakout cone formation and connection breakout, and the connection failure were affected by the cyclic loading. Due to the deterioration in the concrete mechanical properties under repeated cyclic loading within the inelastic range (Erberik & Kurtman, 2010), the connection breakout and ultimate loads decreased. As the applied load approached the connection breakout load, all specimens experienced strength degradation and high residual deformations.

Figure 9-25 shows that at the first breakout cone formation, plastic displacements occurred, i.e., the connection experienced inelastic behaviour. After the first breakout cone formation, the beam mid-span displacements did not change its direction when the pile shaft unloaded and loaded on the other side of the beam. This explains the large crack openings and plastic displacement shown in Figure 9-24. All three beams subjected to cyclic loading failed at their connection breakout load due to the concrete cover failure, followed by the pile cap welding.

Figure 9-26 confirms that the strength and stiffness degradation occurred in both sides of the beam and, consequently, the connection capacity decreased in all three beams.

Finally, beams CS1 and CS3 failed after 3 and 4 cycles of repeating the same load, respectively, which is a manifestation of the strength degradation of connection; and the maximum cyclic load was less than the ultimate load of the identical beams loaded monotonically.
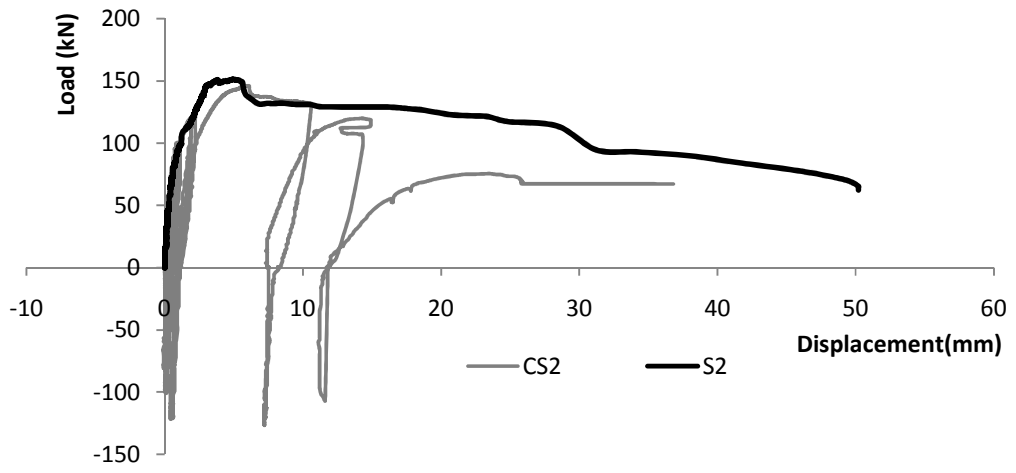
a)
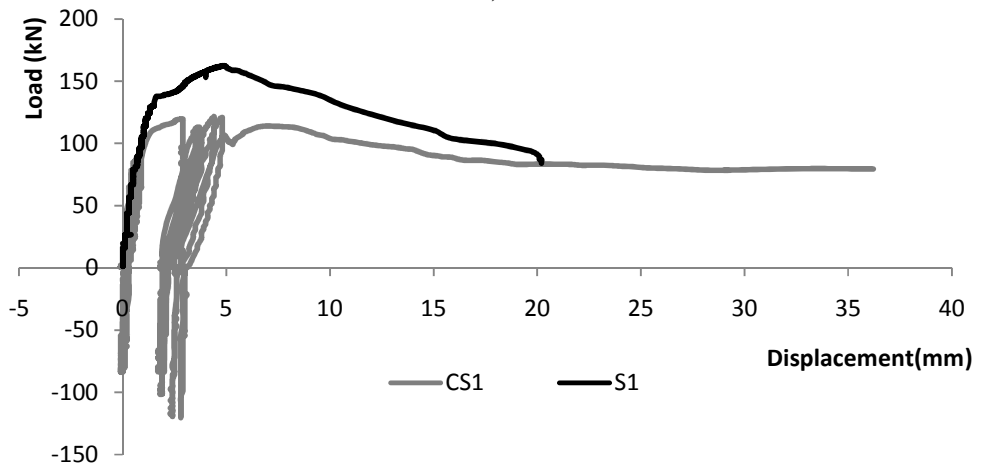
b)
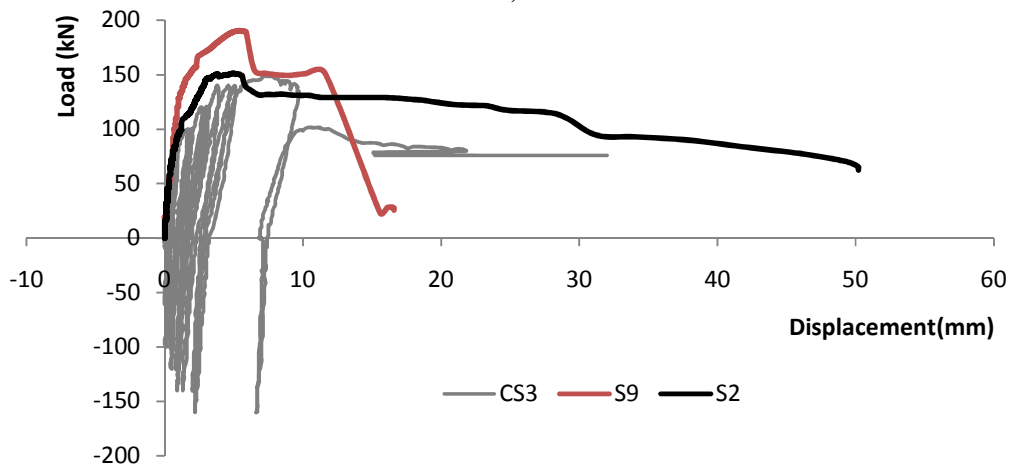
c)

Figure 9- 25 Load mid-span displacement relationship: a) CS2; b) CS1; and c) CS3
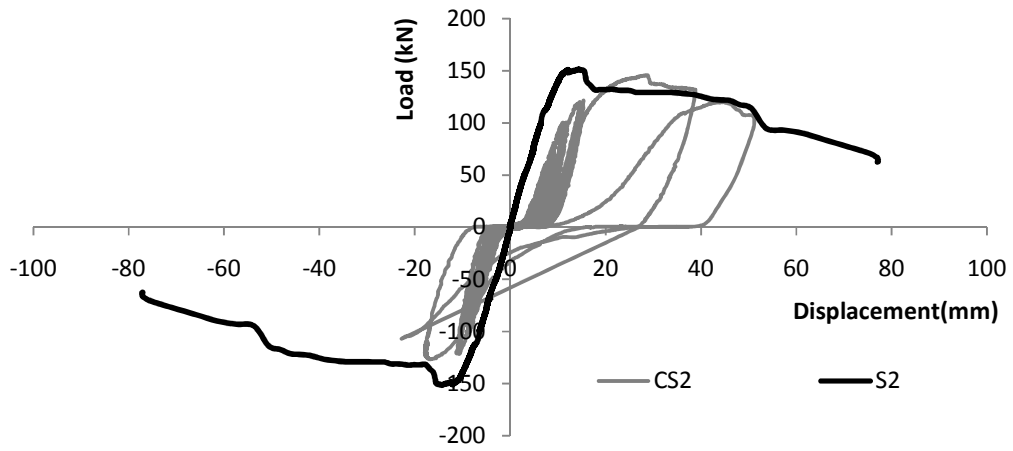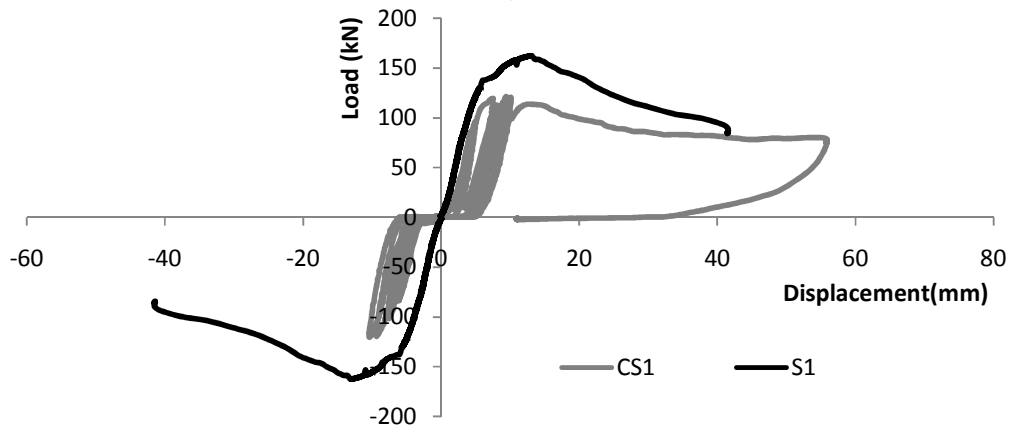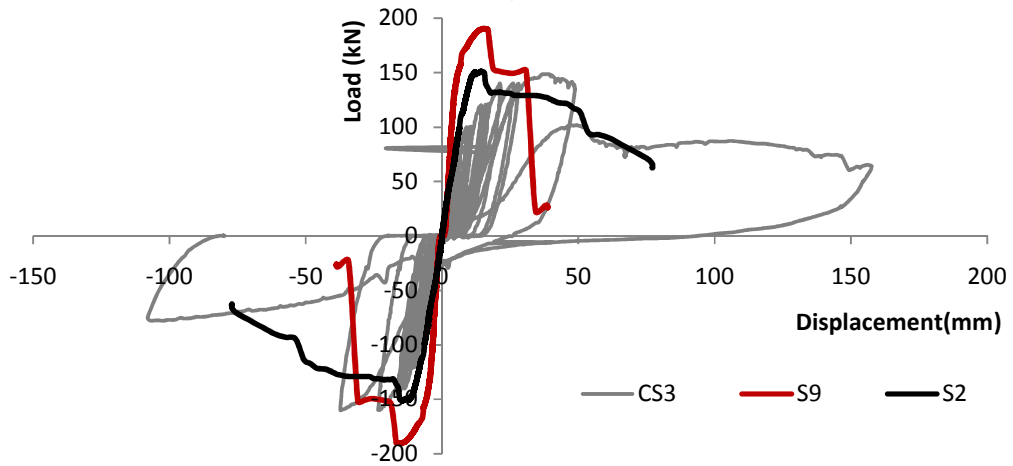
Figure 9- 26 Load-loading jack displacement relationship: a) CS2; b) CS1; and c) CS3

9.10.3 Beam ductility, strain energy and energy dissipation capacity

The three specimens experienced brittle failure at their ultimate load. However, they sustained increased displacements with decreased ultimate loads compared to the identical specimens loaded monotonically due to the cyclic degradation of the concrete stiffness. One the other hand, the pile shafts experienced large displacements and rotations after the specimens' ultimate load was reached, but before the pile cap's welding failure. Thus, the overall behaviour of the connection, including the pile shaft and the pile cap, may be considered as ductile behaviour.

The strain energy stored in the specimen is an indication of its ability to absorb energy before failure. Furthermore, the dissipated energy of a reinforced concrete member during cyclic loading is a favorable characteristic for structures subjected to earthquake loads. The energy dissipation capacity was calculated as the area of each hysteretic loop and the cumulative energy dissipated in each beam was calculated and used for evaluating the performance of different beams. The calculated strain energies and cumulative energies dissipation for the tested beams for only one side of loading are presented in Table 9-4.

Table 9- 4 Test results of specimens subjected to cyclic loading

Group	Specimen	First flexural cracking load(kN)	Connection breakout load(kN)	ultimate load (kN)	mid-span displacement at breakout (mm)	mid-span displacement at ultimate (mm)	Strain energy absorbed by the beam* (kN.mm)	Strain energy absorbed by the connection **(kN.mm)	Cumulative Dissipated Energy*** (kN.mm)	Failure mechanism
First comparison	S2	50	145.03	151.4	3	5	4591	6851	------	Breakout failure with wide pryout cracks
	CS2	22	146	146	5.9	5.9	3084	5625	3165	Breakout failure then welding failure
Second comparison	S1	78.2	137.48	162.39	1.4	4.7	2556	4445	------	Breakout failure then pryout failure
	CS1	22	121.5	121.5	4.4	4.4	1674	2568	2110	Breakout failure then welding failure
Third comparison	S3	75	> 136.8	136.8	--	3.2	318	2716	------	Pile shaft failure
	CS3	40	145.3	148.7 & -160.1 ****	7.7	7.7	3163	6924	3545	Breakout failure then welding failure

*   Strain Energy of Concrete is calculated using the mid-span deformation at the loaded beam side up to 0.6 of its ultimate load after reaching its ultimate load.

**   Strain Energy of Connection is calculated using the loading jack displacement (to take the pile deformation into account) using only one side of loading up to 0.6 of its ultimate load after reaching its ultimate load.

***   The cumulative dissipated energy is the sum of all the areas under the hysteresis loops in the load-displacement curves up to the recorded ultimate load using the loading jack displacement for only one side of loading.

**** In Beam CS3, after reaching the ultimate load in one direction, the other direction was loaded until its ultimate load was reached. Thus, two different ultimate loads were recorded for the two loading directions.

9.10.4 Reinforcement Steel Strain and Pile Cap's plate Strain

Before the first breakout cone formation, the strain gauges recorded the same strain levels for the same load amplitude, which demonstrate that the behaviour of the reinforcing steel and pile cap was linear elastic. After the concrete crushed in front of the pile shaft and the second breakout cone initiated, the longitudinal reinforcement, stirrups and pile

cap's plate strains increased as the number of load cycles increased, especially as the amplitude of cyclic load increased.

9.11 Comparison of connection behaviour under monotonic and cyclic shear loading

9.11.1 Beam CS2 Vs beam S2

Beams CS2 and S2 were identical. From table 9-4 and the load displacement curves shown in Figures 9-25(a) and 9-26 (a), it is noted that the first flexural cracking load of CS2 was less than that of beam S2, but the connection breakout load was approximately the same. On the other hand, the degradation of the connection strength in beam CS2 after breakout load reduced its ultimate load slightly compared to that of S2. Small stiffness degradation was also observed in beam CS2 after the formation of the first breakout cone and up to its ultimate load. Residual displacements, however, increased excessively at the connection breakout load.

Figure 9-27 displays the variation of inner longitudinal reinforcement and inner stirrups strains with the applied load for beams S2 and CS2. It can be noted that approximately the same behaviour existed in both loading cases; however, slightly higher strains were recorded for the cyclic loading case due to the lower first flexural cracking and the concrete degradation under the cyclic loading. Similar behaviour was recorded in the inner longitudinal reinforcement on the other side of the beam and the outer stirrups. The strains recorded in the upper pile cap's plate of beam CS2 were slightly higher than that of beam S2 after the first breakout cone formation but the maximum strain in both beams was much less than their yielding strain. This confirms that the crack opening and plastic

467

displacements caused by the cyclic loading increased the transferred moments to the pile shaft and pile cap's welding. As shown in Table 9-4, beam CS2 absorbed less energy than beam S2 because it had a lower ultimate load.
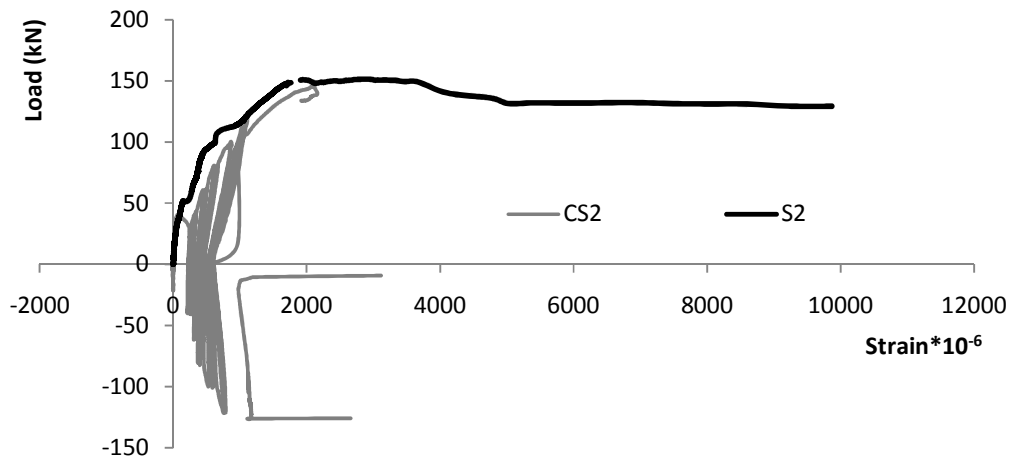
a)
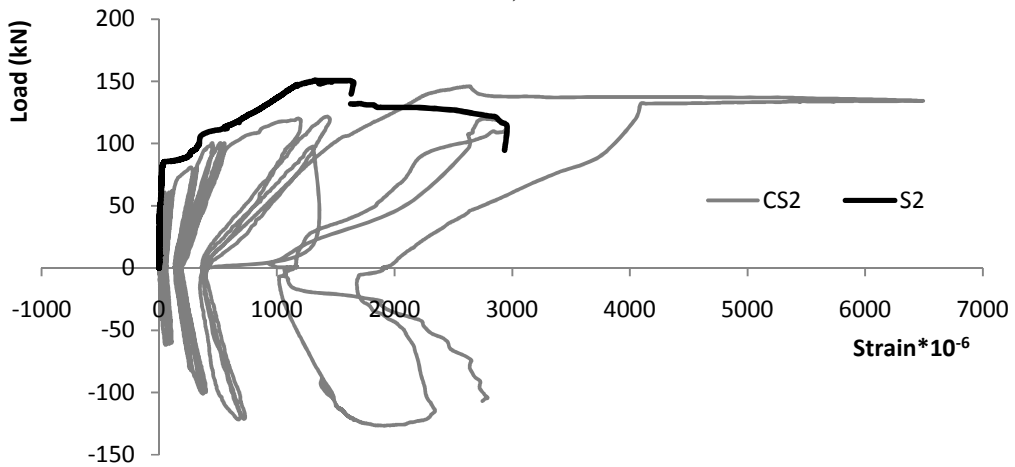
b)

Figure 9- 27 Load- reinforcement strains relation: a) inner longitudinal reinforcement; b) inner stirrups

9.11.2 Beam CS1 Vs Beam S1

Both beams were identical but one was subjected to cyclic loading and the other was subjected to monotonic loading. As shown in table 9-4, beam CS1 had lower breakout

and ultimate loads than S1 (12% and 25% less, respectively). Also, beam CS1 failed after its connection breakout load was exceeded due to the failure of pile cap's welding, while beam S1 exhibited pryout failure. After the first breakout cone formation, beam CS1 experienced large displacements, and concrete degradation, which reached its maximum load in the third cycle of its ultimate load at a mid-span displacement close to the mid-span displacement of beam S1 at its ultimate load.

Figure 9-28 presents the load-strain relationship for longitudinal and transverse reinforcements of beams S1 and CS1. Figure 9-28(a) shows that after the formation of the first breakout cone, the longitudinal reinforcement strains of CS1 increased with each load cycle compared to S1, which confirmed the concrete strength degradation. It also shows that longitudinal steel accumulated residual strains after each load cycle.

Figure 9-28(b) shows that the stirrups strain in beam CS1 increased slightly after each load cycle. Table 9-4 shows that cyclic loading reduced the beam ability to absorb energy before failure by 35% compared to monotonic loading. Furthermore, CS1 experienced failure of pile cap welding while S1 exhibited pryout failure after reaching the connection ultimate load. Finally, the pile cap plate and welding in beam CS1 experienced higher strains than that in beam S1, and the strains of CS1 increased after each load cycle.
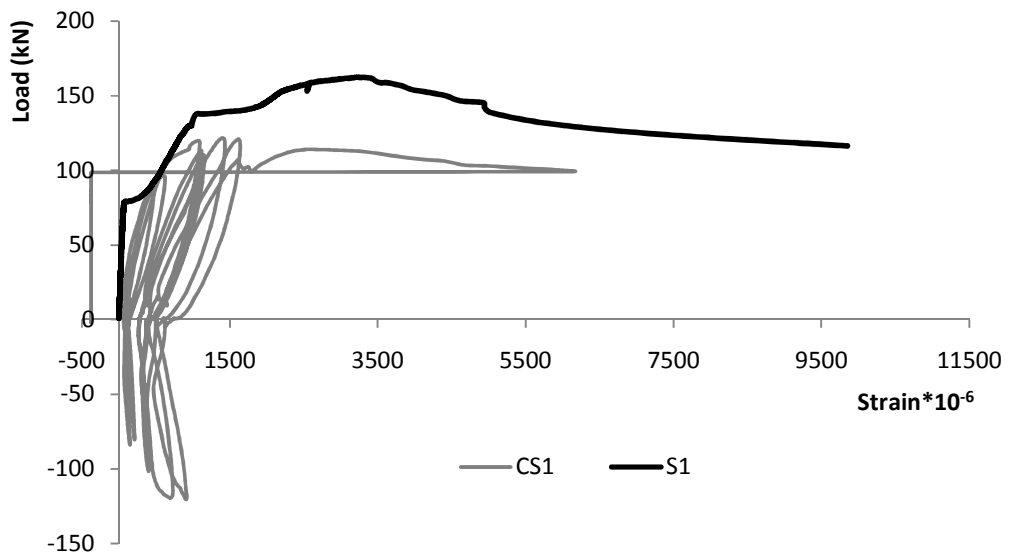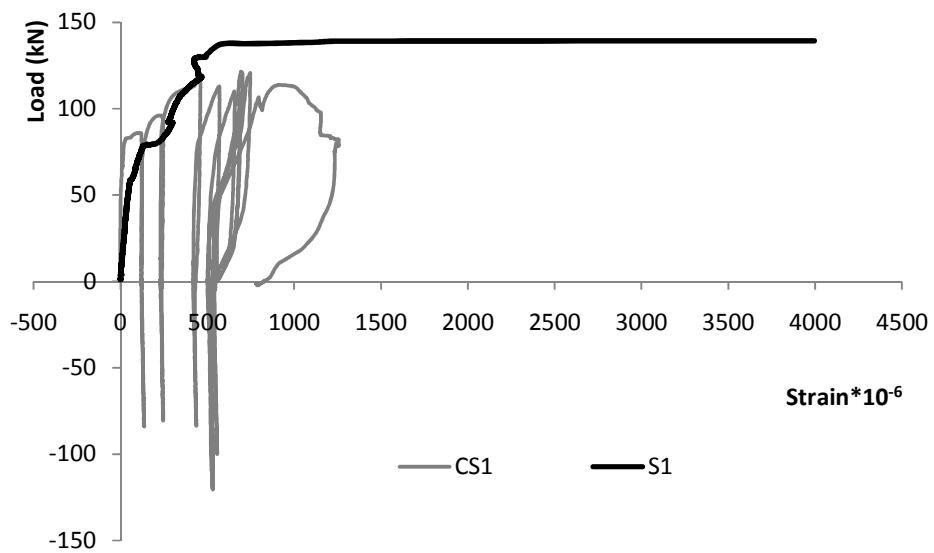
Figure 9- 28 load-strain relationship for: a) longitudinal reinforcement; b) stirrups

9.11.3 Beam S9 Vs beam CS3

Both beams were identical, but Beam S9 had higher compressive concrete strength than that of beam CS3. Thus, beam S2 which had lower transverse reinforcement ratio than other two beams was used in this comparison as a reference beam.

From Table 9-4, beam CS3 had lower capacity than beams S9 and S2. After the ultimate load of beam CS3 was reached on one side, loading on the other side with the shorter span was conducted. As expected, the connection capacity increased due to the shorter span at the other beam side.

Table 9-4 show that beam CS3 had slightly lower first flexural crack and ultimate loads compared to beam S2 and approximately the same connection breakout load. The large difference in connection capacity of beams S9 and CS3 is attributed to the higher concrete compressive strength of beam S9, rather than the effects of the cyclic loading.

As shown in figure 9-29, the longitudinal reinforcement strain of CS3 was approximately the same as in beam S2 up the first breakout cone formation, and increased afterwards with each load cycle. The stirrups strain in beam CS3 increased with each cycle of loading causing to be higher than that in beams S2 and S9 confirming that concrete deterioration existed in beam CS3 due to cyclic loading . Finally, the strain in the pile cap in beam CS3 was higher than that of beams S2 and S9.

a)

471
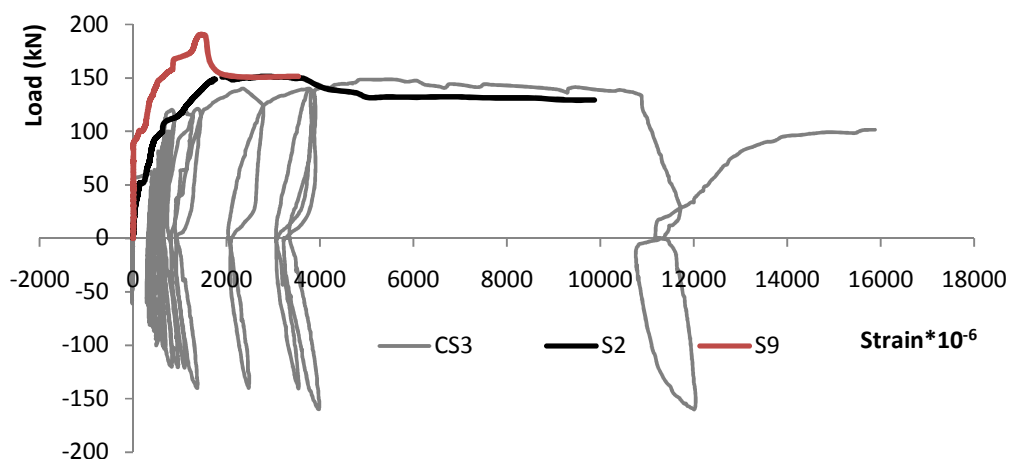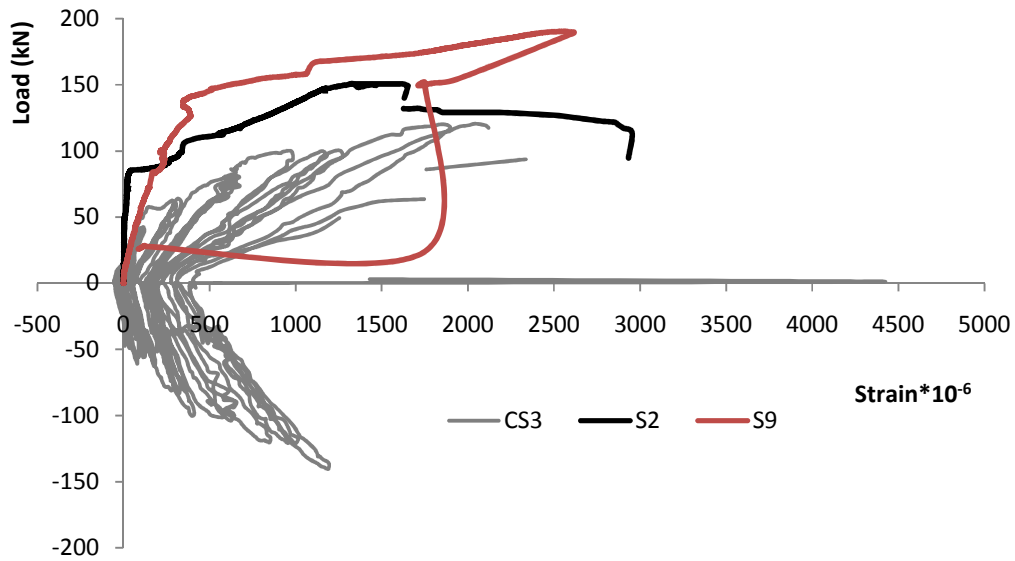
b)
Figure 9- 29 load-steel strain relation for: a) longitudinal reinforcement; b) stirrups

9.11.4 Beam CS2 Vs Beam CS1

Beams CS2 and CS1 were similar but CS1 had 152 mm pile embedment depth while
beam CS2 had 203 mm pile embedment depth. Both beams had similar crack pattern, but
the pile shaft in beam CS1 experienced higher rotation after the concrete crushing
compared to beam CS2. Also, the two beams had generally similar behaviour until the
first breakout cone occurred and the concrete crushed under the pile shaft. At this stage,
the concrete cover of CS1 failed then the pile cap's welding failed, while in beam CS2 a
second breakout cone formed then the pile cap's welding failed. The connection ultimate
shear capacity increased by 20% as the pile embedment depth increase from 152 mm
(CS1) to 203 mm (CS2). Also, the displacement of CS2 at ultimate load was 40% higher
than that of CS1. Moreover, the connection ability to absorb and dissipate energy during
cyclic loading increased as the pile embedment depth increased. Finally, the longitudinal

reinforcement of CS1 did not yield before its ultimate load while that of beam CS2 yielded before its ultimate load indicating higher ductility.

9.11.5 Beam CS2 Vs beam CS3

Beams CS2 and CS3 were similar but beam CS2 had two branches of #2 rebar (6.35 mm diameter) spaced at 200 mm (about 0.07% transverse reinforcement ratio) while beam CS3 had two branches of #2 rebar (6.35 mm diameter) spaced at 100 mm (about 0.14% transverse reinforcement ratio). Beam CS3 was loaded up to its ultimate load of both sides of loading while beam CS2 was loaded up to the ultimate load of one side only.

The load-displacement curves of beams of CS2 and CS3 were similar; with the exception that CS3 sustained maximum displacement of 7.7 mm while maximum displacement of CS2 was 5.9 mm. Thus, the ductility ratio, $\left(\frac{\Delta u}{\Delta y}\right)$, was 2.14 and 1.13 for beams CS3 and CS2, respectively. Moreover, the connection absorbed and dissipated energy was slightly higher for CS3 compared to CS2. In conclusion, increasing the transverse reinforcement ratio had a negligible effect on the beam capacity under cyclic loading but it increased its ductility.

9.12 Conclusions

The capacity of new construction pile bracket used to connect slender shaft piles (e.g. helical piles and micropiles) to grade beams in new RC foundation construction was investigated experimentally. In the first phase of the experimental program, nine foundation models involving simply supported grade beams with new construction pile brackets were subjected to monotonic shear loading. The tested beams were categorized

into four groups according to the parameters investigated. Each group had three beams and only one variable was investigated while the other variables were planned to be constant. The investigated variables were: the pile embedment depth; the width of the steel pile cap's plate; the beam longitudinal reinforcement; and the beam transverse reinforcement. In the second phase, three simply supported grade beams with the new construction pile bracket were subjected to alternating cyclic shear loading. The performance of these beams was compared with that of the similar beams tested under monotonic shear loading. Then these beams were compared with each other. The following conclusions may be drawn from this experimental investigation.

9.12.1 General

1) The studied connection can be considered fixed (i.e. fixed pile head) up to its connection breakout load. Afterwards, the connection becomes hinged and its stiffness and capacity depend on the pile shaft, the longitudinal and transverse reinforcements, and the pile cap configuration.

2) The breakout cracks were close to that reported in ACI 318-11 Appendix D and A23.3-04 CSA code Appendix D (i.e. half pyramid breakout cone with a side length of (3 c_{a1}) and a depth of (1.5 c_{a1}) with 35° crack angles where ca_1 is the distance from the edge to the pile shaft axis).

3) Under monotonic loading, two breakout cones initiated from the pile shaft corners with two different cracking angles of 20° and 35°. The pile shaft rotated after the

474

formation of the 35° breakout cone and the corresponding load was considered as the connection breakout load.

4) The connection breakout load was sustained by the concrete and the longitudinal reinforcement. The longitudinal reinforcement decreased the tensile strains in the concrete and increased its resistance.

5) After the concrete breakout, the concrete ultimate strength was comprised of four parts: the dowel action of longitudinal reinforcement; the stirrups resistance; the pile cap contribution to the connection; and the aggregate interlock resistance.

6) For the connection with shear capacity higher than the concrete bearing capacity, crushing occurred in front of the pile and moments acted on the pile shaft.

7) The connection failure mechanism depended on: the concrete compressive strength, the concrete clear cover, the beam longitudinal and transverse reinforcement ratios, the pile embedded depth, the pile shaft dimensions, the pile cap plate size, the pile shaft material capacity, the welding size, quality, and material strength, and the pile cap's cylinder flexural capacity.

8) The connection stiffness decreased after the connection breakout load.

9) The longitudinal reinforcement close to the beam side (i.e. outer longitudinal reinforcement) resisted the flexural stresses, while the longitudinal reinforcement close to the pile shaft (i.e. inner longitudinal reinforcement) resisted the stresses by dowel action after the breakout cracking.

475

10) The main contribution of the stirrups to the connection capacity occurred after the concrete breakout load (i.e. the 35° breakout cone formation).

11) The connection ductility depended on the connection failure mechanism.

12) The concrete crushing load in front of the pile and the connection breakout load increased with the concrete compressive strength.

13) For slender piles, using more bolts in the pile cap connection close to the pile cap cylinder edge may cause plastic hinge at the first bolt location, which would decrease the straining actions transferred to the pile cap itself and may decrease the connection capacity.

9.12.2 Effect of embedment depth

14) For pile embedment depth less than 4.5 times the pile cap's plate width, pryout cracks occurred. As the pile embedment depth increased, the pile cap contribution to the connection capacity decreased.

15) The connection capacity and stiffness after reaching its ultimate load as well as its ductility and its ability to absorb energy increased as the pile embedment depth increased.

9.12.3 Effect of pile cap's plate width

16) The pile cap size mainly affects the connection ultimate load, and the connection failure mechanism. Using a wider pile cap's plate and adequate welding increased the pile shaft fixation and increased the connection pryout resistance.

476

17) Increasing the pile cap's plate width increased the beam ductility and its ability to absorb energy.

18) Increasing the pile cap's plate width could lead to pile cap's welding failure instead of pryout failure.

9.12.4 Effect of longitudinal reinforcement

19) Increasing the longitudinal reinforcement ratio decreased the tensile strains in the concrete and delayed the concrete cracking.

20) Increasing the longitudinal reinforcement ratio increased the connection breakout and ultimate loads.

9.12.5 Effect of transverse reinforcement

21) Increasing the transverse reinforcement ratio did not affect the concrete behaviour before the first breakout cone formation.

22) Increasing the transverse reinforcement ratio decreased the crack width of the breakout cracks and increased the concrete aggregate interlock contribution to the connection ultimate load and increased the connection stiffness after the connection breakout load.

23) Only the stirrups included within a distance equal to (half the beam width x Cot 35°) from both sides of the pile contributed to the connection ultimate load

9.12.6 Effect of cyclic loading

24) The main effect of the alternating cyclic shear loading on the connection behaviour was observed after the first breakout cone formation.

25) Cracks propagated, displacements increased, and steel strains increased with each cycle of the same load.

26) Under alternating cyclic shear loading, the connection ultimate load and its ability to absorb energy decreased because of the concrete strength degradation, and the connection stiffness degradation.

27) A concrete reduction factor of at least 0.75 should be applied to the connection ultimate load calculation for connections subjected to cyclic shear loading.

28) Under alternating cyclic shear loading, the pile shaft experience higher moments and the steel components should be checked for low cycle fatigue failure. Thus, a reduction factor should be applied to the steel components strength limit states.

29) There is a relation between the connection capacity and the loaded span between the supports that needs more study. It was recorded in this study that a small increase in the connection capacity occurred when the span decreased.

30) Under alternating cyclic shear loading, increasing the pile embedment depth increased the connection ultimate load and its ability to absorb and dissipate energy.

31) Increasing the transverse reinforcement had a negligible effect on the connection capacity but it increased its ductility and ability to sustain more displacements.

9.13 References

Abd Elaziz, A.Y. & El Naggar, M.H., 2015. Performance of Hollow Bar Micropiles under Monotonic and Cyclic Lateral Loads. Journal of Geotechnical and Geoenvironmental Engineering, 141(5), pp.1–11.

 ACI 318, 2011. Building Code Requirements for Structural Concrete (ACI 318-11) and Commentary, Farmington Hills, MI: American Concrete Institute.

ACI 349, 2001. ACI 349-01 Code Requirements for Nuclear Safety Related Concrete Structures, Farmington Hills, MI: American Concrete Institute.

Anderson N. S., & M.D.F., 2005. Pryout capacity of cast-in headed stud anchors. PCI journal, 50(2), pp.90–112.

ASTM Standard E2126–11, 2011. Standard Test Methods for Cyclic (Reversed) Load Test for Shear Resistance of Vertical Elements of the Lateral Force Resisting Systems for Buildings, West Conshohocken, PA, USA: American Society of Testing and Materials.

CSA A23.3, 2004. A23. 3-04: design of concrete structures,

Eligehausen, R., Mallée, R. & Silva, J.F., 2013. Anchorage in Concrete Construction, John Wiley & Sons.

Erberik, M.A. & Kurtman, B., 2010. a Detailed Evaluation on Degrading Behavior of Structural. In Proceedings of the 9th US National and 10 th Canadian Conference on Earthquake Engineering, (369), pp.1–10.

Fuchs, W., 1992. Tragverhalten von Befestigungen unter Querlasten in ungerissenem Beton.(Load-bearing behaviour of fastenings under shear loading in non-cracked concrete). In German. Universität Stuttgart.

Klingner, R.E., Mendonca, J. a. & Malik, J.B., 1982. Effect of Reinforcing Details on the Shear Resistance of Anchor Bolts Under Reversed Cyclic Loading. ACI Journal, 79(1), pp.3–12.

Lee, N.H. et al., 2007. Tensile-Headed Anchors with Large Diameter and Deep Embedment in Concrete. ACI Structural Journal, 104(4), pp.479–486.

Randl, N., John, M. & Eligehausen, R., 2001. Shear anchoring in concrete close to the edge. International Symposium on Connections between Steel and Concrete-RILEM Publications SARL, pp.251–260.

Rieder, A. & Strauss, P., 2009. Seismic response of post-installed anchors in concrete. Universität für Bodenkultur Wien.

Swirsky, R., 1977. Lateral resistance of anchor bolts installed in concrete, California.

Usami, S., Abe, U. & Matsuzaki, Y., 1980. Experimental study on the strength of headed anchor bolts under alternate shear load and combined load (shear and axial). In Proceedings of the Annual Meeting of the Kantou Branch of the Architectural Institute of Japan. Tokyo, Japan: Architectural Institute of Japan.

Vintzeleou, E.N. & Tassios, T.P., 1987. Behavior of Dowels Under Cyclic Deformations. ACI Structural Journal, 84(1), pp.18–30.

Vintzelou, E. & Eligehausen., R., 1992. Behaviour of Fasteners Under Monotonic or Cyclic Shear Displacements. ACI Special Publication, 130(7), pp.181–204.

Zhao, G., 1995. Tragverhalten von randfernen kopfbolzenverankerung bei Betonbruch (Behaviour of headed anchors remote to an edge at concrete failure). In German. Universität Stuttgart.

BEHAVIOUR OF HELICAL PILE CONNECTORS FOR NEW FOUNDATIONS SUBJECTED TO SHEAR LOADING: CONNECTION CAPACITY EQUATIUONS AND DESIGN AID

10.1 Introduction

The experimental investigation on the helical pile-new RC foundation connection under shear loading demonstrated that its failure mechanism is similar to that of cast-in place headed anchors. Therefore, previous researches investigating the anchor shear capacity were reviewed to identify suitable equations that can accurately represent the helical pile-grade beam connection. The main limit states governing the overall connection behaviour were discussed, and the equations that can capture each limit state were presented. The applicability of the selected equations was ascertained through the comparison of their predictions with the experimental results under both the monotonic and cyclic loadings. Finally, a procedure was proposed for the design of the helical pile-new RC foundation connection.

List of notations

A_{se}	effective cross-sectional area of anchor; equal to the least cross-section area of the pile shaft
A_{vc}	projected area of the failure surface as shown in Figure 10-3 for the different applicable cases
A_{vo}	projected area for a single anchor in a deep member
b_{pile}	pile shaft diameter or width; 44.45 mm (1.75") in our case
BED	distance from back row of studs to front edge
b_{rem}	the remaining width after the pile width was decreased by the bolt hole
c'	concrete cover
C_{ev3}	coefficient for eccentric shear force
C_{h3}	coefficient for member thickness
C_{vcr}	coefficient for cracking in a member loaded in shear

C_{x3}	coefficient for overall X spacing of a connection with two or more rows
da	anchor diameter
d_{emb}	the pile embedment depth in the reinforced concrete beam
e	load eccentricity from the load location to the concrete surface
fc'	specified cylinder compressive strength of concrete
f_{cc}	cubic compressive strength of concrete
f_{yp}	the pile shaft yield stress
f_{ult}	specified tensile strength of anchor steel or pile shaft steel
$M_{concrete}$	moment sustained by the concrete due to the induced bearing stresses
M_{rsteel}	anchor maximum moment capacity due to flexural at its weakest point
n	number of anchors or pile shafts involved
l	the load-bearing length of the anchor for shear
R	resistance modification factor
S_p	the pile shaft's section modulus at the critical section
V_{br}	factored concrete breakout resistance in shear in cracked concrete
V_{cbr}	factored concrete breakout resistance in shear of a group of anchors or helical piles
$V_{crushing}$	the concrete crushing in front of the pile shaft limit state
V_{co3}	concrete breakout strength for a single stud connection unaffected by connection or member geometry
V_r	factored shear resistance for a single or multiple stud connection or pile connections, accounting for member and connection geometry
V_{sr}	factored resistance in shear of a single anchor or pile shaft
$V_{sr,mu}$	the anchor maximum steel shear capacity due to induced flexural stresses
λ	modification factor reflecting the reduced mechanical properties of lightweight concrete
$\emptyset_c$	resistance factor for concrete
$\psi_{c,v}$	the modification factor for cracked concrete
$\psi_{ed,v}$	the modification factor for edge
$\psi_{h,v}$	the modification factor for anchors located in a concrete member where the concrete element height (ha) $< 1.5ca1$

10.2 The main limit states governing the connection behaviour

The experimental observations demonstrated that the connection was generally intact and could be treated as a fixed connection before the concrete crushing in front of the pile shaft and before the connection breakout load. After concrete crushing in front of the pile shaft, the pile shaft developed a plastic hinge and rotated around it causing reduction in the steel pile capacity and ductile steel failure may take place; however, the beam remained intact as long as the shaft did not fail. On the other hand, when a breakout cone formed, the pile shaft rotated, the connection failed, and the reinforced concrete integrity was compromised. Thus, after the connection breakout failure, the connection can be considered as a hinged connection.

The longitudinal and transverse reinforcements may increase the connection capacity if sufficient concrete cover is provided to sustain the beam integrity. Eligehausen et al. (2013), Petersen & Zhao (2013), Klingner et al. (1982), and Swirsky (1977) indicated that only the anchor reinforcement in direct contact with the anchor will sustain the anchor connection integrity and enhance the system resisting load. The pryout contribution and the welding capacity of the pile cap also influence the connection behaviour and capacity; however, the experimental results showed that they occurred only after the breakout failure when the connection is considered as hinged connection.

Abd Elaziz & El Naggar (2015) demonstrated that the geotechnical capacity of micropiles increases significantly for fixed connection between the micropile and the pile cap compared to a hinged connection. Therefore, it is recommended to design the helical pile-foundation connection as a fixed connection and this research will focus on finding

483

the most suitable equations to represent the three main limit states that control the fixed connection capacity. These limit states are: the concrete crushing in front of the pile shaft, the concrete breakout failure, and the steel failure of the pile shaft. For each limit state, an equation is proposed and its performance is discussed.

10.3 Calculation of the concrete crushing limit state

Vintzeleou & Tassios (1987), Fuchs (1992) and Randl et al. (2001) studied the concrete crushing mechanism and indicated that it is caused by parabolic bearing stresses distributed over a specific length of the anchor (e.g. bolt). Vintzeleou and Tassios (1987) assumed that the concrete compressive stresses in front of the anchor can reach 5 times the compressive strength of concrete as shown in Figure 10-1. As a result, an induced moment is transferred to the bolt and a plastic hinge occurs at a distance (a). Also, Fuchs (1992) reported the results of FE simulations that indicated that the maximum stress was equal to 3.5 times the cubic concrete compression strength (3.5 f_{cc}) and extended up to one half the anchor diameter below the concrete surface. The bearing compressive stress then decreased linearly over a distance up to twice the anchor diameter. Randl et al. (2001) found that the concrete resistance in front of the anchor was affected by the concrete cover distance because the concrete was pushed over the reinforcement. Thus, the reinforcement effectiveness diminished after concrete crushing occurred. They recorded parabolic distribution of the concrete stress, as shown in Figure 10-2, which was similar to that reported by Fuchs (1992) with zero stress at the reinforcement level. The results of the experimental investigation are reported in Chapter 9, the same crushing behavior indicated by Randl et al. (2001) was observed.
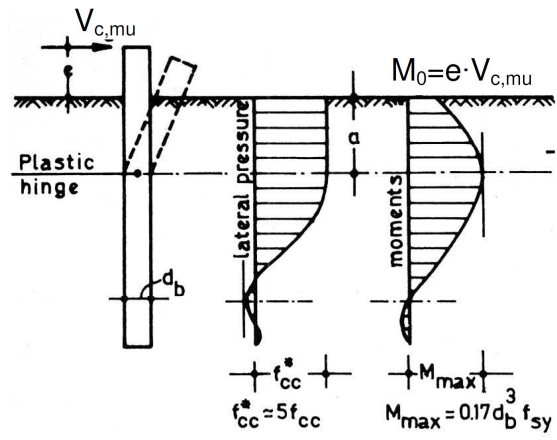
Figure 10-1 Local failure of concrete in front of anchor bar adopted by Vintzeleou & Tassios (1987)
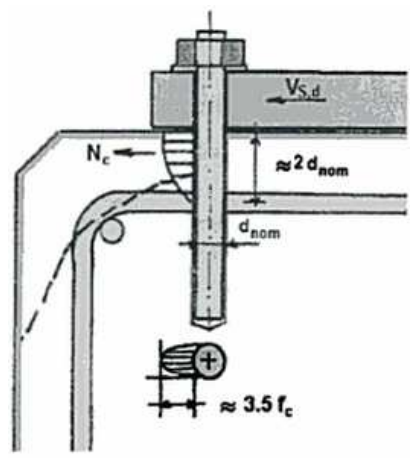
Figure 10-2 Local failure of concrete in front of anchor bar adopted by Randl et al. (2001)

From the above discussion, it may be concluded that the concrete crushing limit state capacity can be calculated as an equivalent uniform stress multiplied by the area of this stress. As the stress distribution is parabolic along the pile diameter and pile length directions, an equivalent uniform stress of 1.83.fc' is proposed. This stress is uniformly distributed on the area dimensioned by the concrete cover and the pile shaft width. Hence, the concrete crushing limit state may be given by:

$$V_{crushing} = 1.83. \emptyset_c\, f_c^{'}.c^{'}.b_{pile} \qquad\qquad \textbf{10.1}$$

where, $\emptyset_c$ will be equal to 1 in the comparison stage with the experimentally recorded data and equal to 0.65 in the design stage.

This equation will be verified later through comparison with the recorded crushing loads from the experimental study.

10.4 Calculation of the concrete breakout limit state

The concrete breakout mechanism of the connection observed in the experimental investigation was approximately the same as that reported in the literature for cast-in - place anchors. For example, the fracture crack of an anchor has an angle of 35° on average with the concrete edge and develops to a depth at the concrete edge of 1.3 to 1.5 times the edge distance (Fuchs et al., 1995). This crack pattern was observed with the helical pile connection. Thus, it is appropriate to employ the equations developed for anchors under shear loading in order to predict the capacity of helical pile connection loaded in shear, after verifying their applicability.

Several equations were developed and used for anchor design. One of the most widely used equations is proposed by ACI 318-11, which is approximately the same as that adopted in CSA 23.3-04. The equation is based on the concrete capacity design (CCD) approach (Fuchs et al., 1995). This equation accounts for the edge distance, size effect, concrete tensile capacity and the distribution of bearing stresses along the anchor length. The equation adopted by the PCI design manual (2004) and the CPCI design manual (2007) is also widely used for design of anchors. It accounts for the edge distance, size effect and concrete tensile capacity, but does not consider the effect of the bearing

stresses along the anchor length. Both equations are presented herein briefly, and for more details and extended conditions reference should be made to (ACI 318, 2011; CPCI, 2007; CSA A23.3, 2004; PCI, 2004).

10.4.1 CSA 23.3-04 and ACI 318-11 concrete breakout calculation

The factored concrete breakout resistance of an anchor subjected to shear loading can be calculated by:

$$V_{cbr} = \frac{A_{vc}}{A_{vo}} \cdot \psi_{ed,v} \cdot \psi_{c,v} \cdot \psi_{h,v} \cdot V_{br} \qquad\qquad \textbf{10.2}$$

Where:

A_{vc} projected area of the failure surface as shown in Figure 10-3 for the different applicable cases

A_{vo} projected area for a single anchor in a deep member and it is equal to $A_{vo} = 4.5 \, c_{a1}^{1.5}$; thus, $\frac{A_{vc}}{A_{vo}} = 1$ for the connection under consideration

c_{a1} The distance from the edge to the anchor axis, equal to half the grade beam width

$\psi_{ed,v}$ The modification factor for edge; equal to 1.0 for the tested specimens

$\psi_{c,v}$ The modification factor for cracked concrete; equal to 1.2 in case of using longitudinal reinforcement bar diameter of 15M or more, and equal to 1.4 in

case of longitudinal bars $\geq 15M$ and stirrups spacing $\leq 100mm$.

$\psi_{h,v}$ The modification factor for anchors located in a concrete member where the concrete element height $(h_a) < 1.5c_{a1}$; equal to 1.0 for the tested specimens

V_{br} The basic concrete breakout strength value for a single anchor, given by:

$$V_{br} = \left(0.58\left(\frac{l}{d_a}\right)^{0.2}\sqrt{d_a}\right)\emptyset_c\sqrt{fc'}(c_{a1})^{1.5}.R \qquad \textbf{10.3}$$

where;

l The load-bearing length of the anchor for shear; $l = d_{emb}$ (anchor embedded depth) for anchors with a constant stiffness over the full length of embedded section and should not exceed 8.da

d_a Anchor diameter; for the tested pile shaft $=44.45$ mm

R the resistance modification factor; for concrete failure in shear, it is equal to 1 where no supplement reinforcement was provided, and equal to 1.15 in case of the potential concrete failure surface are crossed by supplementary reinforcement proportioned to tie the potential concrete failure prism into the structural member

$\emptyset_c$ The concrete material resistance; equal to 1 for the comparison with the experimental results, and equal to 0.65 for the design stage.

(a) If h<1.5cl   (b) If c2 <1.5cl
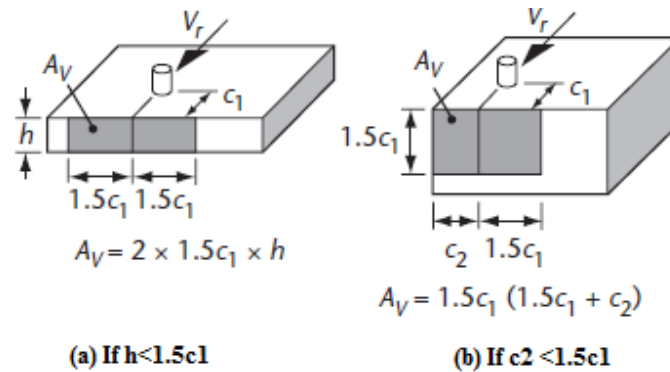
Figure 10-3 Projected areas for single anchor in different cases adopted by CSA 23.3-04

Considering the relevant variables of the helical pile connection, Equation 10.3 is revised to reflect the helical pile connection parameters as follows:

$$V_{br} = \left(0.58 \left(\frac{d_{emb}}{b_{pile}}\right)^{0.2} \sqrt{b_{pile}}\right) \emptyset_c \sqrt{fc'}(c_{a1})^{1.5}. R \ , \ \frac{d_{emb}}{b_{pile}} \leq 8 \qquad \textbf{10. 4}$$

Equation 10.4 can be used in equation 10.2 to account for the different factors discussed before.

10.4.2 CPCI and PCI design manual concrete breakout calculation

The factored concrete breakout resistance of an anchor in shear can be given by

$$V_r = \phi. V_{co3}. C_{x3}. C_{h3}. C_{ev3}. C_{vcr} \qquad \textbf{10. 5}$$

Where;

V_r factored shear resistance for a single or multiple stud connection or pile shafts, accounting for member and connection geometry

489

ϕ   concrete strength reduction factor; will be equal to 1 in the comparison, while it will be equal to 0.65 in the design stage

C_{x3} coefficient for overall X spacing of a connection with two or more rows; equal to 1

C_{h3} coefficient for member thickness; equal to 1

C_{ev3} coefficient for eccentric shear force; equal to 1

C_{vcr} coefficient for cracking in a member loaded in shear; equal to 0.85 when edge reinforcement greater than or equal to 15M bar was used, and equal to 1 if a stirrups with spacing less than or equal to 100mm provided with edge reinforcement.

V_{co3} concrete breakout strength for a single stud connection unaffected by connection or member geometry

$$V_{co3} = 11.5\,\lambda\sqrt{fc'}\,(BED)^{1.33} \qquad \textbf{10. 6}$$

where;

λ   Light weight concrete factor; equal to 1

BED   Distance from back row of studs to front edge, equal to c_{a1} in case of one pile shaft.

Considering the relevant variables of the helical pile connection, Equation 10.6 is revised to reflect the helical pile connection parameters as follows:

$$V_{co3} = 11.5\,\lambda\sqrt{fc'}(c_{a1})^{1.33} \qquad\qquad \textbf{10. 7}$$

The basic breakout shear capacity for the studied helical pile connection can be calculated using Equation 10.7. Equation 10.7 can be used in Equation 10.5 to account for the different factors discussed before.

10.5 The steel failure limit state calculation

Two main conditions govern the pile shaft steel failure. First, the steel pile shaft shear failure may occur if no breakout cracking or concrete crushing existed at the steel pile shear capacity. Second, the pile shaft strength will decrease markedly due to the effect of the induced moments in the pile shaft if concrete crushing or concrete breakout existed before the shear failure of the pile shaft.

For the first condition, the equation proposed by the ACI318-11, CSA 23.3-04, PCI-6th edition, and the CPCI-4th edition will be adopted herein to calculate the steel shear strength, i.e.

$$V_{sr} = n.A_{se}\,.\,\emptyset_s.0.6\,.\,f_{ult}\,.R \qquad\qquad \textbf{10. 8}$$

where;

$\qquad V_{sr}$ $\qquad$ Factored resistance in shear of a single or multiple anchor connection or

n number of anchors or pile shafts involved; equal to 1.

$\emptyset_s$ steel material resistance factor for reinforcement; equal to 1 for comparison with recorded values; equal to 0.9 for design.

f_{ult} specified tensile strength of anchor steel or pile shaft steel

A_{se} effective cross-sectional area of anchor; equal to the least cross-section area of the pile shaft.

R resistance modification factor; equal to 0.75 for ductile steel shear failure

Fuchs (1992) developed an equation that can be used for the second condition. It calculates the shear at which the anchor shaft will fail under flexure when it rotates around a point (i.e. plastic hinge) embedded in the concrete at twice the anchor diameter, i.e.

$$M_{rsteel} = V_{sr,mu}\,(2.\,d_a + e) - M_{concrete} \qquad\qquad \textbf{10. 9}$$

where;

M_{rsteel} anchor maximum moment capacity due to flexural at its weakest point; for the studied connection, it is at the bolts' hole location.

$V_{sr,mu}$ the anchor maximum steel shear capacity due to induced flexural stresses

e   load eccentricity from the load location to the concrete surface

$M_{concrete}$ moment sustained by the concrete due to the induced bearing stresses shown in Figure 10-3. Fuchs (1992) reported that this moment is equal to

$$M_{concrete} = (1.26).\left(3.5f_{cc}\right).d_a^3 \cong (5.2) . fc'.d_a^3$$

Equation 10.9 was also found to be suitable for calculating the steel helical pile shaft capacity as will be discussed later. Incorporating the specific parameters of the helical pile connection into Equation 10.9, the following equation is developed:

$$V_{sr,mu} = \frac{S_p . f_{yp} + (5.2). fc'.b_{pile}^3}{(2.b_{pile}+e)} \qquad \qquad \textbf{10. 10}$$

where,

S_p The pile shaft's section modulus at the critical section (at the bolt's hole location)

f_{yp} The pile shaft yield stress.

For the case where a bolt hole exists exactly at the concrete surface (e.g. beam S3 in the experimental testing program reported in Chapter 9), the moment sustained by the concrete decreases because of the reduced bearing area at the maximum bearing stresses location. The shear load in this case would be less than the loads predicted using Equation 10.10. In this case, the moment sustained by the concrete should be $M_{concrete} =$

$\left(2.7 b_{pile}{}^2 . b_{rem} + 1.737\ b_{pile}{}^3\right) . fc'$, where b_{rem} is the remaining width after the pile width was decreased by the bolt hole.

10.6 Verification of proposed limit state equations for monotonic shear loading of helical pile connection

The proposed equations of the concrete crushing load (Equation 10.1), the breakout cone failure load of the CSA 23.3-04 (Equation 10.2), the breakout failure load of the CPCI design manual (Equation 10.5), the steel pile shear failure load adopted by CSA 23.3-04 (Equation 10.8), and the steel pile shear capacity due to the induced moments (Fuchs, 1992) (Equation 10.10) are used to calculate these limit states and the results are presented in table 10-1. The recorded experimental results for concrete crushing load, breakout load, and ultimate load are also shown in table 10-1. The calculated values are presented in table 10-2 as percentage of the experimental values, along with the percentage average, standard deviation and coefficient of variation. The steel pile shear capacity due to the induced moments was only calculated for the beams that failed in the pile shaft.

From tables 10-1 and 10-2, the calculated values using Equation 10.1 achieved 107.2% mean value, 12.85% standard deviation and 12% coefficient of variation compared to the experimental results. These results indicate the suitability of the Equation 10.1 for calculating the concrete crushing load in front of the pile shaft in the studied connection. In addition, it was found that Equations 10.2 and 10.5 provide conservative predictions of the breakout failure load of the studied helical pile connection. For instance, the breakout loads predicted by Equation 10.2 achieved 88.4% mean value, 7.9% standard deviation

and 8.9% coefficient of variation compared to the experimental results, while Equation 10.5 recorded only 55% mean value, 3.33% standard deviation and 6% coefficient of variation. Therefore, Equation 10.2 (CSA 23.3-04/ ACI318-11) rather than Equation 10.5 (CPCI/ PCI) is recommended for the design of the helical pile connection.

The CCD method provides an equation based on the average value from test results on anchors unlike the CSA 23.3-04/ ACI 318-11 or the CPCI/PCI equations, which are based on the 5% fractile value. It was found that the equation proposed by Fuchs et al. (1995) overestimated the connection breakout capacity as the percentage mean value was found to be 125% of the experimentally recorded values.

In conclusion, it is proposed to use Equation 10.2 (adopted by CSA A23.3-04 and ACI318-11 codes) to calculate the breakout failure limit state of the helical pile connection.

Equations 10.8 and 10.10 were used to calculate the steel failure load of the anchors. The results of Equation 10.8 listed in tables 10-1 and 10-2 indicate that no shear failure occurred in the pile shafts before the lesser of concrete breakout load and concrete crushing load was reached. Even though 4 specimens failed during the experimental program in steel failure (beams S3, S7, S8, and S9) as described in Chapter 9, Equation 10.8 predicted much higher shear capacity for their helical piles. This means that after reaching either the concrete crushing load or the concrete breakout load, the pile shaft shear strength should not be calculated using Equation 10.8 because the induced flexural stresses in the pile shaft would cause a premature steel failure in the anchor which would

be less than the predictions of Equation 10.8. On the other hand, Equation 10.10 predicted the shear force at which these pile shafts had failed with high accuracy (102% mean value, 1.7% standard deviation and 1.67% coefficient of variation). Therefore, Equation 10.10 is recommended for predicting the steel failure of the studied helical pile connection and must be used when the calculated concrete crushing load or the concrete breakout load were less than the helical pile shear load calculated by Equation 10.8. It should be mentioned that Equation 10.10 is particularly applicable in case of large edge distance exists as the failure will be governed by the pile shaft failure mechanism after the concrete crushing load is reached.

In conclusion, the flow chart shown in figure 10-4 can be used for the fixed helical pile-reinforced concrete grade beam connection design implementing all the discussed limit states and using the proposed equations.

Table 10-1 Comparison of calculated and measured limit states of the specimens subjected to monotonic shear loading

Specimen	Experimentally recorded values			Calculated values using the proposed equations				
	$V_{crushing}$ (kN)	V_{cbr} (kN)	V_u (kN)	$V_{crushing}$ Eq. 10.1 (kN)	V_{cbr} (CSA23.3) Eq. 10.2 (kN)	V_r (CPCI) Eq. 10.5 (kN)	V_{sr} Eq. 10.8 (kN)	$V_{sr,mu}$ Eq. 10.10 (kN)
S1	120	137.48	162.39	122.02	128.47	83	**229**	190.49
S2	125	145.03	151.40	122.02	136.13	83	**229**	190.49
S3	130	------	136.83	122.02	-------	83	**229**	138.64
S4	110	148.40	176.00	122.02	128.47	83	**229**	190.49
S5	97	145.40	160.10	122.02	128.47	83	**229**	190.49
S6	95	157.80	164.20	122.02	128.47	83	**229**	190.49
S7	150	183.50	183.50	162.69	148.35	96	**229**	190.49
S8	175	185.20	185.20	162.69	148.35	96	**229**	190.49
S9	155	190.60	190.60	162.69	195.57	112	**229**	190.49

Table 10-2 Comparison of calculated and measured connection limit states under monotonic shear loading: statistical evaluation

Specimen	Experimentally recorded values			(Calculated /Recorded) %				
	$V_{crushing}$ (kN)	V_{cbr} (kN)	V_u (kN)	$V_{crushing}$ Eq. 10.1 (kN)	V_{cbr} (CSA23.3) Eq. 10.2 (kN)	V_r (CPCI) Eq. 10.5 (kN)	V_{sr} Eq. 10.8 (kN)	$V_{sr,mu}$ Eq. 10.10 (kN)
S1	120	137.48	162.39	101.68	93.45	60	141.26	-----
S2	125	145.03	151.40	97.61	93.86	57	151.51	-----
S3	130	------	136.83	93.86	-------	52	167.65	101.32
S4	110	148.40	176.00	110.92	86.57	56	130.34	-----
S5	97	145.40	160.10	125.79	88.36	57	143.28	-----
S6	95	157.80	164.20	128.44	81.41	52	139.70	-----
S7	150	183.50	183.50	108.46	80.84	52	125.01	103.81
S8	175	185.20	185.20	92.96	80.10	52	123.86	102.86
S9	155	190.60	190.60	104.96	102.61	59	120.35	99.94
Average %				107.19	88.40	55.21	138.11	101.98
Standard deviation%				12.85	7.89	3.33	15.17	1.70
Coefficient of variation%				11.98	8.92	6.02	10.99	1.67

10.7 Verification of proposed limit state equations for cyclic shear loading

The experimental results showed that the specimens subjected to cyclic shear loading experienced degradation of concrete strength, and excessive concrete crushing in front of the pile shaft and large deformations were recorded. The maximum reduction in the connection ultimate load due to cyclic loading, as opposed to monotonic loading, was equal to 25% (beam CS1 vs. beam S1). Therefore, it is important to introduce a reduction factor to be applied to the connection capacity in order to account for the cyclic loading effects. Vintzeleou & Tassios (1987) proposed a reduction factor of 0.5 for dowels under cyclic loading, while Pallarés & Hajjar (2010) proposed a reduction factor of 0.75 for the design of anchors subjected to seismic loading. CSA 23.3-04 and ACI 318-11 codes and

CPCI manual propose a reduction factor of 0.75 for both steel and concrete in case of seismic loading.

Thus, a reduction factor equal to 0.75 is proposed to be applied to Equations 10.1, 10.2, 10.8, and 10.10 to account for cyclic loading (e.g. seismic loading). Tables 10-3 and 10-4 compare the measured connection limit states under cyclic shear loading (reported in Chapter 9) and the calculated limit states using the proposed equations employing a reduction factor of 0.75.

Tables 10-3 and 10-4 show that the percentage mean value of the breakout failure load was only 80%. These results demonstrate that the ACI318-11 and CSA 23.3-04 equations provide reasonable, but conservative, prediction of the breakout cone failure load, and therefore can be used for the design of the helical pile connection. Additionally, the concrete bearing resistance as well as steel shear resistance were predicted reasonably well with an adequate design margin of safety.

Based on the above discussion, the recommended equations are shown to be applicable for the design of helical pile-grade beam connections under alternating cyclic shear loading by using a reduction factor equal to 0.75.

Table 10-3 Comparison of calculated and measured limit states of specimens subjected to cyclic shear

Specimen	Experimentally recorded values			Calculated values using the proposed equations			
	$V_{crushing}$ (kN)	V_{cbr} (kN)	V_u (kN)	$V_{crushing}$ Eq. 10.1 (kN)	V_{cbr} (CSA23.3) Eq. 10.2 (kN)	V_{sr} Eq. 10.8 (kN)	$V_{sr,mu}$ Eq. 10.10 (kN)
CS1	100	146.00	146.00	91.51	96.35	172.04	142.87
CS2	100	121.50	121.50	91.51	102.09	172.04	142.87
CS3	100	145.30	148.70	91.51	129.28	172.04	142.87

Table 10-4 Comparison of calculated and measured connection limit states under cyclic shear loading: statistical evaluation

Specimen	Experimentally recorded values			(Calculated /Recorded) %			
	$V_{crushing}$ (kN)	V_{cbr} (kN)	V_u (kN)	$V_{crushing}$ Eq. 10.1 %	V_{cbr} (CSA23.3) Eq. 10.2 %	V_{sr} Eq. 10.8 %	$V_{sr,mu}$ Eq. 10.10 %
CS1	100.00	146.00	146.00	91.51	66.00	117.84	97.86
CS2	100.00	121.50	121.50	91.51	84.03	141.60	117.59
CS3	100.00	145.30	148.70	91.51	88.97	115.70	96.08
Average %				91.51	80	125.04	103.84
Standard deviation%				0.00	12.09	14.38	11.94
Coefficient of variation%				0.00	15.18	11.50	11.50

10.8 The expected failure mechanism, its corresponding load, connection ultimate load, and connection ductility enhancement

From previous discussion, in order to know the type of the expected failure mechanism, and its corresponding failure load, a flow chart was created and demonstrated in Figure 10-4. In this research, most of the tested helical pile connection did not sustain much load after the connection breakout load. Thus, it is hard to recommend a design equation that

will expect the hinged connection ultimate load and further experimental studies should be conducted to provide this design equation.

On the other hand, design recommendation to enhance the beam ductility and increase its shear strength in case of a brittle failure can be given according to the observed behaviour of the cast-in-place headed anchors ,which had a similar behaviour, and the experimentally tested beams with higher connection ultimate load than their breakout load.

As concluded from the experimental program, the ultimate load capacity after the connection breakout cone will mainly depend on the contributions from the stirrups, longitudinal reinforcement dowel action, the aggregate interlock, and the concrete pryout at the pile cap. Furthermore, lots of researches were conducted on anchor connections having hairpin reinforcement and stirrups reinforcement and it was found that hairpin reinforcement is mainly effective when it is in direct contact with the anchor shaft (Eligehausen et al., 2013; Klingner et al., 1982; Swirsky, 1977). In this case the connection ultimate load and ductility increased excessively. From the conducted experimental program and from different investigations, the stirrups effect is totally decreased with the increase of the concrete cover and its effect increases by the spacing reduction (Swirsky, 1977). Therefore, if stirrups will be used to increase the studied connection ultimate load and to enhance its ductility, these stirrups should have the least concrete cover and the least stirrups spacing. ACI318-11 indicated that only the reinforcement spaced less than the lesser of $0.5c_{a1}$ from the anchor center line from each

side should be included as anchor reinforcement. Recently, several investigations were conducted to calculate the anchor reinforcement contribution to the anchor shear capacity and most of them proposed strut-and-tie models to calculate the anchor's connection ultimate load.

From the experimental study, the international codes recommendations, and the previous researches in the literature, a concrete breakout cone failure mechanism is a brittle failure mechanism that is recommend to be avoided if possible and to be prevented in case of seismic loadings. Thus, special design requirement will be proposed in the flow chart presented in figure 10-4 to enhance the connection ductility in case of breakout failure is expected.

In conclusion, the studied helical pile- RC grade beam connection will be designed as a fixed connection using the flow chart indicated in figure 10-4 and in case of a breakout failure mechanism will take place, three recommendations based upon the experimental program findings and previous investigations on the headed anchors will be presented to enhance the studied helical pile connection ductility and increase its ultimate load to be more than or equal to the steel pile capacity.

Calculate the concrete crushing load ($V_{crushing}$) using Equation 9.1

Calculate the concrete breakout load (V_{cbr}) using Equation 9.2

Calculate the helical pile steel shear failure load (V_{sr}) using Equation 9.8

Is $V_{sr} > V_{crushing}$ & $V_{sr} > V_{cbr}$?

No

yes

Ductile Steel failure mechanism $V_u = V_{sr}$

Calculate the helical pile steel failure load ($V_{sr.mu}$) using Equation 9.10

Is $V_{sr,mu} > V_{cbr}$?

No

yes

Ductile Steel failure mechanism $V_u = V_{sr,mu}$

Brittle Concrete breakout cone failure $V_u = V_{cbr}$

The connection ductility must be enhanced or the concrete ultimate load should be increased

Add hairpin reinforcement in contact with the pile shaft and as close as possible to the concrete surface. This hairpin reinforcement should have a tensile capacity $\geq V_{sr,mu}$ (Eligehausen et al., 2013; Klingner et al., 1982; Swirsky, 1977)

Add more stirrups with the least concrete cover and with spacing less than 100 mm. The stirrups included with in a distance of $0.5c_{a1}$ from the two sides of the pile shaft should have a tensile capacity $\geq V_{sr,mu}$, and edge reinforcement must be provided (ACI 318, 2011)

Design the pile cap welding to resist a moment not less than the multiply of $V_{sr,mu}$ by the max. of concrete cover and double the pile shaft width. and use welded stiffeners between the pile cap's plate and the pile cap's cylinder to increase the pryout contribution to the connection ultimate load

Figure 10-4 Flow chart for the fixed helical pile-RC grade beam connection design procedure

10.9 Conclusions

The shear capacity of new construction pile bracket used to connect slender shaft piles (e.g. helical piles and micropiles) to grade beams in new construction was investigated. The results from the experimental program and information collected from the literature on cast-in-pace headed anchors were used to evaluate the performance of the studied connection and to propose equations for its design. The performance of the proposed equations was verified through comparing their predictions with the experimental observations. These equations were incorporated in a design procedure that can be used for the design of the helical pile connection for new construction. The following conclusions may be drawn.

1) Equation 10.1 can be used to calculate the concrete crushing load in front of the pile shaft for the considered connection. It predicted the concrete crushing load with percentage mean value of 107% compared to experimental results and with 12.8% COV.

2) The equations recommended by the ACI 318-11 and CSA 23.3-04 codes for cast-in -place headed anchors design can be employed for calculating the connection breakout load with adequate margin of safety. Therefore, it is recommended to use Equation 10.4 to calculate the single helical pile connection breakout load.

3) The equations proposed to calculate the concrete breakout load for anchors in the ACI 318-11 and CSA 23.3-04 codes expect the helical pile-RC grade beam

connection breakout load capacity more accurately than those recommended by the PCI and CPCI design manuals.

4) The equations recommended by the ACI 318-11 and CSA 23.3-04 codes for design of cast-in -place headed anchors (i.e. Equation 10.8) predicted the pile shaft steel failure under shear loading accurately only if the shear capacity of the steel pile was less than the connection breakout load calculated by Equation 10.2, and the concrete crushing load calculated by Equation 10.1. Otherwise, the shear capacity of the steel pile should be calculated using Equation 10.10. This equation predicted the steel failure load with 102% mean value and with 1.7% COV.

5) If the connection will be subjected to cyclic shear loading, a reduction factor of 0.75 should be applied to the proposed design equations.

6) The flow chart presented in figure 10-4 provides a detailed design procedure that can be used to calculate the fixed connection capacity and to ensure its ductile failure.

10.10 References

Abd Elaziz, A.Y. & El Naggar, M.H., 2015. Performance of Hollow Bar Micropiles under Monotonic and Cyclic Lateral Loads. Journal of Geotechnical and Geoenvironmental Engineering, 141(5), pp.1–11.

ACI 318, 2011. Building Code Requirements for Structural Concrete (ACI 318-11) and Commentary, Farmington Hills, MI: American Concrete Institute.

CPCI, 2007. Canadian Precast and prestressed Concrete Design Manual 4- Edition., Ottawa, ON: Canadian Precast/Prestressed Concrete Institute.

CSA A23.3, 2004. A23. 3-04: design of concrete structures,

Eligehausen, R., Mallée, R. & Silva, J.F., 2013. Anchorage in Concrete Construction, John Wiley & Sons.

Fuchs, W., 1992. Tragverhalten von Befestigungen unter Querlasten in ungerissenem Beton.(Load-bearing behaviour of fastenings under shear loading in non-cracked concrete). In German. Universität Stuttgart.

Fuchs, W., Eligehausen, R. & Breen, J.E., 1995. Concrete Capacity Design (CCD) Approach for Fastening to Concrete. ACI Structural Journal, 92(1), pp.73–94.

Klingner, R.E., Mendonca, J. a. & Malik, J.B., 1982. Effect of Reinforcing Details on the Shear Resistance of Anchor Bolts Under Reversed Cyclic Loading. ACI Journal, 79(1), pp.3–12.

Pallarés, L. & Hajjar, J., 2010. Headed steel stud anchors in composite structures, Part I: Shear. Journal of Constructional Steel Research, 66(2), pp.198–212.

PCI, 2004. PCI Design Handbook: Precast and Prestressed Concrete 6th-Edition ed., Chicago, Ill.

Petersen, D. & Zhao, J., 2013. Design of Anchor Reinforcement for Seismic Shear Loads. ACI Structural Journal, 110(1), pp.53–62.

Randl, N., John, M. & Eligehausen, R., 2001. Shear anchoring in concrete close to the edge. International Symposium on Connections between Steel and Concrete-RILEM Publications SARL, pp.251–260.

Swirsky, R., 1977. Lateral resistance of anchor bolts installed in concrete, California.

Vintzeleou, E.N. & Tassios, T.P., 1987. Behavior of Dowels Under Cyclic Deformations. ACI Structural Journal, 84(1), pp.18–30.

SUMMARY, CONCLUSIONS AND RECOMMENDATIONS

11.1 Introduction

This chapter provides a brief summary of the experimental and numerical studies conducted to evaluate the performance of the connections between slender shaft piles and new reinforced concrete foundations subjected to different loading conditions. The main findings and conclusions drawn from the investigations are presented. Finally, some recommendations for future research are suggested.

11.2 Summary

This thesis is dedicated to investigate the behaviour of the connections between slender pile types, which end with a mono steel bar at the ground level (e.g. helical piles and micro piles) and new reinforced concrete foundations with limited width such as grade beams. The research methodology involved conducting 33 load tests on full-scale pile-foundation connection models subjected to tension, compression, or shear loading in order to clearly understand the behaviour of the connection and its failure mechanism under different loading conditions. This experimental program was focused on four main factors that affect the connection behaviour. These main factors are: the pile embedment depth into the reinforced concrete grade beam; the size of the pile cap's plate; the longitudinal reinforcement of the grade beam; and the transverse reinforcements of the grade beam. The experimental results were used to calibrate and verify three-dimensional nonlinear finite element models that accurately simulated the structural behaviour and

capture the possible failure modes of the connection. The verified finite element models were then used to conduct comprehensive parametric studies that covered the range of connection parameters used in practice. The parametric studies were also extended to investigate additional connection configurations and parameters, including: pile and pile cap parameters; RC concrete beam parameters; and pile-beam connection parameters. The pile and pile cap parameters included: pile shaft embedment depth; pile cap plate size; and pile cap configuration (bolted or welded and the number of used bolts). The RC concrete beam parameters included: longitudinal reinforcement ratio, transverse reinforcement ratio and configuration, anchor reinforcement, concrete strength, shear span/depth ratio (i.e. a/d ratio) and beam height and width. The pile-beam connection parameters included: position of the pile shaft in respect to supports location, support detail (tensile anchor supports or bearing supports on the same side of the beam), corner effect and supports direction (one way or two way supports).

The results of the experimental and numerical studies were used to define the connection performance characteristics under different loading conditions, and to develop analytical equations and design recommendations for the implementation of the connection in foundation design.

11.3 Conclusions

The general findings from the study of all loading conditions will be indicated, followed by the general findings related to the tension and compression loading cases because of their similar behaviour. Finally, the main conclusions pertinent to the specific loading cases will be summarized.

507

11.3.1 General conclusions for tension, compression, and shear loadings

- The connection capacity must be considered explicitly in the foundation design, along with the evaluation of the grade beam capacity.

- The connection behaviour under tension and compression loadings can be presented by the behaviour of the reinforced concrete beams subjected to indirect loading and failing in shear mechanism, while the connection behaviour under shear loading can be presented by the behaviour of the cast-in-place headed anchors subjected to shear loading.

- Cyclic compression loading has limited effect on the connection behaviour, while cyclic shear loading has a major effect on the connection behaviour.

- The connection can be considered fixed (i.e. fixed pile head) up to the breakout cracking load. Afterwards, the connection becomes hinged and its stiffness and capacity depend on the longitudinal and transverse reinforcements.

- The calibrated finite element models developed in this study can accurately predict the behaviour of the pile-new reinforced concrete foundation connection, and are recommended to be used for its detailed design and analysis.

- The first flexural cracking, breakout cracking and ultimate loads as well as the absorbed energy up to the connection failure increase by increasing the longitudinal reinforcement ratio.

- The transverse reinforcement ratio has no effect on the first flexural cracking or breakout cracking loads, but affects the connection ultimate load. Only the

transverse reinforcement contained in the breakout cone can add to the connection capacity.

- The configuration of the transverse reinforcement can change the load transfer mechanism. Higher connection capacity can be achieved by placing higher percentage of transverse reinforcement closer to the pile shaft.

- Placing transverse reinforcement closer to the pile shaft can reduce the breakout crack width, which maximizes the contributions of the concrete aggregate interlock and the longitudinal reinforcement dowel action.

- The connection's first flexural cracking, breakout cracking and ultimate loads increase by increasing the concrete compressive strength.

11.3.2 General conclusions pertinent to tension and compression loading

- Increasing the pile cap-plate size increases the breakout cone size and enhances the connection ductility and its ability to absorb energy.

- Adequate transverse reinforcement can alter the connection failure mechanism from brittle to ductile, as it enhances the connection ability to absorb energy and the beam ductility.

- The connection ultimate capacity is the larger of the ultimate concrete load and the vertical tensile strength of the used transverse reinforcement within the breakout cone.

- As the anchor reinforcement tensile strength increases, the breakout cracking load will slightly increase and the ultimate load will significantly increase.

- Minimum transverse reinforcement is mandatory at the connection location even if there is no transverse reinforcement in the beam. It is recommended to use transverse reinforcement or anchor reinforcement that can sustain the beam shear strength from the two sides of the pile shaft at the pile location.

- Decreasing the shear span to depth ratio (a/d) under 2.5 will increase the connection capacity significantly.

- Increasing the beam height while maintaining the pile embedment depth and the shear span constant leads to increased connection capacity if stirrups are present.

- For connections shifted from the beam mid-span, its capacity should be the sum of shear strengths of the two sides using (a/d) representing each side; however, it is recommended to conservatively use twice the shear capacity of the side with higher (a/d) ratio as the connection shear capacity. Additionally, the connection capacity should be compared with the beam shear capacity considering the lower (a/d) ratio multiplied by $\left(\frac{\text{Span}}{\text{long shear span}}\right)$.

- The corner connection would have lower stiffness and slightly lower capacity than the connection along a beam span.

- The pile connection can sustain higher breakout cracking load if the foundation was supported in two perpendicular directions.

11.3.3 Conclusions pertinent to tension loading

- Connection breakout cracking initiates from the pile cap's plate and extends with a 35$^{\text{o}}$ angle given that the distance to the support is more than three times the pile embedment depth, and the pile cap plate will not yield during loading.

510

- The dimension of the breakout cone can be approximated by the lesser of (b_{plate} +2.5 d_{emb}) or (3 d_{emb}).

- The pile shaft transfers the load to the concrete primarily through the pile cap plate.

- An increase in the pile cap embedment depth increases the breakout cracking and ultimate loads of the connection almost linearly and increases the size of the breakout cone. It also increases the connection stiffness after the first flexural cracking load and enhances the connection's ability to absorb energy before failure.

- Welded and bolted pile cap connections have the same performance and capacity.

- Using tension anchor support has negligible effect on the connection capacity for (a/d) > 1, but it decreases the connection capacity for a/d<1 if compared with the connection in beams with bearing supports.

- Two equations are proposed to calculate the breakout cracking load of the helical pile connection. The first equation (recommended for design) is a modification of the equation proposed by Al-zoubi (2011). It predicted the breakout cracking load with almost 100% mean value and 9.5% COV. The second equation is a modification of the SMCFT to calculate the cracked concrete shear resistance. It predicted the breakout cracking load with 89% mean value and 10% COV.

- Four different limit states should be considered to calculate the pile-connection ultimate capacity. These limit states are: the concrete ultimate strength, the transverse reinforcement ultimate strength, twice the beam shear strength at the

511

pile location, and the crushing of support region strength when (a/d)< 1. This approach predicted the connection ultimate load with 104% mean value and 9% COV.

11.3.4 Conclusions pertinent to compression loading

- Connection breakout cracking initiated from the highest bolt level in case of bolted connection and from the plate level in case of welded connection and unbolted connection. Therefore, the connection capacity should be calculated considering the highest bolt depth for bolted connection and the remaining depth for welded connection.

- The pile shaft transfers the load primarily up to the breakout cracking through the bolt bearing on concrete, pile cap plate bearing on concrete, and the pile-concrete friction. The stirrups resist part of the load only after breakout cracking occurs.

- An increase in the pile cap remaining depth (i.e. reduction in pile embedment depth), increases the connection stiffness throughout loading, the size of the breakout cone, and the absorbed energy up to failure.

- Increasing the size of the pile cap plate increases the size of the breakout cone and slightly enhances the connection ability to absorb energy.

- Using more bolts to connect the pile shaft to the pile cap can increase the connection breakout cracking and ultimate loads.

- Crack propagation was similar to single shear cracking for concrete for member width (b) less than $\left(2\sqrt{2}d_{rem} + b_{plate}\right)$ and $2\sqrt{2}d_{bolt}$. For larger b, cracks

become similar to punching shear cracks. Thus, the connection breakout cracking load increases as the beam width increases up to this specific width.

- During cyclic loading, the connection behaves in a linear elastic manner until first flexural cracking initiation. After the first flexural cracking initiation, the connection behaviour becomes nonlinear inelastic characterized by concrete deterioration and residual deformations.

- Longitudinal and transverse reinforcements can decrease the effect of the concrete deterioration on the connection capacity due to cyclic loading, especially if they do not yield before the connection ultimate load is reached. If the reinforcement yields first, the connection ultimate load is expected to decrease due to cyclic loading.

- The concrete deterioration under compression cyclic loading is more pronounced for connections with larger remaining depth.

- The dissipated energy during cyclic loading increases as the remaining depth increases.

- The transverse reinforcement can increase the dissipated energy during cyclic loading, which enhances the connection structural damping.

- Two equations are proposed to calculate the breakout cracking load of the pile connection. The first equation is a modification to Al-zoubi's equation (2011) and it predicted the breakout cracking load with almost 101% mean value with 5% COV. The second one is a modification of the cracked concrete shear resistance

equation of the SMCFT. It predicted the breakout cracking load with 90.2% mean value and 4.4% COV.

- Four different limit states should be considered to calculate the pile-connection ultimate capacity. These limit states are: the concrete ultimate strength using the modified SMCFT equation, the transverse reinforcement ultimate strength, the beam shear strength at the pile location, and the crushing of support region strength when (a/d) is less than 1. This recommended approach predicted the connection ultimate load for the experimentally tested beams with 98.7% mean value and 5.7% COV. For hinged connection design using limit state design approach, the least value from the four indicated limit states shall be used in the ultimate limit state design.

- For connections with bolts shorter than half the width of the pile cap plate, the remaining depth (d_{rem}) should be used instead of the highest bolt depth (d_{bolt}).

- In case of cyclic compression load is expected as a case of loading on the helical pile- RC grade beam connection, it is recommended to use a reduction factor of at least 0.85.

11.3.5 Conclusions pertinent to shear loading

- The behaviour of the connection is different from the behaviour of the beam directly loaded on its side. The connection capacity is less than the capacity of directly loaded beam.

- Under monotonic loading, two breakout cones initiate from the pile shaft corners at two different angles (20° and 35°). The 35° breakout cone affects the

514

connection behaviour as the pile shaft rotates after its formation, and its corresponding load represents the connection breakout load.

- The breakout cracks are close to the breakout cracks reported in ACI 318-11 Appendix D and A23.3 CSA code Appendix D for cast-in-place headed anchors which expect a half pyramid breakout cone with a side length of (3 c_{a1}) and a depth of (1.5 c_{a1}) with 35° crack angles where ca_1 is the distance from the edge to the pile shaft axis.

- The connection breakout shear load is sustained by the concrete and the longitudinal reinforcement. After the concrete breakout load, the concrete ultimate strength is comprised of four parts: the dowel action of longitudinal reinforcement; the stirrups resistance; the pile cap contribution to the connection; and the aggregate interlock resistance.

- The concrete bearing capacity in front of the pile shaft has a major effect on the connection capacity. If the connection shear capacity is higher than the concrete bearing capacity, crushing will occur in front of the pile and moments will be applied on the pile shaft and the pile cap.

- The connection capacity must be calculated using different limit states. For fixed connection design, these limit states are: the pile shaft shear strength; the concrete bearing capacity in front of the pile shaft; and the concrete breakout load. For hinged connection design, the connection ultimate load may be higher than the connection breakout load and the following limit states should be considered: the

concrete pryout strength after the breakout cracking; the stirrups tensile capacity; the pile shaft strength; and the welding strength.

- The longitudinal reinforcement close to the beam side (i.e. outer longitudinal reinforcement) resists the flexural stresses in the beam, while the longitudinal reinforcement close to the pile shaft (i.e. inner longitudinal reinforcement) resists the stresses by dowel action after the breakout cracking.

- Stirrups contribute to the connection capacity only after the concrete breakout load (i.e. formation of the 35° breakout cone).

- The concrete crushing load in front of the pile increase with the concrete compressive strength increase.

- For pile embedment depth < 4.5 times the pile shaft width, pryout cracks may occur. Increasing the pile embedment depth increases the connection capacity, stiffness, ability to absorb energy, and ductility after reaching its ultimate load. However, the contribution of the pile cap to the connection capacity decreases as the pile embedment depth increases.

- The pile cap size affects the connection ultimate load and the connection failure mechanism. Increasing the pile cap size promotes pile cap welding failure rather than pryout failure.

- Increasing the longitudinal reinforcement ratio increases the connection breakout load and the connection ultimate load.

- Only stirrups included within a distance equal to (half the beam width x Cot 35°) from both sides of the pile contribute to the connection ultimate load.

516

- The formation of first breakout cone and the concrete crushing are the limits at which the connection behaviour changes from an elastic behaviour to an inelastic behaviour under cyclic shear loading.

- With each load cycle of the same load level, cracks propagate, displacements increase, and steel strains increase.

- Cyclic loading causes degradation of concrete strength and stiffness, which leads to concrete crushing and plastic displacements around the pile shaft from the two loaded sides compared to monotonic shear loading.

- Under cyclic shear loading, the connection ultimate load and its ability to absorb energy decrease because of the concrete strength degradation. Therefore, a concrete reduction factor of at least 0.75 must be used when designing the connections for alternating cyclic shear loading.

- Under cyclic shear loading, the pile shaft is expected to be subjected to more moments compared to monotonic loading. Low-cycle fatigue failure may occur in the steel components of the connection. Thus, a reduction factor to the steel components strength limit states must be used.

- The connection capacity increases with the shear span reduction.

- Under cyclic loading, increasing the pile embedment depth, increases the connection ultimate load, and enhances its ability to absorb and dissipate energy.

- Under cyclic loading, the transverse reinforcement has a negligible effect on the connection capacity but it increases its ductility and ability to absorb and dissipate energy.

517

- Equation 10.1 is proposed to calculate the concrete crushing load in front of the pile shaft. This equation showed good agreement with the loads recorded experimentally and it is recommended to be used in the studied connection design. This equation predicted the concrete crushing load with 107% mean value and 12.8% COV.

- It was found that the equations recommended by the ACI 318-11 and CSA 23.3-04 codes for cast-in -place headed anchors design could expect the connection breakout load with adequate conservative margin. Thus, Equation 10.4 is the recommended equation to be used to calculate the basic single pile connection breakout load.

- It was found that the equations recommended by the ACI 318-11 and CSA 23.3-04 codes for cast-in -place headed anchors design could expect the behaviour of the connection breakout load of the helical pile connection more accurately than those recommended by the PCI and CPCI design manuals.

- It was found that the equations recommended by the ACI 318-11 and CSA 23.3-04 codes for cast-in -place headed anchors design (i.e. Equation 10.8) could not accurately expect the pile shaft steel failure under shear loading if the steel pile shear capacity was higher than the connection breakout load calculated by Equation 10.2, and the concrete crushing load calculated by Equation 10.1.

- If the steel pile shear capacity calculated by equation 10.8 is more than either of the breakout cracking load (Equation 10.2) or the concrete crushing load (Equation 10.1), the steel pile shear load shall be calculated using Equation 10.10

adopted by fuchs (1992). This equation predicted the steel failure load with 102% mean value with 1.7% COV when compared with the experimental results.

- The flow chart presented in figure 10-4 is concluding the design procedures required to calculate the fixed connection capacity and to ensure a ductile failure will take place.

- If the connection will be subjected to cyclic shear loading, a reduction factor of 0.75 shall be multiplied by the design equations previously indicated.

11.4 Recommendations for future research

The current research revealed that some further studies on the helical piles connectors for new reinforced concrete foundations may be needed. The following are some suggested recommendations for future research:

- Evaluate the connection behaviour if used with raft foundations and reinforced concrete pile caps.

- Extend the experimental program under shear loading to investigate the observed failure mechanism more explicitly by studying only one failure mechanism preventing the other failure mechanism from occurring (e.g. conduct an experimental testing on the connection under shear loading if the pile cap connection have stiffeners with adequate welding)

- Perform an experimental testing on site under different cases of loading taking into consideration the pile-soil interaction.

- Test the behaviour of the connection under combined tension/compression and shear loading.

- Test the connection behaviour under shear loading for inclined helical piles.

- Investigate the connection behaviour for different sizes of helical piles/micropiles shafts.

- Investigate the connection performance under tension cyclic loading and compression-tension cyclic loading.

- Include the linear and non-linear behaviour of the connection in the development of a representative element of the connection to be used in finite element modeling for soil-structure interaction analysis.

APPENDIX A

CONCRETE CYLINDER TESTS AND STEEL REBAR TESTS

In this appendix, the data of the tests conducted on the used concrete and the steel rebar will be presented.

A.1 Concrete cylinder tests

In the experimental program, four concrete patches were used. The conducted concrete compression tests' results and concrete splitting tests' results will be presented in four tables for the four patches from table A-1 to A-4. It should be noted that the cylinders were tested in the same day of specimens testing. Figures A-1, and A-2 show the compression test and the typical concrete cylinder failure, respectively. Figures A-3 shows the splitting tensile test and its corresponding typical failure. Moreover, figure A-4 shows a report received from the ready mix concrete supplier, Mobile Mix, for 3 tested cylinders.

Figure A- 1 The conducted concrete compression test according to ASTM C39 / C39M

Figure A- 2 The typical observed concrete cylinder failure under compression testing

(a)

(b)

Figure A- 3 (a) The conducted splitting tensile testing according to ASTM C496 / C496M - 11; and (b) its tyical failure

Table A- 1 Concrete test results for the first ready mix concrete patch

Cylinder	Compression failure load (N)	Compressive Strength (f_c') (MPa)	Splitting failure load (N)	Splitting tensile strength (f_{sp}) (MPa)
1	247944	30.6	109426	3.4
2	248344	30.6	106757	3.3
3	245408	30.3	105423	3.3
4	246876	30.5	105423	3.3
5	231308	28.5	108537	3.3

Table A- 2 Concrete test results for the second ready mix concrete patch

Cylinder	Compression failure load (N)	Compressive Strength (f_c') (MPa)	Splitting failure load (N)	Splitting tensile strength (f_{sp}) (MPa)
1	321606	39.7	160136	4.9
2	324275	40.0	176594.4	5.4
3	345404	42.6	166808.3	5.1
4	314489	38.8	174370.3	5.4
5	304703	37.6	172146.2	5.3

Table A- 3 Concrete test results for the third ready mix concrete patch

Cylinder	Compression failure load (N)	Compressive Strength (f_c') (MPa)	Splitting failure load (N)	Splitting tensile strength (f_{sp}) (MPa)
1	247588	30.6	111206	3.4
2	238425	29.4	126774	3.9
3	235756	29.1	121881	3.8
4	252214	31.1	130333	4.0
5	244875	30.2	137895	4.3

Table A- 4 Concrete test results for the forth ready mix concrete patch

Cylinder	Compression failure load (N)	Compressive Strength (f_c') (MPa)	Splitting failure load (N)	Splitting tensile strength (f_{sp}) (MPa)
1	231308	28.5	120102	3.7
2	260666	32.2	140119	4.3
3	257107	31.7	140119	4.3
4	260221	32.1	135671	4.2
5	242428	29.9	125440	3.9

Holcim

COMPRESSIVE STRENGTH - CONCRETE CYLINDERS
TEST REPORT

Date:	June 30, 2011		Report no.:	052011-0052
Project:	Dock 17 Spencer Engineering Building		Client:	Mobile Mix
Date cast:	May 30, 2011		Date received:	June 2, 2011
		Specified 28-day compressive strength (MPa)		25

Cylinder	Average diameter (mm)	Date tested	Age (days)	Unit weight (kg/m³)	Compressive strength (MPa)	Type of fracture*	Average compressive strength (MPa)
A	101.6	6-Jun-11	7	2375	17.8	1	-
B	101.6	27-Jun-11	28	2375	28.0	1	-
C	101.6	27-Jun-11	28	2375	28.0	1	28.0
D							
E							
F							
G							
H							

* Refer to CSA A23.1-09 page 485 Figure 1

Contractor	University of Western Ontario			
Concrete supplier	Mobile Mix	Truck no.		61
Location on structure				
Ticket no.	.	Load no. / size (m³)		
Time batched	1:35 PM	Time cylinders were cast		1:45 PM
Cast by	A. Konu	of		Co-fo Conc. Forming
Type and size of moulds	Plastic – 100x200-mm			
Specified slump (mm)		Measured slump (mm)		160
Specified air (%)	5.0 – 7.0	Measured air (%)		6.7
Concrete temperature (°C)	18.0	Ambient temperature (°C)		22.0
Mix code		Nominal max. size aggregate (mm)		20.0
Cement type		Supplementary cementing material		
Admixture	AEA, WRA			
Initial 24-hour curing temperature (°C)				
Maximum		Minimum		
Water added on job (L)		Authorized by		
Remarks:				

CCIL

Figure A- 4 Report from the ready mix concrete supplier

A.2 Steel rebars tensile testing

In the experimental program, five different bar designation were used. Direct tensile testing was conducted on 3 instrumented bars from each bar designation. Figure A-5 demonstrate the used testing procedure. Table A-5 presents the measured bar diameter, yield stress, ultimate tensile strength, and the typical grade of the used rebars.
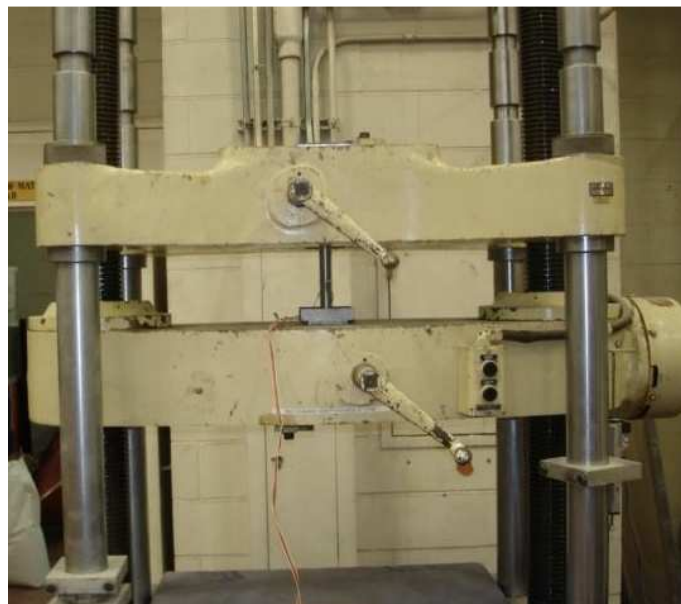
Figure A- 5 The used direct tensile testing system

Table A- 5 The mechanical properties of the used steel rebars

Bar Designation	Bar Diameter (mm)	Bar Type	Grade (yield/ultimate) (MPa)	Yield Stress (f_y) (MPa)	Tensile Strength (f_u) (MPa)
25M	25.2	Deformed	400/600	390	555
20M	19.5	Deformed	400/600	500	600
15M	16	Deformed	400/600	500	630
10M	11.3	Deformed	400/600	431	593
#2	6.35	Plain	450/550	530	609

APPENDIX B

FORM WORK, REBARING, STRAIN GAUGE INSTALLATION, READY MIX CONCRETE CASTING

B.1 Form Work

In this appendix, the form work used for casting the reinforced concrete system and for fixing the pile shaft in its exact location is presented. , Figure B-1 shows the wooden mould, designed and built by the author, used to cast two or three specimens at the same time. It was designed to give the exact dimensions and to be molded and demolded allowing using the wood several times with the same quality. It has vertical posts at the beam mid-span from the two sides to fix the pile in its location. Figure B-2 shows the two posts connected to the pile shaft using two bars inserted into two holes in the pile shaft and in the posts at the required elevation to achieve the required pile embedment depth for each specimen. Also, the pile shaft is prevented from moving laterally during the concrete casting using a wooden frame holding the pile shaft to the wooden mold as shown in figures B-2 and B-3.
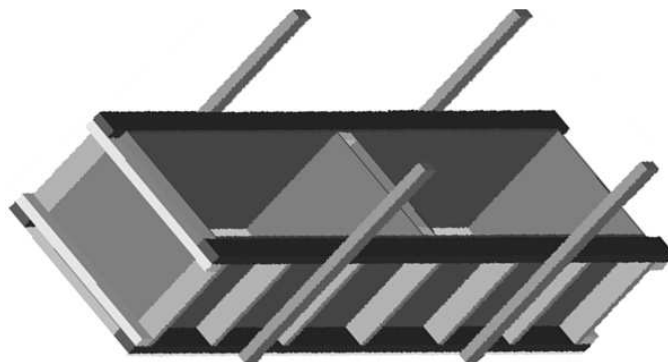
Figure B- 1 3D view of the wooden mould used for concrete casting

Figure B- 2 The used pile fixation system
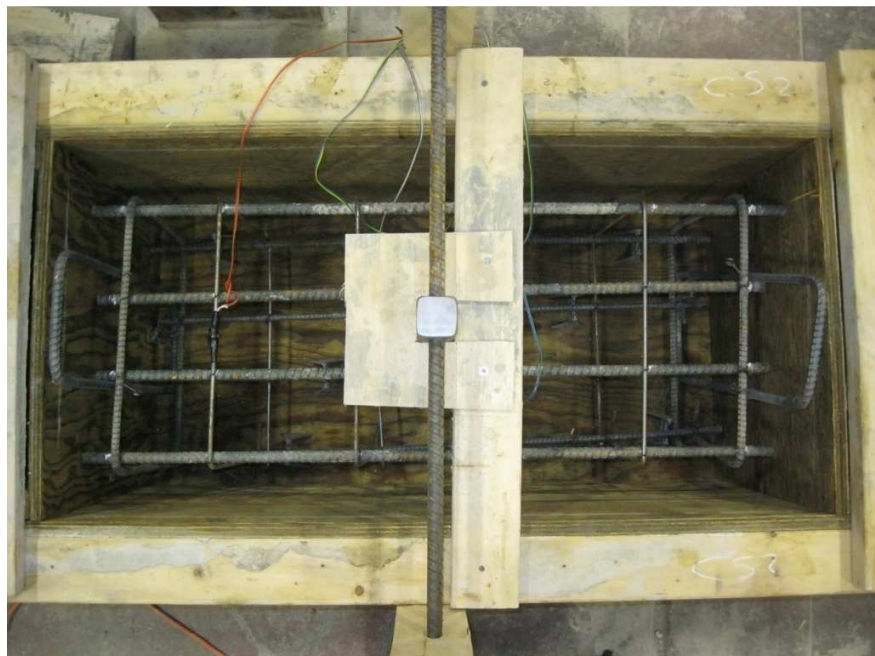
Figure B- 3 Fixing the pile shaft laturally to the wooden mold

B.2 Rebaring

All the rebaring was conducted by the author with the exact required dimensions and location. Figure B-4 shows one of the rebar cages during its tying procedure with annealed steel wire.

Figure B- 4 Rebar cage tying procedure

B.3 Strain gauge installation

All the used strain gauges were installed by the author. The strain gauge installation involved several steps including the surface cleaning, polishing, surfacing, strain gauge bonding to the surface, wires welding to the strain gauge, applying air and water sealing coat, and applying compressible protective coating. Figure B-5 represent one of the rebar cages having the strain gauges bonded, wired, and coated with the water sealant. Figure B-6 demonstrate the strain gauge installation on the new construction bracket (i.e. pile cap). It should be mentioned that the location of the strain gauges installed on the pile cap

528

depended on the type of loading. If the pile cap will be used for shear loading test, the strain gauges was installed facing the holes, and if it is for tension or compression loading test, the strain gauge was installed at the other side of the pile cap.
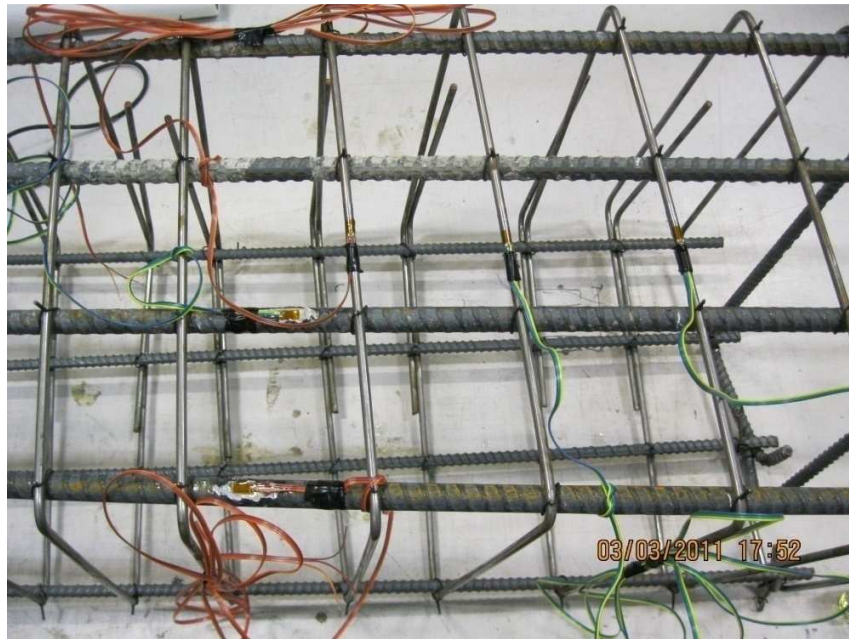
Figure B- 5 Strain gauge installation on the rebars

Figure B- 6 Strain gauge installation on a pile cap used for compression loading test

B.4 Ready mix concrete casting

First, the wooden molds are oil painted. Second, the steel gages are installed in the wooden mold using plastic shoes " cover adjuster " to maintain the required concrete cover from the bottom and from sides. Then, the pile cap get attached to the pile shaft using the required number of bolts. Figure B-7 shows a system ready for concrete casting. After everything is checked to be fixed in place with the required dimensions before pouring the concrete, the concrete pouring began with a continues adequate concrete vibration without touching the rebars. Figure B-8 shows the concrete casting procedure. Afterwards, the concrete surface was formed and concrete cylinders for testing were prepared and a slump flow test was conducted. Finally, the appropriate curing procedure was conducted on both the casted specimens and the concrete cylinders.

Figure B- 7 A ready system for concrete casting

Figure B- 8 Ready mix concrete casting and concrete vibration

APPENDIX C

THE USED KEYWORD INPUT DATA FOR THE FINITE ELEMENT MODELS IN LS-DYNA

This appendix presents the keyword input data used to build the investigated finite element models. These data are reported to be used in future research involving similar specimens behaviour. The data of the nodes and different elements are not included as it will not help the purpose of this appendix. The different concrete materials are presented by different material name, and all the rebar material properties are presented with different part cards, section cards and different material cards. Table C-1 demonstrate the keyword input data for the experimentally tested beams under tension loading as an example of the used models in this research. Moreover, table C-2 presents the keyword input data when the same finite element model was used to analyze the experimental work done by Angelakos et al. ,2001.

Table C- 1 Keyword Input data for beams T1,T2, T3, T4, T5, T6, T7, T7, T8, and T9

```
$$$$$$$$$$$$$$$$$$$$$$$$$$$$$$$$$$$$$$$$$$$$$$$$$$$$$$$$$$$$$$$$$$$$$$$$$$$$$$$$$$$$
$$$$$$$$$$$$$$$$$$$$$$$$$$$$$$$$$$$$$$$$$$$$$$$$$$$$$$$$$$$$$$$$$$$$$$$$$$$$$$$$$$$$
*KEYWORD 600000000 ncpu=6
$   PROJECT :
$     UNITS : mm, N, Sec
$---+----1----+----2----+----3----+----4----+----5----+----6----+----7----+----8
$                     TITLE CARD
$---+----1----+----2----+----3----+----4----+----5----+----6----+----7----+----8
*TITLE
Beam T1/T2/T3
$---+----1----+----2----+----3----+----4----+----5----+----6----+----7----+----8
$                    CONTROL CARDS
$---+----1----+----2----+----3----+----4----+----5----+----6----+----7----+----8
*CONTROL_ACCURACY
$     OSU      INN
        1        1
*CONTROL_TERMINATION
$  ENDTIM   ENDCYC     DTMIN    ENDNEG    ENDMAS
    2.000        0  0.000000  0.000000
*CONTROL_TIMESTEP
$  DTINIT     SCFT      ISDO    TSLIMT      DTMS      LCTM     ERODE     MS1ST
    .000     1.00         0
*CONTROL_ENERGY
$    HGEN     RWEN    SLNTEN     RYLEN
        2        2         2         2
*CONTROL_HOURGLASS
```

```
$        IHQ        QH
          4       0.03
$---+----1----+----2----+---3----+----4----+----5----+----6----+----7----+----8
$                 () Boundary Prescribed Motion at set of nodes Card
$---+----1----+----2----+----3----+----4----+----5----+----6----+----7----+----8
*BOUNDARY_PRESCRIBED_MOTION_SET
$      NSID       DOF       VAD      LCID        SF       VID     DEATH     BIRTH
          1         2         0         1       1.0         0  1.00E+28       0.0
*DEFINE_CURVE
$      LCID      SIDR       SFA       SFO      OFFA      OFFO    DATTYP
          1         0         1         1         0         0         0
$                   A1                  O1
                 0.000                0.00
                 1.000                   5
                 2.001                   5
$
$---+----1----+----2----+----3----+----4----+----5----+----6----+----7----+----8
$                     DATABASE CONTROL CARDS FOR ASCII FILE
$---+----1----+----2----+----3----+----4----+----5----+----6----+----7----+----8
*DATABASE_GLSTAT
$        DT
5.000e-003
$
*DATABASE_MATSUM
$        DT
5.000e-003
$
*DATABASE_RCFORC
$        DT
5.000e-003
*DATABASE_NCFORC
$        DT
5.000e-003
*DATABASE_BINARY_INTFOR
$        DT
5.000e-003
$
*DATABASE_NODFOR
$        DT    BINARY
5.000e-003         3
*DATABASE_NODOUT
$        DT    BINARY
5.000e-003
*DATABASE_elout
$        DT    BINARY
5.000e-003
$
$---+----1----+----2----+----3----+----4----+----5----+----6----+----7----+----8
$                   (5) DATABASE CONTROL CARDS FOR BINARY FILE
$---+----1----+----2----+----3----+----4----+----5----+----6----+----7----+----8
*DATABASE_BINARY_D3PLOT
$  DT/CYCL      LCDT    NOBEAM
5.000e-003
*DATABASE_BINARY_D3THDT
$  DT/CYCL      LCDT    NOBEAM
5.000e-003
$---+----1----+----2----+----3----+----4----+----5----+----6----+----7----+----8
$                               PART CARDS
$---+----1----+----2----+----3----+----4----+----5----+----6----+----7----+----8
*PART
$HEADING
Concrete hexa
$       PID       SID       MID     EOSID      HGID      GRAV    ADPOPT      TMID
          5         1                   1
$
*PART
$HEADING
Welding
$       PID       SID       MID     EOSID      HGID      GRAV    ADPOPT      TMID
          7         2       555
$
*PART
$HEADING
Cylinder
$       PID       SID       MID     EOSID      HGID      GRAV    ADPOPT      TMID
          8         2       666
$
```

```
$
$
*PART
$HEADING
Pile
$       PID       SID       MID     EOSID      HGID      GRAV    ADPOPT      TMID
          9         2       888
$
*PART
$HEADING
Plate
$       PID       SID       MID     EOSID      HGID      GRAV    ADPOPT      TMID
          4         2       999
$
*PART
$HEADING
Bolts
$       PID       SID       MID     EOSID      HGID      GRAV    ADPOPT      TMID
         14         2      1000
$
$
$%%%%%%%%%%%%%%%%%%%%%%%%%%%%%%%%%%%%%%%%%
$---+----1----+----2----+----3----+----4----+----5----+----6----+----7----+----8
$                     MATERIAL CARDS (Cylinder)
$---+----1----+----2----+----3----+----4----+----5----+----6----+----7----+----8
$ STEEL REBAR
*MAT_PIECEWISE_LINEAR_PLASTICITY
$       MID        RO         E        PR      SIGY      ETAN      FAIL      TDEL
        666   7.8E-09    2.0E+5       0.3      344.     2000.       .30       0.0
$         C         P      LCSS      LCSR        VP
        0.0       0.0       0.0       0.0       0.0
$      EPS1      EPS2      EPS3      EPS4      EPS5      EPS6      EPS7      EPS8

$       ES1       ES2       ES3       ES4       ES5       ES6       ES7       ES8

$%%%%%%%%%%%%%%%%%%%%%%%%%%%%%%%%%%%%%%%%%%
$%%%%%%%%%%%%%%%%%%%%%%%%%%%%%%%%%%%%%%%%%%
$---+----1----+----2----+----3----+----4----+----5----+----6----+----7----+----8
$                     MATERIAL CARDS (Pile)
$---+----1----+----2----+----3----+----4----+----5----+----6----+----7----+----8
$ STEEL REBAR
*MAT_PIECEWISE_LINEAR_PLASTICITY
$       MID        RO         E        PR      SIGY      ETAN      FAIL      TDEL
        888   7.8E-09    2.0E+5       0.3     620.0     2000.       .30       0.0
$         C         P      LCSS      LCSR        VP
        0.0       0.0       0.0       0.0       0.0
$      EPS1      EPS2      EPS3      EPS4      EPS5      EPS6      EPS7      EPS8

$       ES1       ES2       ES3       ES4       ES5       ES6       ES7       ES8

$%%%%%%%%%%%%%%%%%%%%%%%%%%%%%%%%%%%%%%%%%%%
$---+----1----+----2----+----3----+----4----+----5----+----6----+----7----+----8
$                     MATERIAL CARDS (Welding)
$---+----1----+----2----+----3----+----4----+----5----+----6----+----7----+----8
$ STEEL REBAR
*MAT_PIECEWISE_LINEAR_PLASTICITY
$       MID        RO         E        PR      SIGY      ETAN      FAIL      TDEL
        555   7.8E-09    2.0E+5       0.3     400.0     2000.       .30       0.0
$         C         P      LCSS      LCSR        VP
        0.0       0.0       0.0       0.0       0.0
$      EPS1      EPS2      EPS3      EPS4      EPS5      EPS6      EPS7      EPS8

$       ES1       ES2       ES3       ES4       ES5       ES6       ES7       ES8

$%%%%%%%%%%%%%%%%%%%%%%%%%%%%%%%%%%%%%%%%%%%
$%%%%%%%%%%%%%%%%%%%%%%%%%%%%%%%%%%%%%%%%%%%
$---+----1----+----2----+----3----+----4----+----5----+----6----+----7----+----8
$                     MATERIAL CARDS (Plate)
$---+----1----+----2----+----3----+----4----+----5----+----6----+----7----+----8
$ STEEL REBAR
*MAT_PIECEWISE_LINEAR_PLASTICITY
$       MID        RO         E        PR      SIGY      ETAN      FAIL      TDEL
        999   7.8E-09    2.0E+5       0.3      344.     2000.       .30       0.0
$         C         P      LCSS      LCSR        VP
        0.0       0.0       0.0       0.0       0.0
$      EPS1      EPS2      EPS3      EPS4      EPS5      EPS6      EPS7      EPS8
```

534

```
$     ES1       ES2       ES3       ES4       ES5       ES6       ES7       ES8

$%%%%%%%%%%%%%%%%%%%%%%%%%%%%%%%%%%%%
$%%%%%%%%%%%%%%%%%%%%%%%%%%%%%%%%%%%%
$---+----1----+----2----+----3----+----4----+----5----+----6----+----7----+----8
$                          MATERIAL CARDS (Bolt)
$---+----1----+----2----+----3----+----4----+----5----+----6----+----7----+----8
$ STEEL REBAR
*MAT_PIECEWISE_LINEAR_PLASTICITY
$       MID        RO         E        PR      SIGY      ETAN      FAIL      TDEL
       1000    7.8E-09    2.0E+5       0.3      655.     2500.       .30       0.0
$         C         P      LCSS      LCSR        VP
        0.0       0.0       0.0       0.0       0.0
$      EPS1      EPS2      EPS3      EPS4      EPS5      EPS6      EPS7      EPS8

$      ES1       ES2       ES3       ES4       ES5       ES6       ES7       ES8

$%%%%%%%%%%%%%%%%%%%%%%%%%%%%%%%%%%%%
$$$$$$$$$$$$$$$$$$$$$$$$$$$$$$$$$$$$$$$$$$$$$$$$$$$$$$$$$$$$$$$$
$---+----1----+----2----+----3----+----4----+----5----+----6----+----7----+----8
$                      Default mat 159 concrete
$---+----1----+----2----+----3----+----4----+----5----+----6----+----7----+----8
*MAT_CSCM_CONCRETE
$       MID        RO     NPLOT     INCRE     IRATE     ERODE     RECOV   ITERTRC
       1222   2.32E-09         1                   0         1         1         1
$      PRED

$       FPC      DAGG     UNITS
       30.0         0         2
$
$$$$$$$$$$$$$$$$$$$$$$$$$$$$$$$$$$$$$$$$$$$$$$$$$$$$$$$$$$$$$$$$$$$$$$$$$$$$$$$$$$$$$
Concrete Model in case of fc'=30 MPa as in T1, T2, and T3
$$$$$$$$$$$$$$$$$$$$$$$$$$$$$$$$$$$$$$$$$$$$$$$$$$$$$$$$$$$$$$$$$$$$$$$$$$$$$$$$$$$$$
*MAT_CONCRETE_DAMAGE_REL3
$       MID        RO        PR
          1    2.4E-09
$        FT        A0        A1        A2        B1     OMEGA       A1F
       3.33     -30.0
$   SLAMBDA      NOUT     EDROP     RSIZE       UCF    LCRate  Locwidth      NPTS
                                        2                    3.94e-02       145
7
$   LAMBD01   LAMBD02   LAMBD03   LAMBD04   LAMBD05   LAMBD06   LAMBD07   LAMBD08

$   LAMBD09  LAMBD010  LAMBD011  LAMBD012  LAMBD013        B3       A0Y       A1Y

$     ETA01     ETA02     ETA03     ETA04     ETA05     ETA06     ETA07     ETA08

$     ETA09    ETA010    ETA011    ETA012    ETA013        B2       A2F       A2Y
                                                         3.1
$$$$$$$$$$$$$$$$$$$$$$$$$$$$$$$$$$$$$$$$$$$$$$$$$$$$$$$$$$$$$$$$$$$$$$$$$$$$$$$$$$$$$
$---+----1----+----2----+----3----+----4----+----5----+----6----+----7----+----8
$    Loading Rate for Mat_072 (MAT_CONCRETE_DAMAGE_REL3)
$---+----1----+----2----+----3----+----4----+----5----+----6----+----7----+----8
*DEFINE_CURVE
$      LCID      SIDR       SFA       SFO      OFFA      OFFO    DATTYP
          7                 0       1.0       1.0       0.0                 0.0
0
$                  A1                 O1
               -30000.0               1.0
                 -300.0               1.0
                 -100.0               1.0
                  -30.0               1.0
                  -10.0               1.0
                   -3.0               1.0
                   -1.0               1.0
                  -0.10               1.0
                 -0.010               1.0
                -0.0010               1.0
               -0.00010               1.0
              -0.000010               1.0
                    0.0               1.0
               0.000010               1.0
                0.00010               1.0
                 0.0010               1.0
                  0.010               1.0
                   0.10               1.0
                    1.0               1.0
```

```
                 3.0                   1.0
                10.0                   1.0
                30.0                   1.0
               100.0                   1.0
               300.0                   1.0
             30000.0                   1.0
$$$$$$$$$$$$$$$$$$$$$$$$$$$$$$$$$$$$$$$$$$$$$$$$$$$$$$$$$$$$$$$$$$$$$$$$$$$$$$
Concrete Model in case of fc'=40 MPa as in T4, T5, T6, T7,T8, and T9
$$$$$$$$$$$$$$$$$$$$$$$$$$$$$$$$$$$$$$$$$$$$$$$$$$$$$$$$$$$$$$$$$$$$$$$$$$$$$$
*MAT_CONCRETE_DAMAGE_REL3
$       MID        RO        PR
          2    2.4E-09
$        FT        A0        A1        A2        B1     OMEGA       A1F
       5.25     -40.0
$   SLAMBDA      NOUT     EDROP     RSIZE       UCF    LCRate  LocWidth      NPTS
                              2   3.94e-02               145         8
$   LAMBD01   LAMBD02   LAMBD03   LAMBD04   LAMBD05   LAMBD06   LAMBD07   LAMBD08

$   LAMBD09  LAMBD010  LAMBD011  LAMBD012  LAMBD013        B3       A0Y       A1Y

$     ETA01     ETA02     ETA03     ETA04     ETA05     ETA06     ETA07     ETA08

$     ETA09    ETA010    ETA011    ETA012    ETA013        B2       A2F       A2Y
                                                         4.3
$$$$$$$$$$$$$$$$$$$$$$$$$$$$$$$$$$$$$$$$$$$$$$$$$$$$$$$$$$$$$$$$$$$$$$$$$$$$$$$$
$---+----1----+----2----+----3----+----4----+----5----+----6----+----7----+----8
$    Loading Rate for Mat_072 (MAT_CONCRETE_DAMAGE_REL3)
$---+----1----+----2----+----3----+----4----+----5----+----6----+----7----+----8
*DEFINE_CURVE
$      LCID      SIDR       SFA       SFO      OFFA      OFFO    DATTYP
          8         0       1.0                 1.0               0.0       0.0
0
$                  A1                  O1
            -30000.0                 1.0
              -300.0                 1.0
              -100.0                 1.0
               -30.0                 1.0
               -10.0                 1.0
                -3.0                 1.0
                -1.0                 1.0
               -0.10                 1.0
              -0.010                 1.0
             -0.0010                 1.0
            -0.00010                 1.0
           -0.000010                 1.0
                 0.0                           1.0
            0.000010                 1.0
             0.00010                 1.0
              0.0010                 1.0
               0.010                 1.0
                0.10                 1.0
                 1.0                 1.0
                 3.0                 1.0
                10.0                 1.0
                30.0                 1.0
               100.0                 1.0
               300.0                 1.0
             30000.0                 1.0
$$$$$$$$$$$$$$$$$$$$$$$$$$$$$$$$$$$$$$$$$$$$$$$$$$$$$$$$$$$$$$$$$$$$$$$$$$$$$$$$$$$
$---+----1----+----2----+----3----+----4----+----5----+----6----+----7----+----8
$                     SECTION CARDS
$---+----1----+----2----+----3----+----4----+----5----+----6----+----7----+----8
$
*SECTION_SOLID_TITLE
Concrete Hexa
$     SECID    ELFORM       AET
          1         1         0

*SECTION_SOLID_TITLE
Steel hexa
$     SECID    ELFORM       AET
          2         1         0
$
$
$---+----1----+----2----+----3----+----4----+----5----+----6----+----7----+----8
$                   Defining point sets
$---+----1----+----2----+----3----+----4----+----5----+----6----+----7----+----8
```

```
*SET_NODE_LIST
$Applied displacement/velocity/force
$       SID        DA1        DA2        DA3        DA4
          1
$      NID1       NID2       NID3       NID4       NID5       NID6       NID7       NID8
       XXXX       XXXX       XXXX       XXXX       XXXX       XXXX       XXXX       XXXX
$
$
$
$
$
$
$
*SET_NODE_LIST
$symetric (IN THE X-Y and z-y  PLANES) x=z=0
$       SID        DA1        DA2        DA3        DA4
          2
$      NID1       NID2       NID3       NID4       NID5       NID6       NID7       NID8
       XXXX       XXXX       XXXX       XXXX       XXXX       XXXX       XXXX       XXXX
$
$
$
$
$
$
$
$
*SET_NODE_LIST
$symetric (In the z-y plane) x=0
$       SID        DA1        DA2        DA3        DA4
          3
$      NID1       NID2       NID3       NID4       NID5       NID6       NID7       NID8
       XXXX       XXXX       XXXX       XXXX       XXXX       XXXX       XXXX       XXXX
$
*SET_NODE_LIST
$Symetric (In x-y plane) z=0
$       SID        DA1        DA2        DA3        DA4
          4
$      NID1       NID2       NID3       NID4       NID5       NID6       NID7       NID8
       XXXX       XXXX       XXXX       XXXX       XXXX       XXXX       XXXX       XXXX
$
*SET_NODE_LIST
$Supports (Y=0)
$       SID        DA1        DA2        DA3        DA4
          5
$      NID1       NID2       NID3       NID4       NID5       NID6       NID7       NID8
       XXXX       XXXX       XXXX       XXXX       XXXX       XXXX       XXXX       XXXX
$
$$$$$$$$$$$$$$$$$$$$$$$$$$$$$$$$$$$$$$$$$$$$$$$$$$$$$$$$$$$$$$$$$$$$$$$$$$$$$$$$
$$$ Printing FORCES IN BEAM ELEMENTS FOR DESIRED BEAM ELEMENTS              $$$$
$$$$$$$$$$$$$$$$$$$$$$$$$$$$$$$$$$$$$$$$$$$$$$$$$$$$$$$$$$$$$$$$$$$$$$$$$$$$$$$$
$*DATABASE_HISTORY_BEAM
$       ID1        ID2        ID3        ID4        ID5        ID6        ID7        ID8
$         4      19203        378        302        445
$$$$$$$$$$$$$$$$$$$$$$$$$$$$$$$$$$$$$$$$$$$$$$$$$$$$$$$$$$$$$$$$$$$$$$$$$$$$$$$$
$$$ Printing reactions of points where prescribed displacements are applied$$$$
$$$$$$$$$$$$$$$$$$$$$$$$$$$$$$$$$$$$$$$$$$$$$$$$$$$$$$$$$$$$$$$$$$$$$$$$$$$$$$$$
$
$$$$$$$$$$$$$$$$$$$$$$$$$$$$$$$$$$$$$$$$$$$$$$$$$$$$$$$$$$$$$$$$$$$$$$$$$$$$$$$$
$
$*database_history_node
$      NID1       NID2
$
$$$$$$$$$$ Printing STRESSES IN SOLID ELEMENTS   $$$$$$$$$$$$$$$$$$$$$$$$$$$$$$$$$
$$$$$$$$$$$$$$$$$$$$$$$$$$$$$$$$$$$$$$$$$$$$$$$$$$$$$$$$$$$$$$$$$$$$$$$$$$$$$$$$
$*database_history_SOLID
$      NID1       NID2
$
$$$$
$$$$$$$$$$$$$$$$$$$$$$$$$$$$$$$$$$$$$$$$$$$$$$$$$$$$$$$$$$$$$$$$$$$$$$$$$$$$$$$$
$$$ Printing reactions of points where prescribed displacements are applied$$$$
$$$$$$$$$$$$$$$$$$$$$$$$$$$$$$$$$$$$$$$$$$$$$$$$$$$$$$$$$$$$$$$$$$$$$$$$$$$$$$$$
*DATABASE_NODAL_FORCE_GROUP
$      NSID        CID
          1
          5
$$$$$$$$$$$$$$$$$$$$$$$$$$$$$$$$$$$$$$$$$$$$$$$$$$$$$$$$$$$$$$$$$$$$$$$$$$$$$$
$$$$$$$                                                          $$$$$$$$$$
```

```
$$$$$$$                                                       $$$$$$$$$$$
$$$$$$$                                                       $$$$$$$$$$$
$$$$$$$ Applying sliding boundary conditions on the edges of the slice $$$$$$$$$$$
$$$$$$$                                                       $$$$$$$$$$$
$$$$$$$                                                       $$$$$$$$$$$
$$$$$$$                                                       $$$$$$$$$$$
$$$$$$$$$$$$$$$$$$$$$$$$$$$$$$$$$$$$$$$$$$$$$$$$$$$$$$$$$$$$$$$$$$$$$$$$
$FACE1-Boundary Condition, symetric (IN THE X-Y and z-y  PLANES)
*BOUNDARY_SPC_SET
$      NSID       CID      DOFX      DOFY      DOFZ     DOFRX     DOFRY     DOFRZ
          2         0         1         0         1         0         0         0
$FACE2-Boundary Conditions symetric (In the z-y plane) x=0
*BOUNDARY_SPC_SET
$      NSID       CID      DOFX      DOFY      DOFZ     DOFRX     DOFRY     DOFRZ
          3         0         1         0         0         0         0         0
$Nodes fixed in the z-Direction Symetric (In x-y plane)
*BOUNDARY_SPC_SET
$      NSID       CID      DOFX      DOFY      DOFZ     DOFRX     DOFRY     DOFRZ
          4         0         0         0         1         0         0         0
$Nodes Supports (x,y,z=0)
*BOUNDARY_SPC_SET
$      NSID       CID      DOFX      DOFY      DOFZ     DOFRX     DOFRY     DOFRZ
          5         0         0         1         0         0         0         0
$---+----1----+----2----+----3----+----4----+----5----+----6----+----7----+----8
$                      (8) NODAL POINT CARDS
$---+----1----+----2----+----3----+----4----+----5----+----6----+----7----+----8
*NODE
$     NID               X               Y               Z        TC        RC
     XXXX      XXXX      XXXX      XXXX      XXXX      XXXX      XXXX      XXXX      XXXX
$
$---+----1----+----2----+----3----+----4----+----5----+----6----+----7----+----8
$                      Solid ELEMENT CARDS
$---+----1----+----2----+----3----+----4----+----5----+----6----+----7----+----8
*ELEMENT_SOLID
$      EID       PID      NID1      NID2      NID3      NID4      NID5      NID6      NID7      NID8
     XXXX      XXXX      XXXX      XXXX      XXXX      XXXX      XXXX      XXXX      XXXX      XXXX
$
$%%%%%%%%%%%%%%%%%%%%%%%%%%%%%%%%%%%%%%%%%%%%%%%%%%%%
$%%%%%%%%%%%%%%%%%%%%%%%%%%%              %%%%%%%%%%%%%%%
$%%%%%%%%%%%%%%%%%%%%%%%%%%%   Solid  ELEMENTS   %%%%%%%%
$%%%%%%%%%%%%%%%%%%%%%%%%%%%              %%%%%%%%%%%%%%%%
$%%%%%%%%%%%%%%%%%%%%%%%%%%%%%%%%%%%%%%%%%%%%%%%%%%%%
*ELEMENT_BEAM
$      EID       PID        N1        N2        N3       RT1       RR1       RT2       RR2     LOCAL
     XXXX      XXXX      XXXX      XXXX      XXXX      XXXX      XXXX      XXXX      XXXX      XXXX
$
$%%%%%%%%%%%%%%%%%%%%%%%%%%%%%%%%%%%%%%%%%%%%%%
$%%%%%%%%%%%%%%%%%%%%%%%%%%%              %%%%%%%%%%%%%%%
$%%%%%%%%%%%%%%%%%%%%%%%%%%%   BEAM ELEMENTS   %%%%%%%%
$%%%%%%%%%%%%%%%%%%%%%%%%%%%              %%%%%%%%%%%%%%%%
$%%%%%%%%%%%%%%%%%%%%%%%%%%%%%%%%%%%%%%%%%%%%%%
$---+----1----+----2----+----3----+----4----+----5----+----6----+----7----+----8
$                      PART CARDS (Beam Elements)
$---+----1----+----2----+----3----+----4----+----5----+----6----+----7----+----8
*PART
$HEADING: 15M
25M
$       PID       SID       MID     EOSID      HGID      GRAV    ADPOPT      TMID
         25      2525        11
*PART
$HEADING: 15M
20M
$       PID       SID       MID     EOSID      HGID      GRAV    ADPOPT      TMID
         20      2020        11
*PART
$HEADING: 15M
15M
$       PID       SID       MID     EOSID      HGID      GRAV    ADPOPT      TMID
         15        11        11
$
*PART
$HEADING: 10M
10M
$       PID       SID       MID     EOSID      HGID      GRAV    ADPOPT      TMID
       1010        12        22
$
*PART
```

```
$HEADING: 6M
6M
$        PID       SID       MID     EOSID      HGID      GRAV    ADPOPT      TMID
          66                  13        33
$
$%%%%%%%%%%%%%%%%%%%%%%%%%%%%%%%%%%%%%%%%%%
$---+----1----+----2----+----3----+----4----+----5----+----6----+----7----+----8
$                        SECTION CARDS (Beam Elements)
$---+----1----+----2----+----3----+----4----+----5----+----6----+----7----+----8
*SECTION_BEAM_TITLE
25M
$      SECID    ELFORM      SHRF    QR/IRID       CST     SCOOR       NSM
        2525         1       1.0        2.0       1.0       0.0       0.0
$       TS1       TS2       TT1       TT2     NSLOC     NTLOC
        25.2      25.2       0.0       0.0       0.0       0.0
*SECTION_BEAM_TITLE
20M
$      SECID    ELFORM      SHRF    QR/IRID       CST     SCOOR       NSM
        2020         1       1.0        2.0       1.0       0.0       0.0
$       TS1       TS2       TT1       TT2     NSLOC     NTLOC
        19.5                19.5       0.0       0.0       0.0       0.0
*SECTION_BEAM_TITLE
15M
$      SECID    ELFORM      SHRF    QR/IRID       CST     SCOOR       NSM
          11         1       1.0        2.0       1.0       0.0       0.0
$       TS1       TS2       TT1       TT2     NSLOC     NTLOC
          16                  16       0.0       0.0       0.0       0.0
*SECTION_BEAM_TITLE
10M
$      SECID    ELFORM      SHRF    QR/IRID       CST     SCOOR       NSM
          12         1       1.0        2.0       1.0       0.0       0.0
$       TS1       TS2       TT1       TT2     NSLOC     NTLOC
        11.3      11.3       0.0       0.0       0.0       0.0
*SECTION_BEAM_TITLE
6M
$      SECID    ELFORM      SHRF    QR/IRID       CST     SCOOR       NSM
          13         1       1.0        2.0       1.0       0.0       0.0
$       TS1       TS2       TT1       TT2     NSLOC     NTLOC
        6.25      6.25       0.0       0.0       0.0       0.0
$%%%%%%%%%%%%%%%%%%%%%%%%%%%%%%%%%%%%%%%%%%
$---+----1----+----2----+----3----+----4----+----5----+----6----+----7----+----8
$                        MATERIAL CARDS (Beam Elements)
$---+----1----+----2----+----3----+----4----+----5----+----6----+----7----+----8
$ STEEL REBAR
*MAT_PIECEWISE_LINEAR_PLASTICITY
$       MID        RO         E        PR      SIGY      ETAN      FAIL      TDEL
          11    7.8E-09    2.0E+5       0.3     400.0    2000.0       .04       0.0
$         C         P      LCSS      LCSR        VP
        0.0       0.0       0.0       0.0       0.0
$      EPS1      EPS2      EPS3      EPS4      EPS5      EPS6      EPS7      EPS8

$       ES1       ES2       ES3       ES4       ES5       ES6       ES7       ES8

$---+----1----+----2----+----3----+----4----+----5----+----6----+----7----+----8
$                        MATERIAL CARDS (Beam Elements)
$---+----1----+----2----+----3----+----4----+----5----+----6----+----7----+----8
$ STEEL REBAR
*MAT_PIECEWISE_LINEAR_PLASTICITY
$       MID        RO         E        PR      SIGY      ETAN      FAIL      TDEL
          22    7.8E-09    2.0E+5       0.3     430.0    2000.0       .04       0.0
$         C         P      LCSS      LCSR        VP
        0.0       0.0       0.0       0.0       0.0
$      EPS1      EPS2      EPS3      EPS4      EPS5      EPS6      EPS7      EPS8

$       ES1       ES2       ES3       ES4       ES5       ES6       ES7       ES8

$---+----1----+----2----+----3----+----4----+----5----+----6----+----7----+----8
$                        MATERIAL CARDS (Beam Elements)
$---+----1----+----2----+----3----+----4----+----5----+----6----+----7----+----8
$ STEEL REBAR
*MAT_PIECEWISE_LINEAR_PLASTICITY
$       MID        RO         E        PR      SIGY      ETAN      FAIL      TDEL
          33    7.8E-09    2.0E+5       0.3     530.0    1666.0       .06       0.0
$         C         P      LCSS      LCSR        VP
        0.0       0.0       0.0       0.0       0.0
$      EPS1      EPS2      EPS3      EPS4      EPS5      EPS6      EPS7      EPS8
```

```
$          ES1          ES2          ES3          ES4          ES5          ES6          ES7          ES8

$%%%%%%%%%%%%%%%%%%%%%%%%%%%%%%%%%%%%%%%%%
$---+----1----+----2----+---3----+----4----+----5----+----6----+----7----+----8
$                    (1) Define Contact Card (pile and cylinder)
$---+----1----+----2----+---3----+----4----+----5----+----6----+----7----+----8
*CONTACT_AUTOMATIC_NODES_TO_SURFACE_TITLE
$      cID    TITLE
        1     PILE-CYLINDER
$     SSID      MSID     SSTYP     MSTYP    SBOXID    MBOXID       SPR       MPR
         9         8         3         3         0                   1         1
$       FS        FD        DC        VC       VDC    PENCHK        BT        DT
      0.75      0.75       0.0       0.0       0.0         0  0.00E+00  1.00E+20
$      SFS       SFM       SST       MST      SFST      SFMT       FSF       VSF
       1.0       1.0
$%%%%%%%%%%%%%%%%%%%%%%%%%%%%%%%%%%%%%%%%%%%
$---+----1----+----2----+---3----+----4----+----5----+----6----+----7----+----8
$                    (2) Define Contact Card (pile and Plate)
$---+----1----+----2----+---3----+----4----+----5----+----6----+----7----+----8
*CONTACT_AUTOMATIC_NODES_TO_SURFACE_TITLE
$      cID    TITLE
        2     PILE-PLATE
$     SSID      MSID     SSTYP     MSTYP    SBOXID    MBOXID       SPR       MPR
         9         4         3         3         0                   1         1
$       FS        FD        DC        VC       VDC    PENCHK        BT        DT
      0.75      0.75       0.0       0.0       0.0         0  0.00E+00  1.00E+20
$      SFS       SFM       SST       MST      SFST      SFMT       FSF       VSF
       1.0       1.0
$---+----1----+----2----+---3----+----4----+----5----+----6----+----7----+----8
$                    (3) Define Contact Card (plate and concrete hex)
$---+----1----+----2----+---3----+----4----+----5----+----6----+----7----+----8
*CONTACT_AUTOMATIC_NODES_TO_SURFACE_TITLE
$      cID    TITLE
        3     PLATE-CONCRETE
$     SSID      MSID     SSTYP     MSTYP    SBOXID    MBOXID       SPR       MPR
         4         5         3         3         0                   1         1
$       FS        FD        DC        VC       VDC    PENCHK        BT        DT
      0.45      0.45       0.0       0.0       0.0         0  0.00E+00  1.00E+20
$      SFS       SFM       SST       MST      SFST      SFMT       FSF       VSF
       1.0       1.0
$---+----1----+----2----+---3----+----4----+----5----+----6----+----7----+----8
$                    (4) Define Contact Card(cylinder and concrete )
$---+----1----+----2----+---3----+----4----+----5----+----6----+----7----+----8
*CONTACT_AUTOMATIC_NODES_TO_SURFACE_TITLE
$      cID    TITLE
        4     CYLINDER FRICTION
$     SSID      MSID     SSTYP     MSTYP    SBOXID    MBOXID       SPR       MPR
         8         5         3         3         0                   1         1
$       FS        FD        DC        VC       VDC    PENCHK        BT        DT
      0.45      0.45       0.0       0.0       0.0         0  0.00E+00  1.00E+20
$      SFS       SFM       SST       MST      SFST      SFMT       FSF       VSF
       1.0       1.0
$%%%%%%%%%%%%%%%%%%%%%%%%%%%%%%%%%%%%%%%%%%%
$---+----1----+----2----+---3----+----4----+----5----+----6----+----7----+----8
$                    (5) Define Contact Card(pile and concrete )
$---+----1----+----2----+---3----+----4----+----5----+----6----+----7----+----8
*CONTACT_AUTOMATIC_NODES_TO_SURFACE_TITLE
$      cID    TITLE
        5     PILE FRICTION
$     SSID      MSID     SSTYP     MSTYP    SBOXID    MBOXID       SPR       MPR
         9         5         3         3         0                   1         1
$       FS        FD        DC        VC       VDC    PENCHK        BT        DT
      0.45      0.45       0.0       0.0      40.0         0  0.00E+00  1.00E+20
$      SFS       SFM       SST       MST      SFST      SFMT       FSF       VSF
       1.0       1.0
$%%%%%%%%%%%%%%%%%%%%%%%%%%%%%%%%%%%%%%%%%%%
$---+----1----+----2----+---3----+----4----+----5----+----6----+----7----+----8
$                    (6) Define Contact Card(Bolt and concrete )
$---+----1----+----2----+---3----+----4----+----5----+----6----+----7----+----8
*CONTACT_AUTOMATIC_NODES_TO_SURFACE_TITLE
$      cID    TITLE
        6     BOLT-CONCRETE
$     SSID      MSID     SSTYP     MSTYP    SBOXID    MBOXID       SPR       MPR
        14         5         3         3         0                   1         1
$       FS        FD        DC        VC       VDC    PENCHK        BT        DT
      0.45      0.45       0.0       0.0      40.0         0  0.00E+00  1.00E+20
$      SFS       SFM       SST       MST      SFST      SFMT       FSF       VSF
```

```
          1.0          1.0
$
$%%%%%%%%%%%%%%%%%%%%%%%%%%%%%%%%%%%%%%%%%%%
$---+----1----+----2----+---3----+----4----+----5----+----6----+----7----+----8
$                   (7) Define Contact Card(Bolt and Cylinder)
$---+----1----+----2----+---3----+----4----+----5----+----6----+----7----+----8
*CONTACT_AUTOMATIC_NODES_TO_SURFACE_TITLE
$      cID     TITLE
         7     CYLINDER-BOLT
$     SSID      MSID     SSTYP     MSTYP    SBOXID    MBOXID       SPR       MPR
        14         8         3         3         0                   1         1
$       FS        FD        DC        VC       VDC    PENCHK        BT        DT
      0.75      0.75       0.0       0.0       0.0         0  0.00E+00  1.00E+20
$      SFS       SFM       SST       MST      SFST      SFMT       FSF       VSF
       1.0       1.0
$
$%%%%%%%%%%%%%%%%%%%%%%%%%%%%%%%%%%%%%%%%%%%
$---+----1----+----2----+---3----+----4----+----5----+----6----+----7----+----8
$                     (8) Define Contact Card(Bolt and Pile)
$---+----1----+----2----+---3----+----4----+----5----+----6----+----7----+----8
*CONTACT_AUTOMATIC_NODES_TO_SURFACE_TITLE
$      cID     TITLE
         8     BOLT-PILE
$     SSID      MSID     SSTYP     MSTYP    SBOXID    MBOXID       SPR       MPR
        14         9         3         3         0                   1         1
$       FS        FD        DC        VC       VDC    PENCHK        BT        DT
      0.75      0.75       0.0       0.0       0.0         0  0.00E+00  1.00E+20
$      SFS       SFM       SST       MST      SFST      SFMT       FSF       VSF
       1.0       1.0
$
*END
```

Table C- 2 Keyword Input data for beams DB120, DB130 and DB140

```
$$$$$$$$$$$$$$$$$$$$$$$$$$$$$$$$$$$$$$$$$$$$$$$$$$$$$$$$$$$$$$$$$$$$$$$$$$$$$$$$$$$$$
$$$$$$$$$$$$$$$$$$$$$$$$$$$$$$$$$$$$$$$$$$$$$$$$$$$$$$$$$$$$$$$$$$$$$$$$$$$$$$$$$$$$$
*KEYWORD 360000000 ncpu=6
$    PROJECT :
$     UNITS : mm, N, Sec
$---+----1----+----2----+----3----+----4----+----5----+----6----+----7----+----8
$                          TITLE CARD
$---+----1----+----2----+----3----+----4----+----5----+----6----+----7----+----8
*TITLE
DB120, DB130, and DB140
$---+----1----+----2----+----3----+----4----+----5----+----6----+----7----+----8
$                        CONTROL CARDS
$---+----1----+----2----+----3----+----4----+----5----+----6----+----7----+----8
*CONTROL_ACCURACY
$      OSU       INN
         1         1
*CONTROL_TERMINATION
$   ENDTIM    ENDCYC    DTMIN    ENDNEG    ENDMAS
    5.000         0 0.000000  0.000000
*CONTROL_TIMESTEP
$   DTINIT      SCFT      ISDO    TSLIMT      DTMS      LCTM     ERODE     MS1ST
     .000      .670         0
*CONTROL_ENERGY
$     HGEN      RWEN    SLNTEN     RYLEN
         2         2         2         2
*HOURGLASS
$     HGID       IHQ        QM
         1         4      0.03
$---+----1----+----2----+---3----+----4----+----5----+----6----+----7----+----8
$             () Boundary Prescribed Motion at set of nodes Card
$---+----1----+----2----+---3----+----4----+----5----+----6----+----7----+----8
*BOUNDARY_PRESCRIBED_MOTION_SET
$     NSID       DOF       VAD      LCID        SF       VID     DEATH     BIRTH
         1         2         0         1       1.0         0  1.00E+28       0.0
*DEFINE_CURVE
$     LCID      SIDR       SFA       SFO      OFFA      OFFO    DATTYP
         1         0         1         1         0         0         0
$                A1                  O1
             0.000                0.00
```

```
                  1.000                    -2.00
                  5.001                    -2.00
$---+----1----+----2----+----3----+----4----+----5----+----6----+----7----+----8
$                   DATABASE CONTROL CARDS FOR ASCII FILE
$---+----1----+----2----+----3----+----4----+----5----+----6----+----7----+----8
*DATABASE_GLSTAT
$         DT
1.000e-002
$
*DATABASE_MATSUM
$         DT
1.000e-002
$
*DATABASE_RCFORC
$         DT
1.000e-002
*DATABASE_NCFORC
$         DT
1.000e-002
*DATABASE_BINARY_INTFOR
$         DT
1.000e-002
$
*DATABASE_NODFOR
$         DT     BINARY
1.000e-002         3
*DATABASE_NODOUT
$         DT     BINARY
1.000e-002
*DATABASE_elout
$         DT     BINARY
1.000e-002
$
$---+----1----+----2----+----3----+----4----+----5----+----6----+----7----+----8
$              (5) DATABASE CONTROL CARDS FOR BINARY FILE
$---+----1----+----2----+----3----+----4----+----5----+----6----+----7----+----8
*DATABASE_BINARY_D3PLOT
$  DT/CYCL      LCDT    NOBEAM
1.000e-002
*DATABASE_BINARY_D3THDT
$  DT/CYCL      LCDT    NOBEAM
1.000e-002
$---+----1----+----2----+----3----+----4----+----5----+----6----+----7----+----8
$                           PART CARDS
$---+----1----+----2----+----3----+----4----+----5----+----6----+----7----+----8
*PART
$HEADING
Concrete
$        PID        SID        MID      EOSID       HGID       GRAV     ADPOPT       TMID
           3          1        111                     1
$
*PART
$HEADING
Plate
$        PID        SID        MID      EOSID       HGID       GRAV     ADPOPT       TMID
           2          2        999                     1
$
$%%%%%%%%%%%%%%%%%%%%%%%%%%%%%%%%%%%%%%%%%%%%%%%%%%%%%%%%%%%%%%%%%%%%%%%%%%%%%%%%%%
$---+----1----+----2----+----3----+----4----+----5----+----6----+----7----+----8
$                      MATERIAL CARDS (Cylinder)
$---+----1----+----2----+----3----+----4----+----5----+----6----+----7----+----8
$ STEEL REBAR
*MAT_PIECEWISE_LINEAR_PLASTICITY
$        MID         RO          E         PR       SIGY       ETAN       FAIL       TDEL
         666    7.8E-06      2.0E+5        0.3       344.      1700.        .30        0.0
$          C          P       LCSS       LCSR         VP
         0.0        0.0        0.0        0.0        0.0
$       EPS1       EPS2       EPS3       EPS4       EPS5       EPS6       EPS7       EPS8

$        ES1        ES2        ES3        ES4        ES5        ES6        ES7        ES8

$%%%%%%%%%%%%%%%%%%%%%%%%%%%%%%%%%%%%%%%%%%%%%%%%%%%%%%%%%%%%%%%%%%%%%%%%%%%%%%%%%%
$%%%%%%%%%%%%%%%%%%%%%%%%%%%%%%%%%%%%%%%%%%%%%%%%%%%%%%%%%%%%%%%%%%%%%%%%%%%%%%%%%%
$---+----1----+----2----+----3----+----4----+----5----+----6----+----7----+----8
$                        MATERIAL CARDS (Plate)
$---+----1----+----2----+----3----+----4----+----5----+----6----+----7----+----8
$ STEEL REBAR
```

542

```
*MAT_PIECEWISE_LINEAR_PLASTICITY
$       MID        RO         E        PR      SIGY      ETAN      FAIL      TDEL
        999    7.8E-03    2.0E+5       0.3       344     1700.       .30       0.0
$         C         P      LCSS      LCSR        VP
        0.0       0.0       0.0       0.0       0.0
$      EPS1      EPS2      EPS3      EPS4      EPS5      EPS6      EPS7      EPS8

$       ES1       ES2       ES3       ES4       ES5       ES6       ES7       ES8

$%%%%%%%%%%%%%%%%%%%%%%%%%%%%%%%%%%%%%%%%%%%%%%%%%%%%%%%%%%%%%%%%%%%%%%%%%%%%%%%%%
$$$$$$$$$$$$$$$$$$$$$$$$$$$$$$$$$$$$$$$$$$$$$$$$$$$$$$$$$$$$$$$$$$$$$$$$$$$$$$$$$$$
$---+----1----+----2----+----3----+----4----+----5----+----6----+----7----+----8
$                        Default mat 159 concrete
$---+----1----+----2----+----3----+----4----+----5----+----6----+----7----+----8
*MAT_CSCM_CONCRETE
$       MID        RO     NPLOT     INCRE     IRATE     ERODE     RECOV   ITERTRC
          1   2.32E-06         1                   0         1         1         1
$      PRED

$       FPC      DAGG     UNITS
       21.0        20         2
$
$$$$$$$$$$$$$$$$$$$$$$$$$$$$$$$$$$$$$$$$$$$$$$$$$$$$$$$$$$$$$$$$$$$$$$$$$$$$$$$$$$$
Concrete Material Model for DB140
$$$$$$$$$$$$$$$$$$$$$$$$$$$$$$$$$$$$$$$$$$$$$$$$$$$$$$$$$$$$$$$$$$$$$$$$$$$$$$$$$$$
*MAT_CONCRETE_DAMAGE_REL3
$       MID        RO        PR
        111    2.4E-09
$        FT        A0        A1        A2        B1     OMEGA       A1F
       3.70       -38
$   sLAMBDA      NOUT     EDROP     RSIZE       UCF    LCRate  LocWidth      NPTS
                    2              3.94e-02       145         7
$   LAMBD01   LAMBD02   LAMBD03   LAMBD04   LAMBD05   LAMBD06   LAMBD07   LAMBD08

$   LAMBD09  LAMBD010  LAMBD011  LAMBD012  LAMBD013        B3       A0Y       A1Y

$     ETA01     ETA02     ETA03     ETA04     ETA05     ETA06     ETA07     ETA08

$     ETA09    ETA010    ETA011    ETA012    ETA013        B2       A2F       A2Y
                                                        2.20
$$$$$$$$$$$$$$$$$$$$$$$$$$$$$$$$$$$$$$$$$$$$$$$$$$$$$$$$$$$$$$$$$$$$$$$$$$$$$$$$$$$$$$
Concrete Material Model for DB130
$$$$$$$$$$$$$$$$$$$$$$$$$$$$$$$$$$$$$$$$$$$$$$$$$$$$$$$$$$$$$$$$$$$$$$$$$$$$$$$$$$$
*MAT_CONCRETE_DAMAGE_REL3
$       MID        RO        PR
        112    2.4E-09
$        FT        A0        A1        A2        B1     OMEGA       A1F
       3.39       -32
$   sLAMBDA      NOUT     EDROP     RSIZE       UCF    LCRate  LocWidth      NPTS
                    2              3.94e-02       145         7
$   LAMBD01   LAMBD02   LAMBD03   LAMBD04   LAMBD05   LAMBD06   LAMBD07   LAMBD08

$   LAMBD09  LAMBD010  LAMBD011  LAMBD012  LAMBD013        B3       A0Y       A1Y

$     ETA01     ETA02     ETA03     ETA04     ETA05     ETA06     ETA07     ETA08

$     ETA09    ETA010    ETA011    ETA012    ETA013        B2       A2F       A2Y
                                                        1.65
$$$$$$$$$$$$$$$$$$$$$$$$$$$$$$$$$$$$$$$$$$$$$$$$$$$$$$$$$$$$$$$$$$$$$$$$$$$$$$$$$$$$$$
Concrete Material Model for DB120
$$$$$$$$$$$$$$$$$$$$$$$$$$$$$$$$$$$$$$$$$$$$$$$$$$$$$$$$$$$$$$$$$$$$$$$$$$$$$$$$$$$
*MAT_CONCRETE_DAMAGE_REL3
$       MID        RO        PR
        113    2.4E-09
$        FT        A0        A1        A2        B1     OMEGA       A1F
       2.75       -21
$   sLAMBDA      NOUT     EDROP     RSIZE       UCF    LCRate  LocWidth      NPTS
                    2              3.94e-02       145         7
$   LAMBD01   LAMBD02   LAMBD03   LAMBD04   LAMBD05   LAMBD06   LAMBD07   LAMBD08

$   LAMBD09  LAMBD010  LAMBD011  LAMBD012  LAMBD013        B3       A0Y       A1Y

$     ETA01     ETA02     ETA03     ETA04     ETA05     ETA06     ETA07     ETA08

$     ETA09    ETA010    ETA011    ETA012    ETA013        B2       A2F       A2Y
                                                        1.55
$$$$$$$$$$$$$$$$$$$$$$$$$$$$$$$$$$$$$$$$$$$$$$$$$$$$$$$$$$$$$$$$$$$$$$$$$$$$$$$$$$$$$$
```

```
$---+----1----+----2----+----3----+----4----+----5----+----6----+----7----+----8
$                   Loading Rate for Mat_072 (MAT_CONCRETE_DAMAGE_REL3)
$---+----1----+----2----+----3----+----4----+----5----+----6----+----7----+----8
*DEFINE_CURVE
$      LCID      SIDR       SFA       SFO      OFFA      OFFO    DATTYP
          7         0       1.0       1.0       0.0       0.0         0
$               A1                  O1
            -30000.0                 1.0
              -300.0                 1.0
              -100.0                 1.0
               -30.0                 1.0
               -10.0                 1.0
                -3.0                 1.0
                -1.0                 1.0
               -0.10                 1.0
              -0.010                 1.0
             -0.0010                 1.0
            -0.00010                 1.0
           -0.000010                 1.0
                 0.0                 1.0
            0.000010                 1.0
             0.00010                 1.0
              0.0010                 1.0
               0.010                 1.0
                0.10                 1.0
                 1.0                 1.0
                 3.0                 1.0
                10.0                 1.0
                30.0                 1.0
               100.0                 1.0
               300.0                 1.0
             30000.0                 1.0
$---+----1----+----2----+----3----+----4----+----5----+----6----+----7----+----8
$                             SECTION CARDS
$---+----1----+----2----+----3----+----4----+----5----+----6----+----7----+----8
$
*SECTION_SOLID_TITLE
Concrete Hexa
$     SECID    ELFORM       AET
          1         1         0
*SECTION_SOLID_TITLE
Steel hexa
$     SECID    ELFORM       AET
          2         1         0
$
$
$---+----1----+----2----+----3----+----4----+----5----+----6----+----7----+----8
$                           Defining point sets
$---+----1----+----2----+----3----+----4----+----5----+----6----+----7----+----8
*SET_NODE_LIST
$Applied displacement
$       SID       DA1       DA2       DA3       DA4
          1
$      NID1      NID2      NID3      NID4      NID5      NID6      NID7      NID8
       XXXX      XXXX      XXXX      XXXX      XXXX      XXXX      XXXX      XXXX
$
$
*SET_NODE_LIST
$y=0
$       SID       DA1       DA2       DA3       DA4
          2
$      NID1      NID2      NID3      NID4      NID5      NID6      NID7      NID8
       XXXX      XXXX      XXXX      XXXX      XXXX      XXXX      XXXX      XXXX
$
$
*SET_NODE_LIST
$y=x=0
$       SID       DA1       DA2       DA3       DA4
          3
$      NID1      NID2      NID3      NID4      NID5      NID6      NID7      NID8
       XXXX      XXXX      XXXX      XXXX      XXXX      XXXX      XXXX      XXXX
$
$
$
$
$
$
```

544

```
$$$$
$$$$$$$$$$$$$$$$$$$$$$$$$$$$$$$$$$$$$$$$$$$$$$$$$$$$$$$$$$$$$$$$$$$$$$$$$$$$$$
$$$ Printing FORCES IN BEAM ELEMENTS FOR DESIRED BEAM ELEMENTS           $$$$
$$$$$$$$$$$$$$$$$$$$$$$$$$$$$$$$$$$$$$$$$$$$$$$$$$$$$$$$$$$$$$$$$$$$$$$$$$$$$$
$*DATABASE_HISTORY_BEAM
$        ID1       ID2       ID3       ID4       ID5       ID6       ID7       ID8
$          4     19203       378       302       445
$$$$$$$$$$$$$$$$$$$$$$$$$$$$$$$$$$$$$$$$$$$$$$$$$$$$$$$$$$$$$$$$$$$$$$$$$$$$$$$
$$$ Printing reactions of points where prescribed displacements are applied$$$$
$$$$$$$$$$$$$$$$$$$$$$$$$$$$$$$$$$$$$$$$$$$$$$$$$$$$$$$$$$$$$$$$$$$$$$$$$$$$$$$
$
$$$$$$$$$$$$$$$$$$$$$$$$$$$$$$$$$$$$$$$$$$$$$$$$$$$$$$$$$$$$$$$$$$$$$$$$$$$$$$$
$
$*database_history_node
$       NID1      NID2
$
$$$$$$$$$$ Printing STRESSES IN SOLID ELEMENTS   $$$$$$$$$$$$$$$$$$$$$$$$$$$$$$$$
$$$$$$$$$$$$$$$$$$$$$$$$$$$$$$$$$$$$$$$$$$$$$$$$$$$$$$$$$$$$$$$$$$$$$$$$$$$$$$$
$*database_history_SOLID
$       NID1      NID2
$
$$$$
$$$$$$$$$$$$$$$$$$$$$$$$$$$$$$$$$$$$$$$$$$$$$$$$$$$$$$$$$$$$$$$$$$$$$$$$$$$$$$$
$$$ Printing reactions of points where prescribed displacements are applied$$$$
$$$$$$$$$$$$$$$$$$$$$$$$$$$$$$$$$$$$$$$$$$$$$$$$$$$$$$$$$$$$$$$$$$$$$$$$$$$$$$$
*DATABASE_NODAL_FORCE_GROUP
$      NSID       CID
          1
          2
          3
$$$$$$$$$$$$$$$$$$$$$$$$$$$$$$$$$$$$$$$$$$$$$$$$$$$$$$$$$$$$$$$$$$$$$$$$$$$$$$$$$
$$$$$$$$                                                           $$$$$$$$$$$
$$$$$$$$                                                           $$$$$$$$$$$
$$$$$$$$                                                           $$$$$$$$$$$
$$$$$$$$ Applying sliding boundary conditions on the edges of the slice $$$$$$$$$$$
$$$$$$$$                                                           $$$$$$$$$$$
$$$$$$$$                                                           $$$$$$$$$$$
$$$$$$$$                                                           $$$$$$$$$$$
$$$$$$$$$$$$$$$$$$$$$$$$$$$$$$$$$$$$$$$$$$$$$$$$$$$$$$$$$$$$$$$$$$$$$$$$$$$$$$$$$
$FACE1-Boundary Condition, symetric (IN THE X-Y and z-y  PLANES)
*BOUNDARY_SPC_SET
$      NSID       CID      DOFX      DOFY      DOFZ     DOFRX     DOFRY     DOFRZ
          2         0         0         1         0         0         0         0
$FACE2-Boundary Conditions symetric (In the z-y plane) x=0
*BOUNDARY_SPC_SET
$      NSID       CID      DOFX      DOFY      DOFZ     DOFRX     DOFRY     DOFRZ
          3         0         0         1         0         0         0         0
$---+----1----+----2----+----3----+----4----+----5----+----6----+----7----+----8
$                    (8) NODAL POINT CARDS
$---+----1----+----2----+----3----+----4----+----5----+----6----+----7----+----8
*NODE
$    NID               X               Y               Z        TC        RC
     XXXX      XXXX      XXXX      XXXX      XXXX      XXXX      XXXX      XXXX
$
$---+----1----+----2----+----3----+----4----+----5----+----6----+----7----+----8
$                    Solid ELEMENT CARDS
$---+----1----+----2----+----3----+----4----+----5----+----6----+----7----+----8
*ELEMENT_SOLID
$    EID       PID      NID1      NID2      NID3      NID4      NID5      NID6      NID7      NID8
     XXXX      XXXX      XXXX      XXXX      XXXX      XXXX      XXXX      XXXX
$
$%%%%%%%%%%%%%%%%%%%%%%%%%%%%%%%%%%%%%%%%%%%%%%%%%%%%%%%%%%%%%%%%%%%%%%%%%%%%%%%%
$%%%%%%%%%%%%%%%%%%%%%%%%%%%%%%%%%%%%%%%%%%%%%%%%%%%%%%%%%%%%%%%%%%%%%%%%%%%%%%%%
$%%%%%%%%%%%%%                                   %%%%%%%%%%%%%%%%%%%%%%%%%%%%
$%%%%%%%%%%%%%%             Beam Elements Card    %%%%%%%%%%%%%%%%%%%%%%%%%%%%
$%%%%%%%%%%%%%                                   %%%%%%%%%%%%%%%%%%%%%%%%%%%%
$%%%%%%%%%%%%%%%%%%%%%%%%%%%%%%%%%%%%%%%%%%%%%%%%%%%%%%%%%%%%%%%%%%%%%%%%%%%%%%%%
*ELEMENT_BEAM
$    EID       PID        N1        N2        N3       RT1       RR1       RT2       RR2     LOCAL
     XXXX      XXXX      XXXX      XXXX      XXXX      XXXX      XXXX      XXXX
$
$%%%%%%%%%%%%%%%%%%%%%%%%%%%%%%%%%%%%%%%%%%%%%%%%%%%%%%%%%%%%%%%%%%%%%%%%%%%%%%%%
$%%%%%%%%%%%%%%%%%%%%%%%%%%%           %%%%%%%%%%%%%%%%%%%%%%%%%%%%%%%%%%%%%%%%
$%%%%%%%%%%%%%%%%%%%%%%%%%%%%%%   BEAM ELEMENTS   %%%%%%%%%%%%%%%%%%%%%%%%%%%%
$%%%%%%%%%%%%%%%%%%%%%%%%%%%           %%%%%%%%%%%%%%%%%%%%%%%%%%%%%%%%%%%%%%%%
$%%%%%%%%%%%%%%%%%%%%%%%%%%%%%%%%%%%%%%%%%%%%%%%%%%%%%%%%%%%%%%%%%%%%%%%%%%%%%%%%
$---+----1----+----2----+----3----+----4----+----5----+----6----+----7----+----8
```

```
$                              PART CARDS (Beam Elements)
$---+----1----+----2----+----3----+----4----+----5----+----6----+----7----+----8
*PART
$HEADING: 30M
30M
$       PID       SID       MID     EOSID      HGID      GRAV    ADPOPT      TMID
          1        11        11
$%%%%%%%%%%%%%%%%%%%%%%%%%%%%%%%%%%%%%%%%%%%%%%%%%%%%%%%%%%%%%%%%%%%%%%%%%%%%%%%%%%
$---+----1----+----2----+----3----+----4----+----5----+----6----+----7----+----8
$                            SECTION CARDS (Beam Elements)
$---+----1----+----2----+----3----+----4----+----5----+----6----+----7----+----8
*SECTION_BEAM_TITLE
30M
$     SECID    ELFORM      SHRF    QR/IRID       CST     SCOOR       NSM
         11         1       1.0       2.0       1.0       0.0       0.0
$       TS1       TS2       TT1       TT2     NSLOC     NTLOC
         30                  30       0.0       0.0       0.0       0.0
$%%%%%%%%%%%%%%%%%%%%%%%%%%%%%%%%%%%%%%%%%%%%%%%%%%%%%%%%%%%%%%%%%%%%%%%%%%%%%%%%%%
$---+----1----+----2----+----3----+----4----+----5----+----6----+----7----+----8
$                           MATERIAL CARDS (Beam Elements)
$---+----1----+----2----+----3----+----4----+----5----+----6----+----7----+----8
$ STEEL REBAR
*MAT_PIECEWISE_LINEAR_PLASTICITY
$       MID        RO         E        PR      SIGY      ETAN      FAIL      TDEL
         11   7.8E-06    2.0E+5       0.3     550.0    5000.0       .30       0.0
$         C         P      LCSS      LCSR        VP
        0.0       0.0       0.0       0.0       0.0
$      EPS1      EPS2      EPS3      EPS4      EPS5      EPS6      EPS7      EPS8

$       ES1       ES2       ES3       ES4       ES5       ES6       ES7       ES8

$%%%%%%%%%%%%%%%%%%%%%%%%%%%%%%%%%%%%%%%%%%%%%%%%%%%%%%%%%%%%%%%%%%%%%%%%%%%%%%%%%%
$---+----1----+----2----+---3----+----4----+----5----+----6----+----7----+----8
$                     () Define Contact Card (plate and concrete hex)
$---+----1----+----2----+----3----+----4----+----5----+----6----+----7----+----8
*CONTACT_AUTOMATIC_SURFACE_TO_SURFACE
$      SSID      MSID     SSTYP     MSTYP    SBOXID    MBOXID       SPR       MPR
          2         3         3         3         0                   1         1
$        FS        FD        DC        VC       VDC    PENCHK        BT        DT
       0.45      0.45       0.0       0.0       0.0         0  0.00E+00  1.00E+20
$       SFS       SFM       SST       MST      SFST      SFMT       FSF       VSF
        1.0       1.0
$      NFLS      SFLS    TBLCID    THKOFF
       1.61      1.61         0         0
$
*END
```

APPENDIX D

THE REST OF THE FINITE ELEMENT CALIBRATION DATA

Due to the large data involved in the finite element calibration with the experimentally tested beams, only small part of the comparison between the predicted finite elements modeling data with the experimentally recorded data are presented in Chapters 4 and 7 in this thesis. Thus, the rest of these data will be presented for the connection behaviour under both tension and compression loading.

As noted in chapters 4 and 7, the finite element models were verified through comparing their predictions with the experimental observations using specific data. These are:

- Load-displacement behaviour including: breakout cracking and ultimate loads and corresponding displacements as well as connection stiffness.
- Longitudinal reinforcement strains for rebars next to the edge of the beam cross-section (denoted outer longitudinal reinforcement), and rebars inside the beam (denoted inner longitudinal reinforcement).
- Strain for stirrups next to the pile shaft (inner stirrups) and farther from the pile shaft (outer stirrups). For 4 branches stirrups, strain in exterior and interior branches for outer and inner stirrups was monitored.
- The pile cap's plate strain.
- The failure mode and the crack pattern.

These data will be presented from Figure D-1 to D-86. The figures demonstrate clearly the accuracy of the verified 3d-nonlinear finite element models in simulating the connection behaviour. Moreover, they confirm that these finite element models is ready to be used in a full analytical parametric study.

D.1 Verification of the finite element model and model calibration for the connections subjected to tension loading

D.1.1 Beam T1
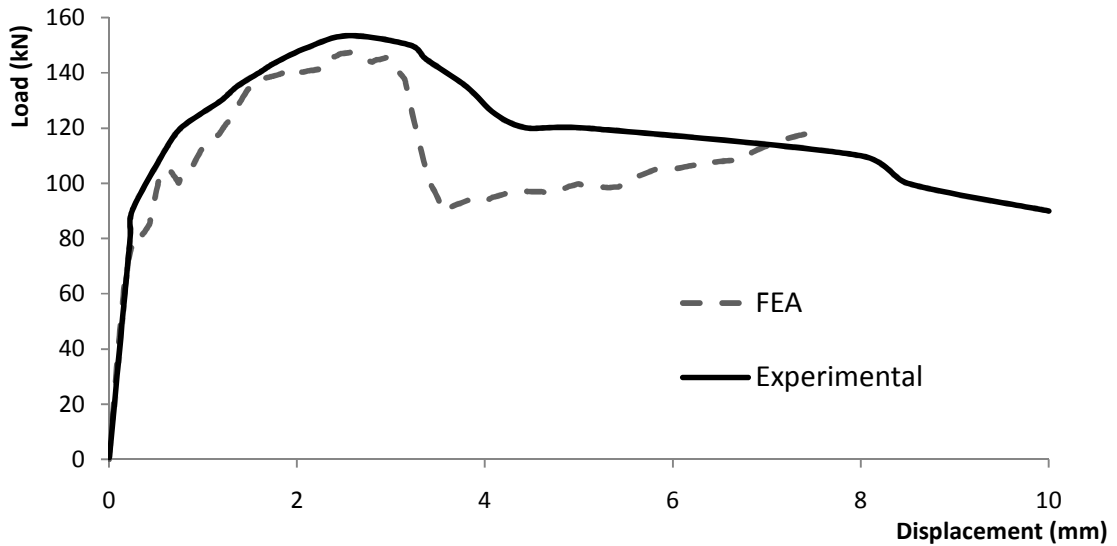
Figure D- 1 Load mid-span displacement relationship verification for beam T1
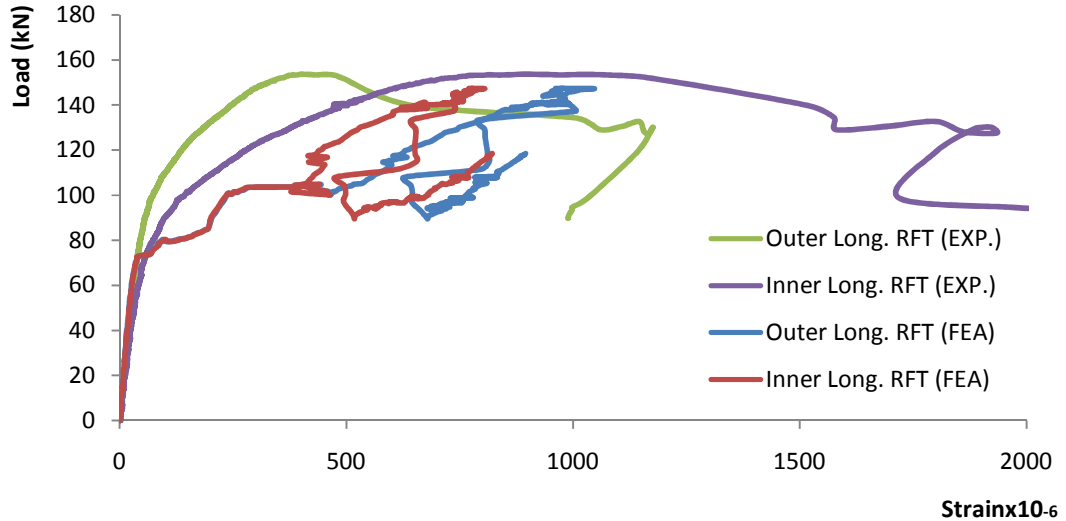
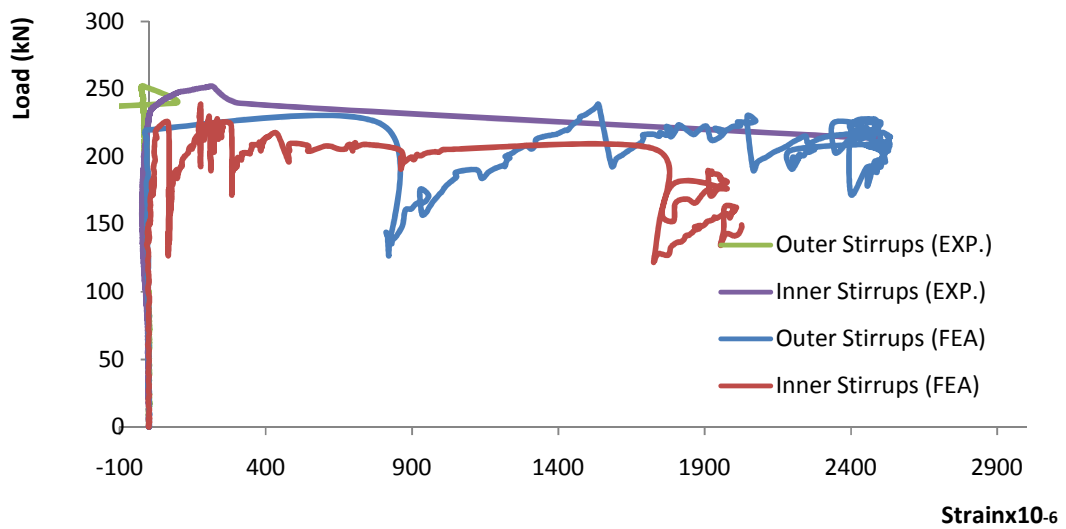**Figure D- 2 Load longitudinal reinforcement strain relationship verification for beam T1**
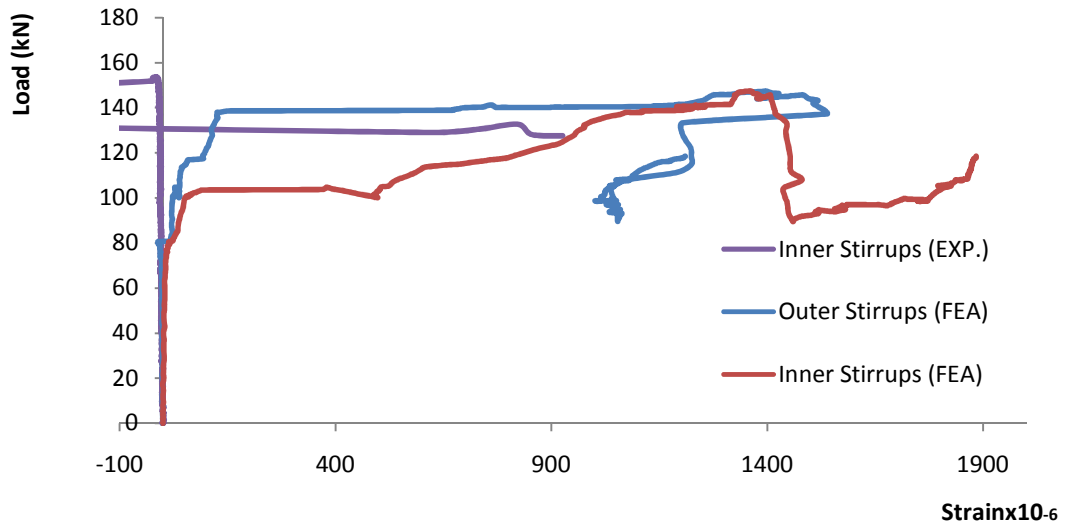
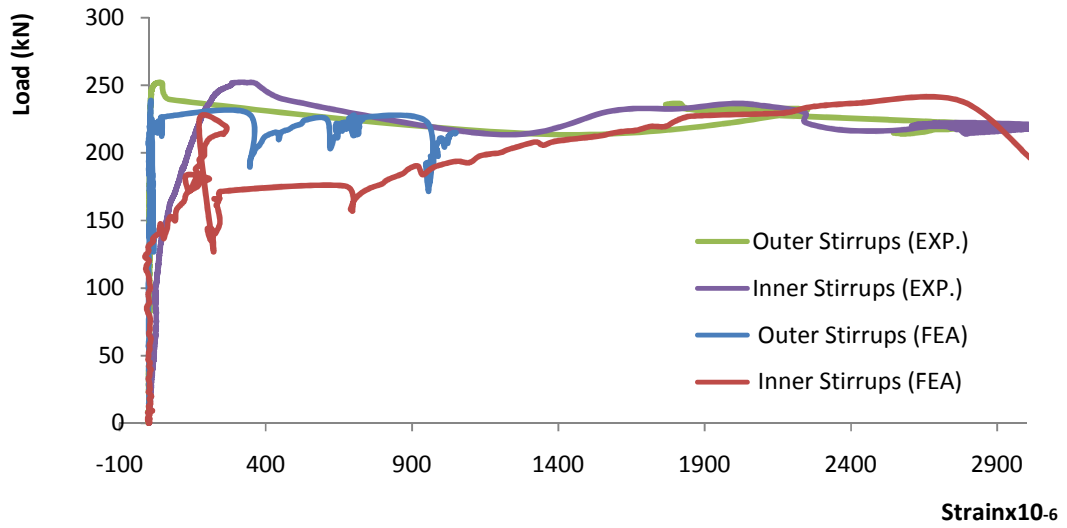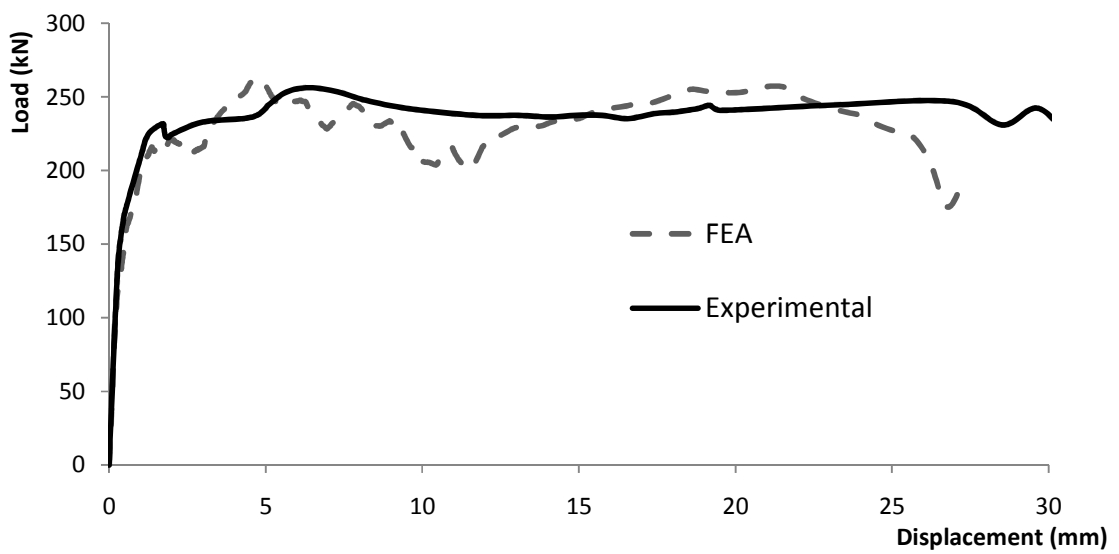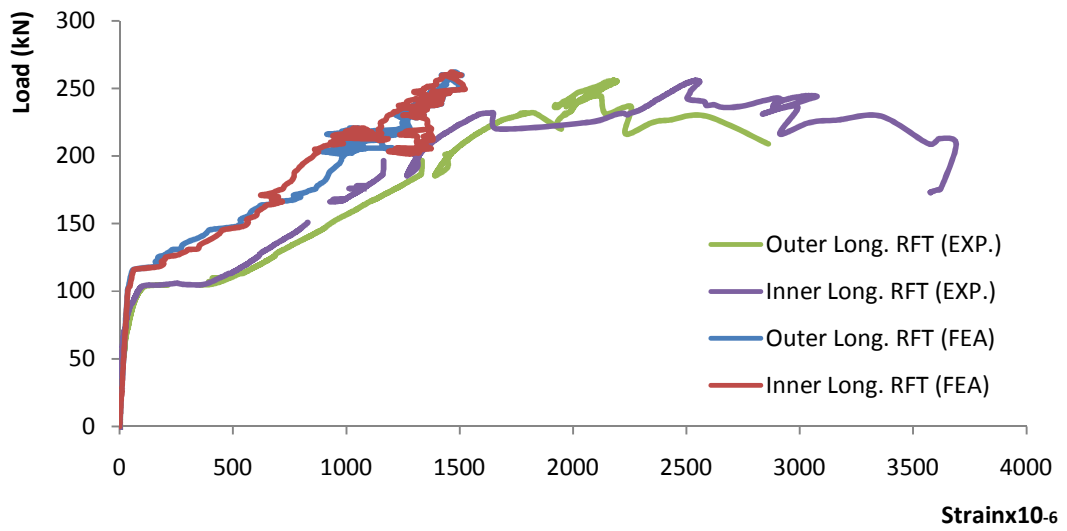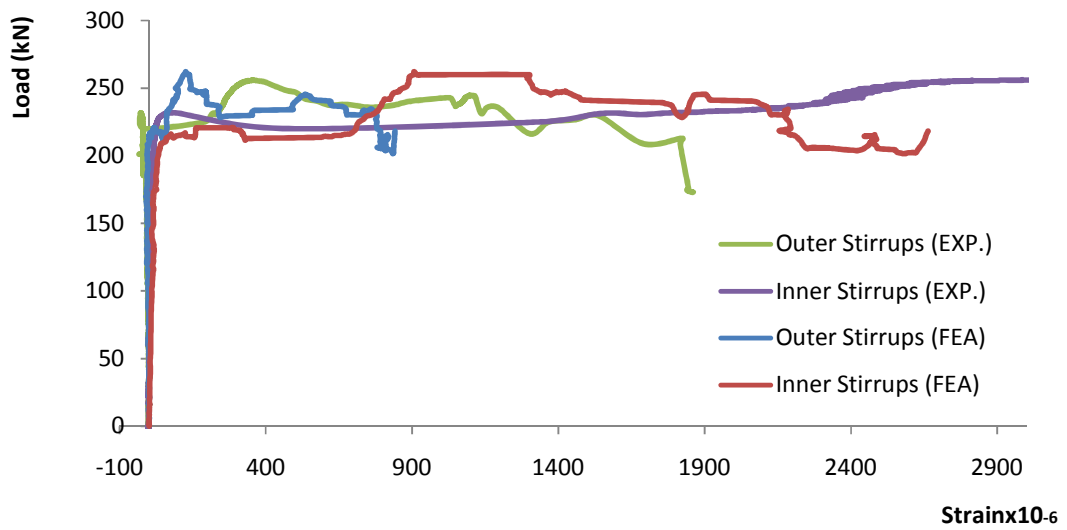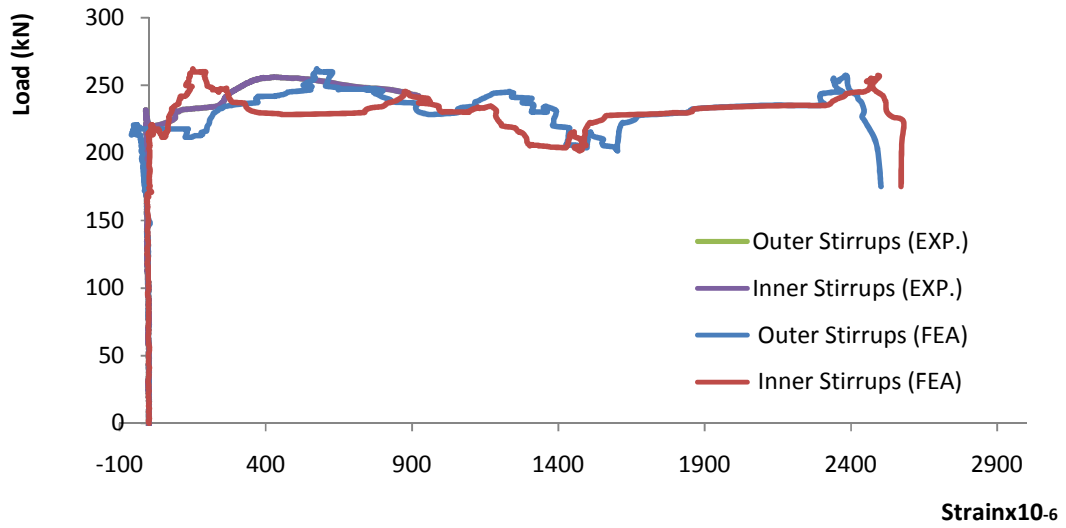**Figure D- 3 Load stirrups strain relationship verification for beam T1**
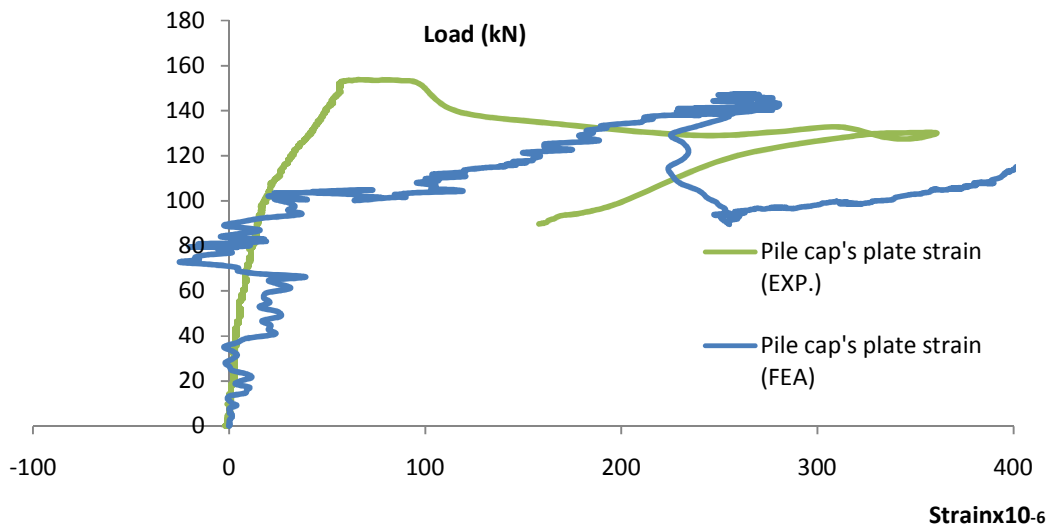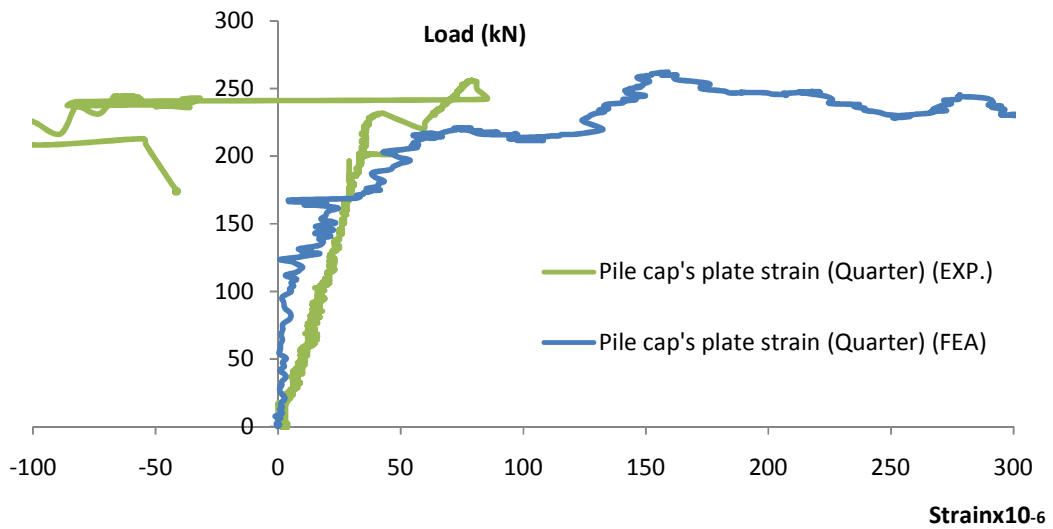

Figure D- 4 Load pile cap's plate strain relationship verification for beam T1

549
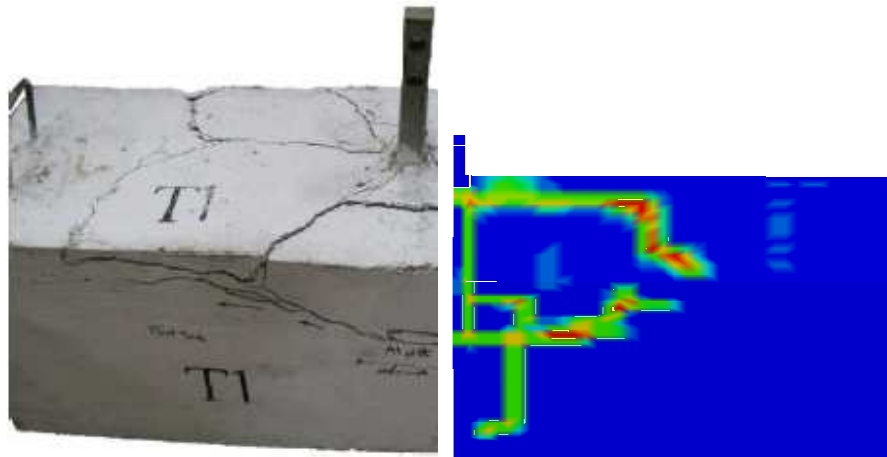
Figure D- 5 Comparison between the crack pattern of the experimental test and analytical model for beam T1

D.1.2 Beam T3
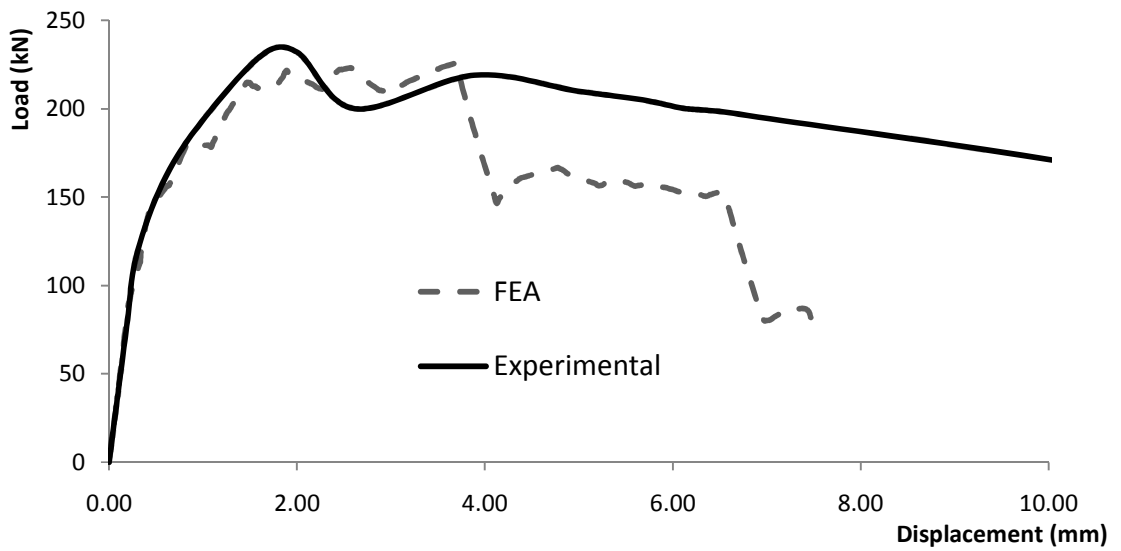
Figure D- 6 Load mid-span displacement relationship verification for beam T3
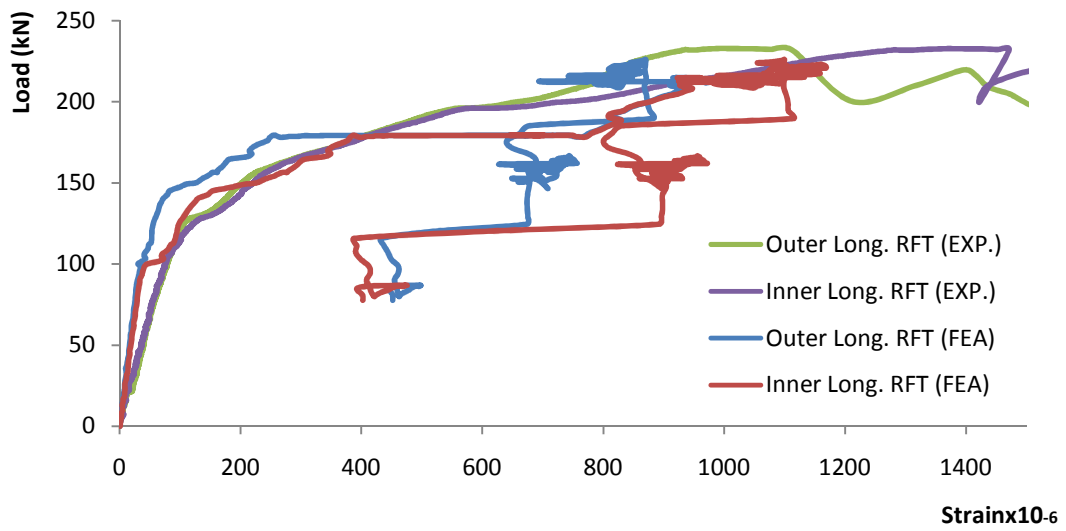
Figure D- 7 Load longitudinal reinforcement strain relationship verification for beam T3
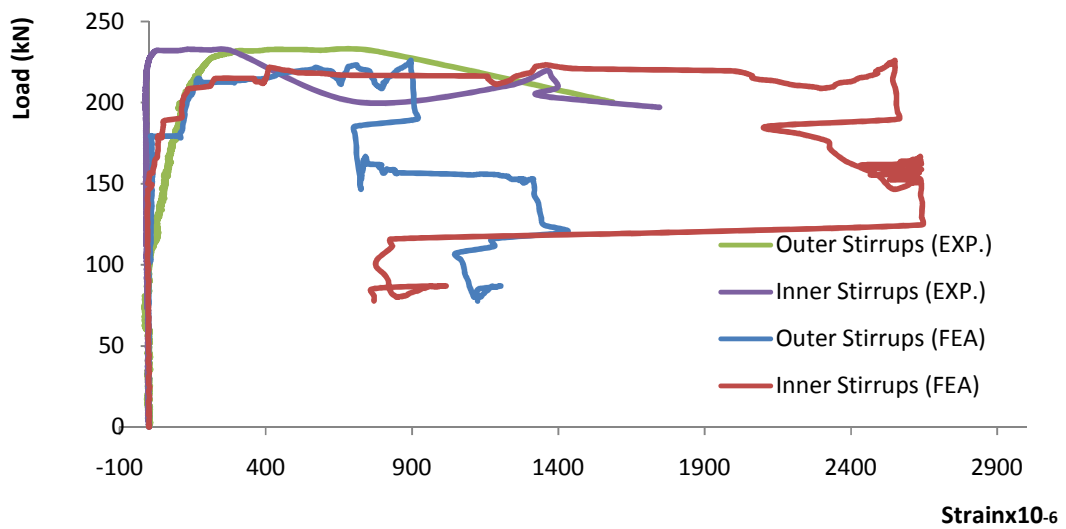
Figure D- 8 Load stirrups strain relationship verification for beam T3

551
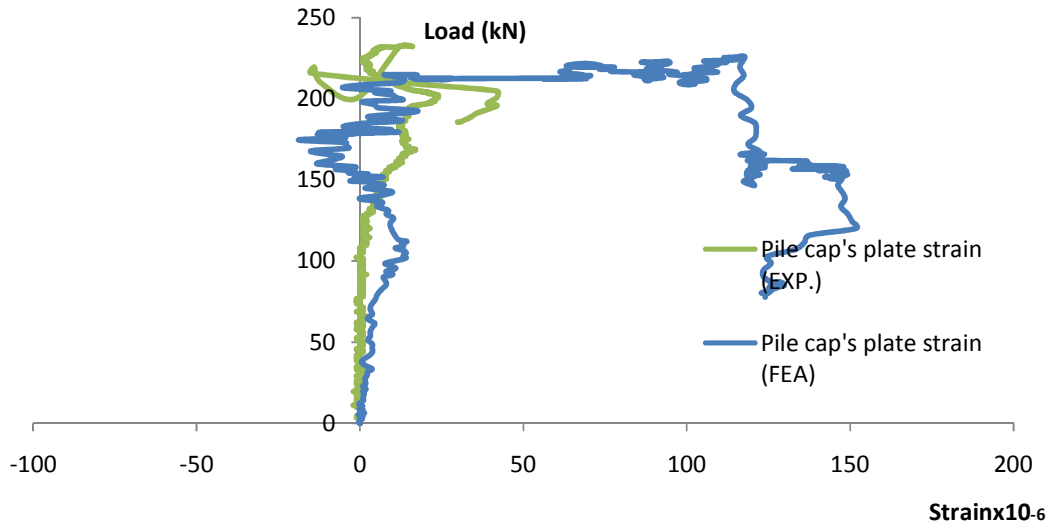
Figure D- 9 Load pile cap's plate strain relationship verification for beam T3
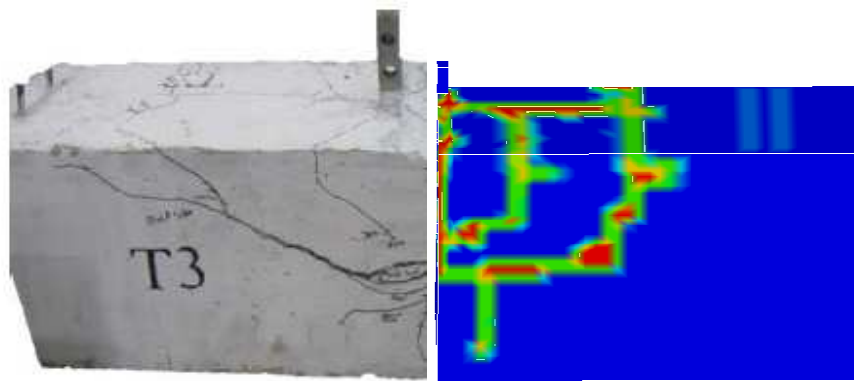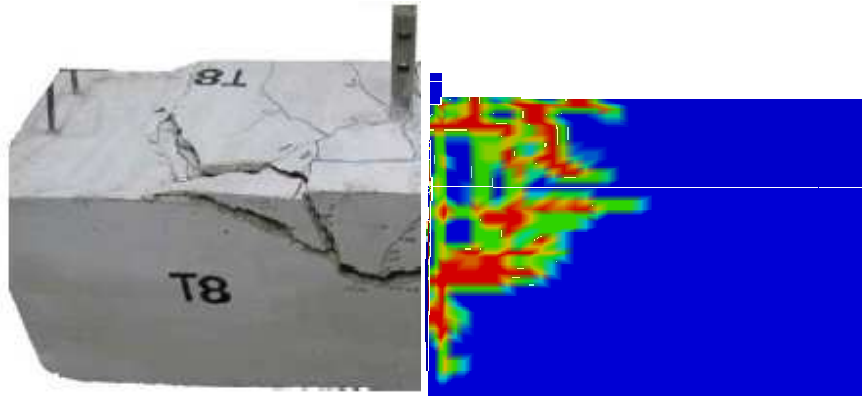

Figure D- 10 Comparison between the crack pattern of the experimental test and analytical model for beam T3
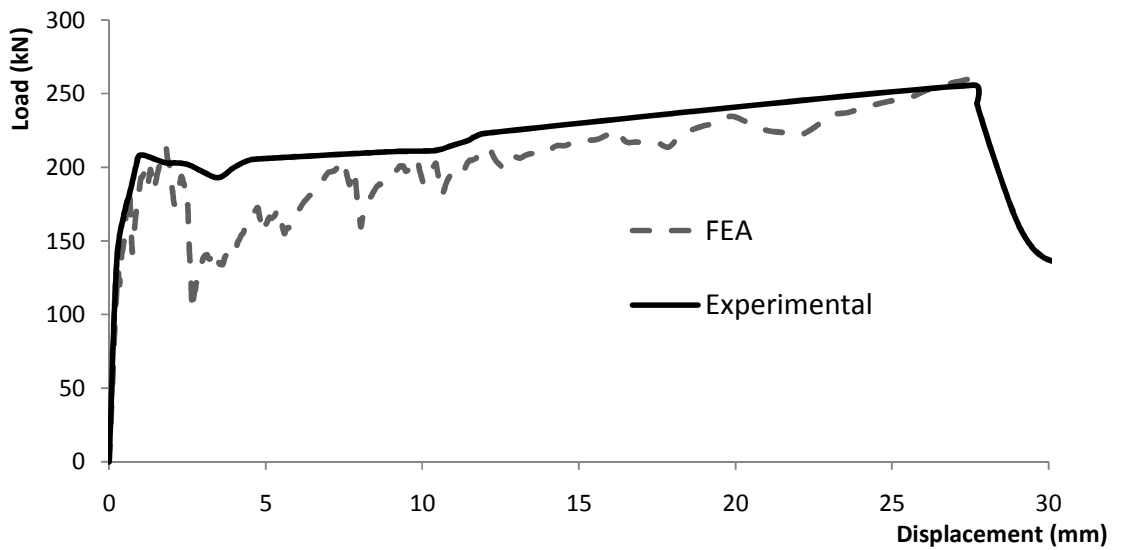
D.1.3 Beam T4
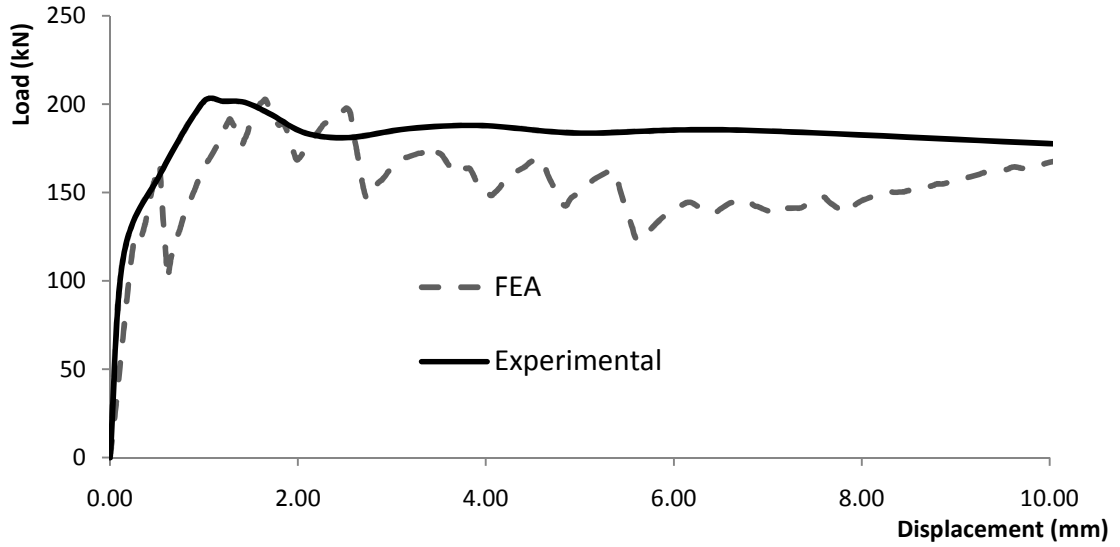
Figure D- 11 Load mid-span displacement relationship verification for beam T4
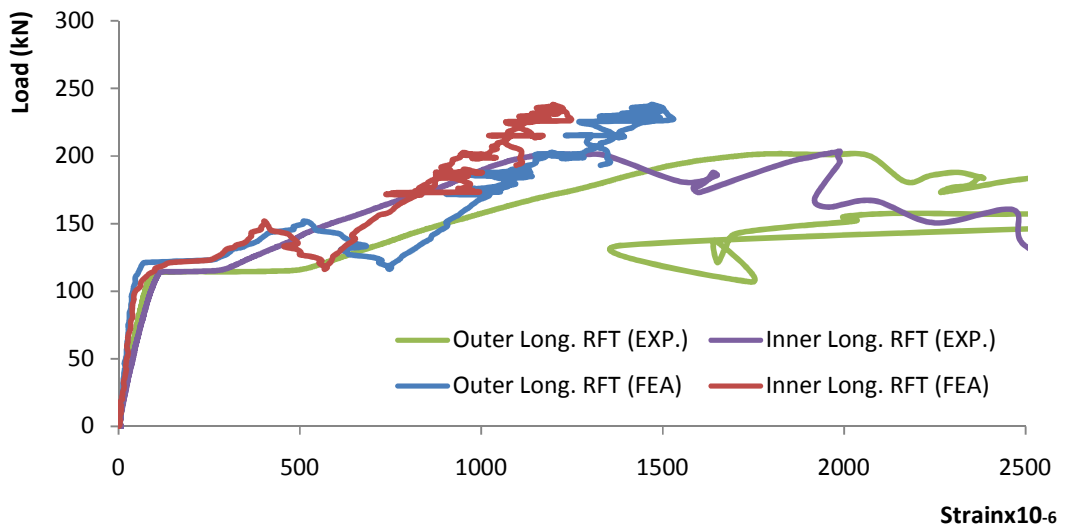
Figure D- 12 Load longitudinal reinforcement strain relationship verification for beam T4
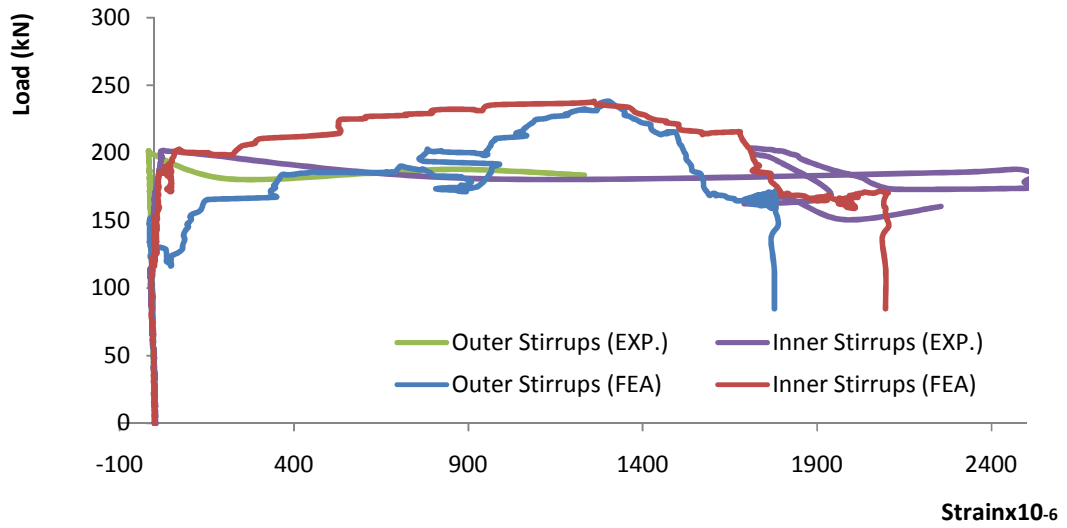
Figure D- 13 Load stirrups strain relationship verification for beam T4
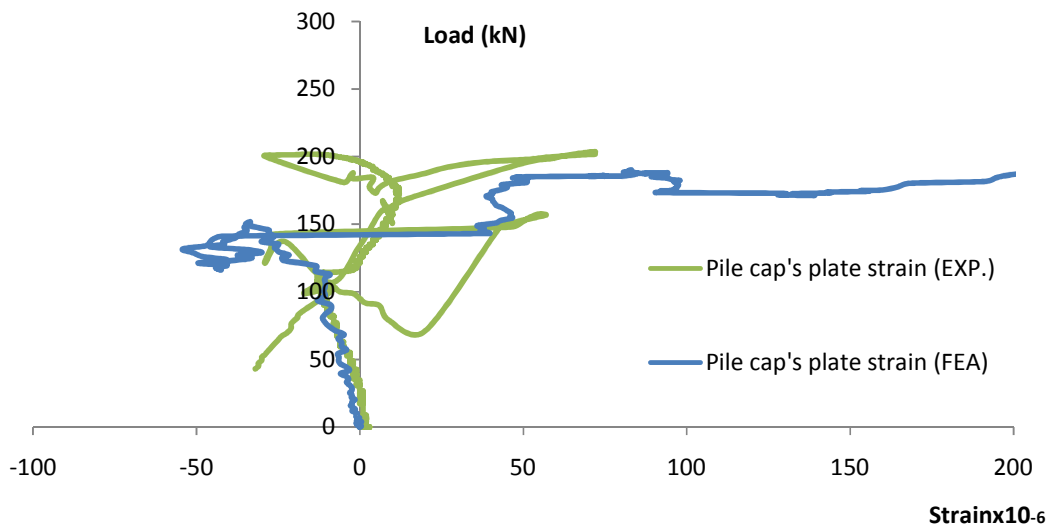
Figure D- 14 Load pile cap's plate strain relationship verification for beam T4

554
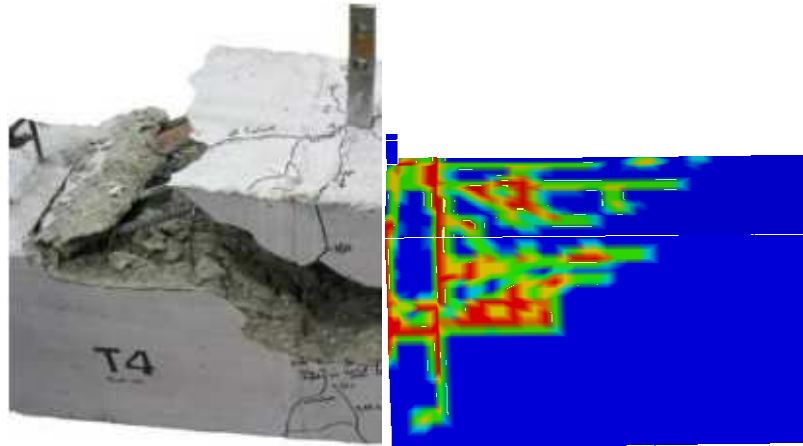
Figure D- 15 Comparison between the crack pattern of the experimental test and analytical model for beam T4

D.1.4 Beam T5
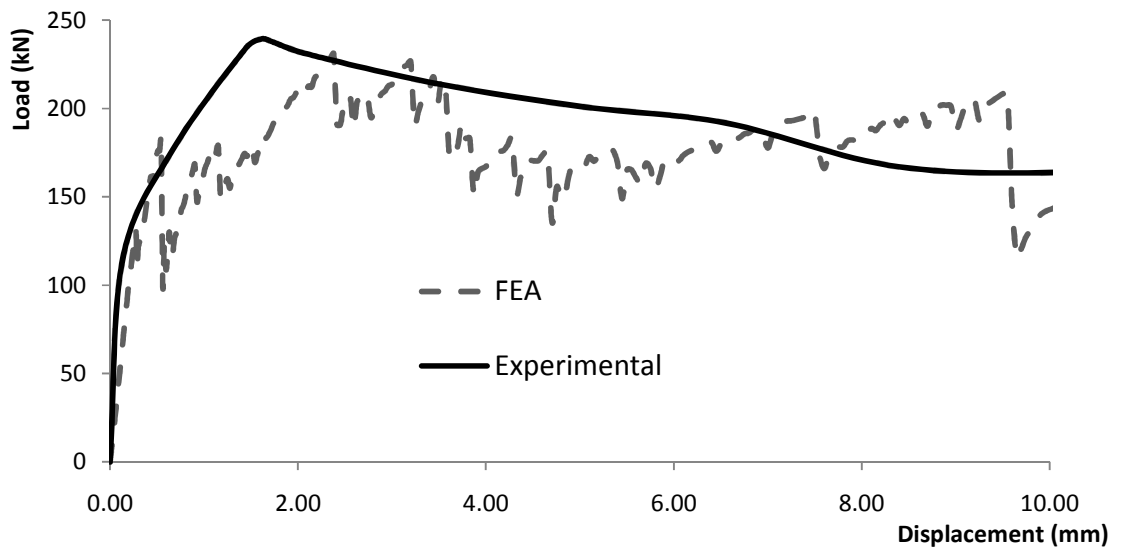
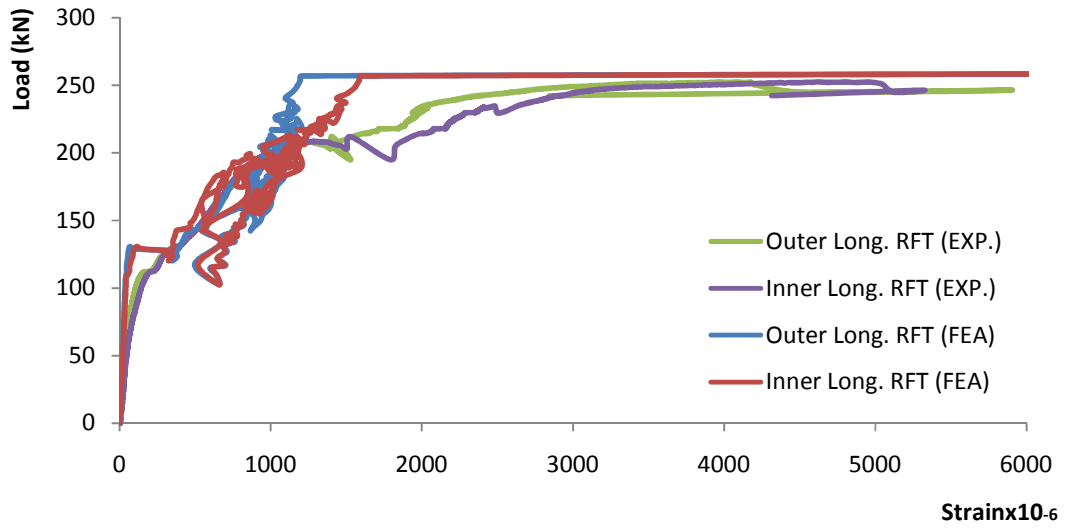**Figure D- 16 Load mid-span displacement relationship verification for beam T5**
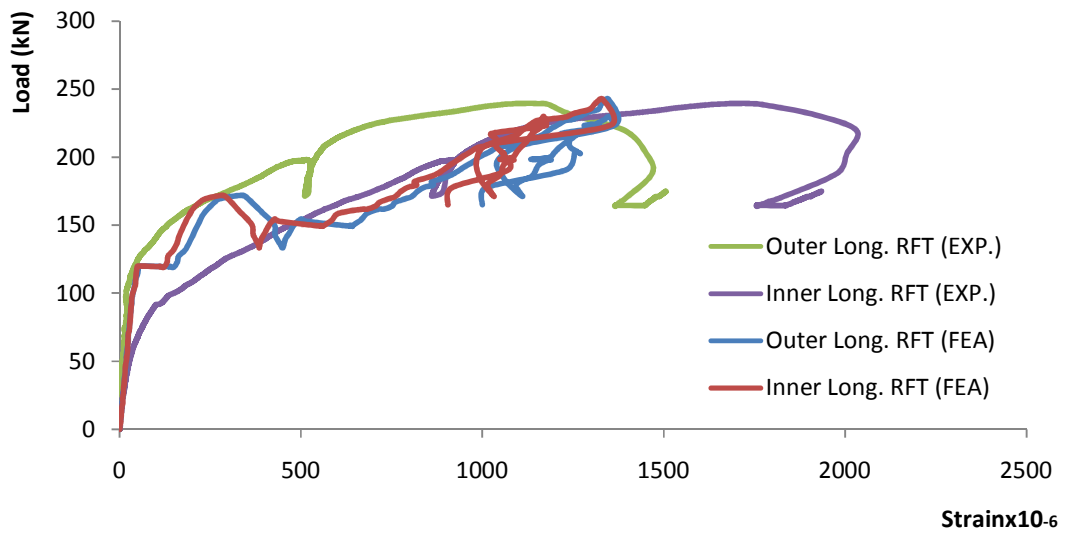
Figure D- 17 Load longitudinal reinforcement strain relationship verification for beam T5
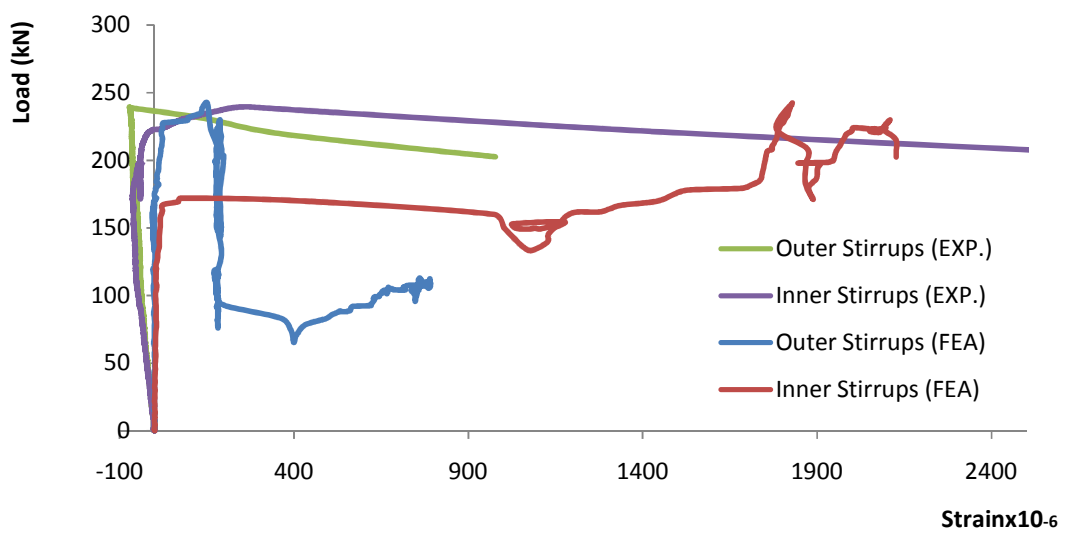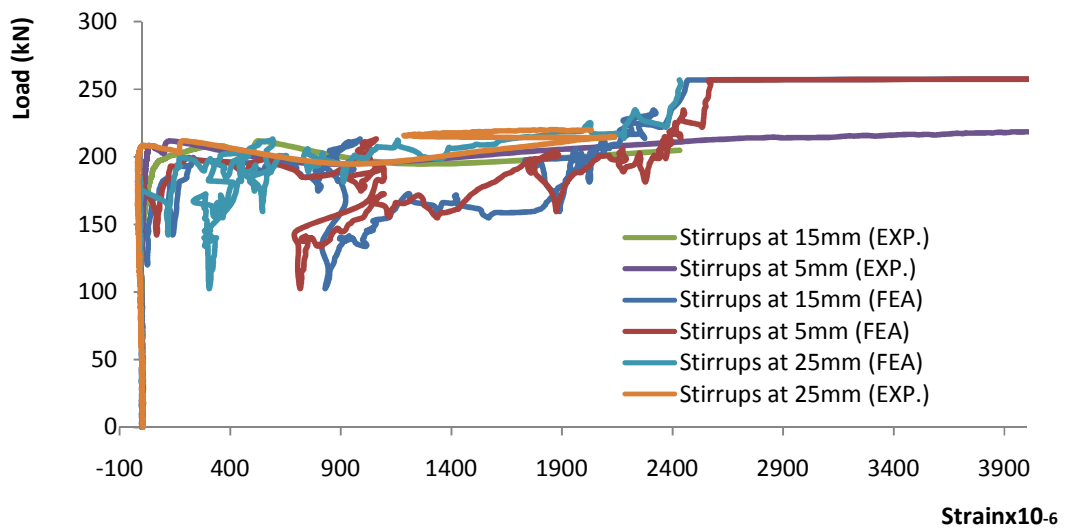

Figure D- 18 Load vertical branch of the stirrups strain relationship verification for beam T5
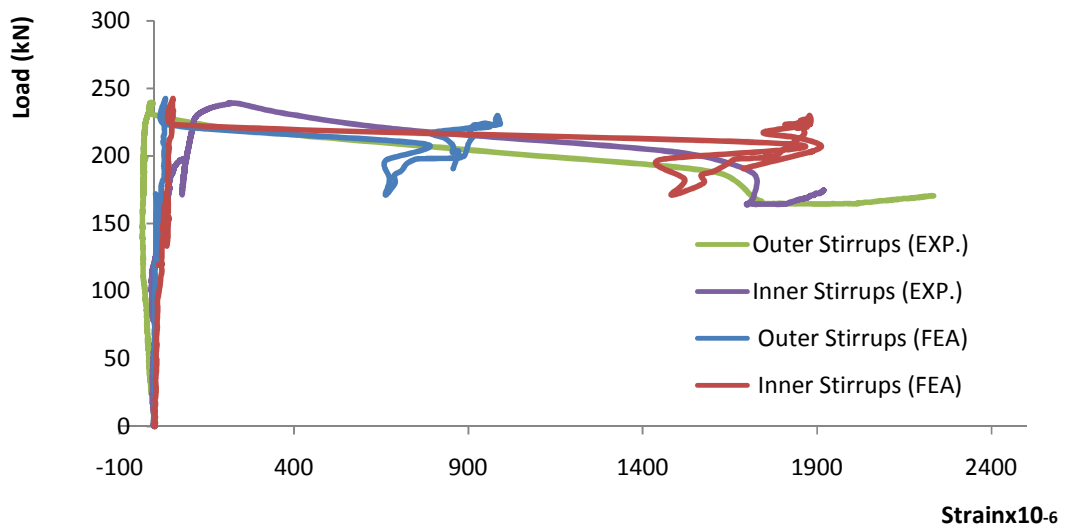
Figure D- 19 Load horizontal top branch of the stirrups strain relationship verification for beam T5
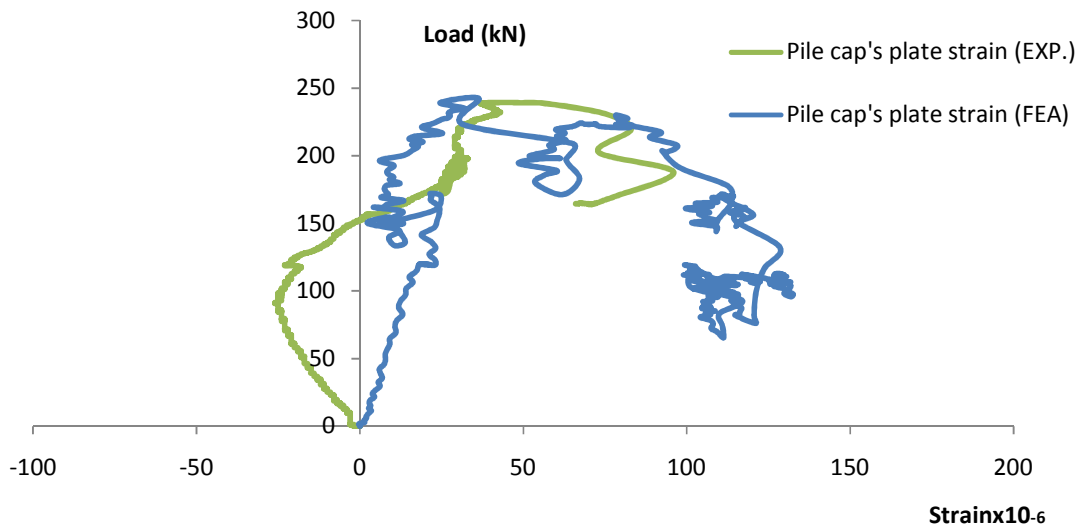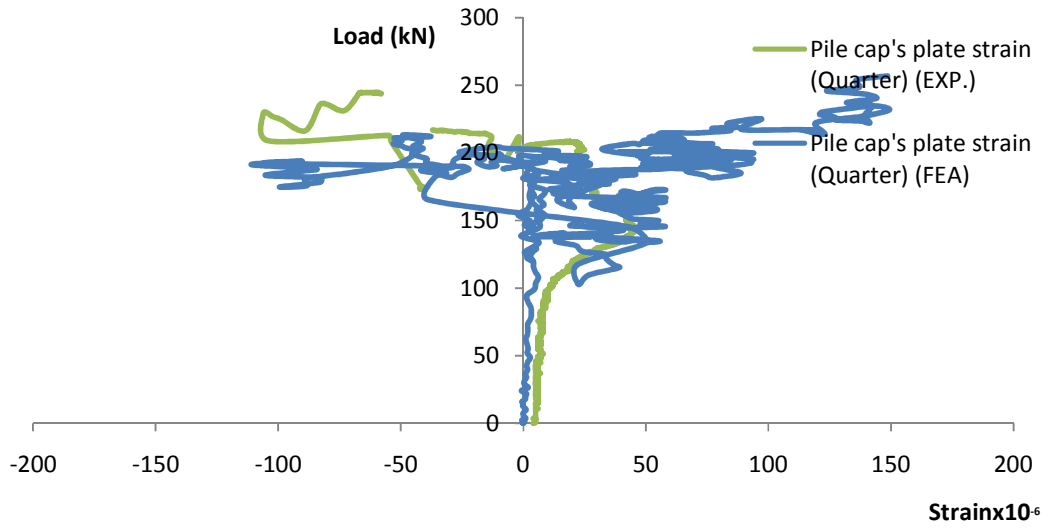

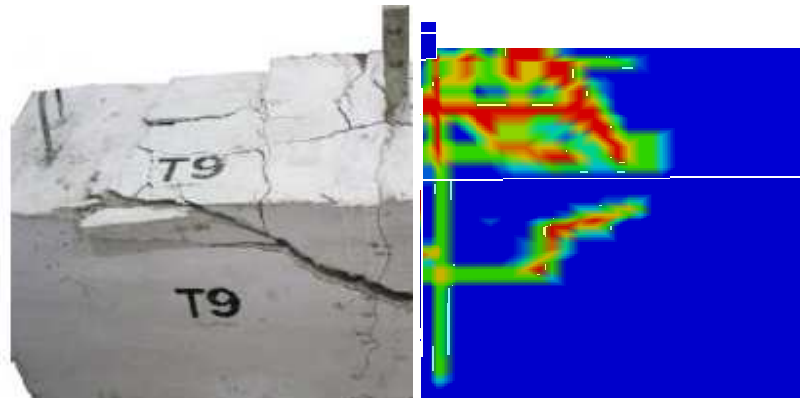**Figure D- 20 Load pile cap's plate strain relationship verification for beam T5**
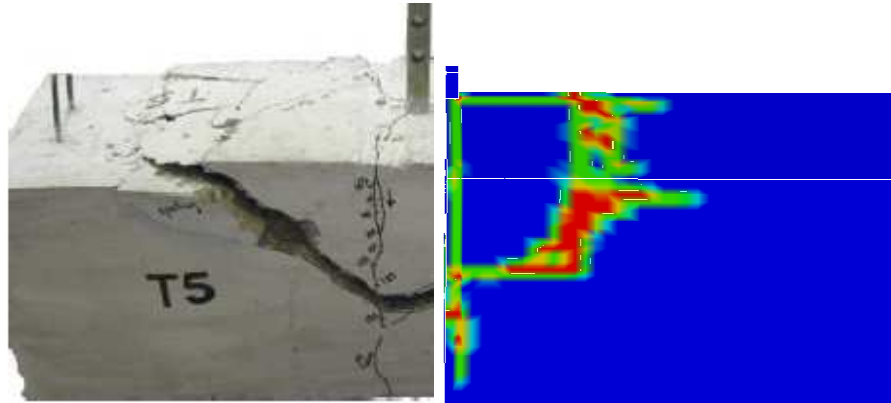
Figure D- 21 Comparison between the crack pattern of the experimental test and analytical model for beam T5

D.1.5 Beam T6
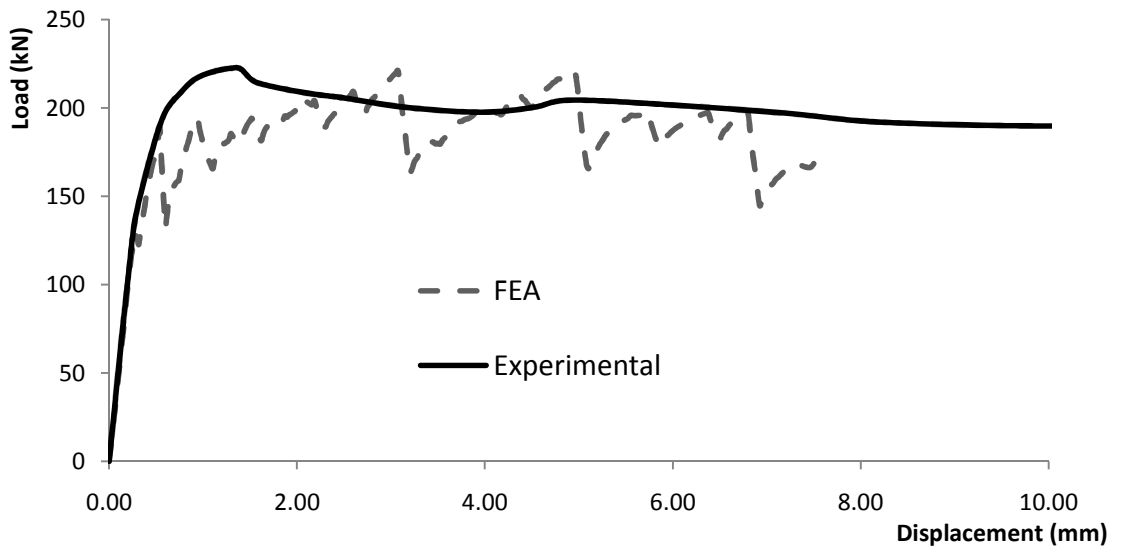
Figure D- 22 Load mid-span displacement relationship verification for beam T6
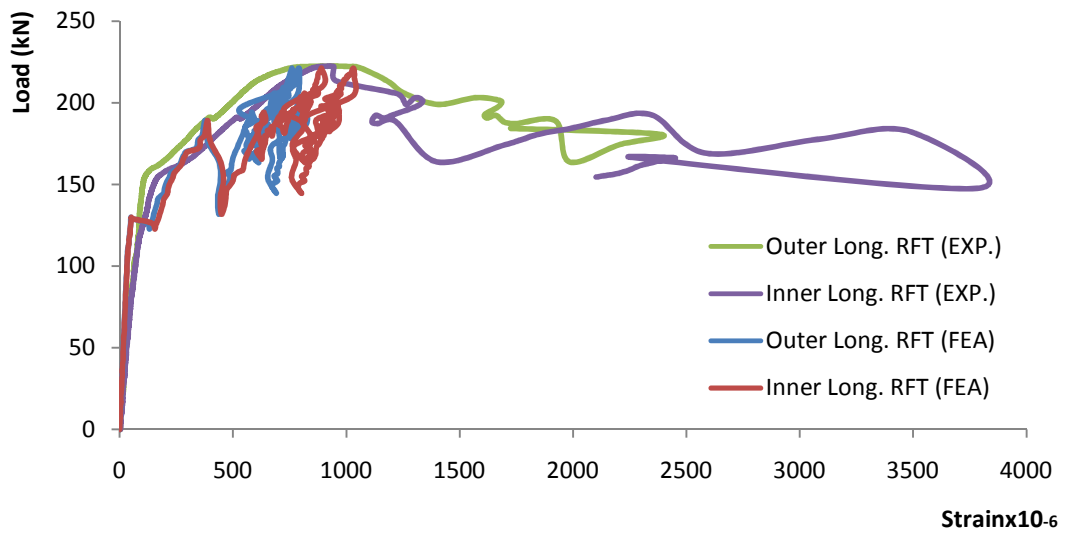
Figure D- 23 Load longitudinal reinforcement strain relationship verification for beam T6
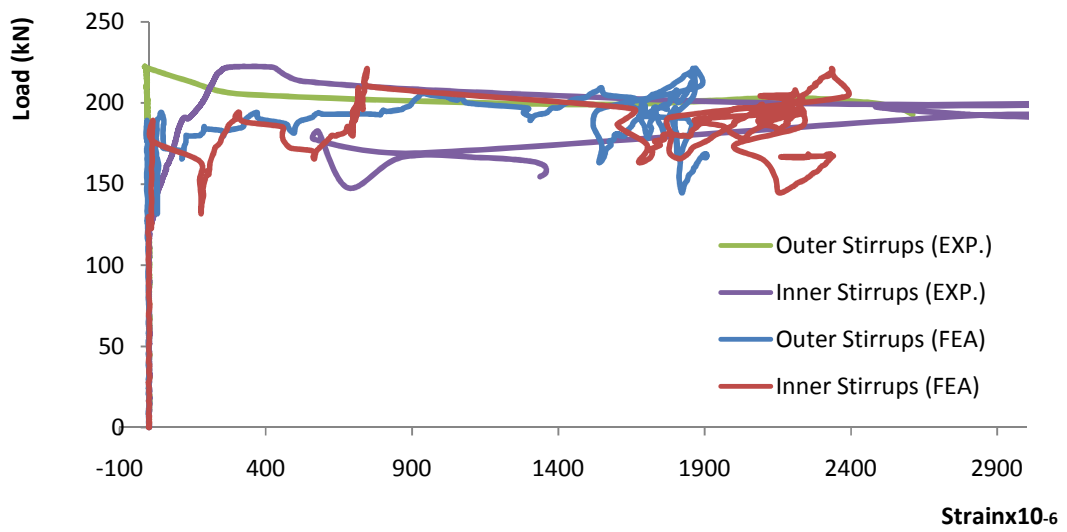
Figure D- 24 Load stirrups strain relationship verification for beam T6
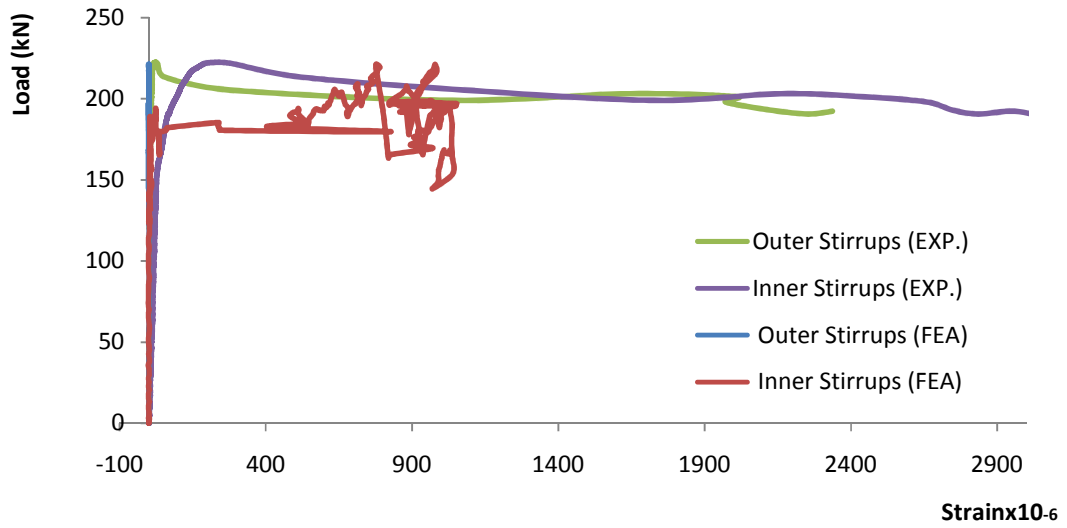
Figure D- 25 Load horizontal top branch of the stirrups strain relationship verification for beam T5
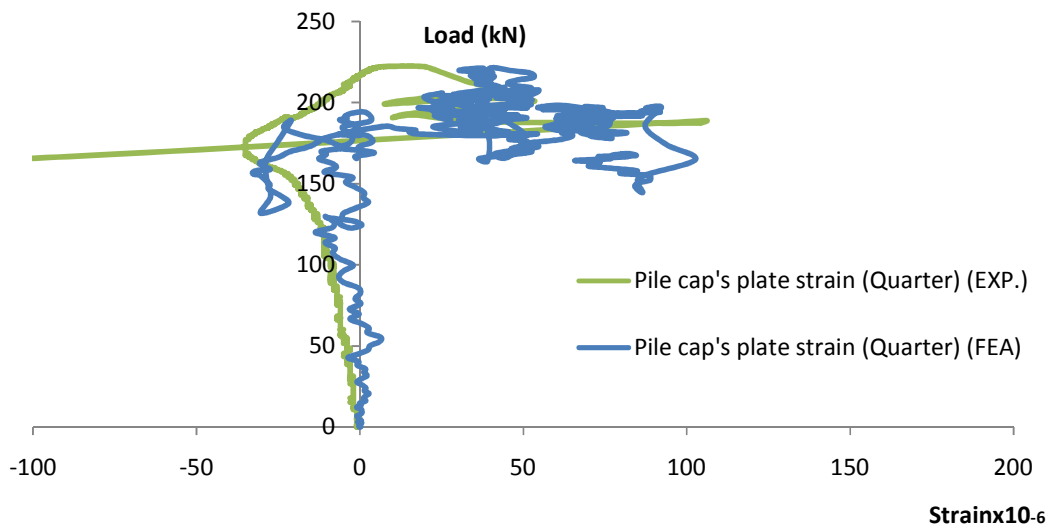
Figure D- 26 Load pile cap's plate strain relationship verification for beam T6
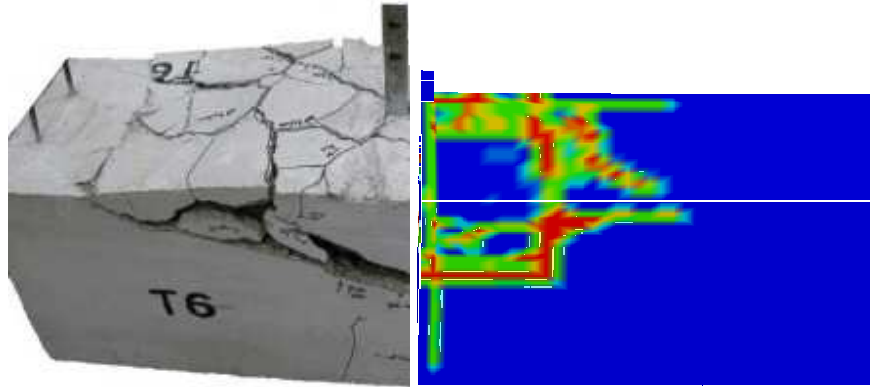
Figure D- 27 Comparison between the crack pattern of the experimental test and analytical model for beam T6
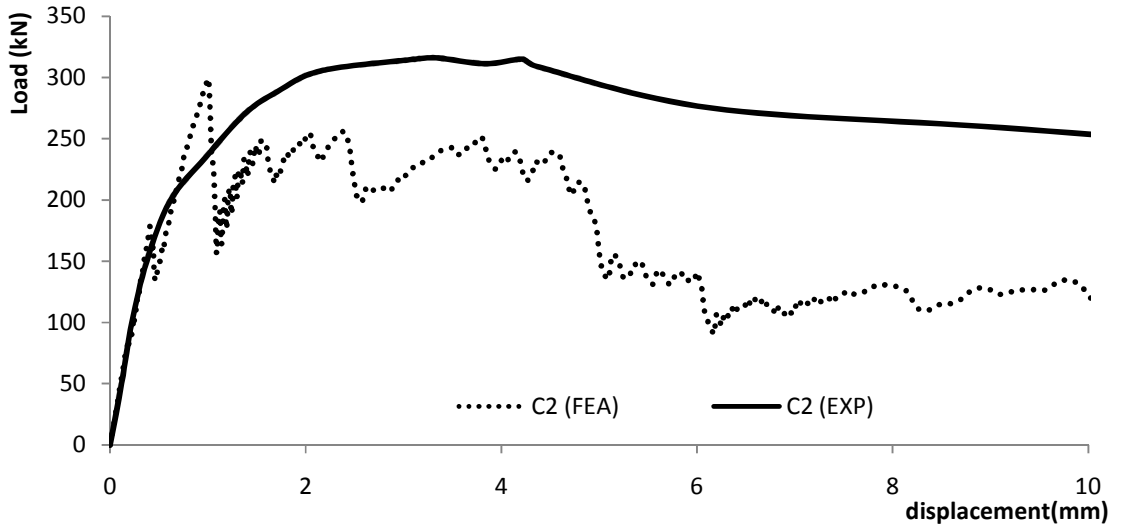
D.1.6 Beam T7
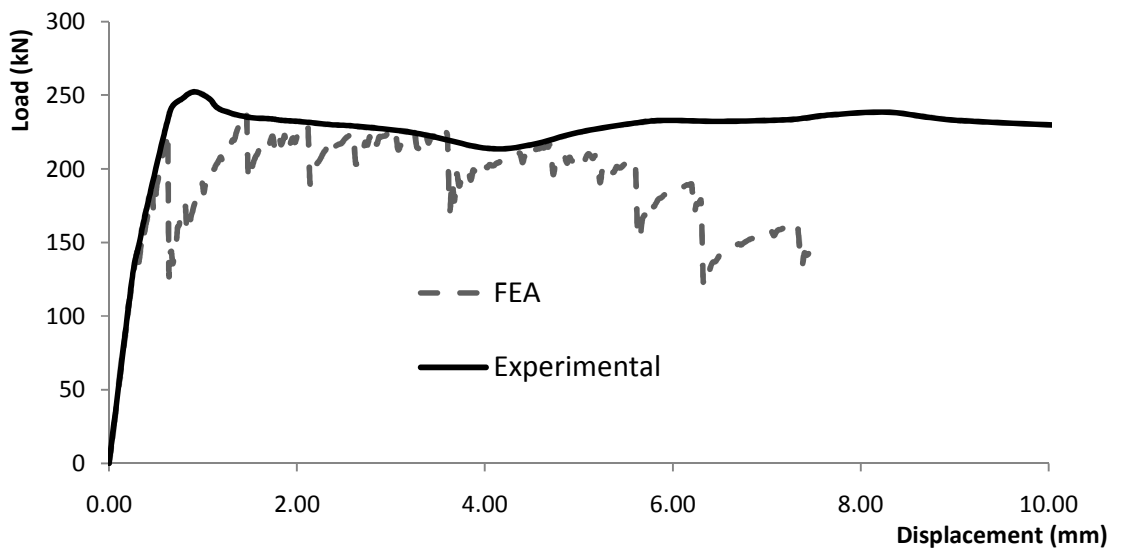
Figure D- 28 Load mid-span displacement relationship verification for beam T7
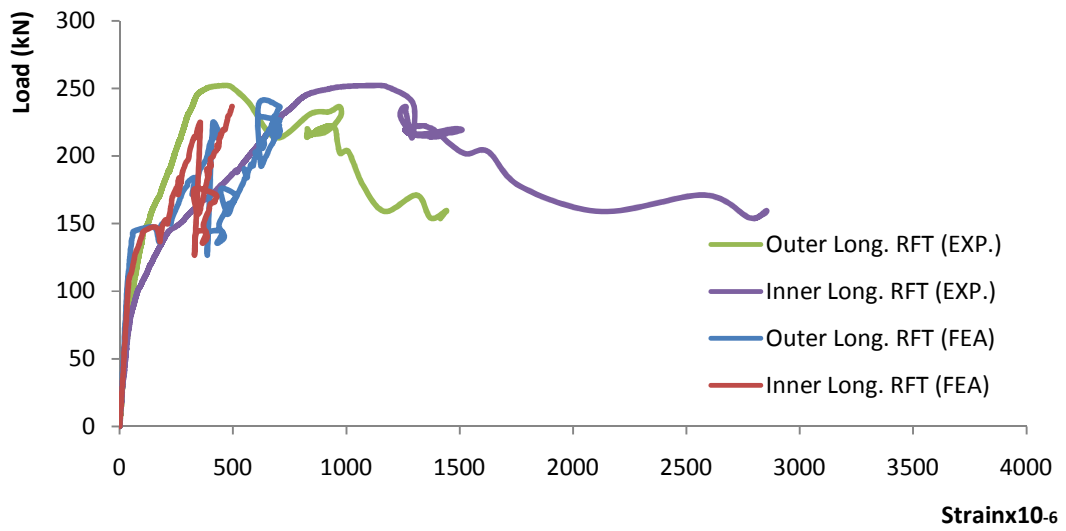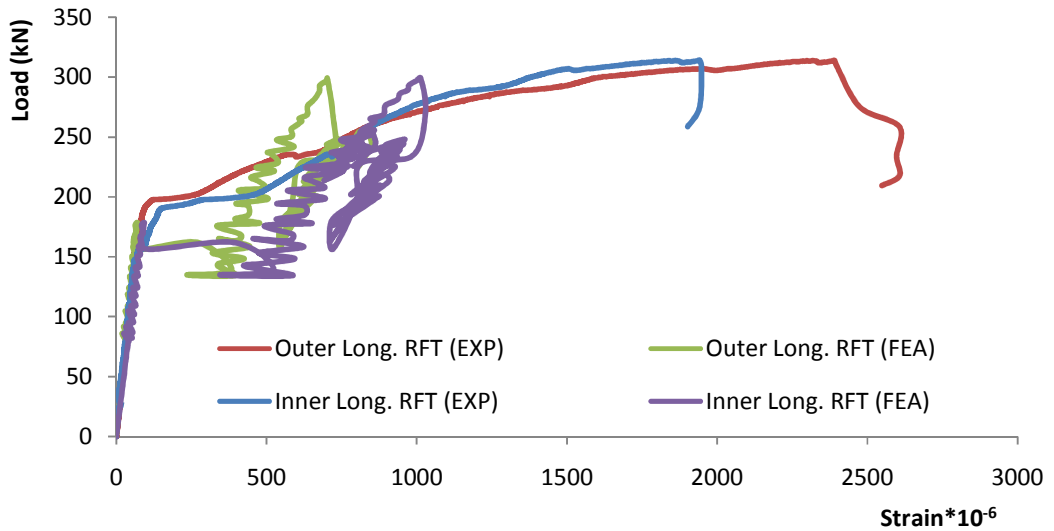
Figure D- 29 Load longitudinal reinforcement strain relationship verification for beam T7
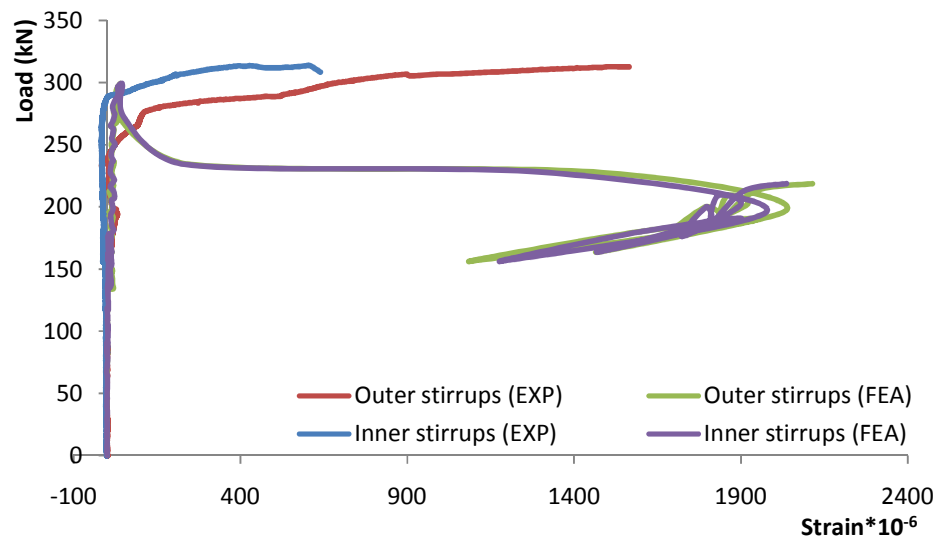

Figure D- 30 Load stirrups strain relationship verification for beam T7

562

Figure D- 31 Load horizontal top branch of the stirrups strain relationship verification for beam T7
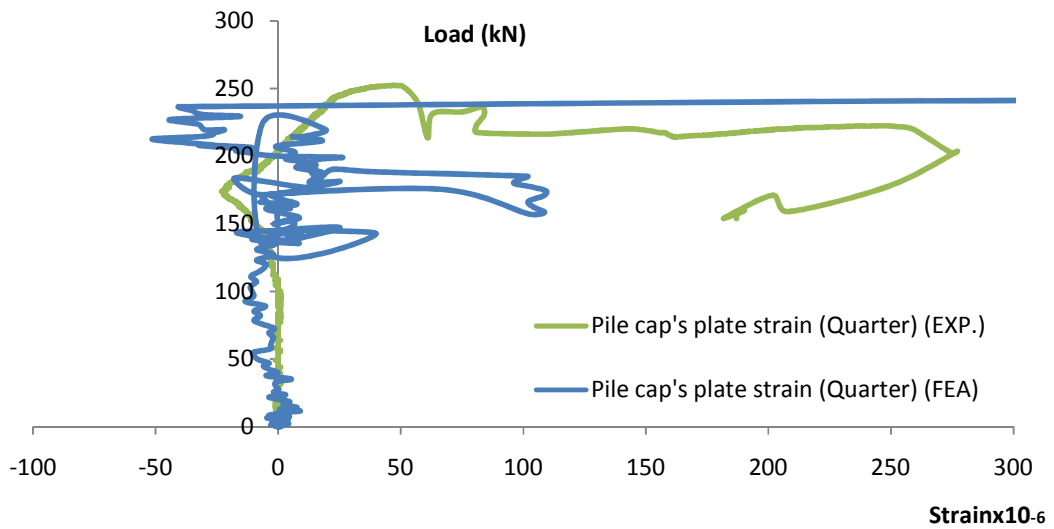
Figure D- 32 Load pile cap's plate strain relationship verification for beam T7
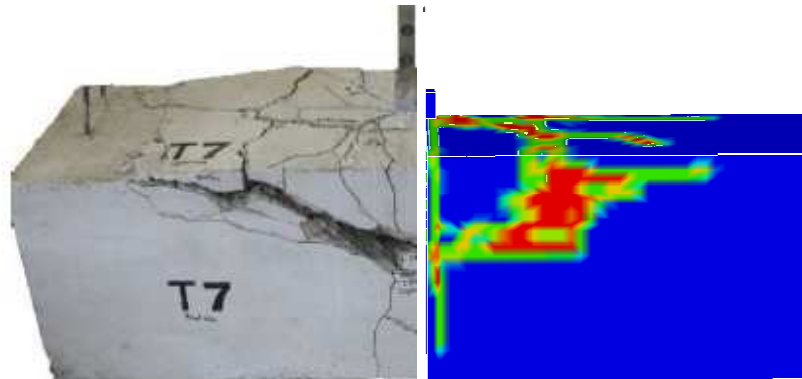
Figure D- 33 Comparison between the crack pattern of the experimental test and analytical model for beam T7

D.1.7 Beam T8

Figure D- 34 Load mid-span displacement relationship verification for beam T8

Figure D- 35 Load longitudinal reinforcement strain relationship verification for beam T8

Figure D- 36 Load stirrups strain relationship verification for beam T8

Figure D- 37 Load strain of the interior branches of the 4 branches stirrups relationship verification for beam T8

Figure D- 38 Load pile cap's plate strain relationship verification for beam T8
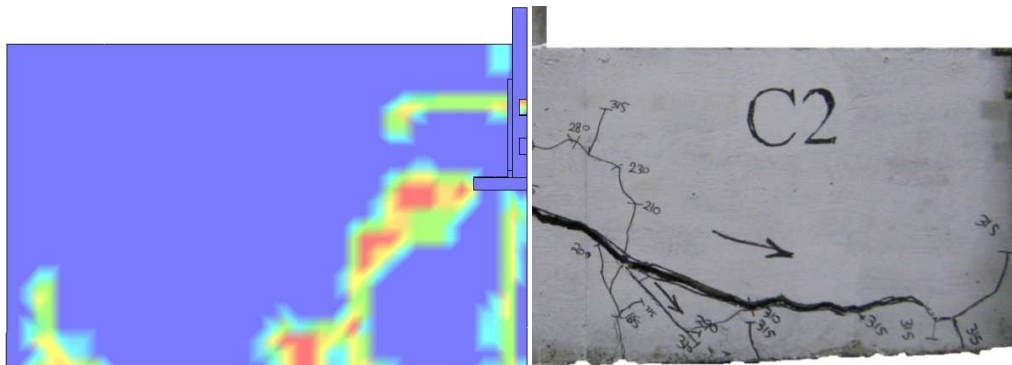
Figure D- 39 Comparison between the crack pattern of the experimental test and analytical model for beam T8
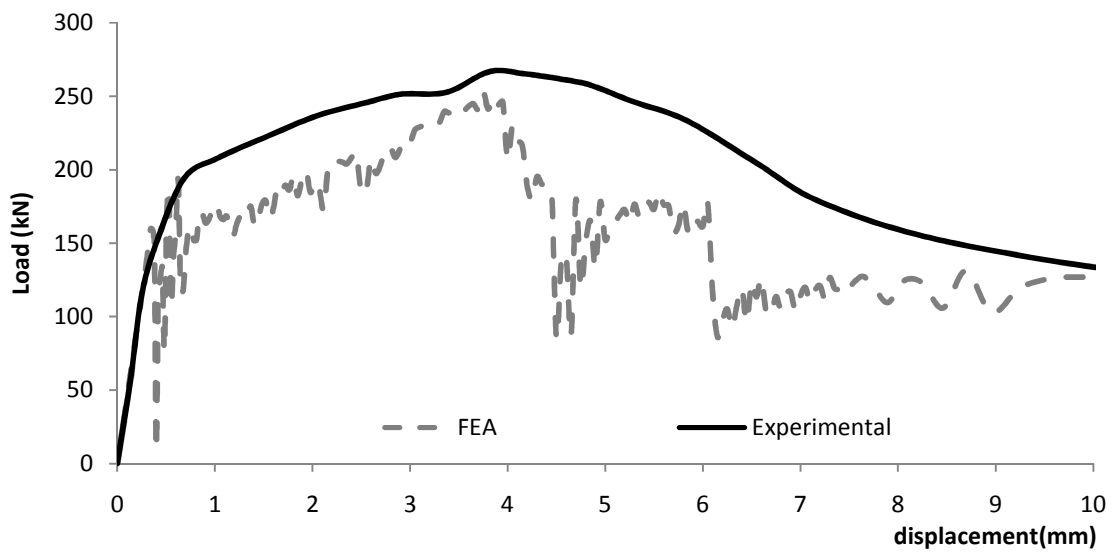
D.1.8 Beam T9

Figure D- 40 Load mid-span displacement relationship verification for beam T9
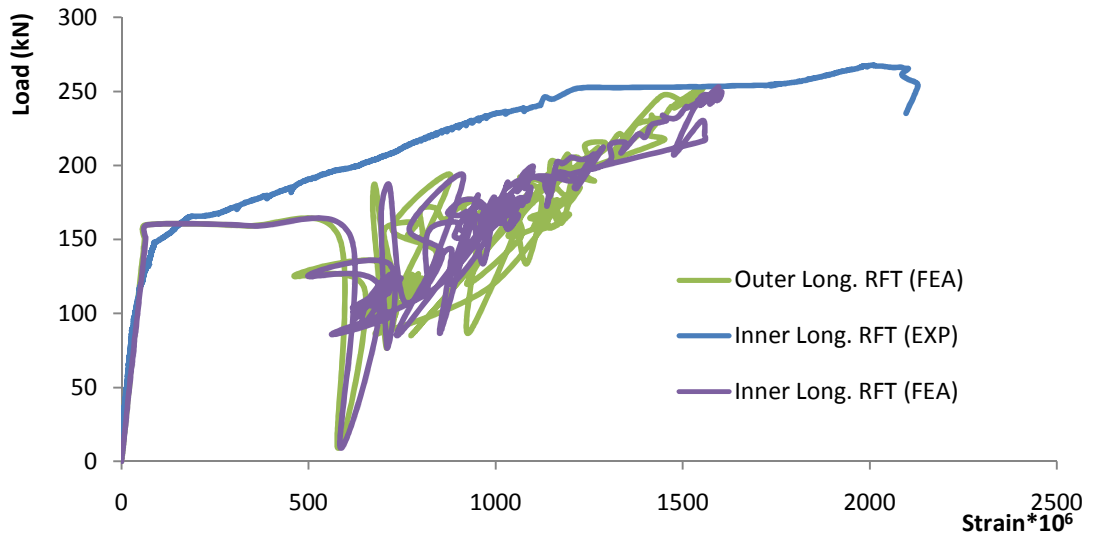
Figure D- 41 Load longitudinal reinforcement strain relationship verification for beam T9

Figure D- 42 Load stirrups strain at different distances from the pile shaft relationship verification for beam T9

Figure D- 43 Load pile cap's plate strain relationship verification for beam T9

Figure D- 44 Comparison between the crack pattern of the experimental test and analytical model for beam T9

D.2 Verification of the finite element model and model calibration for the connections subjected to compression loading

D.2.1 Beam C2

Figure D- 45 Load mid-span displacement relationship verification for beam C2

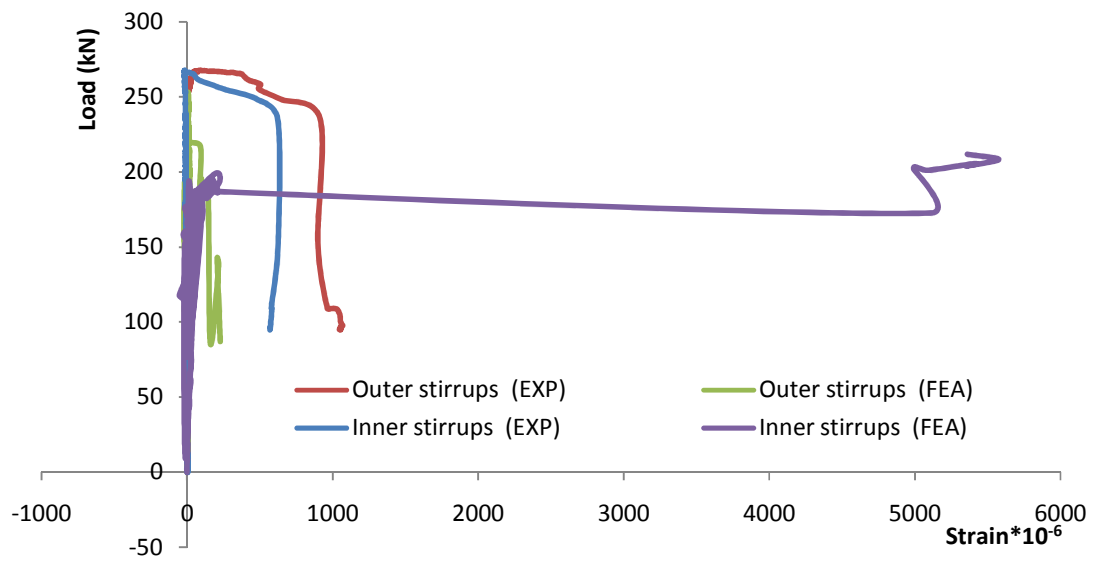**Figure D- 46 Load longitudinal reinforcement strain relationship verification for beam C2**

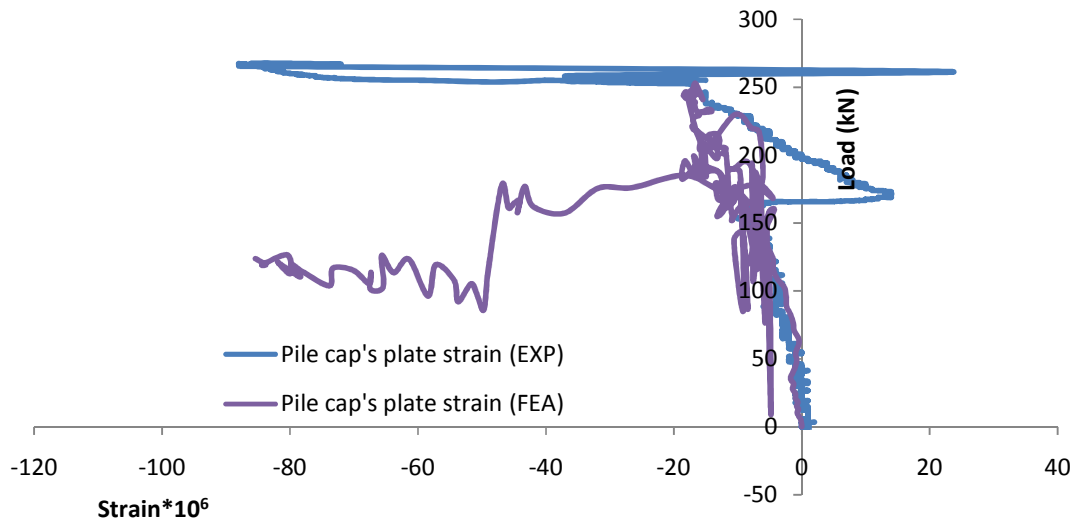**Figure D- 47 Load stirrups strain relationship verification for beam C2**
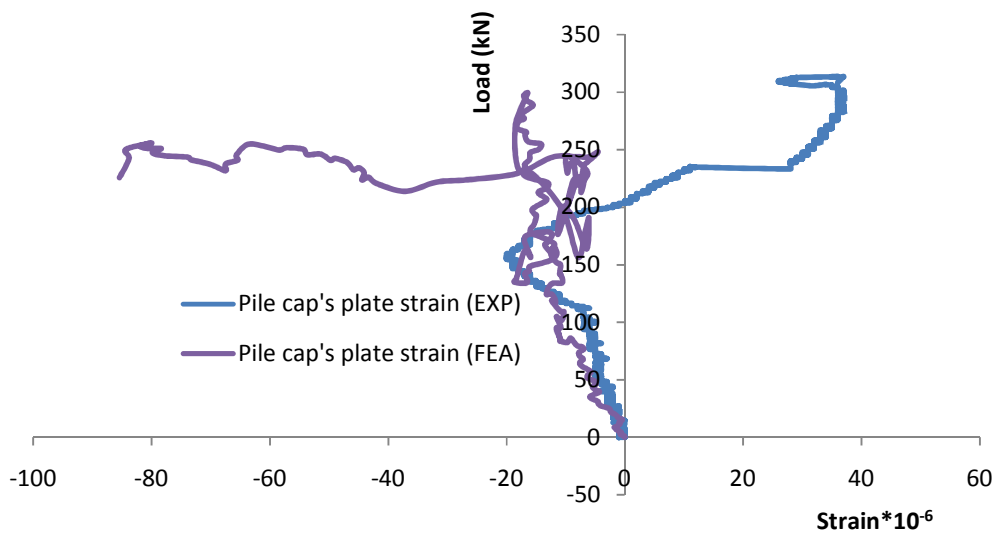
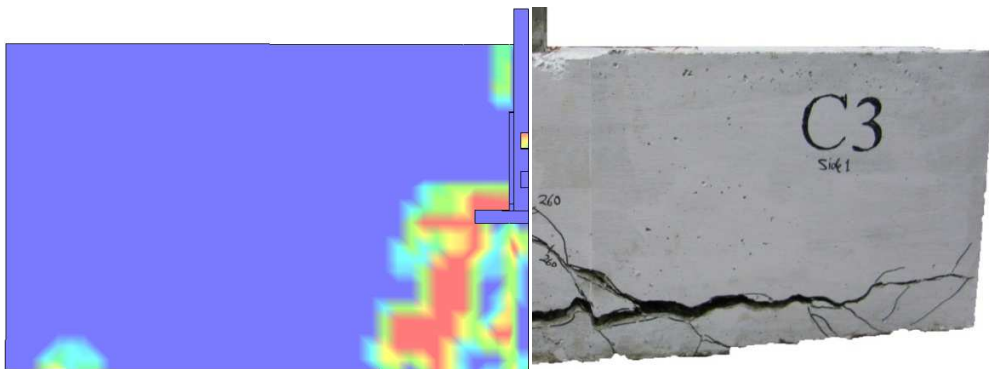**Figure D- 48 Load pile cap's plate strain relationship verification for beam C2**

Figure D- 49 Comparison between the crack pattern of the experimental test and analytical model for beam C2
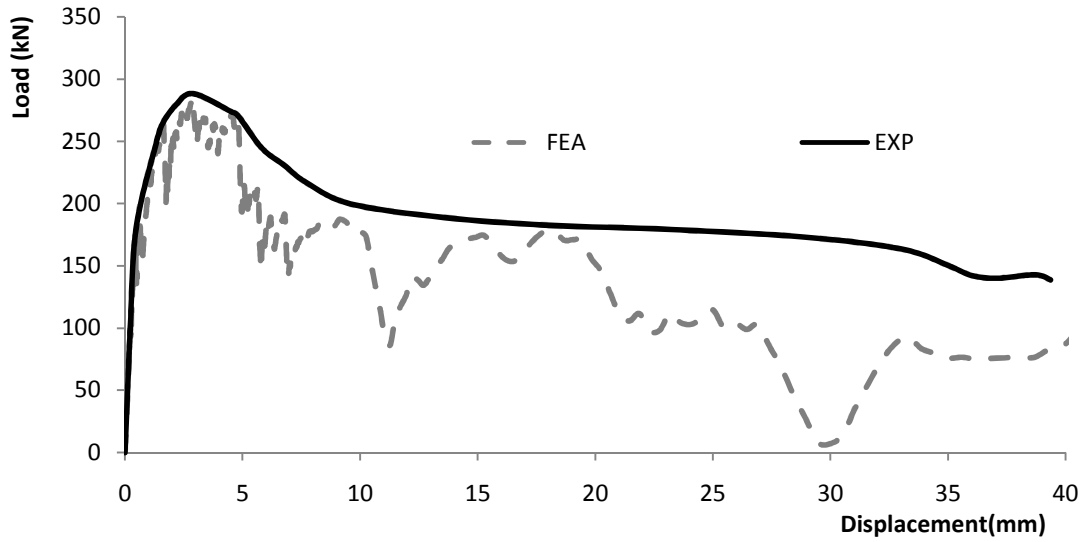
D.2.2 Beam C3

Figure D- 50 Load mid-span displacement relationship verification for beam C3

Figure D- 51 Load longitudinal reinforcement strain relationship verification for beam C3

Figure D- 52 Load stirrups strain relationship verification for beam C3

Figure D- 53 Load pile cap's plate strain relationship verification for beam C3

Figure D- 54 Comparison between the crack pattern of the experimental test and analytical model for beam C3

D.2.3 Beam C4

Figure D- 55 Load mid-span displacement relationship verification for beam C4
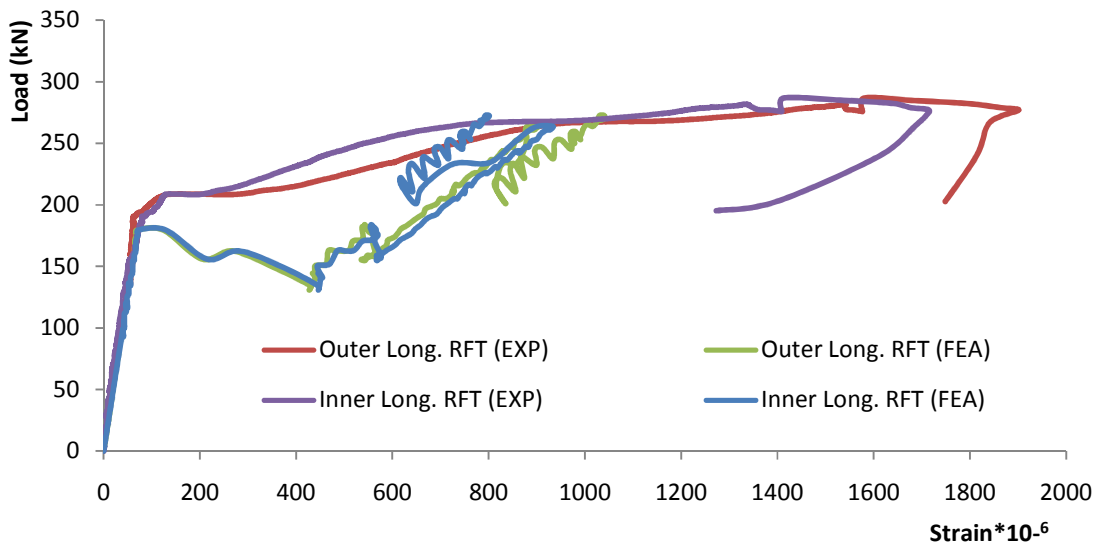

Figure D- 56 Load longitudinal reinforcement strain relationship verification for beam C4
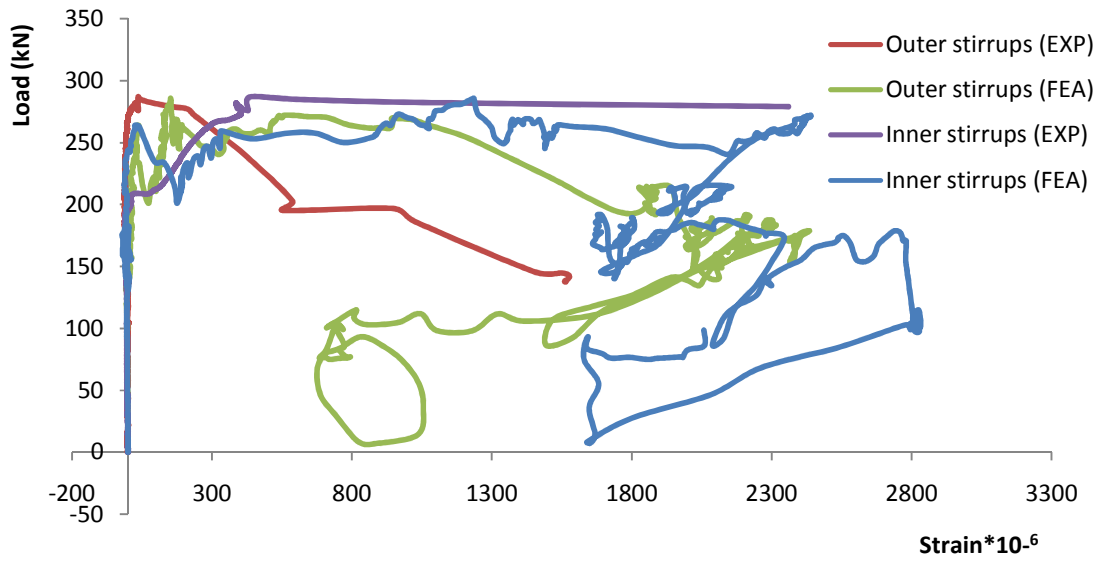
Figure D- 57 Load stirrups strain relationship verification for beam C4

Figure D- 58 Load pile cap's plate strain relationship verification for beam C4

576

Figure D- 59 Comparison between the crack pattern of the experimental test and analytical model for beam C4

D.2.4 Beam C5

Figure D- 60 Load mid-span displacement relationship verification for beam C5

Figure D- 61 Load longitudinal reinforcement strain relationship verification for beam C5

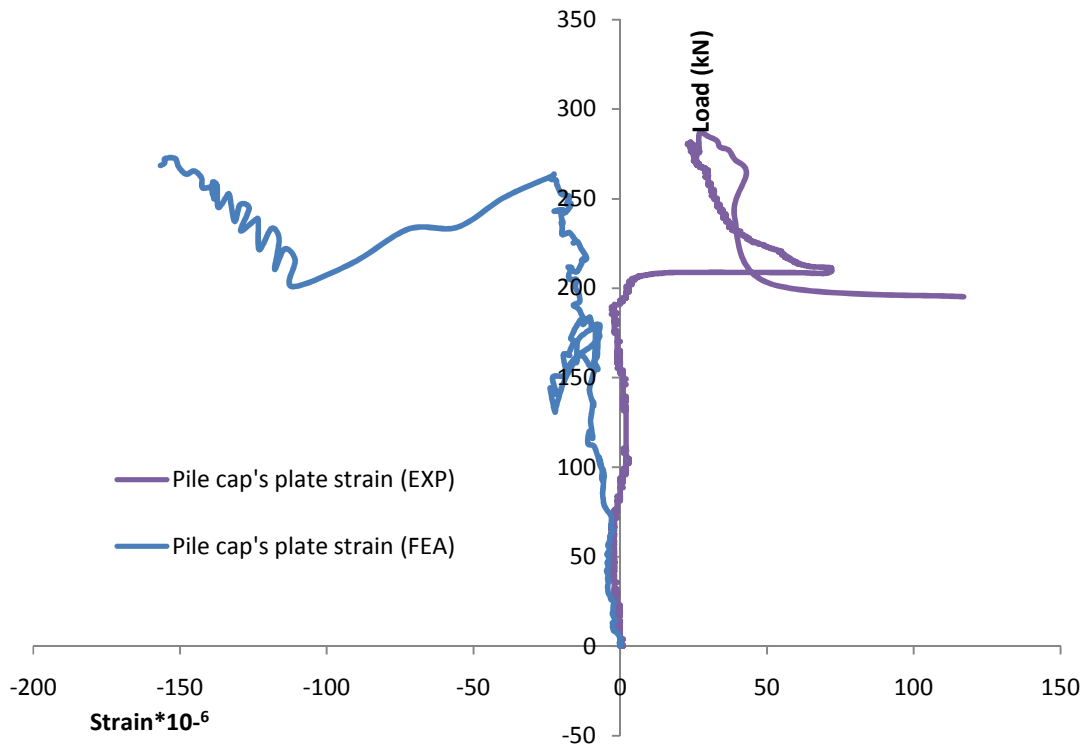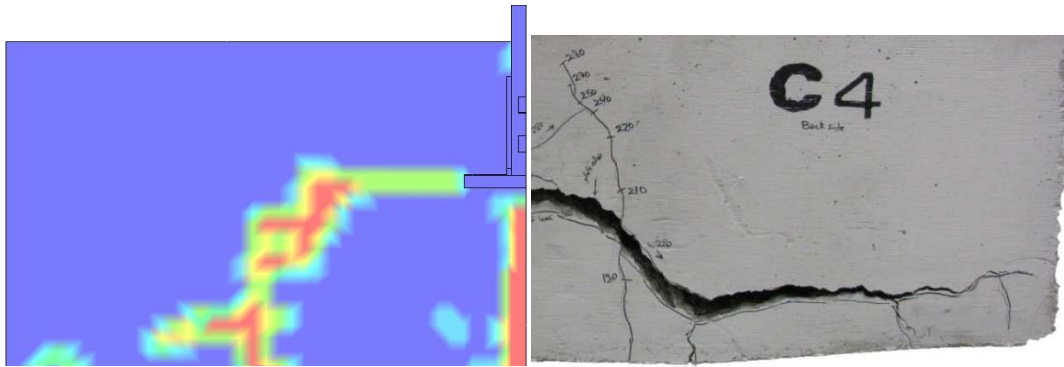**Figure D- 62 Load stirrups strain relationship verification for beam C5**

578

Figure D- 63 Load pile cap's plate strain relationship verification for beam C5

Figure D- 64 Comparison between the crack pattern of the experimental test and analytical model for beam C5
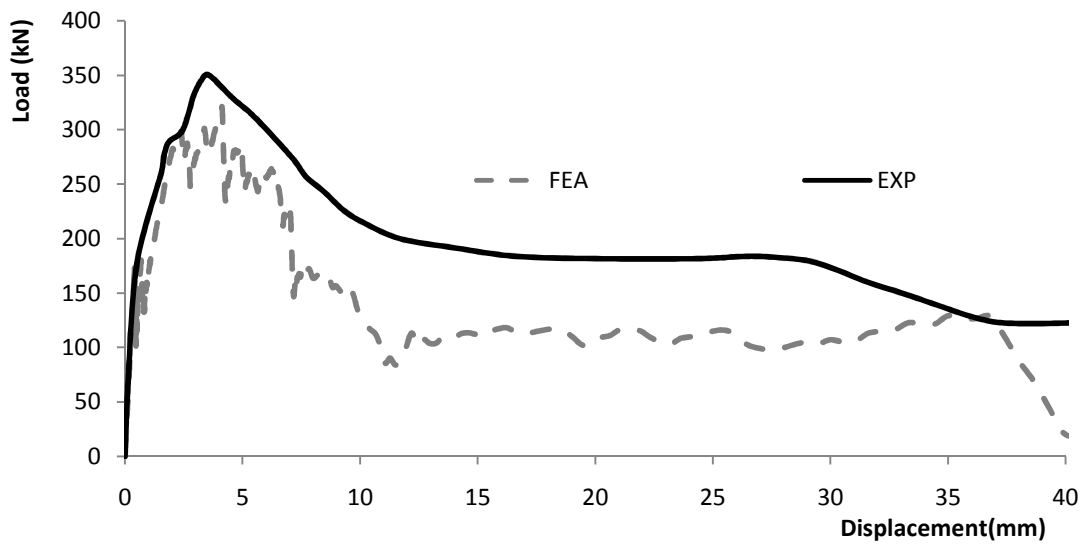
D.2.5 Beam C6

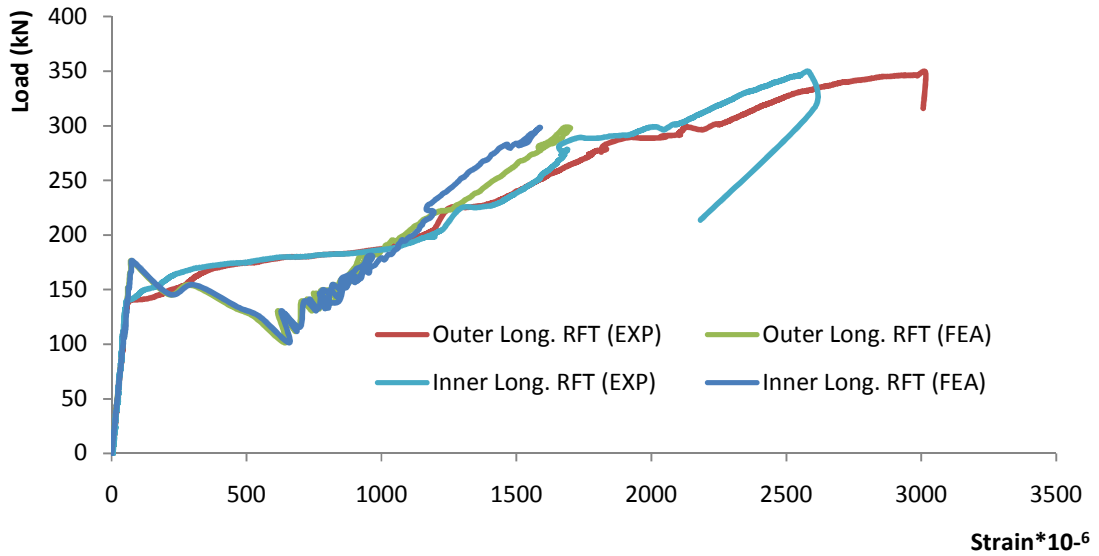**Figure D- 65 Load mid-span displacement relationship verification for beam C6**

Figure D- 66 Load longitudinal reinforcement strain relationship verification for beam C6

Figure D- 67 Load stirrups strain relationship verification for beam C6

Figure D- 68 Load pile cap's plate strain relationship verification for beam C6

Figure D- 69 Comparison between the crack pattern of the experimental test and analytical model for beam C6

D.2.6 Beam C7
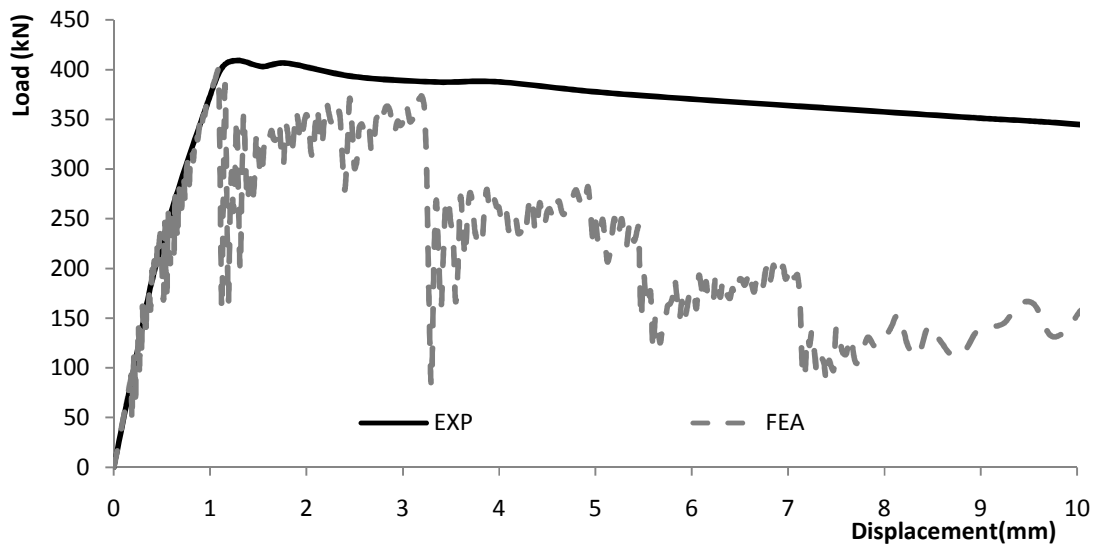
Figure D- 70 Load mid-span displacement relationship verification for beam C7
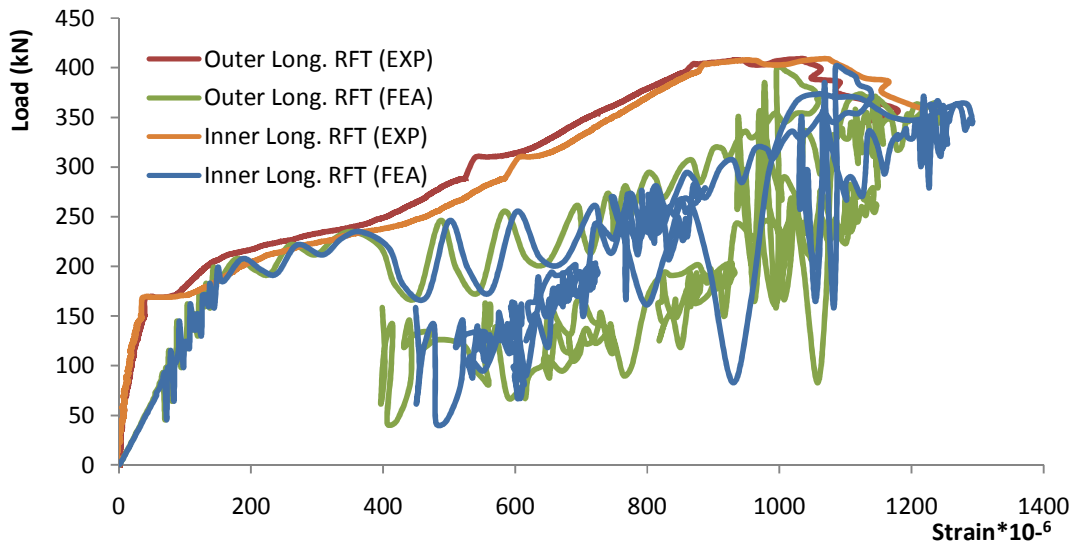
Figure D- 71 Load longitudinal reinforcement strain relationship verification for beam C7
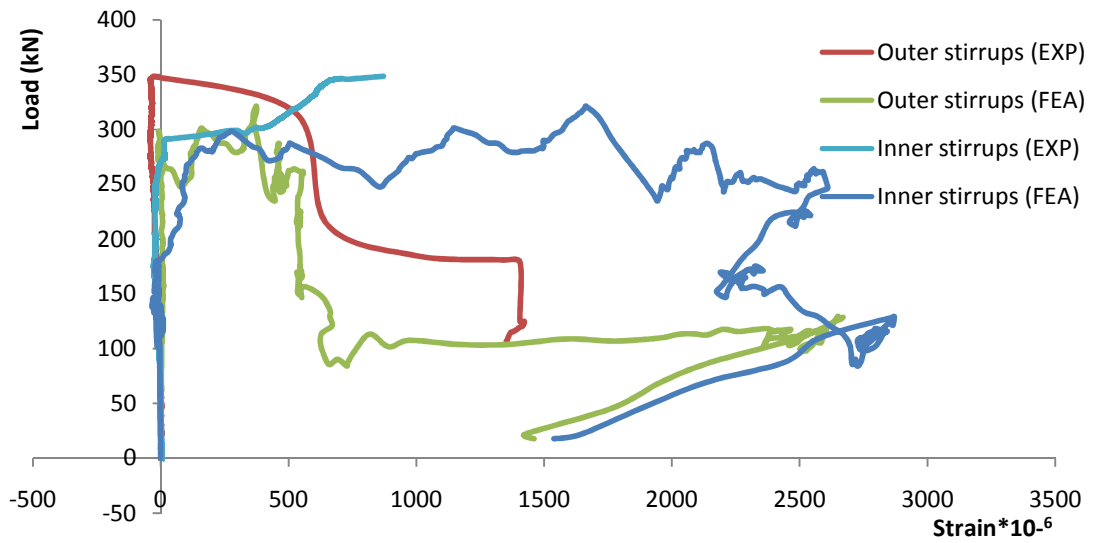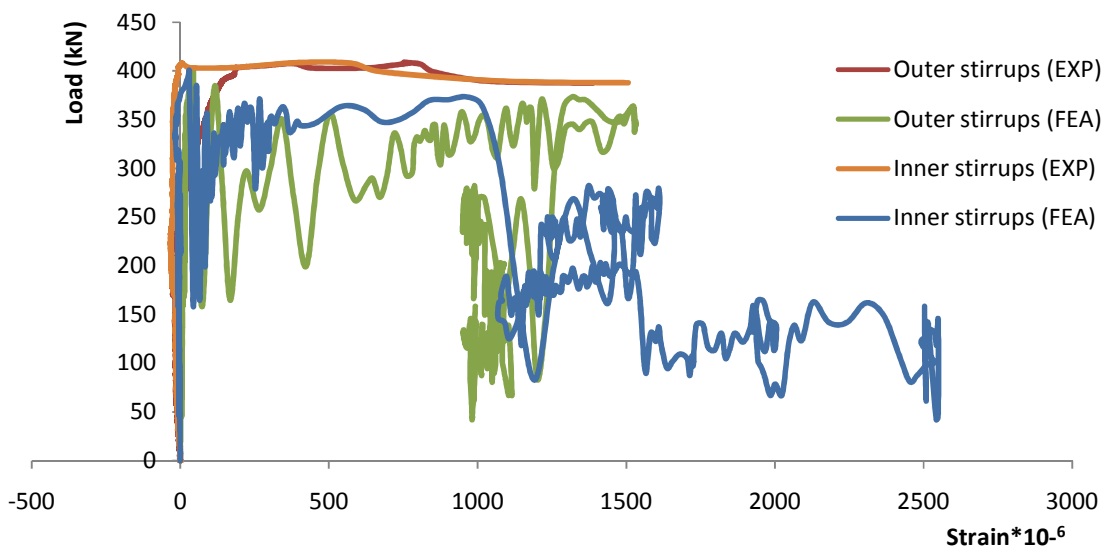

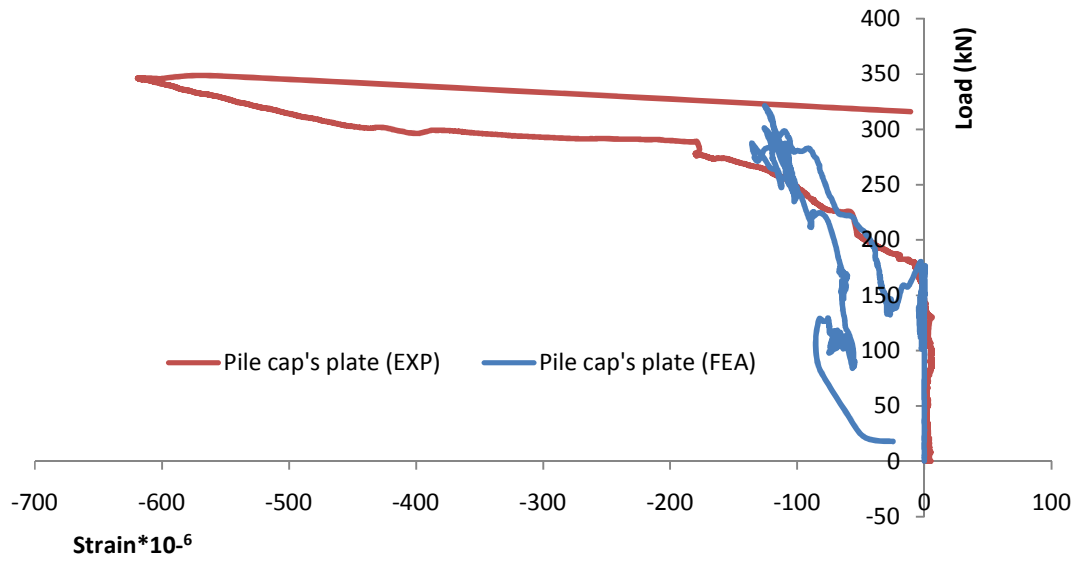**Figure D- 72 Load stirrups strain relationship verification for beam C7**

583

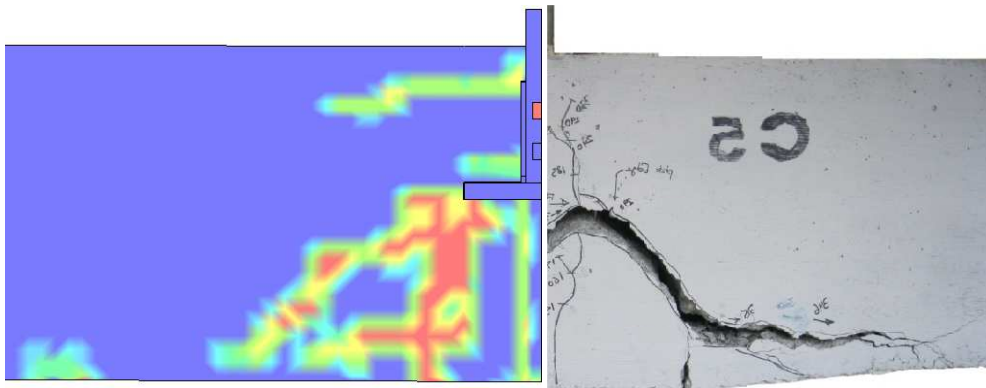**Figure D- 73 Load pile cap's plate strain relationship verification for beam C7**

Figure D- 74 Comparison between the crack pattern of the experimental test and analytical model for beam C7
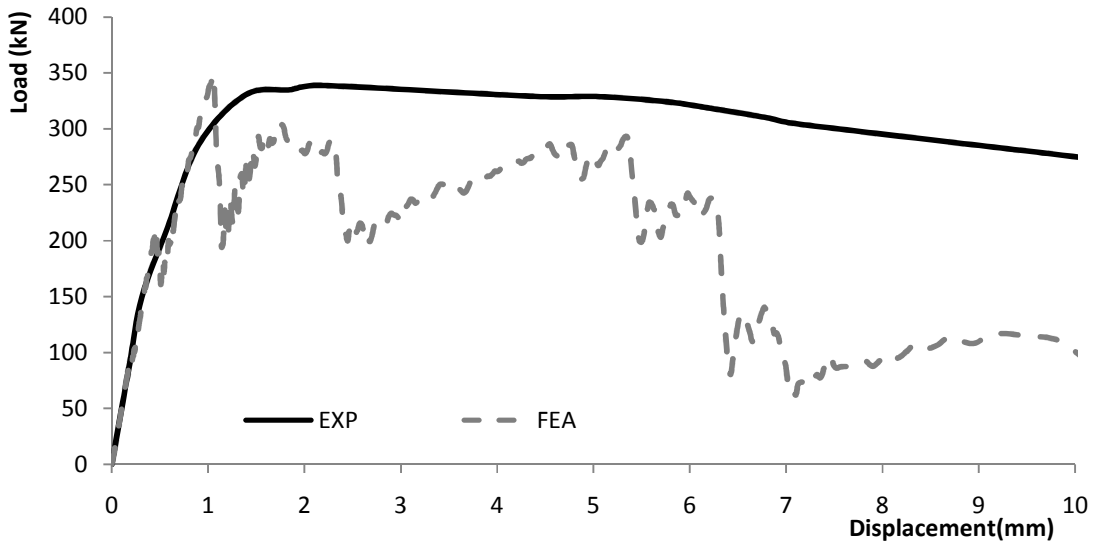
584

D.2.7 Beam C8
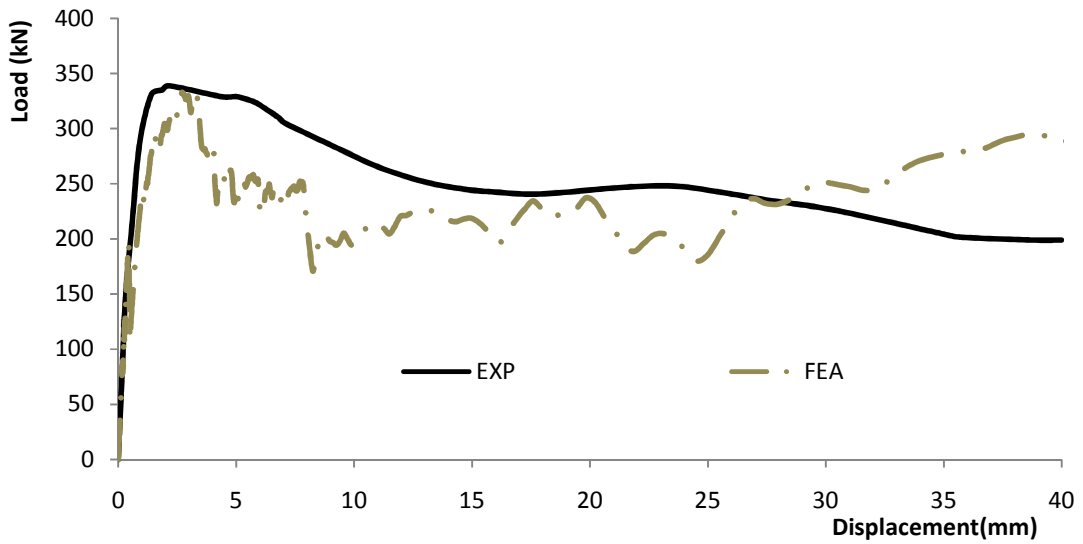
Figure D- 75 Load mid-span displacement relationship verification for beam C8
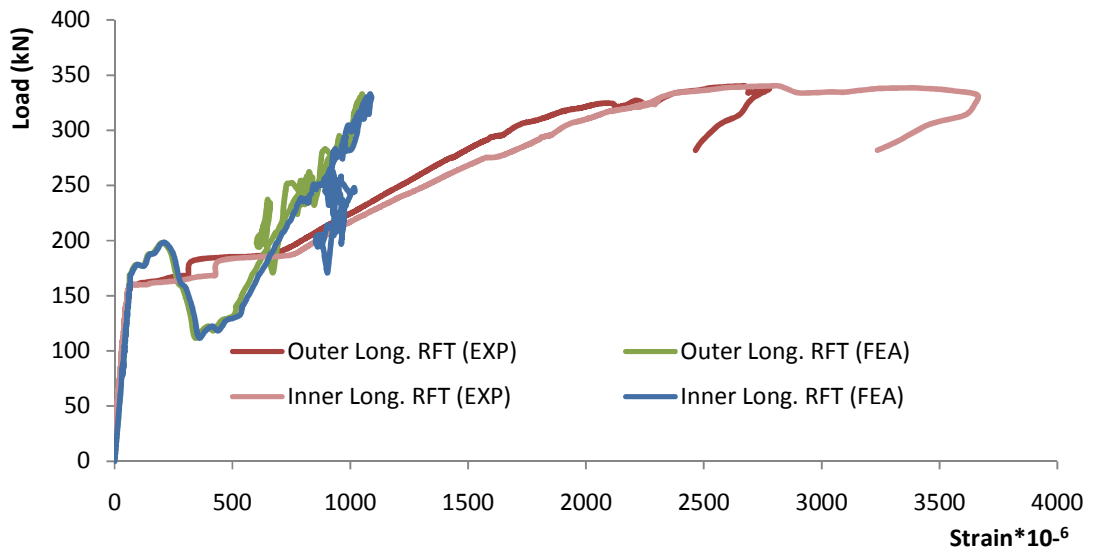
Figure D- 76 Load longitudinal reinforcement strain relationship verification for beam C8
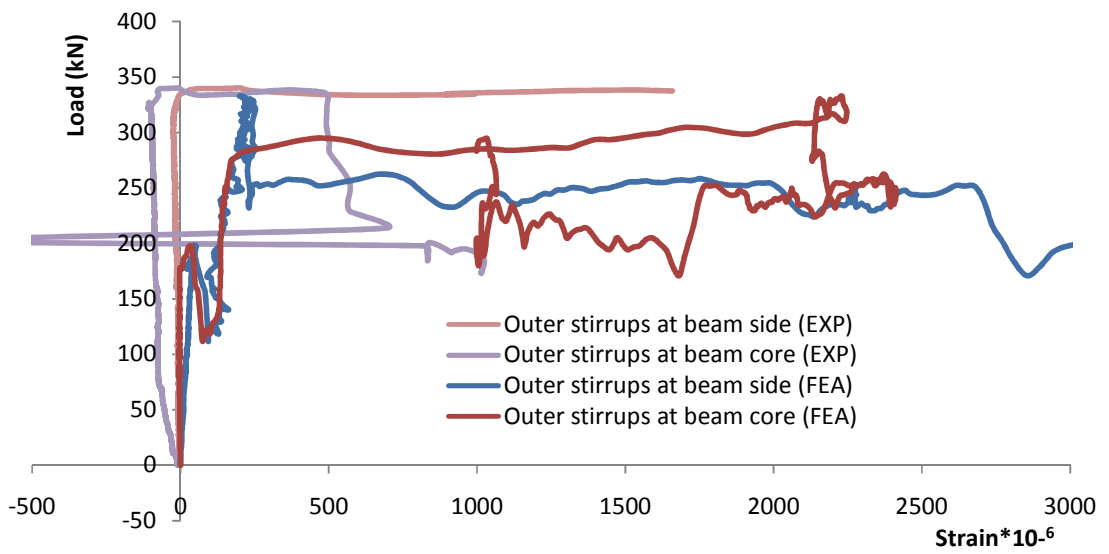
Figure D- 77 Load outer stirrups strain relationship verification for beam C8

Figure D- 78 Load inner stirrups strain relationship verification for beam C8

586

Figure D- 79 Load pile cap's plate strain relationship verification for beam C8
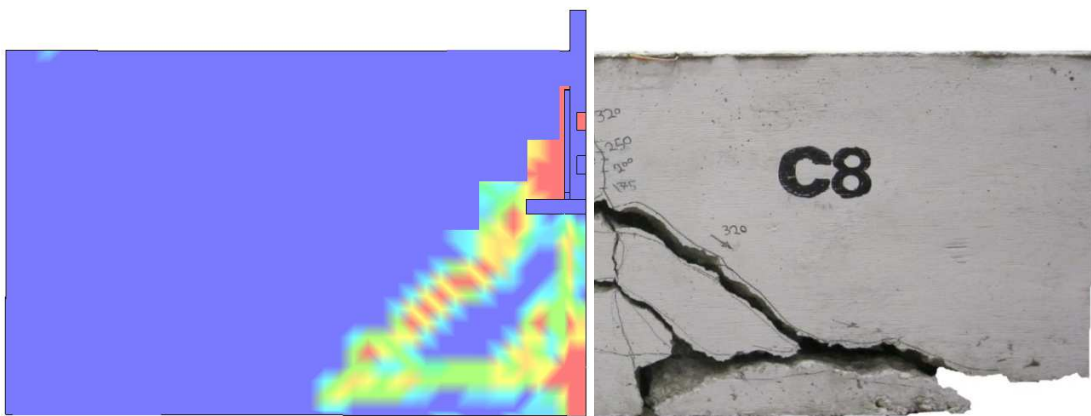
Figure D- 80 Comparison between the crack pattern of the experimental test and analytical model for beam C8

D.2.8 Beam C9
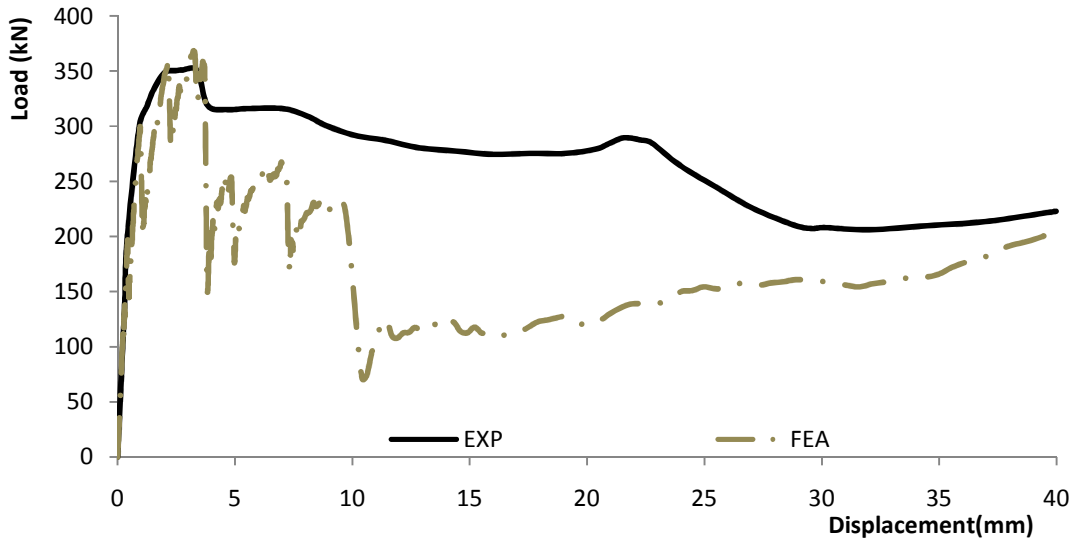
Figure D- 81 Load mid-span displacement relationship verification for beam C9
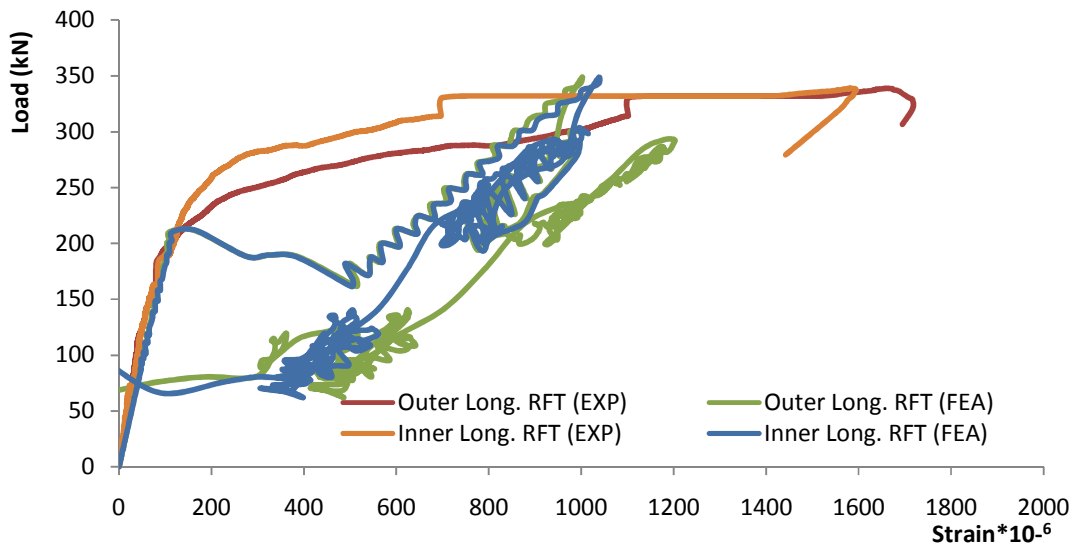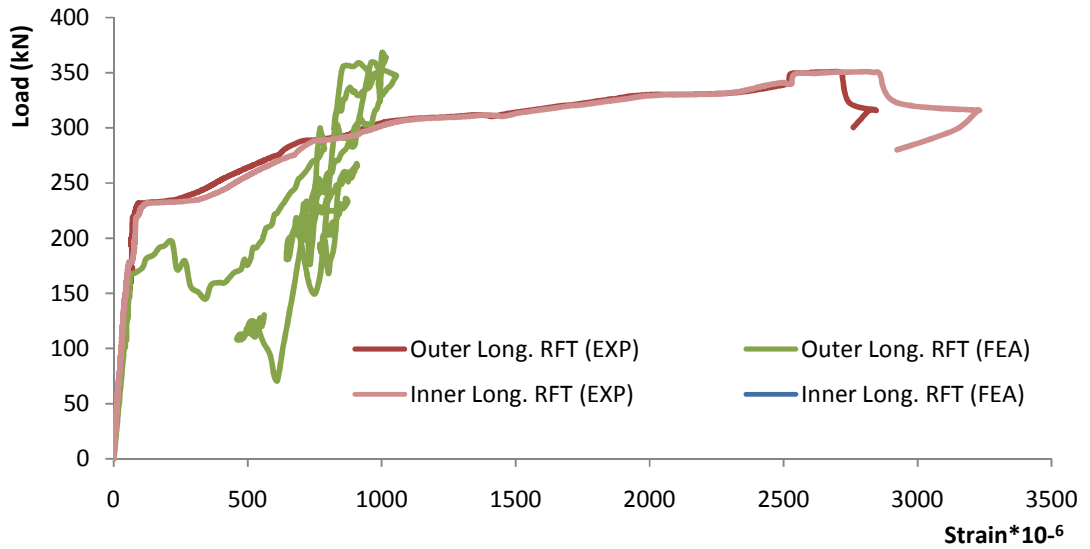

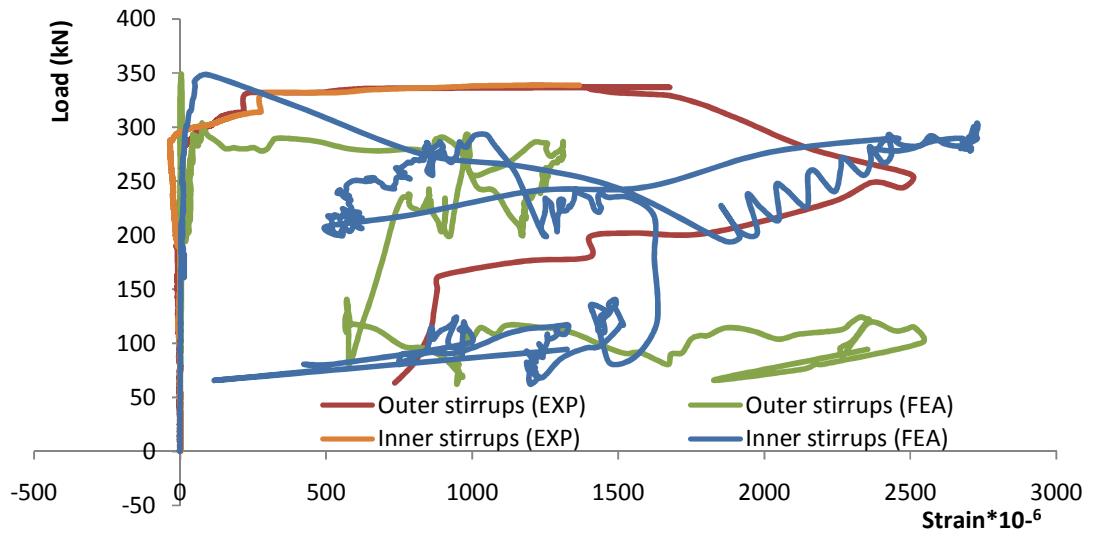**Figure D- 82 Load longitudinal reinforcement strain relationship verification for beam C9**
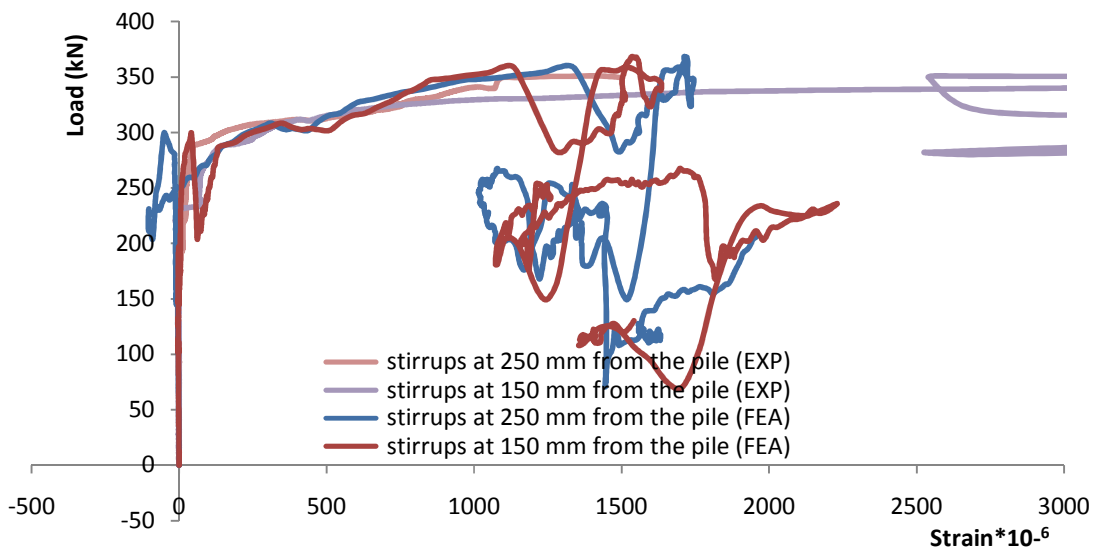
Figure D- 83 Load outer stirrups strain relationship verification for beam C9
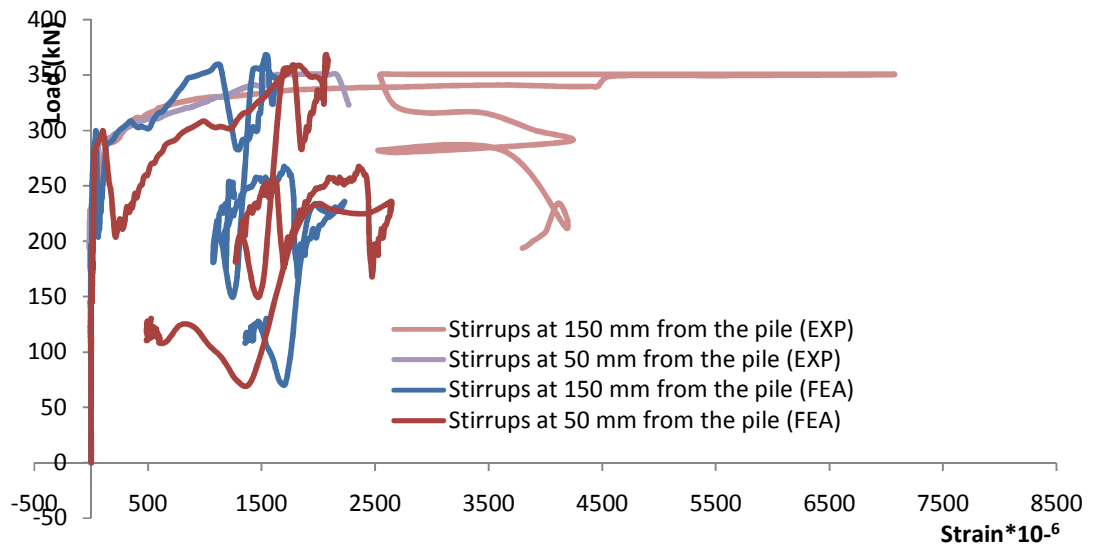
Figure D- 84 Load inner stirrups strain relationship verification for beam C9
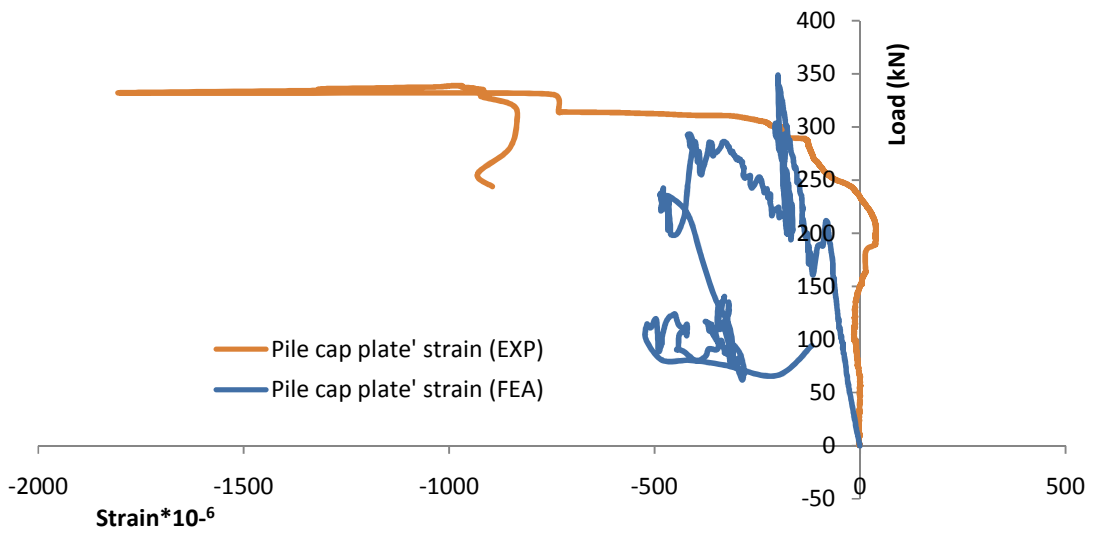
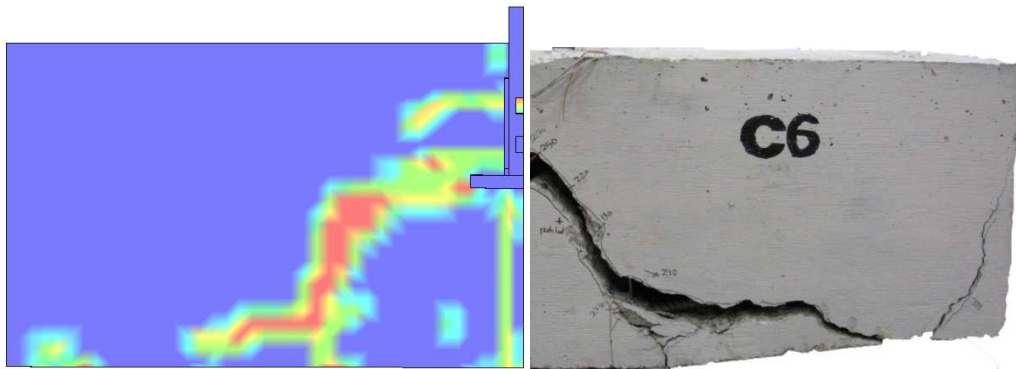**Figure D- 85 Load pile cap's plate strain relationship verification for beam C9**

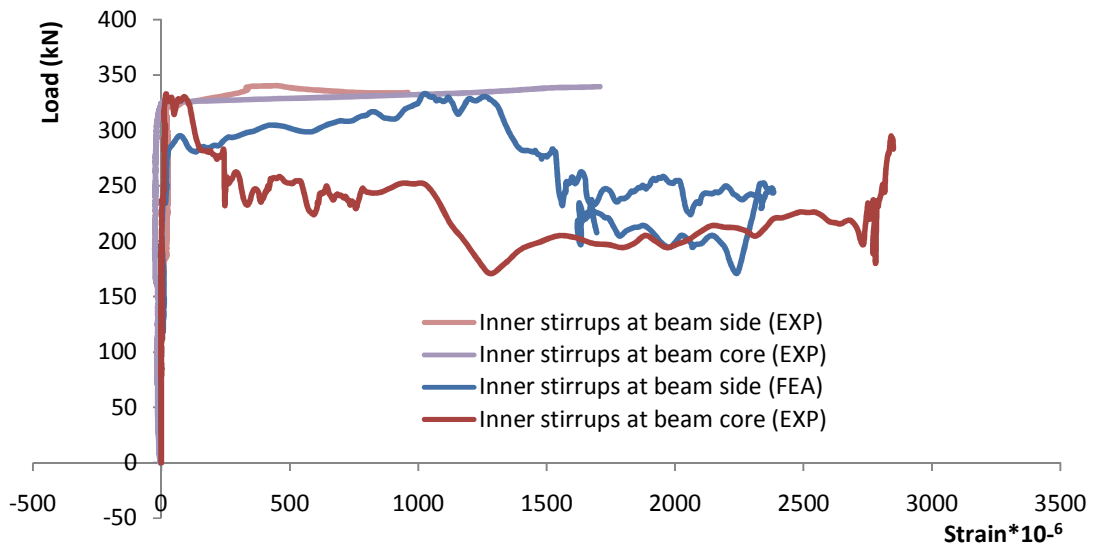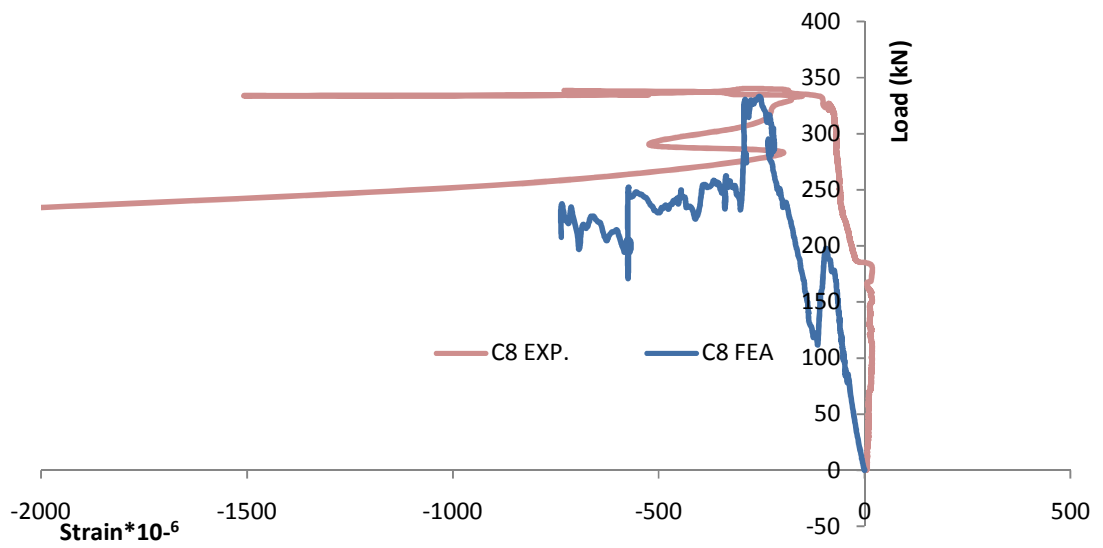**Figure D- 86 Comparison between the crack pattern of the experimental test and analytical model for beam C9**

APPENDIX E

SPECIMENS DATA USED FOR CONNECTION CAPACITY EQUATION GENERATION

In this appendix, the specimens data used in the experimental and analytical studies to develop the connection capacity equations are presented. First, the specimens data used to develop the connection capacity equations under tension loading will be presented in table E-1. Then, the specimens data used to develop the connection capacity equations under compression loading will be listed in table E-2.

Table E- 1 Specimes data used for connection capacity equation generation under tension loading

Specimen ID	B (mm) (width)	d (mm) (depth)	d_{emb} (mm)	fc' (MPa)	$As(mm^2)$ (Steel Area)	Stirrups Configuration	b_{plate} (mm)	$d/a*$	Vcr (kN)	Vu (kN)
T1	500	450	152	30	800	2br#2@200	165	0.853	154	154
T2	500	450	203	30	800	2br#2@200	165	0.853	200	201
F-D-228	500	450	228	30	800	2br#2@200	165	0.853	212.8	229
T3	500	450	254	30	800	2br#2@200	165	0.853	232	232
F-D-280	500	450	280	30	800	2br#2@200	165	0.853	290	290
F-D-305	500	450	305	30	800	2br#2@200	165	0.853	324	324
T-P-100	500	450	203	40	800	2br#2@200	100	0.804	184.5	184.5
T4	500	450	203	40	800	2br#2@200	190	0.874	201.7	201.7
T5	500	450	203	40	800	2br#2@200	229	0.908	239.5	239.5
T-P-305	500	450	203	40	800	2br#2@200	305	0.984	255	255
T-P-380	500	450	203	40	800	2br#2@200	380	1.071	258.6	258.6
T-B-10	500	450	203	40	400	2br#2@200	165	0.853	174	174
T6	500	450	203	40	1200	2br#2@200	165	0.853	222.5	222.5
T7	500	450	203	40	2000	2br#2@200	165	0.853	252.3	252.3
T-B-30	500	450	203	40	2800	2br#2@200	165	0.853	288	288
T-B-35	500	450	203	40	4000	2br#2@200	165	0.853	345	345
T8	500	450	203	40	800	4br#2@200	165	0.853	208.5	256.3
T9	500	450	203	40	800	2br#2@100	165	0.853	208.4	253.2
T-R-2.75 (4-15M)	500	450	203	30	800	2br#2@200	165	0.389	154	154
T-R-1.75 (4-15M)	500	450	203	30	800	2br#2@200	165	0.636	216	216

T-R-1 (4-15M)	500	450	203	30	800	2br#2@200	165	1.224	281	281
T-R-0.5 (4-15M)	500	450	203	30	800	2br#2@200	165	3.158	392	392
T-R-0.25 (4-15M)	500	450	203	30	800	2br#2@200	165	12.000	569	569
T-R-5.5 (4-30M)	500	450	203	30	2800	2br#2@200	165	0.188	175	175
T-R-4 (4-30M)	500	450	203	30	2800	2br#2@200	165	0.262	178	178
T-R-3.5 (4-30M)	500	450	203	30	2800	2br#2@200	165	0.301	192	192
T-R-2.75 (4-30M)	500	450	203	30	2800	2br#2@200	165	0.389	191	191
T-R-2.5(4-30M)	500	450	203	30	2800	2br#2@200	165	0.434	195	195
T-R-2.25 (4-30M)	500	450	203	30	2800	2br#2@200	165	0.480	210	210
T-R-1(4-30M)	500	450	203	30	2800	2br#2@200	165	1.224	386	386
T-R-0.5 (4-30M)	500	450	203	30	2800	2br#2@200	165	2.857	626.4	626.4
T-R-0.25 (4-30M)	500	450	203	30	2800	2br#2@200	165	12.000	644	644
Tension anchor (a/d=1.35)	500	450	203	30	800	2br#2@200	165	0.71	200	174
Tension anchor (a/d=1)	500	450	203	30	800	2br#2@200	165	1.224	242	181
Tension anchor (a/d=0.75)	500	450	203	30	800	2br#2@200	165	1.748	330	196
Tension anchor (a/d=0.5)	500	450	203	30	800	2br#2@200	165	2.857	424	203
Tension anchor (a/d=0.25)	500	450	203	30	800	2br#2@200	165	12	516	217
T2-L-0.75	500	450	203	30	800	2br#2@200	165	0.853 & 1.748	241.64	241.64
T2-L-3.8	500	450	203	30	2800	2br#2@200	165	0.853 & 0.276	210	210
T-A-6	500	450	203	30	800	4anchors-2br#2	165	0.853	204	204.352
T-A-8	500	450	203	30	800	4anchors-2br8$_{mm}$	165	0.853	223	239.8
T-A-10	500	450	203	30	800	4anchors-2br#10M	165	0.853	242	371.424
T-A-15	500	450	203	30	800	4anchors-2br#15M	165	0.853	340	407.68
T-A-20	500	450	203	30	800	4anchors-2br#20M	165	0.853	371.48	371.48
T-A-25	500	450	203	30	800	4anchors-2br#25M	165	0.853	394.24	394.24
2br8@200	500	450	203	30	800	2br8mm@200	165	0.853	200	200
2 br 10@200	500	450	203	30	800	2br10M@200	165	0.853	266	297
2 br 15@200	500	450	203	30	800	2br15M@200	165	0.853	300	428
2 br 8@100	500	450	203	30	800	2br8mm@100	165	0.853	242	300
2 br 10@100	500	450	203	30	800	2br10M@100	165	0.853	286	428
2 br 15@100	500	450	203	30	800	2br15M@100	165	0.853	356	428
4 br 8@200	500	450	203	30	800	4br8mm@200	165	0.853	282	314
4 br 10@200	500	450	203	30	800	4br10M@200	165	0.853	342	428
4-15@200	500	450	203	30	800	4br15M@200	165	0.853	342	428

Table E- 2 Specimes data used for connection capacity equation generation under compression loading

Specimen ID	B (mm) (width)	d (mm) (depth)	d_{bolt} (mm)	fc' (MPa)	As(mm^2) (Steel Area)	Stirrups Configuration	b_{plate} (mm)	d/a*	Rp	Vcr (kN)	Vu (kN)
C1	500	450	392	30	1200	2br#2@200	165	0.71	0.064	400	415.0
C2	500	450	339	30	800	2br#2@200	165	0.71	0.064	295	314.0
C3	500	450	289	30	800	2br#2@200	165	0.71	0.064	250	268.0
C4	500	450	339	30	800	2br#2@200	190	0.72	0.063	280	287.0
C5	500	450	339	30	800	2br#2@200	229	0.74	0.061	289	348.5
C6	500	450	339	30	1200	2br#2@200	165	0.71	0.064	330	339.0
C7	500	450	339	30	2000	2br#2@200	165	0.71	0.064	400	409.3
C8	500	450	339	30	800	4br#2@200	165	0.71	0.064	320	340.0
C9	500	450	339	30	800	2br#2@100	165	0.71	0.064	315	350.9
C-B-10	500	450	339	30	400	2br#2@200	165	0.71	0.064	234	234.0
C-B-7	500	450	339	30	1548	2br#2@200	165	0.71	0.064	360	360.0
C-B-35	500	450	339	30	4000	2br#2@200	165	0.71	0.064	445	445.0
C-B-15	500	450	339	30	800	2br#2@200	165	0.43	0.104	216	219.0
C-B-20R	500	450	339	30	1200	2br#2@200	165	0.43	0.104	287	287.0
C-B-25R	500	450	339	30	2000	2br#2@200	165	0.43	0.104	349	349.0
C2-20	500	450	339	20	800	2br#2@200	166	0.71	0.064	240	245.0
C2-35	500	450	339	35	800	2br#2@200	167	0.71	0.064	338	338.0
C2-40	500	450	339	30	800	2br#2@200	168	0.71	0.064	351	351.0
C2-W	500	450	277	30	800	2br#2@200	165	0.71	0.064	226	233.0
C2-TWO BOLTS	500	450	405	30	800	2br#2@200	165	0.71	0.064	305	327.0
C1-TWO BOLTS	500	450	458	30	800	2br#2@200	165	0.71	0.064	451	451.0
C9-2 BOLTS	500	450	405	30	800	2br#2@100	165	0.71	0.064	353	455.0
C-A-6	500	450	339	30	800	4anchors-2br#2	165	0.71	0.064	294	300
C-A-8	500	450	339	30	800	4anchors-2br8$_{mm}$	165	0.71	0.064	319	360
C-A-10	500	450	339	30	800	4anchors-2br#10M	165	0.71	0.064	330	458
C-A-20	500	450	339	30	800	4anchors-2br#20M	165	0.71	0.064	341	454
C-A-25	500	450	339	30	800	4anchors-2br#25M	165	0.71	0.064	357	476
2-8-200	500	450	339	30	800	2br8mm@200	165	0.71	0.064	295	298
2-10-200	500	450	339	30	800	2br10M@200	165	0.71	0.064	295	342
2-15-200	500	450	339	30	800	2br15M@200	165	0.71	0.064	295	382
2-8-100	500	450	339	30	800	2br8mm@100	165	0.71	0.064	303	405

593

2-10-100	*500*	*450*	*339*	*30*	*800*	*2br10M@100*	*165*	0.71	0.064	304	429
2-15-100	*500*	*450*	*339*	*30*	*800*	*2br15M@100*	*165*	0.71	0.064	341	586
4-8-200	500	450	339	30	800	*4br8mm@200*	165	0.71	0.064	303	405
4-10-200	500	450	339	30	800	*4br10M@200*	165	0.71	0.064	328	518
4-15-200	500	450	339	30	800	*4br15M@200*	165	0.71	0.064	362	694
2-8-200 (4-25M)	500	450	339	30	2000	*2br8mm@200*	165	0.43	0.104	303	298
2-10-200 (4-25M)	500	450	339	30	2000	*2br10M@200*	165	0.43	0.104	317	342
2-15-200 (4-25M)	500	450	339	30	2000	*2br15M@200*	165	0.43	0.104	323	382
C-R-2.75 (4-20M)	500	450	339	27.5	1200	*2br#2@200*	165	0.39	0.115	*260*	*277.0*
C-R-2.50 (4-20M)	500	450	339	27.5	1200	*2br#2@200*	165	0.43	0.104	*287*	*287.0*
C-R-2.00 (4-20M)	500	450	339	27.5	1200	*2br#2@200*	165	0.55	0.082	*305*	*305.0*
C-R-1.75 (4-20M)	500	450	339	27.5	1200	*2br#2@200*	165	0.64	0.071	*301*	*301.0*
C-R-1 (4-20M)	500	450	339	27.5	1200	*2br#2@200*	165	1.22	0.037	*379*	*379.0*
C-R-0.5 (4-20M)	500	450	339	27.5	1200	*2br#2@200*	165	3.16	0.014	*775*	*793.0*
C-R-0.25 (4-20M)	500	450	339	27.5	1200	*2br#2@200*	165	15.00	0.003	*850*	*956.0*
C-R-5.5 (4-30M)	500	450	339	27.5	2800	*2br#2@200*	165	0.19	0.200	*231*	*423.8*
C-R-5 (4-30M)	500	450	339	27.5	2800	*2br#2@200*	165	0.21	0.200	*277*	*449.7*
C-R-4 (4-30M)	500	450	339	27.5	2800	*2br#2@200*	165	0.26	0.172	*269*	*437.5*
C-R-3.5 (4-30M)	500	450	339	27.5	2800	*2br#2@200*	165	0.30	0.150	*280*	*396.4*
C-R-2.75 (4-30M)	500	450	339	27.5	2800	*2br#2@200*	165	0.39	0.116	*313*	*350.0*
C-R-2.25 (4-30M)	500	450	339	27.5	2800	*2br#2@200*	165	0.48	0.094	*362*	*369.2*
C-R-2.0 (4-30M)	500	450	339	27.5	2800	*2br#2@200*	165	0.55	0.082	*396*	*396.2*
C-R-1.75(4-30M)	500	450	339	27.5	2800	*2br#2@200*	165	0.64	0.071	*418*	*418.5*
C-R-1(4-30M)	500	450	339	27.5	2800	*2br#2@200*	165	1.22	0.037	*443*	*604.2*
C-R-0.75(4-30M)	500	450	339	27.5	2800	*2br#2@200*	165	1.76	0.026	*785*	*785.0*
C-R-0.5 (4-30M)	500	450	339	27.5	2800	*2br#2@200*	165	2.86	0.016	*853*	*852.7*

<div align="center">

CURRICULUM VITAE

Muhammad Ahmad Muhammad Diab

</div>

EDUCATION

Ph.D. in Engineering, Civil and Environmental Engineering   **2009-present**

University of Western Ontario, London, Ontario

Academic Average 99.25 %

M.Sc. of Civil Engineering, Structural Engineering   **2005-2009**

Alexandria University, Alexandria; Egypt

Academic Average 99%

Bachelor of Engineering, Civil Engineering   **1998- 2005**

Alexandria University, Alexandria; Egypt

Distinction with Honor (94.08 % - 1st out of 763 Successful students)

Relevant Graduate courses

University of Western Ontario: **2009-2014**

Advanced Design and Behaviour of Concrete, Prestressed Concrete, Finite

Element Analysis for Solids, Seismic Design and Analysis of Buildings,

Geotechnical Earthquake Engineering, and Dynamics of Soil and Foundations

Alexandria University: **2005-2009**

Limit State Design of Reinforced Concrete Structures, Prestressed Concrete,

Mechanics of Concrete Structures, Tall Concrete Buildings, Computer Analysis

of Structures, and Finite Element Method

PROFFESIONAL EXPERIENCE

Structural Designer (Full-Time)   **2015-present**

RIZZ Engineering Inc., Waterloo, ON, Canada

Carried out structural analysis and design for precast concrete buildings

Structural Designer (Full-Time)   **2014-2015**

ASP Design Group Inc. , Waterloo, ON, Canada

Carried out structural analysis and design of various reinforced concrete,

precast/ prestressed concrete, wood, Aluminum, structural glass, light

weight steel, and ordinary steel structures including their foundation design

Structural Designer (Part-Time)   **2010-2013**

EBS Geostructural, Breslau, ON, Canada

(under supervision of M. Hesham El Naggar, , Western University)

Worked with EBS to advance their helical pile foundation system

Teaching Assistant   **2009-2014**

University of Western Ontario

- Finite Element Methods in Engineering
- Structural Design III
- Concrete Design
- Mechanics of Materials
- Natural Disasters: Mitigation, Modeling and Assessment
- Engineering Statics

Structural Engineer (Full-Time)   **2005-2009**

DIAB Consulting Engineering office, Alexandria, Egypt

Carried out structural analysis and design of various concrete and steel

structures (e.g. bridges, high rise and ordinary buildings, water tanks, etc.)

including their foundation design and off shoring system.

Teaching Assistant   **2005-2009**

Alexandria University

- Concrete Structures, Bridges and Tanks-1
- Concrete Structures, Bridges and Tanks-2
- Prestressed Concrete Design and Design of Concrete Bridges
- Reinforced Concrete-1
- Reinforced Concrete-2
- Structural Engineering-3
- Design of Industrial Structures and High Buildings

AWARDS, AND HONOURS

Won the PSAC 610 Scholarship for Community Involvement, UWO, London, Canada, April 2013. **2013**

First place in the international zone award of "The Big Beam Competition 2012" sponsored by the Precast/Prestressed Concrete Institute (PCI), Western University (UWO), London, ON, Canada. **2012**

First Place of the Best Video in USA and Canada award of "The Big Beam Competition 2012" sponsored by the Precast/Prestressed Concrete Institute (PCI), UWO, London, ON, Canada. **2012**

"NSERC Industrial Postgraduate Scholarship (IPS2)", UWO, EBS Engineering and Construction Limited, September 1st 2010- August 31st 2013. **2010**

"Western Graduate Research Scholarship (WGRS)", UWO, Civil and Environmental Engineering, September 1st 2009- August 31st 2013. **2009**

Received the "First Place Academic Award in Alexandria University" Award from the President of Egypt at the National Science Festival in 2005, Cairo, Egypt. **2005**

PUBLICATIONS

Tarabia, A.M., Shoukry, M.S. & Diab, M.A., 2010. Improving the behavior of reinforced concrete beams with lap splice reinforcement. *Challenges, Opportunities and Solutions in Structural Engineering and Construction*, pp.81–86.